Hierarchical and Cellular Structures in Cosmology

Brian Geoffrey Williams

Ph.D. Thesis

University of Edinburgh

1992

This thesis is entirely my own composition with the exception of § 2.2 and Chapter 3, which are largely unaltered parts of the text of the paper "Exact hierarchical clustering in one dimension", by Williams, Heavens, Peacock & Shandarin (1990), which appeared in *Monthly Notices of the Royal Astronomical Society*, **250**, 458. Preliminary results of the work presented in Chapter 5 were published as "Large-scale periodicity: problems for cellular models" by Williams, Peacock & Heavens (1991), which appeared in *Monthly Notices of the Royal Astronomical Society*, **252**, 43.

(March 1992)

Abstract

Though great advances have been made in the field of cosmology by using numerical n-body techniques to investigate large-scale structure formation, these have been hampered by limited dynamic range. Thus there still remains considerable motivation for finding simple methods that link either the final structure or its statistical properties (such as mass and correlation functions) to the initial conditions. This thesis investigates two such approaches — linear theory and the Voronoi foam.

(i) Linear Theory

This is based on the principle of smoothing the non-linear density field in order to recover the underlying linear density field. Bound objects are then identified with regions where the density exceeds some critical value. Such a prescription allows the statistical properties of the bound objects to be described as a function of the power spectrum of the initial density field and the smoothing function.

This thesis checks the accuracy of such models against the adhesion model, a fully non-linear description of gravitational clustering. In order to provide an accurate test of the linear theory predictions, the simulations are carried out in one dimension, where the adhesion model is *exact* and there is sufficient dynamic range to allow a thorough test of the linear theory predictions.

It is found that despite some of the underlying assumptions of linear theory being incorrect in detail, the linear theory mass functions provide an excellent match to those calculated from the simulations. Linear theory correlation functions are also shown to be a good match to those from the simulations, but only in the case where dynamical evolution of the density field is unimportant (i.e. where large-scale power dominates over small-scale power).

(ii) Voronoi foam

This is a simple model where space is divided into cells, each containing a nucleus, with galaxies populating the boundaries between cells, which are equidistant between neighbouring nuclei. The geometric structure of the cells is entirely determined by the

distribution of the nuclei. This forms a continuous network of walls, filaments and nodes, qualitatively similar to that observed.

It is shown that, in comparison to a wide range of statistical measures of galaxy clustering, the Voronoi foam lacks sufficient large-scale power to account for the observed galaxy distribution, if the nuclei are distributed at random. However, if the nuclei are identified with the peaks in a gravitational potential (which are intrinsically clustered), the Voronoi foam can provide an excellent description of the large-scale clustering of galaxies. It is also demonstrated that the Voronoi foam provides, within the context of a cellular model, a natural explanation for the observed phenomenon of large-scale cluster alignment.

Acknowledgments

This thesis is dedicated to my parents and my friends, of whom I am fortunate to have many (friends that is, not parents). I can't say I had a particularly easy or enjoyable time for my first two years in Edinburgh and I'd like to say thank you to everyone who took the time to lend me a helping hand during the bad times.

Academically, I would like to thank my supervisors, John Peacock and Alan Heavens, for their support, help and belief in me over these $3\frac{1}{2}$ years. Thanks also go to Sergei Shandarin for introducing me to the adhesion model and thus the first half of my thesis. Bob Mann and Phil James deserve a big mention for actually *volunteering* to read my thesis and for their many helpful comments. Others deserving of a mention include Lev Kofman, Peter Coles, Tom Shanks, Mike West and Luigi Guzzo, all of whom showed an interest at one time or other and helped make it seem all worthwhile.

On the non-academic front, I owe a great debt to all my friends, especially the York crew and, more recently, the late-nite crew. Special thanks go Vanessa, despite everything, Richard (Worth) for patient support, Suzanne and Jackie-Ann for keeping me sane during my first summer in Pollock, Emma and especially John for keeping me sane in my second year, Kevin for endless support both in person and by e-mail, Aaron, for similar reasons, Jon, for listening, Rachel, for the phone calls, McB., the RPGers, Bobby, Steve, Tim and Joe, and finally (because he's the biggest) Captain Andrew.

Within the ROE, my thanks go to Quentin and also to Phil James for generally brightening the place up, Claire and Chris Collins for noticing and taking the time to say so, Kathy for being daft enough to share an office with, Amadeu for being even dafter to live with me for a year and the late-nite crew — Dave for being Dave, even if there are so few of us who appreciate that, Philbo, Rijdat (and the ever-present Albert) and Penny for putting up with my less than cheerful moments.

I owe a great debt to John Barrow for keeping the computer running so smoothly despite my best efforts to the contrary and also Donald Knuth for writing TEX. Whether he made my life any easier or not, I'm not sure, but thanks anyway. I'm also grateful to Kevin for the 192^3 FFTs. Please note (Alan and Phil) that I intend to deliberately split my infinitives where ever I see fit and finally, a big hand for Lemmy and the boys of MOTÖRHEAD for motivation, company at 2am and hours of loud, loud music.

Table of Contents

Chapter 1

Introduction

1.1 World Models

1.1.1 Introduction

It is quite surprising to consider how far mankind has come in understanding the universe that lies around us. It was only 70 years ago that the nature of the "nebulæ" that we now know to be galaxies external to our own was under vigorous debate. Some held that the nebulæ were merely outlying parts of our own Galaxy. It was not until 1923, when Hubble observed Cepheid variables in the spiral galaxies M31 and M33 and later, in 1925, when he carried out similar observations on the irregular galaxy NGC 6822, that these objects were conclusively shown to be extragalactic in nature.

Hubble (1929) was also responsible for the discovery that the universe is expanding, by showing that galaxies are receding from our own and that the speed of recession is proportional to their distance from us ("Hubble's Law"). This observation was given a firm theoretical footing by Einstein's general theory of relativity and specifically by the work of Friedmann (1922) and Lemaître (1927), which laid down the framework for an expanding universe.

From these early beginnings the field of cosmology has flourished, so much so that less than 70 years after Hubble's discovery of the extragalactic nature of the nebulæ and the expansion of the universe, we now think we understand the global evolution of the universe from the first few hundredths of a second to the present day. We have mapped a good proportion of our local universe and can probe back to the state of the universe when it was less than a million years old through the microwave background radiation.

The work presented in this thesis is an attempt to use simple models to investigate the large-scale distribution of matter in the universe. Though great steps have been made through the use of numerical simulations, which attempt to model the underlying

physics, there is still a place for simple models which can cover a wide range of parameter space (§ 2.1). Three specific models are used — the linear theory approximation, based on the principle of smoothing the non-linear density field to identify bound objects (§ 3.2), the adhesion model, based on Burgers' equation which is a fully non-linear description of gravitational clustering (§ 2.2) and which is used to check the validity of the mass functions in one dimension (Chapter 3), and the Voronoi foam, a simple prescription for the distribution of galaxies confined to thin surfaces surrounding voids (§ 2.3). A large part of this thesis is taken up with an investigation of the Voronoi foam model (Chapters 4 – 7), to see whether such a simple cellular model can account for the complex large-scale distribution of galaxies.

The rest of this introduction is concerned with an overview of present-day cosmology. § 1.1 deals with world models, especially the standard model, the hot Big Bang. § 1.2 discusses the density of the universe and the Hubble constant, the basic physical parameters that govern the expansion of the universe. § 1.3 investigates the origins of the primordial fluctuations that evolved into the present-day large-scale structure, while § 1.4 covers the discovery that we inhabit a universe that is cellular on scales of $20 - 60\,h^{-1}\,\mathrm{Mpc}$, as well as describing our local environment in terms of this cellular picture. § 1.5 is an overview of the remainder of the thesis.

1.1.2 The Cosmological Principle

Underpinning the whole of modern cosmological thinking are two central hypotheses — isotropy and homogeneity — both embodied in the *cosmological principle.* The cosmological principle is based upon the Copernican principle in that it *assumes* that mankind is not a privileged observer, that is, the assumption is made that there is nothing unique or special about our position in the universe. Were the universe observed from any other point in space then its global (i.e. large-scale) properties would be the same.

The cosmological principle also includes the idea of isotropy, that is, there is no preferred direction in space. Thus, wherever one looks, the properties of the universe are the same. Coupled with the Copernican principle, this gives the idea of isotropy — the properties of the universe are the same regardless of the position of the observer and the direction of observation. This implies homogeneity, the other central tenet of the

cosmological principle. Obviously our experience tells us that isotropy and homogeneity are not obeyed on local scales, or even on scales the size of our Galaxy. However, it is assumed that when averaged on very large scales the universe is isotropic and homogeneous. This assumption is considered in more detail in § 1.4.

As well as applying to the distribution of matter, the dual constraints of isotropy and homogeneity also apply to all other physical properties such as temperature and velocity. The latter implies that the velocity field of the universe can only be one of uniform expansion or contraction. Any shear or rotational component would violate the condition of isotropy. Note that Hubble's law of recession velocity being proportional to the distance is the simplest such recession/distance relation that one would expect in a homogeneous, expanding universe.

1.1.3 Steady State versus Big Bang

An extension of the cosmological principle, known as the perfect cosmological principle, includes the idea of temporal as well as spatial homogeneity. Here, the universe is assumed to be such that its global properties are time invariant, that is, all observations reveal the same global properties regardless of epoch. This gave rise to the "Steady State" model of the universe, proposed independently in the late 1940s by Bondi & Gold (1948) and Hoyle (1948, 1949). The basic assumption of such a model is that although the universe is constantly expanding, matter is being produced throughout space in order to maintain a constant density. Under such a model, galaxy formation is a continuous process and hence the global properties of galaxies should show no evolution with time.

The alternative view is that of the "hot Big Bang" model, so named for its predicted beginning of the universe. If space-time is expanding then logically an extrapolation back in time will result in a time when space-time will be infinitely dense and infinitely hot, hence the hot Big Bang. The major consequence of such a model is that there is an evolution in time with global properties of the universe, i.e. the perfect cosmological principle does not hold.

The two conflicting world models can be distinguished between by observations using their predictions of the evolution of the universe. Because light has a finite velocity,

looking at distant objects means looking back in time. If, at cosmological distances, redshift is linked to distance by the Hubble expansion (a matter of debate for some – e.g. Field, Arp & Bahcall 1973; Arp 1989), then objects at high redshift are also young objects. By comparing the basic properties of these objects, such as space density (corrected for the effects of expansion), one can distinguish between the two models. If a given class of objects show an evolution of properties with distance (and hence time) then this supports the hot Big Bang over the Steady State theory. Indeed, this proved to be the case, with both radio galaxies and quasars showing convincing evidence of increasing comoving number density with look-back time (Schmidt 1972, 1978; Longair 1974, 1978).

The other evidence against the Steady State theory was the discovery in 1965 of the microwave background radiation by Penzias & Wilson. This is an isotropic bath of blackbody radiation at $\sim 2.7\,\mathrm{K}$, a feature that could not be explained by the Steady State theory, but which naturally arose in the hot Big Bang model (§ 1.1.4).

1.1.4 The Hot Big Bang

Only the basics of the hot Big Bang model will be outlined here. For a more comprehensive treatment, the reader is referred to the excellent review given by Weinberg (1983).

The "Big Bang" is somewhat a misnomer as it implies some sort of "explosion". The hot Big Bang model actually makes no such assumptions as to the origin of the universe or of the initial expansion which are left as initial conditions. The model starts by assuming that the universe consists of a hot, dense soup of matter and radiation in a state of expansion. Initially, in the first few fractions of a second, the universe is assumed to have been hot enough to allow the spontaneous creation of particle-antiparticle pairs of fundamental particles.

At very early times, with temperatures $\gtrsim 10^{12}\,\mathrm{K}$, the universe contained roughly equal numbers of photons and various elementary particles — the leptons (electrons, muons, etc and their respective neutrinos) and hadrons (protons, neutrons, etc.) — and their antiparticles, which were constantly being produced and annihilated, and were in constant collision, thus maintaining a state of thermal equilibrium. As the

universe cooled, so the temperature dropped below the various thresholds necessary to produce the heavier particles and their antiparticles (i.e. hadrons), which then annihilated. However, the numbers of particles and antiparticles should be equal if the condition of thermal equilibrium was met, and so after annihilation, there should be *no* particles left. However, this is obviously not the case. Furthermore, we live in a matter dominated universe, rather than a matter/antimatter universe, suggesting that there was a global matter/antimatter imbalance in the early universe. The present day baryon-to-photon ratio gives some idea of the magnitude of the asymmetry. Given that the very early universe was expected to be in thermal equilibrium, then for every baryon, one would expect roughly one photon. However, the present day ratio is one baryon for every $\sim 10^9$ photons, though this figure is uncertain by up to an order of magnitude either way due to the uncertainty in the present baryon number density (§ 1.2.4). This suggests a similar fractional excess of protons over antiprotons which has to be built into the standard Big Bang model as an initial condition.

Calculations for these very early times are extremely complicated due to interactions between hadrons (and antihadrons) caused by the strong nuclear force. It is only when the temperature has dropped below that required for π meson production (the lightest hadron, $T \simeq 1.6 \times 10^{12}$ K), that the calculations become relatively simple. Though there are some hadrons left over after annihilation, their numbers are so small (see above) that they can be neglected until the energy density of matter approaches that of the radiation, by which time the density is so low that the strong nuclear force can be neglected except during nucleosynthesis.

About one hundredth of a second after the Big Bang, the universe had cooled to a temperature of $\sim 10^{11}$ K and is composed of a dense soup of photons, electrons, positrons, neutrinos and antineutrinos which, along with a small number of protons and neutrons (all other hadrons that were left over after annihilation, being unstable, had decayed), are in thermal equilibrium. The temperature is so high that the kinetic energy of each particle is many orders of magnitude above its rest mass energy and so they are relativistic and behave in a manner similar to the photons, leading to the universe being radiation-dominated. The remaining protons and neutrons are in a state of constant transition from one to another due to collisions and subsequent reactions with the other, more numerous particles. As the temperature falls it is easier for the heavier neutrons to turn into protons than it is for the reactions to proceed in the opposite direction, thus

introducing an imbalance in the proton/neutron numbers which grows as the universe expands and cools.

After about one second the temperature has fallen to 10^{10} K and the density fallen by a factor of 10^4. The neutrinos and antineutrinos now have such a large mean-free path, due to the decreasing density, that they start to behave like free particles and are no longer in thermal equilibrium with the electrons, positrons and photons. The neutrinos are now "decoupled" and can propagate freely through the universe, taking no further part in any reactions.

Once the temperature falls to about 3×10^9 K, the photons no longer have enough energy to spontaneously create electron-positron pairs, so the electrons and positrons rapidly begin to annihilate. The same matter-antimatter imbalance is present in the leptons as in the baryons, so a small number of electrons are left over after annihilation, matching the number of protons (i.e. the net charge is zero). Though it is now cool enough for stable nuclei such as helium not to be dissociated by energetic photons, they cannot form because the general expansion is so fast that nuclei can only form through a series of two-particle reactions (the probability of even a three-particle reaction occurring is insignificant). The first step of this chain, the combination of a proton and a neutron to form deuterium, readily occurs, but the deuterium nucleus is so weakly bound that it is immediately dissociated, and so no further reactions can occur.

After electron-positron annihilation has occurred, the transformation of protons and neutrons almost ceases due to the relative lack of electrons, but the finite half-life of the neutron ($\sim 10\frac{1}{2}$ minutes) becomes important and a significant fraction of the remaining neutrons start to decay.

As the temperature drops to $\sim 10^9$ K the photons no longer have sufficient energy to dissociate deuterium, so nucleosynthesis begins, rapidly converting all the available neutrons into helium, with a small fraction in other light elements (deuterium, helium three and lithium — there are no elements heavier than lithium due to a lack of stable nuclei with 5 or 8 particles). The epoch of nucleosynthesis finishes a few hundred seconds after the big bang.

Just before the onset of nucleosynthesis sufficient neutrons had decayed into protons that the ratio of protons to neutrons was about 87:13, giving $\sim 26\%$ of helium by

mass with the rest as hydrogen (i.e. protons). The precise onset of nucleosynthesis (in terms of temperature) is determined by the number density of particles, which in turn is governed by the number density of baryons (the number of photons being known). The higher the particle density, the earlier the onset of nucleosynthesis, and hence the less time there is available for neutron decay, giving a larger percentage of helium. In theory observations of present day helium abundance should enable strict limits to be put on the baryon density of the universe by this mechanism. However, the abundances of the other light elements, especially deuterium, are more sensitive and provide more accurate constraints (§ 1.2.3).

After the completion of nucleosynthesis the universe continues to expand and cool, being made up of a soup of photons, light nuclei and electrons with the ever-present background of neutrinos that have been free streaming since decoupling in the first second. The nuclei and electrons are unable to combine to form atoms as they are immediately dissociated by the energetic photons. This relatively stable state continued for another $\sim 720,000$ years while the universe cooled and expanded. One result of this decline in temperature is that the energy density of the radiation began to approach that of the matter (due to the effects of redshift, felt by radiation, but not by matter). At roughly the same time as the radiation and matter energy densities became equal, the temperature fell sufficiently so that atoms were able to form without being dissociated (4,000 K for matter-radiation equality, 3,000 K for the ironically named *re*combination phase). This effectively decoupled the radiation from the matter, leaving it free to propagate in the same manner as the neutrinos, retaining its initial spectral distribution and cooling as the universe expanded. It is this radiation, originally emitted at a redshift of ~1,000 and cooled to a temperature of 2.7 K, that was detected by Penzias & Wilson in 1965.

Though it was only after the detection of the microwave background that the full theory of the hot Big Bang was worked out in detail, it had first been suggested as a logical backward extrapolation of the expanding universe by Alpher, Bethe & Gamow (1948) who did various calculations relating to the primeval fireball and predicted a relic radiation, albeit with the slightly higher temperature of 5 K. This was followed by a series of papers presenting further calculations and cosmological scenarios (e.g. Gamow 1948a,b), though it should be pointed out that Gamow originally assumed all elements could be formed through primordial nucleosynthesis, which makes the details

of his calculations invalid. More accurate and realistic calculations were made shortly before the discovery of the Big Bang by Hoyle & Tayler (1964) and Dicke *et al.* (1965).

It should be mentioned that though the Big Bang has become the *de facto* standard model and is widely accepted, it is not without its problems. They are mostly to do with the proposed initial conditions, especially the generation of the initial expansion and primordial perturbations (§ 1.3). There is also the flatness problem (§ 1.2.3) and the isotropy of the microwave background, which itself is a problem under the standard Big Bang model (see Appendix C). One theory that has proved very successful at solving these problems is inflation (see Appendix C for more details), which itself has become something of a standard model for the pre-Big Bang universe. Despite these problems the hot Big Bang has proved very successful at explaining the universe we inhabit. In some ways the problems faced by the Big Bang are not problems with the model itself, but rather with the theories that precede it and set the initial conditions for the framework of the hot Big Bang.

1.2 Physical Parameters

1.2.1 Introduction

There are two main physical parameters that are required by the Big Bang model, the density of the universe and the rate of expansion. The density is usually expressed in terms of Ω, the ratio of the density, ρ, to the critical density, $\rho_c = (3H^2/8\pi G)$, the density required to just halt the expansion of the universe at infinity (see Appendix A). The rate of expansion is expressed in terms of the Hubble constant, H, which relates the expansion velocity, v, to the distance, d,

$$v = Hd \tag{1.1}$$

and has the somewhat unusual units of $\mathrm{km\,s^{-1}\,Mpc^{-1}}$. The Hubble constant is also related to the expansion rate by (see Appendix A)

$$H = \dot{a}/a, \tag{1.2}$$

where a is the scale factor of the universe (a measure of its size) and $\dot{a}$ is its time derivative (i.e. the expansion rate). Note that the Hubble constant is not actually a constant since it changes with time. It is also a measure of the size of the universe as, the bigger the Hubble constant is, the smaller are the distances measured for a given recession velocity (equation 1.1).

Both these fundamental parameters govern important characteristics of the evolution of the universe and both, unfortunately, are highly uncertain. In the following subsections the current estimates of the Hubble constant and density parameter are given, along with the problems associated with their determination. In all cases the subscript $_0$ refers to the present value of the parameter.

1.2.2 The Hubble Constant, H_0

The Hubble constant should, in theory, be easy to measure. Simply measure the recession velocity (via the redshift) and distance to a sample of galaxies and H_0 is recovered. However, things are not so simple, mainly due to the difficulty in measuring the distance to other galaxies. One of the "Holy Grails" of astronomy is an item called the "standard candle", an object whose intrinsic, observable properties are independent of environment, age, etc. One such standard candle is the cepheid variable star, originally used by Hubble to derive his famous law and to prove the extragalactic nature of the nebulæ (§ 1.1.1). A cepheid variable is a star whose luminosity varies with time in a periodic fashion with its intrinsic luminosity related to its period. By observing its period, one is able to infer its intrinsic luminosity and by comparing this to its observed flux, one can calculate how far away it is by how much it has been diminished.

The problem with such standard candles is that none are 100% accurate and cover only a limited distance range. Cepheids, for example, are only useful out to distances where they can be resolved, making the technique applicable to a limited number of nearby galaxies. Unfortunately, in order to make a clean estimate of the Hubble constant, it is necessary to look out to quite distant objects (those with recession velocities $\gtrsim 2500\,\mathrm{km\,s^{-1}}$; Rowan-Robinson 1985) so that the effects of local perturbations on the Hubble expansion (peculiar velocities) do not introduce unacceptable errors. For example, the Local Group (of which our own Galaxy is a member) has a peculiar velocity (measured with respect to the microwave background) of $\sim 600\,\mathrm{km\,s^{-1}}$ (Davis & Peebles

1983a, Lubin *et al.* 1985).

The requirement to use distant galaxies means that it is necessary to use several independent distance estimators/standard candles with overlapping distance ranges, each of which needs to be calibrated to the previous one. Such a bootstrap procedure (known as the "distance ladder") leads to accumulating errors in the distance measured. An excellent account of the problems associated with the task of measuring the Hubble constant is given by Rowan-Robinson (1985), to whom the reader is referred for further details.

An interesting point is that the errors on individual measurements of the Hubble constant tend to be quite small, despite the accumulated errors described above, whereas the scatter in measurements themselves are quite large and certainly larger than the errors quoted. The two main groups working on the determination of the Hubble constant give radically inconsistent estimates. Sandage and collaborators give $H_0 \simeq 50\,\mathrm{km\,s^{-1}\,Mpc^{-1}}$, with errors of $\simeq \pm 7\,\mathrm{km\,s^{-1}\,Mpc^{-1}}$ (e.g. Tammann & Sandage 1985) while de Vaucouleurs (1982) finds $H_0 \simeq 95\,\mathrm{km\,s^{-1}\,Mpc^{-1}}$ with errors of $\simeq \pm 10$. Neither group's results lie within the errors of the other. Many other authors have attempted to determine the Hubble constant and their results are scattered between the limits of Sandage and de Vaucouleurs. Trying to compile a meaningful table of values of the Hubble constant is almost impossible as there seems to be little consensus or convergence amongst workers in the field. The general method of determining the Hubble constant, free of local perturbations, is to find the relative distances between the Virgo cluster and various more distant objects and then calibrating these distances by the absolute distance to the Virgo cluster. Unfortunately, finding the distance to the Virgo cluster is itself a three step process (e.g. see White 1990), which introduces significant errors (see below).

Problems seem to arise when calibrating the various steps, rather than with scatter or intrinsic errors within the individual methods. A good example is that of Sandage & Tammann (1990), who quote $H_0 = 52 \pm 2\,\mathrm{km\,s^{-1}\,Mpc^{-1}}$ using six different methods to find a distance to the Virgo cluster of 21.9 ± 0.9 Mpc. However, they put 99% confidence limits on the Hubble constant of $40 < H_0 < 76\,\mathrm{km\,s^{-1}\,Mpc^{-1}}$ based on similar confidence limits for the distance to the Virgo cluster of $15 < D < 28$ Mpc. Thus it would seem that errors of $\pm 2\,\mathrm{km\,s^{-1}\,Mpc^{-1}}$ on the Hubble constant are over-optimistic, especially when

given more recent work on the distance to the Virgo cluster that was not available to Sandage & Tammann. Using planetary nebulæ as standard candles Jacoby, Ciardullo & Ford (1990) put Virgo at a distance of 14.7 ± 1.0 Mpc, in excellent agreement with recent work by Tonry (1991), who, using surface brightness fluctuations, finds a distance of 14.9 ± 0.8 Mpc. Both these figures lie at the extreme of Sandage & Tammann's range and using such a distance with their data would give a Hubble constant of $77\,\mathrm{km\,s^{-1}\,Mpc^{-1}}$, in good agreement with the value of $82 \pm 7\,\mathrm{km\,s^{-1}\,Mpc^{-1}}$ found by Tonry (1991) using the infrared Tully–Fisher relationship.

Another method is to use Type Ia supernovæ as standard candles (e.g. Tammann & Leibundgut 1990 and references therein). It is apparent that the maximum bolometric luminosity is a remarkable stable property of Type Ia supernovæ. Like all standard candles, the relationship needs calibrating to nearby supernovæ, which requires the use of an assumed Virgo distance. Using a distance of 21.9 Mpc, Tammann & Leibundgut (1990) have found a Hubble constant of $46 \pm 10\,\mathrm{km\,s^{-1}\,Mpc^{-1}}$ (errors depend on their model of the supernova expansion), which is in good agreement to the Sandage & Tammann (1990) result, given that they used the same distance to the Virgo cluster. Using the value of 14.9 Mpc proposed by Tonry (1991), this gives a Hubble constant of $68 \pm 10\,\mathrm{km\,s^{-1}\,Mpc^{-1}}$. However, Fukugita & Hogan (1991), using a combination of supernovæ data and Virgo distances, find $75 < H_0 < 100\,\mathrm{km\,s^{-1}\,Mpc^{-1}}$.

Other workers have tried to by-pass calibration by the Virgo cluster distance by equating the maximum bolometric luminosity to the instantaneous radioactive decay luminosity of the mass of ^{56}Ni present in the supernova. This allows the luminosity to be fixed without reference to the distance of the individual supernovæ and hence is totally independent of the distance to the Virgo cluster and any other distance measurements. Branch (1979) finds $H_0 = 56 \pm 15\,\mathrm{km\,s^{-1}\,Mpc^{-1}}$ and Arnott, Branch & Wheeler (1985) give $H_0 = 59\,\mathrm{km\,s^{-1}\,Mpc^{-1}}$ with upper and lower limits of 76 and $39\,\mathrm{km\,s^{-1}\,Mpc^{-1}}$ respectively, dependent on the mass of ^{56}Ni present. This method has the potential to make a remarkably clean measurement of the Hubble constant, given sufficient data and a detailed modelling of the production of ^{56}Ni, which could be a useful check of other distance measurements based on the distance to the Virgo cluster.

Another method is to use the geometry of gravitational lensing as a direct probe of the Hubble constant by measuring the time delay between two different light paths

from the same source. This was first suggested by Refsdal (1966) using a quasar as the source, lensed by a foreground object. The source needs to be variable on a time scale of at least a year so that the time delay can be calculated from the shift in the light curves obtained from the two images. Using the quasar 0957+561, a double image lensed by a galaxy and its associated cluster, Falco, Gorenstein & Shapiro (1991) have found that the Hubble constant can be calculated to within 25% if the galaxy's velocity dispersion and the time delay between the two images can each be measured to within 10%. Though their derivation depends on an assumed value of Ω_0, it only affects the Hubble constant by a few percent.

Using the formula of Falco, Gorenstein & Shapiro for the Hubble constant, Rhee (1991) found $H_0 = 50 \pm 17\,\mathrm{km\,s^{-1}\,Mpc^{-1}}$, using a velocity dispersion of $303 \pm 50\,\mathrm{km\,s^{-1}}$ and a time delay of 405 days. Using the same velocity dispersion, but a higher time delay of 511 ± 37 days, Roberts *et al.* (1991) also used the formula of Falco, Gorenstein & Shapiro to obtain $H_0 = 46 \pm 14\,\mathrm{km\,s^{-1}\,Mpc^{-1}}$. (Explicitly assuming $\Omega_0 = 0$. $H_0 = 42 \pm 14\,\mathrm{km\,s^{-1}\,Mpc^{-1}}$ if $\Omega_0 = 1$ is assumed.) However, it is possible that the presence of dark matter in the lensing galaxy will mean the optically measured velocity dispersion is an underestimate by up to 50%, raising the Hubble constant and errors found by both Rhee and Roberts *et al.* by a similar amount. Furthermore, Kochanek (1991) casts doubt on the validity of some of the assumptions of Falco, Gorenstein & Shapiro, suggesting that the uncertainties are larger. Using the velocity dispersion of Rhee and the time delay of Roberts *et al.*, he finds limits on the Hubble constant of $H_0 \lesssim 60 \pm 20\,\mathrm{km\,s^{-1}\,Mpc^{-1}}$, rising as far as $H_0 \lesssim 90 \pm 30\,\mathrm{km\,s^{-1}\,Mpc^{-1}}$ if there is dark matter present.

Though gravitational lensing is a potentially very clean method of determining the Hubble constant and an important independent check of other methods described above, the uncertainties are still large. Even if the observations were improved to the accuracy required by Falco, Gorenstein & Shapiro, there are still many doubts over the theory. For further remarks, see Kochanek (1991).

Though it seems that recent measurements are tending towards a range of $60 \leq H_0 \leq 85\,\mathrm{km\,s^{-1}\,Mpc^{-1}}$ (White 1990; Visvanathan 1990), it is fortunate that the results in this thesis do not require a knowledge of the Hubble constant. All physical distances scale inversely with the Hubble constant, as do all observed distances (from equation 1.1), thus making a knowledge of the value of the Hubble constant unnecessary for a

comparison to be made between theory and observation. For that reason, all distances in this thesis shall be expressed in terms of $h^{-1}\,\mathrm{Mpc}$, where h is the Hubble constant in units of $100\,\mathrm{km\,s^{-1}\,Mpc^{-1}}$.

1.2.3 The Density Parameter, Ω_0

Depending on whether the reader is an optimist or a pessimist, the Hubble constant is either well or poorly determined. However, it is known within a factor two, which is more than can be said for the density of the universe, which is uncertain by at least an order of magnitude. The determination of Ω_0 is very important as it ultimately governs the fate of the universe (Appendix A.2). Though the universe is currently expanding, it is nonetheless slowing down as it expands. This is due to the mutual gravitational attraction of all the mass within the universe. If $\Omega_0 = 1$, i.e. the density matches the critical density, there is sufficient mass in the universe to eventually stop the expansion, but only asymptotically with time. If $\Omega_0 < 1$ then there is insufficient mass in the universe to stop the expansion and the universe will reach a point where it will continue to expand for all time at a constant velocity. If $\Omega_0 > 1$ then not only will the universe stop expanding, but it will also recollapse. Note that this all assumes that the cosmological constant, Λ, is zero (Appendix A).

Because of its association with the deceleration of the expansion, the density parameter can also be expressed in terms of the deceleration parameter, q. For $\Lambda = 0$, $\Omega = 2q$ (Appendix A.4), where q is related to the scale factor by

$$q = -\frac{a\ddot{a}}{\dot{a}^2} = -\frac{dH}{dt} \tag{1.3}$$

where $\ddot{a}$ is the second time derivative, i.e. the acceleration, of the scale factor. In theory the deceleration parameter is easy to measure. Simply plot galaxies' redshifts versus their magnitudes (a Hubble diagram) and look for a deviation from a linear relationship as the redshift increases. This is due to the changing value of the Hubble constant over time, which was larger at higher redshift (earlier times). The observed curve can then be fitted by predicted curves for different values of the present deceleration parameter, q_0.

Unfortunately the deceleration parameter is not so straightforward to measure in practice. The above assumes that galaxies are standard candles (see § 1.2.2) and as such ignores any evolution with time in their magnitudes. Also the scatter in the points is large and the difference in the predicted curves for various q_0 are quite small, even at redshifts of unity and beyond, thus making a unique fit very hard to obtain. Errors on the measurement of q_0 are frequently of the order of the measurement itself and the estimates vary widely. Rowan-Robinson (1985) lists several estimates of q_0 ranging from -0.9 to $+1.6$. Negative values of q_0 imply that the universe is accelerating its expansion, which requires a non-zero cosmological constant (Appendix A.4).

Determinations of Ω_0 are less diverse, though just as inconclusive as those of q_0. The problem is that estimates of the mean density of the universe can only (generally) be made by observing luminous matter. As studies of our own and other spiral galaxies show, there is a considerable halo of non-luminous or "dark matter" that extends far beyond the luminous disk. A further complication is that as one looks on progressively larger scales, so this dark matter content increases. This is normally expressed as the ratio of total mass to luminosity (known as the mass-to-light ratio, which has units such that the sun has a mass-to-light ratio of unity). For our own and similar galaxies, the mass-to-light ratio is $\sim 10 - 20\,h$ (where h is the Hubble constant as defined in § 1.2.2), but the dynamics of binary galaxies and small groups suggest that this rises to $60 - 180\,h$ and to $300 - 500\,h$ for clusters of galaxies (Rowan-Robinson 1985).

The implication of this is that the universe is dominated by dark matter, the luminous matter making up only a small, and perhaps unrepresentative, fraction of the total mass. As the scale increases, so does the mass-to-light ratio (see above). On the largest scales so far probed, mass-to-light ratios of $300 - 500\,h$ for clusters suggest that the amount of dark matter in the intergalactic medium is considerably larger than the total mass contained in small groups, which prompts the question, how much dark matter is present on inter-cluster scales?

This question cannot be answered by considering the spatial distribution of luminous matter alone, nor by considering the dynamics of bound systems. The only way that dark matter can be detected on large scales is via its gravitational attraction and hence its effect on the motions of luminous matter. Recently several studies have been undertaken, using the peculiar motions of galaxies as the tracers of the underlying

large-scale density field. One method, called POTENT (Bertschinger & Dekel 1989; Bertschinger *et al.* 1990; Nusser *et al.* 1991), reconstructs the full three dimensional velocity field from observed radial velocities assuming potential flow (which one would expect on large scales from gravitationally induced peculiar motions). The velocity field is then used to derive the underlying mass distribution which can then be compared to other data to provide an estimate of Ω_0. Work on this method is still underway and as yet no firm limits have been set on Ω_0. However, dynamical arguments strongly suggest that $\Omega_0 \geq 0.5$.

Another method is to use all-sky redshift surveys such as the IRAS survey to predict peculiar velocities via a self-similar iterative procedure (Yahil *et al.* 1991; Davis, Strauss & Yahil 1991). This velocity field can then be compared to the observed motion of the Local Group to estimate Ω_0. This method makes the additional assumption compared to the POTENT method that the galaxies trace the mass distribution, whereas POTENT only assumes that the galaxies trace the velocity field. Again, work is currently underway and no firm limits have been placed on Ω_0. In a similar approach, Heavens (1991) uses the reconstructed mass distribution in the region of the Great Attractor, along with the statistics of Gaussian peaks, to put a lower limit of ~ 0.5 on Ω_0.

A third approach is that of Weinberg (1992), who derives the initial density field from redshift surveys using the assumptions that structure grew from Gaussian fluctuations under the influence of gravity alone (§ 1.3). The final distribution is then "reconstructed" from the initial conditions and compared to the original observations. Provided the above assumptions are correct, the technique can be used to put limits on various physical parameters, including Ω_0. Preliminary work suggests that $\Omega_0 \gtrsim 0.5$ (Weinberg 1989).

1.2.4 Theoretical Considerations and Dark Matter

There are several theoretical constraints that must be borne in mind when considering the value of Ω. One comes from the hot Big Bang itself. During the early phases of the Big Bang the light elements (deuterium, helium and lithium) were produced by nuclear fusion (§ 1.1.4). The amounts of these elements produced or destroyed in stellar processes are very small in comparison, so present day abundances of these elements

such provide very tight constraints on the conditions in the early universe. Calculations by Schramm (1982) show that Ω_b (the ratio of the density of baryons to the critical density) must lie in the region $0.015 \lesssim \Omega_b \lesssim 0.1$. This has been further narrowed down so that the best estimate is now $\Omega_b \sim 0.06$ (Schramm 1991). Estimates of Ω_0 from dynamical arguments give values of 0.2 or higher (see above), which means that unless either Big Bang nucleosynthesis or the dynamical estimates are radically incorrect, at least half the mass of the universe is of a non-baryonic nature (see § 1.3.2).

There are also strong theoretical arguments for assuming $\Omega_0 = 1$. One of the simplest is a "fine tuning" argument. As shown in Appendix A, Ω is a function of redshift, z, of the form

$$\Omega(z) = \frac{\Omega_0(1+z)}{(1+z\Omega_0)}. \tag{1.4}$$

For any $\Omega_0 \neq 1$, $\Omega(z)$ rapidly converges to unity as z increases (see Fig. 1.1).

As one can see, even for a very low value of $\Omega_0 = 0.01$, $\Omega(z = 1000)$ is 0.91 and extrapolating back to even earlier times forces Ω closer and closer to unity. Such a value of Ω, close to, but not exactly equal to unity, is an example of "fine tuning". If $\Omega(z = 1000)$ were only a few percent away from unity then it would have diverged so much by now that either the universe would have recollapsed by the present epoch [$\Omega(z = 1000) > 1$] or the deceleration would have been insufficient to affect the expansion, resulting in the initial expansion being so fast that the local gravitational perturbations would not have been sufficient to overcome the general expansion, hence galaxies could not have formed [$\Omega(z = 1000) > 1$]. At early times there is only a very narrow window in which Ω could lie without excluding galaxy formation. The problem of how Ω could be so close to unity and yet not exactly unity is also known as the "flatness problem" (§ 1.1.4; Appendix C) and caused theorists in the early 1980s to search for natural mechanisms that would force $\Omega = 1$ regardless of its initial value. One such solution came in the form of inflation (see Appendix C), which predicts a period of exponential expansion in the very early universe ($t \lesssim 10^{-35}$ s) that drives Ω to unity.

The problem with asserting that $\Omega_0 = 1$ is that it requires the introduction of an as yet undiscovered non-baryonic dark matter component, which is rapidly becoming

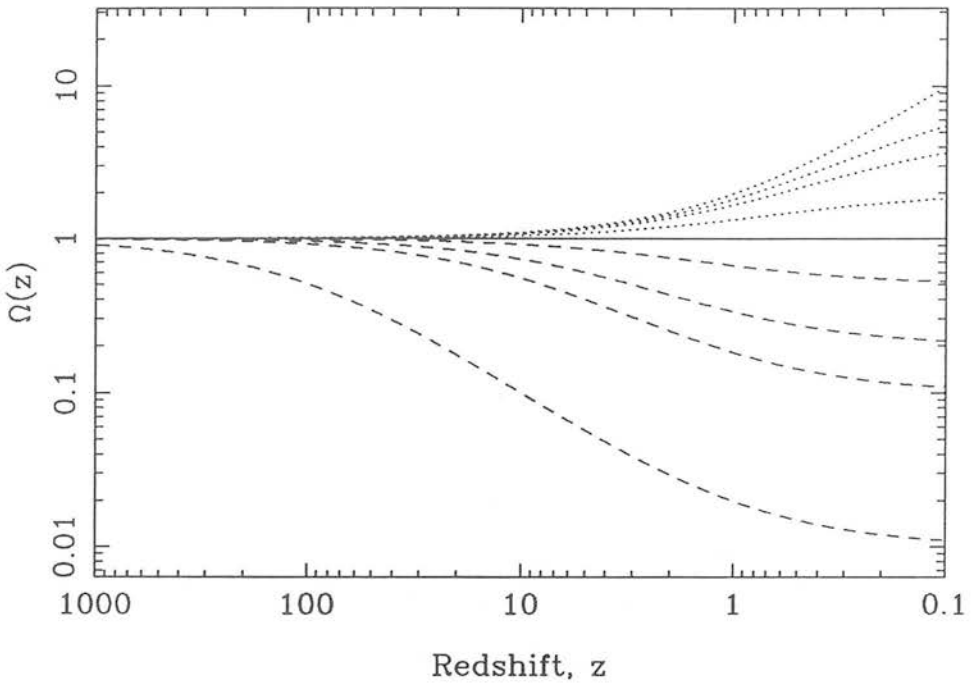

Figure 1.1 Plot showing the evolution of the density parameter, Ω, with redshift, z. The solid line is for the case of $\Omega = 1$ while the broken lines are for an open ($\Omega < 1$) universe and the dotted lines for a closed ($\Omega > 1$) universe. The different curves are for (reading bottom to top), Ω_0 =0.01, 0.1, 0.2, 0.5, 1, 2, 5, 10 and 100.

another Holy Grail of cosmology. However, some would argue that the current conservative estimates of $\Omega \gtrsim 0.2$ (e.g. Rowan-Robinson 1985; White 1990), obtained from dynamical arguments, already "prove" the existence of non-baryonic dark matter, hence the objection is unnecessary. Though it would not prove that $\Omega_0 = 1$, the experimental detection of dark matter particles would go a long way to removing the most serious objections.

Several candidates exist, the least exotic of which is the heavy neutrino. The neutrino has the advantage that it is a real, rather than hypothetical, particle. What remains to be seen is whether the neutrino actually has mass and whether this mass is sufficient to provide closure density. There are three known types (sometimes called "flavours") of neutrino, each associated with one of the three known leptons (the electron, muon and tau particles). If the neutrinos are light ($\lesssim 1\,\mathrm{MeV}$, where $1\,\mathrm{eV}$

$\sim 2 \times 10^{-36}$ kg or 2×10^{-6} times the mass of the electron), then they remain relativistic until the epoch of recombination and hence decouple from the radiation and matter fields in the very early universe (§ 1.1.4). This decoupling conserves the number density, which can then be calculated from the number density of photons in the microwave background. Thus, given the number density, one may calculate the density parameter of neutrinos, Ω_ν, given the neutrino masses.

$$\Omega_\nu = \frac{\sum_{i=1}^{3} m_{\nu_i}(\mathrm{eV})}{100h^2}, \tag{1.5}$$

where m_{ν_i} is the mass of the i^{th} neutrino in electron-volts. This applies for all relativistic species of neutrino with masses $\lesssim 1$ MeV (Schramm 1990, Sadoulet 1990). Obviously, if a neutrino were to be found with a mass $\gg 100$ eV then it would need to be unstable or else the density of neutrinos would vastly exceed the closure density. There has been a tentative discovery of such a neutrino with a mass of 17 keV (Simpson 1985; Simpson & Hime 1989; Hime & Simpson 1989; Hime & Jelley 1991), but due to the extreme difficulty in studying neutrinos, no decay time has been established. Indeed, the reality of such a neutrino has yet to be widely accepted.

There is also the theoretical possibility that there exists a stable neutrino of mass $\gtrsim 3$ GeV (e.g. Schramm 1990). In this case the neutrino would rapidly become non-relativistic and not decouple with the light neutrinos, thus the above constraints on number density and mass would not apply.

Other candidates are the particles predicted as a product of various Grand Unification Theories (GUTs). The most popular of these is the axion (Peccei & Quinn 1977a,b), a spinless boson postulated to conserve charge-parity in strong interactions. Another Grand Unification Theory is supersymmetry, which proposes the existence of a whole new set of supersymmetric partner particles for ordinary particles (e.g. the photino is the supersymmetric partner of the photon, the sneutrino the partner of the neutrino, etc.) Such particles are also considered strong candidates, the most likely being the lightest supersymmetric particle which has mass (e.g. Ellis 1990). For a more detailed discussion of dark matter candidates and their implications see e.g. Audouze & Trân Thanh Vân (1988) or Galeotti & Schramm (1990).

Unfortunately, the one general property of these particles (including neutrinos) is

their extremely weak interaction with matter through any force other than gravity, which makes them exceptionally hard to detect. For a review of current and future experiments aimed at detecting dark matter candidates, see e.g. Sadoulet (1990) or Spiro (1991). However, it is also possible to test the viability of such dark matter candidates via their implications for large-scale structure formation (§ 1.3.2, 1.4.6), though to date few firm conclusions have been reached either confirming or excluding various candidates.

1.2.5 The Age of the Universe

The parameters H_0 and Ω_0 combine to give an estimate of the age of the universe which in turn can be used to constrain the parameters themselves. The Hubble constant has units of one over time, thus one can define $1/H_0$ to be the "Hubble time". Assuming the cosmological constant $\Lambda = 0$, the present day Hubble time is an upper limit to the age of the universe. For $\Omega_0 = 0$ the universe undergoes no deceleration and therefore the expansion rate is constant and the age of the universe is simply given by the Hubble time. For $\Omega_0 > 0$, the universe will be younger as the expansion in the past was greater than it is now. The relationship between the age of the universe, t_0, and Ω_0 is a complicated function (Appendix A.3), but it is given by the excellent approximation

$$t_0 = H_0^{-1}\left(1 + \frac{\Omega_0^{0.6}}{2}\right)^{-1}, \tag{1.6}$$

which simplifies to $\frac{2}{3}H_0^{-1}$ for $\Omega_0 = 1$.

For a Hubble constant of $100\,h\,\mathrm{km\,s^{-1}\,Mpc^{-1}}$, this gives a Hubble time of $\sim 9.5h^{-1}$ Gyr. For the higher estimates of the Hubble constant given in § 1.2.2 ($100\,\mathrm{kms^{-1}}$ Mpc, i.e. $h = 1$), the age of the universe is thus $\lesssim 9.5$ Gyr. This, unfortunately, is far too low. Even for a Hubble constant of $50\,\mathrm{km\,s^{-1}\,Mpc^{-1}}$($h = \frac{1}{2}$), the upper limit to the age of the universe is 19 Gyr, falling to 12.5 Gyr if $\Omega_0 = 1$. Such low ages are in conflict with the ages of globular clusters, derived from the main sequence turn-off. Though the ages of individual clusters vary, a typical age is 16.5 ± 2.4 Gyr (Fowler 1987 and references therein). However, there has been some suggestion that these high ages are overestimates (Willson, Bowen & Stuck–Marcell 1987). Supporting evidence comes from the study of the decay of radioactive heavy elements (Fowler 1987) which gives an age of 11 ± 1.6 Gyr, and a study of the cooling times of white dwarfs (Winget *et al.*

1987) which gives an age of 10.3 ± 2.2 Gyr. Ages of the universe for a range of values of Ω_0 and the Hubble constant are given in Table 1.1.

H_0	Ω_0				
($\mathrm{km\,s^{-1}\,Mpc^{-1}}$)	0.0	0.1	0.2	0.5	1.0
50	19.0	16.9	16.0	14.3	12.7
60	15.8	14.1	13.3	11.9	10.6
85	11.2	9.9	9.4	8.4	7.5
100	9.5	8.4	8.0	7.1	6.3

Table 1.1 The age of the universe in Gyr for various combinations of the Hubble constant, H_0, and the density parameter, Ω_0.

As one can see, for the favoured values of the Hubble constant given in § 1.2.2 ($H_0 = 60 - 85\,\mathrm{km\,s^{-1}\,Mpc^{-1}}$), very low values of Ω_0 are required. If $\Omega_0 = 1$ it is only with a Hubble constant of $\lesssim 60\,\mathrm{km\,s^{-1}\,Mpc^{-1}}$ that the age of the universe is in agreement with the estimates of Fowler (1987) and Winget *et al.*. Even then the globular cluster ages need to have been seriously overestimated. For a Hubble constant of $85\,\mathrm{km\,s^{-1}\,Mpc^{-1}}$, Ω_0 must be very small ($\lesssim 0.2$), the true age of the universe needs to lie at the very lower end of the envelope given by Fowler (1987) and the problems with the globular cluster ages are even worse. The only other alternative is a positive cosmological constant which provides the equivalent of a repulsive force. This leads to a "coasting" period during the past when the expansion velocity was at a minimum. This places the Big Bang further back in time compared to an expansion with a zero cosmological constant, hence increasing the age of the universe (e.g. see Martel 1990; Hoell & Priester 1991).

1.3 Origins of Large-Scale Structure

1.3.1 Primordial Fluctuations

One of the fundamental problems in cosmology is that of the origin of the present large-scale structure of the universe. By far the simplest theory is that of gravitational

instability, which proposes that galaxies and larger structures originated in small fluctuations, present in the density field shortly after the Big Bang, which were then amplified by gravity until there was local collapse into the first generation of gravitationally bound objects. On what scale this collapse occurred is a much debated topic in cosmology. Either the first objects formed were small and clustered together to form progressively larger systems (known generically as a "bottom up" or hierarchical scenario), or were large and fragmented into smaller systems (the "top down" or adiabatic scenario). The distinction between the two depends on the power spectrum of initial fluctuations.

For power spectra dominated by large-scale power, a "top down" scenario will ensue, the first objects to be formed being at the mass scale given by the dominant wavelength. In the absence of non-baryonic dark matter (see § 1.3.2) this type of power spectrum arises from adiabatic fluctuations. Here fluctuations are present in the matter and radiation fields and photon drag damps out any perturbations on scales of less than $\sim 10^{14}\,\mathrm{M}_{\odot}$ for $\Omega = 0.1$ or $\sim 10^{12}\,\mathrm{M}_{\odot}$ for $\Omega = 1$ (Doroshkevich, Sunyaev & Zel'dovich 1974). Power spectra with significant amounts of power on small scales will form structure in a "bottom up" manner, the first objects to collapse being on scales of the Jeans mass ($\sim 10^{6}\,\mathrm{M}_{\odot}$ for $\Omega = 0.1$ and $\sim 2 \times 10^{5}\,\mathrm{M}_{\odot}$ for $\Omega = 1$; Peebles & Dicke 1968), i.e. sub-galactic in scale. One class of fluctuations that will give rise to such a power spectrum (in the absence of non-baryonic dark matter, see § 1.3.2) is isocurvature (sometimes known as isothermal) fluctuations. Here perturbations in the matter field are matched by negative perturbations in the radiation field so that the total density remains unchanged. The Big Bang does not predict the form of the initial fluctuations, nor does it provide any mechanism for their generation. Instead they are assumed as an initial condition.

One form of fluctuations that is theoretically very popular is the so-called scale-invariant spectrum, so named because the fluctuations on the scale of the horizon are always of the same amplitude. Such a spectrum of initial fluctuations has been argued for as long ago as 1972 by Zel'dovich and was also proposed by Harrison (1970). For this reason the scale-invariant power spectrum is also known as the Harrison–Zel'dovich spectrum.

The initial spectrum of perturbations is then modified by the conditions of the early universe. For example, if the fluctuations are adiabatic then all short-wavelength

perturbations are damped. This can be expressed in terms of a transfer function, which links the initial and final power spectra. Thus the final power spectrum, $P(k, t_{\rm f}) \propto |\delta_k|^2$, of matter perturbations can be written as

$$P(k, t_{\rm f}) = \left[\frac{b(t_{\rm i})}{b(t_{\rm f})}\right]^2 T^2(k, t_{\rm f}) P(k, t_{\rm i}), \tag{1.7}$$

where $t_{\rm f}$ is the final (late) time, $t_{\rm i}$ is the initial (early) time, b is the linear growth factor of long-wavelength perturbations (for $\Omega = 1$, $b \equiv a$; see Appendix B) and $T(k, t)$ is the transfer function. Note that even if the form of the power spectrum and transfer function are completely specified, the amplitude of the fluctuations is a free parameter that must be normalised with respect to observations. The rest of this section is given over to a discussion of various theoretical models that dictate the transfer function.

1.3.2 Non-Baryonic Dark Matter

The microwave background provides information about the physical conditions in the early universe, especially the amplitude of the fluctuations, as it allows us to see back to the so-called recombination epoch (§ 1.1.4). Before recombination, matter and radiation were strongly coupled so that the perturbations in one were reflected in the other. After recombination the spectrum of the radiation remained largely unchanged, thus retaining the imprint of matter fluctuations as fluctuations in the temperature of the radiation. Apart from a dipole anisotropy, a consequence of our own peculiar velocity, the microwave background is a pure blackbody spectrum down to the present measurement limits. As yet no fluctuations have been found, placing stringent limits on the inhomogeneities present in the early universe. Upper limits of temperature fluctuations of $\Delta T/T \sim 5 \times 10^{-5}$ on all scales (Silk 1987) place limits of $\delta\rho/\rho \sim 10^{-5}$ on density perturbations.

Simple linear theory predictions allow the growth of such perturbations by a factor $1 + z_{\rm rec}$, where $z_{\rm rec}$, the redshift at the epoch of recombination, is $\sim 1,000$. However, on scales $\lesssim 10\, h^{-1}$ Mpc, density perturbations are of order unity, thus there is a clear discrepancy of two orders of magnitude in the scale of perturbations. Obviously on such small scales, non-linear effects will have become important, but there is still a major problem in creating the large scale structures seen today from such small perturbations.

These problems are much worse for an open universe ($\Omega_0 < 1$) where growth of structure in the linear regime ceases before the present time and the only growth thereafter is in the non-linear regime. For flat and closed universes ($\Omega_0 \geq 1$) growth continues to the present epoch, thus an open universe has less time to achieve the same size perturbations compared to an $\Omega_0 \geq 1$ universe, thus requiring larger fluctuations at the recombination stage.

Thus an $\Omega_0 = 1$ universe is less likely to violate microwave background constraints. As seen in § 1.2.4, an $\Omega_0 = 1$ universe requires non-baryonic dark matter. This can be classified into two generic forms, hot dark matter (HDM), characterised by relativistic ("hot" ≡ light) dark matter particles and cold dark matter (CDM), characterised by non-relativistic ("cold" ≡ heavy) dark matter particles. These two broad classes have very different effects on the initial power spectrum.

In hot dark matter dominated universes, the dark matter particles are assumed to be massive neutrinos (§ 1.2.4). At recombination, these are still relativistic, thus they behave in a roughly similar manner to photons in adiabatic fluctuations (§ 1.3.1), damping out all fluctuations less than a characteristic scale. In this case the characteristic scale is the free-streaming length of the neutrinos when they become non-relativistic, which depends on the mass of the neutrino (the heavier the neutrino, the sooner it becomes non-relativistic). Thus hot dark matter scenarios form structure in a "top down" manner.

In cold dark matter dominated universes, the dark matter particles are assumed to be any one of a number of hypothetical, heavy elementary particles (§ 1.2.4). These rapidly become non-relativistic, so small-scale fluctuations are not damped. The resulting cold dark matter power spectrum tends to form structure on a wide range of scales, so it is not a classical "bottom up" scenario, though structure still forms in a hierarchical manner.

In recent years, cold dark matter has become far more popular than hot dark matter amongst theorists. This is due to the late formation of small-scale structure in the latter model. Galaxies can only form due to fragmentation after the very large-scale structure has formed. This means that to grow such large-scale structure requires either large initial perturbations, violating the microwave background constraints, or an unacceptably late epoch of galaxy formation. Cold dark matter dominated universes

avoid this problem by having the small-scale structure form first, thus allowing larger structures more time to form. However, recent numerical simulations (Centrella *et al.* 1988) have shown that structures in hot dark matter universes go non-linear at very early timescales, thus structure may grow at a faster rate than previously thought using linear theory assumptions. This allows large-scale structures time to form from small perturbations without an unacceptably late epoch of galaxy formation. A further problem is that of galaxy formation outside of the pancakes as galaxies are not predicted to form outwith of the collapsed structures, though isolated galaxies are observed (see § 1.4). This may prove to be a serious constraint on hot dark matter models (e.g. see More, Heavens & Wilson 1990).

1.3.3 Biased Galaxy Formation

Originally proposed to explain the large-amplitude clustering of Abell clusters (Kaiser 1984), biased galaxy formation also provides another prescription by which present day structures may arise from small initial fluctuations. The basic idea of biased galaxy formation is that the efficiency of galaxy formation depends on the local environment, with more galaxies being formed in high density regions (e.g. peaks in the density field), leaving the very low density regions devoid of luminous matter. Thus there is a segregation of luminous and non-luminous (dark) matter, the luminous matter being more strongly clustered than the underlying dark matter. This provides a way of reconciling the highly clustered distribution of luminous matter with the low amplitude fluctuations required by the microwave background, as the fluctuations in the dark matter can still be sufficiently small that they do not violate the microwave background constraints.

1.3.4 Topological Defects

The limitations enforced by the microwave background on the size of initial fluctuations (§ 1.3.2) may yet prove to be so strict that even an $\Omega_0 = 1$ universe with biased galaxy formation cannot produce sufficient growth in the fluctuations to account for the present day large-scale structure. One way round this is to introduce seeds which aid the growth of structure without increasing the amplitude of fluctuations at the recombination phase.

One idea that has come from the study of the interface between particle physics and cosmology in the very early universe is the idea of topological defects in space-

time (Kibble 1976) which could act as seeds for the formation of large-scale structure. The fundamental assumption follows from the various forms of Grand Unified Theories. These assert that at very high temperatures ($\sim 10^{28}$ K, the so-called GUT scale) the four forces were unified. As the universe cooled, so this unification was broken which led to a phase transition during the very early stages of the Big Bang (perhaps during inflation, though this is not a necessary condition). At temperatures below the critical temperature, the energy density of the universe becomes trapped in various ground states. Above the critical temperature there was sufficient energy that the energy density oscillated with an amplitude greater than that of any of the ground states.

When the universe passed through the critical temperature, the energy density of the universe sought to minimise itself at every point by entering a ground state. However, because of the finite speed of light, regions of space that were widely separated were not causally connected and hence became confined in different ground states. At the boundaries of these regions the energy density could not simultaneously minimise itself with respect to all neighbouring regions and hence there would arise a region of trapped energy density, unable to reach a ground state. Such a region forms a topological defect.

A toy model of the formation of topological defects is the spring and pencil model (e.g. see Brandenberger 1990 and references therein). Consider a table with a lattice of pencils, each balanced in its end and connected to its neighbours by a spring. With sufficiently high energy the pencils will vibrate around the vertical, but as the energy falls, they will want to lie flat on the table. One can consider the situation where a pencil's neighbours all fall in different directions. Though the pencil wishes to fall, it cannot do so because it is supported by the springs attached to its neighbours. The pencil (springs) then contains the trapped energy.

Because these topological defects trap energy density, they act as gravitating masses, which can act as non-linear seeds for galaxy formation. Rather than being coherent density fluctuations, these are individual density enhancements that provide deep potential wells for the matter to fall into. The evolution of structure then proceeds along similar lines to the gravitational instability scenario (§ 1.3.1). However, because of the non-linear nature of these seeds, the evolution of structure is not straightforward, thus theoretical modelling of large-scale structure involving topological defects can be very complicated.

There various kinds of topological defects dependent on the particular Grand Unified Theory. The most heavily researched are cosmic strings (e.g. Brandenberger 1990 and references therein), which are one-dimensional lines of trapped energy density. Cosmic strings are proposed to form some 10^{-35} seconds after the Big Bang as the early universe undergoes a phase transition. They are infinite in length and have a mass per unit length, μ, in the order of $10^{16}\,\mathrm{kg\,m^{-1}}$, but a radius of only 10^{-22} times that of the hydrogen atom. Cosmic strings seed structure formation in two ways. The first is by loop production. Cosmic strings interact with themselves and form loops which become detached from the main string. These loops are of a finite mass and act as deep potential wells for the dark matter, hence they seed the formation of individual bound systems from galaxies to galaxy clusters, dependent on the loop mass. In numerical simulations of structure formation with both hot and cold dark matter universes seeded with strings, the presence of loops leads to the early formation of galaxies (Brandenberger 1991). The second mechanism is the dominant one and is due to the motion of cosmic strings. As a segment of a string passes through space it produces turbulence. The perturbations that result then attract matter, forming sheet-like structures (Brandenberger 1991).

The cosmic string model has only one free parameter, the mass per unit length, which is related to the time at which the symmetry breaking occurs in the early universe. If the mass per unit length is normalised via simulations to the observed large-scale structure, this predicts a symmetry breaking at roughly the GUT scale, in line with theoretical predictions (Brandenberger 1991).

Another popular topological defect is texture (e.g. Turok 1989, 1991), which is composed of three-dimensional "knots" of trapped energy density. These slowly contract in size after formation until they "unwind", that is, they spontaneously disappear, radiating away their energy in a burst of free-streaming, massless bosons, so that by the present day all the textures have gone. However, before unwinding, they act as deep potential wells into which the dark matter can fall. The potential wells then remain (due to the dark matter) after the textures are gone. This provides a non-linear amplification to the growth of dark matter perturbations which then proceeds along the lines of the simple gravitational instability theory (§ 1.3.1), which makes the evolution of structure in texture seeded models relatively easy to follow.

Textures obey a simple scaling relation which naturally produces a Harrison-

Zel'dovich spectrum of initial perturbations (Park, Spergel & Turok 1991). Like strings, the model also has only one free parameter — the amplitude of fluctuations, set by the scale of symmetry breaking. Like strings, if this is set to the GUT scale, this naturally produces the correct amplitude fluctuations for present day galaxy clustering.

Analytical modelling has shown that the presence of textures causes early galaxy formation (Gooding, Spergel & Turok 1991) which is supported by N-body simulations of a cold dark matter dominated universe seeded with textures (Park, Spergel & Turok 1991), which also shows that the presence of textures increases the amount of large-scale power. Further work, using a hydrodynamical N-body code (Cen *et al.* 1991) found the both cold and hot dark matter universes provided a better match to observations if seeded by texture. Furthermore, texture seeds in voids failed to form galaxies, thus providing a natural bias towards high density regions (§ 1.3.3).

1.3.5 The Explosion Model

Another class of model is the explosion model (Ostriker & Cowie 1981; Ikeuchi 1981). Like the topological defects (§ 1.3.4), the explosion model is based on the concept of seeds. However it differs from the previous methods as its primary mechanism is not gravitational. Instead, the basic premise behind such a model is that at some cosmologically early time, certainly before the onset of galaxy formation, primordial objects located within what are now voids exploded. The shock fronts from these explosions sweep up the matter before them as they expand, thus creating out large voids. Where two shock fronts meet, the matter collides, stopping the expansion and forming thin walls. Galaxies begin to form by fragmentation of the matter in these walls, thus the explosion model predicts a "top down" scenario.

It should be noted that in early versions of the model it was not assumed that the shock fronts would expand until other fronts were met. Instead the expansion of the shock fronts would have been slowed by the ambient medium, thus the voids would not necessarily form a continuous network. Galaxies would still form in the high density regions of the shock fronts surrounding the voids.

This mechanism naturally produces a cellular structure which is qualitatively not unlike that observed (§ 1.4), which was one of the primary motivations behind the model.

However, it is within the bounds of the model that rather than there being only one generation of explosions, there are several generations. This first generation of explosions sweep out moderate (a few Mpc) voids, and then second generation objects forming in the shells explode, and so on, in a bootstraping procedure. In this way the large voids that are observed today are envisaged to have formed. This does, though, complicate the simplistic picture of structure formation given above for the single generation model.

The seeds for the explosions could be massive first generation stars, quasars or a close spaced series of supernovæ in the first generations of galaxies. Though the explosion model avoids the problem of large amplitude fluctuations at recombination, there may still be problems with the microwave background. The compression and heating of the gas in the shock waves after the explosions is liable to cause unacceptably large small-scale anisotropies in the microwave background due to heating by the Sunyaev-Zel'dovich Compton heating effect (Hogan 1984).

1.4 Present Day Structure

1.4.1 Discovery of a Cellular Universe

One of the fundamental assumptions of modern cosmology is that the universe is homogeneous on large scales (§ 1.1.2). However, the universe about us is manifestly inhomogeneous, so what becomes of the assumption of homogeneity? The problem is one of scale — on very large scales the universe is homogeneous, whereas on small scales it is not. Evidence for very large scale homogeneity comes from the microwave background (§ 1.3.2) and on smaller scales from the lack of clustering of high redshift radio galaxies. Webster (1976b, 1977) and Webster & Pearson (1977), found that the distribution of radio sources on the sky had a remarkably unclustered distribution, suggesting homogeneity on large ($\gtrsim 100\,h^{-1}\,\mathrm{Mpc}$) scales (e.g. Webster 1976b). Note that both these observations refer to the state of clustering in the past. The microwave background probes clustering at the epoch of recombination and the objects used by Webster are characteristically at redshifts of between one and three (Webster 1976b). Evidence of homogeneity at the current epoch comes from the scaling with depth of the angular correlation function. As the correlation function probes to greater depths, so any given angular separation on the sky will measure a larger physical scale. Provided the angular

correlation function measures the same clustering pattern (i.e. the survey is homogeneous over its depth) going to a greater depth will cause the amplitude and absolute angular scale of the correlation function to shift, but without affecting the shape (Groth & Peebles 1977). Angular correlation function analysis on recent surveys have shown that the local universe is homogeneous on scales of $\sim 200\,h^{-1}$ Mpc (e.g. Maddox *et al.* 1990).

However, on small scales the very existence of galaxy clustering shows that the universe is inhomogeneous. Thus the question of homogeneity becomes one of scale and one can ask "what is large scale?" On that topic there has been a quiet revolution over the past 15 years.

In the early 1970s the generally accepted picture of the distribution of galaxies was one of a background ("field") component of galaxies which were distributed homogeneously, with groups and clusters, formed by gravitational growth of local perturbations, superimposed on top. This put "large scale" at quite small scales. As recently as 1983 Shanks and co-authors were arguing for a universe that was homogeneous on scales of $25\,h^{-1}$ Mpc and above, based on a two-point correlation function analysis of a deep redshift survey (Shanks *et al.* 1983). However, data were already accumulating that suggested that this picture was incorrect and that the universe was inhomogeneous on scales far above $25\,h^{-1}$ Mpc.

The evidence came mostly from studies of superclusters, large concentrations of galaxies and clusters of galaxies on the sky. Superclusters had been known from early on in this century from concentrations in the angular distribution of galaxies on the sky, but their reality was disputed by some who claimed them to be merely the effects of extinction (e.g. Holmberg 1974; Fessenko 1978). Surveys such as those of the Perseus supercluster (e.g. Tifft & Gregory 1978; Gregory, Thompson & Tifft 1981) established the physical reality of these systems, revealing long chains consisting of groups and clusters of galaxies with extensive foreground and sometimes background voids (e.g. Gregory, Thompson & Tifft 1981). Also well studied were the Coma/A1367 supercluster (Gregory & Thompson 1978) and the Hercules supercluster (Tarenghi *et al.* 1979, 1980). The striking features of all these surveys were the chain-like nature and size of the superclusters involved, at least $33\,h^{-1}$ Mpc long in the case of the Perseus supercluster (Gregory, Thompson & Tifft 1981), the presence of clearly defined voids, up to $40\,h^{-1}$ Mpc deep

(Tarenghi *et al.* 1979), and the lack of any homogeneously distributed field galaxy component. Indeed, all the authors commented on the lack of isolated galaxies that were not included in any larger structure. This supported previous work by Soneira & Peebles (1977) who found that if a homogeneous field component did exist then it could not contain more than 18% of all galaxies. They also modelled the galaxy distribution using a hierarchical model with no field component, finding a good match to observations.

However, it was the work of Einasto, Jôeveer and co-workers which crystallised the change of thinking. They were the first to emphasis the significance of the voids over that of the superclusters. Starting with an independent survey of the Perseus supercluster and its associated foreground void, Jôeveer & Einasto (1978) went one step further than other authors in the field. Not only did they claim that most of the galaxies were contained in superclusters, but they asserted that these superclusters were interconnected to form a continuous network of sheets and chains of galaxies with voids, or "holes", separating individual sheets and chains, thus giving rise to a cellular structure. This work was extended by Jôeveer, Einasto & Tago (1978) and supported by Chincarini & Rood (1979), before being further refined by Einasto, Jôeveer & Saar (1980). They presented a picture, backed up with observational evidence of the Perseus, Pegasus, Andromeda and Cetus superclusters, of a universe dominated by large voids of linear sizes up to $50\,h^{-1}$ Mpc or more. These voids were almost devoid of bright galaxies and bounded by thin planes or walls of galaxies. Along the edges of the planes, where they intersected with other planes, ran chains of groups and clusters, which in turn intersected with other chains. These points of intersection were then proposed to be the locations of rich clusters. The resulting structure is both cellular and hierarchical. The richest systems (Abell clusters) are joined in a network by chains of less-rich clusters and groups of galaxies, which in turn are joined by thin, essentially two-dimensional planes, only sparsely populated by galaxies and containing no groups or clusters. Each cell is thus made up of a set of walls, chains and rich clusters, all bounding a void, and all interconnected with other cells.

This morphological segregation was demonstrated by Einasto, Jôeveer & Saar (1980), along with a trend of a decreasing spiral population as one went from walls, through chains and into rich clusters. Accompanying this is a reverse trend of increasing elliptical population. In such a picture a supercluster is defined as "one cell wall with surrounding cluster chains". Thus superclusters are not only connected in a continuous

structure, but also share common elements.

This work was partially inspired by the theoretical models of Zel'dovich and collaborators (Zel'dovich 1978 and references therein), who described a scenario based on adiabatic fluctuations (characteristic of the "top down" scenario of § 1.3.1) in which the first structures to form were superclusters of mass $\sim 10^{15}\,M_{\odot}$. These were formed by the collapse of a cloud of gas along one axis and are generically known as "pancakes", due to their two-dimensional nature, and are readily identified with the cell walls of Einasto, Jôeveer & Saar (1980). It is easy to see how a cellular structure could then form from the intersection of various pancakes, provided their collapse occurred at the same epoch, with the remaining material of the clouds that was left in the voids falling onto the pancakes after formation, thus leaving the voids empty of matter. Galaxies were then formed by the fragmentation of the gas within the pancakes. This is also the method of galaxy formation favoured by several other authors, such as Gregory, Thompson & Tifft (1981) who contend that all galaxies were born in superclusters and that the few isolated galaxies that have been observed were ejected by tidal forces during fragmentation and relaxation.

Though Einasto, Jôeveer & Saar may have been guilty of over interpreting their data, going from the evidence they had of the existence of a few walls, chains and voids to the assertion that galaxies were distributed in a cellular structure was a bold step that was to be confirmed by an ever increasing stream of data. Support came with the discovery of the Boötes void (Kirshner *et al.* 1981; 1987), a region $60\,h^{-1}$ Mpc deep lying at a mean distance of over $100\,h^{-1}$ Mpc and which contains few galaxies.

However, up until that point all the evidence had come from deep, narrow-angle surveys, thus the interconnection of the various structures as proposed by Einasto, Jôeveer & Saar (1980) was not conclusively shown to be valid. The wide-angle CfA redshift survey (Davis *et al.* 1982) provided evidence of a network of cells and voids of sizes $20 - 30\,h^{-1}$ Mpc. Further evidence followed with the advent of more, and deeper, wide-angle surveys such as the Perseus–Pisces redshift survey (Haynes & Giovanelli 1986 and references therein), extensions to the CfA survey, both in depth (de Lapparent, Geller & Huchra 1986) and extent (Geller & Huchra 1989), the Southern Sky Redshift Survey (SSRS; da Costa *et al.* 1988) and extension (da Costa *et al.* 1989), the Southern Redshift Catalogue (Fairall *et al.* 1990) and the South Galactic Pole survey of Parker

(1992). Another excellent survey is the QDOT survey (Saunders *et al.* 1991), based on a sparse sampled, all-sky IRAS survey. All of these clearly show the sort of cellular structure predicted by Einasto, Jôeveer & Saar (1980), complete with chains, walls and large voids.

1.4.2 Limits of Inhomogeneity

One thing that soon became apparent from the rapidly growing number of redshift surveys is that the universe is inhomogeneous on very large scales. To date no wide-angle redshift survey has surveyed a large enough volume to be considered a fair sample — all have contained structures of a size comparable to that of the survey.

For example, Geller & Huchra (1989), in an extension to the CfA survey, have found the "Great Wall", a thin sheet of galaxies that stretches right across their survey. Its size, at least $170\,h^{-1}$ Mpc $\times\, 60\,h^{-1}$ Mpc, is limited only by the extent of the survey. Also, all surveys large enough to have done so, have detected voids of linear dimensions $\gtrsim 50\,h^{-1}$ Mpc, which is comparable to the size of the surveys involved (Geller & Huchra 1988).

As survey sizes increase, there is no way of telling if the sizes of the largest voids found so far will not also increase. All of this evidence pushes up the scale of inhomogeneity to $100\,h^{-1}$ Mpc or more. It is possible that an upper limit to the inhomogeneities has been found by Broadhurst *et al.* (1990). They used two deep, one-dimensional redshift surveys ("pencil-beam" surveys) at the north and south galactic poles to probe a baseline of $\sim 1000\,h^{-1}$ Mpc. The remarkable result was a series of regular peaks in the redshift distribution that was interpreted as arising from groups of galaxies with a spatial separation along the line of sight of $128\,h^{-1}$ Mpc. It is suggested by Geller & Huchra (1989) that these peaks are "Great Wall" type structures crossing the line of sight of the survey. This was supported by de Lapparent, Geller & Huchra (1991) and Ramella, Geller & Huchra (1992), who calculate the likelihood of the Broadhurst *et al.* (1990) pencil-beam detecting a "Great Wall" structure and conclude that a periodicity of $\sim 120\,h^{-1}$ Mpc could be achieved from a cellular universe represented by the CfA survey with cells of a characteristic size $20 - 50\,h^{-1}$ Mpc, as the beam will not detect every "Great Wall" it intersects. This is also supported by the simulations of Park & Gott (1991) who suggest that a periodicity of $128\,h^{-1}$ Mpc is indicative of cellular

structure on a smaller scale. Theoretical work to place constraints on the size of the inhomogeneities is also possible. One of the aims of this thesis is to use the Voronoi foam (§ 2.3), a simple cellular model, to see if present day observations can be reproduced by such a model, and if so, what characteristic cell size is required (Chapter 5, 6).

However, more data are needed, especially more pencil-beam surveys, to establish the reliability and statistical significance of the Broadhurst *et al.* (1990) result. If this periodicity proves to be a general feature of future surveys then the extreme regularity may be taken to be an upper limit to the size of the largest structures in the universe, and hence indicate the onset of homogeneity. If, however, the result proves to be a statistical fluke, then it is likely that the scale where homogeneity sets in could be considerably lower and perhaps within the reach of the next generation of redshift surveys. The work of de Lapparent, Geller & Huchra (1991) and Ramella, Geller & Huchra (1992), and that of Park & Gott (1991) suggests the latter, but if more pencil-beam surveys in other directions turn up a similar periodicity, or if wider pencil-beams fail to find the "missing" "Great Walls", then the former may be true, suggesting a larger cellular structure than presently detected. Further, deeper, redshift surveys are also needed to address this question and to ascertain whether the present structures found are limited in size by the size of the survey or whether they extend to yet greater scales.

1.4.3 Voids, Walls, Filaments and Superclusters

One obvious point to arise from all of the large, wide-angle redshift surveys is that the voids are the dominant features, and if the cellular picture of Einasto, Jôeveer & Saar (1980) is correct, the voids should be looked upon as the basic units of large-scale structure (e.g. Geller & Huchra 1989). This is a dramatic turnaround from the approach of investigators who, 15 years ago, were looking at superclusters as the largest coherent structures in the universe and thus as the basic units of very large-scale structure. Indeed, it is now rather uncertain as to what is, or isn't, a supercluster. Though the definition of Einasto, Jôeveer & Saar (1980) of a supercluster as a cell wall is a good working basis, it hasn't been widely adopted. In his review of superclusters, Oort (1983) admits that the term is subjective and used rather loosely.

It is easy to see that in the context of a hierarchical model of structure formation, the supercluster is a logical continuation of the sequence of galaxy to galaxy cluster.

Whereas galaxies are gravitationally bound systems of stars and clusters are gravitationally bound systems of galaxies, it is not obvious that a supercluster is a gravitationally bound system of clusters. Even if it is bound, then it is definitely not relaxed and it is in some ways counter-productive to look at superclusters in the same light as galaxies and galaxies clusters. Most superclusters are probably no more than loose associations of clusters and groups of galaxies, and as such the term supercluster becomes a useful label for a visual concentration of galaxies on the sky, rather than any fundamental building block of very large-scale structure. Instead the emphasis would be much better placed on the cellular nature of the universe, on the topology of the cells and on the fundamental unit of that structure, the void.

However, it is also quite hard to rigorously define a void. Though the voids are striking features in all of the wide-angle redshift surveys, they are not totally devoid of galaxies. This makes it quite difficult to unambiguously define a void. In the terms of a cellular model, such as that of Einasto, Jôeveer & Saar (1980), a void is a clearly defined topological feature, but in reality galaxies are not ideal tracers of the cellular structure as they do not provide a continuous medium. Perhaps the best way to define a void is to use a counts-in-cells approach (de Lapparent, Geller & Huchra 1991) — galaxies are counted in cells of a fixed volume and a void is defined as a contiguous group of cells with counts below a certain threshold. Care must be taken not to make the volume so large as to span across walls, nor too small so as to split walls into discontinuous strips.

Trying to define statistical properties of voids is similarly fraught with difficulty. Linear sizes of voids vary from $20 - 50\,h^{-1}$ Mpc (de Lapparent, Geller & Huchra 1991), though this upper limit is probably set by the size of the survey. Both da Costa *et al.* (1989) and Kirshner *et al.* (1987), in surveys that go deeper than the CfA extension, find voids of linear size $\sim 60\,h^{-1}$ Mpc.

As the voids are not completely empty of galaxies a useful statistic is the density contrast, defined as the ratio of the galaxy density in the void to the mean density. Despite wide variations in the mean density between surveys the density contrast of voids is remarkably stable at ~ 0.2 (de Lapparent, Geller & Huchra 1986; Kirshner *et al.* 1987; da Costa *et al.* 1989), suggesting that the formation and evolution of voids is a universal process that depends only weakly, if at all, on size and environment. However, one caveat must be added. Though the density contrast of 0.2 is obtained for three

separate surveys no investigation of density contrast with void size is made for voids within an individual survey. As each survey is dominated by its largest voids [and in the case of the Boötes void survey of Kirshner *et al.* (1987), only one void], it is possible that this global density contrast relates only to large voids and there is in fact a trend of density contrast with void size that is masked by the dominance of the larger voids. A complementary statistic, the filling factor, measures the amount of space occupied by the geometric structure. This was calculated by de Lapparent, Geller & Huchra (1991) for the CfA survey and found to be $\lesssim 25 \pm 5\%$ for galaxies, leaving $\gtrsim 75 \pm 5\%$ of the volume in voids.

The statistical properties of walls are similarly ill defined. Global properties such as length and height are hard to measure as an individual wall only bounds a single cell in the picture of Einasto, Jôeveer & Saar (1980) whereas observed structures such as the "Great Wall" are highly likely to be composite entities made up from the chance alignment of the walls neighbouring cells, rather than fundamental structures in their own right. However, the width of a wall does not provide such problems and it has been found that the majority of walls have a full width half maximum (FWHM) of $\lesssim 500\,\mathrm{km\,s^{-1}}$ (de Lapparent, Geller & Huchra 1991). The width is given in terms of redshift space as peculiar velocity effects may conspire to make walls look thinner than they actually are due to infall of galaxies onto the walls. However, independent distance estimates based on the infrared Tully–Fisher technique have demonstrated that the structure seen in redshift space is very close to that seen in real space (Geller & Huchra 1988) and so peculiar velocities are unlikely to cause serious distortion. Ignoring possible peculiar velocity effects, the walls thus have a FWHM of only $5\,h^{-1}\,\mathrm{Mpc}$, remarkably thin given the physical extent of the walls and the voids they bound.

Another statistical measure, akin to the density contrast of voids, is the surface density of walls. Again this is roughly constant as measured by de Lapparent, Geller & Huchra (1991) in three of the 6° slices of the CfA extension. They found that the surface density of galaxies varied from 0.25 to 0.44 galaxies per $h^{-2}\,\mathrm{Mpc}^2$ across the three slices, although they made no attempt to calculate the surface density of individual walls in each slice to check for possible variations with surface area. Again, this is made difficult by the problems associated with identifying individual walls.

While the plane-like nature of the structures in the CfA survey (de Lapparent,

Geller & Huchra 1986; Geller & Huchra 1989) and the SSRS (da Costa *et al.* 1988; 1989) is well established, as is the filamentary nature of the superclusters (e.g. Einasto, Jôeveer & Saar 1980; Gregory, Thompson & Tifft 1981), the assertion by Einasto, Jôeveer & Saar (1980) that rich clusters lie at the intersection of filaments is still unproven. Though Geller & Huchra (1988) find that rich clusters such as Coma lie at the intersection of several "bubbles" (their term for cells) in the CfA surveys, da Costa *et al.* (1989) do not find this to be the case in the SSRS, being unable to match the location of several Abell clusters within their survey volume with regions where walls and filaments intersect. However, as both sets of authors point out, there is little overlap in scales between galaxy and cluster surveys. Rich clusters are rare objects and thus one would not expect comparatively small surveys such as the CfA or SSRS to contain many such clusters. Furthermore, as the surveys only go to the relatively bright limit of $m_{B(0)} \lesssim 15.5$, it may be that such clusters are not prominent unless they are very close (e.g. the Coma cluster). Until deeper surveys become available it is hard to validate the claim.

Another feature is the topology of large-scale structure. Gott, Melott & Dickinson (1986) have argued that for structure arising from inflation-generated perturbations and growing under the influence of gravity, the structure on scales larger than the characteristic clustering scale, ought to be "sponge-like". By this they mean that both high and low density regions (defined with respect to the median, rather than mean, density) are interconnected in a continuous manner. They have demonstrated this is the case for both hot and cold dark matter dominated universes as well as for those with Poissonian initial conditions. At first sight a cellular model, such as the one proposed by Einasto, Jôeveer & Saar (1980), does not fulfill this criteria, with isolated voids being completely surrounded by continuous cell walls. However, as Gott, Melott & Dickinson demonstrated, gravitational clustering within cell walls is capable of creating sizeable holes in the walls which allow the voids to become interconnected without destroying the continuous nature of the cell walls. Such a structure also has a sponge-like topology.

A further question is that of the symmetry between high and low density regions. Gott, Melott & Dickinson have argued that for the scenarios described above, high and low density regions should be symmetrical (i.e. if one were to call high density regions low density and low density regions high, then there would be no change in the ensemble properties). This may rule out a cellular model if the walls are very thin compared to the width of the voids. In such a situation there would be a distinct asymmetry between

high and low density regions, with the voids encompassing the majority of the volume. One caveat should be added — though the CfA survey has a filling factor of $\simeq 75\%$ for voids (de Lapparent, Geller & Huchra 1991), a smaller, volume-limited subset of the survey was shown to have a sponge-like topology (Gott, Melott & Dickinson 1986). This is probably due to the fact that the median density is lower than the mean density, due to the effects of non-linear clustering on small scales.

1.4.4 The Local Supercluster

If the preceding concept of a cellular universe is correct, then where does our Galaxy fit into the structure? Evidence of a cellular structure ought to be present in our local ($\lesssim 25\,h^{-1}$ Mpc) environment. In fact, it seems as if we are located in a cell wall, which [somewhat fortuitously, perhaps, though see Flin & Godlowski (1989) for a possible explanation] lies perpendicular to the plane of our Galaxy. Astronomers have been aware of the existence of the local supercluster (or supergalaxy, as our cell wall is termed) for some time. Just as the disk of stars that go to make up our own Galaxy cast a dense strip of stars (known as the Milky Way) across the night sky, so the galaxies of the local supercluster cast a dense strip of galaxies across the sky. Such an excess of galaxies was noticed on deep photographic survey plates of the northern hemisphere by Holmberg (1937) who interpreted the strip as evidence of a disk of galaxies of which we were a member. Though Holmberg's findings were supported by Reiz (1941), it was not until the 1950s, with the advent of large numbers of redshifts, that the reality of the local supercluster was well established.

de Vaucouleurs (1956, 1958) found the local supercluster to be a highly flattened, symmetric disk, centred on, or near to, the Virgo cluster. Virgo, the nearest rich cluster to our own Galaxy, lying some $10-15\,h^{-1}$ Mpc away, was assumed to be the dynamical centre of the supercluster. de Vaucouleurs (1956) estimated that the disk had a diameter of $25-30\,h^{-1}$ Mpc and a thickness of $2-4\,h^{-1}$ Mpc. More recent observations, especially those by Tully (1982), show that the morphology of the local supercluster is considerably more complicated and though it has the form of a flattened disk as proposed by de Vaucouleurs (1956, 1958), it is certainly not the symmetric structure he proposed, nor is it at all obvious that it is centred on the Virgo cluster.

It is clear from the evidence presented by Tully (1982) that our Galaxy lies in

a highly flattened plane (of axial ratios 6:3:1), which is bounded at one edge by the Virgo cluster and the Virgo chain, the latter a prolate structure running from the Virgo cluster along the edge of the plane, with an axial ratio of 10:1 and a linear dimension of at least $14\,h^{-1}$ Mpc (Oort 1983). This fits well with the cellular model of Einasto, Jôeveer & Saar (1980), where the cell walls are bounded by filamentary structures. Further evidence comes from Tully (1982), who proposes a two component model for the local supercluster. His model consisted of a flattened disk containing $\sim 60\%$ of the galaxies plus a roughly spherical halo containing the remaining $\sim 40\%$. However, the distribution of galaxies off the plane is not smooth. In fact it is the direct opposite, with virtually all the galaxies belonging to "clouds" (groups), so that the vast majority of space off the plane is empty. Further more he finds that these groups are prolate in structure and point towards the Virgo cluster, which suggests, in the interpretation of Einasto, Jôeveer & Saar (1980), that they too are filaments. If this is the case then the Virgo cluster should be seen as the focus of the structure. Even though it is apparent that the Virgo cluster is not at the centre of the disk, as was thought by de Vaucouleurs (1956, 1958), it is still the centre of some sort of structure, as suggested by Tully (1982), who found that the number counts of luminous galaxies (averaged over all solid angles) fall off as $1/r_{\rm V}^2$, where $r_{\rm V}$ is the distance of the galaxy from the Virgo cluster.

1.4.5 Beyond the local Supercluster

It is possible to trace the cellular structure out beyond the local supercluster. As well as the early work of Einasto, Jôeveer & Saar (1980), others have found connections between the local supercluster and other superclusters. Haynes & Giovanelli (1986) show that the local supercluster is linked to the Perseus–Pisces supercluster by two cell walls. They also show that the Perseus–Pisces supercluster itself is probably a wall at a distance of $40 - 65\,h^{-1}$ Mpc with a large foreground void between us and it. The Perseus and Pisces clusters lie at opposite corners of the wall and the Perseus chain (Einasto, Jôeveer & Saar 1980) forms the filament bounding the top of the wall. Tago, Einasto & Saar (1984) also find two filamentary structures joining the Virgo region to the Coma–A1367 supercluster, with one filament going to each end of the supercluster, itself filamentary in nature. It may well be that along with the Virgo chain (Oort 1983), this delineates another wall on the far side of Virgo, beyond the local supercluster.

Tully (1986), extending his work on the local supercluster, also finds further evidence that the local supercluster is part of a cellular structure by finding roughly parallel cell walls above and below (in SGZ coordinates) the local supergalactic plane. These walls are connected to the local supercluster by filamentary structures that point towards the Virgo cluster, supporting the claims of Tago, Einasto & Saar (1984) and Haynes & Giovanelli (1986). Both Tago, Einasto & Saar (1984) and Tully (1986) also claim that the local supercluster and associated superclusters form an extended network encompassing the whole survey volume, a feature which is expected if there is a continuous cellular network as proposed by Einasto, Jôeveer & Saar (1980).

1.4.6 Theoretical Implications

The observed cellular nature of the universe poses many theoretical questions and obviously any theory of large-scale structure has to be able to explain such a network of cells. Early theoretical and modelling work seemed to favour scenarios based on adiabatic ("top down") rather than isothermal ("bottom up") fluctuations (§ 1.3.1), due to the former's ability to form large-scale structures such as cells, walls and voids (e.g. see Einasto, Jôeveer & Saar 1980; Gregory, Thompson & Tifft 1981; Frenk, White & Davis 1983). However, as time went on, so the "top down" models, by then characterised by hot dark matter models (§ 1.3.2), fell into disfavour, to be replaced by cold dark matter models (§ 1.3.2). This was mainly due to the late formation of galaxies in a hot dark matter universe, since galaxies were unable to form until after the formation of the first pancakes. However, observations of high redshift galaxies seemed to indicate a much earlier epoch of galaxy formation, which has been used as evidence to rule out adiabatic and hot dark matter models (e.g. White, Frenk & Davis 1983; Frenk, White & Davis 1983).

There was much debate during the 1980s as to whether cold dark matter models could actually produce a cellular structure with sufficiently large voids. However, as both numerical techniques and computing power improved, several authors showed that large voids were a generic feature of cold dark matter dominated universes in both N-body simulations (e.g. White *et al.* 1987; Park 1990) and in simulations based on the adhesion model (e.g. Weinberg & Gunn 1990a,b). More recent work, using improved modelling techniques and larger volumes, have also led to a revival of hot dark matter

dominated universe models (e.g. Melott 1987; Centrella *et al.* 1988), suggesting that they too can produce large voids without violating other observational constraints as was previously thought, most notably the problem of late galaxy formation. However, Zeng & White (1991) claim that hot dark matter models produce voids that are too large in comparison to observations, thus casting further doubt on the model.

When the cellular nature of the large-scale structure was first observed, it was hoped that it would prove to be a powerful discriminant between various classes of model. However, as has been shown, this early optimism seems to have been misplaced as both "top down" and "bottom up" models have proved capable of producing cellular distributions of galaxies. The situation is further complicated by the presence of topological defects (§ 1.3.4), which act as seeds in hot or cold dark matter models, and the explosion model (§ 1.3.5), which was specifically put forward to account for the large voids in the galaxy distribution. Rather than narrow down the range of available models, the discovery of the cellular nature of the galaxy distribution seems to have had the opposite effect, stimulating theorists both to refine current models and produce other, more exotic models, in the attempt to explain the observed cellular structures.

One immediately striking feature of the cellular nature of the universe is the extreme segregation of the luminous matter, which is concentrated into very small volumes. However, it must be stressed that the luminous matter may well be a small and, perhaps, unrepresentative sample of the total mass of the universe. If the universe is dominated by dark matter (§ 1.2.4, 1.3.2) then it is not obvious that the luminous and dark matter will share the same distribution. If light does not trace mass then it is possible that the underlying dark matter distribution is considerably less segregated than the luminous matter. It was found in numerical models used to simulate both hot and cold dark matter dominated universes that the voids were overpopulated with galaxies. However, if galaxies were restricted to forming in high density regions this problem was overcome, thus providing qualitative support that light does not trace mass. Such a concept is known as biased galaxy formation (§ 1.3.3) and has proved highly successful in both hot (Melott 1987; Centrella *et al.* 1988) and cold (Melott 1987; White *et al.* 1987) dark matter universes, though it should be stressed that no natural mechanism has been found to suppress galaxy formation in underdense regions (or, alternatively, trigger galaxy formation in high density regions). An alternative is for simulations to allow the evolution of structure to continue for longer. This allows the voids to naturally

empty of all matter, thus reducing the need for bias (e.g. Couchman & Carlberg 1992). However, this then requires larger initial perturbations which may exceed the microwave background constraints (§ 1.3.2).

Scenarios such as the explosion model (§ 1.3.5) provide a natural way for such a segregation, either by sweeping the voids totally empty of matter, or, more likely, by providing natural sites for galaxy formation at the points where shock fronts collide. However, it should be pointed out that there are doubts as to whether the explosion model can produce sufficiently powerful explosions to create voids of the size observed.

1.5 Outline of the Thesis

The remainder of this thesis is laid out as follows. Chapter 2 gives details of the two computational models used in this work, the adhesion model and the Voronoi foam, as well as a discussion on modelling large-scale structure in general. Physical motivations for the Voronoi foam model are proposed, based on models discussed in § 1.3.

Chapter 3 seeks to test the validity of approximations based on the linear theory principle of smoothing the non-linear density field in order to locate bound objects. The underlying theory is developed and the resulting mass and correlation functions predicted by linear theory are compared with those calculated from one-dimensional simulations using the adhesion model. By restricting the simulations to one spatial dimension, a large mass range is achievable and advantage is taken of the fact that the adhesion model is exact in one dimension. Also tested is the underlying assumption that bound objects form in regions where the one-dimensional density contrast is roughly unity.

Chapter 4 implements the Voronoi foam in two and three dimensions, using two different approaches, the geometrical and kinematical methods. The various parameters of the kinematical method are explored and optimised for simulations used in subsequent chapters. A comparison is made between the geometrical and kinematical methods in two dimensions in order to check the validity of the latter. Also, the framework of the analysis techniques to be used in subsequent chapters are laid down.

Chapter 5 compares the results from Voronoi foam simulations generated with randomly distributed nuclei to various observational measures of galaxy clustering in an

attempt to constrain the normalisation of the length scale of the foam. The measures used are the spatial two-point correlation function for both galaxies and clusters of galaxies and the angular two-point correlation function and the power spectrum of galaxy clustering. Also investigated is the use of the autocorrelation function (i.e. the Fourier transform of the power spectrum) as an alternative to estimating the correlation function via counts of pairs.

Chapter 6 presents an investigation into the use of clustered nuclei in the Voronoi foam. The clustered nuclei are selected from peaks in a gravitational potential, which gives a physical motivation to the distribution of the nuclei. The simulations are compared to the observed galaxy clustering, in order to constrain the various combinations of potential and peak threshold available, as well as the normalisation of the length scale.

Chapter 7 uses the Voronoi foam (with random nuclei) to explain the observed phenomena of cluster alignment, showing it to be a natural feature of cellular models. An attempt is made to model observational uncertainties to see if the alignment strengths present in the Voronoi foam are compatible with those observed.

Finally, Chapter 8 presents the conclusions drawn from the preceding chapters and discusses possible future developments.

Chapter 2

Modelling Large-Scale Structure

2.1 Introduction

2.1.1 Introduction

The aim of modelling large-scale structure is, for a given set of initial conditions, to predict the distribution of matter at the current epoch. Unfortunately the problem is not straightforward. Though on very large scales gravity is the only force that need be considered, the situation is only simple as long as perturbations are small. Once the perturbations grow to a reasonable size (a density contrast, $\delta \sim 1$, see Appendix B), non-linear effects become important and situation is very complex and no longer easily tractable. On small scales, the physical processes that govern galaxy formation are poorly understood. Though one would hope that the process of galaxy formation might be divorced from that of large-scale structure and hence the two could be dealt with separately, this is an untested assumption. There may well be feedback from the process of galaxy formation that disrupts the environment on large scales. Alternatively, the large-scale environment may affect galaxy formation (e.g. biased galaxy formation § 1.3.3, 1.4.6).

A further problem is that most modelling and simulations deal with the distribution of the mass. Unfortunately most observations are constrained to look at the distribution of the luminous matter, which may or may not trace the underlying mass distribution. This makes the understanding of the processes of galaxy formation necessary to convert the underlying mass distribution into a luminous matter distribution that can be compared to the observations. There is also a problem of scale. To adequately model a sufficiently large volume of space in order to obtain a representative sample of the universe (at least $10^6\,h^{-3}\,\mathrm{Mpc}^3$; § 1.4) requires a coverage of several orders of magnitude in both mass and length, from that of galaxies ($\sim 10^{11}\,\mathrm{M}_\odot$, few 10s kpc), to that of cells ($\sim 10^{15}\,\mathrm{M}_\odot$, few 10s Mpc). To accurately model such a wide range of scales can cause serious problems, especially for computationally-based models (§ 2.1.2).

2.1.2 Direct and Indirect Methods

The distinction shall be made here between "direct" and "indirect" methods. Direct methods are those which aim to take the initial conditions and use them directly to predict the statistical properties of the final distribution, whereas indirect methods use the notion of tracers of the distribution and follow their evolution from the initial to the final distribution. The statistical properties are then calculated from the final distribution of the tracers rather than being inferred directly from the initial conditions. The practical difference between direct and indirect methods is that the former are statistical in nature and the latter are iterative and frequently computational in nature.

A good example of a direct method is the Press–Schechter mass function used in Chapter 3 (Press & Schechter 1974). The basic method is to evolve the initial density field (generated according to some given initial conditions; § 1.3) analytically using linear theory well into the non-linear regime and then to regain a linear density field by *smoothing* the non-linear density field with some window function (§ 3.2). Regions with a density contrast equal to a critical value in the smoothed field are identified with objects of a mass given by the size of the window function. If the analysis is restricted to Gaussian density fields (which can be totally described by the power spectrum) then the properties of the density field and the smoothing process can be described analytically and a formula derived that gives the mass function directly from the initial power spectrum (e.g. equation 3.1).

The most familiar indirect technique is the N-body simulation. Here particles are used to map out the mass distribution and are distributed in accordance with a given set of initial conditions (§ 1.3). The gravitational force on each particle is calculated for every other particle in the simulation and each particle is then moved by a small amount. This process is then repeated, step by step, until some condition(s) is (are) met, when the simulation is halted. The particles are usually taken to represent the final positions of galaxies, but often some thresholding principle is applied to prevent galaxies forming in low density regions (i.e. biased galaxy formation, § 1.3.3). The statistical properties of the final "galaxy" distribution are then calculated.

The advantage of the direct methods over the indirect methods is that they are freed from the limitations placed on the indirect techniques by the finite nature of computer processing speed and memory. Thus they can cover the large range of parameter

space needed to provide a fair sample. In contrast, the indirect methods can be severely hampered by the computing requirements. For example, in very large N-body simulations the mass of an individual particle is often much greater than the mass of an individual galaxy, making an identification of particles with galaxies at best a statistical one. Furthermore, it is made very difficult to identify the effect of galaxy formation on large-scale structure. Similarly, N-body simulations can be used to model the formation of individual galaxies or even clusters of galaxies, including (to a limited extent) the effects of hydrodynamics, but these necessarily cannot include any information about the evolution of the large-scale structure in which they would be embedded. More recently large-scale hydrodynamical N-body simulations have been developed, but their treatment of hydrodynamical processes is still very crude (e.g. see Centrella *et al.* 1988; Cen *et al.* 1991 and references therein).

The one big disadvantage of the direct methods is that they cannot accurately deal with the evolution of structure. Instead they must replace very complex physical processes with some very simple, partially physical, prescription such as smoothing. This is not to be taken to imply that indirect methods can accurately model all the processes involved in large-scale structure and galaxy formation, but a better attempt can be made to model these processes rather than replacing them with an ad hoc prescription. One of the aims of this thesis is to see whether the approach of the direct methods, that of smoothing the non-linear density field, is valid in comparison to a fuller treatment of the problem with an indirect method, the adhesion model (§ 2.2; Chapter 3).

The other aim of the thesis is to take the "Voronoi foam" model (§ 2.3; Chapter 4), which uses a very simple prescription to give the location of galaxies and which straddles the border between direct and indirect methods, and see if it is capable of reproducing various statistical measures of the observed galaxy distribution (Chapters 5 – 7).

2.2 The Adhesion Model

2.2.1 Introduction

The adhesion model is a fully non-linear description of gravitational perturbations, based on Burgers' equation (Burgers 1940, 1974). The use of Burgers' equation and the adhesion model in connection with the problem of large-scale structure has been widely

discussed in the literature (e.g. Gurbatov, Saichev & Shandarin 1985, 1989; Shandarin 1987; Kofman, Pogosyan & Shandarin 1990; Nusser & Dekel 1990; Weinberg & Gunn 1990a,b). Burgers' equation is also used extensively in the field of fluid dynamics, where it originated (e.g. Burgers 1950a,b,c,d, 1972; Tatsumi 1969; Tatsumi & Kida 1972; Kida 1979).

The adhesion model can be viewed as an extension of the well-known Zel'dovich approximation (Zel'dovich 1970) where particles' peculiar velocities are determined by the initial gravitational potential. This describes the particle motion up to the point where the trajectories cross, which is where the approximation starts to break down. The adhesion model introduces the notion of "sticky" particles which allows the model to progress beyond this point. Instead of particle trajectories crossing, the particles collide and stick together, moving in a manner that conserves momentum. This allows the formation of bound structures in the form of thin walls. Where these walls intersect, they form string-like filaments and where the filaments intersect, they form point-like nodes.

2.2.2 Basics of the Adhesion Model

The simulations used in Chapter 3 are based on the adhesion model which leads to Burgers' equation. The adhesion model as implemented here was first presented in a paper by Gurbatov, Saichev & Shandarin (1989) and for a full derivation the reader is referred to that paper. Here only the most important parts of the derivation are reproduced.

The model is based on the equations describing the evolution of density inhomogeneities in an expanding dust-like medium in co-moving coordinates. These are (Peebles 1980)

$$\frac{dV_i}{dt} + \frac{\dot{a}}{a}V_i = -\frac{1}{a}\frac{\partial\phi}{\partial x_i}, \tag{2.1}$$

$$\frac{\partial^2\phi}{\partial {x_i}^2} = 4\pi G a^2[\rho(x_i,t) - \rho_b(t)], \tag{2.2}$$

$$\frac{\partial \rho}{\partial t} + 3\frac{\dot{a}}{a}\rho + \frac{1}{a}\frac{\partial}{\partial x_i}(\rho V_i) = 0, \tag{2.3}$$

where the peculiar velocity, V_i, is given by

$$V_i = a\frac{dx_i}{dt}, \tag{2.4}$$

for comoving coordinates $x_i = r_i/a$. r_i is the Eulerian coordinate, ϕ is the perturbation of the gravitational potential, $a(t)$ is the scale factor (the dot signifies the time derivative), ρ the density and ρ_b the mean density.

The Zel'dovich approximation is given by

$$x_i = q_i + b(t) \cdot s_i(\mathbf{q}), \tag{2.5}$$

where x_i and q_i are comoving Eulerian and Lagrangian coordinates respectively, $b(t)$ is a function describing the time evolution of the growing mode of gravitational instability in the linear approximation (for $\Omega \approx 1$, b is equivalent to the scale factor, a) and $s_i(\mathbf{q})$ is the potential vector field :

$$s_i(\mathbf{q}) = \frac{\partial \Phi_0(\mathbf{q})}{\partial q_i}, \tag{2.6}$$

which describes the spatial structure of the gravitational perturbations in the linear stage. Φ_0 is proportional to the initial gravitational potential and it is related to ϕ as follows :

$$\phi = 3\ddot{a}ab \cdot \Phi_0(\mathbf{q}). \tag{2.7}$$

By assuming that the Zel'dovich approximation is valid outside any structure, one can use it to explicitly calculate the acceleration for every point in the fluid. By defining a new set of variables,

$$v_i(x_i,t) = \frac{1}{a\dot{b}} V_i(x_i,t), \tag{2.8}$$

$$\eta(x_i,t) = a^3 \rho(x_i,t), \tag{2.9}$$

and using the Zel'dovich approximation, one obtains the following set of equations describing the time evolution of the peculiar velocity and density :

$$\begin{aligned} \frac{\partial v_i}{\partial b} + v_k \frac{\partial v_i}{\partial x_k} &= 0, \\ \frac{\partial \eta}{\partial b} + \frac{\partial (\eta v_i)}{\partial x_i} &= 0. \end{aligned} \tag{2.10}$$

Thus the Zel'dovich approximation is equivalent to the fluid mechanics of a perfect inviscid fluid. The approximation therefore reveals nothing about the evolution of density after the formation of structure (i.e. after orbit crossing in the Zel'dovich approximation).

The adhesion model is an attempt to extrapolate the Zel'dovich approximation into the non-linear regime. To do this "sticky" particles are used. Though the model is expressed in terms of a continuous medium, it useful to think of it in terms of individual particles that move with the fluid. Every particle moves in accordance with the first equation in (2.10) until it runs into another particle, whereupon the two particles "stick" and move together with a common velocity that conserves momentum. In the case of a continuous medium, this can be described mathematically by inserting a viscous term in the first equation in (2.10), giving :

$$\frac{\partial v_i}{\partial b} + v_k \frac{\partial v_i}{\partial x_k} = \nu \frac{\partial^2 v_i}{\partial {x_k}^2}. \tag{2.11}$$

The form of the viscous term chosen leads to an equation analogous to Burgers' equation (Burgers 1940, 1974), which has a well-known analytic solution.

For the study of large-scale structure only potential motions need be considered, as in linear theory the growing mode is curl-free. Introducing a velocity potential related to the velocity field as

$$v_i(\mathbf{x}, b) = -\frac{\partial \Phi(\mathbf{x}, b)}{\partial x_i}, \tag{2.12}$$

one may solve equation (2.11). Note that this is the opposite sign convention to that taken by Gurbatov, Saichev & Shandarin (1989). The exact solution is given in terms of the usual diffusive Green's function (Gurbatov, Saichev & Shandarin 1989) :

$$v_i(\mathbf{x}, b) = \frac{\int \frac{x_i - q_i}{b} \exp[-\frac{1}{2\nu} G(\mathbf{x}, \mathbf{q}, b)] d^3q}{\int \exp[-\frac{1}{2\nu} G(\mathbf{x}, \mathbf{q}, b)] d^3q}, \tag{2.13}$$

where

$$G(\mathbf{x}, \mathbf{q}, b) = \frac{(\mathbf{x} - \mathbf{q})^2}{2b} - \Phi_0(\mathbf{q}), \tag{2.14}$$

which differs from the expression given by Gurbatov, Saichev & Shandarin (1989) only in the sign of Φ_0.

In the limit $\nu \to 0$, the main contribution to the integrals in equation (2.13) comes from the region where $G(\mathbf{x}, \mathbf{q}, b)$ has a minimum with respect to q. In this case it can be shown that equation (2.13) simplifies to

$$v_i(\mathbf{x}, b) = \frac{x_i - q_i(\mathbf{x}, b)}{b}, \tag{2.15}$$

where $q_i(\mathbf{x}, b)$ is the coordinate of the absolute minimum of $G(\mathbf{x}, \mathbf{q}, b)$ at given $\mathbf{x}$ and b, provided that this is a non-degenerate case.

While the adhesion model has been derived for the full three-dimensional case, it has been decided to restrict its use to one dimension. The benefits of this are two fold. The first is that in one dimension the adhesion model is both simple to implement (§ 2.2.3, 2.3.4) and exact. In higher dimensions, the initial gravitational potential becomes an approximation to the true gravitational potential at late times, whereas in one dimension the initial potential remains valid at all times. The implementation of the geometric method is also straightforward in one dimension, but becomes increasingly complex in two or three dimensions. Indeed, workers using the adhesion model in three

dimensions use a different method of implementing the model, based on the evolution of the gravitational potential (e.g. Weinberg & Gunn 1990a,b).

The second benefit is the dynamic range that can be covered in one dimension. The adhesion model is used in this thesis as a comparison to the linear theory approximations, which by their very nature (§ 2.1.2) can span a wide range of parameter space. Thus, in order for a fair comparison to be made, the adhesion model needs to cover a similarly large range. The one-dimensional adhesion model simulations used in Chapter 3 cover three to four orders of magnitude in mass, whereas the same sized simulation (in terms of the limiting factor, computer memory) in three dimensions would cover only around an order of magnitude in mass.

2.2.3 Geometrical Solution of the Adhesion Model in One Dimension

Restricting the analysis to one dimension, the condition that equation (2.15) is a solution of equation (2.11) is that the function $G(x, q, b)$ (equation 2.14) has a minimum with respect to q at the point $q_i(x, b)$, which leads to the condition

$$x = q_i - b\frac{\partial \Phi_0}{\partial q}\bigg|_{q_i}. \tag{2.16}$$

It is now possible to "solve" equation (2.16) using a geometrical technique. Though this is derived here in one dimension, it is possible to extend it to higher dimensions (Gurbatov, Saichev & Shandarin 1989). If one wishes to find the Eulerian position of a particle whose Lagrangian position is q_t, one can do so by constructing a parabola, P, where

$$P = h + \frac{(x - q)^2}{2b}, \tag{2.17}$$

(h is a constant) and require it to be tangential to the potential $\Phi_0(q)$ at q_t. It shall be shown that x is then the Eulerian position of the particle at a time characterised by the function $b(t)$. The condition that the parabola is tangential to the potential requires

$$\frac{\partial P}{\partial q}\bigg|_{q_t} = \frac{(q_t - x)}{b} = \frac{\partial \Phi_0}{\partial q}\bigg|_{q_t}, \tag{2.18}$$

and hence

$$x = q_l - b\frac{\partial \Phi_0}{\partial q}\bigg|_{q_l}. \tag{2.19}$$

By comparing equations (2.16) and (2.19) it can be seen that $q_l = q_i$ is also a solution of equation (2.11) with the Eulerian position, x, given by equation (2.19), i.e. the solution of equation (2.11) is the minimum of the parabola.

It can also be seen by comparing equation (2.18) with equation (2.15), which gives the velocity of a particle at the point x, that the velocity is given by the gradient of the potential, i.e.

$$v(x, b) = -\frac{\partial \Phi_0}{\partial q}\bigg|_{q_l}. \tag{2.20}$$

Thus for a given time, characterised by $b(t)$, the parabola, P, is a solution to equation (2.11) in the limit $\nu \to 0$ and gives both the position (bottom of the parabola) and velocity (negative of the gradient of the potential) of a particle with Lagrangian coordinate q_l. It is therefore possible to take every point in Lagrangian space and calculate its Eulerian position and velocity at a time characterised by $b(t)$, simply by constructing a parabola tangential to the parabola at that point.

So far this is nothing more than the Zel'dovich approximation. For early times $b(t)$ will be small and there is a one-to-one correspondence between points in Lagrangian and Eulerian space. As $b(t)$ increases, so the parabola broadens and there will come a time where a parabola will satisfy the condition in equation (2.18) at more than one point in Lagrangian space and hence the solution in equation (2.19) is no longer unique.

Looking at Fig. 2.1, it is obvious that matter at both the Lagrangian points q_1 and q_2 will have simultaneously arrived at the point x, bringing with it all the matter in between to form a single object (generically known as a "pancake") at x. In three dimensions the geometrical technique is very similar. Here a paraboloid is fitted to the potential and this may touch the potential once (matter does not come into contact with any other matter), twice (matter collapses along an axis to form a pancake), three times

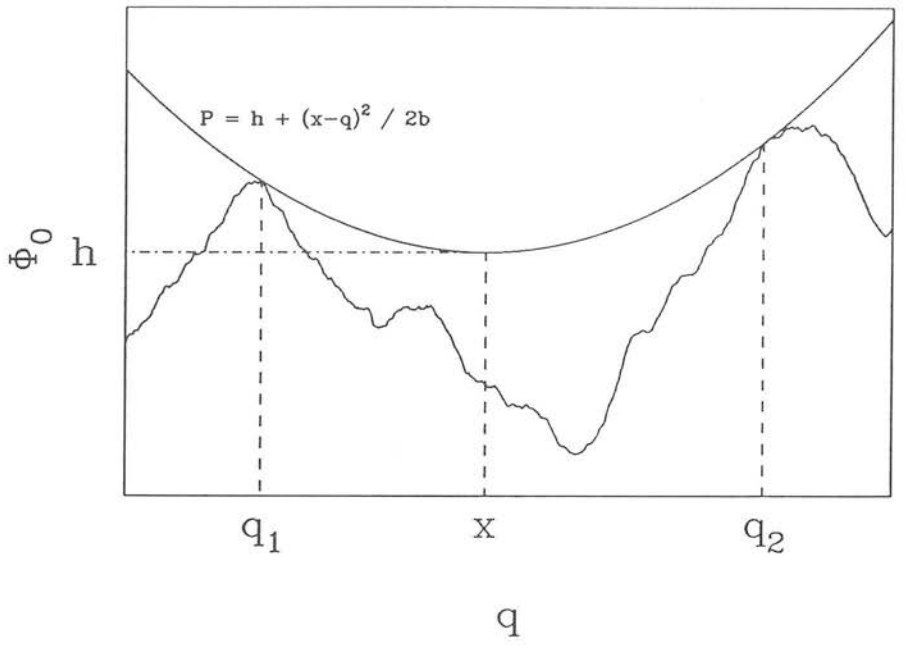

Figure 2.1 Demonstration of the graphical solution to the adhesion model. The parabola P touches the gravitational potential, Φ_0, at two points, q_1 and q_2. As the parabola does not intersect the potential at any point, particles at q_1 and q_2 would both simultaneously end up at the bottom of the parabola, x. In one dimension it is obvious that all matter between these two points must also end up at x.

(pancakes intersect to form filament–like structures) or four times (filaments intersect to form nodes).

In one dimension only the single- or double-touching cases are possible. Though the parabola can simultaneously touch the potential at three points this is just a more complicated version of the double-touching case representing the merging of two pancakes, both pancakes ending up as a single entity at the bottom of the parabola.

As a result of the simplification of allowing $\nu \to 0$, the adhesion model reveals nothing of the internal structure of objects formed. In three dimensions the pancakes are of zero thickness, the filaments of zero radius and the nodes are point objects. In this way the adhesion model is quite close to the Voronoi foam model (§ 2.3) with its

cellular structure of walls (pancakes), filaments and nodes. Indeed, as will be argued, the Voronoi foam is a good late-time approximation to the adhesion model. In one dimension, all objects formed are point objects, completely specified by their location, mass and momentum.

One of the strengths of the adhesion model is that the above process can be carried out for any value of $b(t)$ without the need to refer to previous steps, thus avoiding the cumulative errors that may in principle arise in conventional N-body techniques.

2.2.4 Computer Simulations of the Adhesion Model in One Dimension

The simulations consist of an array holding the gravitational potential and its derivative which is sampled at a discrete number of points, equally spaced in Lagrangian coordinates. The potential and its derivative are generated by means of a fast Fourier transform of a specified power spectrum with random phase (§ 3.3.1). Boundary conditions are imposed such that the potential is periodic. Each of the points in the potential is designated either a "free" or "bound" point; "free" if the point has not yet been included in any pancake and "bound" if it has. The array is shifted so that the global maximum lies at the boundary of the array, with the first point of the array immediately to the right of the maximum and the last point of the array immediately to its left. It is obvious that the global maximum is always a free point.

The geometrical technique described in § 2.2.3 is used to locate the pancakes by looking for instances where a parabola is tangential to the potential at two separate points. The method consists of fitting a parabola, whose curvature is fixed for a given time by the parameter $b(t)$, tangentially to the potential, starting with the first point in the array. For each point all other points to the right are checked to see if the parabola intersects the potential once, more than once or not at all. If the parabola does not intersect the potential at any other point in the simulation then that point is free and the program moves on to the next point.

Due to the discrete nature of the potential it is never possible to tell if the parabola is tangential to the potential at any other point in the simulation. The approximation is therefore made that if the parabola intersects the potential at one, and only one, other point in the array then the parabola is tangential at that point. This then determines

the left-hand edge of the pancake in Lagrangian space.

If the parabola intersects the potential more than once then the point is bound. As the previous point is always free, the left-hand edge of the pancake in Lagrangian space lies between the bound point and the previous free point. The position of the edge is found more accurately by conducting a binary search using values of the potential and its derivative interpolated from the free and bound points. The search continues until the approximate condition that the parabola is tangential at some other point (described above) is met, which determines the position of the left-hand edge.

A further binary search is conducted, fitting a parabola tangentially to interpolated points in the region of the right-hand edge until the parabola is found to intersect the potential once and only once in the region of the left-hand edge. This fixes the position of the right-hand edge of the pancake. The program then resumes at the next point immediately after the right-hand edge of the pancake, as all intervening points are obviously bound.

The mass of the pancake is the linear distance between the two edges in Lagrangian space (i.e. the line density is set to unity) and the pancake's momentum is the difference between the values of the potential at the two edges. The location of the pancake in Eulerian space is taken to be the average of the positions of the bottoms of the two parabolae that accurately determine the left- and right-hand edges of the pancake in Lagrangian space. These differ only by a fraction of a grid point.

There are two simple ways of internally checking the program. One is to calculate the total mass of the objects and the free points. With unit line density this should be equal to the size of the simulation. The other check is to sum the momenta of the objects and the free points, which should come to zero.

2.3 The Voronoi foam

2.3.1 Introduction

The Voronoi foam is a simple statistical description of the distribution of galaxies in which they are confined to sheets, filaments and clusters surrounding voids. It is based on the Voronoi tessellation, a mathematical prescription in which space is partitioned

into polyhedral cells that fill all space. The tessellation is fully determined by the distribution of randomly placed nuclei, with each cell containing a single nucleus such that every point in space within the cell is closer to the enclosed nucleus than to any other. The tessellation is best described in two dimensions, where it can be drawn (Fig. 2.2). Each cell contains a single nucleus (shown an open circle), with the walls that bound the cells being located equidistant between two neighbouring nuclei. The points where the walls intersect are termed the nodes and are equidistant from the nuclei of the three neighbouring cells. In three dimensions the walls that bound the cells are located at the planes midway between adjacent nuclei and intersect to form filaments which in turn intersect to form nodes. Thus the walls are boundaries between two adjacent cells, the filaments boundaries between three cells (and hence are the lines where three walls meet) and the nodes boundaries between four adjacent cells (and hence are the points where four filaments meet). Note that the location of a node is uniquely determined as the node is equidistant from the four nuclei of the adjacent cells.

The Voronoi tessellation is the simplest of a family of tessellations (Voronoi 1908, Dirichlet 1850). Strictly speaking, the Voronoi foam refers to the distribution of galaxies on the geometrical skeleton of walls, filaments and nodes provided by the tessellation, but the two terms are often used interchangeably in the literature. However, in this thesis the term "Voronoi foam" shall refer specifically to the galaxy or particle distribution upon the geometric structure.

Thus the Voronoi foam can be seen as a very simple model. Like the indirect methods of § 2.1.2, it uses the idea of tracer particles to map out the large-scale structure, only here no attempt is made to model the evolution of the particles. The various methods of implementing the model are discussed in Chapter 4, along with various ways of distributing the particles on the walls. In general the particles are distributed in a pseudo-random fashion and serve only to map out the geometric structure provided by the tessellation. In this way the Voronoi foam resembles a direct method (§ 2.1.2) as it uses a simple prescription to provide the location of structure, though in this case it is based on simple mathematical rules rather than on some attempt to model a physical situation. However, it shall be argued (§ 2.3.2, 2.3.3) that the Voronoi foam approach is a valid late-stage approximation to several classes of model rather than simply being an ad-hoc prescription. Unlike the direct methods though, the final properties of the foam are not calculated directly from the initial conditions (i.e. the distribution of the

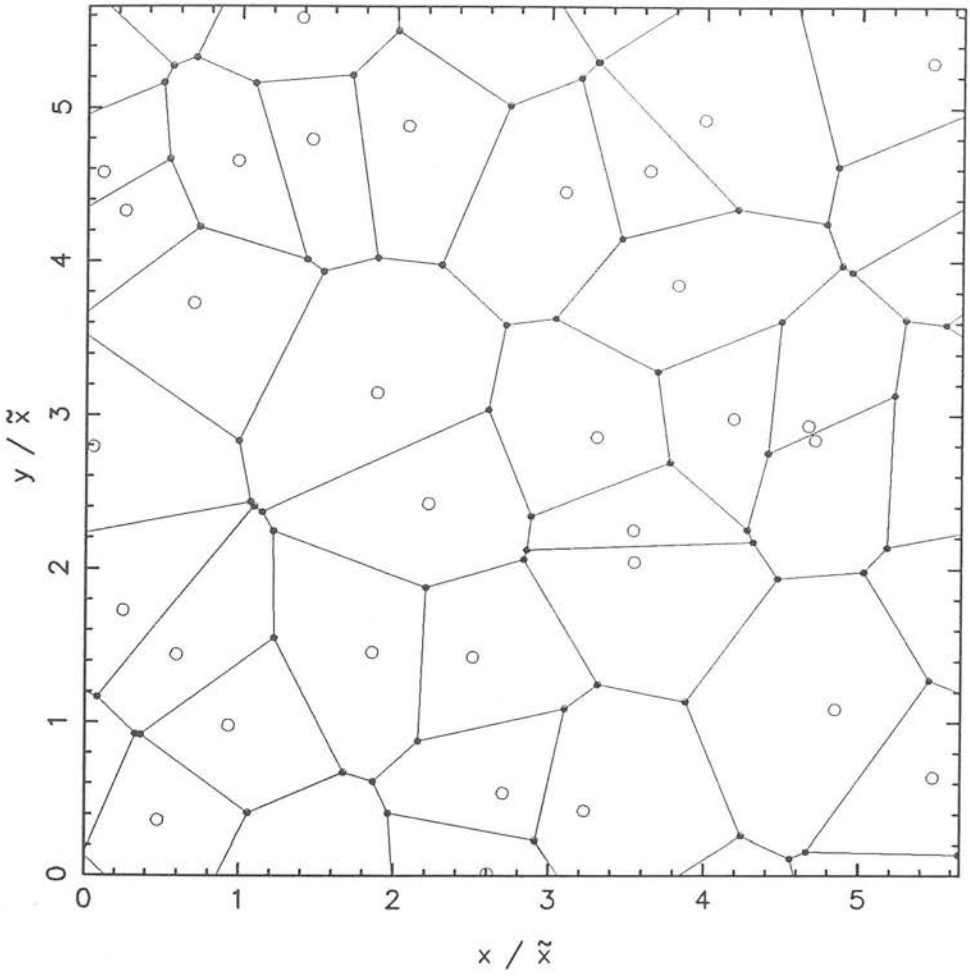

Figure 2.2 A two-dimensional Voronoi foam. The nuclei are denoted by the open circles, the walls by the solid lines and the nodes by the filled points.

nuclei), but from the final particle distribution.

2.3.2 Motivations behind the Voronoi foam

Voronoi tessellation has been widely used in fields as diverse as molecular physics, metallurgy, geology and forestry (cf. Meyering 1953; Miles 1970; Stoyan, Kendall & Mecke 1987). It was first used in astronomy by Kiang (1966) as a potential model for the fragmentation of molecular clouds into proto-stars, though it proved unable to produce

a realistic mass spectrum. The first to consider the application of the Voronoi foam to galaxy clustering were Matsuda & Shima (1984), who noticed the remarkable similarity between a two-dimensional Voronoi foam and N-body simulations performed by Melott (1983) for a neutrino dominated universe. However, they took this no further other than to comment on the potential of the model.

The model was put to practical use by Icke & van de Weygaert (1987), who made extensive investigations into the various statistical properties of two-dimensional Voronoi foams. They extended their work into three dimensions (van de Weygaert & Icke 1989), where they calculated the correlation function of the nodes and found that when the number density of nodes was matched to that of Abell clusters they were able to reproduce the slope and correlation length of the Abell cluster-cluster correlation function as found by Bahcall & Soneira (1983).

This has proved to be one of the main motivations behind the Voronoi foam. As formulated above, the model has only one free parameter, that of the number density of the Voronoi nuclei. As the ratio of nodes to nuclei is fixed, one can fix the number density of the nuclei such that the number density of the nodes matches that of Abell clusters, making the implicit assumption that the Abell clusters lie at the nodes of a Voronoi foam. This effectively fixes the length scale of the model. With only one free parameter it is quite remarkable that the model can reproduce the observed clustering properties of Abell clusters, which was a major success for the model.

Part of the motivation of this thesis is to see whether the Voronoi foam can account for other observational measures of large-scale structure, such as the galaxy-galaxy two-point correlation function, power spectrum and angular two-point correlation function (Chapters 5, 6). The Voronoi foam will also be used to investigate the alignment of galaxy clusters (Chapter 7).

2.3.3 Theoretical Motivations

The Voronoi foam is a natural approximation to the single generation explosion model (§ 1.3.5), provided that the explosions are of roughly the same strength and that the shock fronts expand until they intersect, where the expansion stops. This will happen if the explosions are of sufficient strength or the ambient medium does not decelerate

the shocks by a significant amount. Note that only the component of the expansion perpendicular to the wall is cancelled out by the collision of the shock fronts, thus leaving the matter streaming away from the centres of the walls towards to edges, where it collides with matter streaming out of other walls to form filaments and, by a similar process, streams along the filaments to form nodes.

In the language of the Voronoi foam, the nuclei are the sites of the explosions, the walls are where two shock fronts collide, filaments where three fronts overlap and nodes where four fronts meet. Though extensive calculations and simulations have been carried out in the context of the explosion model (e.g. Weinberg, Ostriker & Dekel 1989; West, Weinberg & Dekel 1990), it is usually to investigate the clustering and other properties of "clusters" which are located at the points where three expanding shock fronts overlap, thus making a direct comparison to the Voronoi foam (where "clusters" are placed at the nodes, points where four shock fronts overlap) impractical. No-one has yet attempted to a make direction comparison between such models and the Voronoi foam approximation.

There is also an alternative theoretical motivation for the Voronoi foam. As was discussed in § 1.4.6, gravitational instability theory, working with both cold and hot dark matter models, has been shown to naturally produce a cellular distribution. It is simple to show (Appendix B) that any density fluctuation in the linear matter-dominated regime will grow in proportion to the scale factor, a. Positive fluctuations will grow in this manner until non-linear effects are no longer negligible. These non-linear terms lead to an acceleration of the growth of the fluctuations, giving rise to local collapse. The objects formed will then break away from the general Hubble expansion and undergo gravitational clustering.

The problem with such an approach is that it is difficult to solve analytically, due to the highly non-linear nature of the evolution of the structure after the formation of bound objects. An alternative approach is to look at the "negative" of the universe. Instead of concentrating on high density regions, it is equally valid to follow the evolution of the low density regions which are the progenitors of the observed voids. This approach has the advantage that in low density regions (where the local density is less than the mean background density) the amplitude of the density contrast never exceeds unity, except at the edges of the voids. Thus linear theory approximations are valid until a

much latter stage than is the case in the collapse of high density regions.

This approach is known as the "Bubble Theorem" (Icke 1984). In an expanding medium, a region whose size is much less than the horizon scale and which has a local density less than that of the global background will expand faster than the surrounding Hubble flow. At the same time the density contrast will increase (in a negative sense — the density within the region will fall at a faster rate than the mean background density) and the region will tend to become more and more spherical as it expands.

This gives a picture of voids originating from the expansion of small, *negative* density perturbations in the early universe, as opposed to the standard picture where structure forms from the gravitational collapse of small, *positive* density perturbations. It should be stressed that these two approaches are not at odds with each other, rather they are complimentary ways of looking at the same process, that of the formation of structure under the influence of gravity.

As the voids expand, they become increasingly spherical and underdense, forming thin shells of matter at their edges. The expansion continues until the shells collide with those of other voids. The matter that was being swept out of the voids by the expansion will then form thin walls between the voids. Matter within the walls then fragments and starts to coalesce into galaxies. Furthermore, only the component of the expansion perpendicular to the wall is cancelled out by the collision of the voids, thus leaving the matter streaming away from the centres of the walls towards to edges, where it collides with matter streaming out of other walls to form filaments and, by a similar process, streams along the filaments to form nodes.

Note that the formation of voids is not a static process. Small voids will merge with larger voids, which are expanding more quickly. Only in the approximation that all voids start equally underdense and hence expand at the same rate, will the gravitational instability scenario tend to the Voronoi foam solution at late times.

This is qualitatively similar to the explosion scenario. There is little, if any, distinction between the two. The only major difference between the two approaches is the nature of the initial expansion and whether gravity alone is sufficient to allow the present day structures to have grown from such small initial fluctuations (§ 1.3). Regardless of the initial assumptions, the final structure will approximate to a Voronoi foam provided

the explosion strengths/void expansion rates are the same.

2.3.4 Clustered Nuclei — Gravitational Peaks as Voronoi Nuclei

The Voronoi foam model, as originally proposed, used randomly distributed nuclei. However, one of the aims of this thesis is to see what effect clustered nuclei have on the structure of the foam (Chapter 6). Of the two theoretical motivations discussed in § 2.3.3, the explosion model (§ 1.3.5) has no natural mechanism for the distribution of the explosive seeds. However, in terms of gravitational instability theory (§ 1.3.1), voids (cells) form under the influence of gravity in low density regions. Hence voids form in regions of *high* gravitational potential. In fact, just as bound objects are thought to form at maxima in the density field, so voids are thought to form at maxima in the gravitational potential. Thus it seems natural to identify Voronoi nuclei (the progenitors of the cells) with peaks in the gravitational potential (progenitors of the voids).

In developing the role of peaks in a gravitational potential as Voronoi nuclei, it is instructive to consider the adhesion model (§ 2.2). The model works by considering the gravitational potential. Matter follows its initial linear trajectories, given by the negative of the gradient of the initial gravitational potential, until it collides with other matter, where it sticks together and moves in a manner that conserves momentum. This forces matter into walls, where it moves along towards the wall edges. Here it enters filaments, colliding with more matter from other walls, and, by a similar process, moves along the filaments and into nodes. Thus the adhesion model builds up a cellular structure, dependent only on the initial gravitational potential. Matter flows away from peaks in the potential, thus locating them in the voids and providing a motivation for their use as Voronoi nuclei.

If one considers the geometrical method used to solve the adhesion model (§ 2.2.3), a further point comes to light. The method fits a paraboloid to the gravitational potential, finding points where the paraboloid is tangential to the potential. The curvature of the paraboloid is inversely proportional to time, thus at early times the sides of the paraboloid are very steep and it only touches the potential at a single point. At later times the curvature of the paraboloid lessens and it begins to touch the potential at more than one point simultaneously. This leads to the formation of structures (walls, filaments or nodes, depending on whether the potential touches the paraboloid two,

three or four times) at the bottom of the paraboloid. As time goes on and the curvature of the paraboloid decreases further, it is no longer possible for the paraboloid to touch small peaks in the potential. At very late times the paraboloid is almost flat, thus it can only touch the potential at the highest peaks. In this case the peaks are of roughly the same height and the bottom of the paraboloid lies equidistant from the peaks (see Fig. 2.3). Thus at late times the adhesion model approximates to a Voronoi foam. However, this suggests that only the high peaks in the gravitational potential may be used as nuclei in a Voronoi foam.

As stressed in § 2.3.3, the requirement for the Voronoi foam to be an approximation to the gravitational instability model is that the voids expand at equal rates. This argues against using small peaks in the potential as they are likely to give rise to small voids that will be subsequently incorporated into larger voids. Chapter 6 investigates the effect of imposing a peak-height threshold on the peaks chosen as Voronoi nuclei. Obviously, such a simple thresholding model is unlikely to be totally realistic as the probability of any void around a given peak surviving is dependent on the size of the surrounding peaks. However, modelling such a situation (perhaps by using a local threshold) vastly increases the complexity of the model and is, perhaps, unwarranted for a simple model such as the Voronoi foam, which is, after all, only a crude, statistical approximation and not an attempt to accurately model the processes of galaxy formation.

The assertion that the Voronoi foam is a good late-time approximation to the adhesion model for high peaks can be checked using the adhesion model itself. Fig. 2.3 shows the location of high mass pancakes in adhesion model with respect to the pancake edges in Lagrangian space (i.e. the peaks in the gravitational potential). The two plots are for (a) pancakes of mass greater than the characteristic mass (see § 3.2.1) and (b) for pancakes of mass greater than twice the characteristic mass. As one can see, the higher the mass of the pancake, the more likely it is to reside midway between the peaks. In Fig. 2.3(b) virtually all the pancakes lie between the two peaks. It should be noted that although high mass pancakes are associated with high peaks in the gravitational potential, there is no one-to-one correspondence between peak height and pancake mass and thus no useful limits can be set on which height peaks should be used as Voronoi nuclei.

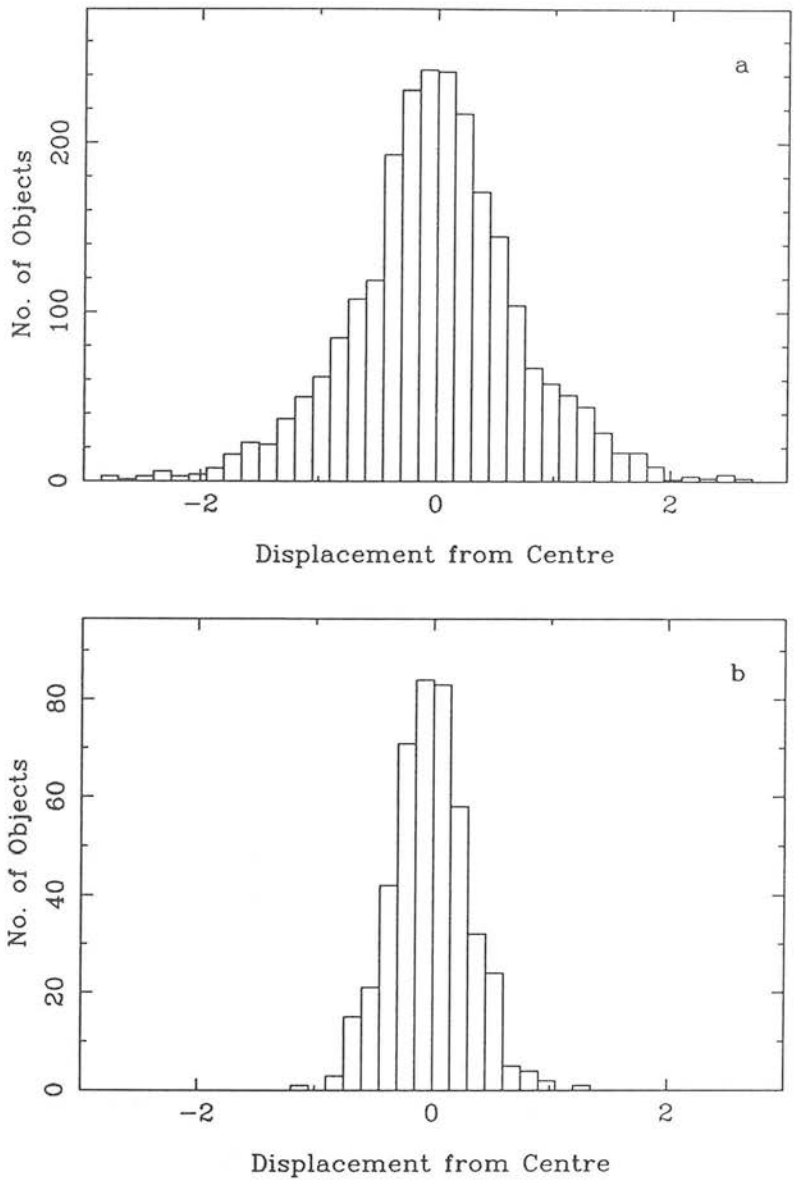

Figure 2.3 Histograms showing the locations of pancakes in Eulerian space with respect to the pancake edges in Lagrangian space. A value of zero indicates that the pancake lies equidistant from the edges and a value of ± 1 indicates that it lies at the edge. The two plots are for (a) all pancakes of mass $M > M_*$ and (b) $M > 2M_*$. The results are the sum of 100 simulations using a 2^{17} point, $n = 1$ potential with a characteristic mass $M_* = 1638.4$ (see § 3.3.1).

2.3.5 Galaxy Formation in the Voronoi Foam

The Voronoi foam model makes no assumptions as to the formation and subsequent

evolution of galaxies. Rather it seeks to provide a simple prescription for their location at late times. In situations where structure forms in a "bottom up" manner (e.g. cold dark matter dominated universes; § 1.3.1, 1.3.2), then galaxies are likely to form in the voids and subsequently move into the geometric structure, unless there is some biasing mechanism that prevents structure formation in low density regions (§ 1.3.3, 1.4.6). Once within the skeleton (either because they only form there or because they have moved in), the galaxies will move towards the filaments as discussed in § 2.3.3, and they will also cluster together under their own self-gravity.

Where structure forms in a "top down" manner [e.g. hot dark matter dominated universes (§ 1.3.1, 1.3.2) or the explosion scenario (§ 1.5.3, 2.2.3)], then the geometric skeleton will go non-linear first and galaxies will form by fragmentation. Recent two-dimensional simulations of the collapse and fragmentation of pancakes have shown that objects fragment into galaxy-sized objects which then cluster and merger together under self-gravity (Yuan, Centrella & Norman 1991). Thus in both scenarios, there is considerable clustering and evolution of structure within the geometric skeleton.

The Voronoi foam prescription makes no attempt to account for this internal structure, nor, in some ways, should it. The model is a very simple attempt to model *large*-scale structure. To model such small-scale clustering would be extremely complicated (and require making assumptions about the methods of galaxy formation) and it would rob the model of its simplicity. However, this deficiency must be borne in mind while comparing the Voronoi foam to observations (Chapters 5, 6). The distribution of particles on walls in the Voronoi foam can best be described as pseudo-random (§ 4.3.4) and there is no sub-clustering built into the distribution. Thus on intra-wall scales one would expect the Voronoi foam to underestimate the small-scale power in comparison to observations, which is indeed the case (Chapter 5). This should not be allowed to detract from the model's principal strength, that of providing a simple prescription for the large-scale distribution of matter.

Chapter 3

Linear Theory and the Adhesion Model

3.1 Introduction

In the matter-dominated, pressure-free regime, linear theory predicts that density perturbations, $\delta(\mathbf{x}) = [\rho(\mathbf{x}) - \bar{\rho}]/\bar{\rho}$, grow in proportion to the scale factor, a, as long as $\Omega = 1$ [Appendix B; note that as long as $\Omega = 1$, the scale factor, a, is equivalent to the time-dependent function $b(t)$ used in § 2.2] and the density field rapidly becomes non-linear. For a large range of initial conditions the linear density field will be dominated by fluctuations on small scales ("bottom up" scenarios; § 1.3). These will be the first to become non-linear, which leads to local collapse. The objects formed will then cluster together and merge to form larger objects as time goes on. The critical idea in continuing to apply linear theory to this non-linear situation is that the location and properties of the non-linear objects might nevertheless be found by *smoothing* the linear-theory density field on a given scale. This approach is aided by the fact that one is often interested in the case where the various Fourier components, $\delta_{\mathbf{k}}$, of the density field are assumed to have random phases, and hence the field is Gaussian. All the statistics of the situation are therefore specified by the power spectrum, $|\delta_{\mathbf{k}}|^2$.

It is the aim of this chapter to introduce several such linear theory methods: the mass function of Press & Schechter (1974), the peaks theory modifications of Peacock & Heavens (1990) and the two-point correlation function for peaks in a Gaussian field (Lumsden, Heavens & Peacock 1989; Coles 1989). The predictions for these mass and correlation functions can then be tested against simulated data. The model chosen for this comparison is the adhesion model of § 2.2. The model is restricted to one spatial dimension because it is then *exact*. Furthermore, by restricting the simulations to one dimension, it is easier to obtain the large dynamical range in mass that is needed to thoroughly test the theoretical predictions.

Whether a test of these theories in one dimension is valid in two and three dimensions is not directly addressed in this chapter. However, there is no immediate reason

why this should not be so, as there are no specific features in these theories that make them unique in one, two or three dimensions, thus there is no reason to believe that the results presented here should not provide a useful guide to further studies in higher dimensions.

3.2 Linear Theory

3.2.1 The Press-Schechter Formalism

An early attempt at using such ideas to determine the mass function of collapsed objects analytically was made by Press & Schechter (1974). Their method was to evolve the density field according to the linear approximation and then, for a given time, implicitly smooth the field on different mass scales, M. Any point with $\delta(x)$ greater than some critical value δ_c (~ 1) was assumed to have collapsed into an object of mass at least M.

Following this prescription it is relatively simple to derive their original mass function :

$$f(M) = \frac{\bar{\rho}\delta_c}{\sqrt{2\pi}\sigma_0 M^2} \exp\left(-\frac{{\delta_c}^2}{2{\sigma_0}^2}\right) \frac{d(\ln \sigma_0)}{d(\ln M)}, \tag{3.1}$$

where ${\sigma_0}^2$ is the variance of the smoothed density field, given by

$${\sigma_0}^2(R_f) = A\int_0^\infty W(k, R_f)^2 |\delta_k|^2 4\pi k^2 dk, \tag{3.2}$$

with A being a normalisation constant and $W(k, R_f)$ a filter function, with the filter radius, R_f, representing smoothing on a given length scale, which corresponds to a given mass, M.

The variance, ${\sigma_0}^2$, is normalised so that it is equal to the square of the critical density, δ_c, for a given filter radius, R_*, corresponding to a cut-off mass, M_*, which represents the boundary between the linear and non-linear regimes. When filtered on a scale $M < M_*$ the density field is non-linear, but for filtering scales corresponding to masses above M_* the density field is still linear. The exact form of the filter function

and the relationship between filter radius and mass are not determined, being left open to choice, but in general $W(k, R_f)$ is a function that drops from unity for $k \lesssim \frac{1}{R_f}$ to zero for $k \gtrsim \frac{1}{R_f}$.

Note that the Press–Schechter formalism only accounts for half of the mass as it does not include the underdense regions where $\delta < 0$. To account for this, Press & Schechter inserted a factor of two in their mass function, thus doubling the *number* of objects at all masses without changing the actual mass of any of the objects. If the filter function contains a sharp truncation in k space then this factor of two is naturally obtained (e.g. Peacock & Heavens 1990). However, for any differentiable filter function this is not the case and the mass function differs from the Press–Schechter form (see Peacock & Heavens 1990).

3.2.2 Peaks Theory Modifications to Press–Schechter

A conceptual problem which is posed by the Press–Schechter formalism is that objects form from spatially unconnected regions. Consider the density field smoothed on some radius, R_f. A point with $\delta = \delta_c$ will be part of an object of mass $M(R_f)$, but adjacent points will have $\delta \neq \delta_c$. However, when smoothed on some other scale $R_f \pm \delta R_f$, these points will then have $\delta = \delta_c$ and thus be incorporated into objects of mass $M(R_f \pm \delta R_f)$, i.e. spatially adjacent points will become incorporated in different objects, a very unphysical process.

A better approach to the formation of structure, which avoids some of these conceptual problems, is to assume that objects form at the sites of maxima in the linear density field (Peacock & Heavens 1985, Bardeen *et al.* 1986). The incorporation of such a constraint into the Press–Schechter formalism has been considered by Peacock & Heavens (1990). The basic approach is to consider the fraction of mass associated with a peak above a given threshold, ν (defined as the dimensionless ratio δ/σ_0), when smoothed on a scale R_f. The physical basis for this approach is to assume that any material within a distance $\sim R_f$ of a peak which has collapsed is part of an object with mass at least $\sim \bar{\rho} R_f^3$ (in three dimensions). The criterion for collapse is that any point in the peak has $\delta \geq \delta_c$. Note that the relationship between the mass of the object formed and the filter radius is very important in determining the final form of the mass function and its overall normalisation. In general, for a pure power law, the peak theory model

predicts more lower mass objects than Press–Schechter, though this effect does depend on the mass assigned to a peak and is more pronounced in three dimensions (see below).

3.2.3 Filter Functions

The above methods have two critical uncertainties: what form of filter function should be used, and what is the relationship between the filtering length, R_f, and the mass?

Several different choices of filter are discussed in this sub-section. Note that in all cases the filter is referred to by its *real* space form, but all filter functions are applied in k-space. The real and k-space filter functions are a Fourier transform pair, where the normalisation of the transform is contained within the normalisation constant, A (equation 3.2).

Press & Schechter used a top-hat filter function. This equally weights all points in real space out to a distance R_f from the centre of the filter function, leading to "ringing" in k-space as its Fourier transform is a sinc function. Is this an undesirable feature? Intuition says that the sidelobes indicate an unreasonable choice of filter, but one should recall that there are no absolute guidelines here. The smoothing process attempts to mimic the effect of non-linearities via a linear filter; if such an attempt is successful at all, the "correct" filter can only be judged by its empirical performance. Nevertheless, the top hat does seem an unwise choice owing to its width in k-space: for many power spectra of practical interest (cold dark matter, for example) the higher moments of the power spectrum, which are of interest for determining the statistical character of the density field, do not converge with this filter. This says that the top hat accepts power from too wide a range of wavenumbers; the whole idea of Press–Schechter-style filtering is to isolate fluctuations arising from a given scale. For this reason it is common to employ the Gaussian filter, since this damps short wavelengths more severely. However, other choices are possible which differ in the rapidity of this damping; "exponential" and "power-law" filters are also used, in order to gain some insight into the sensitivity of the results to filter choice. The definitions of these alternatives are given in Table 3.1.

The relationship between mass and filter radius is similarly open to choice and depends to a large extent on the filter function. One would expect the mass of an object filtered on a scale R_f to be related to the area under the filter function, which means in

Filter Name	$W(x, R_f) \propto$	$W(k, R_f) \propto$	Area under $W(x, R_f)$
Top Hat	R_f, $\lvert x\rvert < R_f$	$\sin(kR_f)/(kR_f)$	$2R_f$
Exponential	$\exp(-\lvert x\rvert/R_f)$	$(1+k^2R_f^2)^{-1}$	$2R_f$
Power Law 1	$[1+(x/R_f)^2]^{-1}$	$\exp(-\lvert k\rvert R_f)$	πR_f
Power Law 2	$[1+(x/R_f)^2]^{-2}$	$(1+kR_f)\exp(-\lvert k\rvert R_f)$	$\pi R_f/2$
Gaussian	$\exp(-x^2/2R_f^2)$	$\exp(-\frac{1}{2}k^2R_f^2)$	$\sqrt{2\pi}R_f$

Table 3.1 Real $[W(x, R_f)]$ and k-space $[W(k, R_f)]$ forms of the various filter functions considered in this chapter, along with the area under the filter.

d dimensions that $M(R_f) \propto \bar{\rho} R_f^d$.

The problem arises when trying to decide upon the constant of proportionality. For the top-hat filter in three dimensions, one has the motivation of the spherical collapse model to set $M = V\bar{\rho}$, where V is the top-hat volume. In general, things are not so simple, and so the scaling

$$M = \beta V \bar{\rho} \tag{3.3}$$

is adopted where β is to be treated as a fitting parameter. In one dimension, V, the volume of the filter function, is replaced by the area under the filter function which is listed in Table 3.1 for the filters considered in this chapter.

The importance of β depends on the power spectrum and the mass-function theory being adopted. For power-law spectra, $|\delta_k|^2 \propto k^n$ in d dimensions,

$$\frac{\delta_c}{\sigma_0} = \left(\frac{M}{M_*}\right)^{(n+d)/2d}, \tag{3.4}$$

which is independent of β. However, M_* is defined to be $\beta\bar{\rho}V_*$, where V_* is the volume of the filter function that corresponds to $\sigma_0 = \delta_c$. For pure Press–Schechter theory,

$M^2 f(M)$ depends only on δ_c/σ_0 and hence is independent of β, except through its effect on the numerical value of M_*. A variation in β simply translates $M^2 f(M)$ by some amount in $\ln M$, but preserves its shape and normalisation; the Press–Schechter factor of 2 is not supplied by putting $\beta = 2$. However, as discussed in § 3.3.2, the peak-based mass functions are sensitive in detail to β.

3.2.4 Steep Spectra

The assumptions that go into Press–Schechter type models are only valid for a limited range of spectral indices. It had been previously thought by various authors (e.g. Press & Schechter 1974; Peebles 1980) that the growth of non-linear perturbations for a power-law power spectrum, $|\delta_k|^2 \propto k^n$, would go as

$$M_* \sim M_0 a^{2d/(n+d)}, \tag{3.5}$$

where d is the number of dimensions and M_0 the characteristic mass at $a = 1$. In one dimension this is indeed the case (see § 3.3.2).

It was widely believed that in three dimensions equation (3.5) would hold for spectral indices between $-3 < n \leq 4$. For spectra steeper than the "minimal" $n = 4$ spectrum it was proposed that the growth would take a limiting value given by

$$M_* \sim M_0 a^{6/7}, \tag{3.6}$$

which is independent of the spectral index for $n \geq 4$. This arises due to the non-linear generation of the long wavelength part of the spectrum where mode-coupling terms dominate over any intrinsic large-scale power. Thus even if there are no long wavelength perturbations at the linear stage (as is the case for steep spectra) the characteristic mass will grow at these scales with the limiting rate given above.

It was suggested by Gurbatov, Saichev & Shandarin (1989) that equation (3.5) only holds as long as the variance of the gravitational potential, $\sigma^2_{\Phi_0}$, diverges as $k \to 0$. For a pure power-law power spectrum with no smoothing, but with a small wavelength

cut-off ($k_{\max}$), and the relationship between matter and gravitational perturbations given by equation (3.27), the variance in d dimensions is given by

$$\sigma^2_{\Phi_0} = \int_0^{k_{\max}} k^{n+d-5} dk. \tag{3.7}$$

Thus one can see that $\sigma^2_{\Phi_0}$ diverges for $n \leq 1$ in three dimensions and for $n \leq 3$ in one dimension, which is contrary to previous assumptions. In this case the limiting rate would be given by

$$M_* \sim M_0 a^{d/2}, \tag{3.8}$$

This conclusion is backed up by the work of Kida (1979) who (although working in the context of turbulence theory) effectively solved Burgers' equation exactly in one dimension to obtain $f(M)$ in the limit of very steep spectra. Not only does M_* scale as in equation (3.8), but the form of $f(M)$ is greatly different from the Press–Schechter prediction (see below). Similar work on Burgers' equation has been carried out by Gurbatov & Saichev (1981), looking at one-dimensional turbulence in Gaussian fields, and Doroshkevich & Kotok (1990), looking at the problem in the context of galaxy formation. Both sets of authors derived a mass function in agreement with that given by Kida.

The mass function derived by Kida is given by

$$f(M) = \frac{\pi\bar{\rho}}{2}\frac{M}{[\ell(a)\bar{\rho}]^3}\exp\left[-\frac{\pi}{4}\left(\frac{M}{\ell(a)\bar{\rho}}\right)^2\right], \tag{3.9}$$

where $\ell(a)$ is a characteristic scale given by

$$\ell(a) = \left(\frac{\pi a}{2B^{\frac{1}{2}}}\right)^{\frac{1}{2}}\left[\ln\left\{\frac{A}{4}(\pi a)^{\frac{1}{2}}B^{-\frac{5}{4}}\right\}\right]^{-\frac{1}{4}}. \tag{3.10}$$

and A and B are constants.

In Kida's work A and B are free parameters which arise in an ansatz that the probability that the highest peak is in the range $[\Phi_0, \Phi_0 + d\Phi_0]$ is

$$P(\Phi_0) = \frac{1}{n_{\rm pk}} A \Phi_0^{\alpha} \exp(-B\Phi_0^{\beta}), \tag{3.11}$$

where $n_{\rm pk}$ is the total number density of peaks.

It is possible to improve on Kida's analysis by using the properties of Gaussian fields to determine the values of α, β, A and B :

$$\begin{aligned} \alpha &= 1, \\ \beta &= 2, \\ A &= \frac{1}{2\pi}\frac{\sigma_1}{\sigma_0^3}, \\ B &= \frac{1}{2\sigma_0^2}, \end{aligned} \tag{3.12}$$

where σ_j^2 the $2j^{\rm th}$ moment of the gravitational power spectrum, i.e.

$$\sigma_j^2 \propto \int_0^{\infty} |\Phi_k|^2 k^{2j} dk. \tag{3.13}$$

Note that this is not the exact form given by Kida, rather it is equivalent to the function $\tilde{f}(\tilde{\mu})$ given in his equation (4.38) and the approximation to $\ell(a)$ given by his equation (4.35) has been used. Though at first sight equation (3.10) may seem dimensionally odd, it is fact valid as the potential, Φ_0, has dimensions of length squared.

Kida's analysis is only valid if the peaks are uncorrelated in position. This is the case for steep power spectra at large values of the scale factor ($a \gg 1$). The lack of any power above some critical length scale means that the peaks are uncorrelated on this scale and above. If the scale factor is sufficiently large, then, in terms of the geometrical solution of the adhesion model (§ 2.2.3), the parabola will only touch the highest peaks; thus the separation of the touching peaks will be large. For a sufficiently steep spectrum and a large enough scale factor, the peak separation will be greater than the critical length and the positions of the peaks are uncorrelated. This is demonstrated in § 3.3.3.

It is interesting to compare this to the Press–Schechter mass function under the assumption that for $n \geq 3$ in one dimension, one may use a constant value of $n = 3$ in the mass function. Both mass functions give the correct low-mass slope [$f(M) \sim M$ for

$M \ll M_*$, where $M_* \sim \ell(a) \sim a^{\frac{1}{2}}$] but the cut-offs are different, Kida's formula going as $\exp[-(M/M_*)^2]$ whereas the Press–Schechter mass function would predict a cut-off going as $\exp[-\frac{1}{2}(M/M_*)^4]$, i.e. Press–Schechter cuts off too quickly, not producing enough high-mass objects. This is because the Press–Schechter formalism does not take into account the non-linear processes that generate the long wavelength fluctuations.

3.2.5 Correlation Functions

The calculation of a two-point correlation function for peaks in a one-dimensional Gaussian field has been carried out by Lumsden, Heavens & Peacock (1989) who derived an exact form for $\xi_{\rm pk-pk}$, the correlation function for all peaks above a threshold ν. The result, which was unfortunately misprinted in the original paper, is

$$\begin{aligned} 1+\xi_{\rm pk-pk}(r) =& \frac{\sigma_0^2\sigma_2^2}{(2\pi)^3 M_{33}^{-1}(\det M)^{1/2} n_{\rm pk}^2(>\nu)} \int\!\!\int_{\nu}^{\infty}\int_{0}^{\infty} q_2 \exp(-Q_0/2) \\ & \times \left[1-\frac{\sqrt{2\pi}}{2}\exp(+a^2/2)\, a\, \mathrm{erfc}(a/\sqrt{2})\right] dq_2\, d\nu_2\, d\nu_1, \end{aligned} \tag{3.14}$$

where

$$\begin{aligned} a =& -\sigma_0 \left(M_{13}^{-1}\nu_1 + M_{16}^{-1}\nu_2 - \frac{\sigma_2}{\sigma_0} M_{36}^{-1} q_2 \right) / \sqrt{M_{33}^{-1}} \\ Q_0 =& M_{11}^{-1}\sigma_0^2(\nu_1^2+\nu_2^2) + 2M_{14}^{-1}\sigma_0^2\nu_1\nu_2 + M_{33}^{-1}\sigma_2^2 q_2^2 \\ & - 2\sigma_0\sigma_2 \left(M_{13}^{-1}\nu_1 q_1 + M_{16}^{-1}\nu_2 q_2 \right), \end{aligned} \tag{3.15}$$

with

$$\begin{aligned} \mathbf{y}^T &\equiv (\delta_1, \delta_1', \delta_1'', \delta_2, \delta_2', \delta_2'') \\ M_{ij} &\equiv \langle y_i y_j \rangle. \end{aligned} \tag{3.16}$$

Note that M_{ij}^{-1} indicates the ij component of the inverse of $\mathbf{M}$. Explicit forms of M_{ij} can be found in Lumsden, Heavens and Peacock (1989).

The expression for the number density of peaks above a height ν is given by equation (8a) in Lumsden, Heavens & Peacock (1989) which can be integrated analytically (see Cartwright & Longuet-Higgins, 1956) to give

$$n_{pk}(>\nu) = \frac{1}{4\pi R}\left\{\mathrm{erfc}\left(\frac{\nu}{\sqrt{2(1-\gamma^2)}}\right) + \gamma e^{-\frac{\nu^2}{2}}\left[1+\mathrm{erf}\left(\frac{\gamma\nu}{\sqrt{2(1-\gamma^2)}}\right)\right]\right\} \quad (3.17)$$

where γ and R are defined in terms of the $2j^{\mathrm{th}}$ moments of the power spectrum by

$$\begin{aligned}\gamma &= \frac{\sigma_1^2}{\sigma_2\sigma_0} \\ R &= \frac{\sigma_1}{\sigma_2}\end{aligned} \quad (3.18)$$

where

$$\sigma_j^2 \propto \int_{-\infty}^{\infty} |\delta_{\mathrm{k}}|^2 k^{2j} dk \quad (3.19)$$

Equation (3.14) is used in § 3.3.4 to generate the peaks theory correlation function. The density field is smoothed on a given mass scale and the threshold is set such that the number of peaks found above the threshold matches the number of pancakes of that mass or above present in the simulation.

It should be noted that the peaks theory correlation function will always give $\xi_{\mathrm{pk-pk}} = -1$ for small separations, i.e. for $r \lesssim R_{\mathrm{f}}$. This is because when smoothed, all substructure on scales less than about R_{f} will be removed and hence there will be no pairs on scales of R_{f} or less. However, the peaks correlation function deals only with the static clustering present within the power spectrum and takes no account of the movement of peaks. One may use the Zel'dovich approximation (equation 2.5) to relate the peculiar velocity, V, to the co-moving displacement, $\Delta\mathbf{x}$ $(= \mathbf{x} - \mathbf{q})$, using equation (2.4) :

$$\mathbf{V} = a\frac{\dot{b}}{b}\Delta\mathbf{x}. \quad (3.20)$$

The mean square peculiar velocity is (from equation 27.22 of Peebles, 1980)

$$\sigma_{\mathbf{V}}^2 \equiv \langle \mathbf{V}^2 \rangle = (a\frac{\dot{b}}{b})^2 \sigma_{-1}^2, \quad (3.21)$$

where σ_{-1}^2 is a moment of the power spectrum as defined in equation (3.19).

The r.m.s. velocity of the peaks in a Gaussian field is somewhat smaller than the r.m.s. peculiar velocity. The relationship between the two can be obtained from equation (4.23) in Bardeen *et al.* (1986) :

$$\sigma_{\mathbf{v},\mathrm{pk}} = \sigma_{\mathbf{v}}(1-\gamma_{\mathbf{v}}^2)^{\frac{1}{2}}, \tag{3.22}$$

where

$$\gamma_{\mathbf{v}} \equiv \frac{\sigma_0^2}{\sigma_{-1}\sigma_1}. \tag{3.23}$$

Thus, from equations (3.20) and (3.21), the r.m.s. co-moving displacement of peaks is

$$\sigma_{\Delta\mathbf{x}} = \frac{1}{a}\left(\frac{b}{\dot{b}}\right)\sigma_{\mathbf{v},\mathrm{pk}} = \frac{1}{a}\left(\frac{b}{\dot{b}}\right)\sigma_{\mathbf{v}}(1-\gamma_{\mathbf{v}}^2)^{\frac{1}{2}} = \sigma_{-1}(1-\gamma_{\mathbf{v}}^2)^{\frac{1}{2}}. \tag{3.24}$$

For a power law spectrum (with $n > -1$) with a Gaussian filter function

$$\begin{aligned} \sigma_{-1} &= \left(\frac{2}{n+1}\right)^{\frac{1}{2}}\sigma_0 R_{\mathrm{f}}, \\ \gamma_{\mathbf{v}}^2 &= \frac{(n+1)}{(n+3)}. \end{aligned} \tag{3.25}$$

Thus one can see that for n not close to -1 peaks on the mass scale M_*, where $\sigma_0 \sim 1$, will move $\sim R_{\mathrm{f}}$. Note that this calculation ignores any correlation between the velocity of peaks which would be needed in order to determine $\xi_{\mathrm{pk-pk}}$. However, it does demonstrate that the displacements associated with the peculiar velocities of the density perturbations are of the right order to lead to correlations on scales $< R_{\mathrm{f}}$. Thus though the peaks theory predicts $\xi_{\mathrm{pk-pk}} = -1$ for $r < R_{\mathrm{f}}$ this is not expected to be the case in reality.

3.3 Results from the Simulations

3.3.1 The Simulations

The aim of this section is to test the predictions for mass and correlation functions made in § 3.2 by comparison with simulations based on the adhesion model. Two sizes of simulation are used, those with a potential sampled on a 2^{14} point grid and larger simulations with a 2^{17} point grid. The total mass of the simulation is equal to the number of grid points and is initially smoothly distributed, giving a line density of $\bar{\rho} = 1$.

For simplicity the power spectra used to generate the potentials are restricted to being power-laws with a short-wavelength Gaussian cut-off. There is also a long-wavelength cut-off, which is imposed by the size of the simulation. The short-wavelength cut-off should not be confused with the smoothing processes discussed in § 3.2. The power spectrum of the potential is thus given by

$$|\delta_k|^2 = k^n \exp(-k^2 R_{\rm i}^2), \tag{3.26}$$

with $R_{\rm i}$ set to two grid points to ensure that the results are not affected by the sampling of short wavelength modes of a size close to that of the resolution of the simulation. The gravitational perturbations are related to the matter density perturbations via Poisson's equation to give

$$\Phi_k = -k^{-2}\delta_k. \tag{3.27}$$

The gravitational potentials, $\Phi(q)$, used in the simulations are calculated by fast Fourier transforming the gravitational perturbations, Φ_k. The variance is expressed as a direct sum, rather than the integral given in equation (3.2),

$$\sigma_0^2(R_{\rm f}) = A \sum_{k_{min}}^{k_{max}} |\delta_k|^2 W(k, R_{\rm f})^2, \tag{3.28}$$

where σ_0^2 is normalised in the same manner as before and $W(k, R_f)$ is given in Table 3.1 for the various filters.

The initial density field was normalised so that $\sigma_0 = \delta_c$, corresponding to a smoothing length $R_f = 0$ and a scale factor $a = 1$. Under linear theory $\sigma_0(R_f)$, for some fixed R_f, grows in proportion to the scale factor, a. Using this and the fact that $\sigma_0(R_*) = \delta_c$, the scale factor can be expressed in terms of the corresponding cut-off mass, M_*, and its associated filter radius, R_* :

$$a = \delta_c \left[\frac{\sigma_0^2(0)}{\sigma_0^2(R_*)} \right]^{\frac{1}{2}} . \tag{3.29}$$

For each power spectrum eight independent realisations of the gravitational potential were generated. This was done rather than generate a single, larger potential because the computational time for a single potential rises faster than the size of the potential. Computer memory restrictions also place a limit on the size of the simulation of $\frac{1}{8}$ million points. Using independent realisations allows an estimation of the errors in any statistical analysis by comparing the results from several simulations.

Parabolæ were fitted to each potential at eight different epochs (§ 2.2.4), the results being combined at each epoch. This allows the investigation of the time evolution of the structure. The different epochs are characterised by the scale factor, a, and as the process of parabola fitting is independent of previous epochs, the choice of the values of the scale factor for each epoch is not constrained.

The scale factor is calculated at each epoch using equation (3.29) with values of R_* calculated from equation (3.3), the volume of the relevant filter function being given in Table 3.1. To provide a wide range of physical scales the values of M_* are logarithmically spaced with a maximum value of 1638.4, one tenth of the size of the 2^{14} point potentials. The scale factors depend on the spectral index and size of the potential used, but the simulations are scaled to M_* at each epoch. This allows a comparison of different potentials, assuming a Press–Schechter style scaling of the cut-off mass with epoch.

3.3.2 Mass Functions

This sub-section presents the mass functions obtained from the adhesion model simulations and compares them to the theoretical mass function derived by Press & Schechter (§ 3.2.1) and from peaks theory (§ 3.2.2). Figs. 3.1 → 3.4 show plots of the mass function in "multiplicity function" form, $M^2 f(M)$, versus the mass, M, scaled by the assumed time dependence of the cut-off mass, M_*. Fig. 3.1 shows the mass functions for three different spectral indices of $n = -\frac{1}{2}$ (a), $n = 1$ (b) and $n = 3$ (c) at three different epochs. The Press–Schechter mass functions (solid lines) are also displayed. They are calculated directly from equation (3.1), with σ_0^2 being calculated using equation (3.28) and the values of R_f obtained from equation (3.3). The parameter β is obtained by fitting the curves by eye to the simulation results. Here $\beta = 1.4$ for all power spectra, which corresponds to setting $\beta = 1$ and using values of δ_c of 0.92 for $n = -\frac{1}{2}$, 0.71 for $n = 1$ and 0.51 for $n = 3$ (see equation 3.4). It should be stressed that using a value of $\beta = 1$ and varying δ_c as given above would give identical results for the unmodified Press–Schechter theory.

One can see the excellent fit of the Press–Schechter curves to the data over a wide range of masses. There are differences, however, at either end of the mass range. The data points from the simulations tail off faster at low mass than the Press–Schechter curves. This is due to the normalisation of the Press–Schechter mass function which automatically accounts for all the mass. However, not all the matter in the simulation is incorporated in pancakes — there are still free points, and these are not included in the data. Thus the Press–Schechter curves will always overestimate the total amount of mass present in the pancakes. There is also the effect of the finite sampling of the simulation. Obviously with a basic length (and hence mass) unit of one grid point this will be the minimum mass of pancake formed, and coupled with the initial removal of small-scale power by smoothing on a scale R_i, there is a downturn in the number of pancakes at low masses. Note that, as one would expect, the difference between the curves is greater for early epochs which have low values of M_*, as here far more pancakes of mass $M \sim M_\mathrm{i}$ form. For late epochs, when $M_* \gg M_\mathrm{i}$, there is very little difference. Also for late epochs, most of the mass is incorporated into pancakes and therefore the Press–Schechter overestimate is only very slight.

The differences at the high-mass end of the mass function are due to the heavy

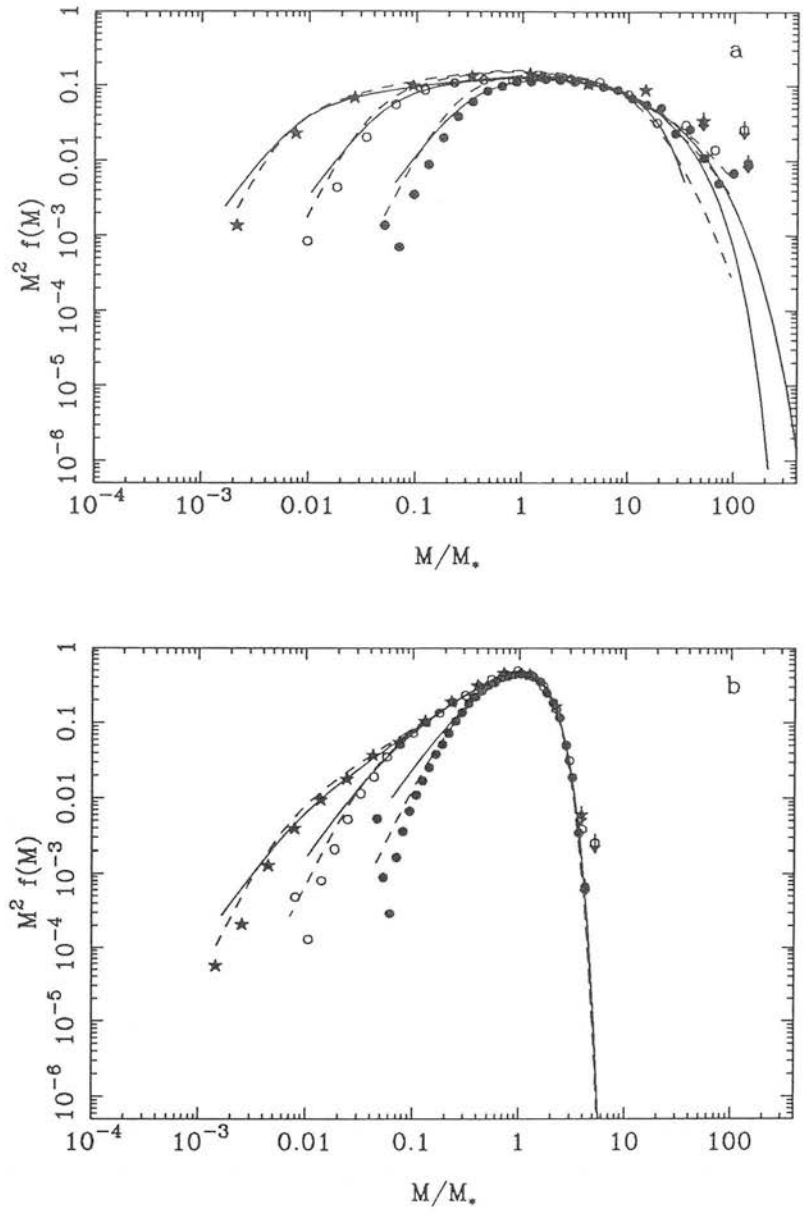

Figure 3.1 The multiplicity function, $M^2 f(M)$, versus M/M_* as given by Press–Schechter (solid line), peaks theory (broken line) and the adhesion model simulations (data points) using a 2^{17} point grid. The three data sets are for epochs 3 (•), 5 (o) and 7 (⋆). The last data point (marked by a superposition of a ↓) is an upper limit, assuming one pancake in the bin after the last data bin. The three panels are for spectral indices of (a) $n = -\frac{1}{2}$, (b) $n = 1$ and (c) $n = 3$ and are plotted on the same scales to facilitate comparison. The Press–Schechter curves are calculated with $\beta = 1.4$ for all spectral indices, which corresponds to setting $\beta = 1$ and using a value of δ_c of (a) 0.92, (b) 0.71 and (c) 0.51. The peaks theory curves are calculated with $\beta = 1$ and δ_c varied as above.

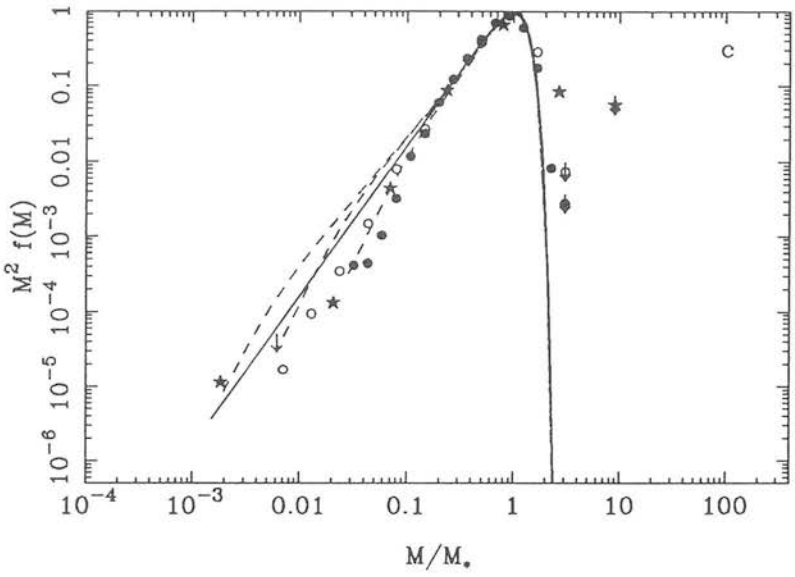

Figure 3.1 — *continued*

smoothing of a discretely sampled power spectrum. For large masses the smoothing radius, $R_{\rm f}$, is sufficiently large that the filter function tends to zero even for very small wavenumbers, k, thus severely curtailing the sampling of the power spectrum. This can be seen in Fig. 3.1a by the rapid fall away of the Press–Schechter curves (solid lines) at high mass, indicating that the $n = -\frac{1}{2}$ power spectrum is insufficiently sampled to produce the self-similar behaviour of a pure power law. Note that, as one would expect, this effect is more pronounced for later epochs as the cut-off mass, M_*, and hence the filter radius, $R_{\rm f}$, at the high-mass end increase with time. In contrast Figs. 3.1b and 3.1c show that the Press–Schechter curves are self-similar at the high-mass end. This indicates that the $n = 1$ and $n = 3$ power spectra are fully sampled. This is due to the lack of large-scale power present in these power spectra, hence there are no pancakes of sufficient mass to curtail the sampling by any noticeable amount. It is interesting to note that for an assumed power-law that extends to arbitrarily low k, then the Press–Schechter mass functions are indeed self-similar at high mass.

Fig. 3.1 also shows peaks theory mass functions (broken lines) generated using a Gaussian filter. For the $n = -\frac{1}{2}$ power spectrum (Fig. 3.1a) β has been set to unity and

a value of $\delta_c = 0.92$ has been adopted (see above). One can see that while both curves agree quite well at the high-mass end, the peaks theory curves give better fits at the low-mass end, more accurately reproducing the tailing off of the data. The discrepancy between the low-mass end of the peaks theory curves and the data can be explained using similar arguments to those given above for the Press–Schechter curves. Note that the peaks curves also suffer from the sampling problem mentioned above, but to a lesser extent. For the $n = 1$ power spectrum (Fig. 3.1b) $\beta = 1$ and $\delta_c = 0.71$ and for the $n = 3$ power spectrum (Fig. 3.1c) $\beta = 1$ and $\delta_c = 0.51$. Again the peaks curves provide a better fit to the data, especially at the low-mass end.

Fig. 3.2 shows the effect of using different filters in the peaks theory mass function. In Fig. 3.2a the peaks theory curves have been calculated using a power-law filter ("Power Law 1", Table 3.1) for an $n = 1$ spectrum with $\beta = 1$ and $\delta_c = 0.71$. One can see that the power-law filter gives a considerably worse fit than either the Press–Schechter or the peaks theory curve using a Gaussian filter (see Fig. 3.1b). The power-law filter vastly underestimates the number of pancakes at low mass and similarly overestimates the number of pancakes around the cut-off mass. It also cuts off a fraction too soon. Fig. 3.2b shows a modified power-law filter ("Power Law 2", Table 3.1) which is a considerably better fit, but still underestimates the number of pancakes with low masses. The exponential and top-hat filters given in Table 3.1 were not used here because the higher moments required by the peaks theory mass function do not always converge. Thus one concludes, that of the filter functions tested here, the Gaussian filter is to be preferred.

Fig. 3.3 shows the effect for the peaks theory of modifying both β and δ_c. The mass functions are for an $n = 1$ power spectrum using a Gaussian filter. Similar results were obtained for different spectral indices and different filter functions. Fig. 3.3a demonstrates that modifying β has a major effect on the shape of the mass function as well as the position of the cut-off. The slope of the low-mass end of the mass function is steepened as β is increased, though the slope of the very low-mass section (introduced by the artificial cut-off; § 3.3.1) remains unaltered. As a result fewer low mass pancakes are predicted which leads to an increased number of pancakes around the cut-off mass, which itself increases with increasing β. It is readily apparent from Fig. 3.3a that altering β, even by relatively small amounts, will significantly alter the mass function.

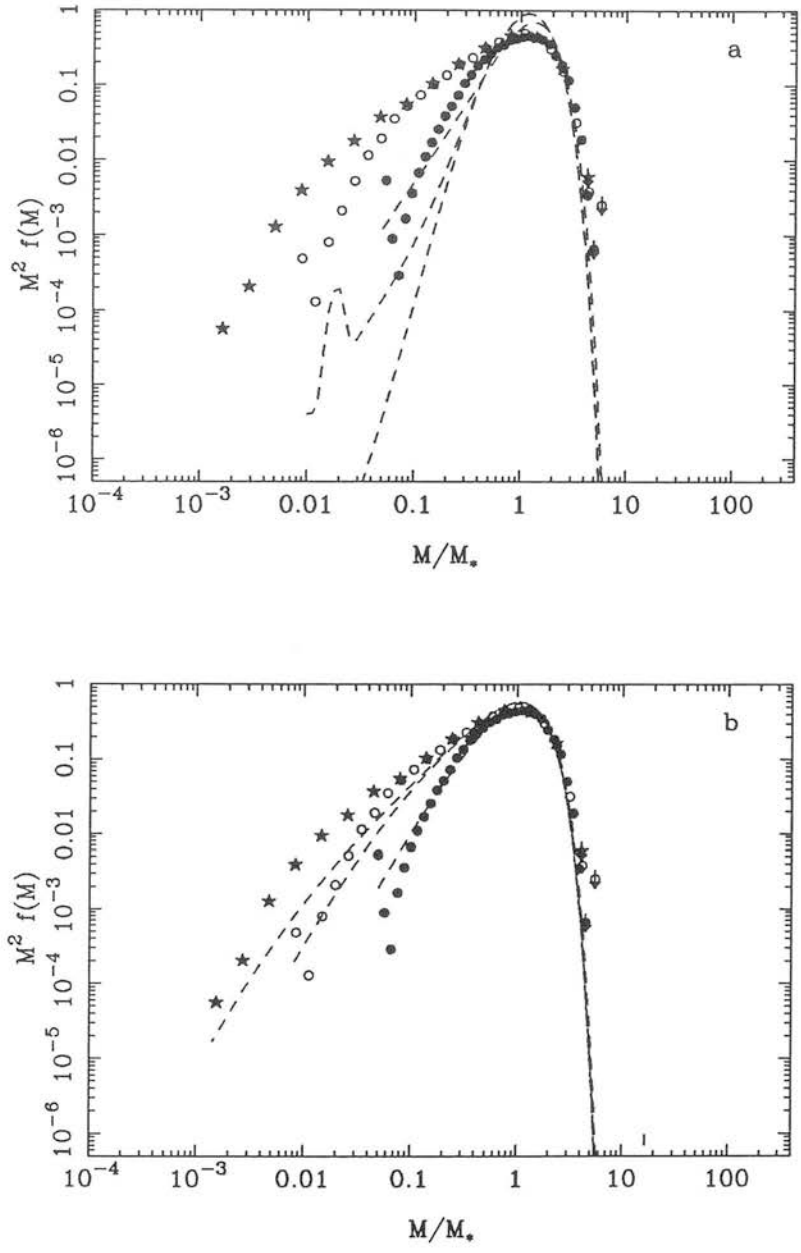

Figure 3.2 As Fig. 3.1b, but showing the effect of different filters on the peaks theory mass function (broken line). (a) shows a power-law filter of k-space form $\exp(-kR_f)$ and (b) a modified power-law filter of k-space form $(1+kR_f)\exp(-kR_f)$ (see Table 3.1).

Unlike the original Press–Schechter case, changes in β and δ_c are not equivalent when using the peaks theory modifications. Altering δ_c (see Fig. 3.3b) produces very little change in the actual form of the mass function, mainly causing the cut-off mass to

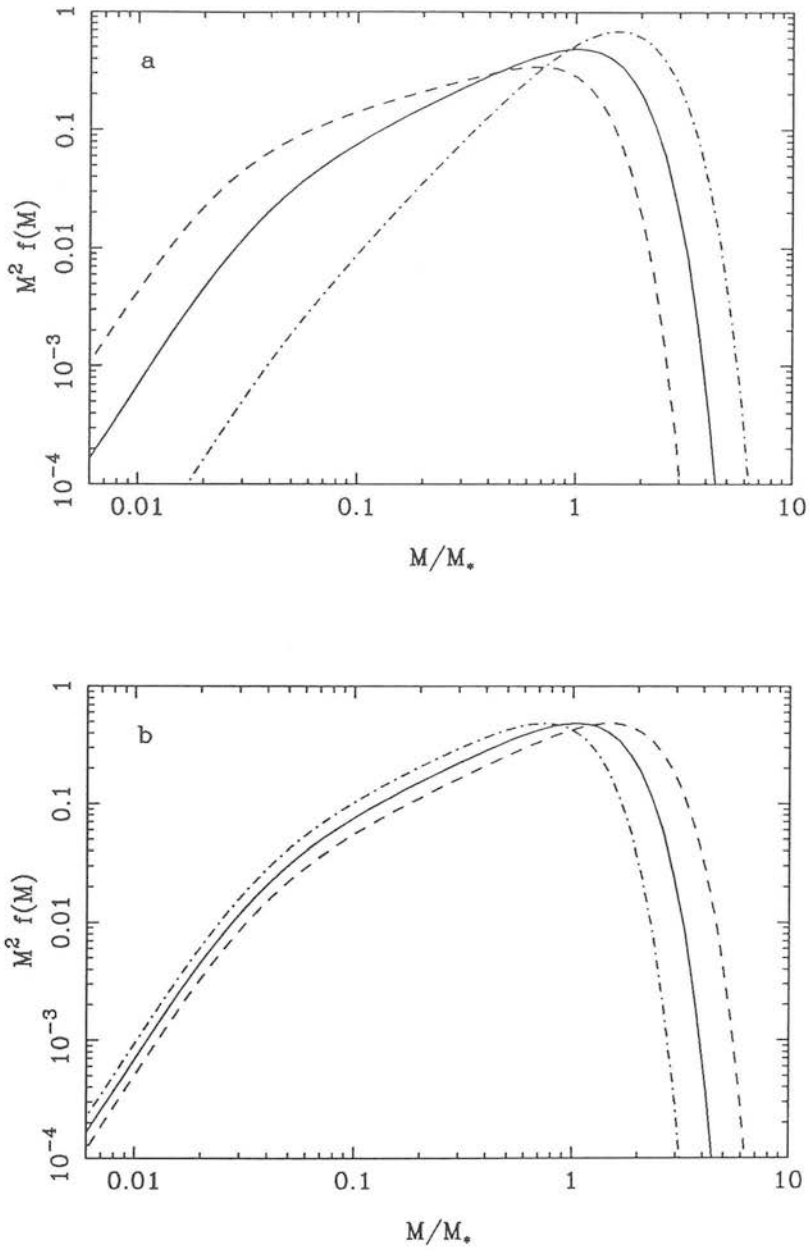

Figure 3.3 The multiplicity function, showing the effect of varying β and δ_c in the peaks theory mass function. The peaks theory curves have been calculated for a spectral index of $n = 1$, using a Gaussian filter and normalised to a single M_*, that of the peaks curve denoted by the solid line. (a) shows the effect of varying the parameter β with δ_c kept at a constant value of 0.71. The three curves are $\beta = 0.7$ (broken line), $\beta = 1.0$ (solid line) and $\beta = 1.4$ (dot-dash line). (b) shows the effect of varying δ_c with $\beta = 1.0$. The three curves are $\delta_c = 0.5$ (broken line), $\delta_c = 0.71$ (solid line) and $\delta_c = 1.0$ (dot-dash line). Unlike the simple Press–Schechter case, the variation of the two parameters is not equivalent.

decrease as δ_c increases.

This suggests that the best procedure for normalising the $M(R_f)$ relation in the context of the peaks theory mass function is to set $\beta = 1$ and that a best fit to the data is then obtained by varying δ_c, given approximately by $\delta_c \simeq 1.4^{-(n+1)/2}$ (see above). It seems that the approach of setting δ_c to a universal constant for all power spectra and then varying β will not give a reasonable fit to the data. Furthermore it is apparent that altering β and δ_c away from those values given for Fig. 3.1 will not significantly improve the fit to the data of the mass functions produced using the two power-law filters, thus leading to the conclusion that out of the filters considered, the Gaussian filter is to be preferred.

3.3.3 Steep Spectra

§ 3.2.4 puts forward the suggestion that the growth of non-linear perturbations would take the limiting form of $M_* \sim M_0 a^{d/2}$, where d is the number of dimensions, rather than the usually assumed value of $\sim M_0 a^{2d/(4+d)}$. It was also claimed that this limiting rate sets in for spectral indices of $n \geq (4-d)$ as opposed to $n \geq (7-d)$.

In order to test this claim in one dimension, a series of simulations were carried out with spectral indices ranging from $n = 3$ to $n = 15$. This verified that the Press–Schechter and peaks theory mass functions break down above $n = 3$, as predicted in § 3.2.4. It also confirmed that the cut-off mass grows as $a^{1/2}$ rather than $a^{2/5}$. The validity of the mass function calculated by Kida (1979) (equation 3.9) was also tested. Fig. 3.4 shows the multiplicity function for a spectral index of $n = 10$ for three different epochs, along with the mass function predicted by Kida (solid line). One can see that the fit of Kida's mass function to data points improves as the simulations go from early epochs (small a) to late epochs (large a), confirming the conclusion reached in § 3.2.4 and supporting the argument that the analysis is only valid for uncorrelated peaks. Kida's mass function has also been fitted to various simulations with spectral indices ranging from $n = 4$ to $n = 15$ and gives good fits for all values of n, though the fit improves with increasing n, as expected from the arguments put forward in § 3.2.4.

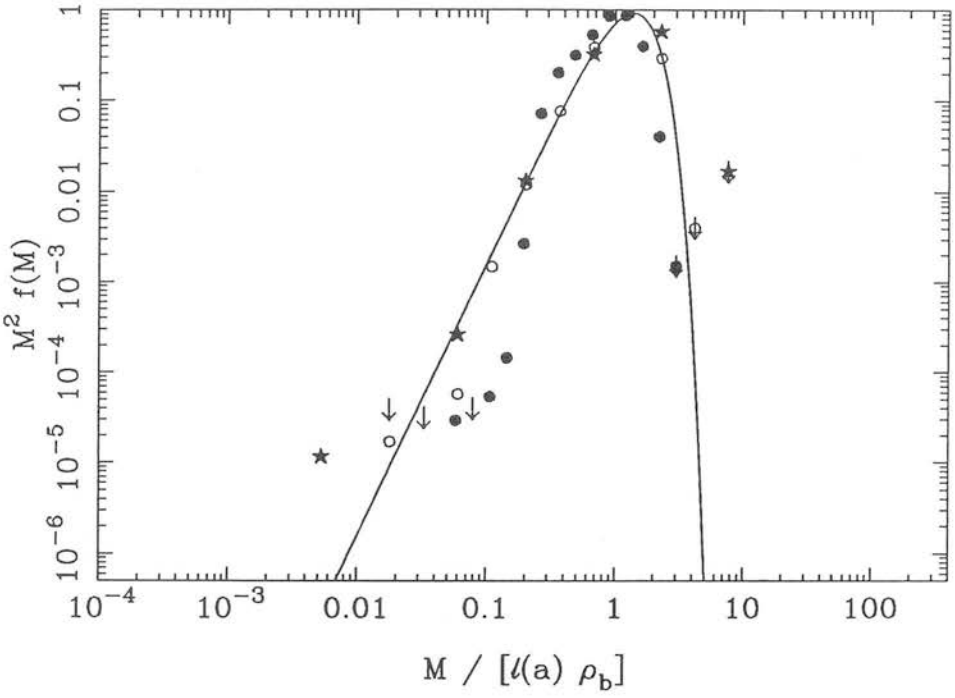

Figure 3.4 Plot of the mass function of Kida (equation 3.9) in the form of the multiplicity function versus M/M_* (solid curve) and adhesion model simulations (data points) for a spectral index of $n = 10$. The three datasets are for epochs 4 (•), 6 (o) and 8 (⋆). The first curve (•) does not fit the theoretical curve as it is only valid for large values of the scale factor, a.

3.3.4 Correlation Functions

This sub-section compares the two-point correlation functions derived from the adhesion model simulations with those calculated from the peaks theory (§ 3.2.5). The two-point correlation function for pancakes is defined as

$$\xi_{\rm p}(r) = \frac{n_{\rm pairs}}{n_{\rm random}} - 1 \tag{3.30}$$

where $n_{\rm pairs}$ is the number of pairs at a given separation, r, and $n_{\rm random}$ is the expected number of pairs at that separation in a random (unclustered) catalogue.

Figs. 3.5 and 3.6 show the correlation function for a 2^{17} point simulation with spectral indices of $n = -\frac{1}{2}$ and $n = 1$ respectively. The four different datasets are for

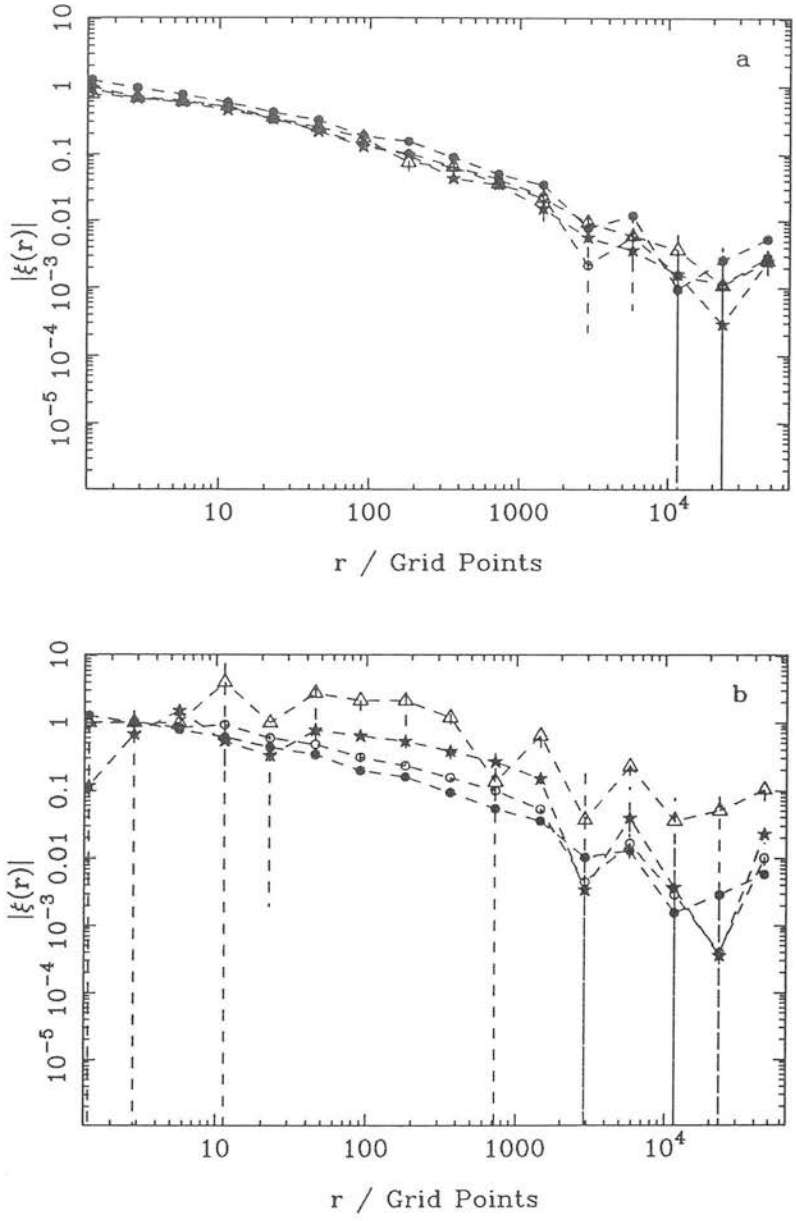

Figure 3.5 The correlation function, ξ_p, for an $n = -\frac{1}{2}$ spectrum. The data points are the mean from eight simulations using 2^{17} point potentials, the error bars representing the standard deviation from the mean. The four different correlation functions are for epochs 2 (•), 4 (○), 6 (⋆) and 8 (△). The two plots show the correlation function calculated using (a) all the pancakes, (b) all pancakes above $M_*/2$.

different epochs, showing the time evolution of the correlation function. The conclusions that one may draw from these figures are heavily dependent on the spectral indices, unlike those for the mass functions.

Considering the data for the $n = -\frac{1}{2}$ power spectrum (Fig. 3.5a) one can see that there is very little change with time in the correlation function calculated using all the pancakes. However, looking at Fig. 3.5b, which shows the correlation function for all pancakes with a mass above $M_*/2$, one can clearly see an increase in amplitude with time which one might naïvely expect from the evolution of the autocorrelation function under linear theory. The difference between the two plots is obviously due to the low-mass pancakes which dominate the counts at all epochs. These low-mass pancakes show very little evolution with time, perhaps because the relative positions of nearby pancakes change little in the absence of small-scale power. Since the low-mass objects dominate the counts, the correlation function of all pancakes shows little evolution. The correlation function of the high-mass pancakes (Fig. 3.5b) has the same slope as the correlation function of all pancakes (Fig. 3.5a) but there is an increase in amplitude with epoch of up to an order of magnitude.

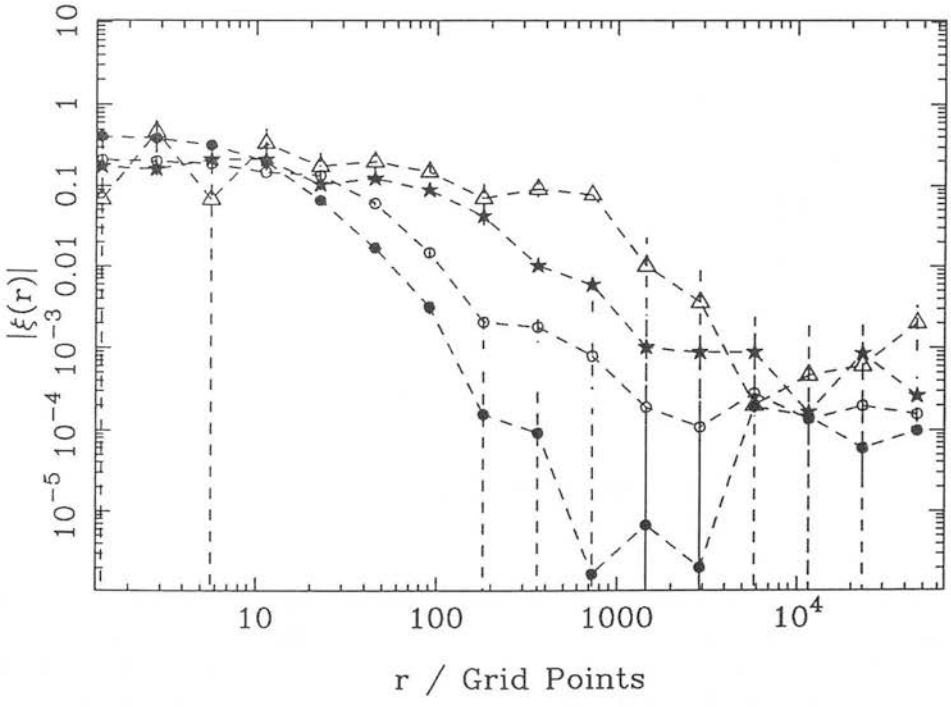

Figure 3.6 As Fig. 3.5a, but for a spectral index of $n = 1$.

In the case of the $n = 1$ power spectrum, Fig. 3.6 reveals the trend towards higher correlation amplitudes with time except at small separations. It should be stressed that, while this effect is similar to that for the $n = -\frac{1}{2}$ potential, the sign of the correlation function is different for the two potentials. For the $n = -\frac{1}{2}$ potential, the correlation function is positive on all except very large scales, but for the $n = 1$ potential, the correlation function is negative, except at very large scales, thus an increase in correlation amplitude means a more negative value of $\xi_p(r)$, i.e. fewer pancakes than expected at a given separation. This is probably due to the large amount of small-scale power leading to high relative motions and mergers of pancakes which gives rise to a complicated evolution of the correlation function.

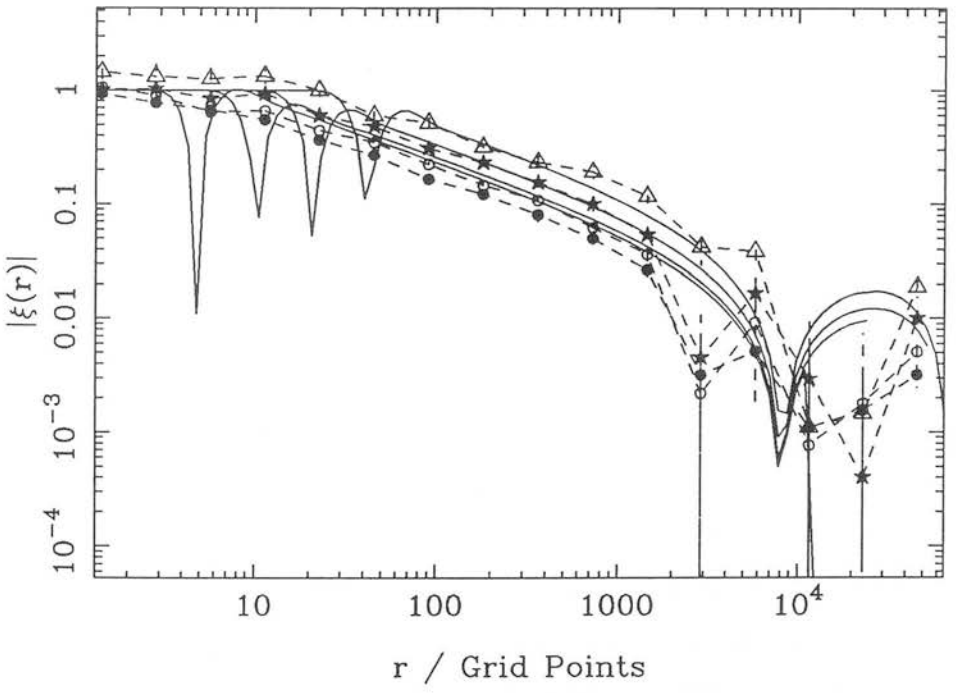

Figure 3.7 The correlation function, ξ_p, (broken line) and the peaks theory correlation function, ξ_{pk-pk}, using a Gaussian filter (solid line) for an $n = -\frac{1}{2}$ potential. The data points are the mean from eight simulations using 2^{17} point potentials, the error bars representing the standard deviation from the mean. All curves are for the same scale factor and show the correlation function calculated using all pancakes above $M_*/8$ (•), $M_*/4$ (o), $M_*/2$ (⋆), and M_* (△).

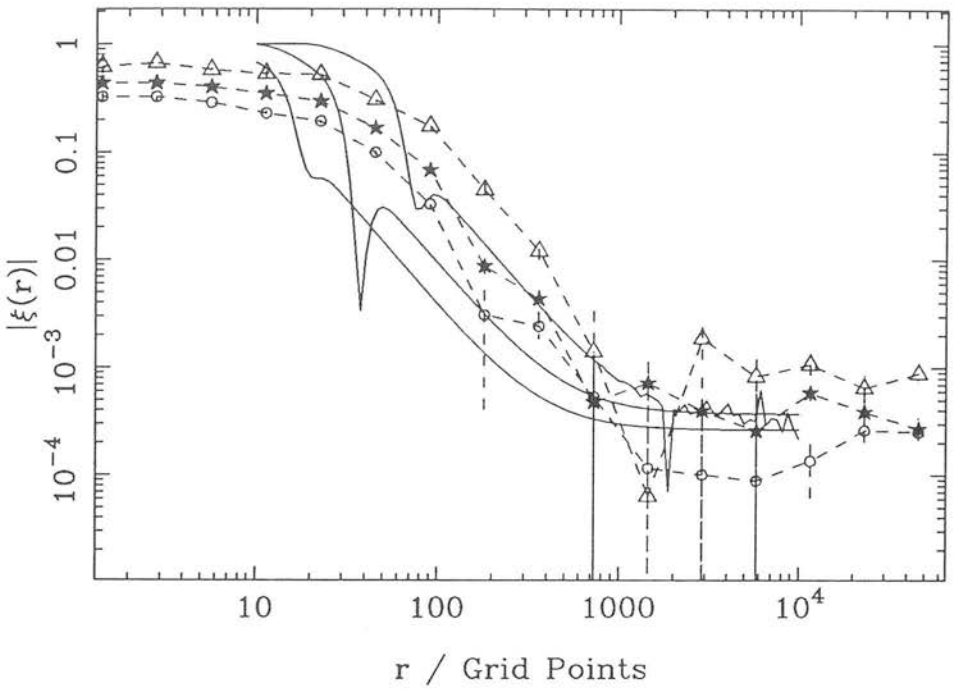

Figure 3.8 As Fig. 3.7, but for a spectral index of $n = 1$. The excessive ringing present in the peaks theory curves is caused by the under sampling of the integral in equation (3.14). No curve is shown for the $M_*/8$ case.

Figs. 3.7 and 3.8 show plots from the same simulations at epoch 4 (corresponding to a value of $M_* = 40.48$). In Fig. 3.7 the four datasets represent correlation functions calculated using only pancakes above $M_*/8$, $M_*/4$, $M_*/2$ and M_* respectively. The four solid lines are correlation functions calculated using peaks theory (equation 3.14) and correspond to the simulations, the density field being smoothed on a mass scale equivalent to the minimum mass of pancake used. In Fig. 3.8 the $M_*/8$ curve is not shown.

Considering Fig. 3.7, one can see that there is quite good agreement between the peaks theory correlation functions and those from the simulations with the same general trends being obeyed. However, Fig. 3.8 shows that the peaks theory correlation functions bear no resemblance to the simulations for the $n = 1$ potential. This is due to the complicated evolution of the correlation function which dominates any statistical

clustering present in the initial conditions. As the peaks theory is a static model which does not take this evolution into account, one would not expect the model to fit the simulations in this case. Also, there is very little power on large scales in the $n = 1$ power spectrum. This means that the correlation amplitude drops rapidly for large separations. However, because peaks theory gives $\xi_{\mathrm{pk-pk}} = -1$ for $r \lesssim R_{\mathrm{f}}$, and the amplitude of $\xi_{\mathrm{pk-pk}}$ goes to zero for $r \gtrsim R_{\mathrm{f}}$, there is only a very small range over which there is sufficient signal to compare the two correlation functions.

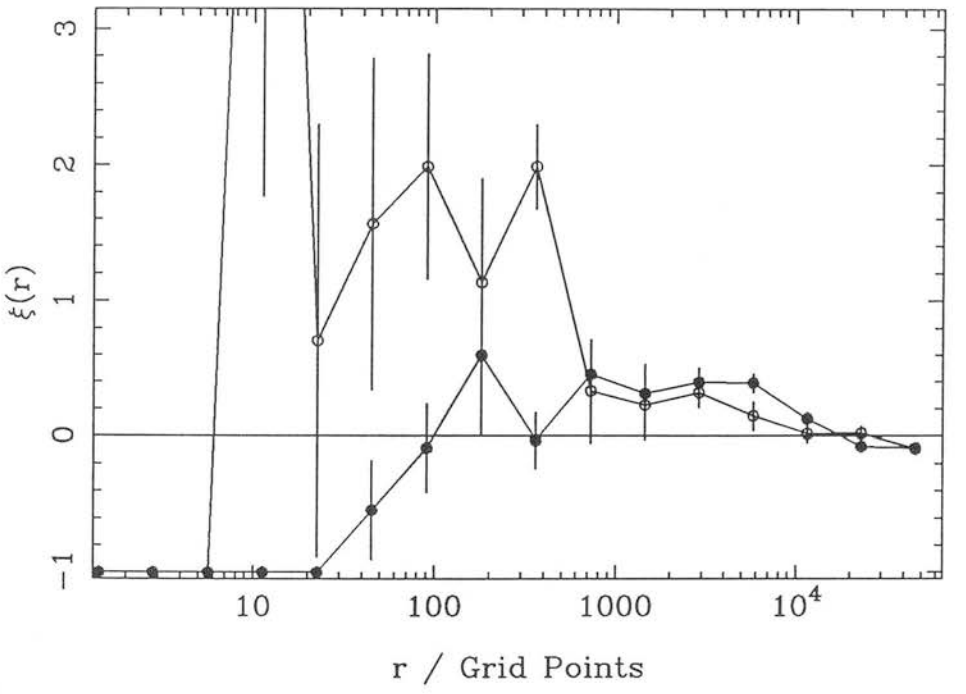

Figure 3.9 The cross-correlation function (•) and the two-point correlation function (o) for an $n = -\frac{1}{2}$ power spectrum at a late epoch with $M_* = 714.3$.

Note that in both cases, although the peaks theory predicts $\xi_{\mathrm{pk-pk}} \to -1$ for $r \lesssim R_{\mathrm{f}}$, this is not the case in the data. As suggested in § 3.2.5, $\xi_{\mathrm{pk-pk}} \neq -1$ for $r \lesssim R_{\mathrm{f}}$ due to movement of peaks over distances of order R_{f}. This assertion may be further supported by performing cross-correlations between the pancake positions and the positions of peaks in the density field when smoothed on a scale $R_{\mathrm{f}}(M)$, where M

is the mass of the pancake. Fig. 3.9 shows the cross-correlation function (filled circles) and two-point correlation function (open circles) for a spectral index of $n = -\frac{1}{2}$ at a late epoch. For small separations, there are no pairs at all, but as the separation increases, so the cross-correlation function increases, until for separations ~ 700 one recovers the two point correlation function. In this case $M_* \simeq 700$ giving $R_* \simeq 1750$. This suggests that though there is not an exact one-to-one correspondence between peaks and pancakes (one would expect a single, large peak at $r = 0$ if this were the case), it suggests that pancakes are located within $\sim R_{\rm f}$ of peaks, accounting for the reduced amplitude of the cross-correlation function in that region. This is consistent with the hypothesis that pancakes form at peaks in the linear density field and then move away from the site of formation by distances of up to $\sim R_{\rm f}$. Indeed, the cross-correlation function suggests that $R_{\rm f}$ should be considered an upper limit to the movement of a pancake.

Note that this movement of peaks is not sufficient to explain the discrepancy between the data and the peaks theory correlation functions in Fig. 3.8. Whereas the movement of the peaks described in § 3.2.5 arises from peculiar velocities in the *linear* density field, the dynamical evolution that causes the clustering for the $n = 1$ power spectrum is non-linear in origin and thus beyond the scope of the peaks theory.

The effect of using different filter functions on the peaks correlation theory has also been investigated. Fig. 3.10 shows the correlation function calculated using a power-law filter equivalent to that used to produce the mass functions in Fig. 3.2b. This clearly predicts far too much clustering on all scales of interest. As with the mass function (§ 3.3.2), the Gaussian filter appears to be the best choice out of the alternative filters that have been investigated.

3.4 Direct Tests of the Linear Theory Assumptions

This section is concerned with the validity of one of the main assumptions of linear theory, namely that objects of mass M form in regions which have $\delta \simeq \delta_{\rm c}$ when smoothed on a scale $R_{\rm f}(M)$ This assumption is checked by finding δ for each pancake formed in the adhesion model simulations used in § 3.3. All the pancakes formed in the simulations are binned by mass into 16 logarithmically spaced bins. The density field is then smoothed with a Gaussian filter of radius $R_{\rm f}(M)$ as given in equation (3.3), where M is the centre of the mass bin. For each pancake in that mass bin the density contrast, δ, at the

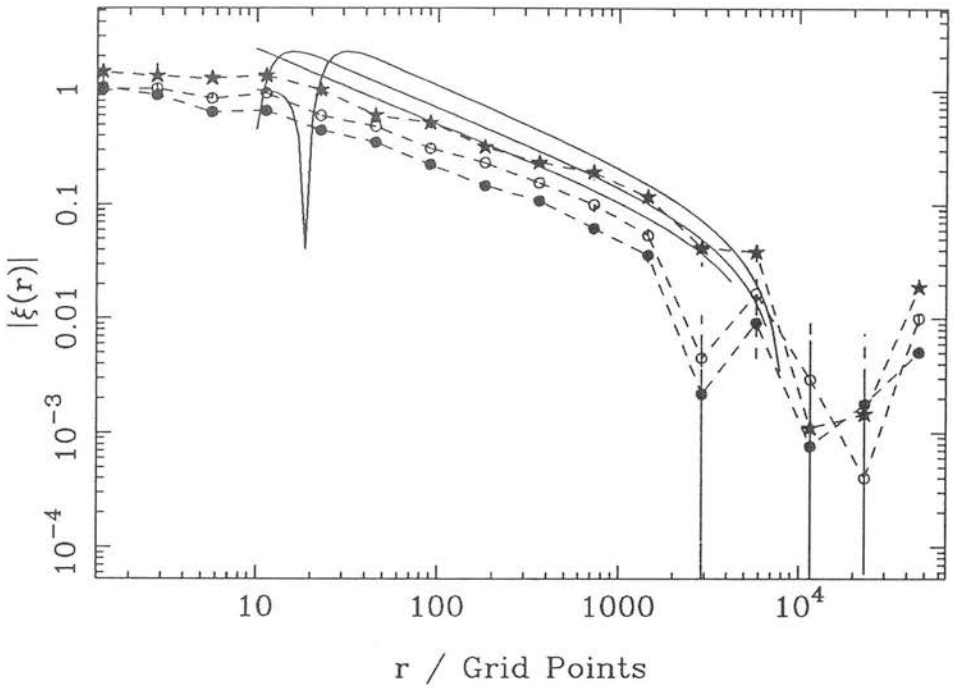

Figure 3.10 As Fig. 3.7, but with the peaks theory correlation function calculated using a power-law filter (see Table 3.1).

Lagrangian co-ordinate half way between the two points of touching of the parabola is calculated for the smoothed density field. An alternative approach, that of finding the density contrast at the highest peak between the two points of touching, has also been used. This is a direct test of the peaks modification of the Press–Schechter formalism described in § 3.2.2 and makes no significant difference to the results presented below.

The results are given in Figs. 3.11 and 3.12 for power spectra with $n = -\frac{1}{2}$ and $n = 1$. Two plots are shown for each power spectrum, the first showing the data for all epochs and the second showing data from pancakes of mass $M \geq M_*$. As it can be seen from the plots, the spread in values of δ is quite small for both spectral indices. Values for the position of the maximum of the distribution, the mean of the distribution, and of its width in terms of the full width at half maximum and standard deviation are shown in Table 3.2.

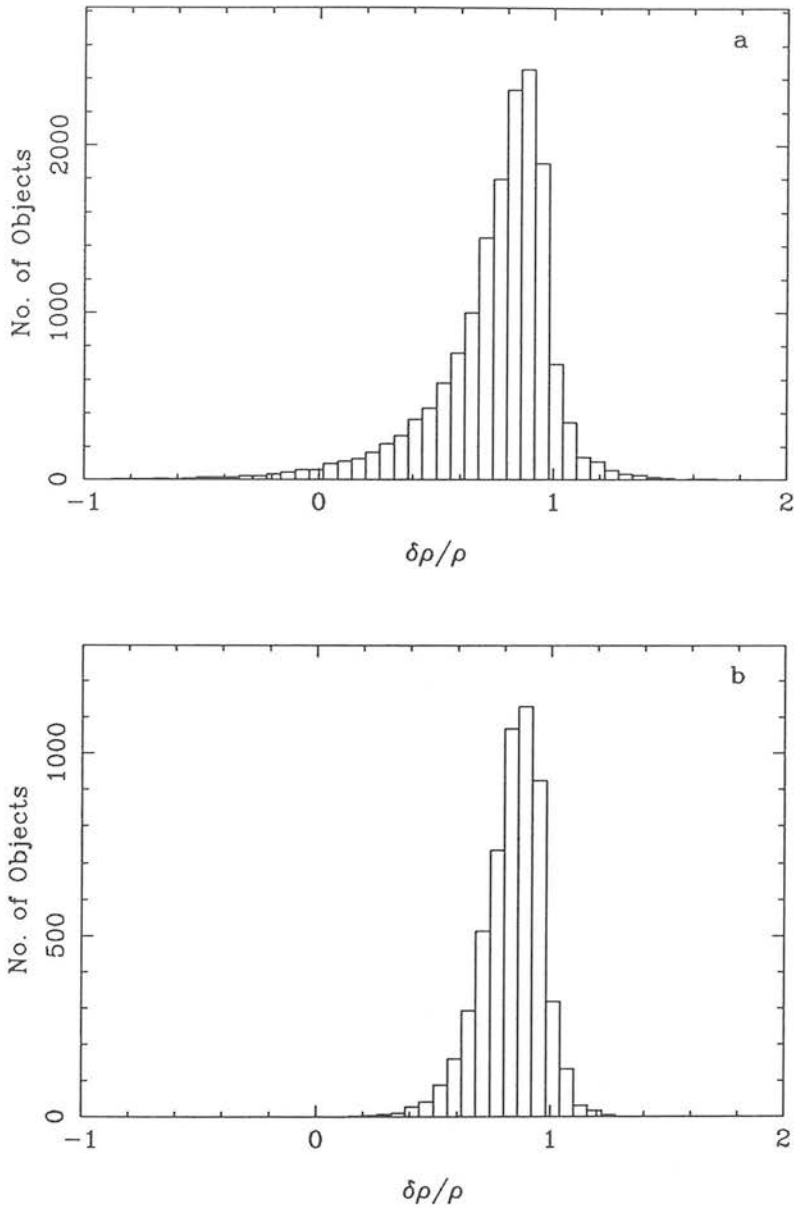

Figure 3.11 Histogram showing the distribution of δ at the centre of the pancake in Lagrangian space when smoothed on a scale $\sqrt{2\pi}M\beta$ with $\beta = 1$. The data are for eight independent realisations of a 2^{14} point simulation with spectral index, $n = -\frac{1}{2}$. The plots are for (a) all pancakes above a minimum mass of 2 grid points for all epochs and (b) all pancakes above the cut-off mass M_* for all epochs.

Looking at Figs. 3.11 and 3.12, one can see the remarkable similarity between the shapes of the histograms and the overall trends in the characteristics of the peak of the distributions, given that they are for two dissimilar power spectra. This is confirmed by

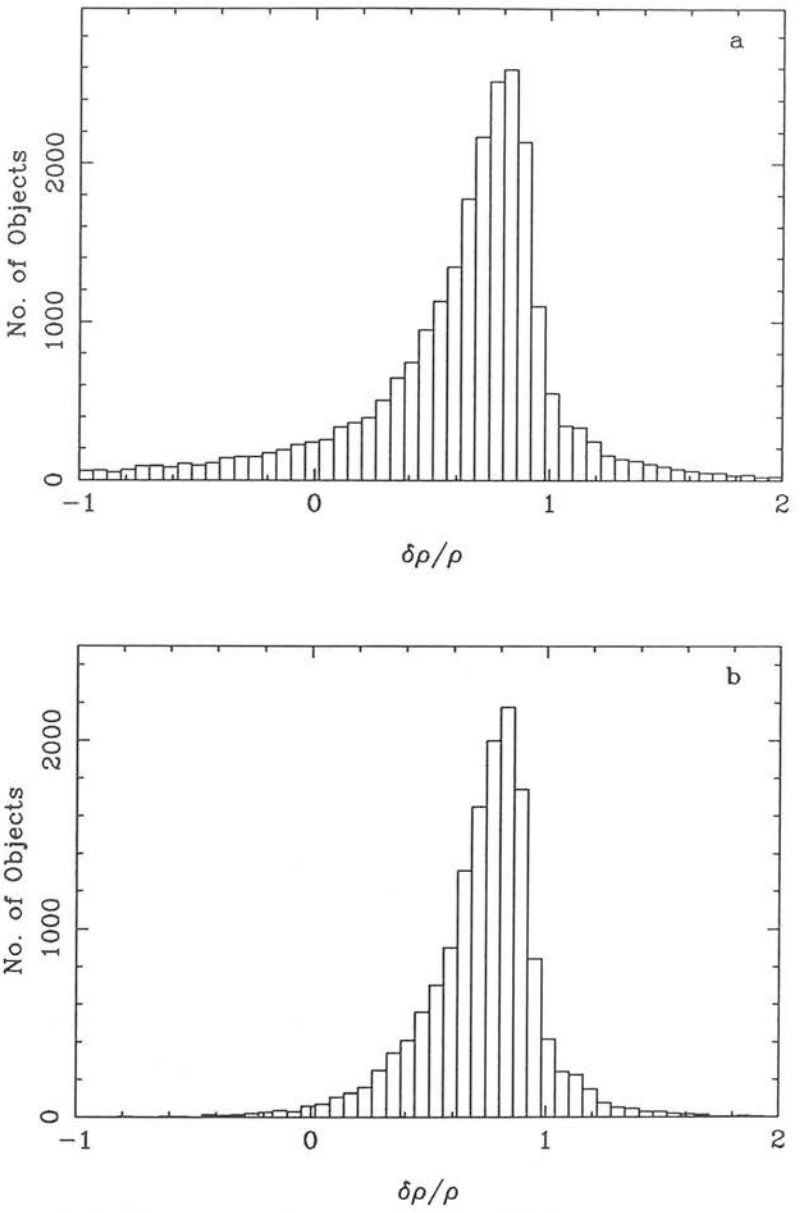

Figure 3.12 As Fig. 3.11, but for $n = 1$.

looking at Table 3.2. However, though the two different power spectra have very similar peak positions and full width half maxima, there is considerable difference between the mean and standard deviations of the two distributions. This is almost entirely due to the tails of the distribution present for the $n = 1$ power spectrum (Fig. 3.12). These are absent in the $n = -\frac{1}{2}$ power spectrum, and arise from pancakes forming in regions

Figure	n	Epoch	Min. Mass	Peak	FWHM	$\bar{x}$	σ_0
11a	$-\frac{1}{2}$	ALL	2.0	0.88±0.02	0.29±0.02	0.75	0.26
11b	$-\frac{1}{2}$	ALL	M_*	0.94±0.02	0.24±0.02	0.83	0.13
12a	1	ALL	2.0	0.85±0.02	0.30±0.02	0.32	3.20
12b	1	ALL	M_*	0.85±0.02	0.30±0.02	0.73	0.26
	$-\frac{1}{2}$	1	2.0	0.91±0.02	0.19±0.02	0.86	0.09
	$-\frac{1}{2}$	8	2.0	0.65±0.05	0.65±0.05	0.51	0.44
	1	1	2.0	0.83±0.02	0.21±0.02	0.80	0.10
	1	3	2.0	0.70±0.05	0.70±0.05	0.52	0.48

Table 3.2 Position of the peak, along with its FWHM, mean and standard deviation for the $\delta\rho/\rho$ histograms shown in Figs. 3.11 and 3.12. Also tabulated are the data for some individual epochs.

where the smoothed density field has $|\delta| \gg 1$. The absence of such extreme variations in the $n = -\frac{1}{2}$ power spectrum is because there is relatively little small-scale power, and hence large local fluctuations are avoided. The location of pancakes in such regions in the $n = 1$ power spectrum can be taken as showing that the linear theory prediction of pancakes forming in regions with $\delta \sim \delta_c$ is not 100% accurate, though inspection of Fig. 3.12 by eye shows that the majority of pancakes are contained within the narrow band $0 < \delta < 1$.

Note that if the peaks theory is a correct interpretation of the physical processes involved in pancake formation then one would expect the histograms to be delta functions located at $\delta = \delta_c$. In linear theory, δ_c is expected to be unity in one dimension. However, best fits for the peaks theory mass functions (§ 3.3.2) were obtained using values of $\delta_c = 0.92$ and 0.71 respectively. Though the data presented in Figs. 3.11 and 3.12 do not support a unique value of δ_c for a given power spectrum, they certainly point towards the majority of pancakes being formed in regions where $\delta < 1$. In all cases the distribution is noticeably skewed towards the left, i.e. low values of δ.

It is also possible to look at data for individual epochs. The statistics of some of these epochs are shown in Table 3.2. From this a general tread with epoch can be seen. At early times the data show a marked decrease in half width, both in comparison with later times and with the data set as a whole. Also note that at later times the

distribution becomes much less peaked (as signified by the rapid increase in half width) and the peak moves away from unity. In the $n = 1$ case this is markedly so, and for late epochs, there is only a broad peak in the range $-2 < \delta < 2$.

This behaviour is to be expected, as for early times the masses of the pancakes will be close to M_*, whereas at late times the majority of the pancakes have mass considerably less than M_*. This can be seen by looking at Fig. 3.1 (§3.3.2), where for late epochs there is a considerable tail to the distribution into the region where $M \ll M_*$. These low-mass pancakes are in the highly non-linear regime and therefore it comes as no surprise if the linear theory prediction of objects forming in regions where $\delta \simeq \delta_c$ does not hold. This is supported by Figs. 3.11b and 3.12b which show data for all pancakes of mass $M \geq M_*$. Removing the low-mass pancakes causes a marked decrease in standard deviation and on visual examination of Figs. 3.11b and 3.12b it can be seen that both distributions have lost their broad wings, confirming that low-mass pancakes form in regions where $\delta \neq \delta_c$. In view of this, it surprising that both the Press–Schechter and, especially, the peaks theory mass functions, predict the correct low-mass slope and give such a good fit to the simulations, especially at late epochs, where the values of δ vary most markedly from the linear theory assumptions.

3.5 Conclusions

The adhesion model has been shown to be a useful tool in the analysis of gravitational clustering and it has been used to test various direct methods, such as the Press–Schechter mass function and the peaks theory mass function of Peacock & Heavens (1990). The tests presented in this chapter are essentially of two types: statistical tests and direct tests of some of the underlying assumptions of linear theory.

Into the first category come the comparisons between the mass and correlation functions, both of which show remarkably good agreement with the simulations. Into the second category comes the investigation of whether pancakes form in regions where $\delta \simeq \delta_c$ and whether pancake positions are closely correlated with the positions of peaks in the smoothed density field.

Both mass functions give accurate fits to the data provided that the spectral index lies in the range $-1 < n \leq 3$. Outside this range the mass function breaks down

completely. The peaks theory mass functions provide a better fit to the data, especially at late times. A best fit is obtained using a Gaussian filter with $\beta = 1$ and δ_c varied according to the power spectrum, but given approximately by $\delta_c \simeq 1.4^{-(n+1)/2}$. For a given power spectrum, the same values of β and δ_c give a good fit to the data for all epochs.

The peaks theory also fares better for low masses where there is a non-power law feature in the power spectrum owing to artificial cut-off imposed by the initial small-scale smoothing. The peaks theory more accurately reproduces this feature in the mass function, suggesting that, in general, it is a better technique than the Press–Schechter mass function.

It has also been shown that *in one dimension* the onset of non-linear effects on the linear part of the perturbation spectrum occurs for lower values of the spectral index than previously thought ($n > 3$ as opposed to $n > 6$) and the validity of the mass function derived for steep spectra by Kida (1979) has been confirmed.

The use of $\delta_c < 1$ (see above) is supported by considering the density contrast of the smoothed density field at the location of the pancakes. The histograms in Figs. 3.11 and 3.12 clearly show that the vast majority of pancakes form in regions where $\delta < 1$, although there is too much spread in the data to support any single value of δ_c for a given power spectrum.

Looking at the two-point correlation functions of the pancake positions, there are considerable differences in behaviour between different power spectra. It should be stressed that peaks theory, which predicts the correlation function from the statistical properties of the initial linear density, fits well for a spectral index of $n = -\frac{1}{2}$, but not for a spectral index of $n = 1$. In the latter case there is little positive correlation statistically and most of the correlation presumably arises out of dynamic evolution of the system. One may speculate that where there is a significant amount of statistical clustering, peaks theory provides a good approximation. However, where statistical clustering is absent, or "anti-clustering" present, the peaks theory is unable to produce an accurate fit to the data.

The choice of filter function has likewise been investigated and several different filter functions have been considered for generating both mass and correlation functions.

It has been shown that the Gaussian filter is preferred over the exponential and power-law filters.

It is clear that although the majority of objects (especially those of low mass) do not form in regions of the linear density field with $\delta = \delta_c$, the resulting linear theory mass functions are an excellent statistical approximation to those obtained from the adhesion model simulations. Also, where the power spectrum contains a significant amount of statistical clustering, the peaks theory correlation function is an excellent approximation to the results of the simulations. All of this suggests that the approach of smoothing the linear density field and identifying objects as peaks above some threshold is a valid statistical approach, although it may not be correct in the detailed location of the objects formed.

Chapter 4

Computer Modelling the Voronoi Foam

4.1 Implementing the Model

4.1.1 The Geometrical Method

As the Voronoi foam is based upon a simple mathematical tessellation, it ought to be possible to construct the Voronoi skeleton from geometrical principles alone, once the initial distribution of the nuclei is known. While this is relatively simple in two dimensions, it will be shown that the algorithm is quite difficult to implement in three.

In two dimensions the algorithm for constructing the Voronoi foam is as follows. A sample two-dimensional foam is shown in Fig. 4.1. The nuclei are shown by open circles. Every wall is terminated by a node at either end and every node has three walls terminating at it. Thus every node is at the boundary of three cells. Visually it is quite easy to construct the geometric skeleton. For each nucleus one takes one of the walls bounding the Voronoi cell and then proceeds in either a clockwise or anti-clockwise direction along the wall until one of the two terminating nodes is reached. One then continues along the next wall that borders the cell and so on, until one returns to the node that one started from.

This is in essence the way that the two-dimensional algorithm used in this thesis constructs the geometrical skeleton. For each nucleus the equation of the line between it and every other nucleus is calculated and the bisector of each line is found. The bisectors form a list of candidate walls. The aim of the algorithm is to find the walls and nodes which surround the chosen nucleus, N_i (see Fig. 4.2).

In order to find the first wall, a line passing through the nucleus and parallel to the x-axis is constructed (broken lines in Fig. 4.2). It is obvious that the first wall that it intersects will be one of the walls bounding the cell containing the nucleus N_i. Let this point be denoted P. The points where the wall intersects all other candidate walls

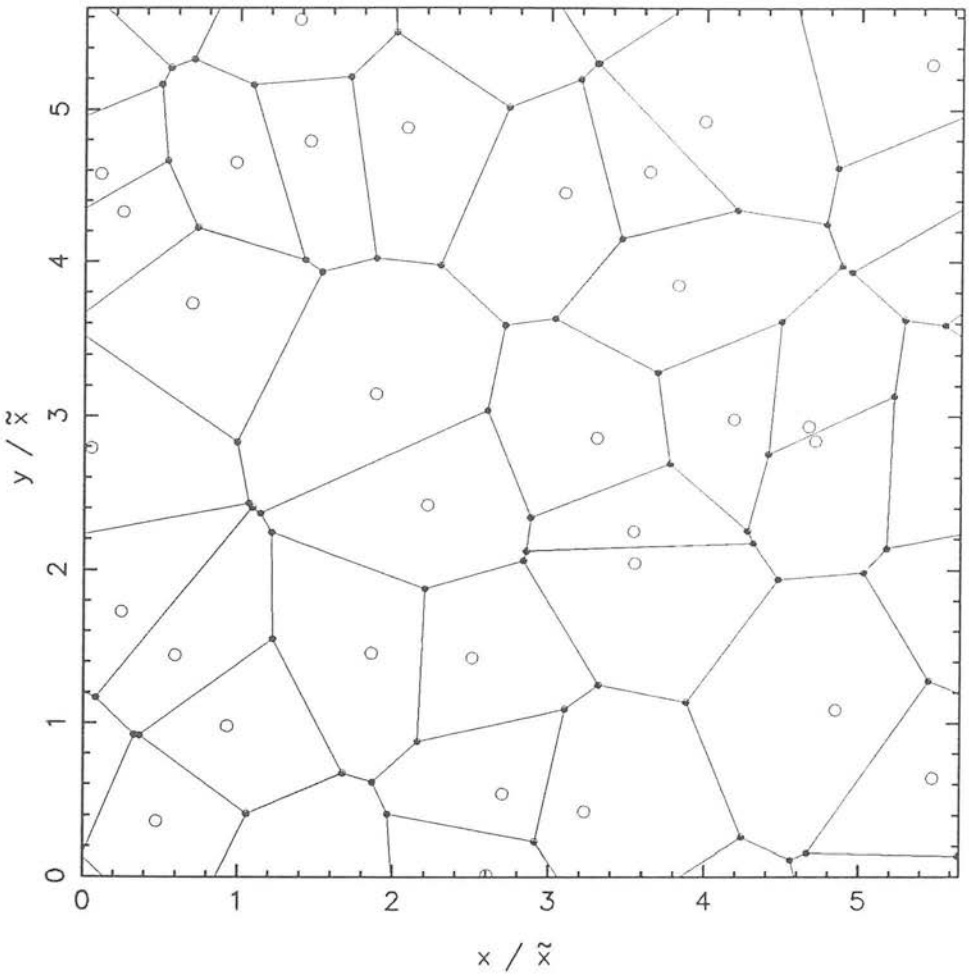

Figure 4.1 A two-dimensional Voronoi foam. The nuclei are denoted by the open circles, the walls by the solid lines and the nodes by the filled points.

are then calculated, these points being candidate nodes. As each wall is terminated by two nodes and the point P lies between the two nodes, it is easy to identify the two true nodes, n_0 and n_1, as those which lie closest to the point P in either direction along the wall.

The node lying in a clockwise direction, n_1, is chosen and an iterative process is then initiated (Fig. 4.3). The position of each node is uniquely defined by the location of the nuclei of the three adjacent cells, N_i, N_j, N_k. The wall between nucleus N_i and the

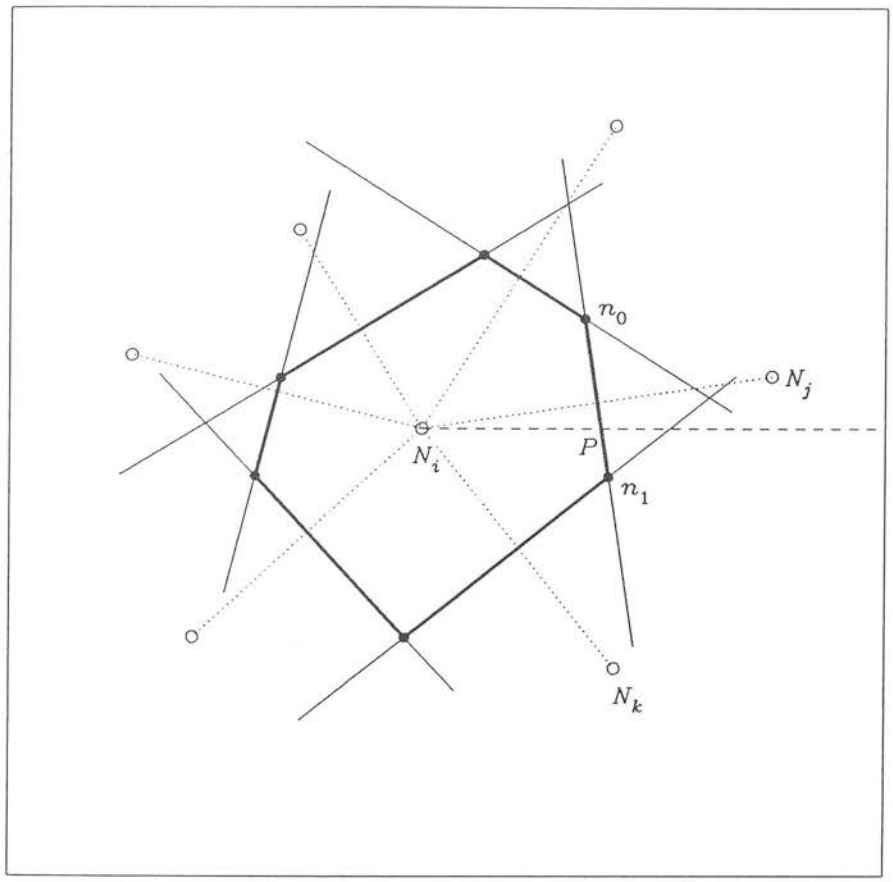

Figure 4.2 Illustration of the geometrical method of solving the Voronoi tessellation in two dimensions. Nuclei are shown by open circles, nodes by filled circles. The walls enclosing the cell occupied by nucleus N_i are shown by the heavy lines. The dotted lines join the other nuclei to N_i and are bisected at their mid-points by the walls. The broken line is described in the text and serves to locate a point, P, on the first wall.

third nucleus, N_k, is constructed and the points where it cuts all other walls are found, one of these points being the node, n_1. From these points, two candidate nodes, n_a and n_b, are chosen using the same criterion as above (see Fig. 4.3). In this case however, one of the nodes, n_a, is false. The true node, n_b, is found by constructing a line (broken line in Fig. 4.3) from each candidate node to the nucleus, N_i. The line between the true node and the nucleus will not cut any other wall whereas the one between the false

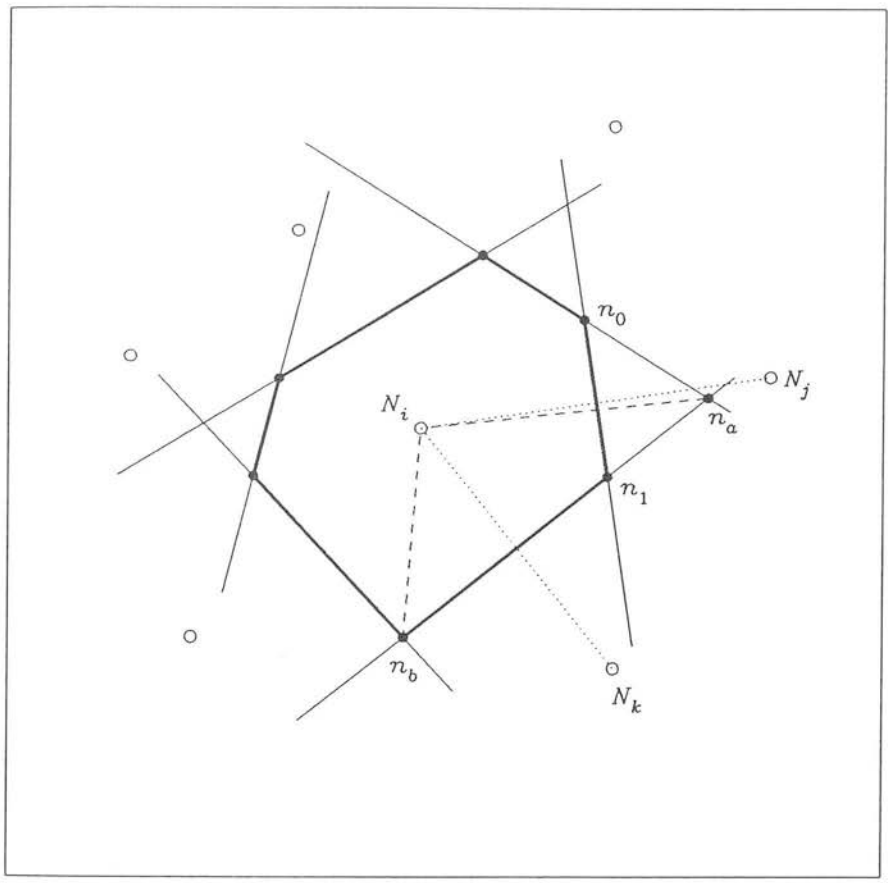

Figure 4.3 As Fig. 4.2, but showing how the true node, n_b, is selected instead of the false node, n_a. Here the broken line joins the candidate nodes (n_a, n_b) to the nucleus, N_i.

node and the nucleus will. The false node is discarded and the true node is used as the starting point for the next iteration. This continues until the new node matches the first node found, n_0.

Rather than identifying each node by its position, which could lead to problems with rounding and computational errors, the nodes are identified by the nuclei of the three adjacent cells, N_i, N_j, N_k. This provides a unique identification of each node. As well as storing each node's position and the three nuclei, the program stores the three

nodes to which each node is connected. This allows the reconstruction of the walls, as they are uniquely defined by the two nodes at which they terminate.

Although this technique is applicable in three dimensions, it has not been implemented. This is because, while relatively straightforward in two dimensions, the three-dimensional case requires the calculation of the equations of planes and the intersection of planes. Whereas in two dimensions the walls are bounded by two points, this is not the case in three dimensions. Here the walls are bounded by many lines. This makes the problem far more complicated than a simple extension of the algorithm. As it took several months to develop the software for the implementation of the two-dimensional algorithm, it was decided that it was not worth the effort required to implement a three-dimensional algorithm.

The code to implement the two-dimensional algorithm is quite straight forward. It is assumed that the distribution of the nuclei has periodic boundary conditions and the program loops through every nucleus in turn, finding the positions of the nodes and walls bounding the cell. The details of the nodes are then compared to those previously found and any repeated nodes are removed. The program produces a list of nodes, recording for each node its position, the three adjacent nuclei and the three adjoining nodes. In two dimensions the total number of nodes is twice the number of nuclei.

4.1.2 The Kinematical Method

The kinematical method described in this section was developed by van de Weygaert & Icke (1989). Rather than constructing the whole of the geometrical skeleton, the basis of the kinematical method is to use test particles to sample the underlying geometrical skeleton. The algorithm is very simple and can be applied to N dimensions. The algorithm is illustrated below for the three dimensional case.

For each test particle, located at $\mathbf{x}$, the nearest nucleus, N_1, is located and the particle is given a velocity, $\mathbf{v}$, directed radially away from the nucleus:

$$\mathbf{v} \propto (\mathbf{x}_0 - \mathbf{p}_1) \tag{4.1}$$

where $\mathbf{x}_0$ is the initial position of the particle and $\mathbf{p}_1$ is the position of the nearest nucleus, N_1.

The particle is moved in a series of time steps, each of length Δt, and its position is modified as follows:

$$\mathbf{x} \rightarrow \mathbf{x} + \mathbf{v}\Delta t \tag{4.2}$$

The particle is moved in this fashion until it is closer to another nucleus, N_2, located at $\mathbf{p}_2$. At this point the particle has crossed through a wall and is now in another cell. By cancelling the particle's velocity perpendicular to the cell wall, the particle is constrained to move along the wall, keeping equidistant between the nuclei of the two adjacent cells. This is achieved by modifying the particle's velocity as follows:

$$\mathbf{v} \rightarrow \mathbf{v} - (\mathbf{v} \cdot \hat{\mathbf{p}})\,\hat{\mathbf{p}} \tag{4.3}$$

where $\hat{\mathbf{p}}$ is the unit vector normal to the plane of the wall given by:

$$\hat{\mathbf{p}} \equiv \frac{(\mathbf{p}_1 - \mathbf{p}_2)}{|\mathbf{p}_1 - \mathbf{p}_2|} \tag{4.4}$$

The particle then moves along the wall as described by equation (4.2) until it is closer to a third nucleus, N_3, located at $\mathbf{p}_3$. The particle has now crossed a filament and entered into a third cell. By cancelling the particle's velocity in the plane defined by the nuclei of the three cells adjacent to the filament, the particle is constrained to move along the filament, keeping equidistant from the three nuclei. This is achieved by modifying the particle's velocity as follows:

$$\mathbf{v} \rightarrow (\mathbf{v} \cdot \hat{\mathbf{f}})\,\hat{\mathbf{f}} \tag{4.5}$$

where $\hat{\mathbf{f}}$ is the unit vector normal to the plane defined by the three nuclei (i.e. the equation of the line describing the filament) and is given by:

$$\hat{\mathbf{f}} \equiv \frac{\frac{\mathbf{p}_1 - \mathbf{p}_3}{|\mathbf{p}_1 - \mathbf{p}_3|} \times \hat{\mathbf{p}}}{\left|\frac{\mathbf{p}_1 - \mathbf{p}_3}{|\mathbf{p}_1 - \mathbf{p}_3|} \times \hat{\mathbf{p}}\right|}. \tag{4.6}$$

The particle then moves along the filament until it is closer to a fourth nucleus. The particle has now reached a node and is stopped. This algorithm may be applied to as many particles as required, each particle being moved independently of the others. In two dimensions all that is required is that the third dimension of all particle and nucleus coordinates are set to zero and the algorithm will automatically stop the particle when it reaches a "filament" (a node in the two dimensional case) as can be seen by inspecting equation (4.3).

4.2 Methods of Analysis

4.2.1 Normalisation of the Length Scale

In order to properly compare two different Voronoi foams it is necessary to ensure that any measurement is made using the same physical units, regardless of the individual simulation. The Voronoi foam is fully defined by the distribution of the Voronoi nuclei and thus the logical physical parameter with which to normalise different simulations is the number density of nuclei. For a given volume this leads to a normalisation of the length scale, namely the characteristic inter-nucleus separation, $\tilde{x}$:

$$\tilde{x} = \sqrt[d]{V/n} = L/\sqrt[d]{n}, \tag{4.7}$$

where n is the number of Voronoi nuclei, V $(= L^d)$ is the area/volume of the simulation, L is the length of side of the simulation and d is the number of dimensions.

In the following work all physical parameters are scaled by the characteristic inter-nucleus separation, $\tilde{x}$. Note that the characteristic inter-nucleus separation is not the mean separation of the nuclei.

4.2.2 The Correlation Function

The two-point correlation function is a much used measure of galaxy clustering and is used in this thesis primarily to provide a comparison with observational data. For this reason its use shall be restricted to three dimensions. For a discussion of its advantages and disadvantages, see Chapter 5.

The two-point correlation function, ξ, is defined (see Peebles 1980) by the joint probability of there being objects present in both of the volume elements δV_1 and δV_2 at a separation r_{12},

$$\delta P = n_0^2 \delta V_1 \delta V_2 \left[1 + \xi(r_{12})\right], \tag{4.8}$$

where n_0 is the mean number density of objects in the sample volume.

When dealing with catalogues of point sources the above definition is not the most useful way of casting the two-point correlation function. Instead the following estimator is used:

$$\xi(r) = \frac{n_s}{n_{exp}} - 1, \tag{4.9}$$

where n_s is the number of *pairs* of objects in the sample at a separation of r and n_{exp} is the expected number of pairs in an unclustered catalogue. In practice $\xi(r)$ is determined for a series of shells of radius r and width $2\Delta r$. For every object in the sample, the distance to every other object is calculated, avoiding double counting, and the number of pairs with separations of $(r \pm \Delta r)$ are counted, giving n_s for each shell. As all the simulations have periodic boundary conditions, any linear separation, $r_i > L/2$ [where $r = (\sum_i r_i^2)^{1/2}$], is modified to $r_i \rightarrow L - r_i$, to account for the wrap around of the structure.

There are two ways of calculating the expected number of pairs, n_{exp}. The first is to distribute an equal number of points at random within the same volume and then follow the same procedure as above, except that the distance is calculated from every object in the sample to every point in the random catalogue. This method is usually used for observational surveys where the boundary conditions of the sample are not uniform.

As the samples generated by the Voronoi foams essentially have no boundaries, one can assume a smoothly distributed catalogue instead. In this case the expected number of pairs in a shell of radius r and width $2\Delta r$ is given by

$$n_{\rm exp} = \frac{4\pi n_0}{3}\left[(r+\Delta r)^3 - (r-\Delta r)^3\right], \tag{4.10}$$

where n_0 is the mean number density of objects in the sample volume.

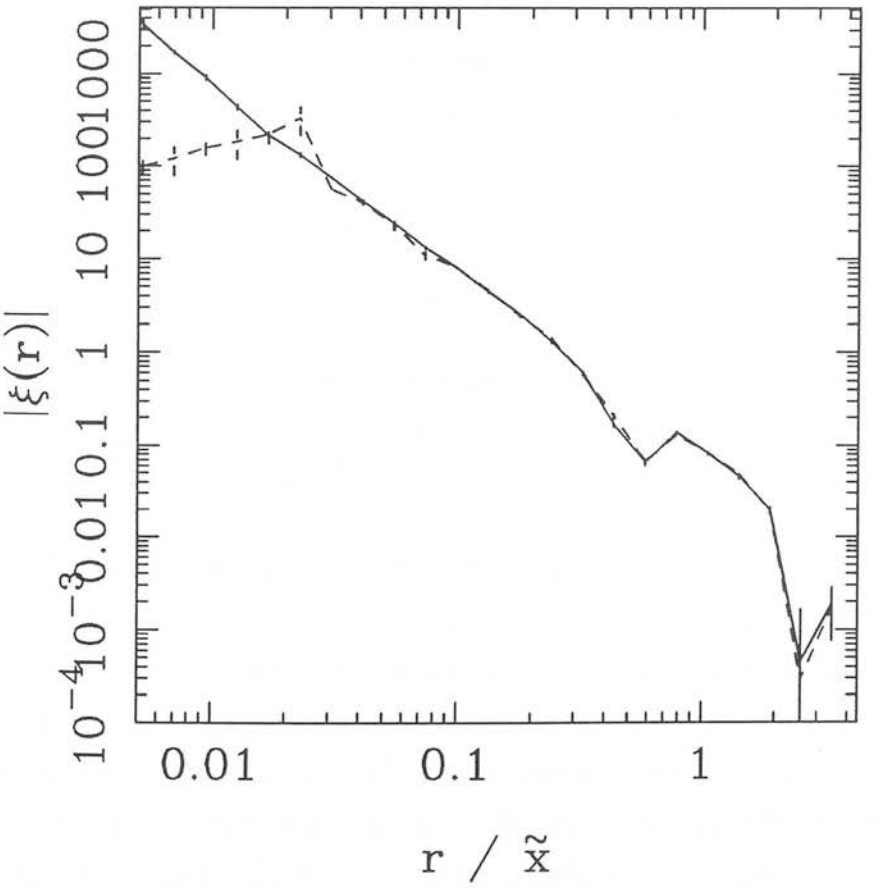

Figure 4.4 The two-point correlation function for the nodes in a Voronoi simulation with 512 randomly distributed nuclei, calculated assuming a smoothly distributed catalogue (solid line) and a randomly distributed catalogue (broken line).

Fig. 4.4 shows the difference between the two methods. The solid line is the two-point correlation function for the nodes in a Voronoi simulation calculated assuming a smoothly distributed catalogue and the dashed line is the same correlation function, but calculated assuming a randomly distributed catalogue. As one can see, the difference between the two correlation functions is negligible for scales of interest ($r > 0.03\tilde{x}$). The difference is due to the lack pairs at extremely small separations in the randomly distributed catalogue. The expected number of pairs can only be an integer in this case, whereas the number of pairs in the smoothly distributed catalogue can be fractional at small separations. This problem can be overcome by using more objects in the random catalogue, thus providing more pairs at all separations. The amplitude of the correlation function is then rescaled to account for the different particle densities in the data and random catalogues. However, as the difference between the two methods is negligible, the assumption of a smoothly distributed catalogue will be adopted for the rest of this thesis on the grounds that it at least halves the time taken to compute the two-point correlation function.

4.2.3 The Angular Correlation Function

The angular two-point correlation function is another much used measure of galaxy clustering and is used in this thesis, like the spatial two-point correlation function, primarily to provide a comparison to observational data.

The angular two-point correlation function is a statistic to measure clustering in the angular distribution of objects. As the angular positions of galaxies are far easier to obtain than their distances, observers have compiled large positional catalogues and have frequently computed the angular two-point correlation function for them (e.g. Groth & Peebles 1977; Maddox *et al.* 1990; Picard 1991a; Collins, Nichol & Lumsden 1992). The advantage of the angular correlation function over its spatial counterpart is that the signal-to-noise is a lot higher. Despite signal being lost due to the lack of a third dimension, this is more than compensated by the increased number of objects available. Due to the difficulty in obtaining redshifts, three-dimensional surveys generally have no more than $\sim 10^4$ galaxies (e.g. Geller & Huchra 1989; Saunders *et al.* 1991) whereas the two-dimensional surveys based on machine scans of wide-angle photographic plates have $\gtrsim 2 \times 10^6$ galaxies (e.g. Maddox *et al.* 1990; Collins, Nichol & Lumsden 1992). This

increase in signal-to-noise also enables the angular correlation function to probe much larger physical scales (where the amplitude of the correlation function is several orders of magnitude below unity) than the spatial correlation function.

In the case of the Voronoi foam simulations, however, the three-dimensional positions are automatically provided and so it is necessary to reduce this information to the angular positions alone. This is done by projecting the positions of the objects in the three-dimensional catalogue onto the back plane of the simulation cube. It is useful to define a set of spherical polar coordinates. Placing the origin at the centre of the $z = 0$ plane leads to an obvious choice of coordinates. r is the radial distance from the origin, ϕ the angle from the x-axis in the x-y plane and θ the angle from the z-axis. All objects within the simulation volume that then lie within a cone of opening angle $\theta_{\rm max}$ centred with its apex on the origin and axis parallel to the z-axis are selected according to some radial selection function, $S(r)$ (to be defined later, see § 5.5.3), and their angular positions (θ, ϕ) are recorded. This provides a catalogue of angular positions of particles in the Voronoi foam.

The angular two-point correlation function, w, is defined in an analogous way to the spatial two-point correlation function (§ 4.2.2), i.e. by the joint probability of objects being present in both of the solid angle elements $\delta\Omega_1$ and $\delta\Omega_2$ at an angular separation θ_{12} (see Peebles 1980),

$$\delta P = N_0^2 \delta\Omega_1 \delta\Omega_2 \left[1 + w(\theta_{12})\right], \tag{4.11}$$

where N_0 is the mean surface density of objects in the sample area.

As with the spatial two-point correlation function, the estimator in equation (4.9) is used for catalogues of point objects, where $n_{\rm s}$ is now the number of pairs of objects in the sample at an *angular* separation of θ.

In practice $w(\theta)$ is determined as for the spatial correlation function, but in a series of annuli of radius θ and width $2\Delta\theta$. As the catalogue is projected, it is not possible to allow the structure to wrap-around , thus the catalogue has definite boundaries and a random catalogue is used instead of a smoothly distributed one. This is generated by distributing an equal number of objects within the sample area. Each object has a ϕ

coordinate chosen at random from $0 - 2\pi$ and a θ coordinate chosen at random from $\cos\theta_{\max} \leq \cos\theta \leq 1$, the latter accounting for the projection of a sphere onto a plane and ensuring a smooth (unclustered) distribution of points in the random catalogue.

4.2.4 The Power Spectrum

Power spectrum analysis is a powerful and flexible tool for the analysis of clustering in the spatial distribution of a set of points. It is the primary method that will be used in the remainder of this thesis to determine the clustering properties of a given distribution of points, such as Voronoi nuclei or particles in a Voronoi foam. The quantity used to describe the power spectrum, $\Delta^2(k)$, is defined as the contribution to the variance per $\ln k$:

$$\Delta^2(k) = \frac{d\sigma^2}{d\ln k} = A|\delta_{\mathbf{k}}|^2 k^d, \tag{4.12}$$

where k is the wavenumber ($= 2\pi/\lambda$) and $\delta_{\mathbf{k}}$ is the Fourier transform of the spatial density field, $\delta_{\mathbf{x}}$:

$$\delta_{\mathbf{k}} = \frac{1}{L^d}\int_0^\infty \delta_{\mathbf{x}} \exp(i\mathbf{k}\cdot\mathbf{x}) d^d x. \tag{4.13}$$

The constant, A, is given by

$$A = \frac{L^d}{2\pi^{d-1}}, \tag{4.14}$$

where L is the size of the square/cube containing the sample and d is the number of dimensions.

The power spectrum, $\Delta^2(k)$, is in practice calculated by binning the data on an $L = 64^3$ or 100^3 grid in three dimensions and an $L = 256^2$ grid in two dimensions. The data are then fast Fourier transformed and the individual Fourier components, $f_{\mathbf{k}}$, are summed over shells in k-space of width $2\Delta k$ centred on k, to give $\Delta^2(k)$:

$$\Delta^2(k) = \frac{\sum_{\text{shell}} |f_{\mathbf{k}}|^2}{\delta \ln k}, \tag{4.15}$$

where $\delta \ln k$ is the width of the shell in log space and

$$\begin{aligned} f_{\mathbf{k}} &= \sum_x f_{\mathbf{x}} \exp(i\mathbf{k} \cdot \mathbf{x}), \\ f_{\mathbf{x}} &= n/N. \end{aligned} \tag{4.16}$$

Here $f_{\mathbf{k}}$ and $f_{\mathbf{x}}$ are the discrete counterparts of the continuous variables $\delta_{\mathbf{k}}$ and $\delta_{\mathbf{x}}$, with n being the number of particles at a given grid point and N being the total number of particles in the simulation. Note that this is equivalent to the more usual formulation $nL^d/N - 1 (\equiv \delta_{\mathbf{x}})$, except that this formulation introduces a $k = 0$ term that must be accounted for in the power spectrum.

The definition of the Fourier transform assumes a continuous distribution of the density field. Any structure sampled by a discrete distribution of points will give rise to a noise component which is independent of any intrinsic clustering in the sample.

The power spectrum, as defined in equation (4.15), involves taking the modulus of the Fourier components. Expanding,

$$|f_{\mathbf{k}}|^2 = \sum_{x,x'} f_{\mathbf{x}} f_{\mathbf{x}'} \exp[i\mathbf{k}(\mathbf{x} - \mathbf{x}')], \tag{4.17}$$

and examining the diagonal terms, $\mathbf{x} = \mathbf{x}'$, reveals that the phase factor is always unity and thus one is left with $\sum f_{\mathbf{x}}^2$. For discrete objects, this is always nonzero, even in the limiting case of an infinitesimally small grid, where each grid point is either empty or has only one particle. In this case the diagonal term reduces to

$$\sum f_{\mathbf{x}}^2 = \sum_i n_i^2/N^2 = 1/N. \tag{4.18}$$

This is the shot-noise term which must be subtracted from the power spectrum to account for discrete sampling. Thus the power spectrum, $\Delta^2(k)$, is given by

$$\Delta^2(k) = \frac{\sum_{\text{shell}} (|f_{\mathbf{k}}|^2 - 1/N)}{\delta \ln k}. \tag{4.19}$$

Note that this derivation is only strictly valid in the case of Poisson sampling of a continuous medium. It is not immediately apparent that this is the case for structures in the Voronoi foam. Even in the case where the particles are distributed initially at random, the final sampling of the structure is not necessarily a Poissonian process. It shall be assumed that despite this non-Poissonian sampling, the shot-noise contribution given by equation (4.18) is applicable and the power spectrum will be calculated according to equation (4.19). Fig. 4.5a shows the power spectra for particles in walls taken from four two-dimensional Voronoi simulations using the kinematical method, each using the same distribution of nuclei, but with different particle densities (2, 8, 32 and 128 particles per nucleus going from top to bottom). The power spectra have been calculated without noise subtraction (equation 4.15). As one can see, the power spectrum changes considerably with changing particle density, the power decreasing as the number of particles increases, which is as expected. Fig. 4.5b shows the power spectra from the same simulations, but calculated with shot noise subtracted (equation 4.19). The four power spectra now agree within the intrinsic noise caused by undersampling (§ 4.3.1), thus supporting the decision to remove shot noise from the power spectra.

However, the non-Poissonian nature of the sampling becomes more important when the initial particle distribution is non-random (e.g. § 4.3.4) The applicability of noise subtraction in this case shall be discussed in more detail in § 4.3.4.

A point where the applicability of the above noise subtraction breaks down is when the particles are weighted in some manner (§ 4.5.2; Appendix D). If each particle is given some weight, W, then $f_{\mathbf{x}}$ (equation 4.16) becomes

$$f_{\mathbf{x}} = \frac{\sum_j W_j}{\sum_k W_k}, \tag{4.20}$$

where j is summed over the n particles in the grid point and k is summed over all particles. Thus, in the limit discussed above, where each grid point contains one or no particles, equation (4.18) becomes

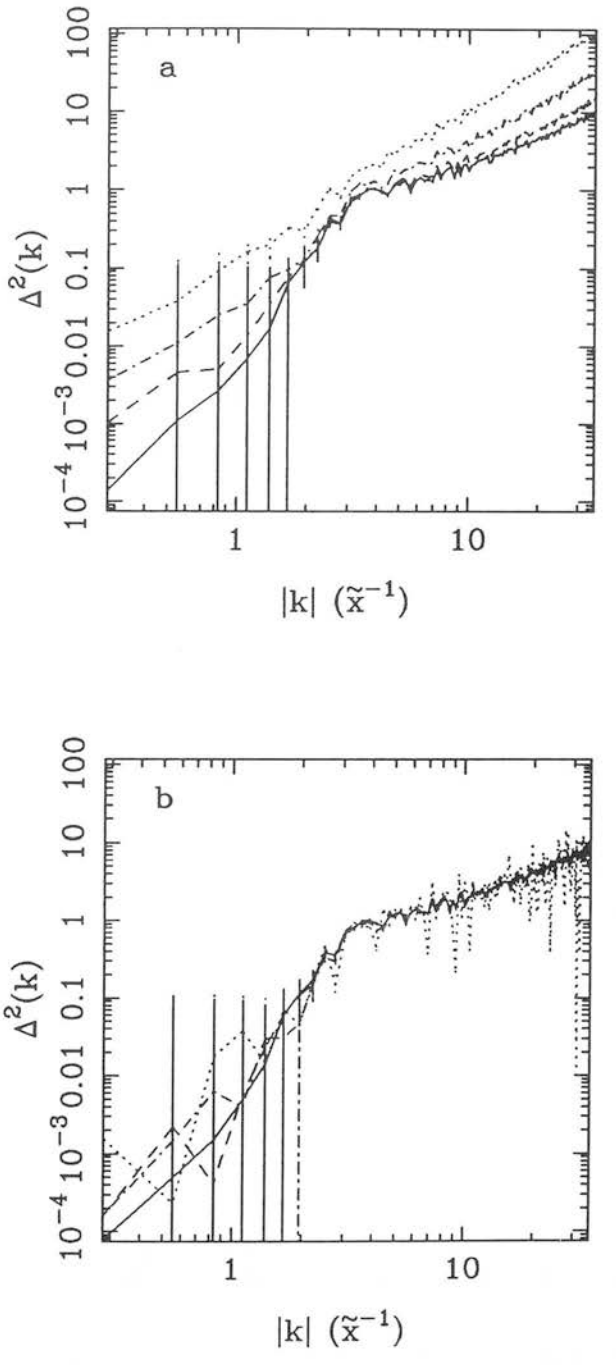

Figure 4.5 Power spectra for particles in walls in a two-dimensional Voronoi foam generated using the kinematical method. The four power spectra represent simulations using the same distribution of nuclei, but with particle densities of 2 (dotted line), 8 (dot-dash line), 32 (broken line) and 128 (solid line) particles per nucleus. (a) shows the power spectra with no noise subtraction while (b) shows the power spectra with the shot-noise component given in equation (4.18) subtracted. The error bars are Poissonian.

$$\sum f_{\times}^2 = \sum_i \frac{W_i^2}{(\sum_k W_k)^2} \tag{4.21}$$

which is now the correct noise component for a weighted power spectrum. The validity of this shall be demonstrated in § 4.5.2.

Noise subtraction is inapplicable in the case where foams are generated using the geometrical method. This is because the structure is exact, thus the correction for discrete sampling is not required. However, as the foam is continuous in this case and the Fourier transform is carried out on a discrete grid, it is necessary to digitise the Voronoi foam onto a two-dimensional grid. The nodes are simply treated as individual particles and given an equal weighting. The contribution of the walls is obtained by calculating the length of wall that passes through each grid point in the Fourier grid and multiplying this by the line density (set to a constant for all walls in a foam). The grid is then Fourier transformed in the normal manner and the power spectrum calculated as above (equation 4.15).

In the case where nodes or Voronoi nuclei are being considered, these are point objects, and it may be argued that they also have an intrinsic shot-noise component. The shot-noise contribution arises in the case where a continuous medium is sampled by a discrete distribution of points. In the limit as $N \to \infty$, this gives over to the continuous case, so no noise component arises. However, for point objects, such as nuclei and nodes, the intrinsic clustering built into the distribution will not be reduced as N is increased. For this reason, no noise subtraction shall be made for distributions of point objects and the power spectrum for nodes or nuclei shall be calculated according to equation (4.15).

4.3 The Kinematical Method — Free Parameters

The kinematical method, as described in § 4.1.2, has several free parameters for a given distribution of Voronoi nuclei, unlike the geometrical method, which has no free parameters. The free parameters of the kinematical method arise as initial conditions and are either set to an optimal value or varied depending on the requirements of the individual simulations. The aim of this section is to present the various initial conditions used in the simulations in the rest of this thesis.

4.3.1 Particle Density

The kinematical approach uses particles to sample the Voronoi foam. It is necessary to sufficiently sample the structure so that any relevant features are not missed and that the noise caused by the discrete sampling of the structure is kept to acceptable levels. However, oversampling the structure, while not bringing any extra information, is wasteful both of storage space and computer time. Thus an optimum particle density is sought.

The particle density is expressed as the ratio of particles to Voronoi nuclei. Fig. 4.6 shows power spectra for the particles at walls (solid lines) in a three-dimensional Voronoi foam. The individual plots (a) → (d) are for particle densities of 16, 20, 24 and 28 particles per nucleus respectively. As one can see, the noise dies down to acceptable levels by the time 20 particles per nucleus are used. There is little to be gained by using more particles (Fig. 4.6c, d). The case of particles in walls is the worst scenario, which is to be expected. Filaments and nodes, being strings and points respectively, need far fewer particles to adequately sample the structure. This is born out by the broken lines in Fig. 4.6 which show particles at the nodes. As one can see, there is essentially no difference despite the increase in sampling. Thus, unless otherwise stated, a particle density of 20 particles per Voronoi nucleus will be used in this thesis.

The power spectrum is not the only analytical tool used to investigate the Voronoi foam. Fig. 4.7 shows the two-point correlation function calculated for the same simulations as the power spectra in Fig. 4.6. As one can see, the two-point correlation function is less sensitive to particle density than the power spectrum. Thus the adopted particle density of 20 particles per nucleus is more than adequate for the two-point correlation function.

The two-dimensional kinematical method is primarily used as a comparison to the geometrical approach, thus the two dimensional particle density will be determined by direct comparison to the geometrical approach (see § 4.5).

4.3.2 Step Size

The kinematical approach advances each particle in a "time step" of length Δt (equation 4.2). This introduces a minimum step length, $\Delta x = v\Delta t$, where v is the particle's

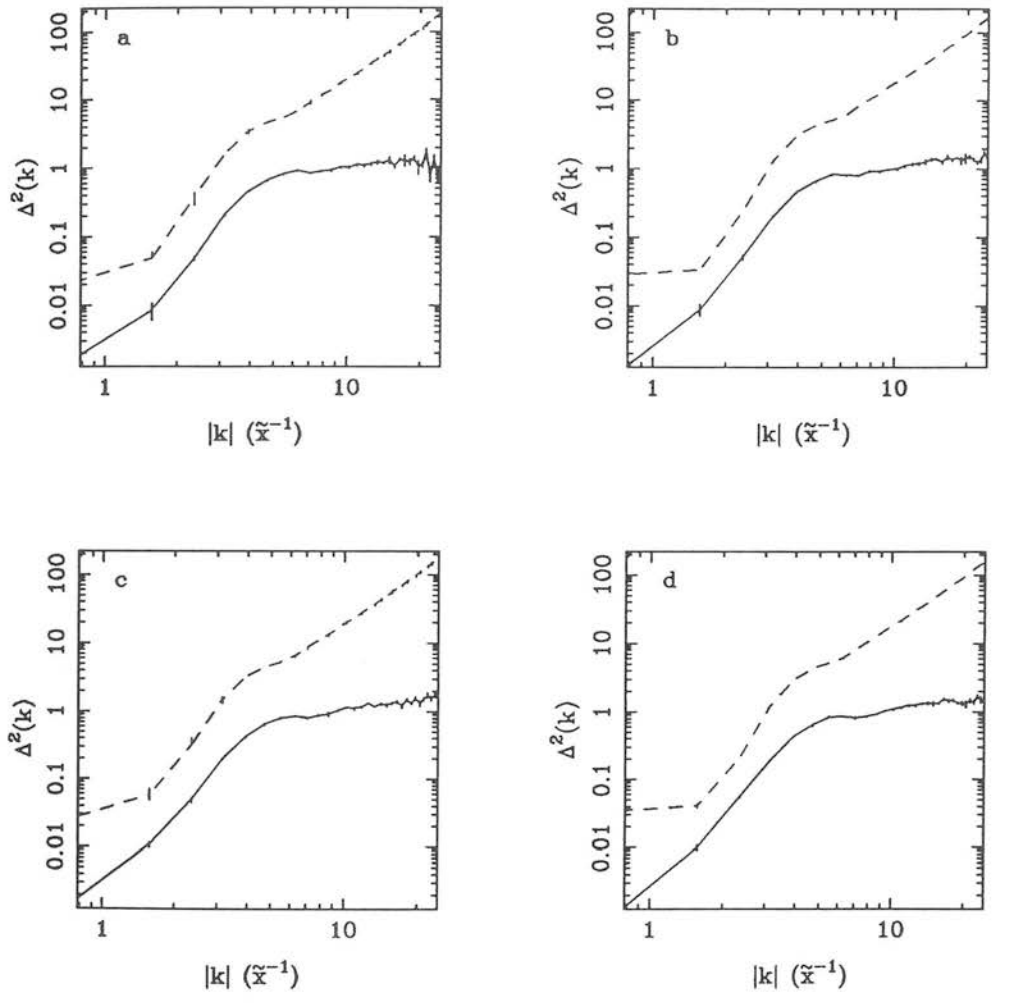

Figure 4.6 The power spectra for particles in walls (solid line) and nodes (broken line) in a Voronoi simulation with 512 randomly distributed nuclei. The four plots are for particle densities of (a) 16 particles per nucleus, (b) 20 particles per nucleus, (c) 24 particles per nucleus and (d) 28 particles per nucleus. Each power spectrum is the mean of five independent realisations and the error bars represent the standard deviation of the mean.

velocity. Particles are advanced until they enter another cell. If Δx is too large, then it is possible that the particle will overshoot the adjacent cell and enter a third cell. However, this is an unlikely event. It is more common that the particle will overshoot the wall by a small amount and this error will be propagated when the particle reaches a filament and then a node.

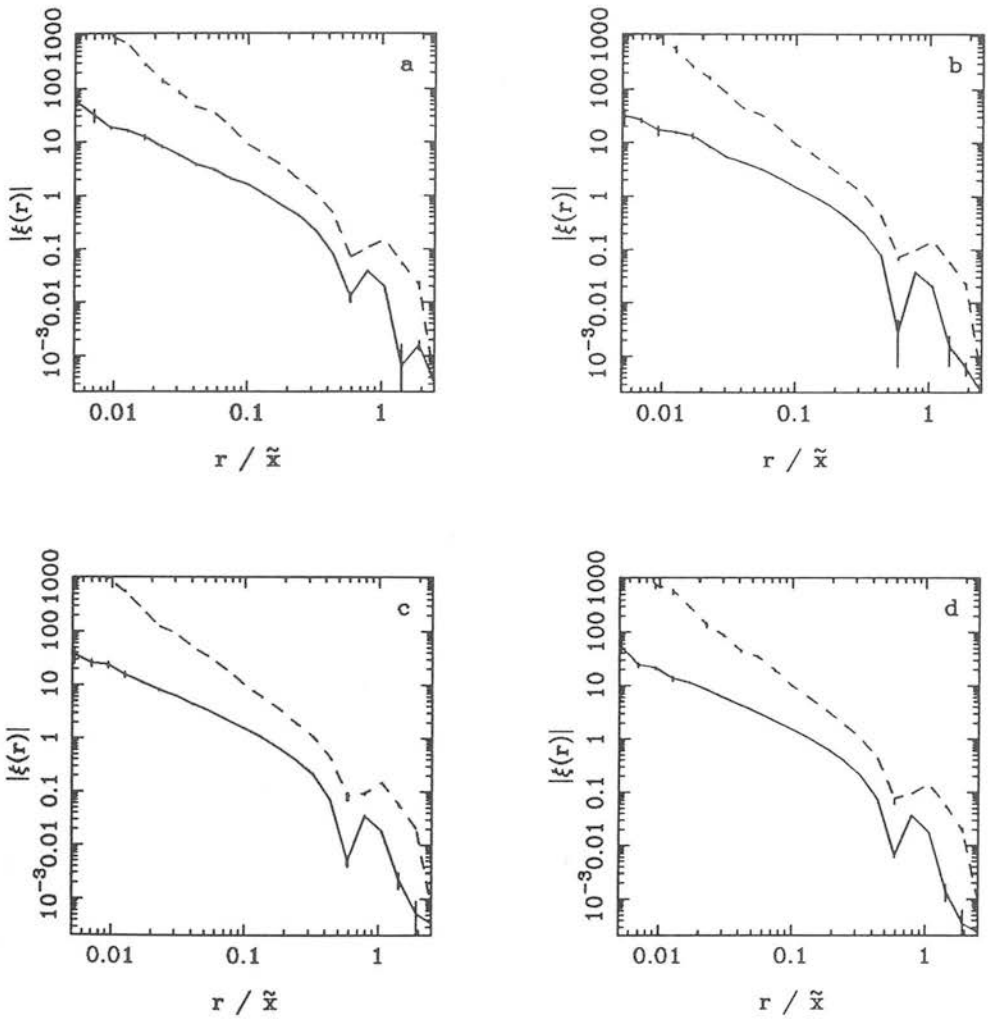

Figure 4.7 As Fig. 4.6, but showing the two-point correlation functions for walls (solid lines) and nodes (broken lines) respectively. The particle densities are the same as in Fig. 4.6.

This leads to walls becoming sheets with a finite width, filaments becoming cylinders and nodes becoming small spheres of particles. In the strict geometrical skeleton the walls, filaments and nodes do not have this "thickness". However, this only affects clustering on the scale Δx and below. Large-scale clustering is unaffected. Thus it is necessary to optimise Δx, depending on the scale of interest. If Δx is too large, then clustering on scales of interest will be affected. If Δx is too small, then no extra resolution will be gained, but the simulation will take a greater number of steps to reach an equivalent position, thus wasting computer time.

For power spectrum analysis, the maximum resolution is set by the largest grid that may be Fourier transformed. In three dimensions this is 100^3, leading to, for a simulation of side of length L, a minimum grid size of $0.01L$. To ensure that only a suitably small number of particles end up at the wrong grid point a step size of $\Delta x = 0.001L = 0.001\sqrt[3]{n}\tilde{x}$ is more than adequate, where n is the number of Voronoi nuclei. In two dimensions the largest grid is 256^2, leading to a step size of $\Delta x = 4 \times 10^{-4}L = 4 \times 10^{-4}\sqrt{n}\tilde{x}$.

For a three-dimensional two-point correlation function, the main aim is to provide a comparison with observational data. In this case it is unlikely clustering on scales of less than $1\,h^{-1}$ Mpc need be considered. This is because of peculiar velocity effects which make the relative distances of close pairs in redshift surveys uncertain on scales up to $\sim 2\,h^{-1}$ Mpc (e.g. de Lapparent, Geller & Huchra 1988). For a conservative value of $\tilde{x} = 100\,h^{-1}$ Mpc (Chapters 5, 6), this gives $\Delta x = 0.01\tilde{x}$. In practice, the analysis technique that requires the lower value of Δx will dictate the step size chosen.

It should be noted here that though a finite step size will give the Voronoi foam a certain "thickness", this is not a problem in the case of the nodes. This is because the nodes are uniquely identified and located by the nuclei of the adjacent cells. Thus, if the positions of the nuclei are known, the position of the corresponding node, i.e. equidistant between the nuclei, is also known. Thus, provided Δx is small enough that particles reach the correct node and do not overshoot into another cell (a rare event, but possible if two or more nodes are only separated by a very small distance), the nodes can be identified exactly using the kinematical method.

4.3.3 Particle Velocities

Two choices must be made with regard to the amplitude of the velocities of the particles. The first concerns the initial velocity. In all cases the particle's initial velocity is directed radially away from the nearest nucleus. However, the amplitude of the velocity can either be fixed to a set value or allowed to vary from particle to particle in some defined manner. The various cases will be discussed in § 4.4. If the particle velocity is fixed, then its initial value must be set in conjunction with Δt, the time step, so as to achieve the required step length, Δx, as discussed in § 4.3.2. Unless otherwise stated, the initial particle velocities will all be set to unity, and Δx fixed by adjusting Δt.

The second choice concerns the normalisation of the particle velocity after it has reached a wall or filament. In all cases the particle's velocity is modified according to equations (4.3) & (4.5). However, this still leaves the normalisation of the velocity undecided. If the particles are required to behave in a physically realistic manner (see § 4.4.1) then the natural normalisation to use is that of equations (4.3) & (4.5), which automatically ensure that momentum is conserved. However, if the particles are merely tracers of the geometrical skeleton (§ 4.4.2) then there is no such constraint on the particle velocity and it may be normalised to any arbitrary value. In such a case the particle velocity will be normalised to unity, thus ensuring that the step length, Δx, is constant throughout the simulation.

4.3.4 Initial Particle Distribution

In general, the particles used in the Voronoi foam simulations will be initially distributed at random. This is the most physically realistic situation, leading to a homogeneous initial background of particles. However, at various points in this thesis, contrived, non-random, initial particle distributions will be used in order to investigate certain phenomena (e.g. § 4.5.4, Chapter 5). In all cases these contrived distributions will introduce large-scale power in addition to that present due to the Voronoi foam. However, unless otherwise stated, the initial particle distributions used in the simulations shall be assumed to be random.

One such non-random initial distribution that will be used in this thesis is known as the "grenade" model. An equal number of particles are placed in each cell, located at the Voronoi nucleus. They are given an isotropic distribution of velocities and thus all particles move away from the nucleus in an expanding spherical shell. Compared to a random initial distribution this ensures a more uniform covering of the walls bounding the cell. However, it does involve a non-homogeneous initial distribution which introduces additional large-scale power as small cells will acquire an equal weight to large cells, which, spread over a smaller area/volume, leads to an enhanced overdensity. This also calls into question the applicability of the method of noise subtraction used on the power spectra (§ 4.2.4). Fig. 4.8 shows power spectra for four simulations using the "grenade" model, which have the same distribution of nuclei, but different particle densities. Fig. 4.8a shows the power spectra with no noise subtraction, while Fig. 4.8b shows

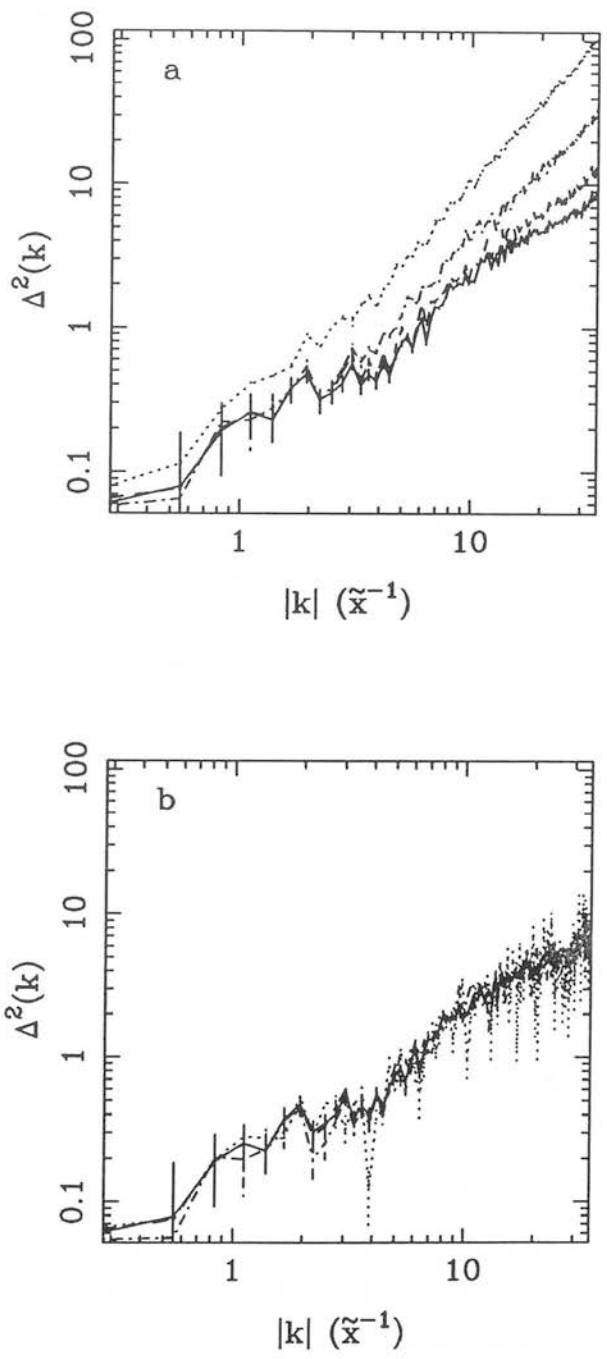

Figure 4.8 As Fig. 4.5, but for simulations using the "grenade" model as opposed to a random initial distribution of particles.

the power spectra with a shot-noise component given by equation (4.18) subtracted. As

one can see, this adequately describes the noise component, despite the non-Poissonian sampling of the structure inherent in the "grenade" model. If there were any additional noise component, then one would not expect the four power spectra to be consistent as they are in Fig. 4.8b.

4.4 The Kinematical Method — Two Different Approaches

4.4.1 Evolution of the Voronoi Foam

The kinematical method can be used to follow the evolution of the Voronoi foam with time. This is achieved by moving each particle an equal number of time steps and then recording the positions of all the particles. This gives a series of "snap shots" of the Voronoi foam at various different times.

This approach can be used to model the underlying physical processes of the Voronoi foam (see § 2.3). However, taking this approach places constraints on the behaviour of the particles, namely that the particles are required to behave in a physically realistic manner. This effectively constrains both the initial velocities of the particles and the way they are modified when a particle enters a wall or filament (see § 4.1.2). In the latter case the particle should move in a manner that conserves momentum and hence the particles' velocities are modified according to equations (4.3) & (4.5), as this ensures the conservation of momentum.

The initial velocities of the particles should also be dictated by the underlying physical process. van de Weygaert & Icke (1989) suggest making the initial velocity proportional to the distance of the particle from the nearest Voronoi nucleus. The motivation for this comes from considering the voids as expanding underdense regions in the gravitational instability scenario (§ 2.3.3). Compared to the surrounding medium, the void is expanding faster than the general Hubble expansion (i.e. co-moving coordinates), so in a frame stationary with respect to the Hubble expansion, particles in the void will move out from the centre with their velocities increasing with distance as they are accelerated by the overdensities at the edges of the voids.

However, if one considers the Voronoi foam as arising from an explosion scenario

(§ 1.3.5, 2.3.3) then the initial velocity of each particle will be that of the shock front of the explosion. To a first approximation this will be constant for all particles regardless of the distance from the nucleus and will certainly not increase with distance. More realistically, particles will be slowed as they encounter the ambient medium, thus their velocities will fall as the distance from the nucleus increases. Furthermore, as a particle will only start moving when it is first hit by a shock front, not all particles will start moving at the same time. To account for this it is necessary to introduce a time delay for each particle equal to the distance from the nearest nucleus divided by the velocity of the shock front.

It could be argued that the strengths of the individual explosions and hence the initial velocities of the particles should be varied from cell to cell, thus cells created by large explosions would be evacuated more quickly than those created by smaller explosions. Similarly, in the gravitational instability scenario, with peaks in the potential as nuclei (§ 2.3.4), bigger peaks should have higher expansion rates and hence higher initial velocities. However, this is an unsatisfactory approach as the Voronoi foam is only a valid approximation to either scenario if the explosions/expansion rates are of roughly equal strength (§ 2.3.3). If this is not the case then the walls, filaments and nodes in the Voronoi foam do not form equidistant from nuclei. Though the kinematical method can be modified to account for this, the situation is complex and it is beyond the scope of this thesis to investigate this scenario.

Using the kinematical method of implementing the Voronoi foam to try to accurately model the underlying physical processes seems fraught with difficulties and complications. Indeed, it is in some ways perverse to try and use an approximate model such as the Voronoi foam to accurately model the physical processes involved (§ 2.3.5). Such an approach is best left to more accurate methods such as the adhesion model (§ 2.2, Chapter 3) and N-body simulations (§ 2.1.2). Any advantages that could be gained are vastly outweighed by the associated difficulties and the loss of simplicity that is the attraction of the Voronoi model. For this reason any investigations of the evolution of the Voronoi foam carried out in this thesis will set the initial velocities of all particles to unity and normalise the velocities on subsequent modifications in accordance with equations (4.3) & (4.5).

4.4.2 Mapping the Geometric Skeleton

An alternative method to that presented in § 4.4.1 is to use the kinematical method to map out the geometric skeleton of the Voronoi foam. This involves moving each individual particle from its starting position until it reaches a node, where it stops, recording on its way the positions where it first encounters a wall and filament. In this way three catalogues are built up, one of particles in walls, one of particles in filaments and one of particles at nodes. The distribution of the particles within the walls and filaments can then be varied by varying the initial particle distributions (see § 4.3.4).

As the particles are merely tracers of the physical structure of the Voronoi foam and no attempt is made to model any physical processes, there are no constraints on the behaviour of the particles. Thus it is simpler to ensure that the velocity of the particle is always normalised to unity. In this case, the time step in equation (4.2) ceases to have any physical meaning. The advantage of this approach is that it allows the geometric skeleton to be sampled and the effect of the various distinct elements, the walls, filaments and nodes, to be investigated independently. In this respect this approach is very much akin to using the geometrical method. Unless otherwise specified the simulations in Chapters 5 – 7 are carried out using this approach.

4.5 Comparing the Kinematical and Geometrical Methods

4.5.1 Introduction

The aim of this section is to compare the kinematical and geometrical methods in an attempt to validate the claim that the kinematical method accurately traces the geometrical skeleton of the Voronoi foam.

Fig. 4.9 shows a two-dimensional Voronoi foam generated using 32 randomly distributed nuclei (open circles). The solid lines show the locations of the walls of the Voronoi foam as found by the geometrical method (§ 4.1.1) and the dots mark the locations of 1,000 particles, initially distributed at random and moved according to the kinematical method (§ 4.1.2) until they first reach a wall. As one can see, the particles delineate the geometric skeleton, but do not sample it in a uniform manner. Some walls

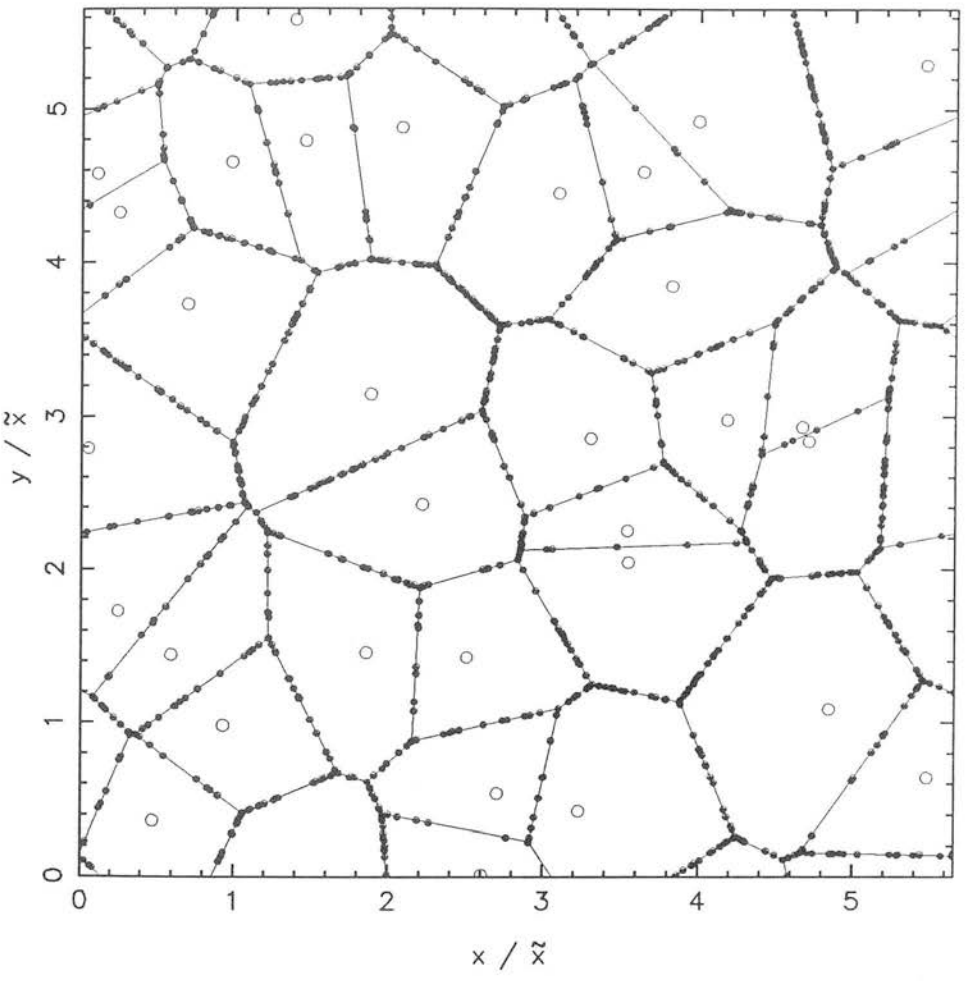

Figure 4.9 A two-dimensional Voronoi foam generated using 32 randomly distributed nuclei (open circles). The walls of the Voronoi foam as found by the geometrical method are shown by lines and particles, initially distributed at random and moved according to the kinematical method until they first reach a wall, are shown by dots.

have many particles per unit length while others have very few.

The reason for this is that the kinematical method effectively projects particles contained within a triangle (in two dimensions, a wedge in three) with a Voronoi nucleus as one vertex onto the wall opposite the nucleus. The number of particles within the triangle is proportional to its area which dictates the number of particles arriving on the wall. The number density is hence determined by the distance of the nucleus from

the wall. Thus a wall bounding a cell where the Voronoi nucleus is very close to the wall will have a lower number density of particles on the wall than a wall with triangle of similar area where the nucleus is much further away (see Fig. 4.9).

4.5.2 Comparing the Walls

Fig. 4.10a shows the power spectra of the walls in a two-dimensional Voronoi foam with 512 randomly distributed nuclei. The solid line is calculated for the foam generated by the geometrical method and the broken line for the kinematical method. As can be seen, the two power spectra are quite dissimilar, in both shape and amplitude. This is primarily due to the differences mentioned above, the excess large-scale power for the geometrical method arising due to each wall being giving a constant line density (§ 4.2.4). This means that small cells, which have many walls in a small area, receive considerably more weight than large cells, creating large-scale inhomogeneity. This situation is reminiscent of the "grenade" model of § 4.3.4. Fig. 4.10a also shows the power spectra of a Voronoi foam generated using the "grenade" model (dot-dash line). This gives considerably more large-scale power than the geometrical method, and also slightly more small-scale power. However, this is not a direct comparison between the two methods as the "grenade" model does not give the walls a constant line density. To correct for this the following scheme is used, which weights each particle according to its position in order to give the walls a constant line density. For a random initial distribution of particles, each particle is assigned a constant weight, W, given by:

$$W \propto \frac{1}{r_{\mathrm{p}}}, \tag{4.22}$$

and for the "grenade" model,

$$W \propto \frac{r^2}{r_{\mathrm{p}}}, \tag{4.23}$$

where r is the distance from the particle to the nucleus and r_{p} is the perpendicular distance from the nucleus to the wall. For a derivation of the weighting scheme in two and three dimensions, see Appendix D.

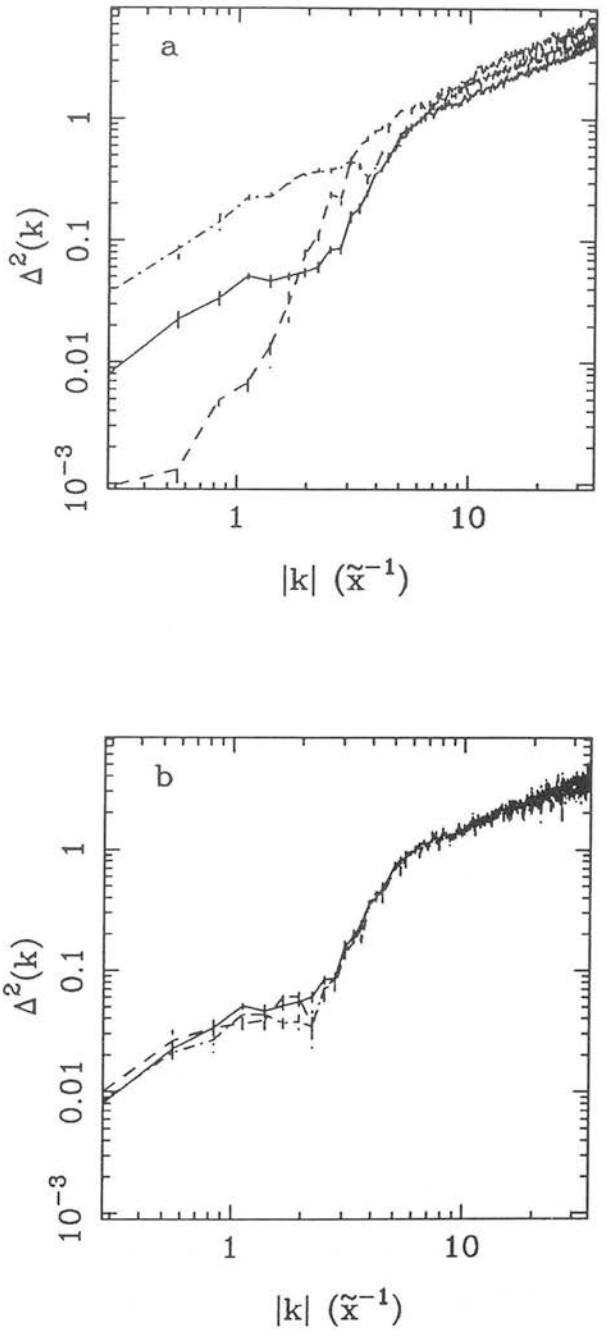

Figure 4.10 Power spectra for walls in a two-dimensional Voronoi foam with 512 randomly distributed nuclei. The three power spectra are for the geometrical method (solid line), the kinematical method with a random initial distribution of particles (broken line) and the "grenade" model (dot-dash line). In (b) the latter two are weighted so as to give the walls a constant line density.

The effect of these two weighting schemes is shown in Fig. 4.10b by the broken and dot-dash lines respectively. The solid line is the power spectrum for the geometrical method. The agreement between all three power spectra is excellent, especially on small scales. The large-scale discrepancies are within the errors. This demonstrates that the kinematical and geometrical methods are tracing the same structure and are equivalent procedures. Note that the power spectra for the weighted cases were calculated using the noise component given in equation (4.21), as opposed to the standard shot-noise contribution of equation (4.18). If the latter is used, the power spectra do not agree on small scales, showing that the correct noise component is given by equation (4.21).

4.5.3 Comparing the Nodes

It is also possible to compare the distribution of the nodes. Fig. 4.11 shows the power spectra of the nodes from the same simulations as above. Here the agreement is more striking. Fig. 4.11a shows the power spectra of the nodes in the geometrical method (solid line), the kinematical method with a random initial distribution of particles (broken line) and the "grenade" model (dot-dash) line. The discrepancy between the kinematical method with random initial positions and the geometrical method is qualitatively similar to that in the case of the walls and is for similar reasons. The geometrical method only finds each node once, whereas the kinematical method (regardless of the initial particle distribution) can find each node many times as more than one particle can stop at a given node. Weighting the nodes equally produces the same sort of large-scale inhomogeneity as for the walls, apparent from the large excess of power in the geometrical method over the kinematical method.

The agreement of the "grenade" model with the geometrical method is excellent. This is not too surprising as the "grenade" model starts an equal number of particles in each cell and the number of nodes per cell shows very little variation, thus the number of particles per node is unlikely to differ from node to node. This gives a very similar distribution to that of the nodes in the geometrical method.

It is very easy to carry out an exact comparison of the three methods by giving each node in the kinematical simulations an equal weighting rather than weighting it by the number of particles at the node. As each node is uniquely identified by the Voronoi nuclei of the three adjacent cells, it is possible to identify each node and its position

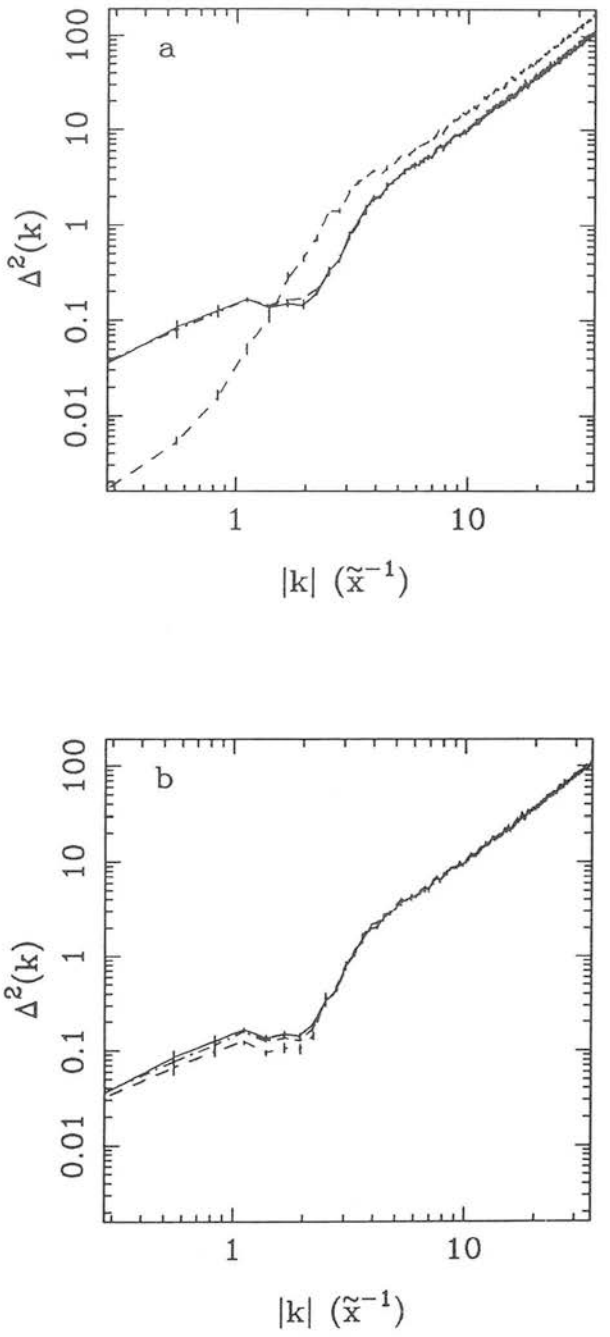

Figure 4.11 (a) as Fig. 4.10a, but for nodes. (b) is the same as (a), but with each node being equally weighted (see text).

exactly, despite the particles at each node being in slightly different positions due to

the finite step size (§ 4.3.2). Fig. 4.11b shows the kinematical method with a random initial distribution of particles (broken line) and the "grenade" model (dot-dash line) with each node being equally weighted. The solid line is the power spectrum for nodes in the geometrical method.

In the case of the "grenade" model this makes very little difference, supporting the claim made above that the nodes are already equally weighted. The agreement between the kinematical method and the geometrical method is also excellent, especially at small scales. There is a slight discrepancy at large scales ($k \lesssim 2\tilde{x}^{-1}$), but this is of only marginal significance.

4.5.4 Conclusions

As shown by the previous three subsections, the particles in the kinematical method adequately sample, in two dimensions, the geometrical skeleton of the Voronoi foam. There is no reason why this method should not work equally well in three dimensions, provided sensible values of Δx and the particle density are chosen. For the simulations in this section a step size of $\Delta x = 0.01\tilde{x}$ was chosen in line with § 4.3.2 and a particle density of 12 particles per nucleus was used.

In many ways it is not desirable to use the kinematical method to reproduce the results of the geometrical method in three dimensions. The choice as to whether to use the kinematical method to reproduce the geometrical solution by giving the walls a constant surface density depends on the situation being modelled. If structure forms in a hierarchical manner, with galaxies forming in the voids and then moving into the geometrical skeleton (§ 1.3, 1.4.6, 2.3.5), then the best method would to use the kinematical method to sample the skeleton without any weighting. If the galaxies are expected to form in situ in the geometrical skeleton [e.g. the explosion model (§ 1.3.5), or "top down" models (§ 1.3.1, 1.3.2)], then it may be preferable to give the walls a constant surface density. However, even in this case, this is only valid if one assumes that galaxies will form at a constant surface density and not in proportion to the mass present in the walls. In the latter case, it would again be preferable to used the dynamical method without additional weighting.

The observational evidence as to the variation of surface density with walls is

uncertain (§ 1.4.3), as is the nature of galaxy formation. Thus, unless otherwise stated, all kinematical method simulations in the remainder of this thesis will use a random initial distribution of particles and the power spectra will be calculated without any weighting schemes. However, the effect on large-scale clustering of both giving the walls a constant surface density and the "grenade model" of § 4.3.4 shall be investigated in Chapter 5.

The case for nodes is a little different. As individual nodes tend to be identified with rich clusters (§ 5.1), it would seem correct to weight the nodes equally. However, as cluster catalogues are selected using richness criteria, this suggests that a one-to-one correlation of nodes with clusters is not ideal. Weighting nodes by the number of particles present would avoid nodes with few particles (equivalent to poor clusters) from being given equal weight to those with many particles present (equivalent to rich clusters). An alternative would be to include a richness cut-off, excluding nodes with less than a given number of particles. These options are explored in § 5.1.

Chapter 5

Comparing the Voronoi Foam with Observations

A crucial test of any theory is how it compares with the experimental evidence. In the case of the Voronoi foam, this evidence comes in the form of observational measurements of large-scale clustering. It is the aim of this chapter to compare the statistical properties of the Voronoi foam model to a variety of observational measures of large-scale clustering. These are the spatial two-point correlation function for both galaxy clusters and galaxies, the angular two-point correlation function for galaxies and the power spectrum of galaxy clustering. These four measures are chosen due to the complimentary way in which they probe different scales and features of large-scale clustering. The Voronoi foam will be restricted to having only randomly distributed nuclei. This leaves only one free parameter, the length scale, given by the characteristic inter-nucleus separation, $\tilde{x}$ (§ 4.2.1). The case of clustered nuclei will be discussed in Chapter 6.

5.1 The Cluster-Cluster Correlation Function

5.1.1 Introduction

One of the original claims made in support of the Voronoi foam model was that it could naturally reproduce the two-point correlation function for Abell clusters (van de Weygaert & Icke 1989). The nodes in a Voronoi foam are the obvious sites for rich concentrations of matter. While matter flows along the walls and filaments in a foam, it congregates at the nodes (§ 2.3). Hence, except at very early times, one would expect the nodes to be the sites of large amounts of mass. This was the approach of van de Weygaert & Icke (1989), who identified nodes in the Voronoi foam as Abell clusters and matched their number density to the observed number density of Abell clusters with richness class $R \geq 1$. As the ratio of nodes to nuclei is fixed at 6.733 to 1 (van de Weygaert & Icke 1989), this enables the number density of nuclei and hence the length scale, the inter-nucleus separation, to be fixed (§ 4.2.1).

van de Weygaert & Icke (1989) used an observed number density of Abell clusters

with richness class $R \geq 1$ of $6 \times 10^{-6}\, h^3\,\mathrm{Mpc}^{-3}$ (Blumenthal, Dekel & Primack 1988; Bahcall 1988) which leads to a characteristic inter-nucleus separation of

$$\bar{x} = \sqrt[3]{\frac{6.733}{6 \times 10^{-6}}} \simeq 104\, h^{-1}\,\mathrm{Mpc}. \tag{5.1}$$

Using this normalisation scheme they calculated the two-point correlation function for nodes in a Voronoi foam, found exactly using a geometrical technique (see van de Weygaert & Icke 1989). The two-point correlation function was found to fit a power law of the standard form

$$\xi(r) = (r/r_0)^{\gamma}, \tag{5.2}$$

where $r_0 = 32\, h^{-1}\,\mathrm{Mpc}$ and $\gamma = -1.97$.

5.1.2 Comparison with Observations

Fig. 5.1 shows the two-point correlation function for nodes in a Voronoi foam generated by the kinematical method using randomly distributed particles and normalised using the same length scale as van de Weygaert & Icke (1989). The solid line represents nodes weighted by the number of particles at each node while the broken line represents equally weighted nodes (equivalent to the correlation function of van de Weygaert & Icke 1989). These follow a power-law behaviour for $r \lesssim 25\, h^{-1}\,\mathrm{Mpc}$ with $r_0 = 36\, h^{-1}\,\mathrm{Mpc}$, $\gamma = -1.85$ (nodes weighted according to number of particles) and $r_0 = 32\, h^{-1}\,\mathrm{Mpc}$, $\gamma = -1.9$ (nodes equally weighted). These latter parameters agree well with van de Weygaert & Icke (1989). Their correlation function is shown in Fig. 5.1 by the dotted line. The values of r_0 agree and the slight discrepancy between the two slopes is well within the errors allowed by the uncertainty of the power-law fit.

However, though the above results are consistent with the previous work of van de Weygaert & Icke (1989), this does not necessarily mean that they are consistent with observations. Of the two correlation functions calculated, it is more realistic to compare the one for equally weighted nodes with observations, as cluster-cluster correlation functions are not generally calculated with clusters weighted by their richness (§ 4.5.4).

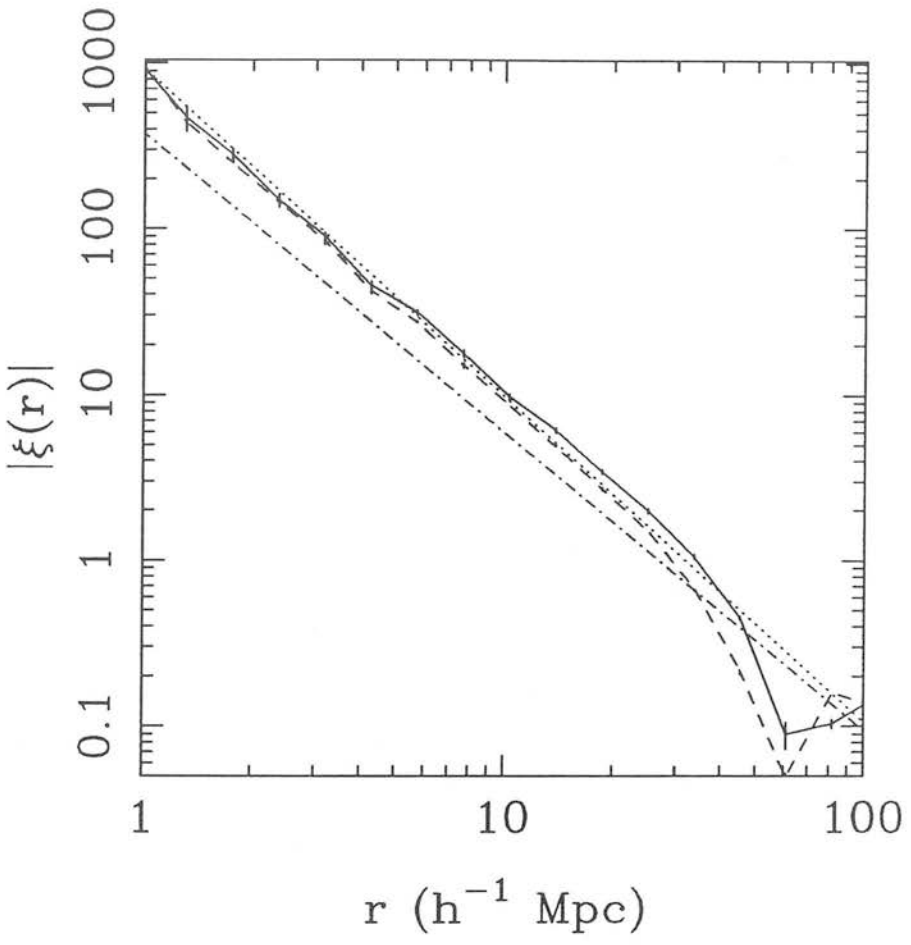

Figure 5.1 Two-point correlation functions for nodes in a Voronoi foam with 512 randomly distributed nuclei, generated by the kinematical method. The solid line represents the two-point correlation function calculated by weighting each node by the number of particles at the node and the broken line is calculated by weighting each node equally. The dotted line is the two-point correlation function for nodes in a Voronoi foam as found by van de Weygaert & Icke (1989) and the dot-dash line the two-point correlation function for Abell clusters (Bahcall & Soneira 1983) The simulation is normalised such that $\bar{x} = 104\,h^{-1}$ Mpc. The correlation functions are the mean of 10 independent simulations and the errors are the standard deviation on the mean.

van de Weygaert & Icke 1989 claim that their result is consistent with the upper bounds given in a review of cluster-cluster correlation functions by Bahcall (1988). A much quoted result is that of the two-point correlation function for Abell clusters of richness class $R \geq 1$ as measured by Bahcall & Soneira (1983). They found power-law behaviour

for $r \lesssim 100\,h^{-1}$ Mpc, with $r_0 = 26\,h^{-1}$ Mpc and $\gamma = -1.8$, shown by the dot-dash line in Fig. 5.1. Though no formal errors were quoted for this result, their two-point correlation function was calculated from only 104 clusters and it is obvious from the visual scatter of their data that there is quite a large error associated with their results. An error of 10% is often used (e.g. Bahcall 1988) and though this puts the slope in agreement with the Voronoi foam model, r_0 still lies outside the quoted error.

There is, however, an uncertainty in determining r_0 for the Voronoi foam data. Both the correlation functions in Fig. 5.1 start to deviate from a power law for $r \gtrsim 25\,h^{-1}$ Mpc, as does the correlation function calculated by van de Weygaert & Icke (1989; see their Fig. 4). This makes the determination of r_0 ambiguous. There are two possible definitions of r_0. The first, used above, is the point where the best-fit power law passes through unity (equation 5.2), and the second, the point where the two-point correlation function, as measured by the data, passes through unity. Strictly speaking, if one is expressing the correlation function as a power law, then one ought to quote r_0 as defined by equation (5.2). However, it seems a little inconsistent to represent the point where the correlation function goes through unity by a fitted power law when one has data that clearly shows the point where the correlation function crosses unity. The difference, though small, is significant. For example, the data in Fig. 5.1 shows $\xi(r) = 1$ at $r = 35\,h^{-1}$ Mpc (solid line) and $r = 28\,h^{-1}$ Mpc (broken line).

The observational data are frequently very noisy and thus such small deviations from power-law behaviour are lost in the errors. This leaves the problem of how to compare the simulated data to the observational data. This becomes more serious when one considers the two-point correlation function of particles in walls (see § 5.2.2), as here the correlation function, though approximating to a power law over small ranges, has a significant curvature over the range of interest and cannot be fitted by a single power law. Thus, although it is possible to give a range of values for the slope of a power law, to do the same for r_0 seems unrealistic. To avoid confusion, r_0 will hereafter refer to the point where $r = r_0$ in the best-fit power law (see equation 5.2) and the term "correlation length" will refer to the point where $\xi(r) = 1$ for the data.

5.1.3 Normalisation of the Length Scale

A serious problem for the Voronoi foam model is that more recent analyses of the

Abell cluster catalogue have produced lower results for the amplitude of the two-point correlation function. Sutherland (1988) and Sutherland & Efstathiou (1991) have argued that projection effects in the catalogue have led to an over-estimate of the amplitude of the two-point correlation function by up to a factor of four. Their analysis of the catalogue puts $r_0 = 14\,h^{-1}$ Mpc, clearly in disagreement with the Voronoi foam model using the normalisation of van de Weygaert & Icke (1989).

However, this normalisation is rather arbitrary. The length scale, $\tilde{x}$, is fixed to an observed number density of clusters with richness class $R \geq 1$. The value used by van de Weygaert & Icke (1989) is $6 \times 10^{-6}\,h^3\,\mathrm{Mpc}^{-3}$ (Blumenthal, Dekel & Primack 1988; Bahcall 1988), but this is uncorrected for obscuration effects. Bahcall (1988) suggests that when this is taken into account the number density is raised to $\sim 10^{-5}\,h^3\,\mathrm{Mpc}^{-3}$, thus reducing the inter-nucleus separation and hence the length scale. Including less-rich $R = 0$ clusters will raise the number density of clusters and hence lower the length scale (equation 5.1. Furthermore, the one-to-one identification of Abell clusters of a given richness with nodes in the Voronoi foam is open to question. Using the number of particles at each node in a kinematical simulation as a guide, it is obvious that if nodes were identified as clusters they would not all have the same richness. It is likely that only some fraction of the nodes would be picked up as rich clusters, effectively reducing the length scale (§ 5.1.4).

There is also evidence that some Abell clusters are elongated along a preferred axis and show alignment with other nearby clusters (see Chapter 7). This suggests that rather than being nodes in a Voronoi foam, Abell clusters may be galaxies aligned or clustered along a filament, hence the elongation and alignment with other clusters/filaments. This further weakens the case for the identification of nodes with Abell clusters and hence for the normalisation used by van de Weygaert & Icke (1989).

An alternative approach is to normalise the length scale such that it agrees with the observed two-point correlation function for Abell clusters, rather than some arbitrary number density of nodes/clusters. However, this leads naturally to the question — which observed correlation function? There is, as yet, no general consensus amongst workers in the field as to the correct form of the correlation function. Table 5.1 shows the correlation functions for six different samples of Abell clusters in terms of the parameters of the power law given in equation (5.2) along with the number of clusters used, richness

class and distance limit. It is obvious that there is a wide and discordant set of values for the cluster-cluster two-point correlation function.

Authors	N	R	Distance	r_0 (h^{-1} Mpc)	Slope, γ
Bahcall & Soneira (1983)	104	≥ 1	$D \leq 4$	26 ± 2.5	-1.8 ± 0.2
Klypin & Kopylov (1983)	158	≥ 0	$D \leq 4$	$40 - 50$	-1.6 ± 0.3
Postman, Geller & Huchra (1986)	154	≥ 0	$z \leq 0.1$	20 ± 10	-1.8 ± 0.2
Sutherland (1988)	588	≥ 0	$z \leq 0.3$	14	-1.8
Huchra *et al.* (1990)	145	≥ 0	$D \leq 6$	$20 \pm 5^{(1)}$	-1.5 ± 0.3
Postman, Huchra & Geller (1992)	208	≥ 0	$z \leq 0.08$	21 ± 5	-1.9 ± 0.2

(1) r_0 given for an assumed slope of -1.8, not the best fit slope.

Table 5.1 Observational determinations of the Abell cluster-cluster two-point correlation function by various authors. The correlation function is expressed in terms of the power law given in equation (5.2) and the number of clusters, N, richness class, R, and limiting distance (Abell distance class, D, or redshift, z), are also given.

According to Bahcall (1988), the existing measurements of the cluster-cluster correlation function at that time were consistent with the Bahcall & Soneira (1983) result. However, given the large errors quoted for most results, this is not surprising. The low value for r_0 found by Sutherland (1988) is attributed by Bahcall (1988) to an overestimation of projection effects leading to a subtraction of real clustering. Sutherland & Efstathiou (1991) support the original claim of Sutherland (1988) by re-analysing the data of Huchra *et al.* (1990) and finding similar projection effects. When these are accounted for they find a value of $r_0 = 14\,h^{-1}$ Mpc, though with large errors. Thus there seems to be a consensus amongst workers in the field that the true value of r_0 for the cluster-cluster two-point correlation function lies somewhere within the range $14 \leq r_0 \leq 26\,h^{-1}$ Mpc*. This range is far too large to constrain theoretical work,

* Klypin & Kopylov's (1983) determination of $r_0 = 40 - 50\,h^{-1}$ Mpc seems to be largely ignored and the review by Bahcall (1988) quotes a value of $r_0 = 25\,h^{-1}$ Mpc for their work, in contrast to the original value given in their paper.

including the Voronoi foam.

More recently there have been two attempts to construct objective cluster catalogues from computer scans of photographic plates [Abell's (1958) catalogue was constructed from "eye-ball" scans of photographic plates and as such is subject to errors that are very hard to quantify]. The aim of these catalogues is to eliminate, or at least quantify, the errors that plague the Abell catalogue, especially the effects of spurious line-of-sight clustering. Cluster redshift surveys have been carried out for both these catalogues and the cluster-cluster two-point correlation function has been calculated (Dalton *et al.* 1992; Nichol *et al.* 1992). They both find low values of r_0 (see Table 5.2) and are substantially free of spurious line-of-sight clustering. There are also two other estimates of the cluster-cluster correlation function, both aimed at eliminating these problems. One is an X-ray selected cluster sample (Lahav *et al.* 1989) and the other, a sample of clusters containing a cD galaxy in their core (West & van den Bergh 1991). Though both find $r_0 \sim 21\,h^{-1}$ Mpc, they have small samples and hence high errors (see Table 5.2).

Authors	Method	N	r_0 (h^{-1} Mpc)	Slope, γ
Dalton *et al.* (1992)	Automated Survey	173	12.9 ± 1.4	-1.9 ± 0.3
Nichol *et al.* (1992)	Automated Survey	79	16.4 ± 4.0	-2.1 ± 0.3
West & van den Bergh (1991)	cD clusters	64	22.1 ± 6.8	-1.70 ± 0.48
Lahav *et al.* (1989)	X-ray clusters	53	21.0 ± 7.0	-1.8

Table 5.2 Observational determinations of the cluster-cluster two-point correlation function by various authors for sources other than the Abell (1958) cluster catalogue. The correlation function is expressed in terms of the power law given in equation (5.2) and the number of clusters and method used to construct the catalogue are also given.

Though the low values of r_0 found by Dalton *et al.* (1992) and Nichol *et al.* (1992) seem to support the claims of Sutherland (1988) and Efstathiou & Sutherland (1991) that the earlier, higher values were overestimates, there is an alternative explanation. Bahcall & Soneira (1983) and Postman, Geller & Huchra (1986) claim to have found

a richness dependence in the clustering of Abell clusters, with the richer clusters being more strongly clustered. This would explain the lower clustering strengths of the Dalton *et al.* and Nichol *et al.* samples, as their clusters are of lower richness than Abell richness class $R = 1$ clusters. However, it should be noted that both Postman, Huchra & Geller (1992) and Dalton *et al.* (1992) find no evidence of clustering strength being dependent on richness in their samples, though the errors are large and such a trend cannot be ruled out.

There is also the question of the slope of the correlation function. Most authors use a value of $\gamma = -1.8$, despite the large associated errors. Huchra *et al.* (1990) actually derive r_0 for an assumed value of $\gamma = -1.8$, even though a best-fit power law to their data gave a slope of $\gamma = -1.5 \pm 0.3$, leaving their assumed value lying on the upper limit of their quoted error. It is not obvious why such a value should be chosen and there is no evidence to suggest that it is the best value. Tables 5.1 and 5.2 give $-1.2 \leq \gamma \leq -2.2$, making the slope obtained for the node-node two-point correlation function consistent with the upper end of the observed range.

5.1.4 Clustering as a Function of Richness

It is possible to investigate any trend in clustering strength with richness in the Voronoi foam scenario. As demonstrated in Fig. 5.1, when the nodes are weighted according to the number of particles present, the clustering is enhanced, suggesting that nodes with more members are more strongly clustered. One can then define node "richness" to be the number of particles, $n_{\rm p}$, present at a node in a kinematical simulation. Note that this definition is dependent on the total number of particles present in the simulation and thus care must be taken when comparing different simulations. All simulations used in this section have the same number of particles.

Fig. 5.2 shows the two-point correlation function for nodes with $n_{\rm p} \geq 1$, 3, 5, 6 and 7. This clearly shows that the amplitude of the correlation function increases with the number of particles at the nodes. Note that there is no trend of changing slope with cluster richness in the Voronoi foam that might explain the wild variations in the observed slope of the two-point correlation function function that were discussed in § 5.1.3.

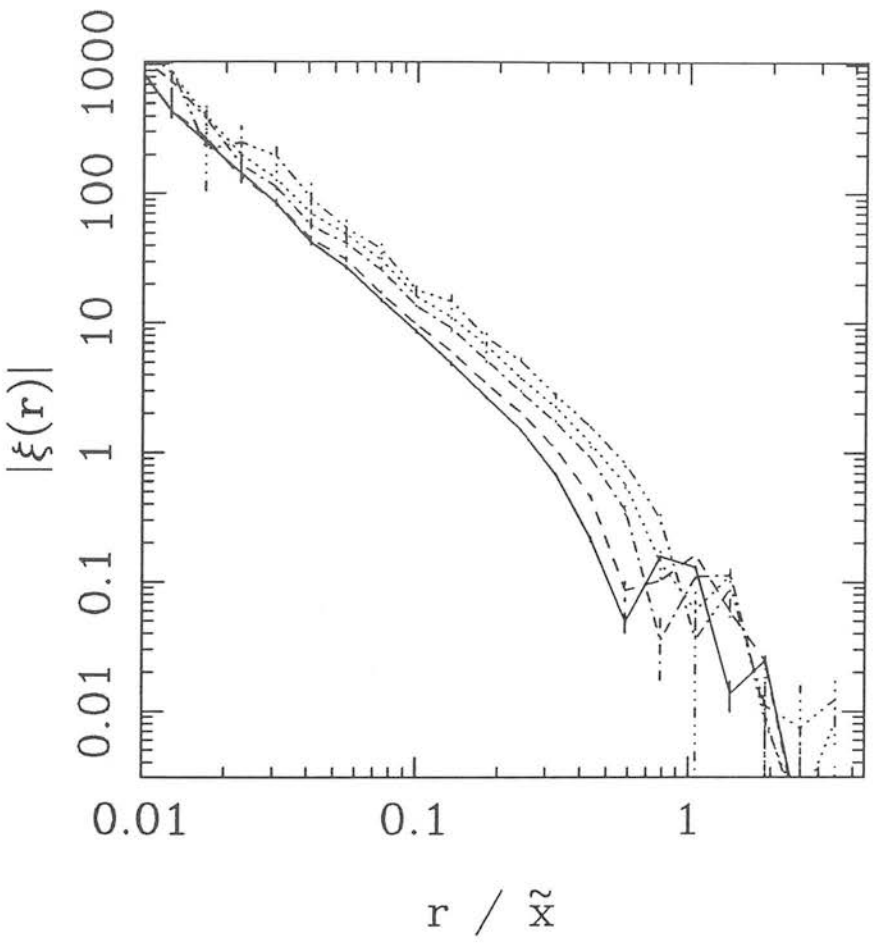

Figure 5.2 The two-point correlation function for nodes in a Voronoi foam with n_p greater than one (solid line), three (broken line), five (dot-dash line), six (dotted line) and seven (dot-dot-dash line) particles per node. The correlation functions are the mean of 10 simulations and the error bars represent the standard deviation on the mean.

Bahcall & Chokshi (1992; see also Bahcall 1988 and references therein) have suggested that there is a universal correlation function, where the amplitude of the correlation function is proportional to the richness of the system. This translates to there being a power-law relationship between correlation length and cluster richness, i.e.,

$$r_0 \propto n_p^{\alpha}, \tag{5.3}$$

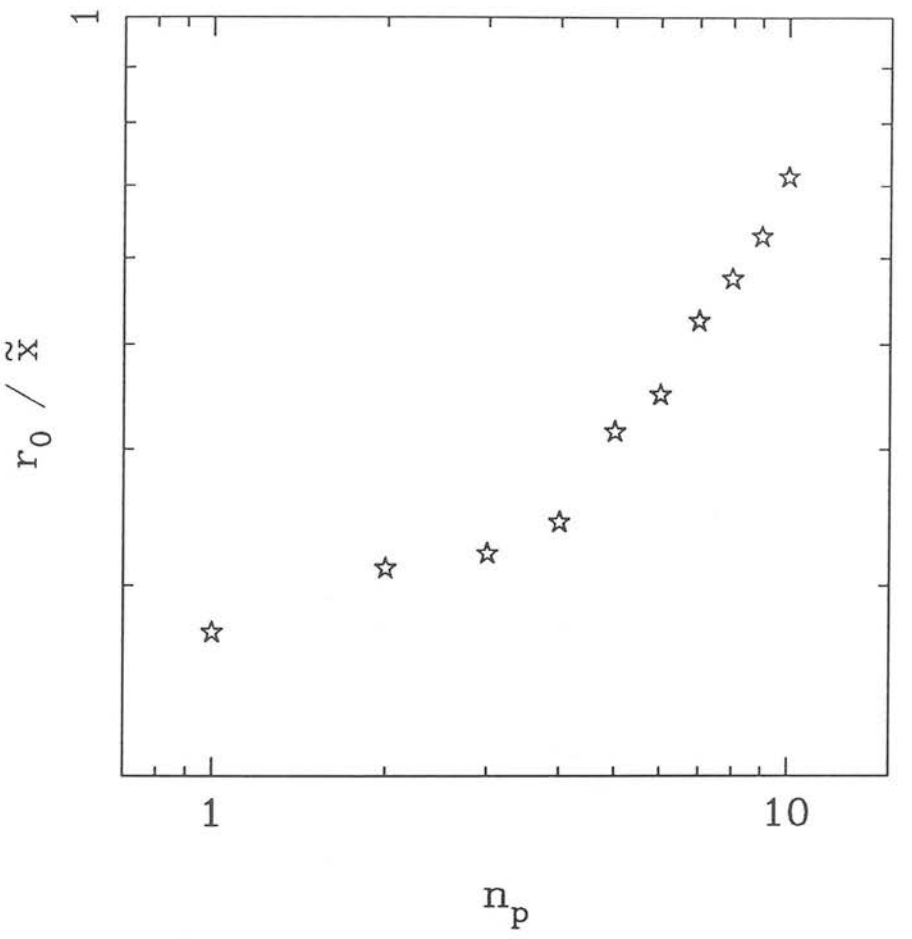

Figure 5.3 Plot of the number of nodes per nucleus, $n_{\rm p}$, against the correlation length, r_0, of the node-node correlation function.

where α is some constant to be determined.

Fig. 5.3 shows a log-plot of $n_{\rm p}$ against correlation length, r_0, for the node-node correlation function. It is clear from this plot that no such universal relationship exists, though for $n_{\rm p} \geq 4$, there is a linear relationship between clustering length and the number of particle per node.

Bahcall & Chokshi (1992) also suggest that there exists a similar relationship between the number density, $n_{\rm d}$, of the clusters (nodes) and the correlation length given

by

$$r_0 \simeq 0.5\, n_{\rm d}^{-0.33}. \tag{5.4}$$

where the number density is used as a guide to richness, richer systems being rarer and hence having a lower number density. This is the form expected if the correlation length scales with the characteristic inter-cluster separation.

Fig. 5.4 shows a log-plot of correlation length versus number density and a clear power-law behaviour is seen, though the data are best fitted by a relationship of the form (shown by the solid line)

$$r_0 \simeq 0.44 n_{\rm d}^{-0.28}, \tag{5.5}$$

rather than the one given by Bahcall & Chokshi (1992) (broken line).

Authors	Richness	Number Density (h^3 Mpc^{-3})	r_0 (h^{-1} Mpc)
Dalton *et al.* (1992)	$\mathcal{R} \geq 20^{(1)}$	2.4×10^{-5}	12.9 ± 1.4
Dalton *et al.* (1992)	$\mathcal{R} \geq 35^{(1)}$	1.2×10^{-5}	14.0 ± 4.0
Postman, Geller & Huchra (1992)	$R \geq 0$	1.2×10^{-5}	20.6 ± 4.5
Nichol *et al.* (1992)	$\mathcal{R} \geq 22^{(2)}$	1.0×10^{-5}	16.4 ± 4.0
Bahcall & Soneira (1983)	$R \geq 1$	0.6×10^{-5}	26.0 ± 2.5

(1) Richness, $\mathcal{R}$, is given for the number of galaxies above a given density threshold.

(2) Richness, $\mathcal{R}$, is given for the number of galaxies with a given radius, two thirds that of the standard Abell radius.

Table 5.3 The richness (Abell richness class, R, or number of galaxies, $\mathcal{R}$, satisfying a given criterion), number density and r_0 for various cluster samples.

However, though Bahcall & Chokshi claim this trend is universal for all systems larger than galaxies, their evidence is not compelling. Table 5.3 shows the richness of

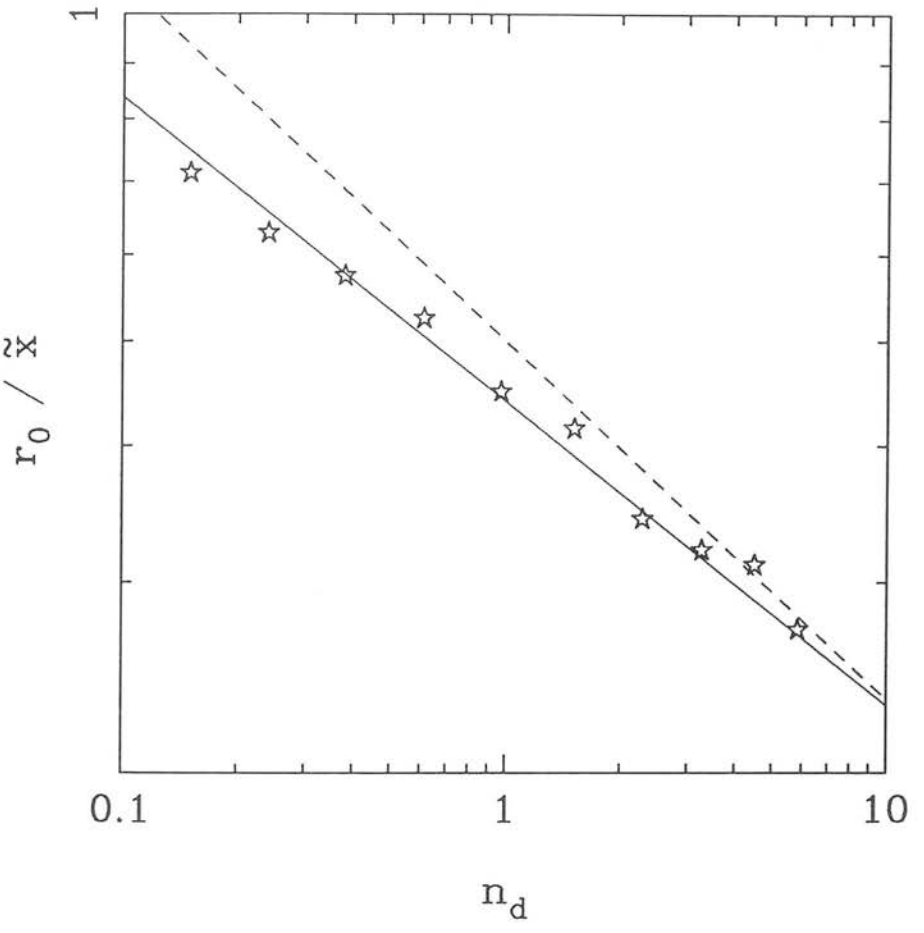

Figure 5.4 Plot of the number density of nodes, n_d, against the correlation length, r_0, for the node-node two-point correlation function. The solid line is given by equation (5.5) and the broken line by equation (5.4) (Bahcall & Chokshi 1992).

various cluster surveys along with the space density of clusters and r_0. Though there is no definite trend with cluster richness and space density as suggested by Bahcall & Chokshi (1992), one might tentatively claim some trend with richness.

The trend of increasing clustering with node richness makes the identification of nodes with clusters more problematic, as one must now ask what richness nodes should be identified with what richness clusters. Table 5.4 lists the number density and correlation length of the node-node correlation functions shown in Fig. 5.2 for a

n_p	$\tilde{x}$		$\tilde{x} = 104\,h^{-1}$ Mpc		$\tilde{x} = 45\,h^{-1}$ Mpc	
	n_d ($\tilde{x}^{-3}$)	r_0 ($\tilde{x}$)	n_d (h^3 Mpc^{-3})	r_0 (h^{-1} Mpc)	n_d (h^3 Mpc^{-3})	r_0 (h^{-1} Mpc)
1	5.84	0.271	5.0×10^{-6}	28.2	6.4×10^{-5}	12.2
3	3.27	0.321	2.9×10^{-6}	33.4	2.3×10^{-5}	14.4
5	1.51	0.415	1.3×10^{-6}	43.2	1.0×10^{-5}	18.7
6	0.97	0.449	8.6×10^{-7}	46.7	6.9×10^{-6}	20.2
7	0.61	0.525	5.4×10^{-7}	54.6	4.3×10^{-6}	23.6

Table 5.4 Number density of nodes and correlation length, r_0, for nodes with $\geq n_p$ particles at each node. Three different normalisations are listed : (i) normalised to the characteristic inter-nucleus separation, $\tilde{x}$, (ii) normalised to $\tilde{x} = 104\,h^{-1}$ Mpc and (iii) normalised to $\tilde{x} = 45\,h^{-1}$ Mpc.

variety of normalisations. It is obvious that for a normalisation of $\tilde{x} = 104\,h^{-1}$ Mpc, the Voronoi foam produces excessively large two-point correlation functions for nodes. However, the normalisation of $\tilde{x} = 45\,h^{-1}$ Mpc that is also used in Table 5.4 provides a much better match to the observations, though due to the uncertainties in the observed number densities and r_0, no single value may be set on $\tilde{x}$.

5.1.5 Conclusions

Though the wide range of cluster-cluster correlation functions makes the task of normalising the Voronoi foam difficult, it is possible to place some limits on the length-scale. From Tables 5.3 and 5.4, it is clear that a characteristic inter-nucleus separation of $\tilde{x} = 104\,h^{-1}$ Mpc, the value used by van de Weygaert & Icke (1989), is too high. A value of $\tilde{x} \sim 45\,h^{-1}$ Mpc seems much more reasonable, but due to uncertainties in the number densities of observed cluster surveys, r_0 for the observed correlation function and which richness nodes should be compared to which richness clusters, it is hard to place firm limits on $\tilde{x}$. However, given that the number density, n_d, scales as $\tilde{x}^{-3}$ and the correlation length scales as $\tilde{x}$, it is possible to place plausible limits.

If one identifies poor ($n_p \geq 1$) nodes with rich (Abell richness class $R \geq 1$) clusters, then $\tilde{x} = 104\,h^{-1}$ Mpc is still a (just) plausible value. However, if poor nodes

are matched with poor systems, then one finds that $\tilde{x} \lesssim 55\,h^{-1}$ Mpc. Similarly, if rich nodes are to be identified as very poor systems [e.g. $(n_{\rm p} = 7) \equiv (\mathcal{R} \geq 20)$], then values of $\tilde{x} = 30\,h^{-1}$ Mpc are plausible, but more realistic limits mean that $\tilde{x} \gtrsim 40\,h^{-1}$ Mpc. Thus, to fit the cluster-cluster two-point correlation function, the most likely normalisation for the Voronoi foam lies in the range $40 \lesssim \tilde{x} \lesssim 55\,h^{-1}$ Mpc, though it should be stressed that these are not absolute limits. Normalisations as low as $\tilde{x} = 30\,h^{-1}$ Mpc and as high as $\tilde{x} = 104\,h^{-1}$ Mpc cannot be ruled out.

The position is by no means hopeless. Extensions to the machine-based surveys of Dalton *et al.* (1992) and Nichol *et al.* (1992) will, if carried out, enable richness dependence to be investigated within a single, well defined catalogue. At the moment, the dependence of clustering strength on cluster richness is inferred from several different catalogues and may prove to be an artifact of differences between them, rather than being an intrinsic feature. Certainly, if no richness dependence is found, then this will be hard to explain in the context of the Voronoi foam model. Also of great help will be the ROSAT X-ray selected cluster catalogue as this should be free of the biases that affect optically selected catalogues, providing an independent check on the results from other surveys. However, even without these results, the Voronoi foam must be able to satisfy other measurements of large-scale structure. If these require normalisations that are at odds with those required for the cluster-cluster two-point correlation function then the model can be rejected.

5.2 The Galaxy-Galaxy Correlation Function

5.2.1 Introduction

Although the galaxy-galaxy two-point correlation function is better determined than the cluster-cluster correlation function, there are problems with using the Voronoi foam model to calculate the two-point correlation function for galaxies. While it is plausible to identify nodes in the Voronoi foam with galaxy clusters, it is less certain how one should identify galaxies in the foam. After all, though the foam has a reasonably strong physical motivation (see § 2.3), it is still only a geometrical prescription for the location of mass in the universe, not the locations of individual units of mass, i.e. galaxies.

The Voronoi foam provides three distinct topological features where matter, and

hence galaxies, can be located. Of the three, nodes have been identified with clusters, leaving walls and filaments. However, observational determinations of the galaxy-galaxy two-point correlation function do not distinguish between galaxies at different sites and thus to carry out a full comparison between the Voronoi foam and observations it is also necessary to work out the fraction of galaxies in nodes, filaments and walls, as well as their locations.

One approach would be to use the kinematical method to sample the population of the geometrical skeleton as it evolves with time. As argued in § 4.4, this approach is likely to be less than fruitful as it raises more questions than it answers. To try to model the locations of galaxies in a realistic manner is beyond the scope of a simple model like the Voronoi foam. Instead the strengths of the Voronoi foam should be brought into play, namely to investigate the effects of the different elements of the geometrical skeleton on the clustering of galaxies.

A further difficulty is that all observed two-point correlation functions for galaxies are measured in redshift space, whereas the two-point correlation functions for particles in the Voronoi foam models are measured in real space. The conversion from redshift space to real space is straightforward, apart from the problem of peculiar velocities which can distort relative separations up to at least $2\,h^{-1}\,\mathrm{Mpc}$ (e.g. de Lapparent, Geller & Huchra 1988). In N-body simulations this is not a problem as particles' peculiar velocities are known, allowing the two-point correlation function to be calculated in redshift space to give a direct comparison with observations. For the Voronoi foam model, this approach is not possible as the velocities assigned to the particles by the kinematical method are not physically meaningful. The peculiar velocities of the particles are not predicted by the Voronoi foam model, thus the two-point correlation function is measured in real space as opposed to redshift space, causing some problems when it is compared to observations. For this reason all two-point correlation functions calculated from Voronoi foam simulations are not plotted for $r < 1\,h^{-1}\,\mathrm{Mpc}$, the region where peculiar velocities are most likely to affect the results. Though on scales of interest ($r \simeq r_0 \gtrsim 4\,h^{-1}\,\mathrm{Mpc}$; see § 5.2.3) peculiar velocities should not affect the correlation function too severely, this point should be borne in mind when comparisons are made between observations and simulations.

5.2.2 Correlation Functions for Particles in Walls, Filaments and Nodes

Fig. 5.5 shows the two-point correlation functions for particles at walls, filaments and nodes in a Voronoi foam. There is a distinct increase in the amplitude and slope of the correlation function as one goes from walls to filaments and a slight increase as one goes from filaments to nodes. To begin with, a normalisation of $\tilde{x} = 104\,h^{-1}$ Mpc will be used here, in line with that put forward by van de Weygaert & Icke (1989) (see § 5.1.1). The parameters for fitted power laws of the form given in equation (5.2) are listed in Table 5.5. Note that the node correlation function is weighted by the number of particles at each node. Also two power laws have been fitted to the correlation function for walls, one for the range $r \lesssim 8\,h^{-1}$ Mpc and one for the range $10 \lesssim r \lesssim 20\,h^{-1}$ Mpc. As noted in § 5.1.2, it is impossible to fit a single power law over the whole range of the correlation function. For small separations ($r \lesssim 8\,h^{-1}$ Mpc) the slope of the correlation function approaches -1, which is to be expected for pairs located primarily within the same wall. The number of pairs of particles distributed uniformly on a two-dimensional plane grows as r^2, whereas the number of pairs of particles distributed uniformly in a three-dimensional volume will grow as r^3, hence a correlation function $\xi(r) \propto r^{-1}$ (cf. equation 5.2). As the separation increases, and the correlation function begins to sample significant numbers of pairs from different walls, as opposed to pairs confined within a single wall, the slope steepens continuously — there is certainly no evidence of a break from one power law to another. The second power law has been fitted to the correlation function at the point where $\xi(r) = 1$ and has a slope of -1.45.

Correlation Function	γ	r_0 (h^{-1} Mpc)	Correlation Length (h^{-1} Mpc)
Nodes	-1.85	36	35
Filaments	-1.80	28	28
Walls, $10 < r < 20\,h^{-1}$ Mpc	-1.45	14	14
Walls, $r < 8\,h^{-1}$ Mpc	-1.05	17	14

Table 5.5 Parameters for power laws fitted to the two-point correlation functions given by solid lines in Fig. 5.5.

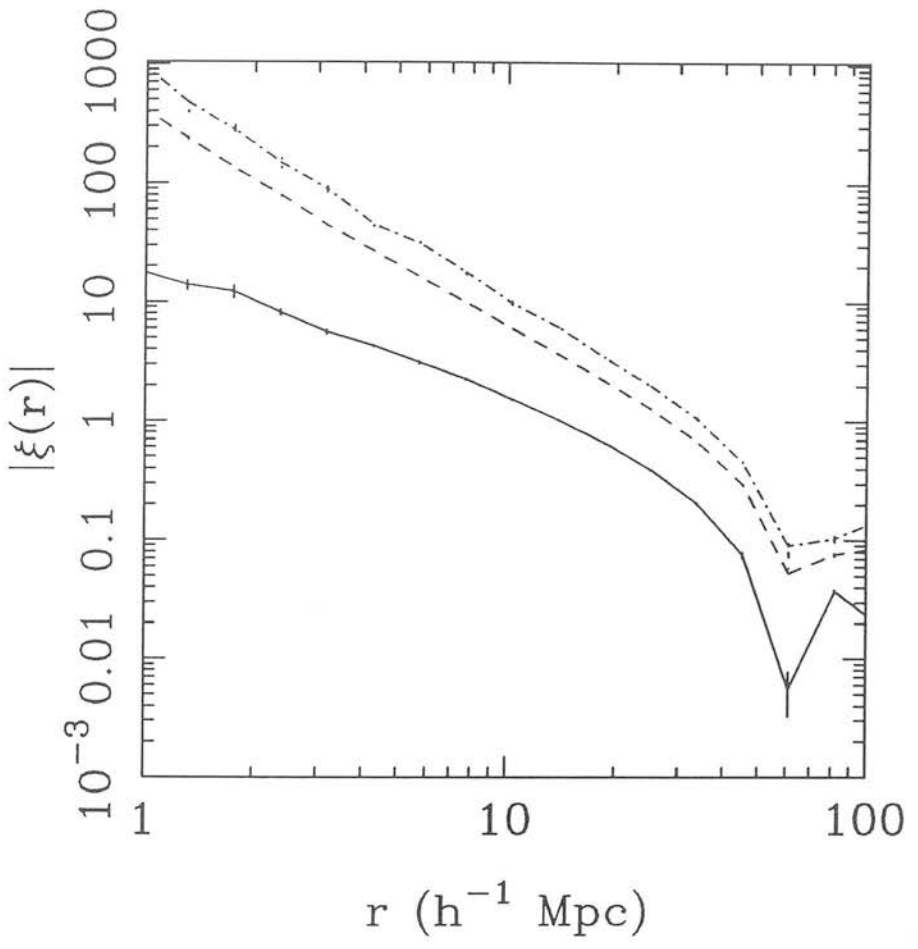

Figure 5.5 Two-point correlation function for particles in a Voronoi foam when they first reach walls (solid line), filaments (broken line) and nodes (dot-dash line). The feature at $r \simeq 70\,h^{-1}$ Mpc is the zero crossing of the correlation function. The correlation functions are the mean of 10 independent simulations and the error bars represent the standard deviation on the mean.

5.2.3 Comparison with Observations

As previously noted in § 5.2.1, comparison between the two-point correlation function for particles in a Voronoi foam and the observed two-point correlation function for galaxies is not straightforward. Further problems arise due to the inconclusive nature of current estimates of the two-point correlation function. Early estimates of the two-point correlation function for galaxies from both three-dimensional galaxy redshift surveys

and fits to the two-point angular correlation function for two-dimensional surveys found a power law form of the correlation function (equation 5.2) with $r_0 \simeq 5\,h^{-1}$ Mpc and $\gamma = -1.8$ (Davis & Peebles 1983b; Groth & Peebles 1977). Later estimates were in rough agreement with this result. Bean *et al.* (1983) found $r_0 = 4.1 \pm 0.3\,h^{-1}$ Mpc when they fitted a power law with the slope fixed at $\gamma = -1.8$, while Shanks *et al.* (1983), working from essential the same catalogue, found no clear evidence for power-law behaviour and obtained a correlation length of $5.5\,h^{-1}$ Mpc from the data.

The distinction should be made here between redshift and real-space correlation functions. Davis & Peebles (1983b) measured the correlation function in real space, whereas in redshift space they found increased clustering strength, due to spurious line-of-sight clustering caused by peculiar velocities. Denoting redshift space by s as opposed to r, the corresponding correlation length, s_0, was found by Davis & Peebles (1983b) to be $\simeq 7\,h^{-1}$ Mpc. This should be borne in mind as many recent calculations of the two-point correlation function for galaxies are given exclusively in redshift space, which may lead to the results being overestimated.

For example, Shanks *et al.* (1989), working with an extended version of the survey used by Shanks *et al.* (1983), again found no clear evidence of power law behaviour and found a correlation length (in redshift space) of $6 - 7\,h^{-1}$ Mpc. de Lapparent, Geller & Huchra (1988), working with a complete 12° declination slice of the CfA survey, found that the two-point correlation function depended strongly on the estimator used and on the assumed mean density of galaxies. They found evidence for power-law behaviour on scales $s \lesssim 10 - 20\,h^{-1}$ Mpc, with $5 \lesssim s_0 \lesssim 12\,h^{-1}$ Mpc and $-1.3 \lesssim \gamma \lesssim -1.9$, depending on the estimator used, though they give a "best estimate" of $s_0 = 7.5\,h^{-1}$ Mpc, $\gamma = -1.6$. Note that the line-of-sight anisotropies caused by peculiar velocities are not as great as those of Davis & Peebles (1983b), so this result may not be too great an overestimate of r_0.

Davis *et al.* (1988) measured the two-point correlation function for three redshift surveys — the CfA, the SSRS (da Costa *et al.* 1988) and a survey based on galaxies selected by the IRAS satellite (Strauss & Davis 1988). They found that r_0 varies with sample volume for the two optically selected surveys (CfA and SRSS), but not for the IRAS survey, an effect they put down to many causes, but mostly due to luminosity effects. Correcting for these they tentatively put $r_0 \sim 5\,h^{-1}$ Mpc for all three surveys.

Pellegrini *et al.* (1990) also measured the two-point correlation function for the CfA and SRSS surveys, finding $5 \lesssim r_0 \lesssim 8\,h^{-1}$ Mpc and $-1.45 \lesssim \gamma \lesssim -1.6$ for both.

Thus there seems to be some consensus amongst authors that the galaxy-galaxy two-point correlation function has $r_0 = 4 - 8\,h^{-1}$ Mpc. Supporting evidence comes from the angular two-point correlation function, which can be fitted by a projected spatial two-point correlation function (Appendix F). A power law with $r_0 = 4.7\,h^{-1}$ Mpc and $\gamma = -1.77$ provides an excellent fit to the data at small separations (Groth & Peebles 1977). Measurements of the slope of the spatial two-point correlation function give $\gamma \sim -1.4 - -1.8$, though like the cluster-cluster correlation function (§ 5.1.3), many authors adopt a slope of $\gamma = -1.8$ rather than a best fit slope, perhaps motivated by the fit to the angular correlation function, which exhibits well-defined power-law behaviour over several decades and is much less noisy than its spatial counterpart, allowing for a far better determination of the slope (see § 5.5.4).

A note of caution should be made here. As pointed out by de Lapparent, Geller & Huchra (1988) and Geller & Huchra (1988), it is wise not to put too much weight on the results provided by currently available redshift surveys. Surveys such as the CfA survey cannot be said to constitute a fair sample of the universe (de Lapparent, Geller & Huchra 1988; Geller & Huchra 1988; Davis *et al.* 1988; Pellegrini *et al.* 1990) as the volume sampled contains structures on the scale of the survey itself (§ 1.4). Also, the wide range of parameters for the power-law fit (equation 5.2) shows that the resulting two-point correlation function is heavily dependent on such ill-determined factors as the estimator used and the mean number density of galaxies. Indeed, it is not at all certain that the two-point correlation function can be fitted by a single power law, though evidence from the angular correlation function (see above) suggests that the situation may not be as bad as perhaps it first seems.

However, it is still possible to try to make some sort of a comparison between the two-point correlation function for particles in a Voronoi foam and the observed two-point correlation function for galaxies. Given the wide range of slopes found by de Lapparent, Geller & Huchra (1988), it seems premature to rule out the two-point correlation function for particles in walls, filaments or nodes (see Table 5.5), though the slope for particles in walls does seem a little shallow. It would be possible to steepen the slope of the correlation function for particles in wall by adding a percentage of

particles in filaments and perhaps nodes. This is a more realistic situation as there is no observational evidence that galaxies are confined exclusively to walls. However, the fraction of particles in walls, filaments and nodes is observationally undetermined, thus making a comparison the matter of finding the best fit.

The correlation length, however, is a better discriminant. As normalised above, all three two-point correlation functions have far too great a correlation length to be compatible with current observations. Of the three, the two-point correlation function for particles in walls provides a minimum correlation length of $14\,h^{-1}$ Mpc. However, even this lies outside the quoted range of $5 - 12\,h^{-1}$ Mpc given by de Lapparent, Geller & Huchra (1988), which in itself has a generous upper limit (especially as it was derived in redshift space). Thus the first indication is that the Voronoi model as normalised above will generate excessive small-scale galaxy correlations. The correlation length for particles in walls could easily be lowered to a more acceptable value of $7\,h^{-1}$ Mpc simply by halving the length scale used in the normalisation of the Voronoi foam. This move would be more in line with the results from the cluster-cluster correlation function (§ 5.1.5), but rather than take this step, it would seem prudent to first see if this conclusion can be weakened by varying the way in which particles populate the walls in the Voronoi foam. After all, the correlation functions in Fig. 5.5 represent only one way of populating the geometric skeleton of the Voronoi foam. Alternative methods are investigated in § 5.3.

5.3 Varying the Particle Distribution

In this section the effects of varying the way particles are distributed within the Voronoi foam model are investigated, with the aim of seeing if it is possible to reduce the correlation length of the two-point correlation function for particles in the Voronoi foam. This is motivated by the desire to see if the conclusion of § 5.2.3 can be weakened without resorting to reducing the length scale used in the normalisation of the Voronoi foam simulations. For this reason the investigations shall be limited in the majority of cases to particles in walls, as these already provide a minimum correlation length (see § 5.2.2).

5.3.1 Varying the Skeleton Thickness

In the Voronoi model, the geometric skeleton has zero thickness. Obviously this is not

the case in the real universe, so it is important to investigate the effects of giving the skeleton a finite thickness to see if this can lower the correlation length. This is achieved by giving each particle a random displacement characterised by a Gaussian of given half-width. The broken lines in Fig. 5.6 show the effect a 10 h^{-1} Mpc half-width compared to the correlation functions for the normal Voronoi foam (solid lines). Though this changes the correlation function, it does so only on scales less than the correlation length. In order to reduce the correlation length to $5\,h^{-1}$ Mpc, a smoothing length of $\sim 15\,h^{-1}$ Mpc is required. This is clearly too large as the half-width of the walls in the CfA survey is $\lesssim 2.5\,h^{-1}$ Mpc (de Lapparent, Geller & Huchra 1988). Thus even the value used here, that of $10\,h^{-1}$ Mpc, is too large and does not actually lower the correlation length for any of the correlation functions.

5.3.2 Varying the Particle Distribution with Time

In Fig. 5.5, the particles are distributed on the walls in a pseudo-random manner (see Chapter 4) Each particle is moved radially away from the nearest nucleus until it reaches a wall, where its position is recorded. This gives a particular distribution of particles within the walls. An alternative distribution may be obtained by using the kinematical method to follow the particles, calculating the correlation function of particles after a given number of time steps. After the particles hit the walls they move away from the centre of the wall and towards the filaments, which lie at the edges of the walls. This should achieve a different distribution of particles on the walls.

Fig.	Nodes	Filaments	Walls	Voids
a	0.0 %	1.3 %	23.3 %	75.5 %
b	0.6 %	11.1 %	42.7 %	45.7 %
c	9.6 %	40.1 %	37.8 %	12.5 %
d	42.2 %	45.9 %	10.8 %	1.2 %

Table 5.6 Percentage of particles in nodes, filaments, walls and voids for particles in the two-point correlation functions shown in Fig. 5.7.

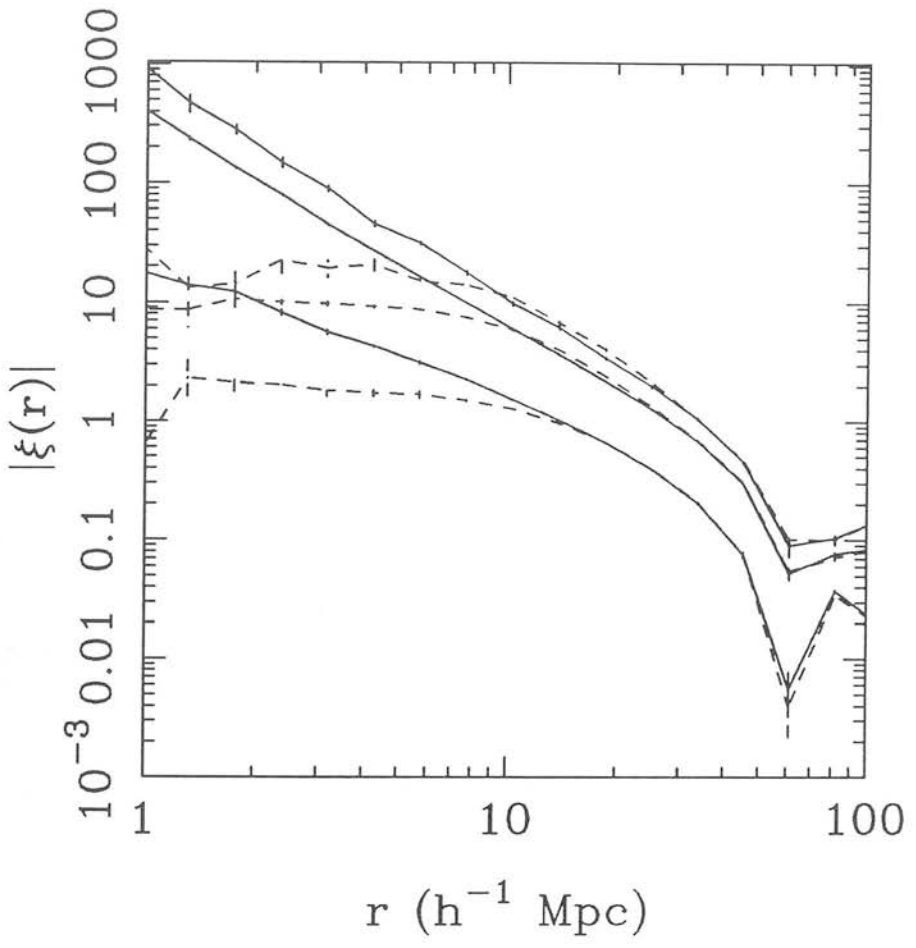

Figure 5.6 Two-point correlation function for particles in a Voronoi foam when they first reach walls (bottom line), filaments (middle line) and nodes (top line). The dashed line shows the effect of adding a random displacement to each particle, drawn from a Gaussian of half-width $10\,h^{-1}$ Mpc, to simulate the finite thickness of the Voronoi skeleton. The correlation functions are the mean of 10 independent simulations and the error bars represent the standard deviation on the mean.

Fig. 5.7 shows the two-point correlation function of the particles in walls at increasing times (a $\rightarrow$ d) during a kinematical method simulation (broken lines), with the solid line representing the two-point correlation function for particles when they first reach walls (cf. Fig. 5.5). Though the number of particles in walls and the percentage of particles in nodes, filaments, walls and voids varies quite dramatically (see Table 5.6), the correlation functions are all very similar, except at small separations

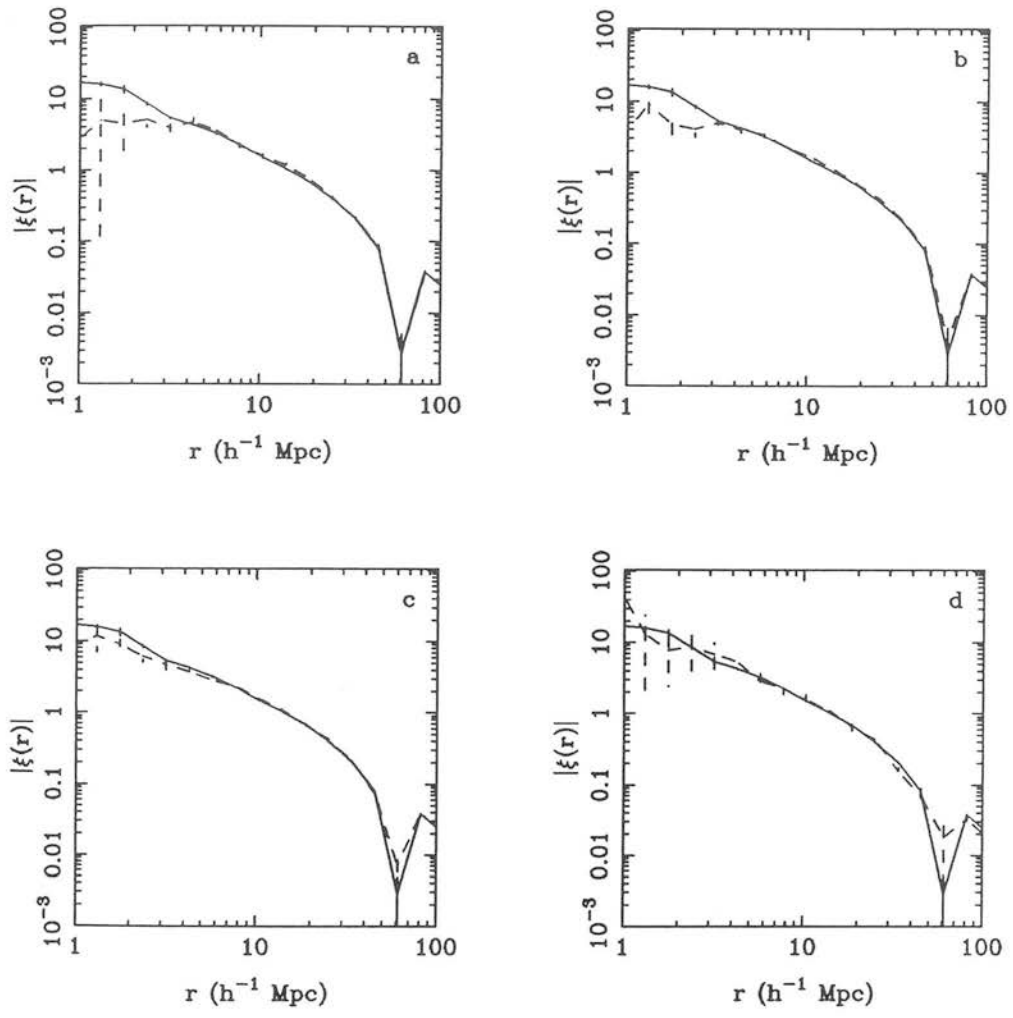

Figure 5.7 The two-point correlation functions for particles (initially distributed at random) on walls in a Voronoi foam. The solid line is for particles when they first reach a wall and the broken line for wall particles after a given number of time steps in a kinematical simulation. Panels (a) to (d) represent progressively later times. The percentages of particles in nodes, filaments, walls and voids are given in Table 5.6. The correlation functions are the mean of 10 independent simulations and the error bars represent the standard deviation on the mean.

($r \lesssim 3\,h^{-1}$ Mpc). There are two possible explanations for this. One is that the two-point correlation function is insensitive to the distribution of particles on the walls. The other is that despite the migration of particles from the centres of wall outwards to the filaments, the overall distribution of particles is the same regardless of the time. This may be because as the particles move outwards, there are always particles moving in

from the voids to take their place and the particle distribution on the walls changes little with time. Regardless of which of the two explanations is correct, it is clear that the minimum correlation length cannot be lowered by such an approach.

5.3.3 Non-random Initial Conditions

To investigate the effect of varying the surface density and distribution of particles on the walls, various simulations were carried out. Fig. 5.8 shows the results of several such simulations. The solid line represents the two-point correlation function for particles (initially distributed at random) when they first reach a wall (cf. Fig. 5.5) and is included for comparison.

The broken line shows the two-point correlation function for particles when they first reach a wall for the "grenade" model (see § 4.3.4). This increases the correlation length over the random initial distribution (solid line), though this is to be expected, as the surface density of particles on walls falls off quite rapidly with distance from the centre compared to the case of a random initial distribution (see Appendix D). Thus one would expect stronger clustering on small scales in the case of the "grenade" model.

The dot-dash line in Fig. 5.8 represents the two-point correlation function for the particles on walls in the "grenade" model, weighted by position to give a constant surface density of particles (see Appendix D). This gives a considerably lower correlation length than in the unweighted case, but it is still too large at $11.5\,h^{-1}$ Mpc, as this is only just inside the quoted range of $5 - 12\,h^{-1}$ Mpc given by de Lapparent, Geller & Huchra (1988) and is in conflict with other work (see § 5.2.3).

A further, highly contrived, initial particle distribution was tried. 26 particles were located at each Voronoi nucleus and given initial velocities along each cartesian axis in both directions and at 45° to each axis. This imposes a highly regular distribution of particles on the walls and leads to quite a different correlation length, as shown by the dotted line in Fig. 5.8. Though this achieves the required lowering of the correlation length to $6.5\,h^{-1}$ Mpc, these highly contrived initial conditions cannot be representative of a physically realistic situation. However, this situation serves as an example that the distribution of particles on the walls can be used to reduce the correlation length. It is not possible on the evidence presented here to categorically rule out the lowering of the

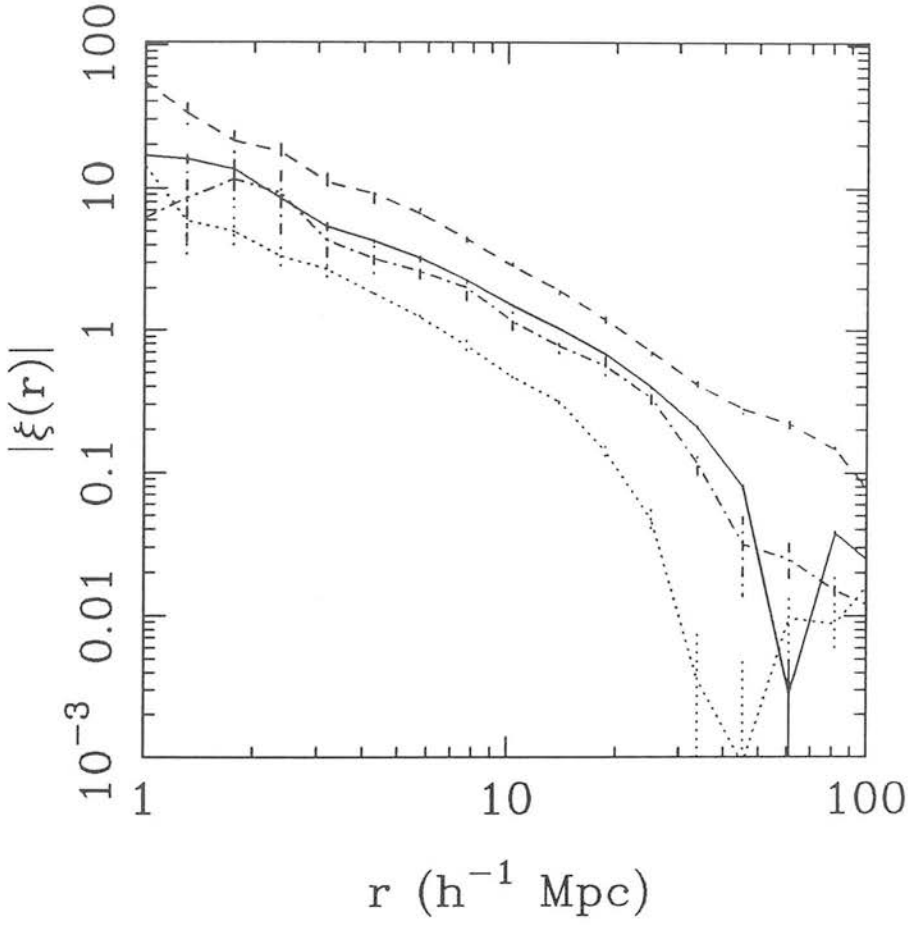

Figure 5.8 The two-point correlation functions for particles when they first reach walls in a Voronoi foam for a variety of different initial conditions. The solid line represents a random initial distribution of particles (cf. Fig. 5.5), the broken line, the "grenade model", the dot-dash line, the "grenade" model, weighted to give a constant surface density of particles, and the dotted line, a highly regular initial distribution of particles along and at 45° to the cartesian axes. The correlation functions are the mean of 10 independent simulations and the error bars represent the standard deviation on the mean.

correlation length by a physically realistic clustering of particles within the walls, but this is highly unlikely.

5.3.4 Particles in the Voids

One further approach is to include particles in the voids. Though this goes against the spirit of the Voronoi foam, it is worth investigating the effect as voids in the observed universe are not totally devoid of galaxies (§ 1.4.3).

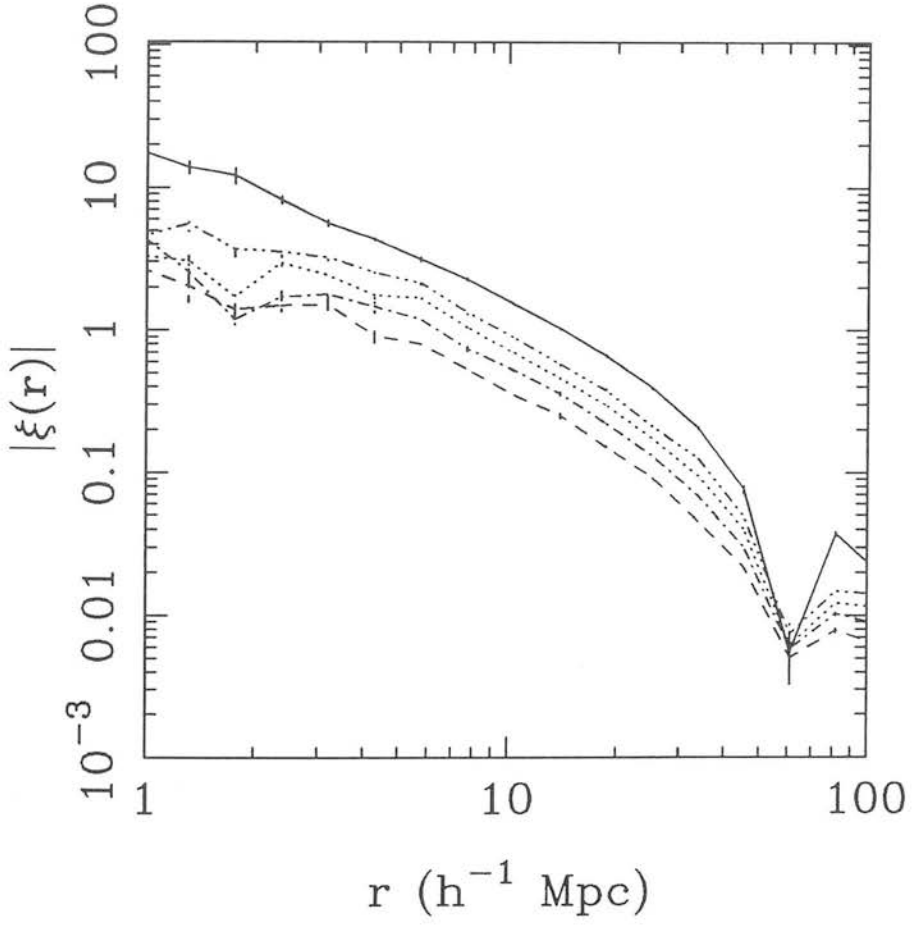

Figure 5.9 Two-point correlation functions for *all* particles (initially distributed at random) in a kinematical Voronoi simulation after a given number of time steps (see text) to illustrate the effects of including particles still in the voids. The first four correlation functions have 58% (broken line), 51% (dot-dash line), 46% (dotted line) and 41% (dot-dot-dash line) of particles in the walls respectively. The solid line represents the two-point correlation function for particles when they first reach a wall. The correlation functions are the mean of 10 independent simulations and the error bars represent the standard deviation on the mean.

The best way to see the effect of including particles in voids is to use the kinematical method to trace the time evolution of the geometrical skeleton, including any particle that has not yet reached a wall, filament or node. The simulations of § 5.3.2 were used and the resulting two-point correlation functions are shown in Fig. 5.9. The correlation length increases as the number of particles in the voids decreases, i.e. increases with time, until it reaches the limiting value of the correlation function calculated using only particles in walls (solid line in Fig. 5.9). Note that the four correlation functions shown in Fig. 5.9 are not equivalent to those shown in Fig. 5.7.

Fig. 5.9 clearly shows that by including the void particles, the correlation length may be lowered so as to be compatible with the observed two-point correlation function without altering the slope of the correlation function. However, is such an approach justified? Though voids are not entirely empty, visual inspection of slices though recent redshift surveys (e.g. de Lapparent, Geller & Huchra 1986; Haynes & Giovanelli 1986; da Costa *et al.* 1988; Fairall *et al.* 1990) show that only a few percent of galaxies lie within voids, not the 40%+ needed in Fig. 5.9 to lower the correlation length to an acceptable value.

What is important though is not the percentage of particles in the voids, but their distribution. After all, in the Voronoi foam particles are clearly marked as either being in voids or in walls, filaments or nodes, but the various redshift surveys do not share this advantage. Particles moving away from Voronoi nuclei in the kinematical method will vacate the centres of the voids first and it may be possible that at latter times the centre of the void is empty and the so-called void particles lie near the edges of the voids, continuous with and indistinguishable (by eye) from the particles in the walls. Fig. 5.10 shows a slice through one of the simulations in Fig. 5.9, corresponding to the dot-dash line where 50% of particles are in the voids. The plot clearly shows that the particles in the voids (open circles) populate space in a reasonably random manner, and do not cluster along the walls, which are clearly delineated by the wall particles (filled circles). Thus the above suggestion that the particles in the voids may cluster along the void edges is obviously incorrect.

Note that the particles in the voids are still clustered. Because they are being moved by the kinematical method radially away from the Voronoi nuclei, there will be an element of clustering in the void particle distribution, not unlike that of the particles

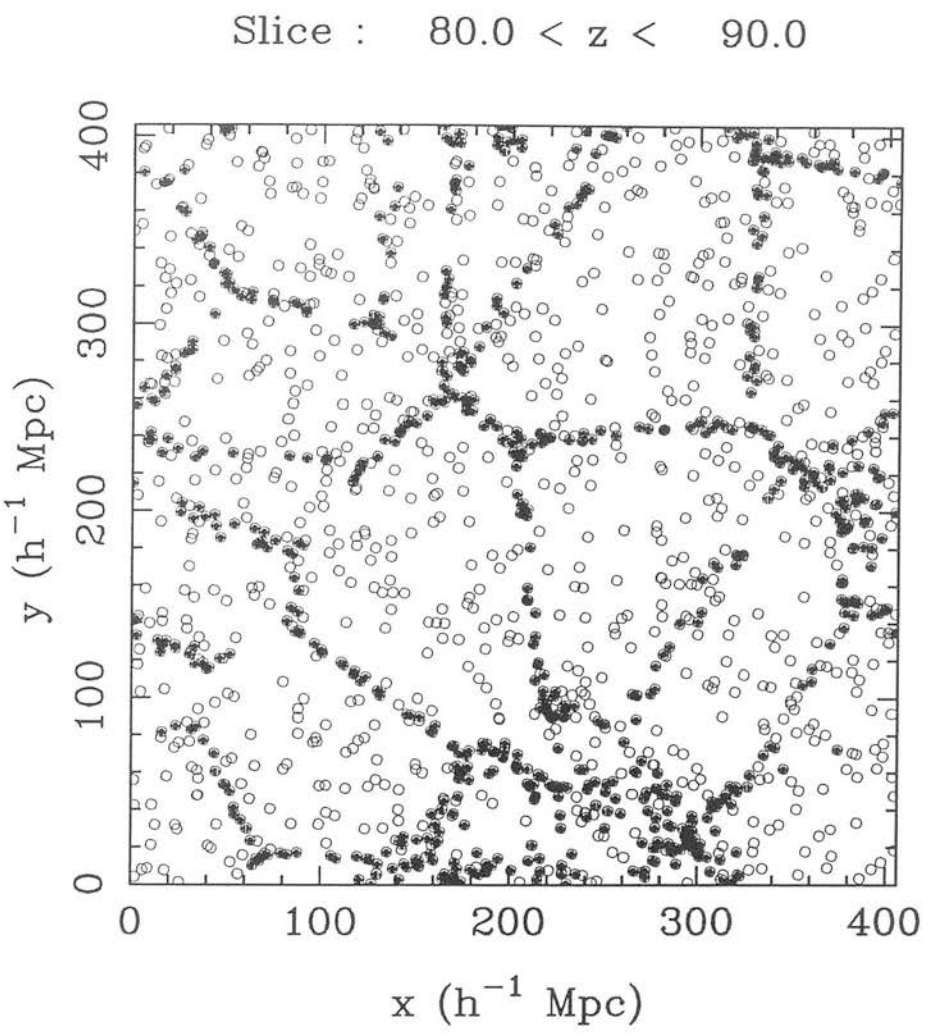

Figure 5.10 A slice through the left hand corner of a kinematical simulation used in Fig. 5.9 (dot-dash line) showing the particles on walls (filled circles) and particles still in voids (open circles).

in the walls. This probably explains why the shape of the two-point correlation function in Fig. 5.9 is changed at small separations ($r \lesssim 3\,h^{-1}$ Mpc) by the addition of the void particles. Small-scale clustering will have had time to take effect, but on large scales the distribution of the void particles will still be largely homogeneous, leading to a general suppression of the clustering strength.

An alternative approach, which avoids the intrinsic clustering of the void particles, is to add a number of particles, distributed at random, to a catalogue of particles on

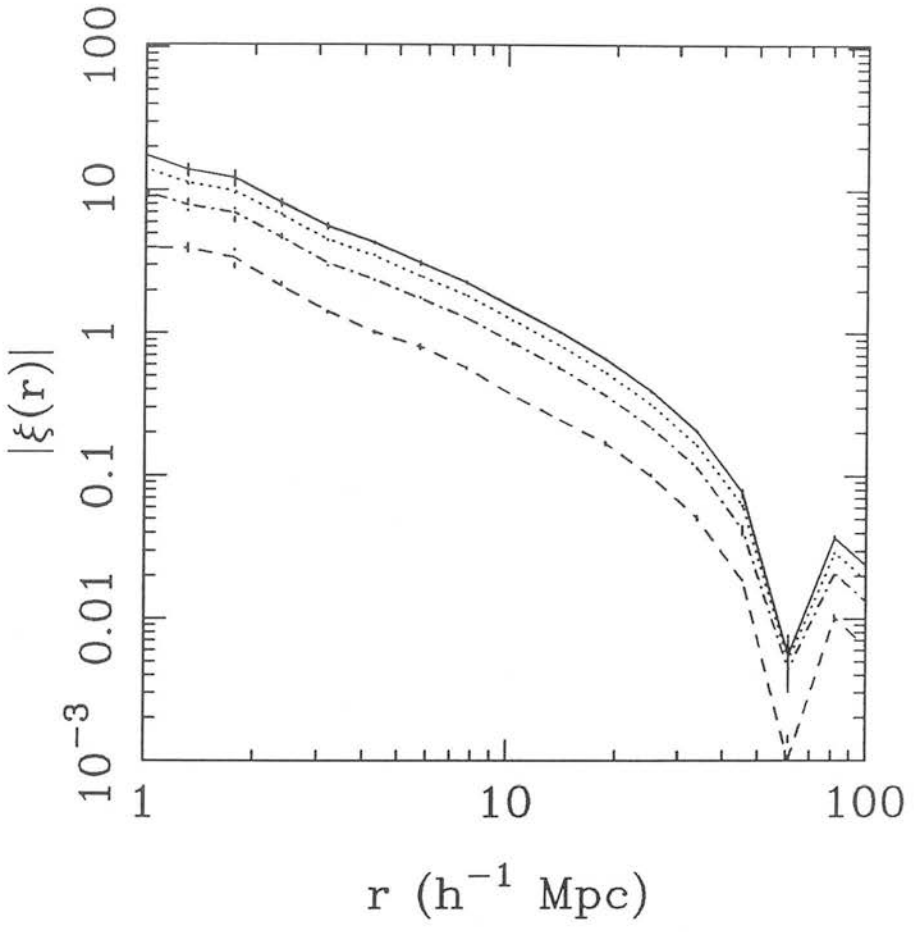

Figure 5.11 Two-point correlation functions for particles when they first reach a wall in a kinematical Voronoi simulation plus an added number of randomly distributed particles. The first three correlation functions have 50% (broken line) of particles randomly distributed, 25% (dot-dash line) and 10% (dotted line) respectively. The solid line represents the two-point correlation function for particles when they first reach a wall. The correlation functions are the mean of 10 independent simulations and the error bars represent the standard deviation on the mean.

walls. The effect of this is shown in Fig. 5.11, where the solid line is the two-point correlation function for particles in walls without any added particles. There is little difference between the correlation functions for particles added at random and those in voids (Fig. 5.9) and the same conclusions apply. To reduce the correlation length to an acceptable level, $\sim$ 50% of the particles must be distributed at random, clearly at odds

with observations. A slice similar to that in Fig. 5.10 is shown in Fig. 5.12, but with 50% of the particles randomly distributed as opposed to being in voids. As with the case of the void particles, the random particles fill the voids in a manner incompatible with the observed population of voids (e.g. de Lapparent, Geller & Huchra 1986; Haynes & Giovanelli 1986; da Costa *et al.* 1988; Fairall *et al.* 1990).

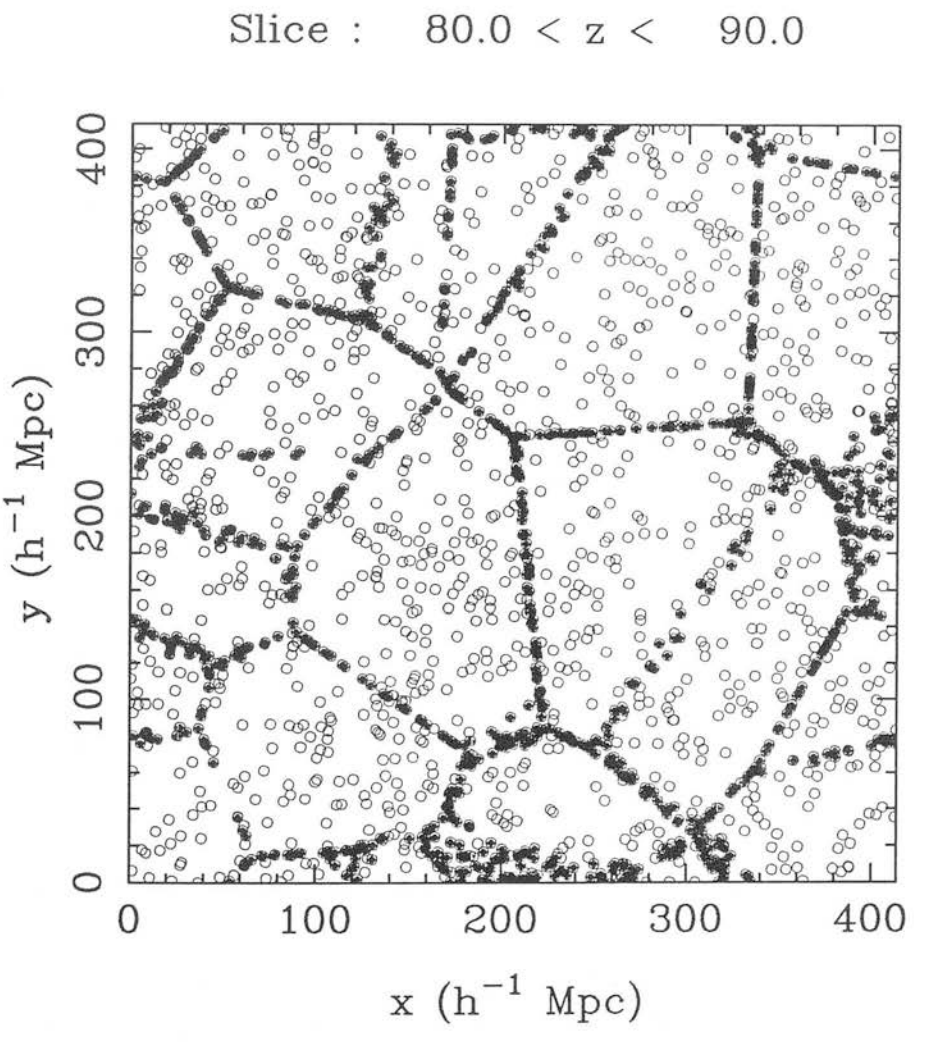

Figure 5.12 A slice through the left hand corner of a kinematical simulation used in Fig. 5.11 (broken line) showing the particles on walls (filled circles) and the particles distributed at random (open circles).

In conclusion, adding particles to the voids, either at random, or as part of a kinematical simulation, though reducing the correlation length to a level compatible

with the observed galaxy-galaxy two-point correlation function, cannot do so without filling the voids in a manner contradictory to present observations.

5.3.5 Conclusions

The aim of this section has been to see if the correlation length of the two-point correlation function for particles in walls can be lowered to a level compatible with that of the observed two-point correlation function for galaxies without altering the normalisation of the length scale used in the Voronoi foam simulations. As has been shown, this has not been possible without resorting to highly unphysical solutions such as imposing a regular distribution onto the particles (§ 5.3.3) or locating $\sim$ 50% of the particles in voids (§ 5.3.4).

The obvious conclusion is that as presently normalised, the two-point correlation function for particles in walls in the Voronoi foam model is incompatible with the observed two-point correlation function for galaxies. Adding particles in either filaments or nodes will only make the position worse as the correlation lengths for these particles are far in excess of those for particles in walls (see Table 5.5). Thus the conclusion may be extended to say that the two-point correlation function for particles in the Voronoi foam model, when normalised to an inter-nucleus separation of $104\,h^{-1}$ Mpc, is incompatible with the observed galaxy-galaxy two-point correlation function. However, it is worth pointing out that the adoption of the value $\tilde{x} = 45\,h^{-1}$ Mpc would bring the correlation length down to $\simeq 6\,h^{-1}$ Mpc, a value more in line with the majority of current estimates of r_0. This is also a more reasonable normalisation when one considers the cluster-cluster correlation function (§ 5.1.5).

One caveat must be born in mind at this point. As shown in § 5.3.3, the clustering (or anti-clustering) of particles within the walls can affect the correlation length, either increasing, it in the case of clustering (the "grenade" model), or decreasing it, in the case of anti-clustering (the highly regular structure of § 5.3.3). The Voronoi foam model does not claim to provide a detailed simulation of the underlying physical processes of galaxy clustering and there will inevitably be some additional clustering of galaxies/particles within the walls of the Voronoi foam due to self-gravitation. It is likely that this clustering will *increase* the correlation length (see above), but this conclusion is based on only a few specific examples. Without a full simulation of the effects of mutual gravitational

attraction for particles within the walls this caveat must remain, though it is extremely unlikely that any realistic particle clustering would reduce the correlation length.

5.4 The Power Spectrum

5.4.1 Introduction

Power spectrum analysis is a powerful tool for the investigation of galaxy clustering. Despite its early use in two-dimensional surveys (Yu & Peebles 1969; Peebles 1973; Webster 1976a,b 1977; Webster & Pearson 1977) it has languished somewhat since then, the preferred statistics being the spatial and angular two-point correlation functions. Recently, however, several authors have calculated the power spectrum from a variety of galaxy redshift surveys (Baumgert & Fry 1991; Peacock 1991; Peacock & Nicholson 1991; Gramann & Einasto 1992), which has rekindled the interest in the power spectrum as a statistic for quantifying large-scale clustering. The power spectrum, $\Delta^2(k)$ (see § 4.2.4), is the contribution to the variance per unit $\ln k$, and is given by $\Delta^2(k) = \partial\sigma^2/\partial \ln k \propto k^3|\delta_k|^2$.

The power spectrum is the Fourier transform of the correlation function (see § 5.5.3; Appendix E). However, despite this common basis, the power spectrum, when calculated directly, has a significant advantage over its Fourier transform counterpart. Because of the way the two-point correlation function is defined (§ 4.2.2; equation 4.9), it is sensitive to the mean density of the sample. For the power spectrum, this mean density simply adds to the overall normalisation, thus it does not affect the shape of the power spectrum. This can be of critical importance on scales where the amplitude of the two-point correlation function is considerably less than unity. For example, if the $\xi(r) = 0.1$, then errors in the mean density (and hence the expected number of pairs) of 10% induce errors of a similar magnitude in the correlation function. Such variations in the mean density of present redshift surveys are common (e.g. Davis *et al.* 1988; Pellegrini *et al.* 1990). Thus it is very hard for the correlation function to probe on such scales. These scales ($\gg 10\,h^{-1}\,\mathrm{Mpc}$) are often of great interest as here the clustering is assumed to still be in the linear regime and thus free from the complex effects of non-linear clustering processes which are poorly understood and hence very difficult to model (§ 2.1). Because of its insensitivity to fluctuations in the mean density, the power

spectrum is an ideal tool to probe clustering on these scales, as shall be demonstrated in this section.

Following the approach presented in § 5.2 and § 5.3, this section shall seek to investigate the effects on the power spectrum of particles in different topological regions of the Voronoi foam and compare them to the observed power spectrum for galaxies.

5.4.2 Power Spectra for Particles in Walls, Filaments and Nodes

Fig. 5.13 shows the power spectra for particles in walls, filaments and nodes of a Voronoi foam. The power spectra may be fitted by two power laws, one in the region $k \gtrsim 5\tilde{x}^{-1}$ (small-scale) and the other in the region $k \lesssim 4\tilde{x}^{-1}$ (large-scale), with a well defined break in between. The slopes of these power laws are given in Table 5.7. The break occurs between $k \simeq 4 - 5\tilde{x}^{-1}$, which corresponds to a physical scale of $\lambda = 2\pi/k \simeq 1.25 - 1.60\tilde{x}$, i.e. on scales slightly larger than, but comparable to, the characteristic inter-nucleus separation. This break reflects the transition from one form of clustering to another. In the case of the Voronoi foam, the transition is from predominantly intracellular clustering on small scales to predominantly intercellular clustering on large scales. This is supported by the fact that the break occurs on a scale slightly larger than that of the characteristic inter-nucleus separation (i.e. the characteristic cell size, $\simeq \sqrt{3}\tilde{x}$) and by the fact that the power spectra for all three topological regions break at roughly the same scale. As the three topological regions are embedded within the same cellular structure, one would expect the break to occur on similar scales if the break were associated with the transition from intra- to intercellular clustering. Though the small-scale slope increases as particles go from walls through filaments to nodes, which is expected from the behaviour of the spatial two-point correlation function (§ 5.2.2), the large-scale slopes are roughly equal, at $\simeq 4.5$. This further supports the idea that beyond the break scale, clustering is predominantly intercellular, as the three distinct topological regions are now essentially sampling the same structure, i.e. the intrinsic clustering of the cells, albeit with differing amplitudes.

Note that the power spectrum probes scales much larger than that of the spatial two-point correlation function. The power spectra in Fig. 5.13 all reach scales of $7 - 8\tilde{x}$, whereas the spatial two-point correlation functions in § 5.1 – § 5.3 only sample structures out to a scale of $\simeq \tilde{x}$. A consequence of this is that the power spectrum does not

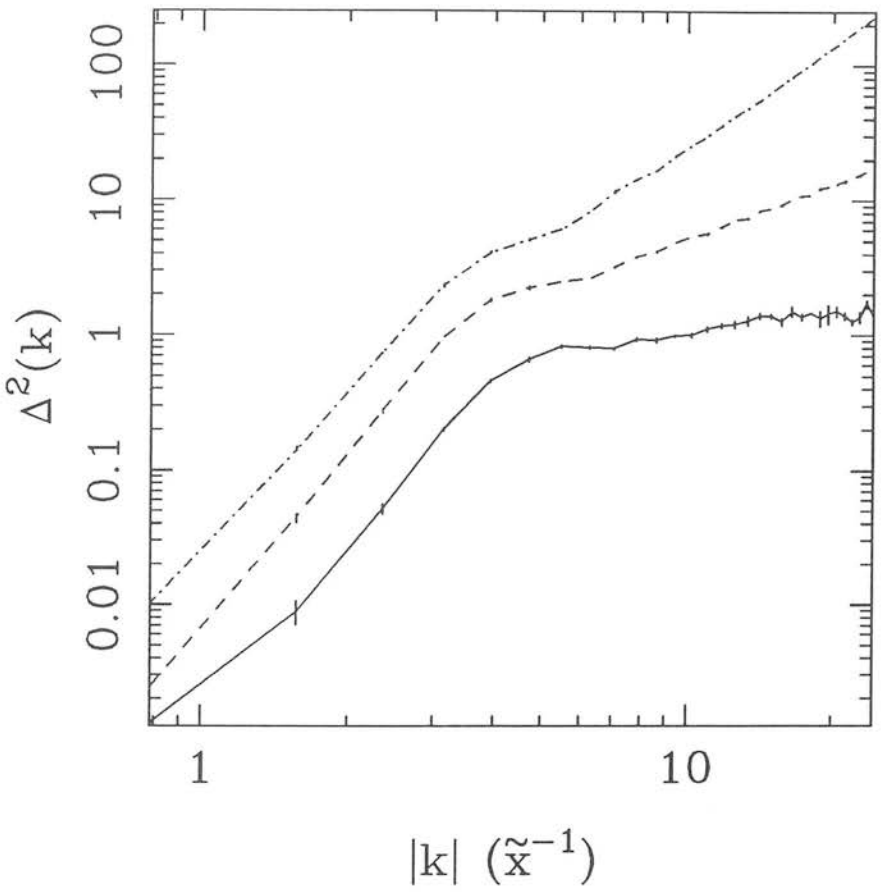

Figure 5.13 Power spectra for particles in a Voronoi foam when they first reach walls (solid line), filaments (broken line) and nodes (dot-dash line). The power spectra are the mean of five independent simulations and the error bars represent the standard deviation on the mean.

probe small scales. The smallest scale probed by the power spectra in Fig. 5.13 is $k \simeq 25\tilde{x}^{-1} \Rightarrow r = 0.25\tilde{x}$, whereas the spatial correlation functions of § 5.1 – 5.3 easily reach scales as small as $0.01\tilde{x}$. It is possible for the power spectrum to probe such small scales, as the limitation is set by the size of the cube that can be Fourier transformed (see § 4.3.2). However, every halving of the minimum scale probed requires an eight-fold increase in computer memory, thus it is very difficult in practice to probe very small scales.

Power Spectrum	Small-Scale Slope ($k \gtrsim 5\tilde{x}^{-1}$)	Large-Scale Slope ($k \lesssim 4\tilde{x}^{-1}$)
Nodes	2.35	4.95
Filaments	1.35	4.40
Walls	0.65	4.50
Observed	0.95	2.50

Table 5.7 Parameters for power laws fitted to the power spectra given in Fig. 5.13 and Fig. 5.14.

5.4.3 Comparison with Observations

Fig. 5.14 shows the power spectra for particles in walls in a Voronoi foam (lines) along with the observed power spectrum for three galaxy redshift surveys (symbols). The normalisation of the three observed power spectra are fixed to the IRAS survey (circles; Peacock 1991). This is because, in the case of the CfA results (triangles; Baumgart & Fry 1991), the normalisation is uncertain and in the case of the radio galaxies (squares; Peacock & Nicholson 1991), the actual power spectrum has been reduced in amplitude by a factor three. Whether this approach is justified is discussed below. The two power spectra for the Voronoi foam are normalised such that $\tilde{x} = 104\,h^{-1}\,\mathrm{Mpc}$ (broken line) and $\tilde{x} = 45\,h^{-1}\,\mathrm{Mpc}$ (broken line).

It is possible to fit a two component power-law model to the observed power spectrum as in § 5.4.2, though there is quite a large scatter in the data and the errors bars are quite large, especially at long wavelengths. The best fit parameters are given in Table 5.7.

As one can see, the Voronoi foam, when normalised to $\tilde{x} = 104\,h^{-1}\,\mathrm{Mpc}$, fails to match the observations, providing too much power at all but the smallest and largest wavenumbers. The normalisation of $\tilde{x} = 45\,h^{-1}\,\mathrm{Mpc}$, suggested by § 5.1.5, and § 5.3.5, provides a better fit, but not an ideal one. The Voronoi foam breaks at roughly the right scale, though it may break a little too soon. However, as the break scale is poorly defined in the observed power spectrum, it is difficult to place any firm constraints on the break, though it seems that the power spectrum for the Voronoi foam also breaks

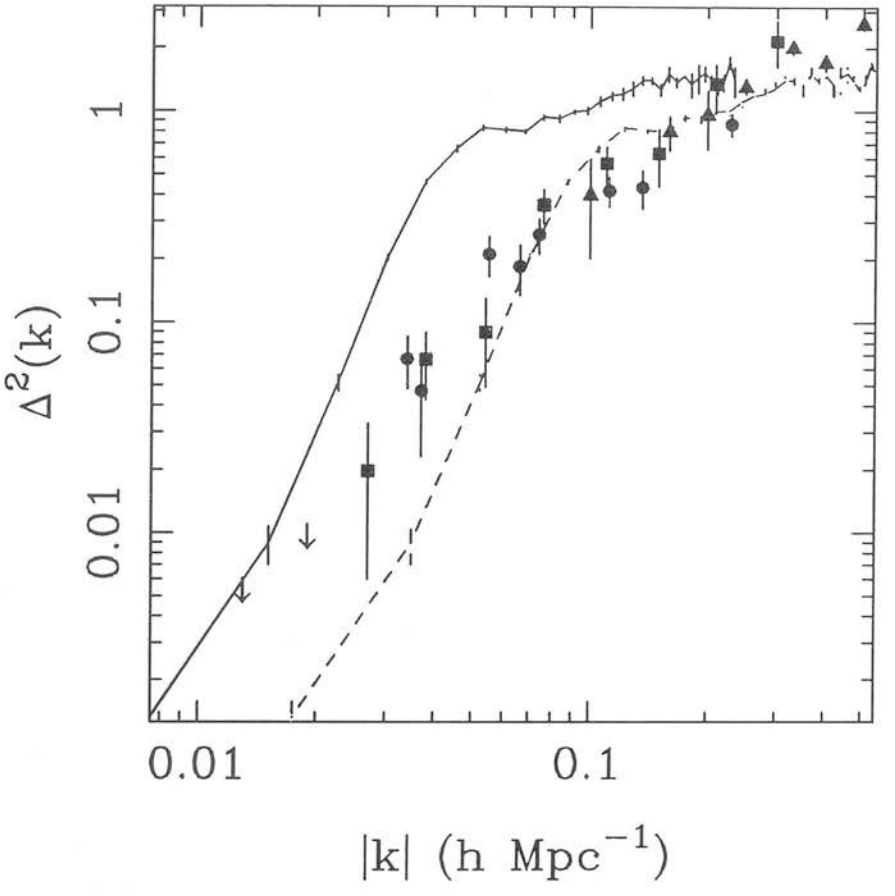

Figure 5.14 The power spectra for particles in walls in a Voronoi foam, normalised such that $\tilde{x} = 104\,h^{-1}$ Mpc (solid line) and $\tilde{x} = 45\,h^{-1}$ Mpc (broken line). Both power spectra are the mean of five independent simulations and the error bars represent the standard deviation on the mean. The symbols show the observed power spectra for three galaxy redshift surveys — the CfA survey (triangles; Baumgart & Fry 1991), the IRAS survey (circles; Peacock 1991) and radio galaxies (squares; Peacock & Nicholson 1991). The three observed power spectra are all normalised to the IRAS data. See text for details.

too sharply. Even when normalised to $\tilde{x} = 45\,h^{-1}$ Mpc, the Voronoi foam still slightly overestimates the amount of power at the break scale, as well as underestimating the amount of power on very small scales.

The small-scale slope of the observed power spectra, at 0.95, is steeper than that

for particles at walls in the Voronoi foam, but given the large scatter, this is not too significant, though if this behaviour extends to smaller scales then there will be a serious discrepancy between the observed data and the Voronoi foam. However, the large-scale slope, at 2.50, is considerably less steep than that of the Voronoi foam. This is born out by the fact that at very large scales ($k \lesssim 0.5\,h\,\mathrm{Mpc}^{-1}$, $r \gtrsim 125\,h^{-1}\,\mathrm{Mpc}$) the Voronoi foam seriously underestimates the amount of power present in the observed power spectrum.

In Fig. 5.14 the radio-galaxy data of Peacock & Nicholson (1991) has had its amplitude artificially reduced by a factor three so that it matches the IRAS data (Peacock 1991). Is this justified? Radio galaxies are well known to cluster more strongly than "normal" galaxies (e.g. Prestage & Peacock 1988; Yates, Miller & Peacock 1989), which suggests that they are preferentially situated in some topological feature or environment that exhibits stronger clustering properties. This argues against reducing the power as it suggests that it is intrinsic clustering that is being removed. However, what is more important is the shape of the power spectrum. As demonstrated in Fig. 5.13, the three power spectra for walls, filaments and nodes all have a common shape at large-scales, thus to artificially reduce the amplitude of the radio-galaxy data to help to constrain the shape of the power spectrum is a valid approach, provided that the real clustering properties of galaxies follow that of a Voronoi foam type scenario. If the Voronoi foam prescription is radically incorrect (i.e. the large-scale clustering of objects in regions of high-amplitude clustering does not have the same shape as the low-amplitude clustering) then this approach is invalid, though recent evidence suggests that this is not the case. Gramann & Einasto (1992) find that the power spectrum for galaxies in nearby "superclusters" increases in amplitude with luminosity, but retains a constant shape. Peacock & West (1992) find that the power spectrum of Abell clusters is of roughly the same shape as that of galaxies (Peacock 1991), albeit with a tenfold increase in amplitude.

5.4.4 Varying the Particle Distribution

The first suggestions are thus that the Voronoi foam is incapable of matching the observed large-scale distribution of galaxies. The Voronoi foam has been shown to have too little large-scale power, and though the power spectrum does not match the observa-

tions perfectly on small scales, the general aim of this subsection is to find a method of introducing extra large-scale power without significantly affecting the small-scale power and the amplitude of power spectrum around the break.

Following the lead of § 5.3, various methods of populating the geometric skeleton shall be considered. Varying the skeleton thickness (§ 5.3.1) may be rejected, along with taking snapshots of the distribution at different times (§ 5.3.2) and adding particles in voids (§ 5.3.4), as these either only affect the small-scale power or lead to a reduction of power on all scales. Of the methods suggested in § 5.3, only that of introducing non-random initial conditions (§ 5.3.3) is capable of increasing the amount of large-scale power present.

Fig. 5.15 shows the power spectrum for particles in walls of a "grenade" model simulation (§ 4.3.4). The data for the observed power spectra are as in Fig. 5.14. The two continuous curves are for the Voronoi foam normalised such that $\tilde{x} = 45\,h^{-1}$ Mpc (solid line) and $\tilde{x} = 30\,h^{-1}$ Mpc (broken line). The "grenade model" has totally the wrong shape. It provides too much power on all scales when normalised to $\tilde{x} = 45\,h^{-1}$ Mpc and when normalised such that $\tilde{x} = 30\,h^{-1}$ Mpc, though it matches the observed power spectrum on small scales, it still has far too much large-scale power.

The alternative suggested in § 5.3.3, that of weighting each particle such that each wall has a constant surface density, is shown in Fig. 5.16. The solid line is for unweighted particles, initially distributed at random (cf. Fig. 5.14), while the broken and dot-dash lines are the power spectra for particles initially distributed at random and the "grenade" model respectively, both weighted to give the walls a constant surface density (Appendix D). All three power spectra are normalised such that $\tilde{x} = 45\,h^{-1}$ Mpc and the observed data are given by the usual symbols.

As in § 4.5.2, both weighted power spectra agree, indicating that the weighting scheme (Appendix D) is working correctly. The same general trends exhibited in two dimensions also hold in three (cf. Fig. 4.10). On scales smaller than the break scale, the constant surface density case provides less power than the unweighted case, as it does on intermediate scales beyond the break, where the two follow similar power-law behaviour with differing amplitudes. It is only at very large scales ($k \lesssim 0.5\,h\,\mathrm{Mpc}^{-1}$, $r \gtrsim 125\,h^{-1}$ Mpc) that the power spectrum for weighted particles exceeds that of the unweighted case. Compared to the observations, one can see that giving the walls a

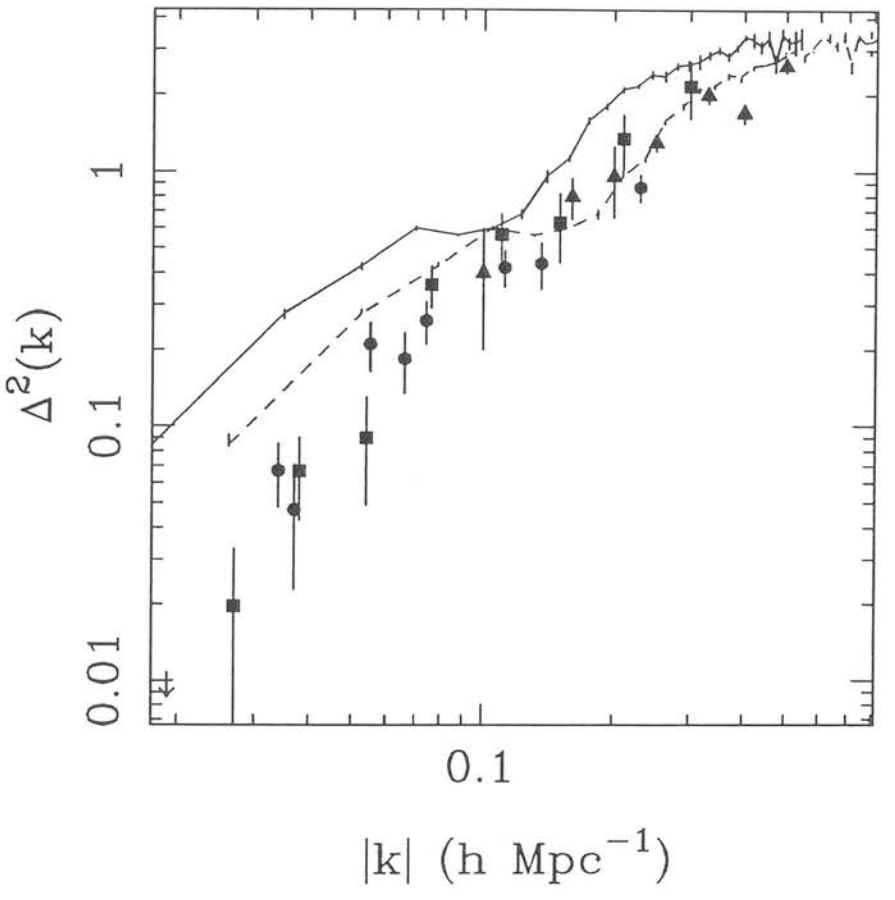

Figure 5.15 The power spectra for particles in walls in the "grenade" model, normalised such that $\bar{x} = 45\,h^{-1}$ Mpc (solid line) and $\bar{x} = 30\,h^{-1}$ Mpc (broken line). Both power spectra are the mean of five independent simulations and the error bars represent the standard deviation on the mean. The symbols show the observed power spectra for three galaxy redshift surveys — the CfA survey (triangles; Baumgart & Fry 1991), the IRAS survey (circles; Peacock 1991) and radio galaxies (squares; Peacock & Nicholson 1991). For details of the normalisation, see Fig. 5.14.

constant surface density of particles makes agreement with the data considerably worse. Though the power spectrum tentatively agrees with the observations at around the break scale and at very large scales, it provides too little small-scale power and serious underestimates the power on intermediate scales beyond the break.

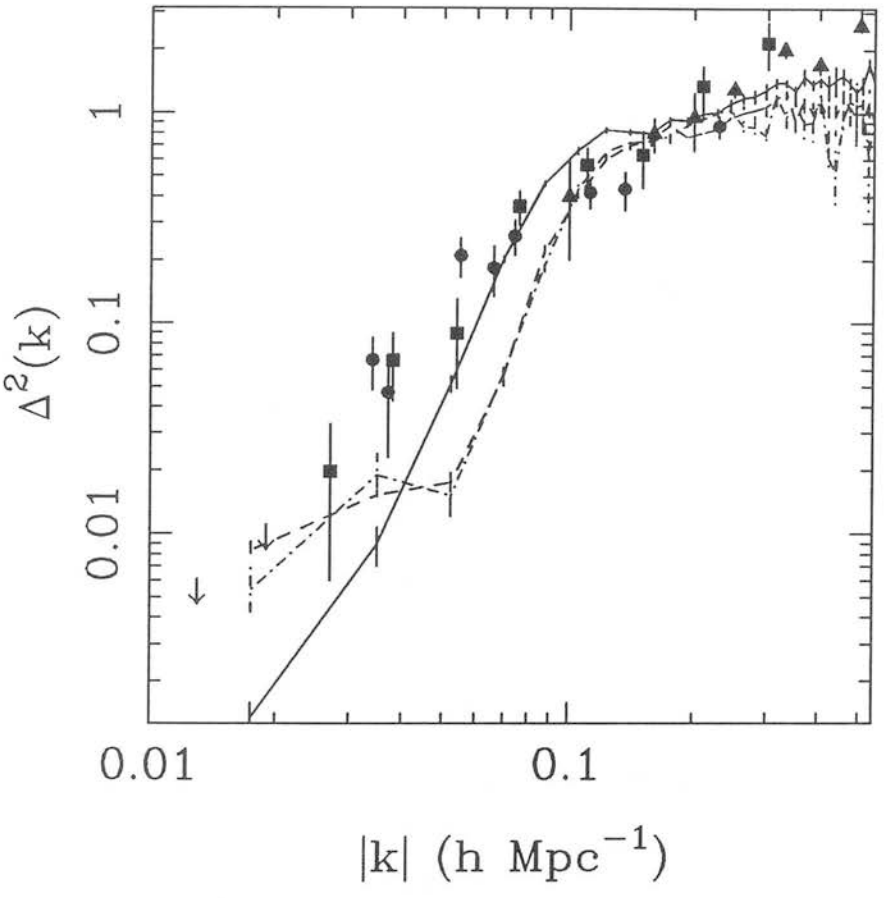

Figure 5.16 The power spectra for particles in walls in a Voronoi foam. The solid line is the power spectrum for unweighted particles, initially distributed at random, the broken line for the same simulation, but with particles weighted to give the walls a constant surface density, and the dot-dash line a "grenade" model simulation similarly weighted. All simulations are normalised such that $\bar{x} = 45\,h^{-1}$ Mpc and are the mean of five independent simulations with the error bars representing the standard deviation on the mean. The symbols are as in Fig. 5.14.

5.4.5 Conclusions

As stressed in the introduction (§ 5.4.1), the power spectrum is an excellent tool for probing large-scale clustering. Unlike the two-point correlation function correlation function for both galaxies and clusters of galaxies, the power spectrum is capable of constraining both the shape of the clustering spectrum and its overall normalisation.

Consistent with § 5.1.5 and § 5.3.5, a normalisation of $\tilde{x} \sim 45\,h^{-1}\,\mathrm{Mpc}$ is preferred. However, though the Voronoi foam qualitatively predicts the form of the large-scale clustering of galaxies, it lacks sufficient large-scale power to accurately account for the observed galaxy clustering. However, the evidence presented by the power spectrum is more suggestive than that. As well as lacking large-scale power, the global shape of the power spectrum for the Voronoi foam seems wrong, lacking both small and large-scale power and, as a result, breaking too sharply. Whereas in the Voronoi foam, the two clustering regimes are clearly defined, the observed power spectrum turns over much more gently and it is hard to define a single break scale. Various methods have been tried to overcome this deficiency (§ 5.4.4), but none has proved successful. Thus one is forced to conclude that the Voronoi foam model, with randomly distributed nuclei, is incapable of matching the observed power spectrum of galaxy clustering. See § 5.6 for a further discussion.

5.5 The Angular Correlation Function

5.5.1 Introduction

Although it contains less information, the angular correlation function has one major advantage over its three-dimensional counterparts, the spatial two-point correlation function (§ 5.2, 5.3) and the power spectrum (§ 5.4). Due to the difficulty in obtaining redshifts (distances), three-dimensional surveys are limited to small numbers and hence small volumes (see § 4.2.3). As discussed in § 5.2.3, this leads to the problem of whether or not the survey constitutes a fair sample. By concentrating only on the angular positions of the galaxies, two-dimensional surveys, such as the APM (Maddox *et al.* 1990) and EDSGC (Collins, Nichol & Lumsden 1992) surveys, are able to cover extensive areas of the sky containing large numbers of galaxies, thus improving the signal-to-noise, even when the amplitude of the correlation function is low (§ 4.2.3). Furthermore, the advent of modern plate scanning machines, such as those used in the APM and EDSGC surveys, has enabled the galaxy selection to be placed on a much more objective footing than was previously possible.

As in previous sections of this chapter, the aim is to compare the angular correlation functions computed from these new, automated surveys with that obtained from

the Voronoi foam. Again this work shall concentrate on the clustering of particles in the different topological regions of the foam.

5.5.2 Correlation Functions for Particles in Walls, Filaments and Nodes

As shown in § 5.2.2, the amplitude and slope of the spatial two-point correlation function increases as particles move from walls through filaments to nodes. As the angular two-point correlation function is merely a projected version of its three-dimensional counterpart, one would expect similar behaviour (see Appendix F). Fig. 5.17 shows the angular two-point correlation functions for particles at walls, filaments and nodes in a Voronoi foam. As one can see, the angular two-point correlation function roughly approximates to a power law at small θ, followed by a break at some critical angle, the break angle, θ_b. The slope of the power-law section and the amplitude of the correlation function at $\theta = 1$ are shown in Table 5.8. As one can see, both slope and amplitude increase as one would expect from the behaviour of the spatial two-point correlation function.

Correlation Function	Slope	$w(\theta = 1°)$
Nodes	−1.22	0.49
Filaments	−1.09	0.28
Walls	−0.68	0.08

Table 5.8 Parameters for power laws fitted to the angular two-point correlation functions given in Fig. 5.17.

If the spatial correlation function is modelled as a pure power law (equation 5.2) and the angular correlation function is also considered as such, then it may be fitted by (Groth & Peebles 1977) :

$$w(\theta) \propto \theta^{1+\gamma}, \qquad (5.6)$$

where γ is the power-law index of the spatial correlation function (equation 5.2).

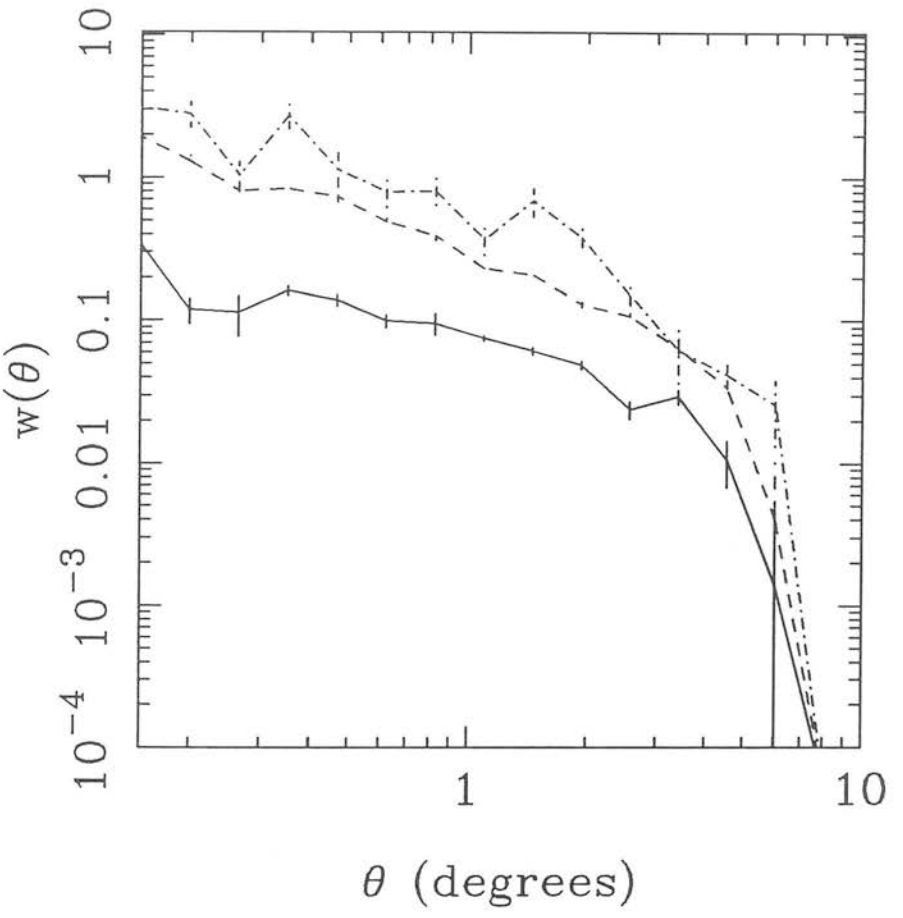

Figure 5.17 Angular two-point correlation function for particles in a Voronoi foam when they first reach walls (solid line), filaments (broken line) and nodes (dot-dash line). The Voronoi foam is normalised such that $\tilde{x} = 52\,h^{-1}$ Mpc, with the selection function chosen to match that of the APM survey and scaled to the depth of the Lick survey (see § 5.5.3). The correlation functions are the mean of five independent simulations and the error bars represent the standard deviation on the mean.

Comparing the parameters in Table 5.8 with those for the spatial correlation function in Table 5.5 it is obvious that the relation in equation (5.6) does not hold. This confirms the conclusion of § 5.2.2, that the spatial correlation function cannot be fitted by a single power law, even for small r. This is also true for the angular correlation function, as seen in Fig. 5.17, where for particles in walls, the correlation function shows evidence of turning over at small θ towards the limiting case of particles confined to

a two-dimensional plane. This is qualitatively similar to the behaviour of the spatial correlation function (see Fig. 5.5 and § 5.2.2 for a discussion).

The break angle, though not very well delineated, is similar for all three correlation functions in Fig. 5.17. This is to be expected and mirrors the behaviour of the power spectrum (Fig. 5.13), where all three power spectra break at roughly the same scale. This supports the conclusion reached in § 5.4.2 that the break is related to the transition from intra- to intercellular clustering.

5.5.3 Angular Two-Point Correlation Function vs. Autocorrelation Function

The angular correlation functions plotted in Fig. 5.17 were calculated by binning pairs with angular separations of $\theta \pm \Delta\theta$, using the estimator introduced in § 4.2.3,

$$w(\theta) = \frac{n_{\text{pairs}}}{n_{\text{exp}}} - 1, \tag{5.7}$$

where n_{pairs} is the number of pairs at a given angular separation θ and n_{exp} is the expected number of pairs at the same separation in an unclustered catalogue. Though the angular two-point correlation function allows a vast improvement in signal-to-noise over the spatial correlation for observational data, for the Voronoi foam simulations the reverse is true. Due to the periodic boundary conditions employed in the simulations, the spatial two-point correlation function can be calculated over the volume of the whole simulation (§ 4.2.2). To compute the angular two-point correlation function, the data needs to be projected in order to produce a two-dimensional catalogue, a process which discards $\sim \frac{2}{3}$ of the particles and destroys the sample's periodicity (§ 4.2.3). This means that the angular two-point correlation functions are considerably more noisy than their spatial counterparts (cf. Figs. 5.5 and 5.17). A further consequence of this is that the angular correlation function only probes to angular separations of $\theta \gtrsim 0.2°$ whereas the observed angular correlation function extends to $\theta \lesssim 0.02°$. Because the correlation function begins to break at $\theta \simeq 3°$, this means that there is only a limited range over which the correlation functions can be compared.

One way around this problem is to use the angular autocorrelation function (Appendix F). This is calculated directly from the power spectrum, thus the whole simula-

tion volume is used. Note that the angular auto- and two-point correlation functions are not different statistics, rather they are complimentary estimators of the same statistic.

The angular correlation function is related to the spatial correlation function by Limber's equation (e.g. Peebles 1980; Peacock 1991),

$$w(\theta) = \frac{\int_0^\infty y^4 S(y)^2 dy \int_{-\infty}^{\infty} \xi(\sqrt{x^2 + y^2\theta^2}) dx}{\left[\int_0^\infty y^2 S(y) dy\right]^2}, \tag{5.8}$$

where $S(y)$ is a radial selection function (see below) and y is the radial comoving co-ordinate. The spatial separation, r, is given by $\sqrt{(x^2 + y^2\theta^2)}$. The spatial correlation function is related to the power spectrum by a Fourier transform (equation E.18),

$$\xi(r) = \frac{1}{r} \int_0^\infty \Delta^2(k) \sin(kr) \frac{dk}{k^2}. \tag{5.9}$$

One may then recast Limber's equation in terms of the power spectrum to give (Peacock 1991; Appendix F)

$$w(\theta) = \frac{\int_0^\infty y^4 S(y)^2 dy \int_0^\infty \pi \Delta^2(k) J_0(ky\theta) \frac{dk}{k^2}}{\left[\int_0^\infty y^2 S(y) dy\right]^2}, \tag{5.10}$$

where $J_0(ky\theta)$ is the Bessel function. For the form of selection function used here (equation 5.12), this becomes (Appendix F) :

$$w(\theta) = \frac{\pi}{2\Gamma^2(5/4)} \int_0^\infty \Delta^2(k) \exp\left(-[k\theta y_*]^2/8\right) \left(1 - [k\theta y_*]^2/8\right) \frac{dk}{k^2 y_*}. \tag{5.11}$$

In order to comparE the angular two-point correlation function of the Voronoi foam with observations, it is necessary to ensure that the projected catalogue is reaching a similar depth to that of the observations. This requires the use of a radial selection function, $S(y)$ (see § 4.2.3), which approximates to that of the observational survey. The angular correlation functions used for comparison with the Voronoi foam are those computed from the APM (Maddox *et al.* 1990) and EDSGC (Collins, Nichol & Lumsden

1992) surveys. Both catalogues use the same plate material and thus can be expected to have similar selection functions. The selection function

$$S(y) = \exp\left(-\left[\frac{y}{y_*}\right]^2\right)\left(\frac{y_*}{y}\right)^{\frac{1}{2}}, \tag{5.12}$$

has been found to provide a reasonable approximation, where $y_* = 233\,h^{-1}\,\mathrm{Mpc}$ (Peacock 1991), chosen such that the angular correlation function scales to the depth of the original Lick survey (Groth & Peebles 1977). It should be noted that the selection function is normalised such that it gives the probability that a galaxy at distance r is included in the projected catalogue.

A practical difficulty that arises in computing the angular autocorrelation function from the power spectrum on small scales. As the power spectrum does not extend to scales of $\lesssim 10\,h^{-1}\,\mathrm{Mpc}$ (§ 5.4.2), it is necessary to use an assumed power spectrum in this region. Three approaches have been considered. The first is to assume that there is no power beyond the minimum scale provided by the power spectrum. The second is to model the power spectrum at small scales as a power law (a reasonable assumption, see § 5.4) and to extrapolate the power spectrum to indefinitely small scales using a best-fit power law. The third approach is to extrapolate the power spectrum by a power law of unit slope. The last approach is motivated by the knowledge that at small scales the power spectrum will tend to the theoretical case for particles confined to a two-dimensional sheet in three-dimensional space, which is a power law of unit slope (see § 5.2.2)

To check the validity of these approaches Fig. 5.18 shows the angular two-point correlation function (solid line) with the autocorrelation function calculated using the three approaches given above. All three agree at large scales and are only just starting to diverge at small θ, where all three are still compatible with the two-point correlation function which, unfortunately, does not extend to small enough angular separations to distinguish between the three different approaches. Fortunately, one is able to appeal to the spatial two-point correlation function, which extends to much smaller separations. Fig. 5.19 shows the spatial two-point and autocorrelation functions. While the autocorrelation functions agree with each other at large separations, the three methods diverge at small separations, with only the power spectrum extrapolated with a power law of

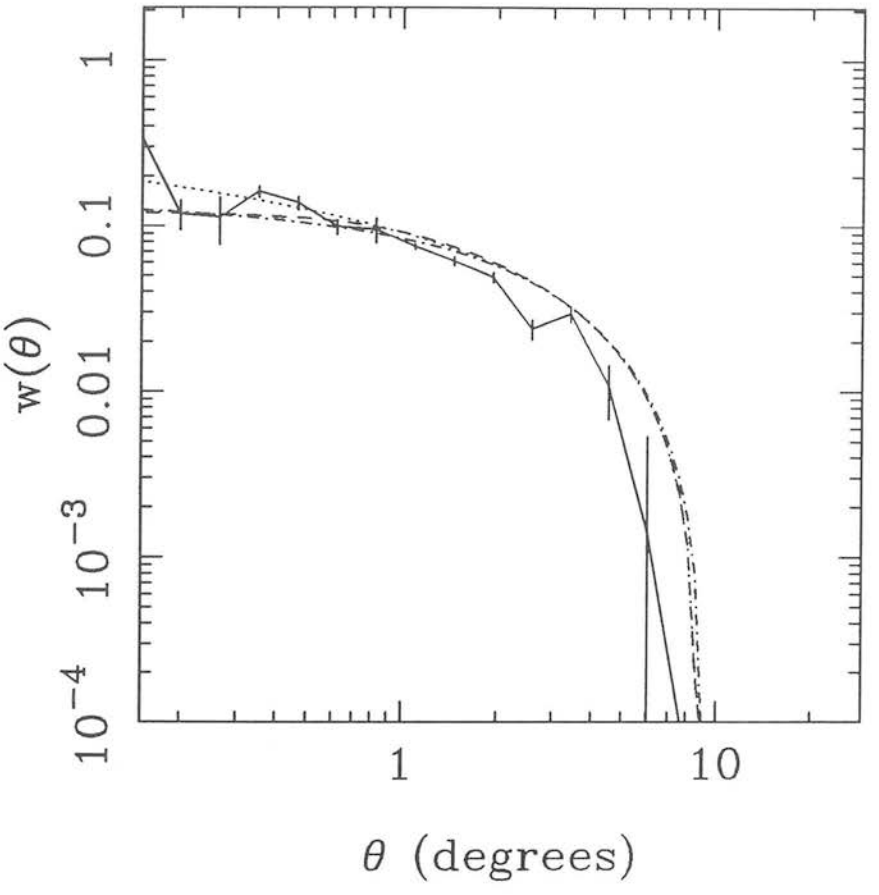

Figure 5.18 The angular two-point and autocorrelation functions for particles in walls in a Voronoi simulation. The solid line is the two-point correlation function (taken from Fig. 5.17), the broken line, the autocorrelation function calculated for the power spectrum with no extrapolation, the dot-dash line, the power spectrum extrapolated as a best-fit power law and the dotted line, the power spectrum extrapolated as a power law of unit slope. The simulations are normalised such that $\tilde{x} = 52\,h^{-1}$ Mpc, with the selection function chosen to match that of the APM survey and scaled to the depth of the Lick survey (see above). The correlation functions are the mean of five independent simulations and the error bars represent the standard deviation on the mean.

unit slope (dotted line) giving an adequate fit to the two-point correlation function. The other two methods underestimate the amount of power on small scales.

Looking at Figs 5.18 and 5.19, one can see that there is some discrepancy between

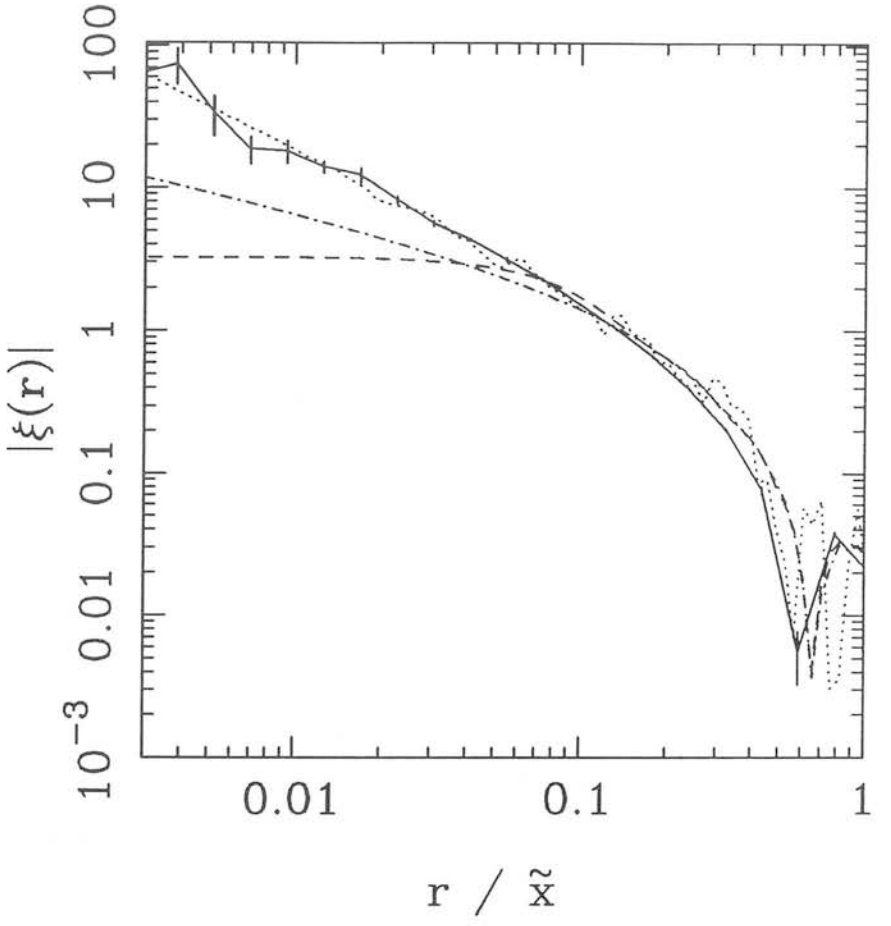

Figure 5.19 The spatial two-point and autocorrelation functions for particles in walls in a Voronoi simulation. The solid line is the two-point correlation function (taken from Fig. 5.5), the broken line, the autocorrelation function calculated for the power spectrum with no extrapolation, the dot-dash line, the power spectrum extrapolated as a best-fit power law and the dotted line, the power spectrum extrapolated as a power law of unit slope. The correlation functions are the mean of five independent simulations and the error bars represent the standard deviation on the mean.

the auto- and two-point correlation functions at large separations, with the autocorrelation functions producing slightly more power. However, the amplitudes of the two-point correlation functions at these scales are considerably less than unity. As discussed in §5.4.1, the two-point correlation function can suffer from considerable uncertainties when the amplitude is small, even for samples with well established mean densities such

as the Voronoi foam simulations. With such uncertainties in mind, the discrepancies at large separations are not considered to be too serious.

5.5.4 Comparison with Observations

Due to the noisy nature of the angular two-point correlation function, the angular autocorrelation function shall be used in comparison with the observations. As demonstrated in § 5.5.3, the two are equivalent estimators of the same statistic. The advantage of the autocorrelation function is that not only does it provide a cleaner estimate, but it extends to much smaller angular separations. Fig. 5.20 shows the angular autocorrelation function, normalised such that $\tilde{x} = 104\,h^{-1}$ Mpc (solid line) and $\tilde{x} = 45\,h^{-1}$ Mpc (broken line), along with the observed correlation function (symbols) of Maddox *et al.* (1990).

As one can see, when normalised to $\tilde{x} = 104\,h^{-1}$ Mpc, the Voronoi foam fails to account for the observations. Even for a normalisation of $\tilde{x} = 45\,h^{-1}$ Mpc, the Voronoi foam is a poor match to the observed data. Though the correlation functions match at the break scale, the Voronoi foam has insufficient small-scale power as well as breaking too sharply, thus providing far too little large-scale power. This supports the findings of the power spectrum (§ 5.4.3), except that the angular correlation function extends to sufficiently small scales to make clear the discrepancy here.

As the autocorrelation function on these small scales is calculated by extrapolating the power spectrum as an assumed power law of unit slope, it may be that the missing power is a product of this process. However, there is good evidence from the spatial autocorrelation function (§ 5.5.3; Fig. 5.19) that this procedure matches the small-scale clustering properties of its two-point equivalent, suggesting that the missing power is inherent to the model and that the angular autocorrelation function is an accurate extension of the angular two-point correlation function. Even if this is not the case, Figs 5.18 and 5.19 show that extrapolating the power spectrum with a unit slope overestimates the power present if extrapolated with a best-fit power law (dotted and dot-dash lines respectively). It is hard to see how this procedure could underestimate the true power present on small scales, thus strengthening the above conclusions.

However, one may ask, how well determined is the observed angular correlation function? A similar survey to that used by Maddox *et al.* (1990) has been carried out

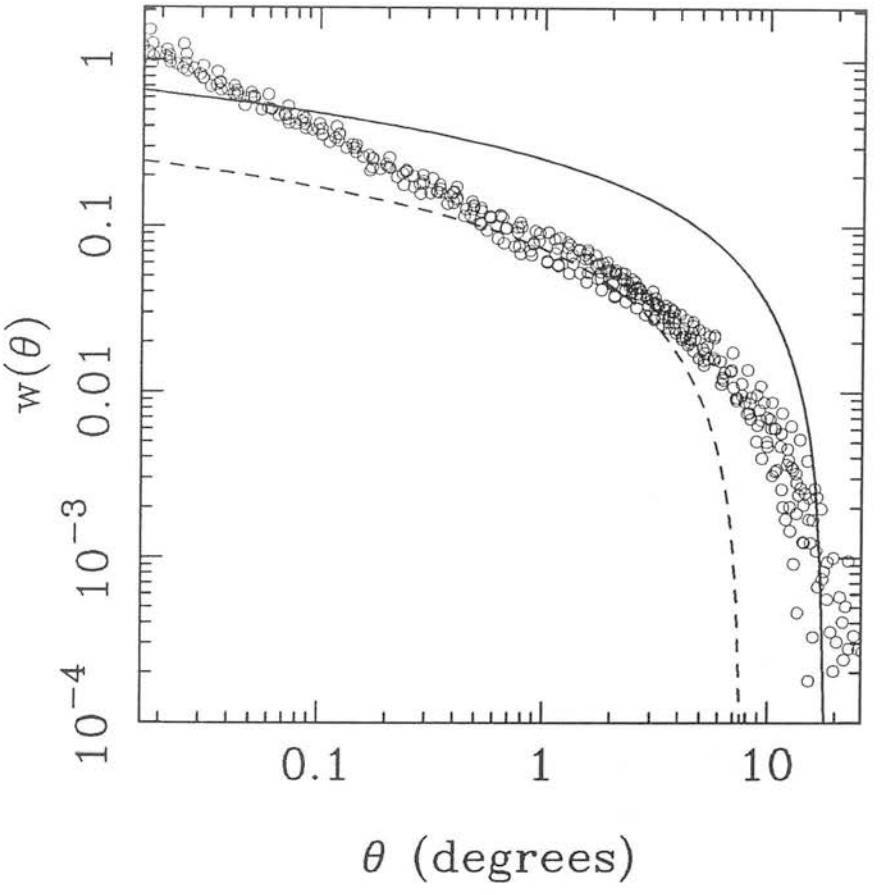

Figure 5.20 The angular autocorrelation functions for particles in a Voronoi foam when they first reach walls (lines) and observations (open circles). The solid line is for $\tilde{x} = 104\,h^{-1}$ Mpc and the broken line for $\tilde{x} = 45\,h^{-1}$ Mpc. Both use the selection function given in equation (5.12) and are the mean of five independent simulations. The observed correlation function is that of Maddox *et al.* (1990). All correlation functions are scaled to the Lick depth.

(Collins, Nichol & Lumsden 1992 and references therein) using the same plate material and a similar computerised scanning technique. They find a similar angular correlation function, agreeing with Maddox *et al.* (1990) on small and intermediate scales, but suggesting that there might be even more power on large ($\theta \gtrsim 10°$) scales, thus making the disagreement between the Voronoi foam and the observed correlation function even greater. A smaller study by Picard (1991a), using different plate material, also finds

a correlation function in agreement with those of Maddox *et al.* (1990) and Collins, Nichol & Lumsden (1992), although there may be more power on scales just before the break, again worsening the discrepancy between observations and the Voronoi foam. Further supporting evidence comes from Peacock (1991), who computes the angular autocorrelation function from a best-fit power spectrum and finds excellent agreement with the angular correlation function of Maddox *et al.* (1990).

It should be noted that this level of agreement has only recently been achieved. Earlier results for the angular correlation function gave break scales of a similar size or less than that of the Voronoi foam, with a similarly rapid drop in amplitude after the break. However, these surveys suffer from several problems. For example, the result of Groth & Peebles (1977), which shows a similar correlation function to that determined for the Voronoi foam, is based on an "eye-ball" survey of photographic plates and is thus prone to considerably larger errors than the automated plate surveys [e.g. see Maddox *et al.* (1990) or Collins, Nichol & Lumsden (1992) and references therein for a discussion].

Other automated surveys (e.g. Shanks *et al.* 1980; Stevenson *et al.* 1985; Collins, Heydon-Dumbleton & MacGillivray 1988), which avoid the type of errors possibly present in the Groth & Peebles result, have found breaks on even smaller scales than that found by Groth & Peebles (1977). These surveys are universally restricted to small regions of the sky and suffer from two effects as a result. One is the integral constraint, which results in small-area surveys systematically under-estimating the amplitude of the angular correlation function (e.g. see Collins, Heydon-Dumbleton & MacGillivray 1988, Collins, Nichol & Lumsden 1992). The second, more serious problem, is that such small-area surveys may not constitute a fair sample (Collins, Heydon-Dumbleton & MacGillivray 1988; Picard 1991a,b). It is interesting to note that the break scale tends to grow with the size of the survey (Collins, Nichol & Lumsden 1992), which lends credence to these arguments, suggesting that the smaller surveys of Shanks *et al.* (1980), Stevenson *et al.* (1985) and Collins, Heydon-Dumbleton & MacGillivray (1988) simply failed to cover large enough an area to include the large-scale power found in larger surveys.

5.5.5 Varying the Particle Distribution

As with previous sections, the possibility remains that altering the distribution of par-

ticles on the walls may provide a better fit to the observations. As discussed in § 5.4.4, introducing non-random initial conditions to the particle distribution is the only method capable of increasing the large-scale power, though this was demonstrated to provide an even worse fit to the data. This conclusion is supported by Fig. 5.21, which shows the angular correlation function for the "grenade" model (broken and dot-dash lines) and the case of walls with a constant surface density (dotted line). The correlation function for particles initially distributed at random (cf. Fig. 5.20) is shown for comparison (solid line) along with the correlation of Maddox *et al.* (1990). The simulations are normalised such that $\tilde{x} = 45\,h^{-1}$ Mpc, with the exception of one of the "grenade" model simulations, which is normalised to $\tilde{x} = 20\,h^{-1}$ Mpc (dot-dash line).

One can see that the "grenade" model, when normalised to $\tilde{x} = 45\,h^{-1}$ Mpc, provides far too much power on virtually all scales, but when normalised to $\tilde{x} = 20\,h^{-1}$ Mpc, it provides a fair fit at the break scale and beyond, though the break is still quite steep compared to the data. On small scales it is consistent with the case for randomly distributed particles and thus underestimates the small-scale power by a considerable amount.

In any case, a normalisation of $\tilde{x} = 20\,h^{-1}$ Mpc is very unrealistic. This would lead to a node-node correlation function with a correlation length of only $\simeq 5\,h^{-1}$ Mpc, which is in conflict with the cluster-cluster correlation function (§ 5.1) and the correlation function for particles in walls would have a correlation length of $\lesssim 4\,h^{-1}$ Mpc, which is in conflict with the galaxy-galaxy correlation function (§ 5.2.3). Thus one may exclude such a low normalisation, even though it provides an excellent fit to the observed angular correlation function at large scales.

The other alternative, that of weighting the particles so as to give each wall an equal surface density, is also shown in Fig. 5.15 (dotted line). Like the power spectrum (§ 5.4.4), this provides too little power on all but the largest scales ($\theta \gtrsim 10°$) where it provides too much power. Thus this too can be excluded and one is forced to conclude that, as in § 5.3 and § 5.4, varying the distribution of particles on the walls is incapable of accounting for the discrepancy between the observations of large-scale structure and those predicted by the Voronoi foam.

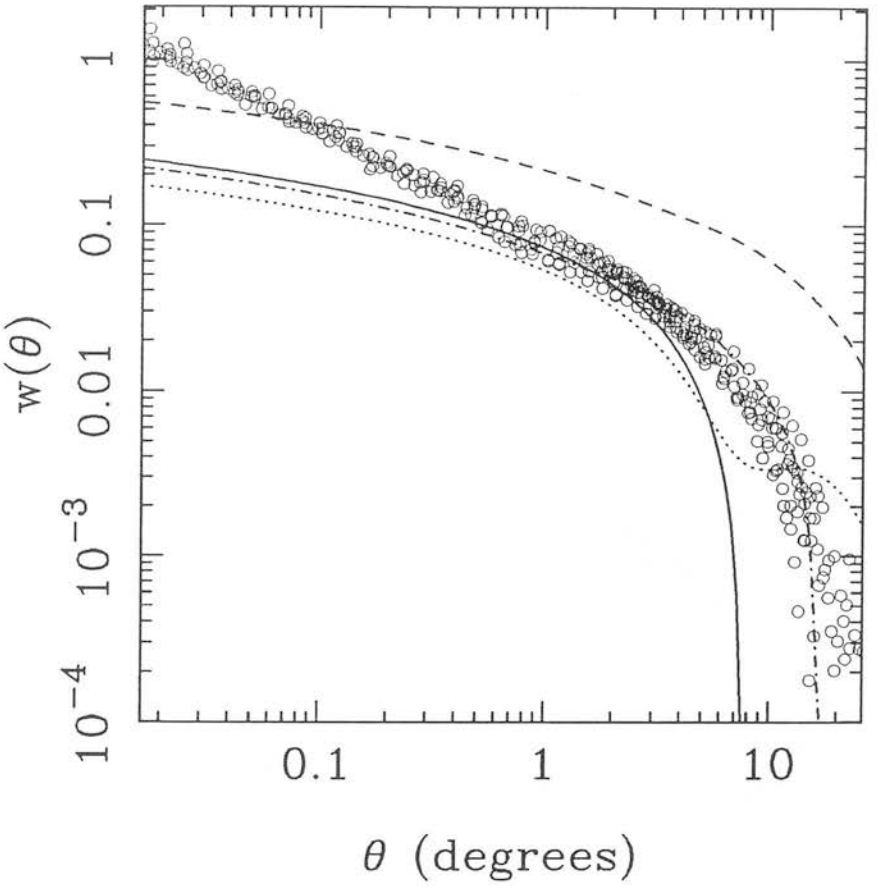

Figure 5.21 Angular autocorrelation function for particles on walls in a Voronoi foam (lines) and the observed angular correlation function (symbols) of Maddox *et al.* (1990). The four curves are for particles initially distributed at random (solid line), the "grenade" model (broken and dot-dash lines) and the case of particles weighted so as to give the walls an equal surface density (dotted line). The correlation functions are the mean of five individual simulations and are normalised such that $\tilde{x} = 45\,h^{-1}$ Mpc, except one of the "grenade" model simulations (dot-dash line), which is normalised to $\tilde{x} = 20\,h^{-1}$ Mpc. All the correlation functions are scaled to the Lick depth.

5.5.6 Conclusions

This section has shown the angular two-point correlation function to be an excellent discriminant between theory and observation. Like the power spectrum (§ 5.4), the angular correlation function can constrain both the amplitude and shape of the clustering

spectrum. In line with § 5.1.5, § 5.3.5 and § 5.4.5, a normalisation of $\tilde{x} \sim 45\,h^{-1}$ Mpc is preferred. However, due to the high signal-to-noise of the observed angular correlation function, the limit of $40 \lesssim \tilde{x} \lesssim 55\,h^{-1}$ Mpc may be placed on the normalisation (see Fig. 5.22). This agrees with the plausible limits set on the normalisation by the spatial two-point correlation function for clusters (§ 5.1.5).

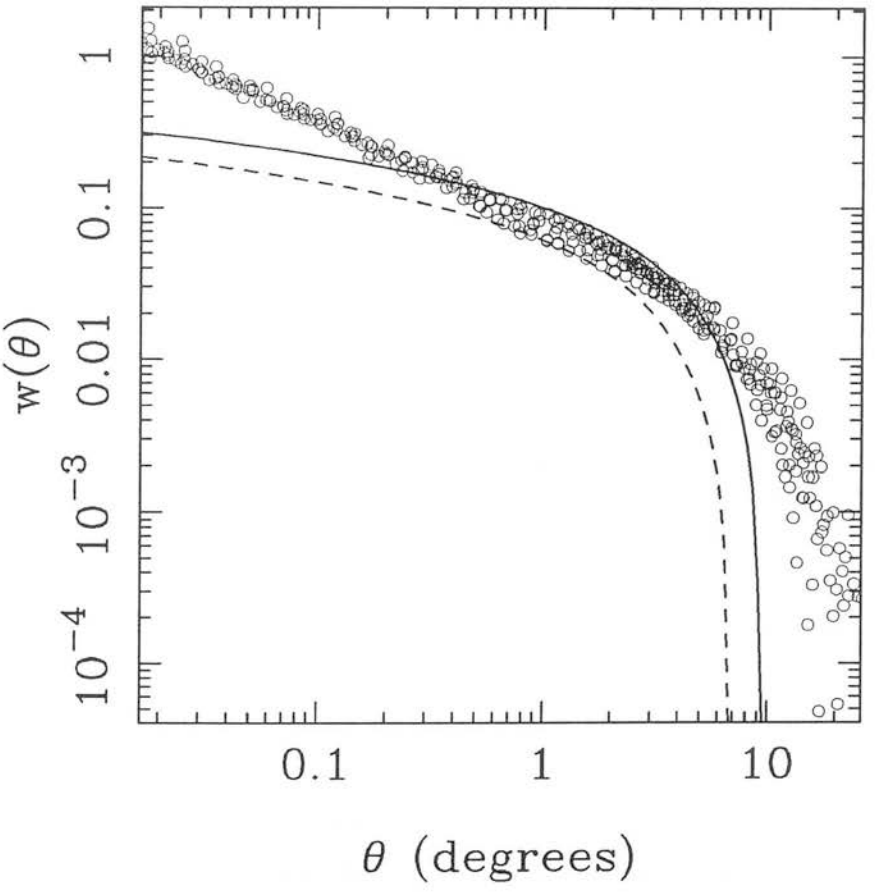

Figure 5.22 The angular autocorrelation function for normalisations of $\tilde{x} = 55\,h^{-1}$ Mpc (solid line) and $\tilde{x} = 40\,h^{-1}$ Mpc (broken line), compared to the observed angular correlation function of Maddox *et al.* (1990). All correlation functions are scaled to the depth of the Lick survey.

The shape of the angular correlation function also supports the conclusions reached

by comparison with the power spectrum. The Voronoi foam model lacks both small- and large-scale power in comparison to the observed galaxy distribution. Once again, the fundamental problem is the shape of the clustering spectrum — the Voronoi foam breaks too sharply, whereas the turnover in the observed data is much smoother.

With a high degree of confidence one is now able to rule out the standard Voronoi foam model (i.e. randomly placed nuclei and a random initial particle distribution) as a prescription for the large-scale structure of the universe. Similarly, altering the distribution of particles within the Voronoi skeleton does not make the Voronoi foam model compatible with the observed angular correlation function. Once again, the shape of the correlation function is wrong. Thus it is with a high degree of confidence that one is able to say that the Voronoi foam model with randomly distributed nuclei is unable to account for the observed large-scale angular clustering of galaxies.

5.6 Conclusions

It has been the aim of this chapter to provide a comparison between the observed large-scale distribution of galaxies and that predicted by the Voronoi foam model. The goal of this investigation is to see whether the model can provide an accurate description of the large-scale galaxy distribution and to put limits on the model's one free parameter, $\tilde{x}$, the inter-nucleus separation and the model's physical length scale.

In order to achieve this aim three related statistics have been used — the spatial two-point correlation function for both galaxies (§ 5.2, 5.3) and clusters of galaxies (§ 5.1), the angular two-point correlation function (§ 5.5) and the power spectrum (§ 5.4).

There are two independent criterion to be met. Any model of large-scale structure has to account for both the shape of the observed distribution (i.e. the amount of clustering, or power, on different scales) and the overall amplitude of the clustering. The latter is set by the normalisation of the model and is independent of the shape, this being largely determined by the geometric structure of the foam.

The original normalisation suggested for the Voronoi foam model, that of $\tilde{x} = 104\,h^{-1}\,\mathrm{Mpc}$, was put forward by van de Weygaert & Icke (1989), who claimed that it naturally accounted for both the observed number density of Abell richness class $R \geq 1$ clusters and the cluster-cluster two-point correlation function. However, the

majority of work in this chapter points to a normalisation of $\tilde{x} \simeq 45\,h^{-1}$ Mpc. With $\tilde{x} = 104\,h^{-1}$ Mpc, the Voronoi foam consistently predicts clustering amplitudes that are far too high. Even the cluster-cluster two-point correlation function has an amplitude that is in conflict with more recent determinations of the two-point correlation function for clusters. It is reassuring to note that the preferred normalisation of $\tilde{x} \simeq 45\,h^{-1}$ Mpc is consistent with the observed sizes of voids in recent redshift surveys (e.g. de Lapparent, Geller & Huchra 1986; Geller & Huchra 1989; da Costa *et al.* 1988, 1989; Fairall *et al.* 1990; Parker 1992).

There is a further observation that needs to be taken in account. Broadhurst *et al.* (1990) carried out two pencil-beam surveys at the north and south galactic poles (§ 1.4.2) and, on combining their data, found a remarkable periodicity, with galaxies being clustered at redshift intervals equivalent to a comoving separation of $128\,h^{-1}$ Mpc. This has been taken as evidence of a cellular structure of characteristic size $\sim 128\,h^{-1}$ Mpc. van de Weygaert (1991) used the Voronoi foam model to simulate the Broadhurst *et al.* surveys and, using a normalisation of $\tilde{x} = 104\,h^{-1}$ Mpc, found periodicities of $100 - 150\,h^{-1}$ Mpc in $\sim 15\%$ of his simulations. However, as has been demonstrated in this chapter, this normalisation is inconsistent with other observed measures of galaxy clustering. Thus one is forced to consider how an apparent $128\,h^{-1}$ Mpc cellular structure on large scales can be reconciled with a local one of size $\sim 45\,h^{-1}$ Mpc.

As discussed in § 1.4.2, both de Lapparent, Geller & Huchra (1991) and Ramella, Geller & Huchra (1992) argue that the Broadhurst *et al.* result is consistent with the CfA survey, which itself has voids of linear size $\sim 40\,h^{-1}$ Mpc. This is due to pencil-beams not picking up every wall they pass through. At the characteristic depths of the survey, Broadhurst *et al.*'s pencil-beams are only $\sim 5\,h^{-1}$ Mpc in diameter, roughly the clustering length of the galaxies in the walls. Thus it is not surprising that a pencil-beam can intersect a wall and yet detect no galaxies (de Lapparent, Geller & Huchra 1991; Ramella, Geller & Huchra 1992). The same conclusion was reached by Ikeuchi & Turner (1991), working within the context of the Voronoi foam model. Thus it seems that there may be no discrepancy between a cellular network of characteristic size $\sim 45\,h^{-1}$ Mpc and a large-scale periodicity of $128\,h^{-1}$ Mpc.

The conclusion therefore reached is that the optimum normalisation of the Voronoi foam model lies in the range $40 - 55\,h^{-1}$ Mpc (§ 5.1.5, 5.3.5, 5.4.5, 5.5.6), a conclusion

which is confirmed for a variety of observational results . However, when addressing the question of shape, the Voronoi foam is not so successful.

The observed spatial two-point correlation function has a poorly determined shape, most authors preferring to model it as a single component power law over the range where there is significant signal. Fortunately, both the angular two-point correlation function and the power spectrum have a much more clearly defined shape — a power law at small scales, followed by a break at some characteristic scale. Beyond the break there is evidence in the power spectrum for a further power-law component.

This is qualitatively what is seen in the Voronoi foam. However, quantitatively, there are significant differences. Whereas for the spatial two-point correlation functions, where the normalisation simply sets the amplitude of the correlation function, the presence of a break in the clustering properties implies a preferred scale (which, in the case of the Voronoi foam, is related to the characteristic cell size), which is also set by the normalisation of the length scale. With $40\,h^{-1}\,\mathrm{Mpc} \lesssim \tilde{x} \lesssim 55\,h^{-1}\,\mathrm{Mpc}$, the Voronoi foam correctly predicts the scale of the break and the amplitude of both the angular correlation function and the power spectrum at the break. However, the model predicts too little power on scales both smaller and greater than the break scale. Though the shape of the angular correlation function/power spectrum is largely fixed by the geometric skeleton of the Voronoi foam, various methods of altering the distribution of the particles on the skeleton have been tried in the hope of supplying the missing power, but with no success. The problem seems to be one fundamental to the geometric structure of the Voronoi foam.

That the Voronoi foam predicts too little power on small scales is none too surprising and is no great problem. The model is a very simple prescription of the *large*-scale distribution of matter. The foam provides surfaces on which galaxies are distributed. and in this implementation of the model, galaxies are distributed roughly at random across the walls, hence it should come as no surprise that the Voronoi foam lacks small-scale power, as none is put in by the model, save that intrinsic to the walls (§ 5.2.2). In more realistic circumstances the particles in the walls would be under the influence of local gravitational forces and hence would cluster on small scales. Whether this additional gravitational clustering would be sufficient to account for the excess observed clustering is unknown, but such clustering is likely to be complex and non-linear in nature, thus

making it hard to model.

A more serious problem is the lack of power beyond the break. The break scale itself is set by the transition from intracellular to intercellular clustering. Beyond the break scale the clustering must reflect the initial distribution of the nuclei, which determines the large-scale properties of the cells. As the nuclei were distributed at random, this probably accounts for the very rapid fall off of power beyond the break. Obviously, this discrepancy cannot be explained by appealing to the action of local gravitational forces. The problem is fundamental to the geometric construction of the Voronoi foam and the initial distribution of the Voronoi nuclei.

Thus the conclusion of this chapter is that the standard Voronoi foam model, with randomly distributed nuclei and particles initially distributed at random, is incapable of accounting for the observed large-scale clustering of galaxies, due to a lack of large-scale power.

There are two avenues for further exploration. The first is to vary the way in which the particles are distributed on the geometric skeleton of the Voronoi foam. Some basic variations have been investigated in this chapter, mostly in § 5.3, but with little success. However, one caveat must be added. It is not impossible, as was shown in § 5.3.3, to finely tune the initial particle distribution so as to achieve the desired result. Highly contrived distributions can be used to achieve the required effect, in the case of § 5.3.3, the imposition of an extremely regular initial distribution in order to reduce the correlation length of the spatial two-point correlation function without changing the normalisation. It should be stressed that such initial conditions are contrived and as such are very unphysical. It seems highly unlikely that a satisfactory distribution can be found that will account for the lack of both small and large-scale power, but it cannot be ruled out on the evidence presented here. The work presented in this thesis does not constitute an exhaustive exploration of the possibilities offered by varying the particle distribution.

The second avenue of exploration is to vary the distribution of the Voronoi nuclei themselves. This offers more promise in that the large-scale power in the Voronoi foam model is determined by the distribution of the Voronoi nuclei, thus altering their distribution could provide the missing large-scale power. This will be explored in detail in Chapter 6.

Chapter 6

Clustering of Voronoi Nuclei

6.1 Peaks in a Gravitational Potential as Voronoi Nuclei

6.1.1 Introduction

Previous work on the Voronoi foam (e.g. Matsuda & Shima 1984; Pierre, Shaver & Iovino 1988; van de Weygaert & Icke 1989; van de Weygaert 1991; Coles 1990) has largely concentrated on using randomly distributed nuclei, as has the work presented so far in this thesis. This is not too surprising when one considers the background of work on the Voronoi foam.

Voronoi tessellation has long been looked at from a mathematical point of view and there are many analytical results known for the case of randomly distributed nuclei (e.g. see Møller 1989 and references therein). Hence early work on the Voronoi foam in cosmology may have used randomly distributed nuclei as it allowed the results from simulations to be compared to the analytical results. Furthermore, as there has been little effort to link the Voronoi tessellation to any underlying physical processes, there is no physical basis for the manner in which the nuclei are distributed. Clustering the nuclei introduces an extra free parameter that needs to be considered. Given the remarkable early success that the Voronoi foam had in reproducing various observations (e.g. van de Weygaert & Icke 1989; van de Weygaert 1991), the introduction of clustered nuclei without any physical motivation may well have been deemed unnecessary.

One of the physical mechanisms proposed to account for the Voronoi foam, the explosion model (§ 1.3.5, 2.3.3), has no intrinsic mechanism for distributing the initial explosive seeds which equate to the Voronoi nuclei and so they are often assumed to be randomly distributed. However, a Voronoi foam may also arise from a gravitational instability picture (§ 1.3.1). Viewing the dynamics of structure formation in the gravitational instability scenario in terms of the underdense regions (§ 2.3.3), one finds that

as they expand to form the present day voids, they become increasingly spherical and, provided the expansion rates are roughly equal, the late stages naturally approximate to a Voronoi foam. The peaks in the gravitational potential are the progenitors of the voids and thus are identified with the nuclei in the Voronoi foam (§ 2.3.4). It is the aim of this chapter to investigate the effect of using peaks in a gravitational potential as the nuclei in a Voronoi foam and to compare the resulting large-scale clustering to observations to see if the missing large-scale power in the standard Voronoi foam model (§ 5.6) can be supplied by the use of non-random nuclei.

6.1.2 Generating the Gravitational Potentials

In order to provide clustered nuclei, peaks in a gravitational potential are identified with Voronoi nuclei. The gravitational potentials are generated in a manner similar to that described in § 3.3.1, only here the process is extended into two and three dimensions. It is again assumed that the various Fourier components, $\delta_{\mathbf{k}}$, of the density field have random phases, and hence the field is Gaussian and can be specified entirely by its power spectrum. For simplicity only power-law spectra with a short wavelength Gaussian cut-off are considered. Note that a long-wavelength cut-off is implicitly set by the size of the grid (see below). The power spectrum is given by

$$|\delta_k|^2 = k^n \exp(-k^2 R_i^2), \tag{6.1}$$

with R_i set to one grid point to ensure that the results are not affected by the sampling of short wavelength modes of a size close to that of the resolution of the simulations. The gravitational perturbations are related to the matter perturbations via Poisson's equation to give

$$\Phi_{\mathbf{k}} = -k^{-2}\delta_{\mathbf{k}}. \tag{6.2}$$

The spatial gravitational potential, $\Phi(\mathbf{x})$, is generated by fast Fourier transforming the gravitational perturbations, $\Phi_{\mathbf{k}}$. This results in a two- or three-dimensional gravitational potential which is discretely sampled on a square or cubic grid, the size of which imposes a long wavelength cut-off. Peaks in the potential are identified by finding cells

in the grid where $\Phi(\mathbf{x})$ is greater than all neighbouring cells. The peak is then placed at the centre of the cell and given a random displacement of up to $\pm\frac{1}{2}$ grid points in each of the three cartesian coordinates. These peaks are then used as nuclei for the Voronoi simulations.

The addition of a random displacement ensures that the structure generated by the Voronoi tessellation can almost never be degenerate, which could happen if the Voronoi nuclei lie on a square or cubic grid. This process is justified as the peak finding algorithm only locates the peak to within one grid point, the resolution of the generation process. Thus the true location of the peak could lie anywhere within that cell. It would be possible to locate the peak more accurately within the cell, but such small variations in the position of the nuclei have a negligible effect on the resulting Voronoi foam (e.g. see § 6.2.1).

The gravitational potential is normalised such that the mean potential is zero. As the absolute values of the potential are not required, the heights of the peaks are characterised by the dimensionless quantity, ν, defined by :

$$\nu = \Phi(\mathbf{x}_p)/\sigma_0, \tag{6.3}$$

where $\mathbf{x}_p$ is the position of the peak and σ_0 is the variance of the potential, defined as

$$\sigma_0^2 = \frac{1}{l^d} \sum_{k_{min}}^{k_{max}} |\Phi_\mathbf{k}|^2, \tag{6.4}$$

where L is the length of the side of the grid and d is the number of dimensions.

Rather than use all of the peaks in a given potential, peaks are selected above a given threshold, ν_c, where ν_c is usually one of $-\infty$ (i.e. all peaks), 0, 1, 2, 2.5, 3, 3.5.

6.1.3 Comparing Different Distributions

In comparing the different distributions of the Voronoi foam, it is important to choose a statistic that can distinguish between the different features and provide a comparison with observations. Very little work has been done on investigating clustered nuclei,

with the exception of Icke & van de Weygaert (1987), who considered clustered and anti-clustered nuclei in two dimensions, the distributions of the nuclei being generated by empirical processes. In comparing their different Voronoi foams they used various geometrical properties of the distribution. Though such an approach may well be able to distinguish between different sets of nuclei, it does not provide a useful comparison with observational data (e.g. Chapter 7).

Of the three statistics considered in Chapter 5, the spatial two-point correlation function is the least suitable. As pointed out in § 5.4.1 and § 5.4.2, the spatial correlation function for galaxies only probes scales dominated by intracellular clustering, which are not expected to be very sensitive to the different distributions of nuclei. The angular correlation function (§ 5.5) and the power spectrum (§ 5.4) are both superior measures of the large-scale structure, as they probe out to the break scale and beyond where clustering is predominantly intercellular in nature and hence determined by the distribution of the nuclei (§ 5.6). The power spectrum is preferred over the angular correlation function as the angular correlation function is not well defined beyond the break. This is due to the rapid decline in amplitude beyond the break to levels where small errors in the correlation function can be of order the size of the signal. However, the angular correlation function shall be used to help constrain the Voronoi foam model in comparison with observations. The other main measure of large-scale clustering used in this thesis, cluster alignment (Chapter 7), is not particularly useful as a method for comparison due to the difficulty in providing an accurate and meaningful comparison to observations, a fault in common with the geometric tests of Icke & van de Weygaert (1987).

This chapter uses six gravitational potentials, characterised by spectral indices of $n = -2, -1, 0, +1, +2$ and $+4$. The results for randomly distributed nuclei obtained in Chapter 5 are also used for comparison purposes. As the gravitational potential becomes less steep (i.e. $n \rightarrow -\infty$ and there is more power on long wavelengths), so the number density of peaks decreases. This means that in order to obtain sufficient numbers of peaks to act as Voronoi nuclei (at least 100 per potential and preferably ~ 500), it is necessary to use very large volumes to generate the gravitational potentials for $n \lesssim 0$. This fall off in peak number density also means that it is hard to impose high thresholds, as the number of peaks rapidly decreases with increasing height. Table 6.1 lists the available potentials by spectral index, n, and peak-height threshold, ν_c, giving

$n\backslash\nu_c$	$-\infty$	0	1	2	2.5	3.0	3.5
-2	$118^{(1)}$						
-1	$2133^{(1)}$	$1333^{(1)}$	$606^{(1)}$	$111^{(1)}$			
0	$542^{(3)}$	$425^{(3)}$	$714^{(2)}$	$830^{(1)}$	$270^{(1)}$		
$+1$	$1376^{(3)}$	$1167^{(3)}$	$653^{(3)}$	$628^{(2)}$	$225^{(2)}$		
$+2$	$968^{(4)}$	$907^{(4)}$	$570^{(4)}$	$461^{(3)}$	$178^{(3)}$		
$+4$	$626^{(5)}$	$613^{(5)}$	$480^{(5)}$	$1328^{(3)}$	$528^{(3)}$	$563^{(2)}$	$112^{(2)}$

(1) 192^3 grid

(2) 100^3 grid

(3) 64^3 grid

(4) 45^3 grid

(5) 32^3 grid

Table 6.1 The sets of peaks available for use as Voronoi nuclei, listed by the spectral index, n, of the gravitational potential and the peak-height threshold, ν_c.

the mean number of peaks for each sample.

The largest volume available was a 192^3 grid. This limited the $n = -2$ potential to a single threshold of $\nu_c = -\infty$ and the $n = -1$ potential to thresholds of $\nu_c \leq 2$. The highest thresholds were usually $\nu_c = 2.5$, but higher thresholds were available for the $n = 4$ potential.

The following sections shall use the above sets of peaks as Voronoi nuclei and investigate the trends in clustering of the Voronoi foam for variation of both the peak-height threshold, ν_c, and spectral index, n.

6.2 Clustering of Peaks

6.2.1 Variation of Spectral Index

Fig. 6.1 shows the power spectra for four different potentials with spectral indices of $n = +4$ (broken line), $+1$ (dot-dash line), -1 (dotted line) and -2 (dot-dot-dash line). The power spectrum of randomly distributed nuclei (solid line) is shown for comparison. All the power spectra converge for high k, to a power law of slope $+3$, the expected

value for the case of randomly distributed particles [$\Delta^2(k) \propto k^3$]. For low k, there is a deviation from power-law behaviour, either in the form of an excess of power ($n \lesssim 0$) or a deficit ($n \gtrsim +1$) over the power spectrum for randomly distributed nuclei.

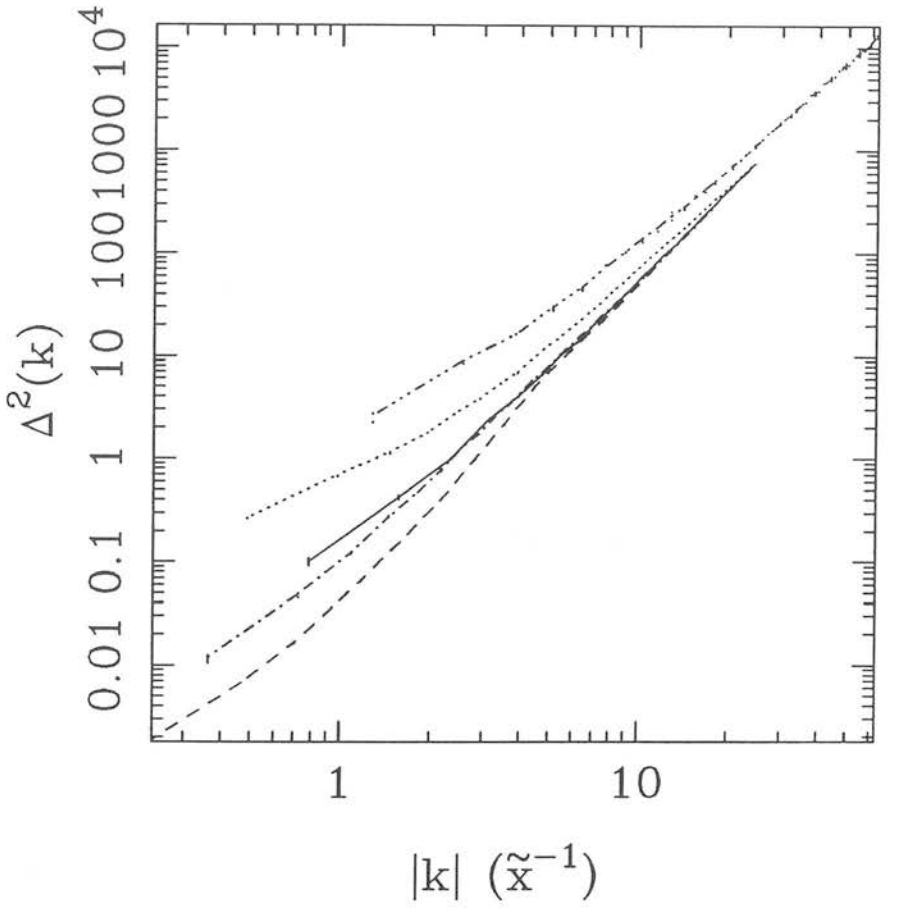

Figure 6.1 Power spectra for peaks in a gravitational potential with spectral indices of $n = +4$ (broken line), $+1$ (dot-dash line), -1 (dotted line) and -2 (dot-dot-dash line). The power spectrum of randomly distributed nuclei (solid line) is shown for comparison. All the power spectra are the mean of five independent realisations and the errors represent the standard deviation from the mean.

It is possible that the convergence of the different potentials at high k is a consequence of the peak assignment procedure that is used to identify peaks in the potential (§ 6.1.2). This procedure locates the peak to within one grid point and then gives it a

random position within that grid point. However, this has been checked by recomputing the power spectra, but with each peak located exactly at the centre of its grid point. If the convergence were due to the random process, then one would expect a different behaviour on the same scales due to this extremely regular distribution of peaks. Instead it was found that the power spectra for the original peak distributions and for the altered ones matched at all wavenumbers, thus the convergence at high k is an intrinsic property of the gravitational potential, most likely associated with the smoothing of the raw potential on scales of one grid point (equation 6.1). This introduces a shot-noise component at high k, regardless of the spectrum, hence the $\Delta^2(k) \propto k^3$ behaviour.

The divergence at low k from the case of randomly distributed nuclei is due to the large-scale distribution of the peaks. In the case where there is significant excess power ($n \lesssim 0$) on large scales, this is due to the dominance of large-wavelength over small-wavelength fluctuations. As the spectral index becomes more negative (less steep), so the gravitational potential is increasingly modulated by the large-scale power present in the power spectrum. This leads to the formation of large, contiguous regions where the average value of the potential is below the global mean. However, the distribution of peaks in the potential is skewed towards regions of high local potential, thus introducing large-scale inhomogeneities in the peak distribution, and hence leading to an increase in large-scale power over the random case (cf.Kaiser 1984; Peacock & Heavens 1985; Bardeen *et al.* 1986).

In the case of steep power spectra ($n \gtrsim 1$), there is a deficit of power compared to the randomly distributed nuclei. Such a situation is sometimes known as "anti-clustering", i.e. the distribution is more regular than a random distribution. This arises because there is significantly more power present on small scales than large scales, thus there is little large-scale modulation of the potential field. The result of this is that large, contiguous regions of low potential are not formed, thus even though there are few peaks in regions of low potential (see Table 6.1), there is little large-scale inhomogeneity, and hence little large-scale power.

6.2.2 Variation of Peak Height

Fig. 6.2 shows the power spectra for four potentials with differing peak-height thresholds of $\nu_c = -\infty$, 0, 1 and 2 (running bottom to top), with the exception of the $n = 4$

potential (Fig. 6.2d) where thresholds of $\nu_c = -\infty$, 2, 2.5 and 3.5 are shown. In all cases the solid line is the power spectrum for randomly distributed nuclei, which is included for comparison. The power spectra show a marked increase in large-scale power as the threshold is increased. The point where the power spectra start to deviate from the power spectrum of randomly distributed nuclei also shifts to larger k as the threshold increases.

The act of increasing the threshold means that low peaks are being progressively removed. As low peaks lie predominantly in regions of low local potential, this merely aggravates the effect described in § 6.2.1 for shallow ($n \lesssim 0$) potentials. As very high thresholds ($\nu_c \gtrsim 2$) are imposed, the only peaks left lie in small, isolated regions of high potential, thus causing large amplitude inhomogeneities on relatively small scales, accounting for the shift towards high k of the deviation from the random case. This behaviour even occurs in the case of the relatively steep $n = 1$ potential (Fig. 6.2c). However, as the spectrum gets steeper, the excess large-scale power definitely diminishes. In the case of the $n = 4$ potential (Fig. 6.2d) there is little increase in large-scale power with threshold, despite taking thresholds as high as $\nu_c = 3.5$, though it should be noted that for very high thresholds ($\nu_c \geq 2.5$) the generation process lacks the size necessary to probe out to very large scales. This is again due to a lack of large-scale power in the potential (see § 6.2.1), which means that rather than large, contiguous volumes of space being depopulated of peaks as the threshold increases, only relatively small large-scale inhomogeneities are introduced as the peaks removed are from a much wider range of locations. Only when the thresholds of the order $\nu_c \gtrsim 3$ are introduced is there a significant increase in large-scale power of type seen in more shallow potentials (see above).

6.3 Clustering of the Voronoi foam

It is the aim of this section to investigate the clustering properties of the Voronoi foam generated by nuclei which are peaks in a gravitational potential and to see how this clustering depends on the spectral index, n, of the potential and peak-height threshold, ν_c. As with Chapter 5, this will be done by considering the clustering of particles at the three topological sites in the foam, the walls, the filaments and the nodes. Following the findings of Chapter 5, the Voronoi foams will be generated using the kinematical

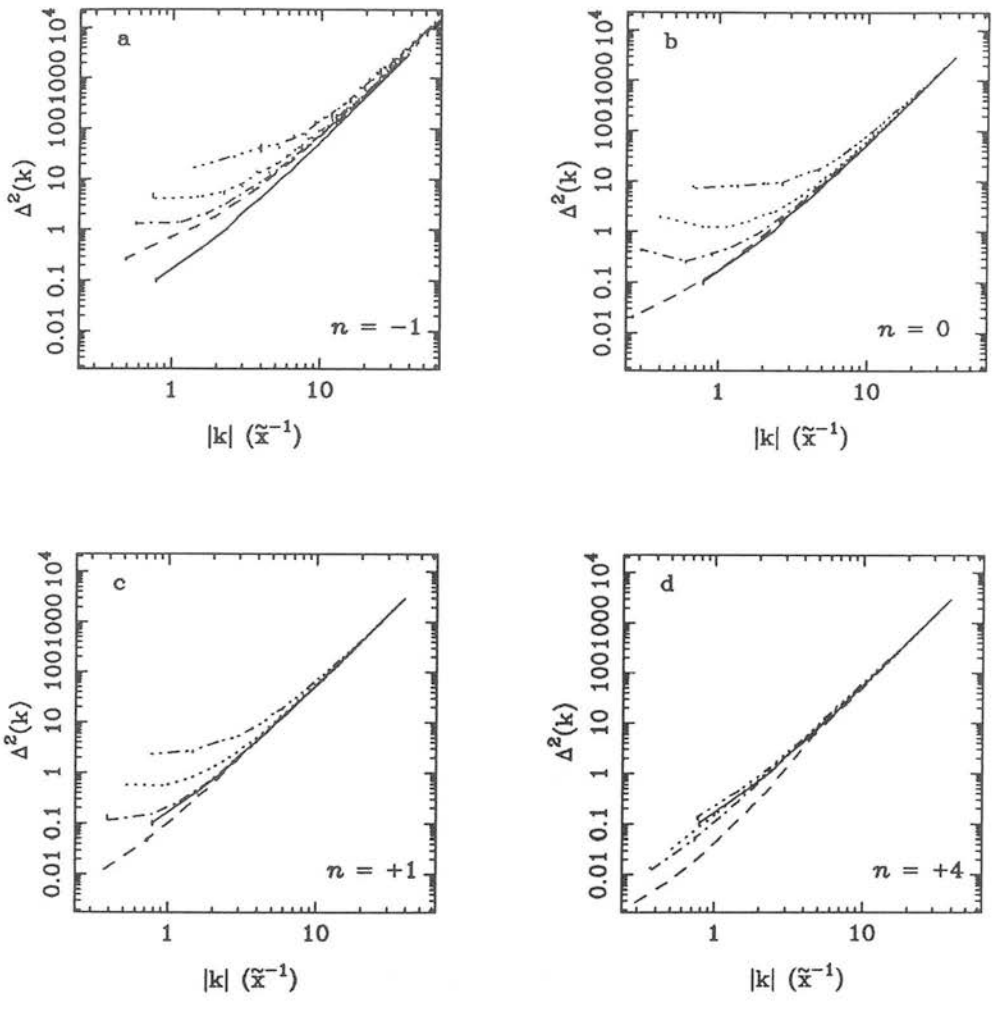

Figure 6.2 Power spectra for the peaks in a gravitational potential with spectra index $n = -1$ (a), 0 (b), +1 (c) and +4 (d). The different power spectra in each panel are for different peak-height thresholds of $\nu_c = -\infty$ (broken line), 0 (dot-dash line), 1 (dotted line) and 2 (dot-dot-dash line), except for (d) where the thresholds are $\nu_c = -\infty$ (broken line), 2 (dot-dash line), 2.5 (dotted line) and 3.5 (dot-dot-dash line). In all cases the solid line is the power spectrum for randomly distributed nuclei. All power spectra are the mean of five independent realisations and the errors represent the standard deviation from the mean.

method, with particles initially distributed at random.

6.3.1 Variation with Spectral Index

Figs. 6.3, 6.4 and 6.5 show the power spectra for particles in walls, filaments and nodes

respectively for four different spectral indices from $n = -2$ to $n = +4$ (top to bottom). The solid line is, in all cases, for particles in a foam generated from randomly distributed nuclei. The power spectra all have the same form, that of a power law at high k, breaking to a steeper power law at low k. The slope and amplitude of the low-k power law depends on the potential. As with the power spectra of peaks (§ 6.2.1), there is an increase in large-scale power and the slope becomes less steep as the gravitational potential becomes less steep (i.e. $n \to -\infty$). Also, the break from small to large-scale clustering is less severe and moves towards larger scales. The main difference between the behaviour of the peaks and the Voronoi foam lies in the increase in amplitude, though not slope, of the small-scale power-law portion of the power spectrum for shallow ($n \lesssim 0$) potentials. This occurs despite there being no such increase in the small-scale power of the peaks (Fig. 6.1).

Though for shallow potentials the nuclei (peaks) exhibit a spatial distribution in which they are clustered in regions of locally high gravitational potential, while the regions of locally low potential have few peaks, this large-scale inhomogeneity is not reflected in the mass distribution of the Voronoi foam. Here, regions with few nuclei are threaded by walls and filaments and the regions inhabited by clusters of nuclei have a tight packed association of small cells. Overall, the distribution is much more homogeneous than that of the nuclei, which accounts for the lower absolute amplitude of the power spectrum for particles in walls and filaments. In the case of the nodes, there is less difference, as the distribution of the nodes is a point process and hence does not fill space as effectively as the sheet- and string-like walls and filaments.

When compared to the mass distribution of the foam for randomly distributed nuclei, the mass distribution for the shallow potentials ($n \lesssim 0$) is much less homogeneous. The distribution of mass in the Voronoi foam depends to a large extent on the size of the cells, which in turn depends on the separation of the associated nuclei. For randomly distributed nuclei, the characteristic inter-nucleus separation, $\tilde{x}$, is actually a good measure of the true inter-nucleus separation and hence the characteristic cell size. This is because there is relatively little spread in the cell sizes. For shallow potentials this is not the case, there being a large spread in cell sizes, with small cells inhabiting regions with many nuclei and large cells inhabiting regions where there are few. This introduces large-scale inhomogeneities in the mass distributions, leading to extra large-scale power over the random case.

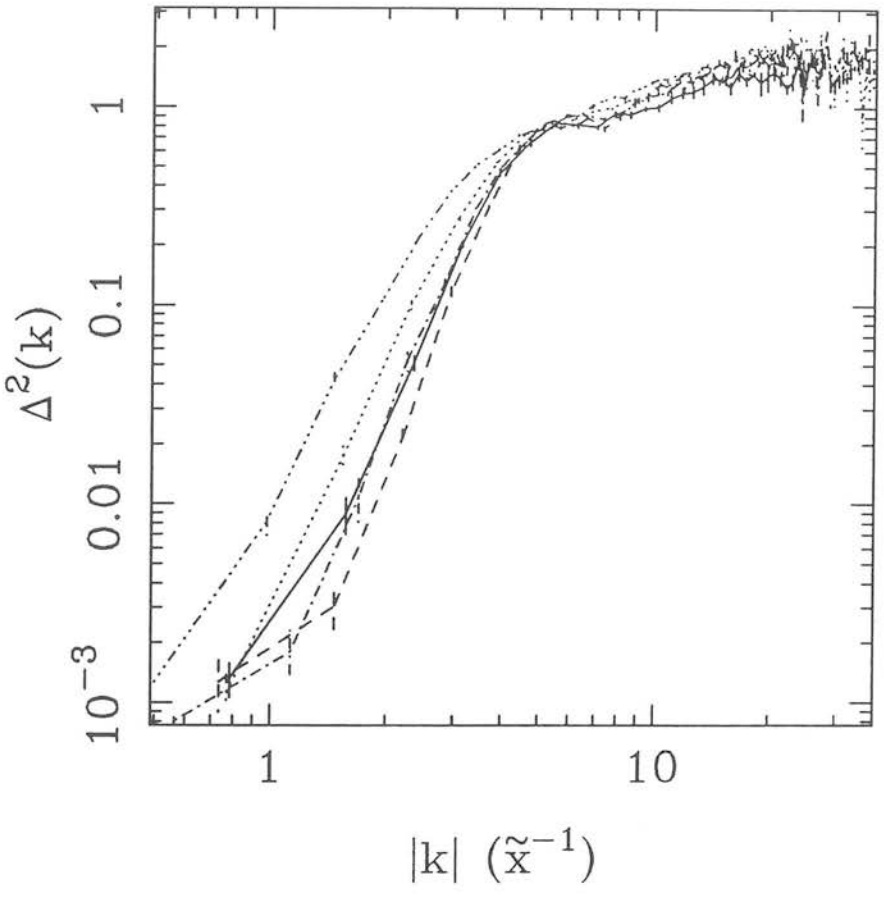

Figure 6.3 Power spectra for particles in walls in a Voronoi simulation generated from peaks in a gravitational potential with spectral index of $n = +4$ (broken line), $+1$ (dot-dash line), -1 (dotted line) and -2 (dot-dot-dash line). In all cases, $\nu_c = -\infty$. The solid line is for a Voronoi foam generated from randomly distributed nuclei. All power spectra are the mean of five independent realisations and the errors represent the standard deviation from the mean.

For steep ($n \gtrsim 1$) potentials, the reverse is true as there is less large-scale power than the random case. This is a result of the lack of large-scale power in the potential, which leads to there being a quasi-regular distribution of nuclei (§ 6.4.1). This means there is very little spread in the cell sizes and hence no large-scale inhomogeneity, leading to a deficit of large-scale power compared to the random case. This deficit increases as the potential becomes steeper.

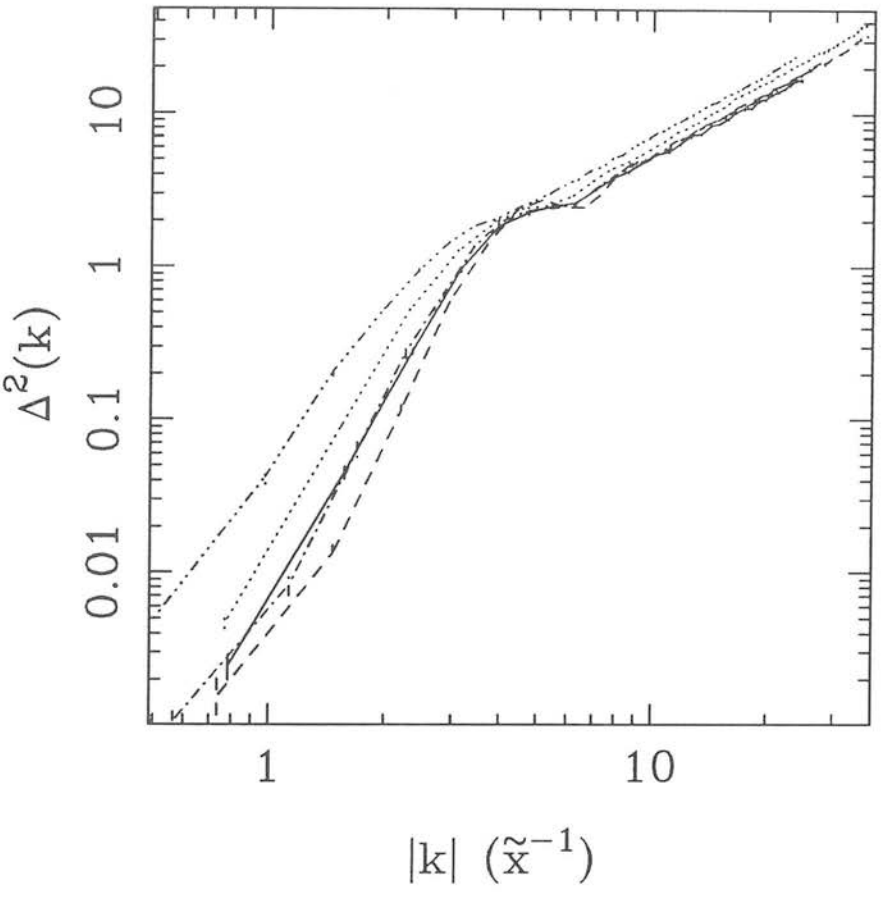

Figure 6.4 As Fig. 6.3, but for particles in filaments.

This is illustrated in two dimensions by Figs 6.6 and 6.7. Fig. 6.6 shows a Voronoi foam generated from a two-dimensional potential with spectral index $n = -1$. Clearly visible are the large cells, which dominate the simulation, with one noticeable cluster of very small cells in the bottom left-hand corner. This contrasts with Fig. 6.7, which was generated using an $n = +1$ potential. Here there are only a few large cells and no clusters of very small cells. Overall the distribution is much more homogeneous.

The spread in cell sizes also accounts for the changing nature of the break from small to large-scale clustering. In the case of random nuclei, the break is characterised

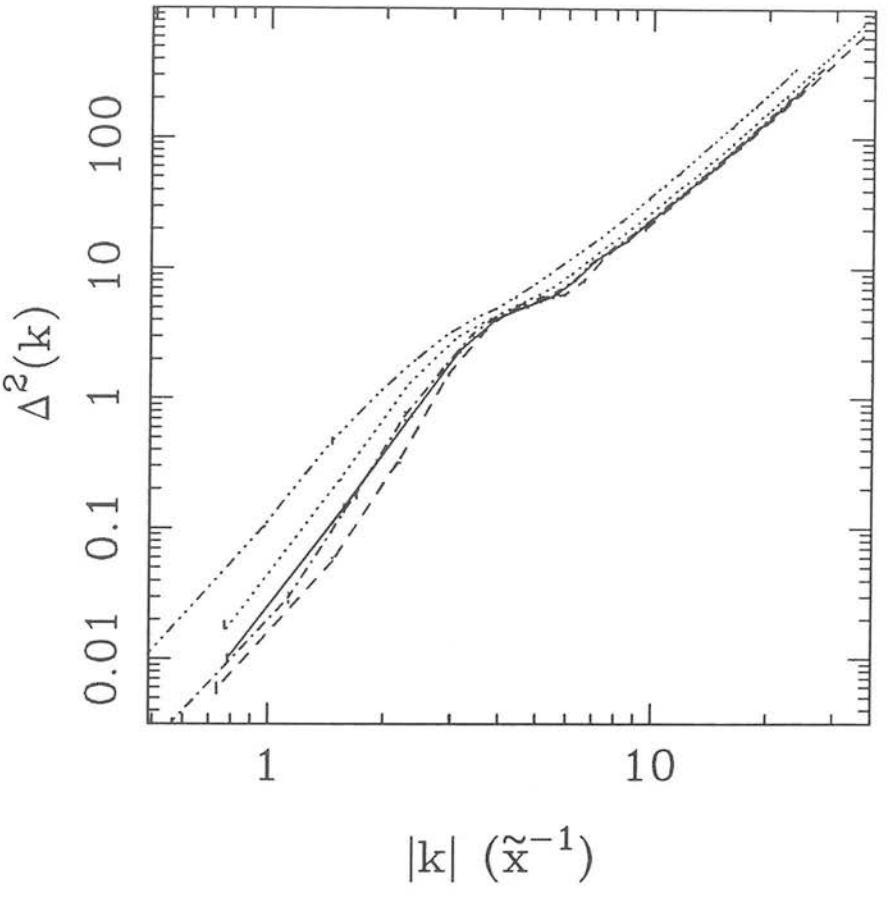

Figure 6.5 As Fig. 6.3, but for particles at nodes, weighted by the number of particles at each node.

by a "shoulder" feature in the power spectrum which is quite pronounced (solid line in Figs. 6.3, 6.4 and 6.5). As the potential becomes more shallow, the break becomes more gentle and the "shoulder" less pronounced. It also moves to larger scales. The reverse is true as the potential becomes steeper.

The break marks the transition from intracellular clustering to intercellular clustering. When the distribution of cell sizes is quite tight, the transition is quite sharp and the "shoulder", which measures the excess power on scales equivalent to the dimensions of the cells, is quite pronounced. However, as the spread of cell sizes increases, this

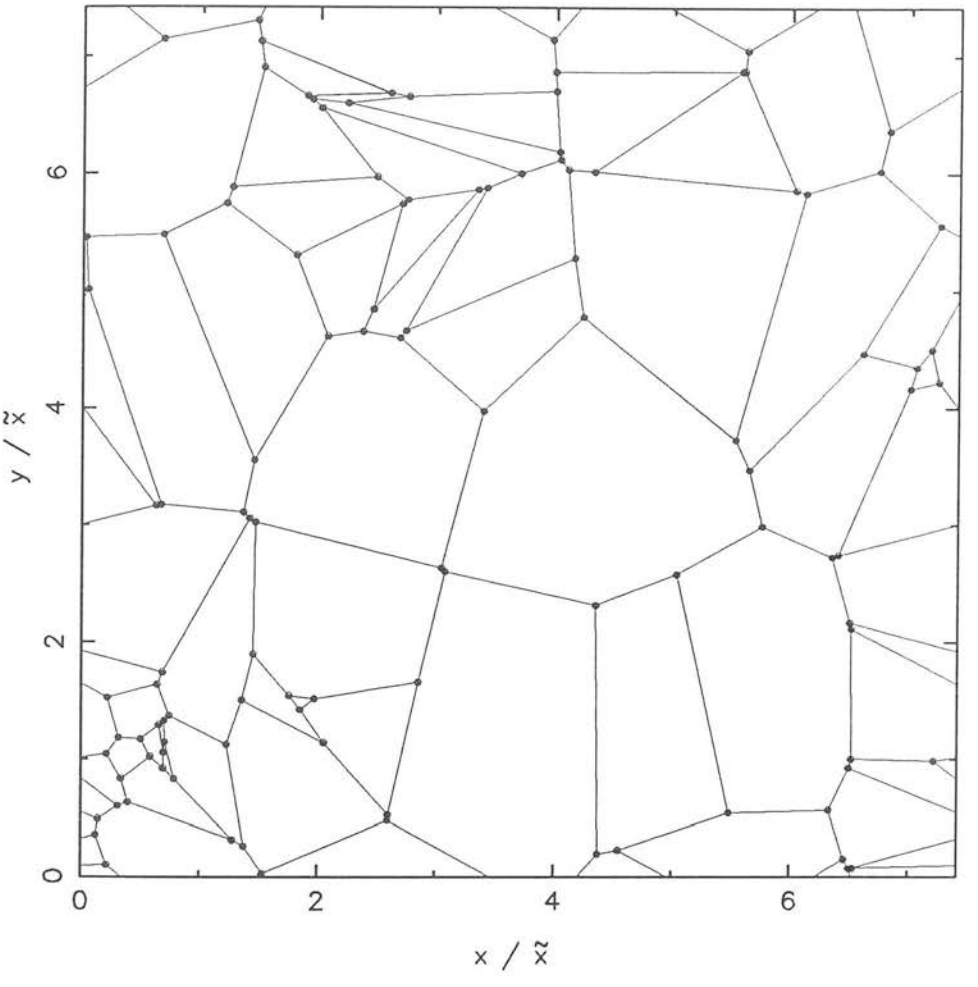

Figure 6.6 Two-dimensional Voronoi foam generated by the geometrical method using nuclei taken from an $n = -1$ two-dimensional gravitational potential with $\nu_c = -\infty$.

transition is "smeared out" over a range of scales rather than being concentrated at a single physical scale, that of the characteristic inter-nucleus separation. Thus the break is more gentle and the shoulder less pronounced.

The onset of the break is governed by the start of the change from intra- to intercellular clustering. One might expect this to occur at relatively small scales for shallow spectra, due to the presence of many small cells. However, on these scales the power spectrum is still probing intra-cellular scales for the large cells. It is only when

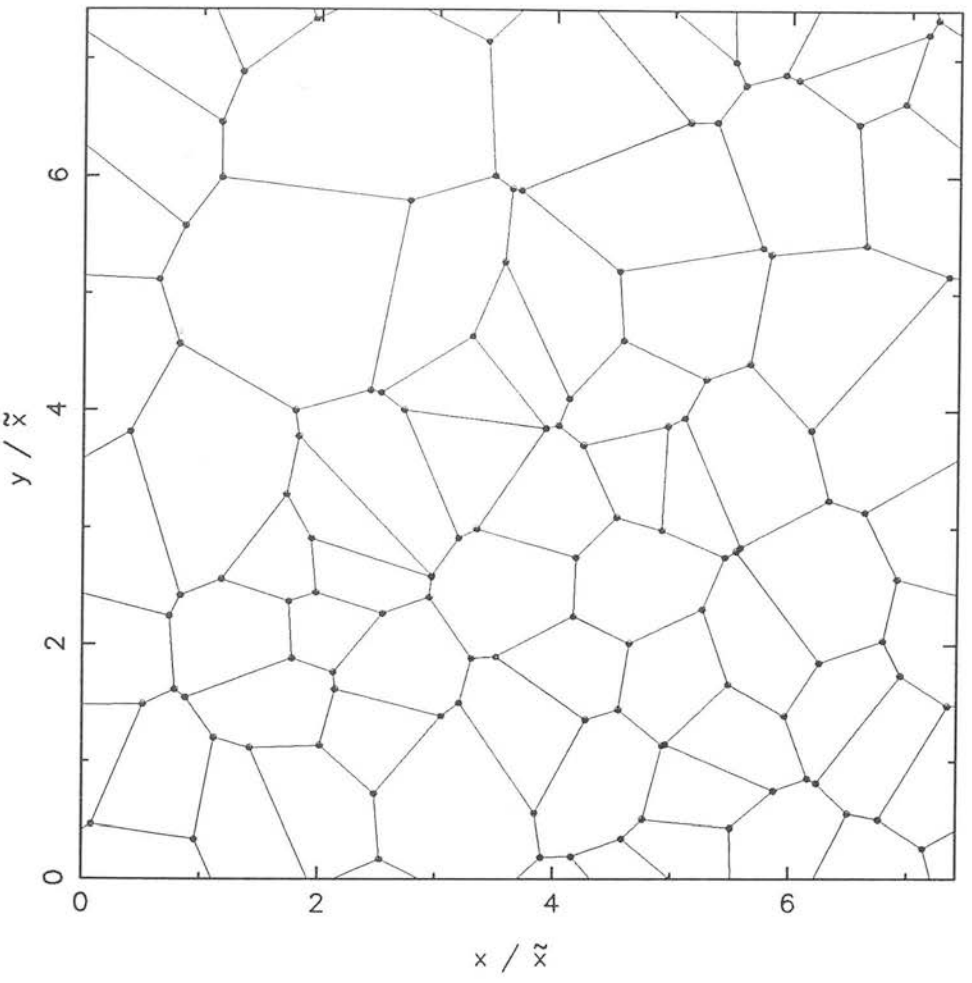

Figure 6.7 As Fig. 6.6, but generated using an $n = +1$ potential. The number of nuclei is the same.

the power spectrum begins to probe scales comparable to the size of the larger cells that the power spectrum beings to turn over. This is because the clustering produced by the larger cells is dominant over the clustering of the smaller cells (see below).

The dominance of the larger cells also accounts for the excess of small-scale power over the random case, which increases in size as the potential becomes less steep, despite there being no corresponding excess in the same region for the nuclei. As shown in Appendix D (equation D.12), the surface density of particles on a wall is proportional to the perpendicular distance to the neighbouring nucleus. Hence, larger cells have

higher surface densities, leading to increased small-scale clustering. The same argument applies to filaments and also to nodes, remembering that the latter are weighted by the number of particles present at each node. This means that the nodes associated with large cells have a high weight, while those associated with small cells have a low weight. In regions where small and large cells bound each other, this can lead to small-scale inhomogeneities and hence excess small-scale power.

6.3.2 Variation of Peak-Height Threshold

Fig. 6.8 shows the power spectra for particles in walls for four different potentials with different peak-height thresholds of $\nu_c = -\infty$, 0, 1 and 2 (bottom to top), except for the $n = 4$ potential (Fig. 6.8d) which has thresholds of $\nu_c = -\infty$, 2, 2.5 and 3.5. In all cases the solid line is the power spectrum for Voronoi foams generated from randomly distributed nuclei.

As with the case of the nuclei (§ 6.2.2), increasing the threshold serves to amplify the effects caused by varying the spectral index of the potential (§ 6.3.1). For the shallow potentials ($n \lesssim 0$) and even $n = +1$, the progressive removal of low peaks leads to a relative increase in the maximum cell size and a greater spread in cell sizes, thus contributing to the large-scale inhomogeneity, and hence to the excess power. This also causes a more gentle turnover of the power spectrum from small to large-scale clustering. Again, for very steep potentials (e.g. $n = 4$), the effect of increasing the threshold is very much diminished. Even imposing thresholds as high as $\nu_c = 3.5$ has little effect (Fig. 6.8d).

The process can again be illustrated in two dimensions. Fig. 6.9 shows a Voronoi foam generated using a two-dimensional potential with $n = +1$ and $\nu_c = +1$. Compared to Fig. 6.7, one can see the large-scale inhomogeneities that have been introduced by removing the low peaks. Large cells now dominate, with the smaller cells clustering together. The overall distribution is much more inhomogeneous than the case with $\nu_c = -\infty$.

Note that there is no simple relationship between the slope of the power spectrum and the potential used. At small scales (high k), there is no difference, either for variation of spectral index (Figs 6.3, 6.4 and 6.5) or peak-height threshold (Fig. 6.8),

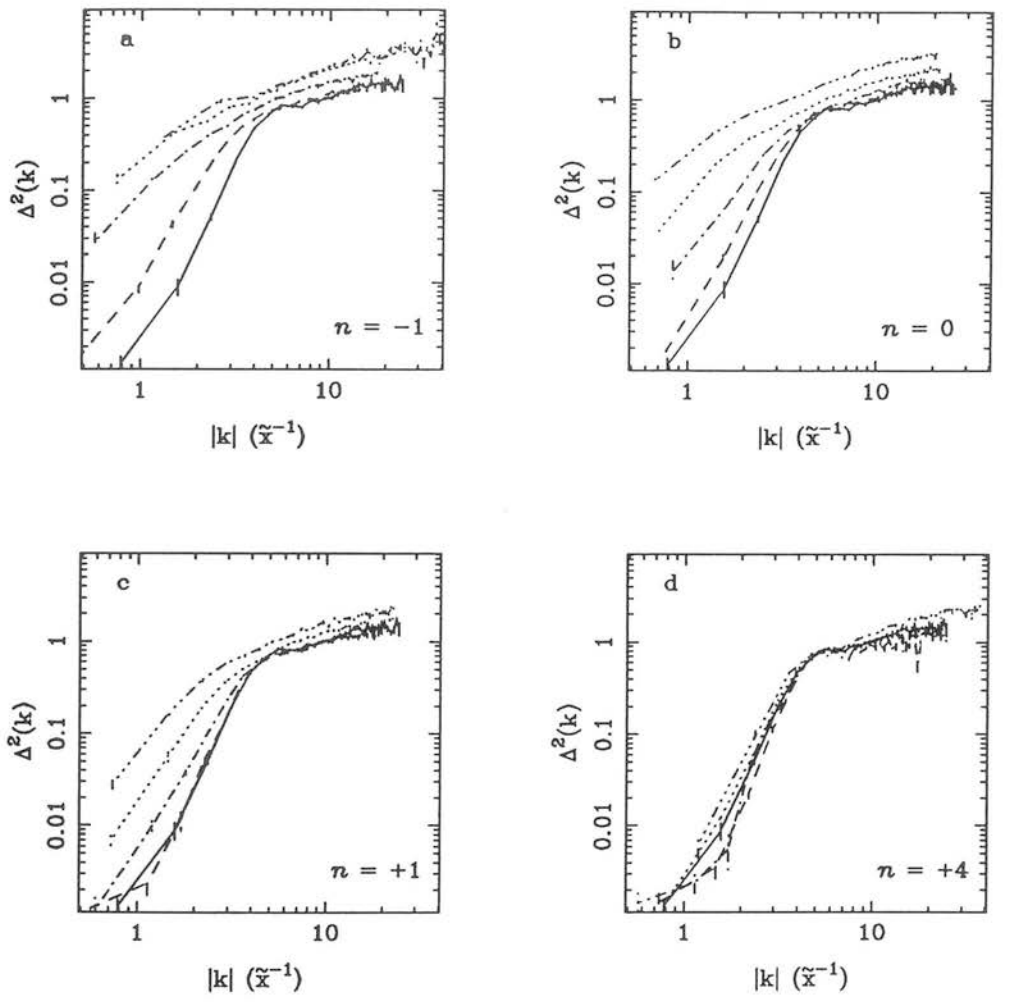

Figure 6.8 Power spectra for the particles in walls in a Voronoi foam generated from peaks in a gravitational potential with spectra index $n = -1$ (a), 0 (b), +1 (c) and +4 (d). The different power spectra in each panel are for different peak-height thresholds of $\nu_c = -\infty$ (broken line), 0 (dot-dash line), 1 (dotted line) and 2 (dot-dot-dash line), except for (d) where the thresholds are $\nu_c = -\infty$ (broken line), 2 (dot-dash line), 2.5 (dotted line) and 3.5 (dot-dot-dash line). In all cases the solid line is the power spectrum for a Voronoi foam generated from randomly distributed nuclei. All power spectra are the mean of five independent realisations and the errors represent the standard deviation from the mean.

reinforcing the conclusion that clustering on these scales is intracellular and unaffected by the clustering of the nuclei. However, on large scales (low k), while there is very little difference in slope between different spectral indices, there is a significant difference when the peak-height threshold is varied. Though it is possible that this is due to differences

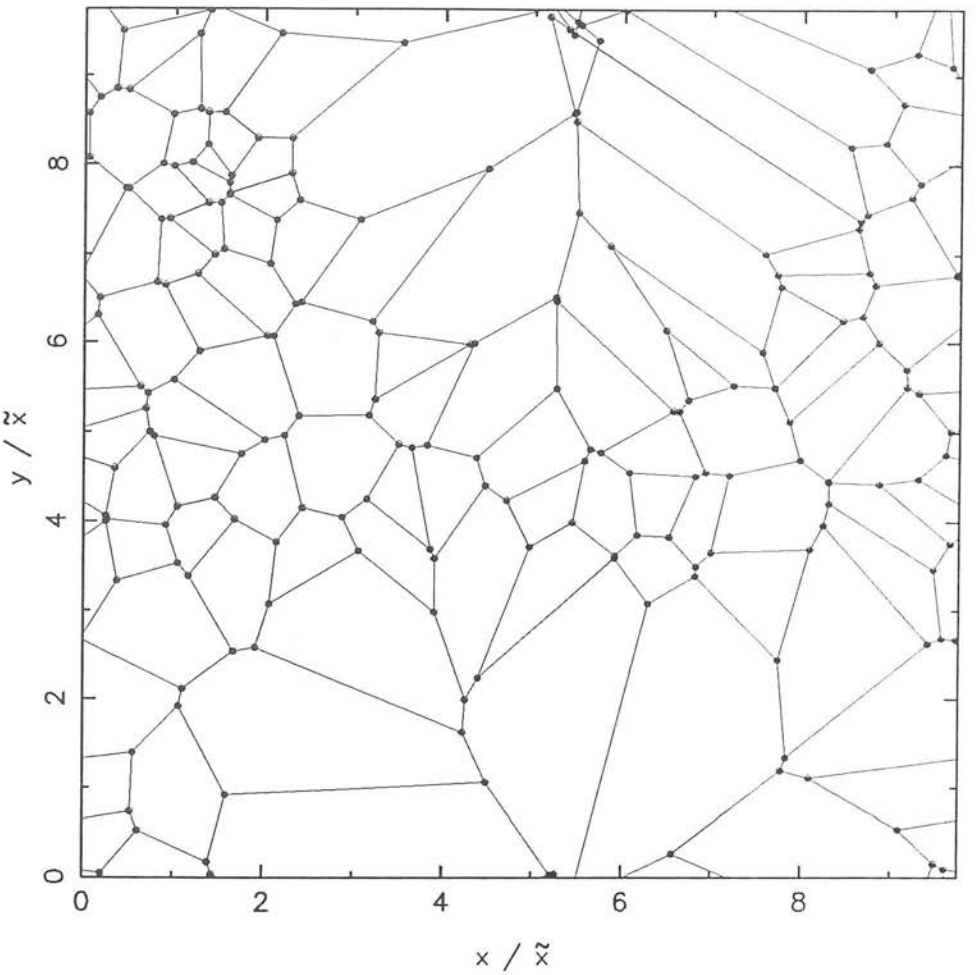

Figure 6.9 Two-dimensional Voronoi foam generated by the geometrical method using nuclei taken from an $n = +1$ two-dimensional gravitational potential with $\nu_c = +1$. The feature at $x \approx 5\tilde{x}$, $y \approx 10\tilde{x}$ is caused by individual cells having linear sizes approaching half the size of the simulation, which causes the geometrical method to fail to construct the cell in the correct manner.

in the way the clustering of the nuclei is changed by the varying of the two parameters, this is unlikely. As it has been argued that varying the spectral index and peak-height threshold have similar effects, it is likely that the shape of the power spectrum at large scales is only a slowly varying function when compared to the amplitude. Note that while the amplitude only varies by a factor ≈ 5 for variations in the spectral index (Figs 6.3, 6.4 and 6.5), it varies by up to two orders of magnitude when the threshold is varied

(Fig. 6.8). This suggests that when the spectral index is varied the clustering of the nuclei is not sufficiently different for the difference in slope to be detected.

6.4 Comparison with Observations

6.4.1 Introduction

The main conclusion reached in Chapter 5 was that the Voronoi foam, when generated using randomly distributed nuclei, lacked both small and large-scale power compared to the observed galaxy distribution. As stressed in § 5.6, the lack of small-scale power is not critical to the model, indeed, by the nature of the simulations used (Chapter 4), one would expect the small-scale clustering to be underestimated. A far more important problem for the Voronoi foam is the lack of large-scale power (i.e. power beyond the break). § 5.4 and § 5.5 show that what is required is a more gentle break from small to large-scale clustering coupled with an increase in large-scale power. § 6.2 and § 6.3 show that these requirements are qualitatively met by introducing clustered nuclei, without adversely affecting the small-scale power.

Identifying nuclei with peaks in a gravitational potential, the method used in this thesis for generating clustered nuclei, provides two free parameters, the spectral index, n, of the potential and the peak-height threshold, ν_c. In some ways these two parameters are complementary, both inducing the same effect of increasing large-scale power and producing a less severe break. Thus it is highly likely that there is no unique combination of spectral index and threshold that matches observations. However, the choice of peaks in a gravitational potential is theoretically motivated (§ 2.3.4) and this motivation suggests that for the Voronoi foam to be a reasonable approximation to the full gravitational instability model, one must look to a late-time approximation. Using the adhesion model as a guide (§ 2.2, 2.3.4), this implies that only high peaks should be considered, implying a high peak-height threshold.

6.4.2 Results from Comparisons

Fig. 6.10 shows the power spectra for particles in the walls of Voronoi foams generated from a variety of different gravitational potentials and peak-height thresholds, along

with the observed power spectra for galaxies of Baumgert & Fry (1991), Peacock (1991) and Peacock & Nicholson (1991). All the observed power spectra are normalised to the data of Peacock (1991), the approach adopted in § 5.4.3. Fig. 6.11 shows the angular autocorrelation functions for the same potentials and thresholds as in Fig. 6.10, compared to the angular two-point correlation function of Maddox *et al.* (1990). All the simulations are normalised such that the characteristic inter-nucleus separation, $\tilde{x}$, is $55\,h^{-1}$ Mpc, the upper limit suggested in Chapter 5.

For a normalisation of $\tilde{x} = 55\,h^{-1}$ Mpc, few combinations of the spectral index and peak-height threshold provide a reasonable fit to the data. The power spectra (Fig. 6.10) that match the observations on large scales generally have too severe a break and consequently overestimate the power at the break scale, whereas the power spectra that have a more gentle break generally have too much power on all scales. The only power spectra that provide a reasonable fit are those with $n = 0$, $\nu_c = -\infty$ (Fig. 6.10a, broken line), $n = +1$, $\nu_c = 0$ (Fig. 6.10b, solid line) and $n = +2$, $\nu_c = 1$ (Fig. 6.10c, dot-dot-dash line).

The situation is even worse for the angular correlation functions (Fig. 6.11), where no correlation function can be said to provide a reasonable fit to the data. Again, those that have a sufficiently gentle break possess too much power on all bar the smallest scales, where one would not expect any agreement (§ 5.6).

One way to counter this is to reduce the overall amplitude by reducing the characteristic inter-nucleus separation, $\tilde{x}$. This will result in a reduction of power on all scales as shown in Fig. 6.12 – Fig. 6.15, where the simulations are normalised such that $\tilde{x} = 40\,h^{-1}$ Mpc, the lower limit found in Chapter 5. In this case there is a much better fit to the data, both at the break scale and beyond. Excellent fits are provided by the $n = 0$ potential with $\nu_c = 0$ (Fig. 6.13, broken line) and the $n = +1$ potential with $\nu_c = +1$ (Fig. 6.14, solid line). The $n = +2$ potential with $\nu_c = +2$ also provides a very good fit to the observed power spectrum (Fig. 6.15a, dot-dot-dash line), but the angular correlation function lacks sufficient power on very large angular scales (Fig. 6.15b, dot-dot-dash line).

It should be stressed that these are not the only combinations of parameters that could produce a satisfactory fit. There are two constraints — the shape, set by the particular combination of n and ν_c, and the overall amplitude, set by both n and ν_c

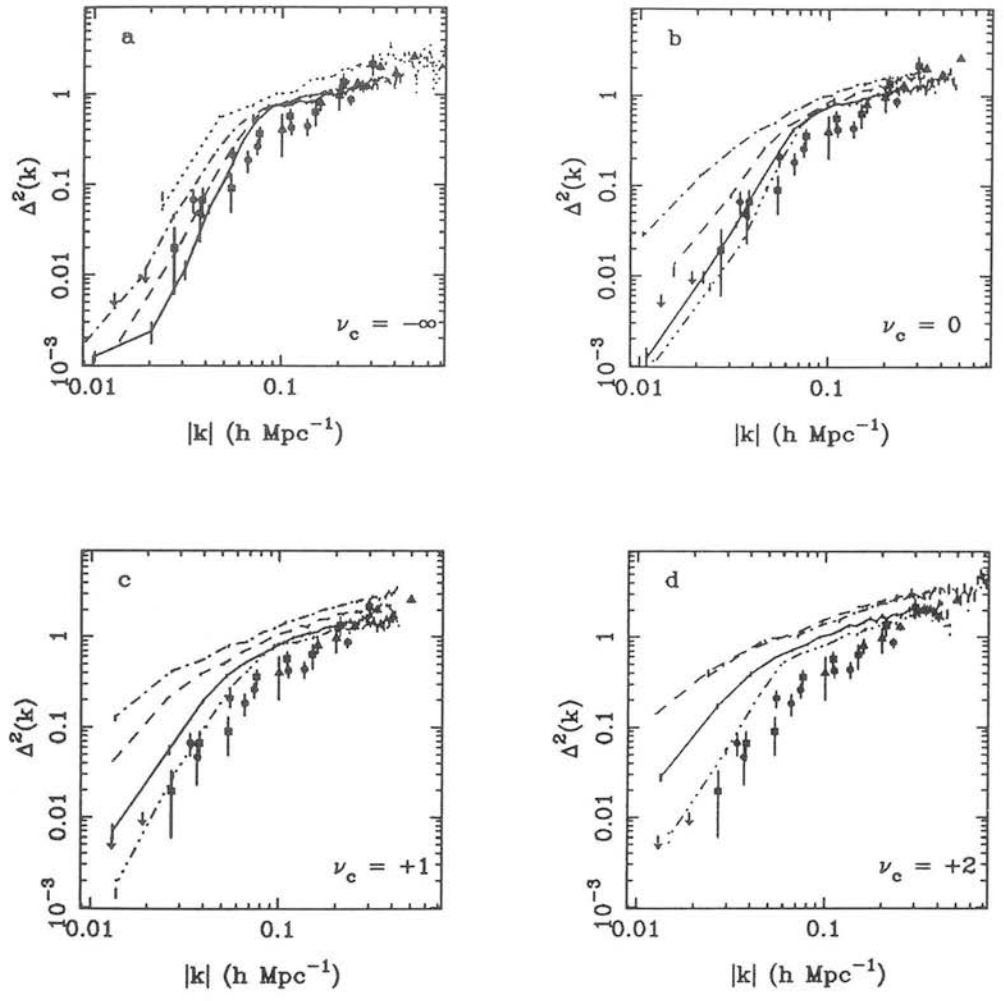

Figure 6.10 Power spectra for particles in walls in a Voronoi foam generated by peaks in a gravitational potential with spectral index $n = +2$ (dot-dot-dash line), $n = +1$ (solid line), 0 (broken line), -1 (dot-dash line) and -2 (dotted line). The four panels show the effect of increasing peak-height threshold : $\nu_c = -\infty$ (a), 0 (b), 1 (c) and 2 (d). The symbols show the observed power spectra for three galaxy redshift surveys — the CfA survey (triangles; Baumgart & Fry 1991), the IRAS survey (circles; Peacock 1991) and radio galaxies (squares; Peacock & Nicholson 1991). The three observed power spectra are all normalised to the IRAS data. See § 5.4.3 for details. The power spectra are the mean of five independent simulations and the error bars represent the standard deviation on the mean. The simulations are normalised such that $\tilde{x} = 55\,h^{-1}$ Mpc.

and the normalisation, $\tilde{x}$. As the potential becomes more shallow ($n \to -\infty$) and the threshold increases, so the break becomes less severe and the overall amplitude increases, leading to a decrease in the normalisation. However, there are practical

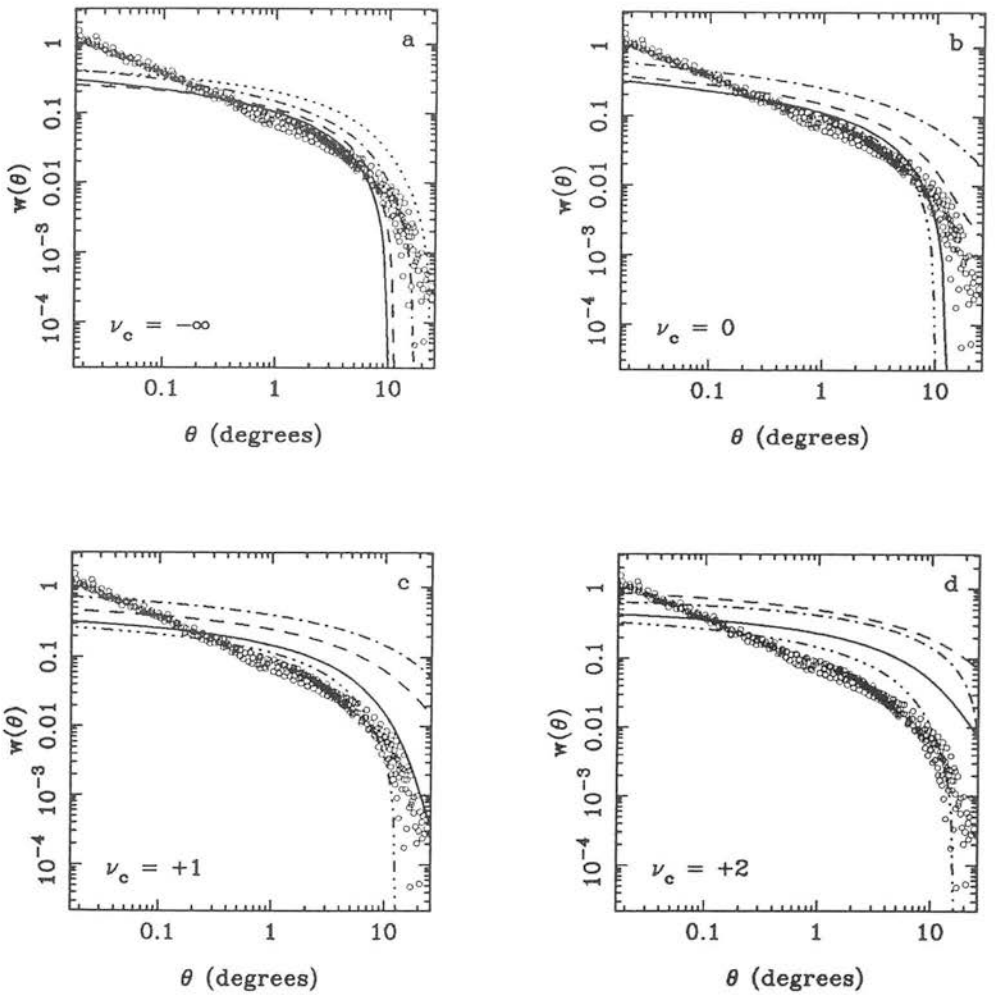

Figure 6.11 The angular autocorrelation functions for the same potentials as in Fig. 6.10. The open circles show the angular two-point correlation function of Maddox *et al.* (1990). All the correlation functions are scaled to the Lick Depth. The correlation functions are the mean of five independent simulations and the error bars represent the standard deviation on the mean. The simulations are normalised such that $\tilde{x} = 55\,h^{-1}$ Mpc.

limits to the parameters that will fit the data. Making the potential more shallow, or increasing the threshold, pushes the break in the correlation function up and to the right, whereas decreasing the normalisation moves it the other way, though the two are not complementary. For very high thresholds, or very shallow potentials, the overall amplitude of the correlation function is too high. Reducing the normalisation then brings the break back to too small a scale. Thus it seems there is a definite window

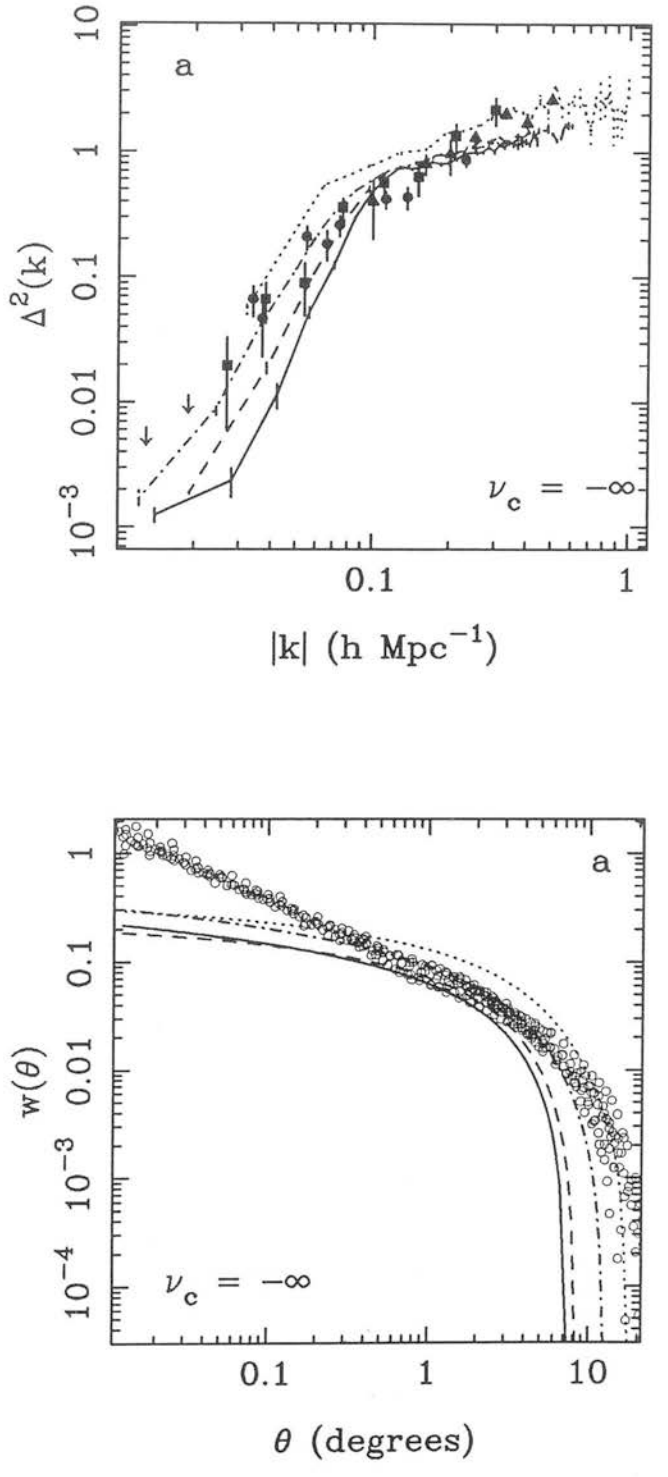

Figure 6.12 (a) As Fig. 6.10a and (b) as Fig. 6.11a, except that the simulations are normalised such that $\tilde{x} = 40\,h^{-1}$ Mpc.

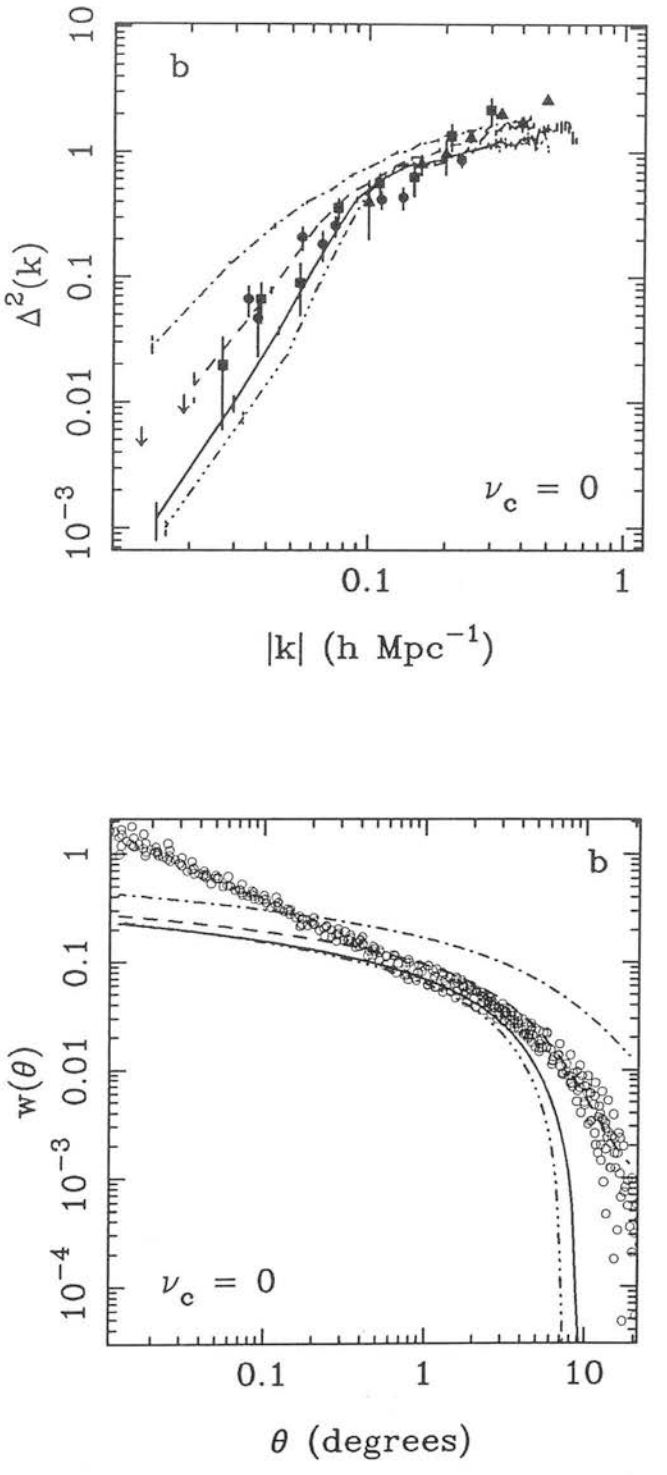

Figure 6.13 (a) As Fig. 6.10b and (b) as Fig. 6.11b, except that the simulations are normalised such that $\tilde{x} = 40\,h^{-1}$ Mpc.

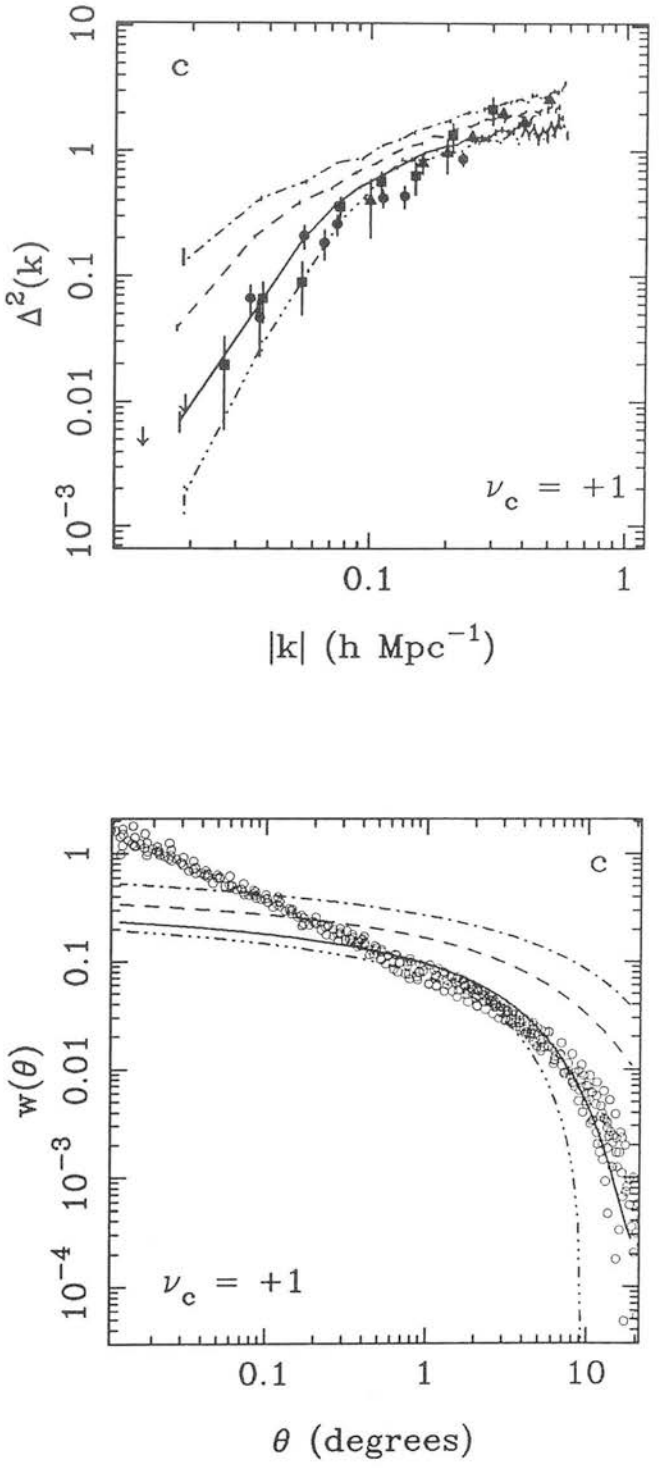

Figure 6.14 (a) As Fig. 6.10c and (b) as Fig. 6.11c, except that the simulations are normalised such that $\tilde{x} = 40\,h^{-1}$ Mpc.

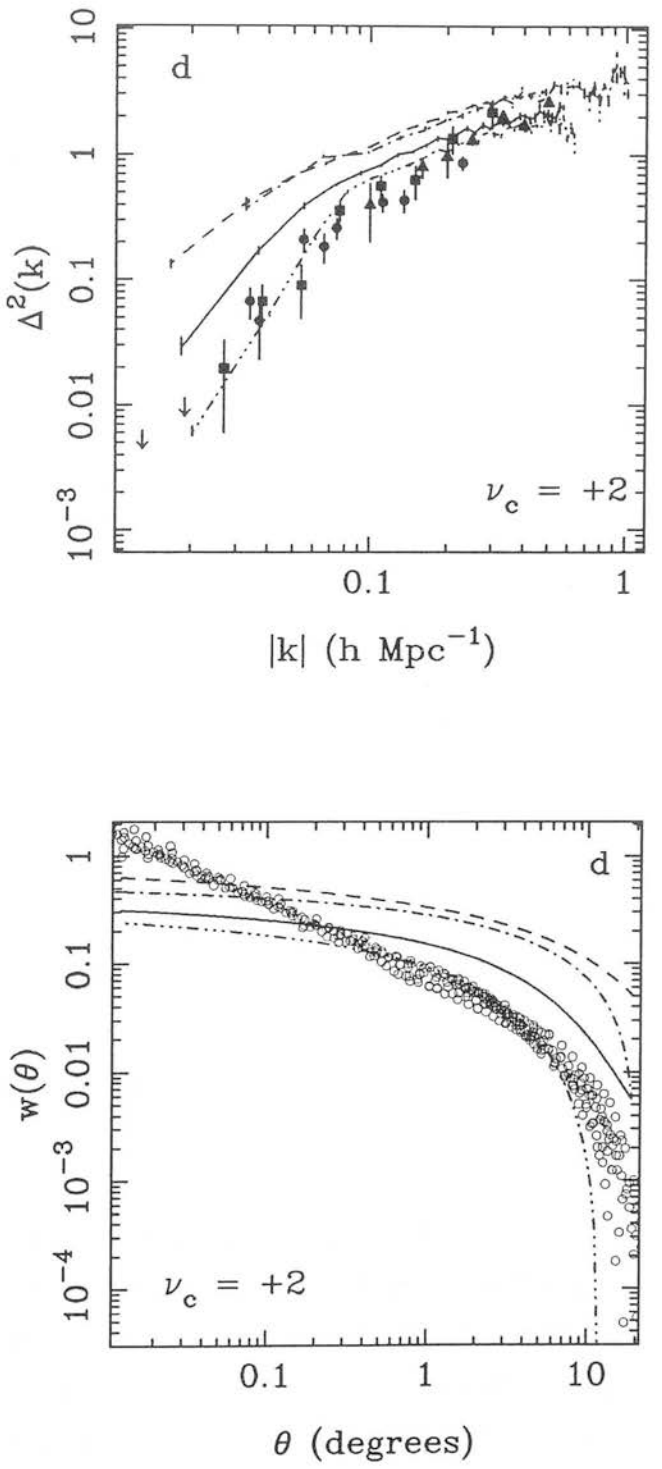

Figure 6.15 (a) As Fig. 6.10d and (b) as Fig. 6.11d, except that the simulations are normalised such that $\tilde{x} = 40\,h^{-1}$ Mpc.

in parameter space of $0 \lesssim n \lesssim 1$ and $0 \lesssim \nu_c \lesssim 1$ where the Voronoi foam provides a satisfactory fit to the data, provided $\tilde{x} \simeq 40\,h^{-1}$ Mpc.

The angular correlation function has also been calculated for a separate survey by Collins, Nichol & Lumsden (1992), who give very similar results as the APM correlation of Maddox *et al.* used in Fig. 6.12 – Fig. 6.15. The only difference is that they find more power beyond the break when compared to the APM correlation function. However, within the errors, which are significant at these scales, both correlation functions agree, making any discrepancy between the Voronoi foam and the correlation function of Collins, Nichol & Lumsden (1992) not very significant.

It is also necessary to check that the Voronoi foams generated using clustered nuclei are compatible with the spatial two-point correlation function for galaxies and galaxy clusters. The first indication from the angular correlation function is that there is no serious problem on small scales, and this is supported by Fig. 6.16, which shows the spatial two-point correlation function for particles on walls (lower curves) for the $n = 1$, $\nu_c = 1$ (dot-dash line), $n = 0$, $\nu_c = 0$ (broken line) and random cases (solid line), normalised to $\tilde{x} = 40\,h^{-1}$ Mpc. As stressed in § 6.1.3, due to the spatial correlation function for particles on walls only probing intracellular scales, there is very little difference between the three cases. As one would expect, the correlation functions for the two foams generated using clustered nuclei maintain a power-law behaviour to greater separations when compared to the unclustered case. However, the correlation lengths are very similar, $\simeq 5.5\,h^{-1}$ Mpc for the unclustered nuclei and $\simeq 6.5\,h^{-1}$ Mpc for the clustered nuclei, which lies within the range of current observations ($4 \lesssim r_0 \lesssim 8\,h^{-1}$ Mpc; § 5.2.3).

Fig. 6.16 also shows the spatial two-point correlation function for nodes (equally weighted) for the same three cases as above (upper lines). The behaviour is very similar to the case for particles on the walls, with foams generated with clustered nuclei showing power-law behaviour to greater scales. Again, the correlation lengths are very similar, $\simeq 11.5\,h^{-1}$ Mpc for the unclustered nuclei and $\simeq 12.5\,h^{-1}$ Mpc for the clustered nuclei. Although these are a little low ($r_0 \gtrsim 14\,h^{-1}$ Mpc; § 5.1.3), this is not too serious as here all the nodes have been used, which may well correspond to using very poor clusters. Richer nodes would give correspondingly higher correlation lengths (§ 5.1.4).

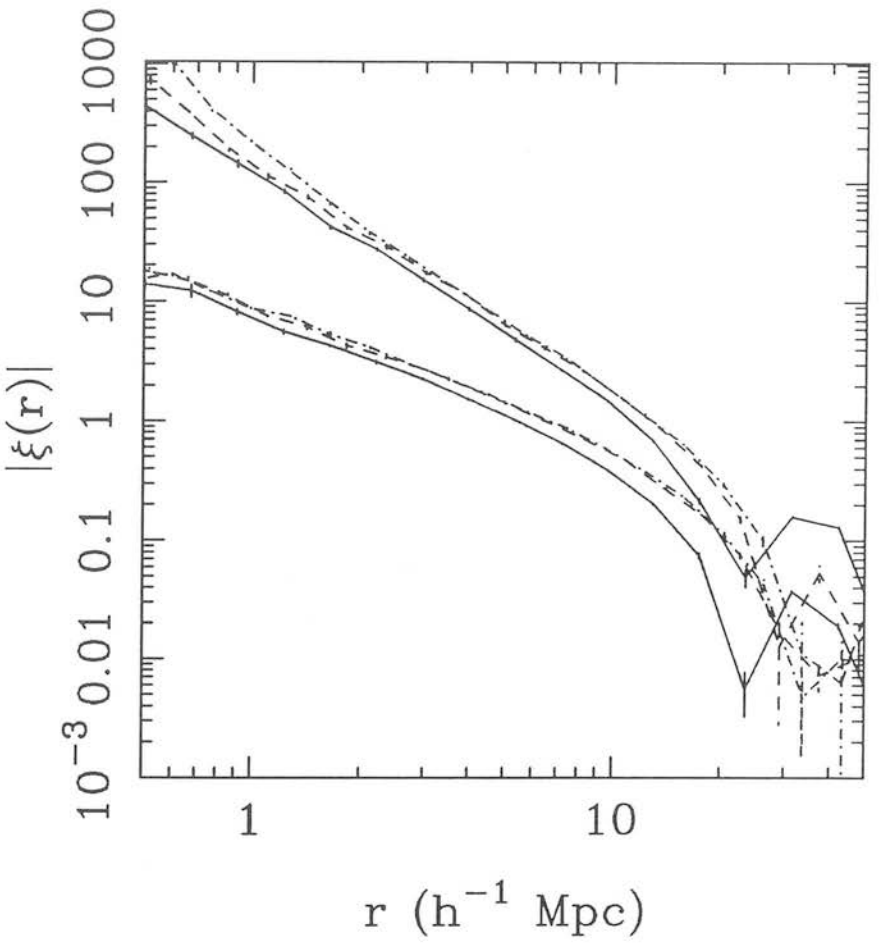

Figure 6.16 The spatial two-point correlation function for particles on walls (lower lines) and at nodes (equally weighted; upper lines). The three correlation functions are for Voronoi foams generated using randomly distributed nuclei (solid line), nuclei taken from an $n = 0$ potential with $\nu_c = 0$ (broken line) and an $n = 1$ potential with $\nu_c = 1$ (dot-dash line). The correlation functions are the mean of five independent simulations and the error bars represent the standard deviation on the mean. The simulations are normalised such that $\tilde{x} = 40\,h^{-1}$ Mpc.

6.5 Conclusions

The introduction of clustered nuclei in the form of peaks in a gravitational potential can supply the missing large-scale power that the Voronoi foam model lacks. However, the window in parameter space is quite small: $0 \lesssim n \lesssim 1$, $0 \lesssim \nu_c \lesssim 1$, $\tilde{x} \simeq 40\,h^{-1}$ Mpc. Also, the observational determination of the amplitude of the galaxy clustering on large

scales is still ambiguous. The data from the power spectra (principally that of Peacock & Nicholson 1991) and the angular correlation function (Maddox *et al.* 1990; Collins, Nichol & Lumsden 1992) agree quite well, but the errors are quite large in the region beyond the break.

A spectral index of $0 \lesssim n \lesssim 1$ is in keeping with modern theories of large-scale structure formation that suggest an initial $n = 1$ Harrison-Zel'dovich spectrum (see § 1.3) at large scales which is modulated on smaller wavelengths. For example, the standard cold dark matter model has a slow turnover to a small-scale slope of $n = -3$, while on the scales of interest (i.e. beyond the break) it predicts $-1 \lesssim n \lesssim 1$.

A threshold in the range $0 \lesssim \nu_c \lesssim 1$ is a little worrying from a theoretical point of view. Viewing the Voronoi foam in terms of a gravitational instability scenario, arguments based around the adhesion model suggest that the Voronoi foam approximates to the full case of gravitational collapse only if high peaks are considered (§ 2.3.4). When smaller peaks are included, the walls no longer lie equidistant between peaks. However, it has been shown that the large-scale structure is dominated by the large cells, which, in the case of the adhesion model, would be more likely to form equidistant between peaks regardless of peak height, unless there was a significant difference in heights (e.g. see § 2.3.4). Thus it may be that the Voronoi foam only fails to approximate to the full case of gravitational collapse on small scales, where the model is expected to be inaccurate. However, to fully answer this question requires further work based more directly on the adhesion model.

Despite the difficulties noted above, the Voronoi foam with clustered nuclei provides an excellent fit to the observed large-scale clustering of galaxies. It is also consistent with the spatial two-point correlation function of galaxies and galaxy clusters. It provides a simple phenomenological model of the formation of large-scale structure, which though probably inaccurate in detail, provides a very good framework and basis for understanding the large-scale distribution of matter in the universe.

Chapter 7

Cluster Alignment

Cluster alignment is a recent cosmological phenomenon. Though observations are contradictory, the weight of the evidence seems to point towards the reality of this effect, whereby clusters of galaxies, separated by tens of Mpc, point towards each other. This chapter sets out to examine the phenomenon in the context of the Voronoi foam model, where cluster alignment naturally arises, and attempts to see if the model can reproduce the observed levels of cluster alignment. It is found that if clusters are located at the nodes in the Voronoi foam, then the alignment may be too weak to account for the observations. Unlike previous Chapters, the restriction that clusters may reside only at nodes is relaxed and clusters are also placed in filaments and walls, which gives rise to a much stronger alignment signal. Due to the observational difficulties in detecting alignment, a review of the evidence for and against cluster alignment is also presented.

7.1 Introduction

Cluster alignment was first suggested by Binggeli (1982), who found that clusters of galaxies point towards their neighbours. That is, the major axis of a cluster (as defined by its position angle) is aligned with the projected vector joining the cluster with the centre of its neighbour. Using a sample of 44 Abell clusters, Binggeli observed this effect out to cluster separations of $15\,h^{-1}$ Mpc when considering only nearest neighbour pairs and out to $50\,h^{-1}$ Mpc when considering all pairs in his sample. However, Binggeli's result was only of marginal significance due to the small number of clusters involved.

Following Binggeli's original work several authors sought to establish the reality or otherwise of what became known as the "Binggeli Effect". The most authoritative recent work, that of West (1989a,b) suggests that the effect is real, which is supported by the complimentary work of Lambas *et al.* (1990) and West (1991). However, several authors (Struble & Peebles 1985; Ulmer, McMillan & Kowalski 1989; Fong, Stevenson & Shanks 1990) found no evidence of alignment, though due to their large errors, none are confident enough to rule out alignment at a weak, but statistically significant level.

Flin (1987) and Rhee & Katgert (1987) also find evidence for alignment, but they only claim marginal support. Thus the observational evidence for cluster alignment is rather scant and contradictory, despite the considerable effort involved in the investigation of the phenomenon. However, it seems that the weight of the evidence lies in favour of cluster alignment, though the effect seems quite weak.

Despite these problems with the observational data, cluster alignment is an important phenomenon. If real, it presents evidence of coherence in the density field, that, due to the large scales involved (up to $\approx 60\,h^{-1}\,\mathrm{Mpc}$ in the case of West 1989b), is highly unlikely to have evolved by gravitational effects and is therefore a feature of the primordial density field. Some authors (e.g. Binggeli 1982; West 1989a,b) have used the suggested evidence of alignment to argue for "top down" models of large-scale structure formation (§ 1.3.1), where the largest scale structures (i.e. superclusters) form first and smaller scale structures form from fragmentation. While this would naturally account for the alignment, it does not automatically argue against "bottom up" scenarios (§ 1.3.1), where the small scale structure forms first and then larger scale structures are constructed from gravitational collapse/attraction. Alignment will occur provided that there is sufficient large-scale power. Conversely, evidence that clearly shows no alignment does not necessarily rule out "top down" models, as alignment after fragmentation is not strictly required.

West, Villumsen & Dekel (1991) have found that clusters tend to point to each other in N-body simulations involving a cold dark matter cosmogony. This alignment is on scales of $\sim 15\,h^{-2}\,\mathrm{Mpc}$ and matches well with the observations of alignment, albeit on a small scale compared to that of some authors who see alignment on scales of $30\,h^{-1}\,\mathrm{Mpc}$ and beyond (e.g. West 1989b). The Voronoi foam model, which can be explained in terms of either a "bottom up" or "top down" type scenario (§ 2.3), also gives rise, in a natural way, to alignments between clusters. In previous chapters (e.g. see § 5.1), nodes in the Voronoi foam have been identified as Abell clusters, though there is no reason why all clusters need to be confined to nodes. The existence of highly elongated clusters lends itself to the suggestion that some, if not the majority of clusters, lie along filaments in the Voronoi foam.

In the gravitational instability picture (though a similar chain of events would take place in an explosion model picture), matter vacates the voids and moves into walls. The

matter then moves across the walls towards the filaments. It seems inconceivable that in such a picture, local gravitational interaction will not act to bind galaxies together into groups or even clusters. On entry into filaments, a much higher density environment, it seems likely that this process will continue at an accelerated rate. As the filaments are one-dimensional in nature, this will naturally account for the elongated nature of the clusters, whereas groups/clusters in walls would be more likely to have an irregular morphology, flattened along the axis perpendicular to the plane of the wall.

The final stage of the gravitational instability picture of the Voronoi foam is the flow of matter from the filaments into the nodes. There is no reason to suspect that a cluster that would form at the node would have to be spherical as it would have matter (i.e. galaxies) flowing into it along four preferential axes (the filaments). The final morphology of the cluster would therefore be dependent on the spatial distribution of the filaments (§ 7.2.1). The only certainty is that the richest clusters would be most likely to reside in nodes.

Thus alignment would naturally arise, even if clusters were confined to nodes, though if clusters populated filaments this would lead to very strong intrinsic alignments. It is the aim of this chapter to investigate alignments within the Voronoi foam and make quantitative comparisons to the present observations. As the observations are at the level of deciding the reality or not of the phenomenon, they are not capable of placing tight constraints on the model. Thus this chapter is a feasibility study to see if the intrinsic alignments in a cellular model such as the Voronoi foam can account for the observations. As there are already several free parameters (see § 7.2), randomly distributed nuclei shall be used, as the introduction of another free parameter (clustered nuclei) will further complicate the situation.

7.2 Alignments in the Voronoi Foam

In order to use the Voronoi foam to investigate cluster alignment, it is first necessary to define both the position and orientation of a cluster. As in previous chapters (e.g. Chapter 5), the aim is to see what effect the various topological features of the Voronoi foam have on the alignment of clusters.

7.2.1 Nodes

Nodes are uniquely located spatially in the Voronoi foam by the nuclei of the four adjacent Voronoi cells, leaving only the orientation of any cluster present at the node to be decided. The simplest method is to add the position vectors defining the four adjacent filaments (taken so that they point towards, not away from, the node). This leaves a residual vector, its direction defining the major axis of the cluster and its magnitude giving some measure of its asphericity. This is the approach that shall be adopted in the rest of this chapter, though it should be noted that this is by no means the only prescription for assigning cluster major axes at nodes. A more realistic measure would be to weight the contribution from each filament by the number of particles in the filament, thus the cluster at the node would be more aligned with the "richer" filaments.

The basic approach of assigning cluster axes by "inflow" from the filaments is justified on the grounds that although the cluster will virialise soon after formation, there will be an almost continuous inflow of galaxies along the filaments in the Voronoi foam picture. These new galaxies will affect the shape of the cluster, reflecting the orientation of the filaments, as they have yet to reach any sort of equilibrium. This further complicates the situation of weighting the contribution of the filaments and, in the absence of detailed modelling of cluster formation and evolution, the simplest scheme, that suggested above, shall be adopted.

7.2.2 Filaments

The case of filaments is a lot less straightforward than that of nodes. In a physically realistic simulation, one would expect a variable number of groups/clusters to be present in each filament with varying richness. The positions of these groups/clusters would also vary along the filament. One approach would be to model the location of clusters by particles in a kinematical simulation of the Voronoi foam (§ 4.4.1) and assign them orientations equal to the direction of their velocity vectors, which should lie parallel to the filament. However, this leads to the problem of what proportion of particles should be in filaments, and, if too many particles are within a single filament, an extremely large alignment signal will arise as all the particles within the filament align.

Instead the approach adopted by this chapter will be to assign two clusters to each

filament detected in a kinematical simulation. Matter flowing into a filament will flow away from the centre and towards the two nodes at either end of the filament. This leads to two sites for clusters and two orientations which are at 180° to each other. The position of the cluster is determined by the mean position of all the particles lying on the filament and moving in same direction. The orientation is given by the mean of the velocity vectors of the particles. The idea here is to map the filaments rather than realistically populate them with particles/clusters. In order to achieve as wide as possible coverage of particles, their positions are recorded when they first reach a filament (§ 4.4.2) and the "grenade" model of § 4.3.4, with 40 particles per nucleus, is used to ensure as even a coverage as possible within each cell.

7.2.3 Alignments of Nodes/Filaments

The search for cluster alignments provides a host of possible configurations for the data, arising both from the methods of assigning the cluster positions and orientations discussed above and from the nature of the phenomenon itself. Taking the latter first, there are two straightforward measures of cluster alignment.

Binggeli (1982) investigated the tendency for clusters to point towards each other, that is the tendency of a cluster's major axis to point towards the centre of another cluster (the "Binggeli Effect"). Note that this is different from the case of alignment of the clusters' major axes (i.e. pointing in the same direction). It is perfectly feasible for a cluster to point towards another cluster while having their major axes at 90° to each other and equally feasible for two clusters to have parallel major axes and not to point to each other at all. Although the case of clusters pointing towards each other has been the more closely studied in the literature, the study of axis alignment is a complementary approach.

The work of West (1989a,b) puts strong emphasis on the alignment of clusters within superclusters, suggesting that clusters form part of another cohesive level of large-scale structure, i.e. superclusters. In his work on groups, West (1989a) found no evidence of alignment in his northern hemisphere sample when considering all groups, but found alignment when he considered the sub-sample of all groups contained in superclusters. However, as discussed in § 1.4.1, the definition of a supercluster is somewhat subjective. In the framework of the Voronoi foam model it is important to disentangle the relative

alignments of the two topological regions. Taking a mixed model of nodes and filaments, there are four filament clusters for every node cluster, which can serve as a simple definition of a "supercluster". One can see from the simple geometry of the Voronoi foam that filaments will point directly towards their associated nodes and there will certainly be a tendency for filaments within a given "supercluster" to point towards each other, though this effect will be less pronounced than that of the filaments pointing towards the node. There will also be a considerable amount of filament-filament axis alignment and, due to the definition of the node's major axis, alignment between filament and node axes. Thus if one restricts alignments to the same "supercluster", one will obtain enhanced alignment over all pairs of clusters (§ 7.3.3).

However, the alignments between nodes and filaments in different superclusters is another matter. Splitting each filament into two clusters ensures that there will be some large-scale alignment. Filaments will point towards nodes in neighbouring superclusters and, of course, will point towards and align their axes exactly with the cluster at the other end of the filament. There will also be some axis alignment of filaments which bound opposites of a wall. Beyond this though, it is hard to see what sort of alignment one would expect on large-scales for filaments. For nodes the case is even less clear. The underlying geometric structure of the Voronoi foam gives very little clue as to the large-scale alignments for nodes. Thus it is important to test alignments not only in mixed filament/node samples, but also in samples containing only nodes and those containing only filaments.

7.2.4 Calculating Cluster Alignments

For the Voronoi foam model, each cluster has a position vector and a direction vector which describes the cluster's major axis. In the case of axis alignment, the alignment angle, ϕ, is defined as the acute angle between the two cluster axes. The alignment angle runs from 0° (parallel axes) to 90° (perpendicular axes). In the case of the "Binggeli Effect" a pointing angle, θ, is defined as the acute angle between the vector joining the centres of the two clusters and the major axis of the first. The pointing angle also runs from 0° (pointing directly at the cluster) to 90° (pointing perpendicular to the cluster).

While this provides full information on the alignment of the Voronoi foam, observational surveys are unable to reconstruct the three-dimensional structure of a cluster.

Even if full redshift information were available for all cluster members, this would be an indication of the individual galaxies' peculiar velocities within the cluster rather than their positions. Thus observed cluster position angles are calculated from the projected two-dimensional image of a cluster. To mimic this, the pointing and alignment angles in the Voronoi foam can also be defined for a projected survey.

In the case of the alignment angle, the two axes are projected onto a constant distance surface and the angle, ϕ, is then the difference between the two projected axes. For the pointing angle, the vector joining the two clusters is computed as normal in three dimensions and then it and the first cluster's major axis are projected onto the constant distance surface. The pointing angle, θ, is then the difference between these two angles. As before, both angles run from 0° to 90°.

In order to allow comparison with observations, all results from the simulations shall be presented as the two-dimensional pointing and alignment angles, though the same general trends are followed in three dimensions. The distance, D, between the two clusters is calculated to be the full three-dimensional separation in all cases, rather than the projected separation.

7.3 Results from Simulations

7.3.1 Distance Dependence of the Pointing and Alignment Angles

Fig. 7.1 shows the pointing angle, θ, for a series of four separation ranges. The distributions are significantly skewed towards $\theta = 0°$, clearly showing that clusters in the Voronoi foam tend to point towards one another on scales of up to $45\,h^{-1}$ Mpc. The evidence for alignment is only very marginal in the distance range $45-60\,h^{-1}$ Mpc. Fig. 7.1 clearly shows that the tendency for clusters to point at each other is distance dependent, the effect diminishing as the separation increases, which is as expected. Fig. 7.2 shows the alignment angle, ϕ, from the same simulations as used for Fig. 7.1. Comparing this to Fig. 7.1, one can see that a tendency for cluster axes to align is also present, but on a much weaker level. The distribution is less skewed and the effect only apparent for small separations, there being no convincing evidence for alignment for separations greater than $15\,h^{-1}$ Mpc.

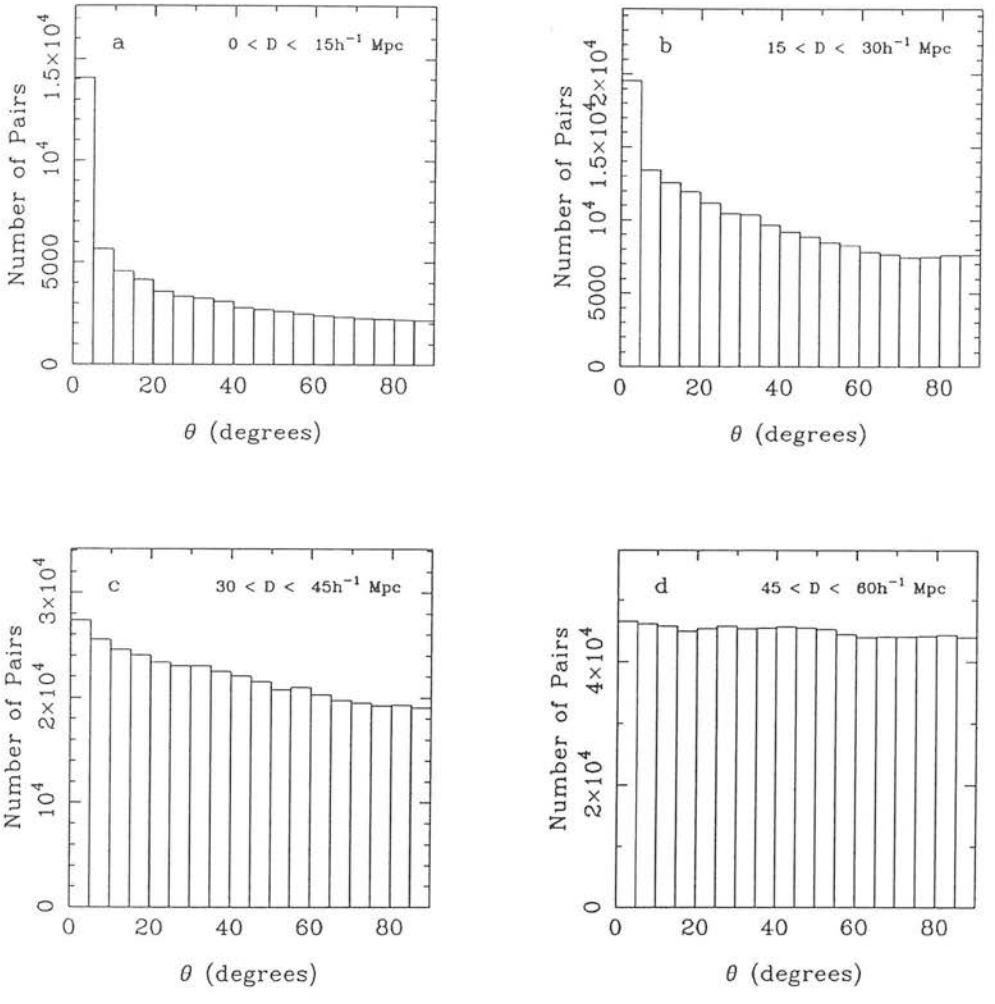

Figure 7.1 The frequency distribution of the pointing angle, θ, plotted as a function of the number of pairs of clusters at a given separation, including both clusters at nodes and clusters in filaments, but excluding clusters within the same filament. The four plots are for four different separations. The simulation is normalised such that $\bar{x} = 52\,h^{-1}$ Mpc.

As discussed in § 7.2.3, it is possible for clusters to point towards each other without actually aligning. This would seem to be the case in the Voronoi foam model, where the distribution of the pointing angle is much more skewed than that of the alignment angle. Any alignment that is present rapidly diminishes with distance, whereas the distribution of the pointing angle is still significantly skewed towards $\theta = 0°$ on scales of up to $45\,h^{-1}$ Mpc. As explained in § 7.2.3, on these large scales the pointing is probably

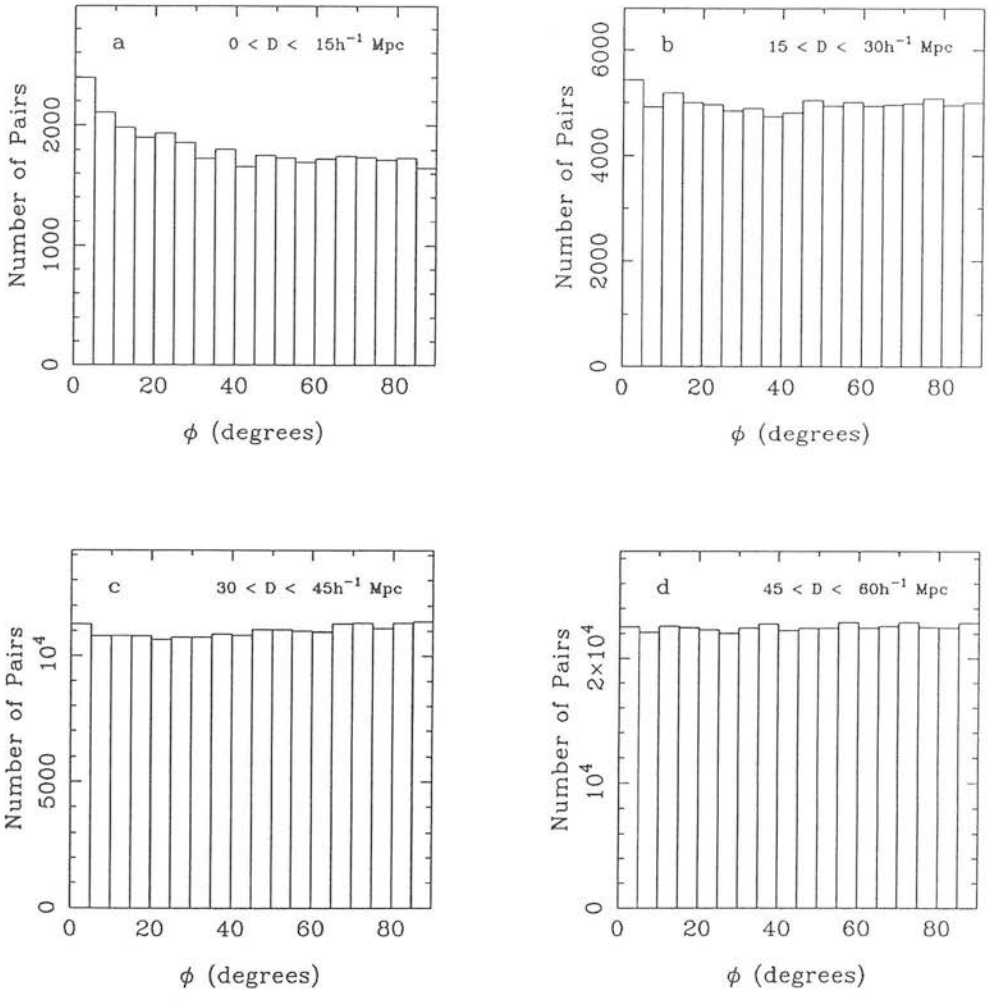

Figure 7.2 As Fig. 7.1 but for the alignment angle, ϕ.

due to clusters at one end of a filament pointing to the cluster at the node at the other end of the filament (pairs of clusters in the same filament having been specifically excluded — see below), supplemented by some clusters in extended superclusters (the supercluster signal still being strong out to $45\,h^{-1}$ Mpc and beyond — see Figs. 7.5 and 7.6).

The data plotted in Figs. 7.1 and 7.2 are for all cluster pairs, including both clusters at nodes and in filaments, but not clusters in the same filaments (see § 7.2.2 and § 7.2.3). The inclusion of these clusters would significantly boost the number of pairs

in the $\theta/\phi = 0°$ bin for both alignment and pointing angles, thus further increasing the significance of the result. The decision to exclude these pairs is somewhat ad hoc, but it should be borne in mind that there is no "correct" method. The aim is to try to find the alignment between filaments, not the alignment within filaments, and excluding pairs within the same filament provides the minimum alignment. In a realistic model, a variable number of clusters would be present in each filament, so if one were to include intra-filament pairs then it would be equally ad hoc to allow only two clusters per filament. Thus, in the spirit of the present investigation, intra-filament pairs are excluded.

7.3.2 Clusters in Filaments and Nodes

Fig. 7.3 shows the relative strengths of alignment for clusters in filaments and nodes. Fig. 7.3a, b shows all cluster pairs for clusters in filaments and nodes with separations less than $15\,h^{-1}$ Mpc. Fig. 7.3a shows the pointing angle and Fig. 7.3b shows the alignment angle (cf. Figs. 7.1a and 7.2a). Similarly Fig. 7.3c, d shows cluster pairs where only clusters in filaments are considered and Fig. 7.3e, f shows cluster pairs for nodes.

Taking the pointing angle first (Fig. 7.3a, c, e), the tendency for clusters to point at each other is strongest when considering the sample including both nodes and filaments (Fig. 7.3a), which is to be expected as filaments naturally point directly towards their associated nodes (§ 7.2.3). Removing the nodes (Fig. 7.3c) weakens the signal, but there is still a very strong tendency for filaments to point towards each other, which is also to be expected (§ 7.2.3). When considering solely the nodes (Fig. 7.3e), the signal is still strong, but it is weaker than either the case of the filaments and nodes or the case of the filaments alone.

In the case of the alignment angle (Fig. 7.3b, d, f) the strength of the alignment is roughly equivalent for the case of clusters in nodes and filaments and in the case of filaments alone. However, when one considers nodes alone, it is plain that there is no clear evidence for alignment. This might be more a reflection of the method used to assign a major axis to a cluster at a node (see § 7.2.1) , rather than the result of any underlying physical phenomenon.

The above conclusions are only strictly valid for small separations. As the separa-

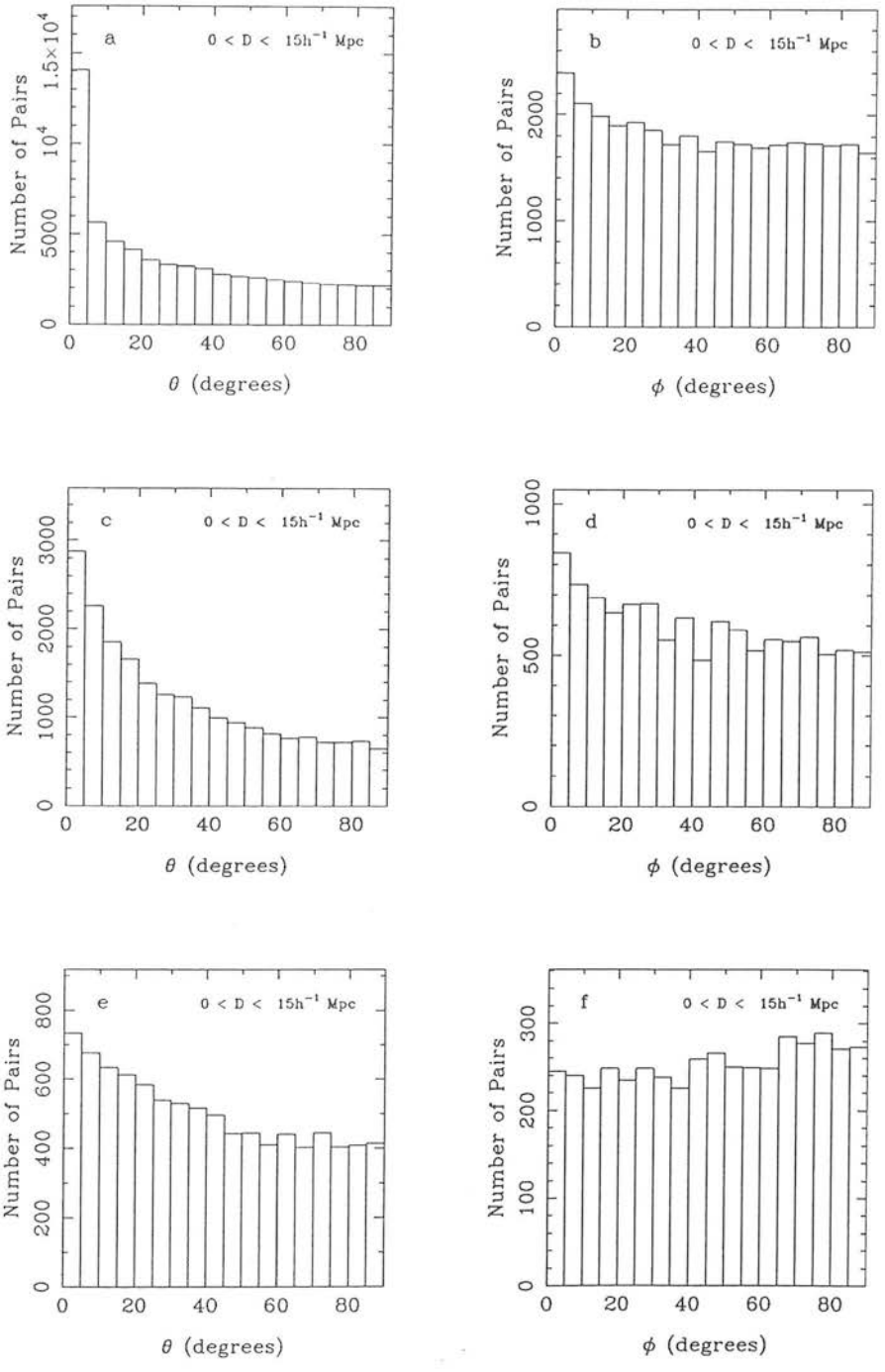

Figure 7.3 The frequency distribution of the pointing angle, θ, and alignment angle, ϕ, for all cluster pairs with separations less than $15\,h^{-1}$ Mpc. The different plots are : (a) and (b) clusters at nodes and in filaments, excluding clusters in same filament, (c) and (d) clusters in filaments, excluding clusters in same filament, (e) and (f) clusters at nodes. The simulation is normalised such that $\bar{x} = 52\,h^{-1}$ Mpc.

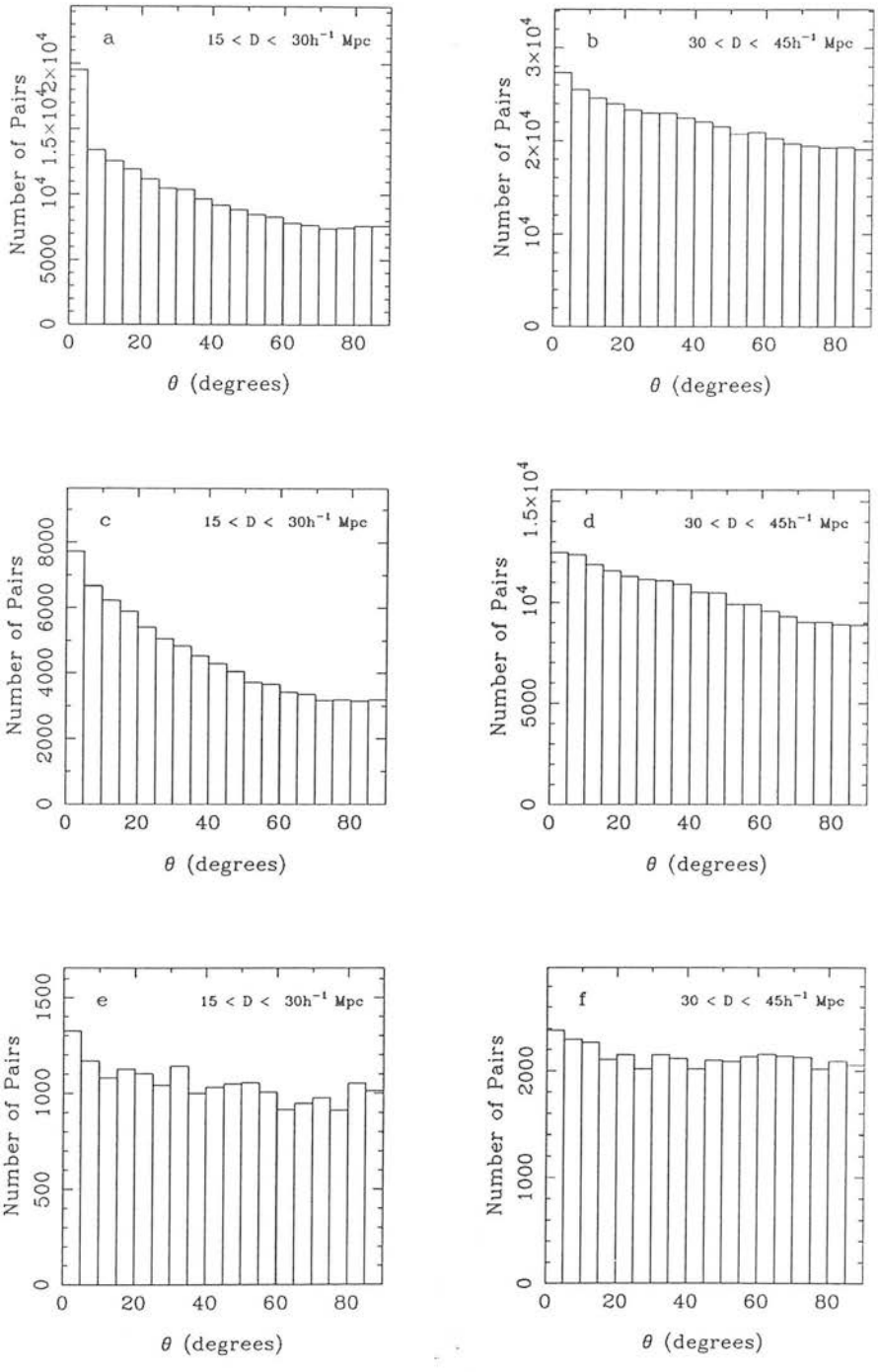

Figure 7.4 The frequency distribution of the pointing angle, θ, for all cluster pairs in two separate distance ranges : (a), (c) and (e) $15 < D < 30\,h^{-1}$ Mpc; (b), (d) and (f) $30 < D < 45\,h^{-1}$ Mpc. The different plots are as in Fig. 7.3. The simulation is normalised such that $\bar{x} = 52\,h^{-1}$ Mpc.

tion increases, so the differences between the three samples decrease as all the samples tend towards the case of homogeneity. This is shown in Fig. 7.4 for the pointing angle, though it is qualitatively similar for the alignment angle. This is because at small ($< 15\,h^{-1}$ Mpc) separations, the majority of node-filament and filament-filament pairs are closely linked, usually being part of the same "supercluster". As the separation increases, the percentage of pairs from unrelated structures grows, leading towards homogeneity in the angular distribution. This can be clearly seen in Figs. 7.1 and 7.2 and is also supported by Fig. 7.4 where the differences in strengths between the different samples decrease as the separation increases, suggesting that they are ceasing to sample coherent structures on those scales and are instead sampling randomly aligned clusters.

7.3.3 Cluster Environment

Fig. 7.5 shows the effect of cluster environment on the pointing angle for three different separation ranges : (a), (d) and (g) up to $15\,h^{-1}$ Mpc, (b), (e) and (h) 15 to $30\,h^{-1}$ Mpc, (c) and (f) 30 to $45\,h^{-1}$ Mpc. Fig. 7.5a, b, c shows all pairs (cf. Figs. 7.1a & 7.2a), Fig. 7.5d, e, f all pairs within the same "supercluster" (see § 7.2.3 for a definition) and Fig. 7.5g, h nearest neighbour pairs. The effect is similar for the alignment angle, but does not extend to such great separations.

There is a significant difference between the three cluster environments, with the strongest signal coming from the nearest neighbours, followed by superclusters, then all pairs. The difference is also much more prominent at larger separations. For separations up to $15\,h^{-1}$ Mpc the three environments produce almost the same distribution of pointing angles, although there is a slight trend in the data of increasing signal strength, but it is not as pronounced as it is at greater separations. Though the three different environments are subject to differing selection rules, in reality excluding pairs with separations greater than $15\,h^{-1}$ Mpc means that most of the pairs in the all pairs sample arise from the same supercluster and only a relatively small minority arise from pairs originating from two different superclusters (where pointing/alignment is less likely). Thus the three different environments show very little difference as they are effectively sampling the same alignment.

In the $15 - 30\,h^{-1}$ Mpc sample this is not so often the case and the differences are much greater between the three environments. In the $30 - 45\,h^{-1}$ Mpc sample there are

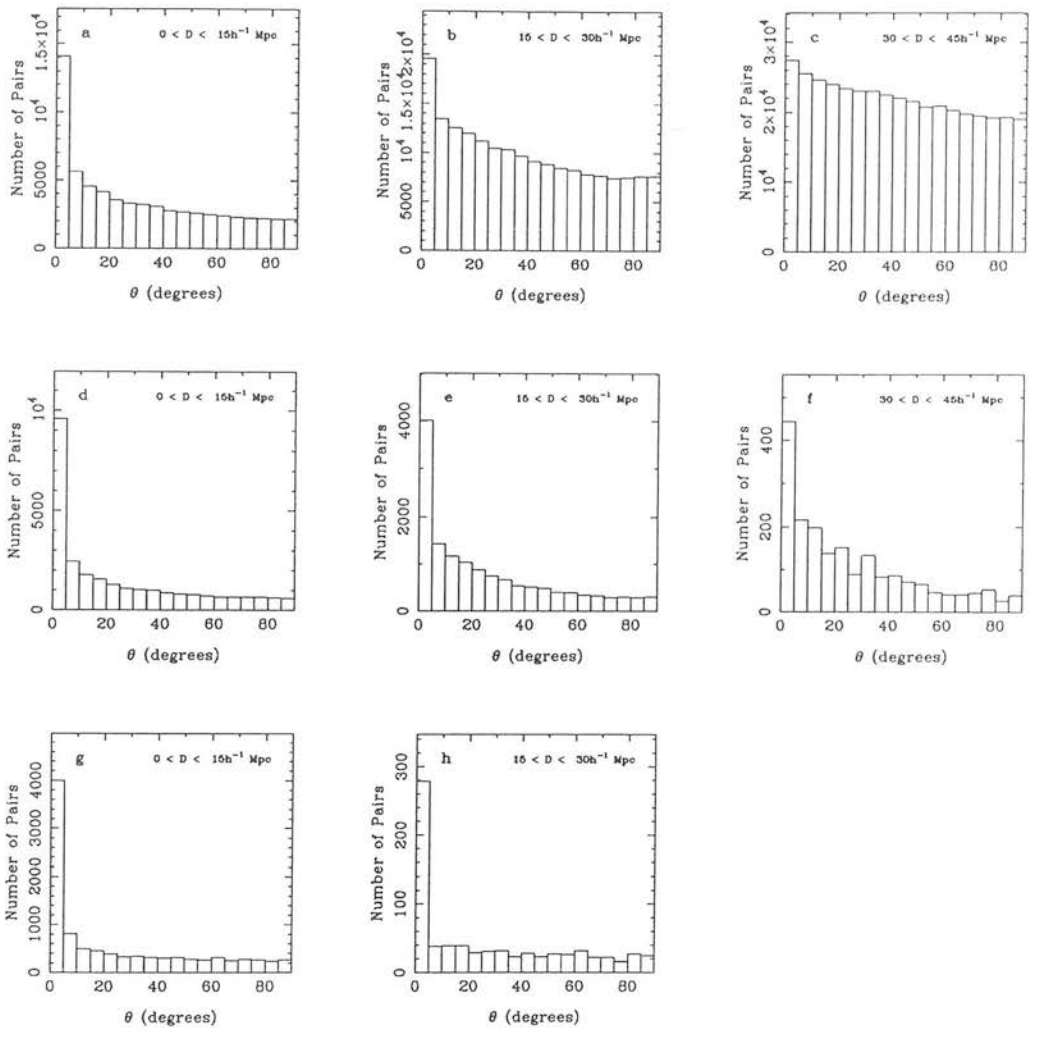

Figure 7.5 The pointing angle, θ, for pairs, including both clusters at nodes and clusters in filaments, but excluding clusters within the same filament. The different plots show the effects of differing environment : (a), (b) and (c) all cluster pairs, (d), (e) and (f) clusters within the same "supercluster", (g) and (h) nearest neighbour clusters. The simulation is normalised such that $\tilde{x} = 52\,h^{-1}$ Mpc.

very few pairs within superclusters (2×10^3 compared to a total of 4×10^5 pairs in the all pair sample; the nearest neighbour sample was not plotted as it only has four pairs!) and hence in the all pairs sample, pairs of clusters from different superclusters go to make up the majority of the pairs plotted. However, there is still a small excess of pairs in the $\theta = 0°$ bin, showing that even on inter-supercluster scales there is a significant tendency for clusters to point to one another.

As shown in Fig. 7.1, the pointing angle is almost uniformly distributed for all pairs in the separation range $45 - 60\,h^{-1}$ Mpc, showing that there is a limit to the extent of the alignment on inter-supercluster scales. However, the signal for pairs in superclusters extends well beyond these scales. Fig. 7.6 shows the distribution of the pointing angle for clusters confined to superclusters on scales between 60 and $500\,h^{-1}$ Mpc. As the signal to noise is poor at such large separations, the pointing angles shown are the sum of five independent simulations. The signal is still very strong in the range $45 - 60\,h^{-1}$ Mpc (Fig. 7.6a) where the distribution for all pairs is close to homogeneity (Fig. 7.1d), but beyond that the significance drops somewhat, though there is still a strong signal for separations of $100 - 200\,h^{-1}$ Mpc (Fig. 7.6c). For separations greater than $200\,h^{-1}$ Mpc there is a clear excess in the $\theta = 0°$ bin, but no other evidence of alignment.

As well as showing that the physical scale of superclusters extends to well beyond $200\,h^{-1}$ Mpc in the Voronoi foam, Fig. 7.6 also shows considerable large-scale alignment when one considers clusters confined to coherent structures, i.e. clusters that one would intrinsically expect to align. The distance dependence of the alignment is, of course, dependent on the normalisation of the simulations. The normalisation used in this chapter, that of an inter-nuclear separation, $\tilde{x} = 52\,h^{-1}$ Mpc, is consistent with that suggested by Chapter 5 and half that used by van de Weygaert & Icke (1989; see § 5.1). The distances are simply proportional to the normalisation used, thus if a value of $\tilde{x} = 104\,h^{-1}$ Mpc, as used by van de Weygaert & Icke (1989), were adopted this would lead to the doubling of all distances quoted here.

7.4 Comparison to Observations

7.4.1 Introduction

The observations of cluster alignment can only deal with the two-dimensional pointing and alignment angles. In general authors have concentrated on the distribution of the pointing angle for nearest neighbour pairs, though West (1989b) considered all pairs within the same supercluster and Fong, Stevenson & Shanks (1990) also considered the alignment angle. The small numbers of observed objects make it difficult to extend the samples beyond nearest neighbour pairs in most cases. The small numbers of objects in the surveys often mean that few objects have more than one or two neighbours

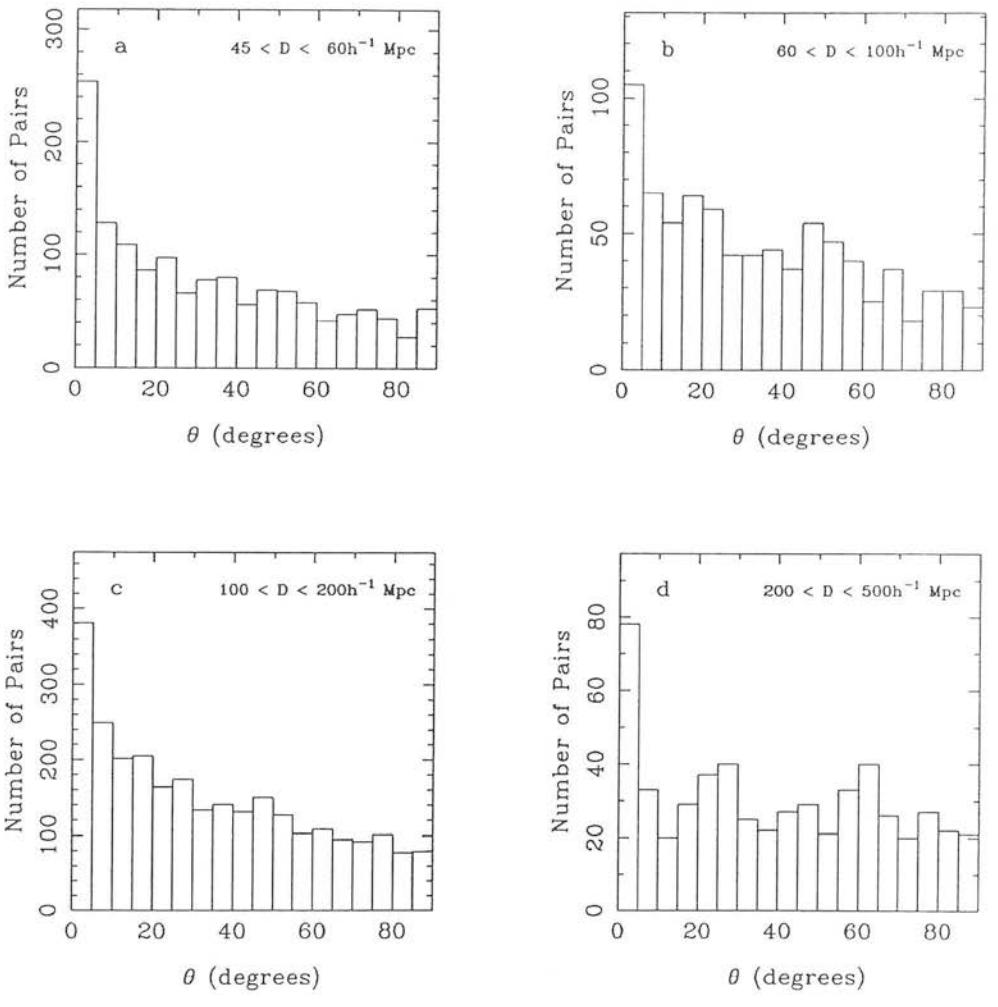

Figure 7.6 The frequency distribution of the pointing angle, θ, for pairs of clusters within the same supercluster, including both clusters at nodes and clusters in filaments, but excluding clusters within the same filament. The results shown here are the sum of five independent simulations, normalised such that $\bar{x} = 52\,h^{-1}$ Mpc.

within a $100\,h^{-1}$ Mpc radius. Extending the sample to all pairs would then swamp any signal present with many pairs of clusters with randomly orientated position angles. As shown in Fig. 7.5, the strongest alignment signal comes from the nearest neighbour pairs, followed by pairs within the same supercluster, thus justifying the observational approach of considering only nearest neighbour or supercluster pairs. However, the alignments shown in Fig. 7.5 are much stronger than any observed alignment signal and

also of a different character.

The frequency distributions shown in this chapter invariably show a steady increase in the number of pairs as one goes from $\theta = 90°$ to $\theta = 0°$, with a peak (often quite sharp) at $\theta = 0°$. Observed frequency distributions tend to show a less-smooth distribution, with a general excess of objects for $\theta < 45°$. Various statistical tests are used to establish the significance of these excesses, whereas as the peaks at $\theta = 0°$ in this chapter are frequently clearly significant to the eye and so no test need be applied. One attempt to quantify the distribution of pointing angles made in the literature is to quote the mean angle, $\langle\theta\rangle$, and its standard error ($\sigma/\sqrt{\text{No. pairs}}$). For a random sample, $\langle\theta\rangle = 45°$, and for a sample showing alignment, $\langle\theta\rangle < 45°$. The smaller $\langle\theta\rangle$ is, the more significant the alignment.

To attempt to provide a comparison with observations, the mean pointing and alignment angles and their associated standard errors are listed in Table 7.1 for the frequency distributions plotted in Figs. 7.1, 7.2, 7.3 and 7.5, along with several random samples which use the clusters' positions, but with randomly assigned position angles. As one can see, these give values of $\langle\theta\rangle$ and $\langle\phi\rangle$ of around 45°, with the standard error depending mostly on the number of pairs, which depends on the environment and separation. Thus the standard error gives a measure of the reliability of the result and the random samples give a measure of the significance of the deviation from 45°. As all the random sample results are within three standard errors of the expected value of 45°, it is possible to say with confidence that any distribution with a mean angle more than three standard errors away from 45° shows some level of alignment. The actual significance of the alignment depends on the difference between the mean angle and the expected value of 45°.

7.4.2 Observational Uncertainties

There are two possible reasons for the cluster alignments in the simulations being considerably more significant that those in the observed sample. The first is that the position angles for clusters in the Voronoi foam simulations are exactly determined. By far the largest source of error in the observations of cluster alignment arise from the difficulty in accurately determining the position angle (§ 7.5). Even in the most accurate work, that of West (1989b), the standard deviation of the position angle was found to be as large as

Fig.	Cluster Sample	$0-15$ h^{-1} Mpc	$15-30$ h^{-1} Mpc	$30-45$ h^{-1} Mpc	$45-60$ h^{-1} Mpc
7.1	all, θ, nf	32.47 ± 0.10	38.37 ± 0.06	42.35 ± 0.04	44.59 ± 0.03
7.2	all, ϕ, nf	41.98 ± 0.15	44.83 ± 0.09	45.35 ± 0.06	45.12 ± 0.04
7.3	all, θ, f	33.71 ± 0.18	37.69 ± 0.09	42.12 ± 0.06	44.91 ± 0.04
7.3	all, ϕ, f	41.71 ± 0.25	44.80 ± 0.13	45.75 ± 0.08	45.38 ± 0.06
7.3	all, θ, n	40.22 ± 0.27	43.20 ± 0.19	44.29 ± 0.13	44.37 ± 0.09
7.3	all, ϕ, n	46.47 ± 0.39	45.05 ± 0.27	44.68 ± 0.19	44.77 ± 0.13
7.5	sc, θ, nf	25.00 ± 0.16	25.62 ± 0.21	26.62 ± 0.54	33.25 ± 1.41
7.5	sc, ϕ, nf	41.10 ± 0.23	43.09 ± 0.31	41.83 ± 0.82	43.28 ± 2.00
7.5	nn, θ, nf	25.00 ± 0.27	28.39 ± 1.01		
7.5	nn, ϕ, nf	39.33 ± 0.27	41.38 ± 0.95		
	all, θ, r	45.00 ± 0.10	44.99 ± 0.06	45.09 ± 0.04	45.05 ± 0.03
	all, ϕ, r	44.69 ± 0.14	45.03 ± 0.08	45.02 ± 0.06	45.02 ± 0.04
	sc, θ, r	44.92 ± 0.07	44.87 ± 0.10	45.14 ± 0.26	44.98 ± 0.70
	sc, ϕ, r	44.94 ± 0.10	44.87 ± 0.14	44.78 ± 0.38	44.99 ± 1.00
	nn, θ, r	44.95 ± 0.12	45.78 ± 0.43		
	nn, ϕ, r	45.16 ± 0.12	44.87 ± 0.43		

Key to Cluster Sample

all All cluster pairs

sc All cluster pairs within a given supercluster

nn Nearest Neighbour pairs

θ Pointing Angle

ϕ Alignment Angle

nf Clusters in Nodes and Filaments

f Clusters in Filaments

n Clusters in Nodes

r Random Sample

Table 7.1 The mean pointing or alignment angle with standard error for the cluster samples in Figs. 7.1, 7.2, 7.3 and 7.5 along with various random samples for comparison.

20°. Any clusters with a standard deviation greater than this were rejected. Obviously

any error in the position angle will serve only to dilute the observed alignment, thus any alignment seen in the simulations will be more significant than the corresponding observed alignment.

The second reason arises from the way in which clusters' major axes are assigned. Clusters in the Voronoi foam are automatically aligned with their associated filament, thus leading to the cluster always pointing towards the associated node at the end of the filament. This accounts for the huge signal seen in the nearest neighbour pointing angle distribution for $\theta = 0°$ (see Fig. 7.5). In any realistic simulation this alignment of clusters with their filament would not be absolute. Rather it would be an alignment in a statistical sense, with a range of different cluster orientations around the filaments. Note, however, that this is a problem that applies only to filaments, as the distribution of pairs of clusters at nodes shows considerably less alignment (see Fig. 7.5).

There are other, less severe, effects that contribute to a weakening of the observed alignment signal. One is the effect of inaccurate cluster distances. Often cluster redshifts are based on only a single redshift measurement which may be highly unrepresentative of the cluster as a whole. This means that a true nearest neighbour may well be excluded due to a false estimate of its own distance or by the inclusion of a false true neighbour with an inaccurate distance. This will serve to dilute the signal.

The observational selection of clusters is another process that is prone to error. Previous "eye-ball" surveys, such as the Abell (1958) survey, have been highly subjective in nature (e.g. see Dalton *et al.* 1992; Nichol *et al.* 1992 for comment) which could lead to the misidentification of clusters and the production of spurious nearest neighbour pairs which are, in fact, unaligned. This too could be due to either finding a non-existent cluster or missing the true nearest neighbour. Again this acts to dilute the alignment signal. Indeed, almost any systematic or random error that one can think of will lead to a reduction in significance of the alignment in the case of the pointing and alignment angles. The exception to this is a systematic error in the measurement of the position angle which leads to the position angles becoming aligned in some preferred direction (usually the plate edge). Though this will still lead to a decrease in the significance of any signal in the pointing angle, it will introduce an artificial signal for the alignment angle.

Thus the presence of errors and uncertainties in the observations of cluster align-

ment will inevitably lead to a decrease in the significance of any alignment present whereas alignments in the Voronoi foam simulations, which do not suffer from these errors and uncertainties, will, as a result, have significantly stronger alignments. The following subsection deals with the simulation of such uncertainties in the alignment of clusters.

7.4.3 Simulating Observational Uncertainties

In order to allow for the observational uncertainties, it is necessary to make the position angles of clusters in the Voronoi foam less well determined. This can be achieved by adding to each position angle a further "error angle", $\theta_{\rm E}$, drawn at random from a Gaussian distribution with standard deviation, σ_θ. Fig. 7.7 shows the effect on the distribution of the pointing angle for nearest neighbours of adding random angles with $\sigma_\theta = 20°$ and $\sigma_\theta = 40°$, compared to the original distribution for two different separations. As one can see, the addition of a random component to the position angles greatly reduces the significance of the alignment. For $\sigma_\theta = 50°$ there is no significant evidence of alignment.

Obviously it is hard to know what value of σ_θ to use in order to accurately account for observational uncertainties, but the alignments measured by West (1989b), are a useful comparison, assuming that he has indeed found the underlying alignment signal, subject to the aforementioned errors. In order to carry out a direct comparison with the work of West (1989b) the pointing angles for all pairs of clusters within the same supercluster have been recalculated for values of $\sigma_\theta = 20°$ and $\sigma_\theta = 30°$. Fig. 7.8 shows the distributions of the pointing angle in the separation ranges $0 - 30\,h^{-1}$ Mpc and $30 - 60\,h^{-1}$ Mpc with the mean angle listed in Table 7.2, along with the observed alignments as found by West (1989b).

West (1989b) created two samples, his main one of 84 clusters, in which all clusters had measured position angles with a standard deviation of less than 20°, and a subsample of 40 clusters with $\sigma < 10°$. As this subsample has so few members it was not feasible to split it into two samples on the basis of separation. As stressed in § 7.4.1 and § 7.4.2, the alignment of clusters with $\sigma_\theta = 0°$ is considerably stronger than that observed by West (1989b). However, when random angles with $\sigma_\theta = 20°$ are applied, the mean pointing angle (at $\simeq 35°$) agrees remarkably well with West's $\sigma < 10°$ sample, though

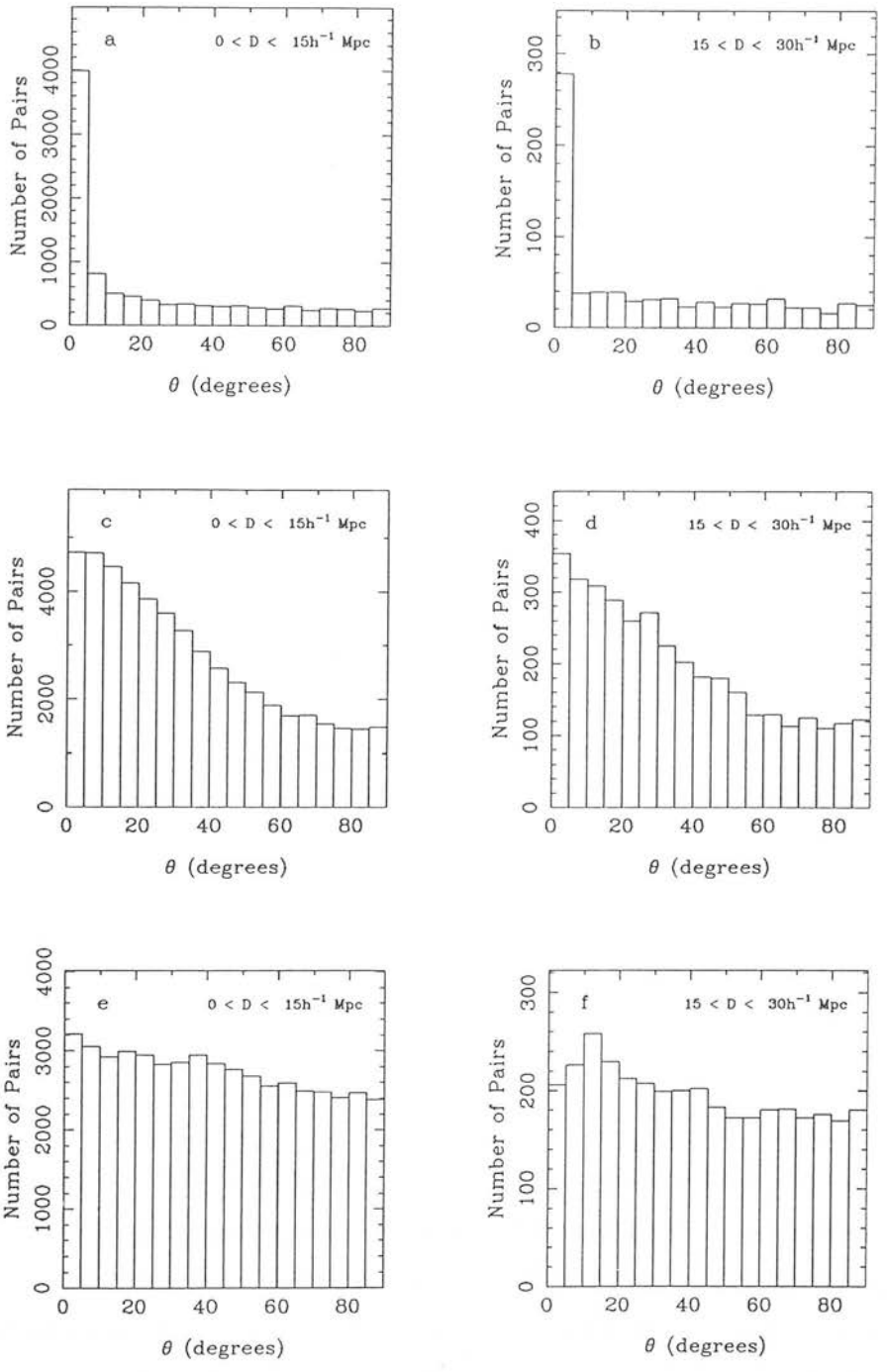

Figure 7.7 The frequency distribution of the pointing angle, θ, for nearest neighbour pairs of clusters, including both clusters at nodes and in filaments but excluding clusters within the same filament. The different plots show the effect of adding random angles to the cluster position angles for varying values of σ_θ. (a) and (b) $\sigma_\theta = 0°$, (c) and (d) $\sigma_\theta = 20°$ and (e) and (f) $\sigma_\theta = 40°$. The results for panels (c) — (f) are the sum of five independent simulations. The simulations are normalised such that $\tilde{x} = 52\,h^{-1}$ Mpc.

Fig.	σ_θ	$0-30$ h^{-1} Mpc	$30-60$ h^{-1} Mpc	$0-60$ h^{-1} Mpc
7.8	$0°$	25.28 ± 0.06	28.23 ± 0.23	25.43 ± 0.05
	$20°$	34.47 ± 0.05	35.58 ± 0.23	34.52 ± 0.05
	$30°$	39.61 ± 0.06	40.01 ± 0.25	39.63 ± 0.05
	$40°$	43.06 ± 0.06	43.50 ± 0.25	43.08 ± 0.05
West	$< 10°$			35.01 ± 1.61
(1989b)	$< 20°$	38.95 ± 1.57	40.23 ± 1.57	39.96 ± 1.17

Table 7.2 The mean pointing angle with standard error for the cluster samples in Fig. 7.8 along with the observed alignments as found by West (1989b).

the error on West's result is rather large. The $\sigma < 20°$ sample has a larger value of $\langle\theta\rangle \simeq 38°-40°$, which matches well with the $\sigma_\theta = 30°$ analysis, although again the error on West's results is still rather large.

There are two points worth noting here. First is that the distribution of pointing angles for the Voronoi foam in the range $0 - 60\,h^{-1}$ Mpc is dominated by the $0 - 30\,h^{-1}$ Mpc subsample, something that is not so in the case of West (1989b), where roughly equal numbers of pairs reside in each separation range. Also, the two samples of West ($\sigma < 10°$ and $\sigma < 20°$) should not be taken to be equivalent to pointing angles which are normally distributed about the mean with standard deviations of $10°$ and $20°$ respectively. The standard deviation given by West is a measure of the *uncertainty* of the individual measurements of the cluster position angle.

The addition of random angles to the pointing angles of clusters in the Voronoi foam simulates two distinct processes, the inaccurate determination of the pointing angle (some measure of which is given by the observations) and the uncertainty of alignment between clusters and filaments in the foam (a model dependent property). Each of these will have its own associated standard deviation, which will add in quadrature to give the final standard deviation, $\sigma_{\rm E}$:

$$\sigma_{\rm E} = \sqrt{\sigma^2_{\rm obs} + \sigma^2_{\rm mod}} \tag{7.1}$$

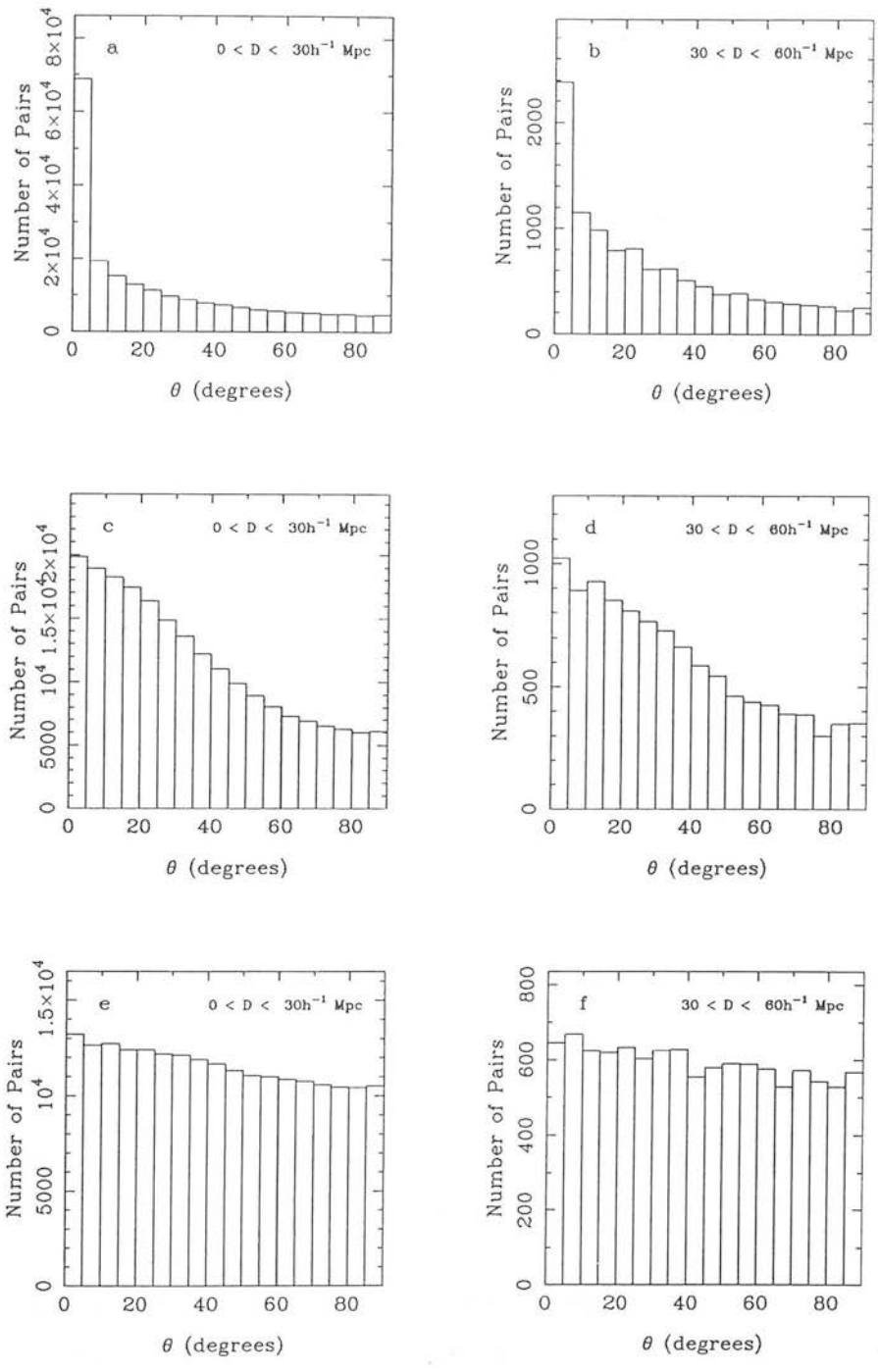

Figure 7.8 The frequency distribution of the pointing angle, θ, for pairs of clusters within the same supercluster, including both clusters at nodes and in filaments but excluding clusters within the same filament. The different plots show the effect of adding random angles to the cluster position angles for varying values of σ_θ. (a) and (b) $\sigma_\theta = 0°$, (c) and (d) $\sigma_\theta = 20°$ and (e) and (f) $\sigma_\theta = 30°$. The results are the sum of five independent simulations. The simulations are normalised such that $\bar{x} = 52\,h^{-1}$ Mpc.

where σ_{obs} is the uncertainty in the observed position angle and σ_{mod} is the uncertainty in the cluster/filament alignment.

For the values of σ_E given in Table 7.2, equation (7.1) may be solved for σ_{obs} and σ_{mod} given that σ_{mod} will not change with σ_E. Taking the extreme case of $\sigma_{mod} = 0°$, this assumes that all errors are in the determination of the pointing angle. This leads to $\sigma_{obs} = 20°$ for the $\sigma < 10°$ sample of West and $\sigma_{obs} = 30°$ for the $\sigma < 20°$ sample. These values seem a little high, especially as they are higher than the cut-off standard deviation of West, but they are not totally implausible. The opposite extreme is to assume $\sigma_{obs} = 0°$ for the $\sigma < 10°$ sample of West. This leaves $\sigma_{mod} = 20°$ and $\sigma_{obs} \simeq 22°$ for the $\sigma < 20°$ sample. Again these values are not too high and it is likely that the "true" values would lie somewhere in between. Given the poor state of the observational data, it is not possible to tie these parameters down any further, but nonetheless, this has demonstrated that the approach of adding random angles to the cluster position angles in order to account for the observational uncertainties is not an unreasonable one.

It is worth mentioning at this point that the case of alignment for nodes and filaments is in some ways the worst possible scenario as here the intrinsic alignment is at its strongest (Fig. 7.3 and Table 7.1). The following two subsections look at the effect of selecting clusters in various different ways and compare the strengths of the alignments present.

7.4.4 Clusters at Nodes

If the selection of clusters was restricted to only those at nodes then, as shown by Fig. 7.3 and Table 7.1, the strength of the alignment is drastically reduced. As most of the evidence for alignment comes from samples of rich clusters (Binggeli 1982; Struble & Peebles 1985; Flin 1987; Rhee & Katgert 1987; West 1989b; Lambas *et al.* 1990) this is a reasonable restriction to make, as one would expect the richest clusters to be located at the nodes of a Voronoi foam (§ 7.1). However, this suggests that the less-rich clusters would be *more* strongly aligned than their rich counterparts, as they would then lie on filaments. Fong, Stevenson & Shanks (1990) used a catalogue of groups and clusters of varying richness to search for alignment, but were unable to find any significant evidence for alignment in the distribution of either the pointing angle or the alignment angle. It

is important to note that they did not attempt to carry out a detailed analysis of the richness dependence of the alignment and their work may well be prone to some quite severe errors which could mask any alignment present (see § 7.5).

West (1989a) also investigated the alignment of groups, finding no alignment in a northern hemisphere sample, but finding alignment in a southern hemisphere sample. He also found alignment for groups in the north when considering only groups that reside within superclusters. A possible explanation of this within the context of the Voronoi foam is that the groups in superclusters lie in filaments and hence show alignment and the other groups lie in walls and hence show no alignment (the groups in the southern hemisphere sample mostly reside in superclusters). In this case the alignment signal for the groups in superclusters should be stronger than that found by West (1989b) for the clusters. Unfortunately the sample used by West (1989a) was not large enough to thoroughly test this hypothesis as the significance of his result is prone to large errors (standard errors of $3°-5°$ were quoted for the mean pointing angle) due both to the small number statistics of the sample and the fact that errors in the position angle for groups are likely to be much larger than those of clusters, thus further diluting any signal present. However, the mean pointing angle for the distributions of groups was similar or smaller than those of the clusters, albeit over a smaller separation range ($0 - 15\,h^{-1}$ Mpc as opposed to $0 - 30\,h^{-1}$ Mpc). Despite the large errors in the mean angles for groups, this is encouraging, as alignments in groups are even more likely to be underestimated than those in clusters due to the poorer determination of the pointing angle (West 1989a). Ideally the alignment strength should be tested for any correlation with cluster richness. However, this has not been possible in previous studies as the samples used have been so small as to preclude any statistically meaningful subsamples from being taken.

Considering only clusters located at nodes, it is worth investigating the effect of adding random components to the position angles of clusters at nodes to mimic observational uncertainties (§ 7.4.3). Fig. 7.9 shows the nearest neighbour pointing angles for clusters at nodes for $\sigma_\theta = 10°$ and $\sigma_\theta = 20°$ as well as the original data, with the mean pointing angle and its standard error listed in Table 7.3 along with the results of West (1989b).

This is not a direct comparison to the work of West (1989b), who used pairs of

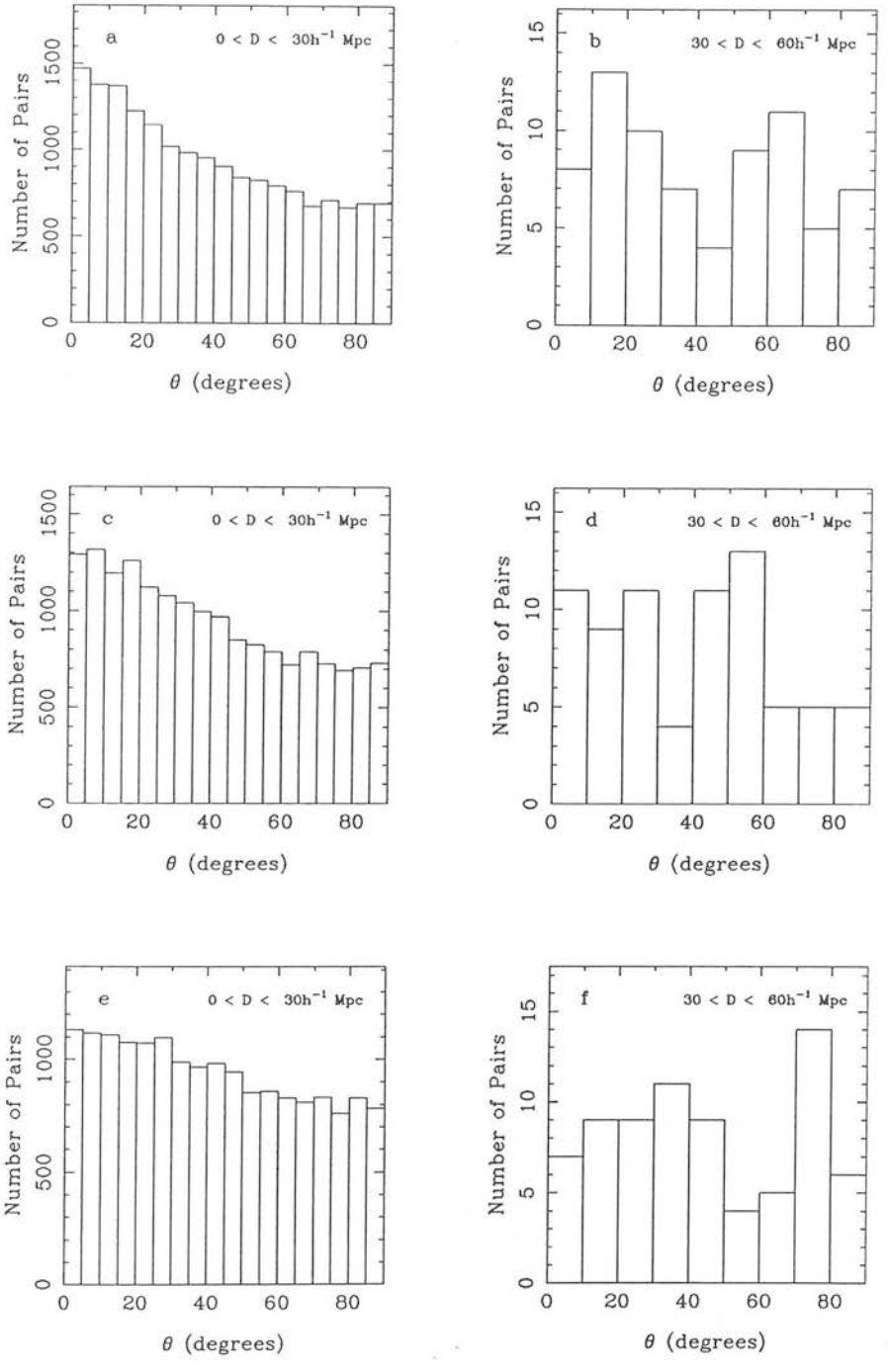

Figure 7.9 The frequency distribution of the pointing angle, θ, for nearest neighbour pairs of clusters, including only clusters at nodes. The different plots show the effect of adding random angles to the cluster position angles for varying values of σ_θ. (a) and (b) $\sigma_\theta = 0°$, (c) and (d) $\sigma_\theta = 10°$ and (e) and (f) $\sigma_\theta = 20°$. The results are the sum of five independent simulations and are normalised such that $\bar{x} = 52\,h^{-1}$ Mpc.

Fig.	σ_θ	$0-30$ h^{-1} Mpc	$30-60$ h^{-1} Mpc	$0-60$ h^{-1} Mpc
7.9	$0°$	38.32 ± 0.20	41.69 ± 2.99	38.33 ± 0.19
	$10°$	39.38 ± 0.20	39.80 ± 2.90	39.38 ± 0.20
	$20°$	41.66 ± 0.20	44.59 ± 3.00	41.67 ± 0.20
	$30°$	43.13 ± 0.20	46.19 ± 3.26	43.14 ± 0.20
	$40°$	44.89 ± 0.20	48.51 ± 3.34	44.91 ± 0.20
West	$< 10°$			35.01 ± 1.61
(1989b)	$< 20°$	38.95 ± 1.57	40.23 ± 1.57	39.96 ± 1.17

Table 7.3 The mean pointing angle with standard error for the cluster samples in Fig. 7.9 along with the observed alignments as found by West (1989b).

clusters within the same supercluster. Due to the definition of a supercluster in the Voronoi foam given in § 7.2.3, no two nodes may be in the same supercluster, therefore the analysis in the case of the Voronoi foam has had to be restricted to nearest neighbour pairs. Note also that the number of pairs in the $30-60\,h^{-1}$ Mpc separation range is very small, leading to large errors in the mean angle. As with the distribution of pointing angles in § 7.4.3, the mean angle for the $0-60\,h^{-1}$ Mpc range is dominated by the mean angle of the $0-30\,h^{-1}$ Mpc subsample.

Table 7.3 shows that the strength of the intrinsic cluster alignment ($\sigma_\theta = 0°$) for nodes alone is weaker than that of the $\sigma < 10°$ sample of West (1989b). Even allowing for the large error on West's result, the two mean pointing angles lie about two standard errors apart. The $\sigma < 20°$ sample matches quite well with the $\sigma_\theta = 10°$ sample, though it is marginally consistent with the $\sigma_\theta = 0°$ sample. Even allowing that the error angle is made up entirely of uncertainties in the pointing angle (there being no clusters in filaments), these values of $\theta_{\rm E}$ are very low, suggesting that the intrinsic alignment in the nodes only case may be too weak to account for the observed alignment.

It is worth bearing in mind that the method of assigning major axes to node clusters (§ 7.2.1) is not the only available method and so the result could be a reflection on the method used rather than the intrinsic geometry of the foam. However, it serves to illustrate the fact that even though the cluster alignment in the Voronoi foam initially seems very strong, it is possible to reduce it quite significantly without taking any

unreasonable steps.

7.4.5 Clusters in Walls and Filaments

The suggestion made in § 7.4.4, that clusters used in observational surveys to determine the cluster alignments lie preferentially at nodes in a Voronoi foam, is at one extreme of the possible cluster distributions. At the other extreme is the suggestion that few, if any, clusters lie at nodes and instead the vast majority of clusters lie either in walls or filaments. This is akin to arguing in the gravitational instability scenario for the Voronoi foam that matter is still streaming from voids into walls, and from walls into filaments, but has not yet reached the nodes.

In this scenario the richest clusters would reside in the filaments, but rich clusters could still reside in walls. Though this seems unlikely, it is possible that large associations of galaxies can form within the walls provided that the transit time across the walls is long enough to allow sufficient gravitational clustering to take place. The alignment signal, though strong for filaments (Fig. 7.3), would be weakened by the presence of pairs of clusters in walls that have essentially no alignment.

As suggested in § 7.1, there would be a difference in morphology between clusters in walls and filaments, the former being more oblate and the latter more prolate. Once again, observational surveys lack sufficient numbers of objects to see if there is a trend in cluster alignment with ellipticity. On average, one would expect oblate (wall) clusters, when viewed in projection, to be more circular and exhibit little or no alignment, whereas prolate, (filament) clusters would be more elliptical and exhibit stronger alignment. However, as it is more difficult to accurately measure a position angle for a circular cluster than for a highly elliptical one (e.g. see Rhee & Katgert 1987), such a trend may well appear in the data due solely to measurement uncertainties.

There is indirect evidence from the morphology of superclusters (West 1989b) that bears upon this question. If clusters reside in walls then one would also expect their superclusters to be oblate for similar reasons, whereas clusters in filaments would be likely to reside in prolate superclusters. West (1989b) studied the morphology of 48 probable superclusters and found that the predominant morphology was prolate with typical axis ratios of 3:1:1 and 4:2:1, suggesting that typical rich clusters reside in

filaments.

It is possible to appeal to other theoretical work, as well as observational evidence, to test this claim. N-body simulations by West, Villumsen & Dekel (1991) using a cold dark matter cosmogony show alignment of clusters on scales of $15\,h^{-2}$ Mpc. They also determined, from the mean cluster morphology, that clusters in their simulations tended to lie in filamentary structures, which argues against the proposition that a large number of clusters lie in walls.

However, retaining the idea that a significant number of rich clusters reside in walls, it is interesting to see what effect adding increasing numbers of clusters in walls to a catalogue of clusters in filaments has on the strength of the alignment signal. This is a different process to that of adding random elements to position angles, as it concerns the addition of unaligned wall clusters. In order to simulate this, the particles in a kinematic Voronoi foam simulation have their positions recorded on first reaching a wall. Each such particle is assigned a position angle parallel to its velocity vector and is then treated as a candidate cluster. This produces a catalogue of candidate clusters from which a given number are drawn at random so as to fix the ratio of clusters in filaments to those in walls to the required value. The alignment analysis then proceeds as normal.

Although this method does not assign random position angles, it ensures that the position angles lie within the plane of the wall, which is a reasonable assumption. This will introduce some cluster pointing as clusters in walls will point towards the filament that they will eventually reach. However, the majority of nearest neighbour clusters will lie within walls and hence won't point to each other, thus depressing any cluster pointing signal. On the other hand, the nearest neighbour clusters will then tend to be moving in the same direction, so this should lead to an enhanced cluster axis alignment signal.

Fig. 7.10 shows the distribution of the pointing angle for nearest neighbour pairs with separations less than $30\,h^{-1}$ Mpc for three samples, each with $\sigma_\theta = 0°$, $20°$ and $40°$. The three samples are Fig. 7.10a, b, c – all clusters in filaments, Fig. 7.10e, d, f – 50% of clusters in filaments, 50% of clusters in walls and Fig. 7.10g, h, i – all clusters in walls. Fig. 7.11 shows the distribution of the alignment angle for the same samples. The mean pointing and alignment angles are listed, along with their standard errors,

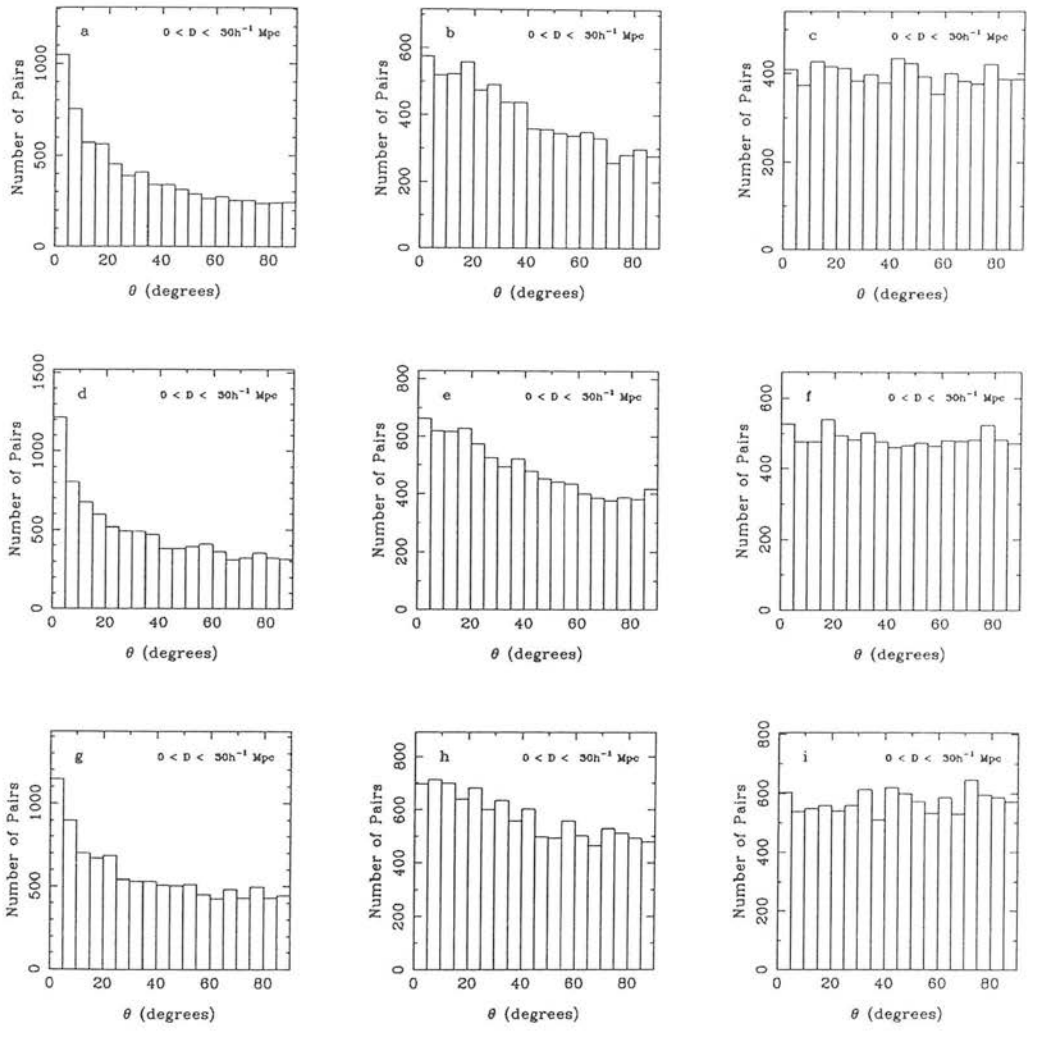

Figure 7.10 The frequency distribution of the pointing angle, θ, for nearest neighbour pairs of clusters. The nine plots show three different samples, each with $\sigma_\theta = 0°$ (a), (d) and (g), $\sigma_\theta = 20°$ (b), (e) and (h) and $\sigma_\theta = 40°$ (c), (f) and (i). The three samples are for clusters in (a), (d) and (g), filaments only, (b), (e) and (h), filaments and walls in equal numbers and (c), (f) and (i), walls alone. Pairs of clusters within the same filament have been excluded. The simulations are normalised such that $\tilde{x} = 52\,h^{-1}$ Mpc.

in Table 7.4 which also lists the mean angles for samples with 10, 25, 75 and 90% of clusters in walls with $\sigma_\theta/\sigma_\phi = 0°$, 10°, 20°, 30° and 40°.

The pointing angle shows considerable anisotropy, even for the sample with all the clusters in the walls (Fig. 7.10g). This is probably due to wall clusters "lining up", i.e. clusters that are moving across walls and towards filaments following roughly the same

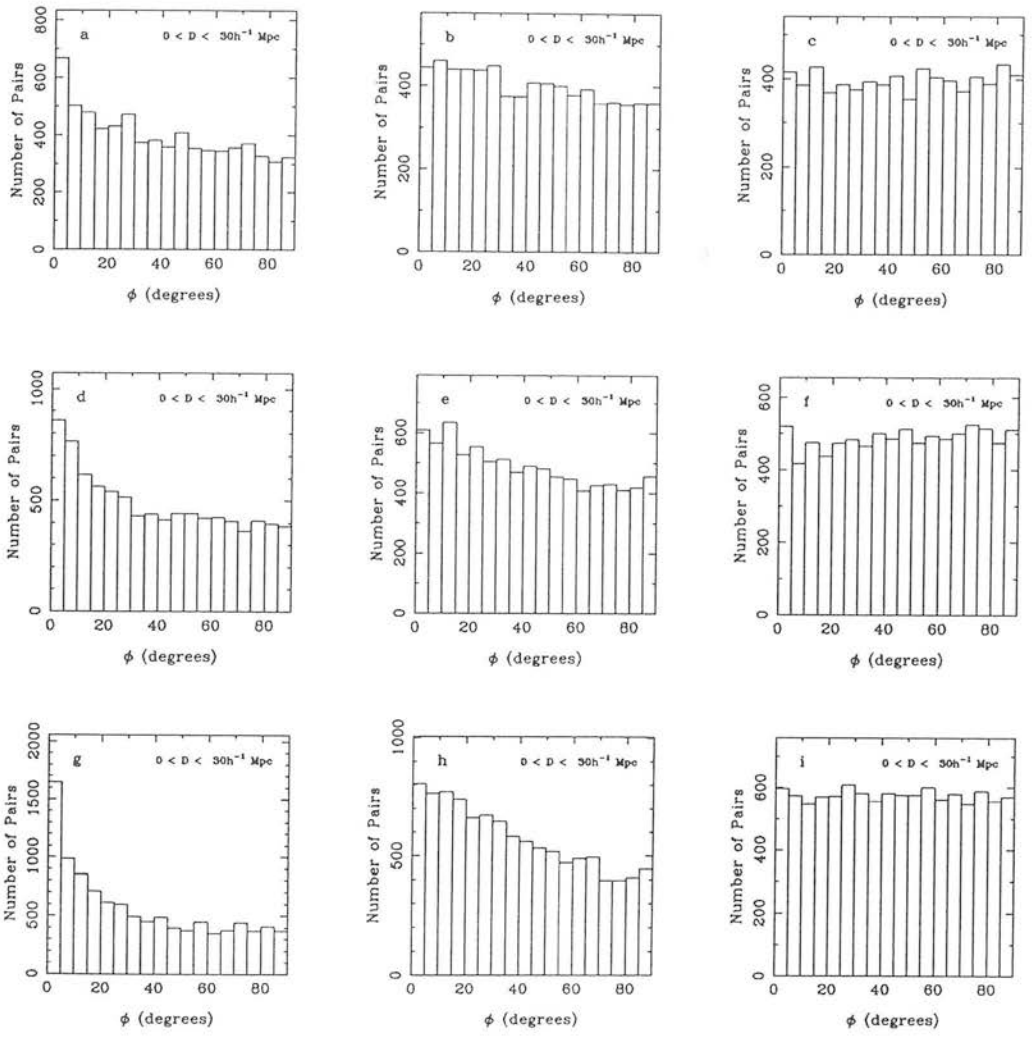

Figure 7.11 As Fig. 7.10, but for the alignment angle, ϕ.

trajectory and hence pointing towards each other. However, as predicted, the strength of the alignment in the case of the pointing angle does decrease as the percentage of wall clusters increases.

The signal for the alignment angle is also quite strong and strengthens rather than decreases as the percentage of wall clusters increases. Though the difference between pointing and alignment angles is significant for the simulation data with $\sigma_\theta/\sigma_\phi = 0°$, the significance lessens as the uncertainty increases. This means that the difference is unlikely to be too large for observationally determined pointing/alignment angles and

Pointing Angle, θ, for separations $0 - 30\,h^{-1}$ Mpc					
Percentage	σ_θ				
in Walls	0°	10°	20°	30°	40°
0	33.72 ± 0.31	35.53 ± 0.30	38.81 ± 0.30	42.20 ± 0.30	44.66 ± 0.31
10	33.83 ± 0.31	35.82 ± 0.30	38.99 ± 0.30	42.34 ± 0.31	44.19 ± 0.30
25	33.94 ± 0.30	35.70 ± 0.29	38.93 ± 0.29	42.23 ± 0.29	44.35 ± 0.30
50	35.59 ± 0.28	37.07 ± 0.28	40.27 ± 0.28	42.84 ± 0.28	44.64 ± 0.28
75	37.13 ± 0.27	38.59 ± 0.27	40.84 ± 0.27	43.30 ± 0.27	44.87 ± 0.27
90	38.15 ± 0.27	39.42 ± 0.27	41.67 ± 0.26	43.75 ± 0.26	45.40 ± 0.26
100	38.44 ± 0.26	39.50 ± 0.26	41.64 ± 0.26	43.84 ± 0.26	45.37 ± 0.26

Pointing Angle, ϕ, for separations $0 - 30\,h^{-1}$ Mpc					
Percentage	σ_ϕ				
in Walls	0°	10°	20°	30°	40°
0	40.49 ± 0.31	41.31 ± 0.31	42.96 ± 0.31	44.37 ± 0.31	45.23 ± 0.31
10	40.53 ± 0.31	41.34 ± 0.30	42.91 ± 0.30	44.54 ± 0.30	44.50 ± 0.30
25	40.83 ± 0.30	41.81 ± 0.30	43.29 ± 0.29	44.97 ± 0.29	45.40 ± 0.29
50	39.27 ± 0.29	40.29 ± 0.28	41.89 ± 0.28	44.03 ± 0.28	45.72 ± 0.28
75	37.03 ± 0.27	38.20 ± 0.27	40.65 ± 0.27	43.46 ± 0.27	44.79 ± 0.27
90	36.42 ± 0.28	37.86 ± 0.27	40.53 ± 0.26	43.09 ± 0.26	45.06 ± 0.26
100	34.44 ± 0.27	36.23 ± 0.26	39.22 ± 0.25	42.18 ± 0.26	44.86 ± 0.25

Table 7.4 The mean pointing and alignment angles with standard error for the cluster samples in Figs. 7.10 and 7.11.

as the errors on the mean angles are likely to be large ($\sim \pm 1°$), it may be quite hard to attach any significance to the result.

However, when compared to the case of a mixed sample of clusters at nodes and in filaments, the pointing angle is much more skewed than the alignment angle (Figs. 7.1 and 7.2) and the mean pointing angle is significantly less than the mean alignment angle (Table 7.1). The opposite is true when the wall clusters form the majority. Hopefully this difference will be detectable in observational surveys of cluster alignment. A clear prediction of the Voronoi foam is that if significant numbers of clusters reside in walls then the mean alignment angle will be much less than the mean pointing angle, whereas if there are no wall clusters, then the opposite is true. In the case where the two angles are similar, then either the observational errors are large (in which case the angles would be close to 45°) or about 75% of clusters reside in walls with a mean angle of $\sim 37°$

(see Table 7.4). If both mean pointing and alignment angles were much less than this and still equal it would seem hard to explain the fact within the context of the Voronoi foam.

Unfortunately, apart from Fong, Stevenson & Shanks (1990), who found no evidence for alignment in either the pointing or alignment angles, no other studies have considered the distribution of the alignment angle. Though it requires no extra data and little extra work to compute the alignment angle as well as the pointing angle, this has not been done, mainly due to the extra uncertainties involved. Calculating the pointing angle for a given cluster pair only requires the knowledge of one of the position angles, whereas calculating the alignment angle requires that both the position angles are known. As the position angle is the biggest source of observational error, this significantly increases the uncertainty in any alignment signal, which is already weak, and may be swamped by these extra errors. Again, the observational difficulties conspire to mimic the desired effect.

It should be noted that the method of assigning major axes to clusters in walls is likely to ensure the largest alignment signals in both pointing and alignment angles. If, for example, random angles were to be assigned to the wall clusters then the mean alignment and pointing angles would both increase towards 45° as the number of wall clusters was increased. For a sample of all wall clusters then the mean angles would be identical to 45° within the errors. Thus the results here should be taken to represent the maximum alignment possible. The only mechanism that could possibly increase the alignment signal would be tidal interaction between close pairs of clusters, though it would be doubtful if this could achieve a significant affect.

It is difficult to compare the mean pointing angle directly with the observed cluster alignment as measured by West (1989b), as he considered all pairs of clusters within the same supercluster, whereas here only nearest neighbour pairs have been included. It may be possible to use some sort of percolation technique similar to that used by West to define a supercluster, but that would require a matching of particle to cluster surface densities to ensure a meaningful result. Even then, as the Voronoi foam does not simulate any physical processes and merely uses the particles (i.e. clusters) as a tracer of the geometric structure, it would be doubtful as to whether the superclusters found bore any resemblance to those in West's survey. Due to these difficulties it was decided not to

pursue this line of inquiry and instead to directly compare the results of the simulations to those of West (1989b), which are listed in Tables 7.2 and 7.3, bearing in mind the differences noted above, along with the fact that the alignment for a sample of nearest neighbour clusters has been shown to be stronger than that of a sample including all pairs within the same supercluster at small separations (§ 7.3.3).

West obtained a mean pointing angle of $38.95°\pm1.57°$ for clusters with $\sigma < 20°$ and separations less than $30\,h^{-1}$ Mpc. For his $\sigma < 10°$ sample he obtained $35.01°\pm1.61°$ for clusters with separations less than $60\,h^{-1}$ Mpc. However, as there are few nearest neighbour pairs ($\lesssim 10$ in almost all cases) for separations greater than $30\,h^{-1}$ Mpc in the simulations, the $\sigma < 10°$ sample is compared directly to the data from the simulations. From Table 7.4 it is apparent that the mean pointing angles are too weak for the cases where wall clusters are in the majority. Although samples with the majority of clusters in filaments have mean pointing angles consistent with West's result for the $\sigma < 10°$ sample, this is only so if $\sigma_\theta \leq 10°$. This assumes very little error in the measured pointing angle and no other source of error. All samples with the majority of clusters in the walls have alignment signals that are too weak to account for the observed alignment in the $\sigma < 10°$ sample.

Considering the $\sigma < 20°$ sample of West, the mean pointing angle of $38.95°\pm1.57°$ is compatible with samples with a majority of clusters in walls only if $\sigma_\theta \leq 10°$, an extremely low value given the uncertainties in the observed position angles in West's survey. For samples with a majority of clusters in filaments the alignment is too weak unless $\sigma_\theta = 20°$. Even this is a low value, unless one considers all the uncertainty to be in the pointing angle, which is unlikely.

Bearing in mind that the alignments presented here for the simulations are likely to be the strongest possible and any modification in the assumptions made is likely to weaken the alignment strength, then the alignment present in the pointing angle seems too weak to account for the observations unless at least 75% of clusters are located in filaments. Even then the signal may well prove to be too weak.

7.5 Discussion of the Observational Evidence

The reason for the lack of clear evidence of cluster alignment is almost certainly due to

the difficulties associated with obtaining an unambiguous measurement of the position angle of a cluster. Position angles for clusters are generally found by considering the brightest n galaxies within a given radius from the nominal cluster centre (usually the brightest galaxy) on a photographic plate. The centre of mass is found and the major axis (and hence position angle) is then defined by the line through the centre which minimises the sum of perpendicular distances of the galaxies to the line (e.g. Binggeli 1982; Rhee & Katgert 1987). As found by Flin (1987), West (1989b) and Ulmer, McMillan & Kowalski (1989), calculations of the position angle for a given cluster vary from author to author by quite large amounts.

In order to reduce this source of error, Flin (1987) took the mean of several different authors' published values. This approach was improved on by West (1989b), who only included clusters with at least three independent measures of the position angle and rejected those with a variance of greater than 20°. Rhee & Katgert (1987) took the approach of including the brightest 100 galaxies in the region of the cluster, as opposed to the brightest 50 (as used by Binggeli 1982). They also determined the positions of the galaxies using an automated procedure based on machine scans of the photographic plates, rather than making the measurements by eye. All three authors found evidence for alignment, the strongest claim being that of West (1989b), who found clear evidence for alignment on scales of up to $30\,h^{-1}$ Mpc and strong evidence on scales of up to $60\,h^{-1}$ Mpc. He also found weak evidence of alignment on scales of $15 - 30\,h^{-1}$ Mpc, comparable to that of Binggeli (1982), for a sample of 59 groups (West 1989a).

Optically determined position angles for clusters suffer from several drawbacks, not least of which is that the luminous matter of galaxies may not be a reliable tracer of the mass distribution within the clusters. Other problems arise from contamination of the cluster by foreground and background galaxies and from the possibility that a rich cluster may be a chance superposition of small clusters or groups along the line of sight. A further problem comes with the arbitrary nature of including either a set number of galaxies or all galaxies within a given radius. Obviously the choice of these parameters will affect the determination of the position angle as, by excluding or including certain galaxies, one can radically alter the position angle.

To avoid these problems Ulmer, McMillan & Kowalski (1989) used the X-ray morphology of 44 clusters to determine the clusters' principal axes, arguing that the hot,

X-ray emitting gas was an equivalent or superior tracer of the mass in the cluster than the galaxies. Though they found no evidence for alignment, their analysis is restricted by their small number statistics. Indeed, small survey sizes are a great problem, as this diminishes the statistical significance of any result. The biggest of the surveys discussed above, that of West (1989b), only contained 84 clusters. A complementary approach was taken by Lambas *et al.* (1990) in an attempt to increase the sample size. They studied the position angle of the brightest cluster galaxy in 204 Abell clusters and found strong evidence that the brightest galaxy pointed towards the neighbouring cluster on scales up to $15\,h^{-1}$ Mpc. It is well established that the brightest galaxy in a cluster tends to be aligned with the cluster's major axis (e.g. see Carter & Metcalfe 1980; Binggeli 1982; Struble & Peebles 1985; Rhee & Katgert 1987) and Lambas *et al.* argued that the evidence showing the brightest galaxy pointing towards the neighbouring cluster was also evidence that the cluster itself was pointing towards its neighbour. Note that by using the galaxy's position angle as an equivalent measure of the cluster position angle, Lambas *et al.* (1990) are introducing a further measurement error that may well account for the weakness of the alignment they observed when compared to the work of West (1989b).

This approach was taken one step further by West (1991), who used the radio axes of 136 radio-loud galaxies and quasars at redshifts greater than 0.5 and found alignment on scales of up to $45\,h^{-1}$ Mpc (in comoving coordinates). Arguing that at these redshifts such galaxies exhibit a tendency to have their radio axes aligned with their optical axes and are likely to be found in the centre of clusters (see West 1991 and references therein), he argued that this was further evidence, albeit at high redshift, for the "Binggeli Effect". Even if this two step argument proves to be false, the evidence still remains that the radio axes are aligned on large scales, suggesting some form of large-scale structure present at those high redshifts.

Two other large surveys have been carried out, but both found no evidence of alignment. Struble & Peebles (1985) used 237 clusters, but their survey has the disadvantage that the position angles may be poorly determined. The major axis of the cluster was measured by eye, using the technique described above and no other measurement of the position angle was used. The measurement procedure was repeated three times per cluster and the mean taken to help eradicate human error, but this still leaves the measurement prone to systematic error. It is hard to tell how accurate any single

measurement of a cluster's position angle is, as it can only be compared to other measurements, which may themselves be highly inaccurate. However, as noted by Struble & Peebles and by Rhee & Katgert (1987), there are significant differences between the determinations of the position angle by Struble & Peebles and Binggeli (1982) where the two samples overlap. Though this does not necessarily mean that the position angles as measured by Struble and Peebles are incorrect, it is certainly a possibility. Also, the angular distribution of cluster position angles, which one would expect to be isotropic regardless of alignment effects, shows some deviation from isotropy (see Struble & Peebles 1985; Lambas *et al.* 1990). This would suggest some sort of systematic error which leaves the position angles of the clusters more likely to adopt a preferential value. The addition of noise to well defined position angles, whether random or systematic can only serve to dilute any signal present (see § 7.4.2). As Struble & Peebles (1985) found alignment at the 1 or 2σ level, it is possible that they detected a weak signal that was swamped by noise caused by poorly defined position angles.

The survey of Fong, Stevenson & Shanks (1990) has 629 groups and clusters taken from COSMOS scans of Schmidt plates. The position angles have been determined by an objective, computerised approach, not dissimilar to that described above. Though this puts the position angles on a more firm footing than say those of Struble & Peebles (1985), it is nonetheless only a single measurement per cluster and still prone to systematic errors arising from the technique involved. The authors also present evidence that the cluster position angles are preferentially aligned with the plate edge. Although they have attempted to allow for this in their analysis, it is still likely to dilute any signal present.

The survey itself could also introduce some errors as it includes groups and clusters regardless of richness. Though one may well expect groups within rich environments to show alignment (see West 1989a), Fong, Stevenson & Shanks (1985) made little attempt to subdivide their sample into richness or environment dependent sub-samples. Thus any signal from aligned rich clusters may well have been swamped by the more numerous, less-rich clusters and groups. Also, as groups have only a few members (minimum membership in the survey was seven) the position angle is more prone to errors of projection and contamination as discussed above, thus further diluting the signal.

A final problem with the survey is that it contains no distance information and so the separations between clusters are their projected separations. This will inevitably lead to a weakening of the "Binggeli Test" as this considers the likelihood of clusters pointing to their nearest neighbours, whereas a two-dimensional catalogue will contain false nearest neighbour pairs arising due to spurious line of sight projections of clusters which are spatially far removed. As such pairs are not true neighbours, one would have no reason to expect any alignment, leading to the dilution of any real alignment signal by pairs of clusters with randomly orientated axes.

Note that these objections to the work of Struble & Peebles (1985) and Fong, Stevenson & Shanks (1990) are speculative and should not be taken as to imply that such signals are present but are being missed. They are merely put forward as a possible reason for the contradictory nature of the various surveys. At the time of writing there is no conclusive evidence as to the reality or otherwise of cluster alignment. Further work needs to be carried out, both in terms of bigger samples and more accurate determination of position angles. It is hoped that the work on automated cluster catalogues from plate measuring machines such as the APM (e.g. Dalton *et al.* 1992 and references therein) and COSMOS (e.g. Nichol *et al.* 1992 and references therein) machine will lead to improvements on both counts, as will the X-ray selection of clusters and X-ray morphology of clusters from the ROSAT mission.

7.6 Conclusions

This chapter constitutes an investigation of cluster alignment within the context of the Voronoi foam model, plus a review of the current observational evidence for and against cluster alignment, the weight of which falls in favour of the phenomenon. There can be no doubt that cluster alignment exists within the framework of the Voronoi foam. What is unknown is the strength of this alignment, something which this chapter has sought to investigate by establishing trends in alignment strength of both pointing and alignment angle with cluster location and cluster environment. The most obvious result is that the pointing angle shows greater anisotropy than does the alignment angle, mainly due to the large signal caused by the filaments pointing exactly at their associated nodes. It has also been shown that the alignment is strongest for mixed samples of nodes and filaments, followed by filaments alone, then nodes.

The main result of this chapter comes from the comparison of cluster alignment in the Voronoi foam with the cluster alignment observed by West (1989b). Though there are many free parameters in the model and the observational data themselves are poor, it has been shown that, despite the strong intrinsic alignment of clusters in the Voronoi foam, the addition of reasonable uncertainties in cluster position angle can lead to distributions of pointing angles similar to those observed.

The main assumption of this chapter is that clusters can reside not only in nodes in the Voronoi foam, but also in walls and filaments. Evidence presented in this chapter suggests that if clusters are confined exclusively to nodes, then the alignment is too weak in comparison to the observed alignment. A similar argument applies if more than 25% of clusters reside in walls. This implies that some clusters must be located in filaments in order for the alignment in the Voronoi foam to match the observed alignments of West (1989b). This is supported by evidence that clusters are located in prolate (hence filamentary) superclusters, though observational evidence for prolate clusters and superclusters need not exclude clusters at nodes, as there is no reason for such clusters to be spherical. Indeed, given that matter flows into them from four preferential axes (§ 7.2.1), one might expect non-spherical clusters to be in the majority.

The evidence presented in § 5.1.4 on cluster and node richness can be used to place limits on the location of clusters. As the cluster number density is an observable quantity, one should be able to use it to fix the node density (set by the length scale, $\tilde{x}$). Using $\tilde{x} = 52\,h^{-1}\,\mathrm{Mpc}$, which is compatible with the normalisations suggested by Chapter 5, this gives a node density of $\sim 4 \times 10^{-5}$ nodes/$h^{-3}\mathrm{Mpc}^3$ (Table 5.4). This is a factor three greater than the observed number density of Abell richness class $R \geq 0$ clusters. Given that most of the surveys detecting alignment (most notably that of West 1989b) use these clusters, this suggests that only rich nodes can be identified as Abell clusters and argues against locating clusters in filaments (which would increase rather than decrease the node density). Using a normalisation of $\tilde{x} = 104\,h^{-1}\,\mathrm{Mpc}$ would reconcile the number densities, but is incompatible with the findings of Chapter 5 and would produce strong alignments on too large a scale to be compatible with observations.

The tentative result of West (1989a) that groups are more strongly aligned than clusters is certainly very exciting, suggesting that the less-rich systems may well reside in filaments alone, leaving rich clusters to inhabit the nodes. The above discussion

suggests that less-rich clusters are also to be found in nodes, which may suggest that groups are left to reside in filaments. However, this still leaves the problem of how the alignment of nodes alone is to account for the strong observed alignment of clusters. While this is not ruled out, it seems unlikely (§ 7.4.4).

While the observational data remain poor and its analysis is restricted to testing the significance of any result, it is difficult to see any further progress being made. However, it is hoped that new, more objective cluster surveys currently underway (e.g. Dalton *et al.* 1992; Nichol *et al.* 1992; and references therein) will lead to the firm establishment of cluster alignment and allow it to become more quantifiable, in which case more concrete predictions can be tested. The biggest step forward would be to allow statistically meaningful subsamples of the data to be taken in order to test for trends of alignment strength with cluster morphology and richness, as well as separation. This would allow some of the speculation of § 7.2 and § 7.4 to be put on a more firm footing.

At the time of writing cluster alignment has yet to become the powerful tool some authors have predicted (e.g. Rhee & Katgert 1987; West 1989a,b), but with larger surveys and more robust results it promises to be a useful predictive tool. Certainly, if the alignment found by Binggeli (1982), Flin (1987), Rhee & Katgert (1987), West (1989a,b) and Lambas *et al.* (1990) proves to be a statistical fluke that goes away with larger surveys, then this will almost certainly rule out the Voronoi foam model. If, on the other hand, it proves to be a real feature as many suspect, then the following predictions can be tested. There should be a trend of decreasing cluster alignment with increasing richness if groups reside in filaments and clusters of varying richness reside in nodes. However, if a significant majority of groups reside in walls then the alignment signal should be significantly stronger for the alignment angle than the pointing angle, whereas this will not be the case if the majority reside in filaments. Taking the reasonable scenario where poor groups reside in walls, rich groups reside in filaments and clusters are found at nodes, then the alignment for the pointing angle will be the strongest for rich groups and for the alignment angle it will be strongest for poor groups. In the meantime it would be interesting to see if similar predictions are made by the various models of large-scale structure formation, which should shed light on the applicability of the Voronoi foam approximation to these various scenarios.

Chapter 8

Conclusions

The aim of this thesis has been to investigate simple models of large-scale structure and to test their validity against a combination of more realistic models and observational data. The results of this investigation can be split into two parts — the use of linear theory to predict the statistical properties of non-linear objects (Chapter 3) and the Voronoi foam model (Chapters 4, 5, 6 and 7), a simple model where space is divided into cells, with galaxies populating the boundaries between cells. Both approaches have proved extremely successful within their limitations.

8.1 Linear Theory and the Adhesion Model

The basic concept of smoothing the linear density field to recover the properties of objects in the non-linear regime was used by Press & Schechter (1974) to obtain a mass function for bound objects which has since proved highly successful. However, carrying out a full test of such an approach has been a difficult process. Numerical simulations generally lack sufficient dynamic range to thoroughly test the theory and comparisons with observations are hampered by the uncertain relation between mass and light (e.g. see § 1.2.3, 1.3.3, 1.4.6). In this thesis, the Press–Schechter mass function, along with the peaks theory modifications of Peacock & Heavens (1990), are compared to those obtained from numerical simulations based on the adhesion model, a fully non-linear extension to the Zel'dovich (1970) approximation of gravitational collapse (§ 2.2). The simulations were carried out in one spatial dimension as here the adhesion model is exact and a sufficiently large range in mass can be covered to allow the linear theory predictions to be thoroughly tested.

Two types of test were applied, statistical tests, such as a comparison of the mass and correlation functions, and direct tests of the underlying assumptions of linear theory. For power-law spectra ($|\delta_k|^2 \propto k^n$), both the Press–Schechter (§ 3.2.1) and peaks theory (§ 3.2.2) mass functions give accurate fits to the data provided that the spectral index lies in the range $-1 < n \leq 3$ (§ 3.3.2). Outside this range the predicted mass function breaks

down completely. Of the two approaches, the peaks theory mass functions provide a better fit to the data, especially at late times. The peaks theory also fares better for low masses where there is a non-power law feature in the power spectrum owing to the artificial cut-off imposed by the initial small-scale smoothing (§ 3.2.1). The peaks theory more accurately reproduces this feature in the mass function, suggesting that, in general, it is a better technique than the Press–Schechter mass function.

Peaks theory (and, implicitly, Press–Schechter) filter the linear density field in order to remove power on scales below the filter scale (equivalent to the mass scale of interest). There is no a priori way of telling what is the "correct" method for such filtering, either in terms of the filter function used, or in terms of the relation between the mass of an object and the filter scale (specified by the variables β and δ_c). Various combinations of these parameters have been tried and it is found that a best fit is obtained using a Gaussian filter with $\beta = 1$ and δ_c (the critical overdensity at which objects are assumed to collapse in linear theory) varied according to the power spectrum, but given approximately by $\delta_c \simeq 1.4^{-(n+1)/2}$. For a given power spectrum, the same values of β and δ_c give a good fit to the data at all epochs.

It has also been shown that, in one dimension, the onset of non-linear effects on the linear part of the perturbation spectrum occurs for lower values of the spectral index than previously thought ($n > 3$ as opposed to $n > 6$) and the validity of the mass function derived from the adhesion model for steep spectra by Kida (1979) has been confirmed (§ 3.3.3). It is also possible to calculate some of the free parameters of Kida's mass function using Gaussian statistics (§ 3.2.4).

When the two-point correlation function of pancake positions in the adhesion model is considered, agreement is less impressive (§ 3.3.4). Peaks theory predicts the correlation function using the statistical properties of the initial density field and provides a good fit to the data from the simulations for a spectral index of $n = -\frac{1}{2}$, but not for a spectral index of $n = 1$. In the former case, the clustering is not significantly affected by dynamical evolution in the density field, but in the latter case it is likely that the discrepancy between the peaks theory and adhesion model correlation functions arises from the latter's consideration of the non-linear evolution of the density field. Thus one may speculate that where there is a significant amount of statistical clustering, peaks theory provides an excellent approximation. However, where statis-

tical clustering is absent, or "anti-clustering" present, the peaks theory is unable to produce an accurate fit to the data.

The direct tests (§ 3.4) were aimed at seeing whether objects form at regions in the smoothed density field where $\delta = \delta_c$, as assumed by linear theory. In one dimension, $\delta_c = 1$ for standard linear theory, whereas peaks theory gives $\delta_c \simeq 1.4^{-(n+1)/2}$ (see above). However, though the vast majority of objects form in regions where $0 < \delta < 1$, supporting the assumption of peaks theory that $\delta_c < 1$, there was no unique value of δ_c supported by the data. The distribution of δ was quite tight though, suggesting that the principle that objects form in regions where the smoothed density field has $\delta \sim \delta_c$ is not radically incorrect. Despite the fact that this underlying assumption of both linear theory and the peaks theory modifications is incorrect in detail, the resulting mass functions are an excellent statistical approximation to the mass functions obtained from the adhesion model simulations, suggesting that the approach of smoothing the linear density field and identifying objects as peaks above some threshold is a valid statistical approach, although it may not be correct in the detailed location of the objects formed.

8.2 The Voronoi Foam

The Voronoi foam is a simple statistical description of the distribution of galaxies in which they are confined to sheets, filaments and clusters, surrounding large voids. The geometrical skeleton of the foam is fully determined by the distribution of the Voronoi nuclei, with each cell (i.e. void) containing a single nucleus. The distribution of galaxies on the geometrical skeleton is not specified by the model, but is usually taken to be random.

In Chapter 5, various statistical measures of the Voronoi foam (the galaxy-galaxy and cluster-cluster two-point correlation function, the angular two-point correlation function for galaxies and the power spectrum of galaxy clustering) were compared with observations. The nuclei were distributed at random, with the particles also distributed in a pseudo-random fashion on the geometrical skeleton (Chapter 4), thus the only free parameter was the characteristic inter-nucleus separation, $\bar{x}$, which sets the physical length scale of the model. It was found that while a normalisation of $40 \lesssim \bar{x} \lesssim 55\, h^{-1}\,\mathrm{Mpc}$ was consistent with the observed spatial correlation function for both galaxies and clusters and provided the correct break scale in comparison with the

angular correlation function and the power spectrum, the Voronoi foam model lacked both small- and large-scale power. This resulted in the *shape* of the clustering spectrum being incorrect — the Voronoi foam produced too sharp a break.

Extensive investigations were carried out to see if this was an artefact of the particle distribution or the restrictions caused by assuming that particles do not inhabit the voids (§ 5.3, 5.4.4, 5.5.5). None of the various methods tried could account for the missing power. That the Voronoi foam predicts too little power on small scales is none too surprising and is no great problem. The model is a very simple prescription of the *large*-scale distribution of matter. The foam provides surfaces on which galaxies are distributed and, in this implementation of the model, galaxies are distributed roughly at random across the walls, hence it should come as no surprise that the Voronoi foam lacks small-scale power, as none is put in by the model over that of particles randomly distributed on a plane. In more realistic circumstances, the particles in the walls would be under the influence of local gravitational forces and hence would cluster on small scales, providing more small-scale power. The more serious problem is the lack of power beyond the break. The break scale itself is set by the transition from intracellular to intercellular clustering. Beyond the break scale, the clustering must reflect the initial distribution of the nuclei, which determines the large-scale properties of the cells. As the nuclei were distributed at random, this probably accounts for the very rapid fall off of power beyond the break. Obviously, this discrepancy cannot be explained by appealing to the action of local gravitational forces. The problem is fundamental to the geometric construction of the Voronoi foam and the initial distribution of the Voronoi nuclei.

In order to see if the missing large-scale power could be supplied, the restriction on the distribution of the nuclei was lifted, allowing non-random distributions to be used. Using the motivation that the Voronoi foam model is a good late-time approximation to the case of a gravitational instability scenario (§ 2.3), Chapter 6 introduces the notion of nuclei as peaks in the gravitational potential, as high peaks would naturally be located in voids, thus making them natural candidates to be identified with nuclei in the Voronoi foam picture. Restricting the gravitational potential to power-law power spectra and choosing peaks above some threshold, ν_c, where ν is the peak height in units of the r.m.s. variance, it was found that the extra large-scale power could be supplied if $0 \lesssim n \lesssim 1$, $0 \lesssim \nu_c \lesssim 1$ and $\tilde{x} \sim 40\,h^{-1}\,\mathrm{Mpc}$ (§ 6.4). An excellent fit to the observations was provided for both the power spectrum and the angular correlation function, though the Voronoi

foam still lacked small-scale power.

The Voronoi foam model was also used to investigate the phenomenon of cluster alignment, that is, the tendency for clusters, separated by tens of Mpc, to point towards each other (Chapter 7). This naturally occurs due to the geometry of the Voronoi foam. In previous Chapters, clusters are assumed to lie solely at nodes, as suggested by number density arguments (§ 5.1, 7.6). However, if this is the case, the resulting alignment may well be too weak to account for the observed alignment strength (§ 7.4.4), though this could be an artifact of the method used to assign cluster principal axes (§ 7.2.1). Allowing clusters to reside in filaments produces a very strong intrinsic alignment (§ 7.3), but the addition of reasonable uncertainties in the clusters' position angles to mimic observational uncertainties/errors can reduce this to levels that are in agreement with observations (§ 7.4.3). The possibility of clusters being located in walls has been examined and found to be unlikely (§ 7.4.5), especially considering the number density constraints.

The Voronoi foam makes the following prediction about the relative strengths of alignment with cluster/group richness, which, due to the small size of present observational surveys, cannot be tested. Assuming that groups and clusters of different richness inhabit different environments (poorest systems in the walls, richest systems at the nodes, with rich groups/poor clusters in the filaments), there will be a peak in alignment strength for the pointing angle for intermediate richness systems and a steady decline for the alignment angle with increasing richness. It is hoped that future, larger, surveys will be able to test this prediction.

8.3 Concluding Remarks

The aim of this thesis has been to investigate the use of simple models of large-scale structure. It has been shown that despite their simplistic approach to the complex underlying physical processes, the two methods studied here have been remarkably successful. The basic approach of linear theory (and of the peaks theory extensions) is to evolve the linear density field into the highly non-linear regime and then smooth it, identifying regions or peaks in the smoothed density field with a given overdensity as bound objects of mass equivalent to the smoothing scale. This provides an excellent approximation to the mass functions of the (fully non-linear) adhesion model. However,

using the sites of these regions as positions for the bound objects meets with limited success. Linear theory fails in some cases to match the correlation functions calculated from the adhesion model, but this is probably due to the complex dynamical evolution of the density field which is not incorporated into the basic linear theory prescription and as such is not too surprising. Even in these cases though, the mass functions still agree. As a general rule, a Gaussian filter should be used, with a "collapse" overdensity, $\delta_c \sim 1.4^{-(n+1)/2}$, for which the mass functions are reliable for $n \leq 3$ and the correlation functions for $n \lesssim 0$. This gives added confidence to those using the Press–Schechter and associated mass functions, which have been widely used in cosmology, despite not having been directly verified by observational evidence.

The basis of the Voronoi foam model is even simpler — on very large-scales luminous matter is assumed to be distributed on the surfaces of a cellular structure, the geometry of which is totally determined by the distribution of the Voronoi nuclei, be they identified with primordial explosions or peaks in the gravitational potential. Despite this simple approach, the Voronoi foam (with clustered nuclei) can provide an excellent match to observations on scales beyond the break scale, which, for the first time, is clearly visible in both the observed angular correlation function and power spectrum of galaxies. This supports the notion that has been growing in the last $10 - 15$ years that the universe is cellular on very large scales. In the Voronoi foam, the break in the clustering spectrum signifies the transition from intercellular clustering to intracellular clustering and thus, if this interpretation is correct, this implies a limit of the scale of inhomogeneities in the distribution of matter in the universe.

Though it is very simplistic in its approach, the Voronoi foam model is not without its physical motivations. As demonstrated in § 2.3, the Voronoi foam provides a good late-time approximation to both the explosion model and to gravitational instability theory. The latter is further supported by the success of the Voronoi foam model in accounting for the observed large-scale distribution of matter when using the peaks in a gravitational potential as nuclei (Chapter 6). However, a more direct test would be helpful as it is not certain that the present day large-scale structure grew via gravitational amplification of initially small perturbations. Ideally, one would like to test the Voronoi foam against N-body simulations using the same gravitational potentials as the initial conditions for both models. This would provide a direct test of the applicability of the Voronoi foam model as a late-time approximation of the gravitational instability

scenario.

If such tests were successful, then one would be in a position to start using more realistic power spectra than the simple power laws used here. By comparison to observations, one might then be able to rule out some of the various theories of large-scale structure formation suggested in § 1.4.1. In theory the various power spectra could be tested by N-body simulations, but these are frequently hampered by the lack of a sufficiently large dynamic range that is required to probe out to scales where the different theories can easily be distinguished (i.e. the break scale and beyond, $\gtrsim 80\,h^{-1}\,\mathrm{Mpc}$). The Voronoi foam on the other hand, if correct, offers an easy and quick method of probing out to very large scales. The simulations presented in this thesis took a few hours to calculate and were carried out using fairly modest computing facilities. However, large-scale clustering is not the only criterion that a theory must satisfy if it is to prove successful and as the Voronoi foam model provides no information on small-scale clustering or topics such as galaxy formation, other tools such as N-body simulations will still play a major role in validating any theory of large-scale structure formation.

It also remains to be seen whether the Voronoi foam is a valid approximation to the various scenarios discussed in § 1.4 that are based on the presence of non-linear seeds. In the case of the explosion model, the answer is almost certainly yes, provided the explosions are of equal strength, but detailed modelling is needed if a more generic explosion scenario is to be tested. Similarly, the Voronoi foam can then be used to test the initial conditions chosen against the observations, though once again, questions such as galaxy formation and small-scale clustering need to be addressed separately. For models seeded by topological defects, the situation is more complex. In cosmic-string scenarios, where the seeds play a dynamic role via string wakes, it seems highly unlikely that a simple model such as the Voronoi foam can provide a reasonable approximation, but for texture-seeded models, where the seeds modify the gravitational potential in some non-linear fashion at early times, it is more likely that the Voronoi foam approximation will be applicable, though once again, more detailed modelling and direct comparisons are necessary.

The Voronoi foam has shown itself to be a useful tool for investigating large-scale structure. As well as being able to account for current observations of large-scale clustering, it can be used to investigate other phenomena, such as cluster alignment, as

has been demonstrated in Chapter 7. The Voronoi foam has also been used to investigate the phenomenon of large-scale periodicity as observed by Broadhurst *et al.* (1990). van de Weygaert (1991) used the Voronoi foam to simulate the Broadhurst *et al.* survey and found periodicities of $100 - 150\,h^{-1}$ Mpc in $\sim 15\%$ of his simulations. However, he used unclustered nuclei and a normalisation of $\bar{x} = 104\,h^{-1}$ Mpc, which has been shown to be incompatible with other measures of large-scale structure (Chapter 5). The introduction of clustered nuclei may be able to account for the observations using a low ($\bar{x} \simeq 45\,h^{-1}$ Mpc) normalisation without appealing to the arguments of de Lapparent, Geller & Huchra (1991) and Ramella, Geller & Huchra (1992), who claim that the Broadhurst *et al.* survey fails to detect roughly 50% of the walls their probe intersects (§ 5.6). Because of the bimodal nature of the distribution of cell sizes, with clusters of small cells being surrounded by larger cells, it may be that our local environment (as probed by redshift surveys such as the CfA) lies in such a cluster, while at the large scales probed by the Broadhurst *et al.* survey, the cellular structure may be dominated by larger cells. Preliminary work suggests that, for a normalisation of $\bar{x} = 45\,h^{-1}$ Mpc, the periodicity is larger than that obtained by van de Weygaert, but smaller than that observed.

To summarise, the Voronoi foam is a useful tool for the investigation of large-scale structure. Its strengths lie in its simplicity, ease of use and ability to quickly simulate large sample volumes. Its main weakness lies in its complete lack of information about small-scale clustering. For this reason it must be seen as a complementary tool to other modelling techniques such as N-body and adhesion model simulations.

References

Abell, G.O., 1958. *Astrophys. J. Suppl.*, **3**, 211.

Albrecht, A. & Steinhardt, P.J., 1982. *Phys. Rev. Lett.*, **48**, 1220.

Alpher, R.A., Bethe, H.A. & Gamow, G., 1948. *Phys. Rev.*, **73**, 803.

Arnott, W.D., Branch, D. & Wheeler, J.C., 1985. *Nature*, **314**, 337.

Arp, H., 1989. *Comm. Astrophys.*, **13**, 57.

Audouze, J. & Trân Thanh Vân, J., 1988. Eds. *Dark Matter*, (Editions Frontieres, Gif-sur-Yvette Cedex).

Bahcall, N.A., 1988. *Ann. Rev. Astron. Astrophys.*, **26**, 631.

Bahcall, N.A. & Soneira, R.M., 1983. *Astrophys. J.*, **270**, 20.

Bahcall, N.A. & Chokshi, A., 1992. *Astrophys. J.*, **385**, L33.

Bardeen, J.M., Bond, J.R., Kaiser, N. & Szalay, A.S., 1986. *Astrophys. J.*, **304**, 15.

Baumgart, D.J. & Fry, J.N., 1991. *Astrophys. J.*, **375**, 25.

Bean, A.J., Efstathiou, G., Ellis, R.S., Peterson, B.A. & Shanks, T. 1983. *Mon. Not. R. astr. Soc.*, **205**, 605.

Bertschinger, E. & Dekel, A., 1989. *Astrophys. J. (Letters)*, **336**, L5.

Bertschinger, E., Dekel, A., Faber, S.M., Dressler, A. & Burstein, D., 1990. *Astrophys. J.*, **364**, 349.

Binggeli, B., 1982. *Astr. Astrophys.*, **107**, 338.

Blumenthal, G.R., Dekel, A. & Primack, J.R., 1988. *Astrophys. J.*, **326**, 539.

Bondi, H. & Gold, T., 1948. *Mon. Not. R. astr. Soc.*, **108**, 252.

Branch, D., 1979. *Mon. Not. R. astr. Soc.*, **186**, 609.

Brandenberger, R.H., 1985. *Rev. Mod. Phys.*, **57**, 1.

Brandenberger, R.H., 1990. in *Physics of the Early Universe*, eds. Peacock, J.A., Heavens, A.F. & Davies A.T. (SUSSP, Edinburgh).

Brandenberger, R.H., 1991. *Physica Scripta*, **T36**, 114.

Broadhurst, T.J., Ellis, R.S., Koo, D.C. & Szalay, A.S., 1990. *Nature*, **343**, 726.

Burgers, J.M., 1940. *Proc. Roy. Neth. Acad. Sci.*, **43**, 2.

Burgers, J.M., 1950a. *Proc. Acad. Amst.*, **53**, 247.

Burgers, J.M., 1950b. *Proc. Acad. Amst.*, **53**, 393.

Burgers, J.M., 1950c. *Proc. Acad. Amst.*, **53**, 718.

Burgers, J.M., 1950d. *Proc. Acad. Amst.*, **53**, 732.

Burgers, J.M., 1972. in *Statistical Models and Turbulence*, eds. Rosenblatt, M. & Van Atta, C. (Springer).

Burgers, J.M., 1974. *The Nonlinear Diffusion Equation*, (Reidel, Dordrecht).

Carter, D. & Metcalfe, N., 1980. *Mon. Not. R. astr. Soc.*, **191**, 325.

Cartwright, D.E. & Longuet-Higgins, M.S., 1956. *Proc. Roy. Soc. A.*, **237**, 212.

Cen, R.V., Ostriker, J.P., Spergel, D.N. & Turok, N., 1991. *Astrophys. J.*, **383**, 1.

Centrella, J.M., Gallagher, J.S., Melott, A. & Bushouse, H.A., 1988. *Astrophys. J.*, **333**, 24.

Chincarini, G. & Rood, H.J., 1979. *Astrophys. J.*, **230**, 648.

Coles, P., 1989. *Mon. Not. R. astr. Soc.*, **238**, 319.

Coles, P., 1990. *Nature*, **346**, 446.

Collins, C.A., Heydon–Dumbleton, N.H. & MacGillivray, H.T., 1988. *Mon. Not. R. astr. Soc.*, **236**, 7P.

Collins, C.A., Nichol, R.C. & Lumsden S.L., 1992. *Mon. Not. R. astr. Soc.*, **254**, 295.

Coleman, S., & Weinberg, E.J., 1973. *Phys. Rev. D*, **7**, 1888.

Couchman, H.M.P. & Carlberg, R.G., 1992. *Astrophys. J.*, in press.

da Costa, L.N., Pellegrini, P.S., Sargent, W.L.W., Tonry, J., Davis M., Meiksin, A., Latham, D.W., Menzies, J.W. & Coulson, I.A., 1988. *Astrophys. J.*, **327**, 544.

da Costa, L.N., Pellegrini, P.S., Willmer, C. & Latham, D.W., 1989. *Astrophys. J.*, **344**, 20.

Dalton, G.B., Efstathiou, G., Maddox, S.J. & Sutherland, W.J., 1992. *Astrophys. J.*, in press.

Davis, M. & Peebles, P.J.E., 1983a. *Ann. Rev. Astron. Astrophys.*, **21**, 109.

Davis, M. & Peebles, P.J.E., 1983b. *Astrophys. J.*, **267**, 465.

Davis, M., Strauss, M.A. & Yahil, A., 1991. *Astrophys. J.*, **372**, 394.

Davis, M., Huchra, J.P., Latham, D.W. & Tonry, J. 1982. *Astrophys. J.*, **253**, 423.

Davis, M., Meiksin, A., Strauss, M.A., da Costa, L.N. & Yahil, A., 1988. *Astrophys. J. (Letters)*, **333**, L9.

de Lapparent, V., Geller, M.J. & Huchra, J.P., 1986. *Astrophys. J. (Letters)*, **302**, L1.

de Lapparent, V., Geller, M.J. & Huchra, J.P., 1988. *Astrophys. J.*, **332**, 44.

de Lapparent, V., Geller, M.J. & Huchra, J.P., 1991. *Astrophys. J.*, **369**, 273.

de Vaucouleurs, G., 1956. *Vistas in Astronomy*, **2**, 1584.

de Vaucouleurs, G., 1958. *Astron. J.*, **63**, 253.

de Vaucouleurs, G., 1982. *Nature*, **299**, 303.

Dicke, R.H., Peebles, P.J.E., Roll, P.G., & Wilkinson, D.T., 1965. *Astrophys. J.*, **142**, 414.

Dirichlet, G.L., 1850. *J. reine angew. Math.*, **40**, 209.

Doroshkevich, A.G. & Kotok, T.V., 1990. *Mon. Not. R. astr. Soc.*, **246**, 10.

Doroshkevich, A.G., Sunyaev, R.A. & Zel'dovich, Ya.B., 1974. in *IAU Symposium 63, Confrontation of Cosmology with Observational Data*, ed. Longair, M.S. (Reidel, Dordrecht).

Einasto, J., Jôeveer M. & Saar, E., 1980. *Mon. Not. R. astr. Soc.*, **193**, 353.

Ellis, J., 1990. in *Physics of the Early Universe*, eds. Peacock, J.A., Heavens, A.F. & Davies A.T. (SUSSP, Edinburgh).

Fairall, A.P., Palumbo, G.G.C., Vettolani, G., Kauffmann, G., Jones, A. & Baiesi-Pillastrini, G., 1990. *Mon. Not. R. astr. Soc.*, **247**, 21P.

Falco, E.E., Gorenstein, M.V. & Shapiro, I.I., 1991. *Astrophys. J.*, **372**, 364.

Fessenko, B.E., 1978. in *IAU Symposium 79, Large-Scale Structure of the Universe*, eds. Longair, M.S. & Einasto, J. (Reidel, Dordrecht).

Field, G.B., Arp, H.C. & Bahcall, J.N., 1973. *The Redshift Controversy.* (W.A. Benjamin, Inc., Reading, Massechusetts).

Flin, P., 1987. *Mon. Not. R. astr. Soc.*, **228**, 941.

Flin, P. & Godlowski, W., 1989. *Sov. Astron. Lett.*, **15**, 374.

Fong, R., Stevenson, P.R.F. & Shanks, T., 1990. *Mon. Not. R. astr. Soc.*, **242**, 146.

Fowler, W.A., 1987. *Qtr. J. R. astr. Soc.*, **28**, 87.

Friedmann, A., 1922. *Z. Phys.*, **10**, 377.

Frenk, C.S., White, S.D.M. & Davis, M., 1983. *Astrophys. J.*, **271**, 417.

Fukugita, M. & Hogan, C.J., 1991. *Astrophys. J. (Letters)*, **368**, L11.

Galeotti, P. & Schramm, D.N., 1990. Eds. *Dark Matter in the Universe* (Kluwer, Dordrecht).

Gamow, G., 1948a. *Phys. Rev.*, **73**, 505.

Gamow, G., 1948b. *Nature*, **162**, 680.

Geller, M.J. & Huchra, J.P., 1988. in *Large Scale Motions in the Universe, Proc. Vatican Conf., 1987*, ed. V.C. Rubin.

Geller, M.J. & Huchra, J.P., 1989. *Science*, **246**, 897.

Gooding, A.K., Spergel, D.N. & Turok, N., 1991. *Astrophys. J. (Letters)*, **372**, L5.

Gott, J.R., Melott, A.L. & Dickinson, M., 1986. *Astrophys. J.*, **306**, 341.

Gramann, M. & Einasto, J., 1992. *Mon. Not. R. astr. Soc.*, **254**, 45.

Gregory, S.A. & Thompson, L.A., 1978. *Nature*, **274**, 450.

Gregory, S.A., Thompson, L.A. & Tifft, W.G., 1981. *Astrophys. J.*, **243**, 411.

Groth, E.J. & Peebles, P.J.E., 1977. *Astrophys. J.*, **217**, 385.

Guth, A.J., 1981. *Phys. Rev. D*, **23**, 347.

Guth, A.J. & Steinhardt, P.J., 1984. *Sci. Am.*, **250**, No. 5, 90.

Gurbatov, S.N. & Saichev, A.I., 1981. *Sov. Phys. JETP*, **53** 347.

Gurbatov, S.N., Saichev, A.I. & Shandarin, S.F., 1985. *Sov. Phys. Dokl.* **30**, 921.

Gurbatov, S.N., Saichev, A.I. & Shandarin, S.F., 1989. *Mon. Not. R. astr. Soc.*, **236**, 385.

Harrison, E.R., 1970. *Phys. Rev. D*, **1**, 2726.

Haynes, M.P. & Giovanelli, R., 1986. *Astrophys. J. (Letters)*, **306**, L5.

Heavens, A., 1991. *Mon. Not. R. astr. Soc.*, **251**, 267.

Hime, A. & Simpson, J.J., 1989. *Phys. Rev. D*, **39**, 1837.

Hime, A. & Jelley, N.A., 1991. *Phys. Lett. B*, **257**, 441.

Hogan, C.J., 1984. *Astrophys. J. (Letters)*, **284**, L1.

Hoell, J. & Priester, W., 1991. *Astr. Astrophys.*, **251**, L23.

Holmberg, E., 1937. *Lund Obs. Ann.*, **6**, 52..

Holmberg, E.B., 1974. *Astr. Astrophys.*, **35**, 121.

Hoyle, F., 1948. *Mon. Not. R. astr. Soc.*, **108**, 372.

Hoyle, F., 1949. *Mon. Not. R. astr. Soc.*, **109**, 365.

Hoyle, F. & Tayler, R.J., 1964. *Nature*, **203**, 1108.

Hubble, E., 1929. *Proc. Nat. Acad. Sci.*, **15**, 168.

Huchra, J.P., Henry, J.P., Postman, M. & Geller, M.J., 1990. *Astrophys. J.*, **365**, 66.

Icke, V., 1984. *Mon. Not. R. astr. Soc.*, **206**, 1P.

Icke, V. & van de Weygaert, R., 1987. *Astr. Astrophys.*, **184**, 16.

Ikeuchi, S., 1981. *Publs astro. Soc. Japan*, **33**, 211.

Ikeuchi, S. & Turner, E.L., 1991. *Mon. Not. R. astr. Soc.*, **250**, 519.

Jacoby, G.H., Ciardullo, R. & Ford, H., 1990. *Astrophys. J.*, **356**, 332.

Jôeveer, M. & Einasto, J., 1978. in *IAU Symposium 79, Large-Scale Structure of the*

Universe, eds. Longair, M.S. & Einasto, J. (Reidel, Dordrecht).

Jôeveer, M., Einasto, J. & Tago, E., 1978. *Mon. Not. R. astr. Soc.*, **185**, 357.

Kaiser, N., 1984. *Astrophys. J. (Letters)*, **284**, L9.

Kiang, T., 1966. *Zeitschr. f. Astrophys.*, **64**, 433.

Kibble, T.W.B., 1976. *J. Phys. A*, **9**, 1387.

Kida, S., 1979. *J. Fluid Mech.*, **93**, 337.

Kirshner, R.P., Oemler, A., Schechter, P.L. & Schectman, S.A., 1981. *Astrophys. J. (Letters)*, **248**, L57.

Kirshner, R.P., Oemler, A., Schechter, P.L. & Schectman, S.A., 1987. *Astrophys. J.*, **314**, 493.

Klypin, A.A., & Kopylov, A.I., 1983. *Sov. Astron. Lett.*, **9**, 41.

Kochanek, C.S., 1991. *Astrophys. J.*, **382**, 58.

Kofman, L.A., Pogosyan, D. & Shandarin, S.F., 1990. *Mon. Not. R. astr. Soc.*, **242**, 200.

Lahav, O., Edge, A.C., Fabian, A.C. & Putney, A., 1989. *Mon. Not. R. astr. Soc.*, **238**, 881.

Lambas, D.G., Nicotra, M., Muriel, H. & Ruiz, L., 1990. *Astron. J.*, **100**, 1006.

Lemaître, G., 1927. *Ann. Soc. Sci. Bruxelles*, **47A**, 49.

Linde, A.D., 1982. *Phys. Lett. B.*, **108**, 389.

Linde, A.D., 1987. *Physics Today*, **40**, No. 9, 61.

Longair, M.S., 1974. in *IAU Symposium 63, Confrontation of Cosmology with Observational Data*, ed. Longair, M.S. (Reidel, Dordrecht).

Longair, M.S., 1978. in *IAU Symposium 79, Large-Scale Structure of the Universe*, eds. Longair, M.S. & Einasto, J. (Reidel, Dordrecht).

Lubin, P., Villela, T., Epstein, G. & Smoot, G., 1985. *Astrophys. J. (Letters)*, **298**, L1.

Luke, Y.L., 1965. in *Handbook of Mathematical Functions*, eds. Abramowitz, M. & Stegun, I.A. (National Bureau of Standards, Washington).

Lumsden, S.L., Heavens, A.F. & Peacock, J.A., 1989. *Mon. Not. R. astr. Soc.*, **238**, 293.

Maddox, S.J., Efstathiou, G., Sutherland, W.J. & Loveday, J., 1990. *Mon. Not. R. astr. Soc.*, **242**, 43P.

Martel, H., 1990. in *Dark Matter in the Universe*, eds. Galleotti, P. & Schramm, D.N.

(Kluwer, Dordrecht).

Matsuda, T. & Shima, E., 1984. *Prog. theor. Phys.*, **71**, 855.

Melott, A.L., 1983. *Mon. Not. R. astr. Soc.*, **202**, 196.

Melott, A.L., 1987. *Mon. Not. R. astr. Soc.*, **228**, 1001.

Meyering, J.L., 1953. *Philips Res. Rept.*, **8**, 270.

Miles, R.E., 1970. *Math. Biosci.*, **6**, 85.

Møller, J., 1989. *Adv. Appl. Prob.*, **21**, 37.

More, J.G., Heavens, A.F. & Wilson, M.J., 1990. *Mon. Not. R. astr. Soc.*, **243**, 413.

Nichol, R.C., Collins, C.A., Guzzo, L. & Lumsden, S.L., 1992. *Mon. Not. R. astr. Soc.*, **255**, 21P.

Nusser, A. & Dekel, A., 1990. *Astrophys. J.*, **362**, 14.

Nusser, A., Dekel, A., Bertschinger, E. & Blumenthal, G.R., 1991. *Astrophys. J.*, **379**, 6.

Olver, F.W.J., 1965. in *Handbook of Mathematical Functions*, eds. Abramowitz, M. & Stegun, I.A. (National Bureau of Standards, Washington).

Oort, J.H., 1983. *Ann. Rev. Astron. Astrophys.*, **21**, 373.

Ostriker, J.P. & Cowie L.L., 1981. *Astrophys. J.*, **243**, L127.

Park, C., 1990. *Mon. Not. R. astr. Soc.*, **242**, 59P.

Park, C. & Gott, J.R., 1991. *Mon. Not. R. astr. Soc.*, **249**, 288.

Park, C., Spergel, D.N. & Turok, N., 1991. *Astrophys. J. (Letters)*, **372**, L53.

Parker, Q.A., 1992. in *Digital Optical Sky Surveys*, eds. MacGillivray, H.T. & Thompson, E.B. (Kluwer, Dordrecht).

Peacock, J.A., 1991. *Mon. Not. R. astr. Soc.*, **253**, 1P.

Peacock, J.A. & Heavens, A.F., 1985. *Mon. Not. R. astr. Soc.*, **217**, 805.

Peacock, J.A. & Heavens, A.F., 1990. *Mon. Not. R. astr. Soc.*, **243**, 133.

Peacock, J.A. & Nicholson, D., 1991. *Mon. Not. R. astr. Soc.*, **253**, 307.

Peacock, J.A. & West, M.J., 1992. In preparation

Peccei, R.D. & Quinn, H.R., 1977a. *Phys. Rev. Lett.*, **38**, 1440.

Peccei, R.D. & Quinn, H.R., 1977b. *Phys. Rev. D*, **16**, 1791.

Peebles, P.J.E., 1973. *Astrophys. J.*, **185**, 413.

Peebles, P.J.E., 1980. *The Large Scale Structure of the Universe*, (Princeton University Press).

Peebles, P.J.E & Dicke, R.H., 1968. *Astrophys. J.*, **159**, 891.

Penzias, A.A. & Wilson, R.W., 1965. *Astrophys. J.*, **142**, 419.

Pellegrini, P.S., Willmer, C.N.A., da Costa, N. & Santiago, B.X., 1990. *Astrophys. J.*, **350**, 95.

Picard, A., 1991a. *Astrophys. J. (Letters)*, **368**, L7.

Picard, A., 1991b. *Astron. J.*, **102**, 445.

Pierre, M., Shaver, P.A. & Iovino, A., 1988. *Astr. Astrophys.*, **197**, L3.

Postman, M., Geller, M.J. & Huchra, J.P., 1986. *Astron. J.*, **91**, 1267.

Postman, M., Huchra, J.P. & Geller, M.J., 1992. *Astrophys. J.*, **384**, 404.

Press, W.H. & Schechter, P., 1974. *Astrophys. J.*, **187**, 425.

Prestage, R.M. & Peacock, J.A., 1988. *Mon. Not. R. astr. Soc.*, **230**, 131.

Ramella, M., Geller, M.J. & Huchra, J.P., 1992. *Astrophys. J.*, **384**, 396.

Refsdal, S., 1966. *Mon. Not. R. astr. Soc.*, **132**, 101.

Reiz, A., 1941. *Lund Obs. Ann.*, **9**, 65.

Rhee, G., 1991. *Nature*, **350**, 211.

Rhee, G. & Katgert, P., 1987. *Astr. Astrophys.*, **183**, 217.

Roberts, D.H., Lehár, J., Hewitt, J.N. & Burke, B.F., 1991. *Nature*, **352**, 43.

Rowan-Robinson, M., 1985. *The Cosmological Distance Ladder.* (Freeman, New York.)

Sadoulet, B., 1990. in *Dark Matter in the Universe*, eds. Galleotti, P. & Schramm, D.N. (Kluwer, Dordrecht).

Sandage, A., & Tammann, G.A. 1990. *Astrophys. J.*, **365**, 1.

Saunders, W., Frenk, C., Rowan–Robinson, M., Efstathiou, G., Lawrence, A., Kaiser, N., Ellis R., Crawford, J., Xia, X. & Parry, I., 1991. *Nature*, **349**, 32.

Schmidt, M., 1972. *Nature*, **240**, 399.

Schmidt, M., 1978. in *IAU Symposium 79, Large-Scale Structure of the Universe*, eds. Longair, M.S. & Einasto, J. (Reidel, Dordrecht).

Schramm, D.N., 1982. in *The Big Bang and Element Creation*, ed. Lynden-Bell, D. (The Royal Society, London).

Schramm, D., 1990. in *Dark Matter in the Universe*, eds. Galleotti, P. & Schramm, D.N. (Kluwer, Dordrecht).

Schramm, D., 1991. in *Physical Cosmology*, eds. Blanchard, A., Celnikier, L., Lachièze-Rey, M. & Trân Thanh Vân, J. (Editions Frontieres, Gif-sur-Yvette Cedex).

Shandarin, S.F., 1987. in *IAU Symposium 130, Evolution of Large-Scale Structures in the Universe*, eds. Audouze J. & Szalay A. (Reidel, Dordrecht).

Shanks, T., Fong, R., Ellis, R.S. & MacGillivray, H.T., 1980. *Mon. Not. R. astr. Soc.*, **192**, 209.

Shanks, T., Hale–Sutton, D., Fong, R., Metcalfe, N., 1989. *Mon. Not. R. astr. Soc.*, **237**, 589.

Shanks, T., Bean, A.J., Efstathiou, G., Ellis, R.S., Fong, R. & Peterson, B.A., 1983. *Astrophys. J.*, **274**, 529.

Silk, J., 1987. in *A Unified View of the Macro- and the Micro-Cosmos*, eds. De Rújula, A., Nanopoulos, D.V. & Shaver, P.A. (World Scientific, Singapore).

Simpson, J.J., 1985. *Phys. Rev. Lett.*, **54**, 1891.

Simpson, J.J. & Hime, A., 1989. *Phys. Rev. D*, **39**, 1825.

Soneira, R.M. & Peebles, P.J.E., 1977. *Astrophys. J.*, **211**, 1.

Spiro, M., 1991. in *Physical Cosmology*, eds. Blanchard, A., Celnikier, L., Lachièze-Rey, M. & Trân Thanh Vân, J. (Editions Frontieres, Gif-sur-Yvette Cedex).

Stevenson, P.R.F., Shanks, T., Fong, R. & MacGillivray, H.T., 1985. *Mon. Not. R. astr. Soc.*, **213**, 953.

Stoyan, D., Kendall, W.S. & Mecke, J., 1987. *Stochastic Geometry and Its Applications*, Akademie–Verlag, Berlin.

Strauss, M.A. & Davis, M., 1988. in *Lecture Notes in Physics*, Vol. **297**, *Comets to Cosmology*, ed. Lawrence, A. (Springer–Verlag, Berlin).

Struble, M.F. & Peebles, P.J.E., 1985. *Astron. J.*, **90**, 583.

Sutherland W.J., 1988. *Mon. Not. R. astr. Soc.*, **234**, 159.

Sutherland, W.J. & Efstathiou, G., 1991. *Mon. Not. R. astr. Soc.*, **248**, 159.

Tago, E., Einasto, J. & Saar, E., 1984. *Mon. Not. R. astr. Soc.*, **206**, 559.

Tammann, G.A. & Sandage, A., 1985. *Astrophys. J.*, **294**, 106.

Tammann, G.A. & Leibundgut, B., 1990. *Astr. Astrophys.*, **236**, 9.

Tarenghi, M., Chincarini, G., Rood, H.J. & Thompson, L.A., 1980. *Astrophys. J.*, **235**, 724.

Tarenghi, M., Tifft, W.G., Chincarini, G., Rood, H.J. & Thompson, L.A., 1979. *Astrophys. J.*, **234**, 793.

Tatsumi, T., 1969. *Phys. Fluids*, **12**, II-258.

Tatsumi, T. & Kida, S., 1972. *J. Fluid Mech.*, **55**, 659.

Tifft, W.G. & Gregory, S.A., 1978. in *IAU Symposium 79, Large-Scale Structure of the Universe*, eds. Longair, M.S. & Einasto, J. (Reidel, Dordrecht).

Tonry, J.L., 1991. *Astrophys. J. (Letters)*, **373**, L1.

Tully, R.B., 1982. *Astrophys. J.*, **257**, 389.

Tully, R.B., 1986. *Astrophys. J.*, **303**, 25.

Turok, N., 1989. *Phys. Rev. Lett.*, **63**, 2625.

Turok, N., 1991. in *The Birth and Evolution of Our Universe*, eds. Nilsson, J.S., Gustafsson, & Skagerstam B.-S. (*Physica Scripta*, **T36**, 135.).

Ulmer, M.P., McMillan, S.L.W. & Kowalski, M.P. 1989. *Astrophys. J.*, **338**, 711.

van de Weygaert, R., 1991. *Mon. Not. R. astr. Soc.*, **249**, 159.

van de Weygaert, R. & Icke, V., 1989. *Astr. Astrophys.*, **213**, 1.

Visvanathan, N., 1990. *Aust. J. Phys.*, **43**, 189.

Voronoi, G., 1908. *J. reine angew. Math.*, **134**, 198.

Webster, A.S., 1976a. *Mon. Not. R. astr. Soc.*, **175**, 61.

Webster, A.S., 1976b. *Mon. Not. R. astr. Soc.*, **175**, 71.

Webster, A.S., 1977. *Mon. Not. R. astr. Soc.*, **179**, 511.

Webster, A.S. & Pearson, T.J., 1977. *Mon. Not. R. astr. Soc.*, **179**, 517.

Weinberg, D.H., 1989. *Ph.D. Thesis* (University of Princeton).

Weinberg, D.H., 1992. *Mon. Not. R. astr. Soc.*, **254**, 315.

Weinberg, D.H. & Gunn J.E., 1990a. *Astrophys. J.*, **352**, L25.

Weinberg, D.H. & Gunn J.E., 1990b. *Mon. Not. R. astr. Soc.*, **247**, 260.

Weinberg, D.H., Ostriker, J.P. & Dekel, A., 1989. *Astrophys. J.*, **336**, 9.

Weinberg, S., 1983. *The First Three Minutes* (Fontana, London).

West, M.J., 1989a. *Astrophys. J.*, **344**, 535.

West, M.J., 1989b. *Astrophys. J.*, **347**, 610.

West, M.J., 1991. *Astrophys. J.*, **379**, 19.

West, M.J. & van den Bergh, S., 1991. *Astrophys. J.*, **373**, 1.

West, M.J., Weinberg, D.H. & Dekel, A., 1990. *Astrophys. J.*, **353**, 329.

West, M.J., Villumsen, J.V. & Dekel, A., 1991. *Astrophys. J.*, **369**, 287.

White, S.D.M., 1990. in *Physics of the Early Universe*, eds. Peacock, J.A., Heavens, A.F. & Davies A.T. (SUSSP, Edinburgh).

White, S.D.M., Frenk, C.S. & Davis, M., 1983. *Astrophys. J. (Letters)*, **274**, L1.

White, S.D.M., Frenk, C.S., Davies, M. & Efstathiou, G., 1987. *Astrophys. J.*, **313**, 505.

Willson, L.A., Bowen, G.H. & Stuck–Marcell, C., 1987. *Comm. Astrophys.*, **12**, 17.

Winget, D.E., Hansen, C.J., Leibert, J., van Horn, H.M., Fontaine, G., Nather, R.E., Kepler, S.O. & Lamb, D.Q., 1987. *Astrophys. J. (Letters)*, **315**, L77.

Yahil, A., Strauss, M.A., Davis, M. & Huchra, J.P., 1991. *Astrophys. J.*, **372**, 380.

Yates, M.G., Miller, L. & Peacock, J.A., 1989. *Mon. Not. R. astr. Soc.*, **240**, 129.

Yu, J.T. & Peebles, P.J.E., 1969. *Astrophys. J.*, **158**, 103.

Yuan, W., Centrella, J.M. & Norman, M.L., 1991. *Astrophys. J. (Letters)*, **376**, L29.

Zel'dovich, Ya. B., 1970. *Astron. Astrophys.*, **5**, 84.

Zel'dovich, Ya. B., 1972. *Mon. Not. R. astr. Soc.*, **160**, 1P.

Zel'dovich, Ya. B., 1978. in *IAU Symposium 79, Large-Scale Structure of the Universe*, eds. Longair, M.S. & Einasto, J. (Reidel, Dordrecht).

Zeng, N. & White, S.D.M., 1991. *Astrophys. J.*, **374**, 1.

Appendix A

The Newtonian Approximation

This appendix derives some of the basic equations governing the evolution of the universe that are drawn upon in the main body of the text. Rather than using the full theory of general relativity, the results shall be derived from the Newtonian theory of gravity, which is not only more intuitive, but gives the same results as the full general relativistic treatment.

A.1 The Dynamics of the Universe

Though it is possible to derive the equations governing the dynamic evolution of the universe via a full general relativistic treatment, it is possible to recover the same result from considering an approximation to the full case using Newtonian gravity. The following analysis is valid for a matter-dominated universe.

Consider a very large cloud of gas (or galaxies), of size much greater than an individual galaxy, but much less than the present horizon, which is isotropic, homogeneous and undergoing a Hubble-type expansion. The acceleration of a galaxy of mass m at a distance r from some observer is determined only by the mass inside the sphere of radius r, centred around the observer (Birkhoff's theorem).

$$m\ddot{r} = -\left(\frac{4\pi}{3}\rho r^3\right) Gm/r^2, \tag{A.1}$$

where ρ is the mean density of the cloud. However, as the cloud is undergoing expansion, $\rho \propto 1/r^3$. Denoting the present epoch by the subscript $_0$,

$$\frac{\rho}{\rho_0} = \frac{r_0^3}{r^3}, \tag{A.2}$$

which gives

$$\ddot{r} = -\frac{4\pi}{3}\rho_0 G r_0^3/r^2. \tag{A.3}$$

Integrating leads to

$$\dot{r}^2 - \frac{8\pi}{3}\rho_0 G r_0^3/r = \kappa, \tag{A.4}$$

where κ is a constant. This is no more than an energy equation, Kinetic Energy + Potential Energy = Constant. Remarkably, this solution is recovered from the full General Relativistic treatment (provided the cosmological constant, Λ, is zero — see § A.4), which also gives the constant, which is determined by the curvature of space. However, a detailed knowledge of the constant is not required for the following discussion.

Defining the scale factor, a, to be

$$a = r/r_0, \tag{A.5}$$

and the Hubble constant (see equation 1.1) to be

$$H = \dot{r}/r = \dot{a}/a, \tag{A.6}$$

gives

$$\begin{aligned} \frac{\dot{r}^2}{r^2} &= \frac{8\pi}{3}\rho_0 G r_0^3/r^3 - \kappa/r^2, \\ H^2 &= \frac{8\pi}{3}\rho G - \kappa/r^2. \end{aligned} \tag{A.7}$$

As the universe expands, so $\rho \to 0$, thus equation (A.7) is governed by κ/r^2. There are three distinct cases.

- $\kappa > 0$: As $\rho \to 0$, there comes a point where $\frac{8\pi}{3}\rho G - \kappa/r^2 = 0$, thus $H^2 = 0$, implying $\dot{a} = 0$. Thus the universe ceases in its expansion. However, because the

acceleration is always negative (equation A.1), the universe immediately begins to contract, the scale factor decreases in size and the density increases. Thus the universe has a definite maximum size and minimum density. This leads to a closed, finite universe. Space-time is said to be positively curved.

- $\kappa < 0$: As $\rho \to 0$, κ is always non-zero, thus H^2 never approaches zero and the expansion is continuous. The universe is then infinite and open. Space-time is said to be negatively curved.

- $\kappa = 0$: As $\rho \to 0$, so $H^2 \to 0$, but only asymptotically. Thus expansion will eventually cease, but only at infinity. Hence the universe is still infinite. Space-time is said to be flat.

The last case, that of a flat universe, introduces the notion of a critical density. For $\kappa = 0$, equation (A.7) gives

$$\rho_c = \frac{3H^2}{8\pi G}. \tag{A.8}$$

The density is often expressed as the dimensionless ratio

$$\Omega = \rho/\rho_c. \tag{A.9}$$

In general relativity the curvature of space-time is linked to its mass content and, though it is not apparent from equation (A.7), the value of κ is dependent on the value of ρ. Thus for $\Omega < 1$ (i.e. $\rho < \rho_c$), $\kappa < 0$ and the universe is open and for $\Omega > 1$ (i.e. $\rho > \rho_c$), $\kappa > 0$ and the universe is closed.

A.2 H and Ω as Functions of Redshift

It is convenient to measure time in an observable quantity, namely redshift. The redshift, z, of an object is given by the wavelength shift :

$$\frac{\lambda_0}{\lambda} = 1 + z, \tag{A.10}$$

where λ_0 is the observed wavelength and λ is the emitted wavelength. Considering the redshift to be a result of the expansion of the universe (i.e. the light has been "stretched" on its journey from emission to the present day) the ratio of wavelengths is just the ratio of scale factors at time of observation and emission, i.e.

$$\frac{\lambda_0}{\lambda} = \frac{a_0}{a}. \tag{A.11}$$

As $a_0 = 1$ by definition (equation A.5), this gives

$$\frac{1}{a} = 1 + z. \tag{A.12}$$

One may recast equation (A.7) as

$$H^2 = \frac{8\pi}{3}\rho G - \frac{\kappa}{a^2}. \tag{A.13}$$

This becomes

$$H^2 = \frac{8\pi}{3}\frac{\rho_0}{a^3}G - \frac{\kappa}{a^2} \tag{A.14}$$

and, from equation (A.8),

$$H^2 = \frac{\rho_0}{\rho_c}H_0^2(1+z)^3 - \kappa(1+z)^2. \tag{A.15}$$

However, from equation (A.14),

$$\frac{\kappa}{a_0^2} = H_0^2 - \frac{8\pi}{3}\frac{\rho_0}{a_0^3}G, \tag{A.16}$$

and, as $a_0 = 1$, this simplifies to

$$\kappa = -H_0^2(1 - \Omega_0), \tag{A.17}$$

and substitution in equation (A.15) leads to

$$H = H_0^2(1+z)^2[1+z\Omega_0]. \tag{A.18}$$

Similarly, one may express Ω as a function of redshift :

$$\begin{aligned} \frac{\Omega}{\Omega_0} &= \left(\frac{\rho}{\rho_c}\right)\left(\frac{\rho_{c_0}}{\rho_0}\right) = \left(\frac{\rho}{\rho_0}\right)\left(\frac{\rho_{c_0}}{\rho_c}\right) \\ &= (1+z)^3\left(\frac{8\pi G}{3H^2}\right)\left(\frac{3H_0^2}{8\pi G}\right). \end{aligned} \tag{A.19}$$

From equation (A.18), $H_0^2/H^2 = (1+z)^{-2}(1+z\Omega_0)^{-1}$, giving

$$\Omega = \Omega_0(1+z)/(1+z\Omega_0). \tag{A.20}$$

A.3 The Age of the Universe

The age of the universe, t_0, is given by

$$t_0 = \int_0^{t_0} dt = \int_0^{a_0} \frac{da}{\dot{a}}. \tag{A.21}$$

From equation (A.4)

$$\dot{a} = \left(\frac{H_0^2\Omega_0 a_0^3}{a} + \kappa\right)^{1/2}, \tag{A.22}$$

where κ is given by equation (A.17). With $a_0 = 1$, this gives

$$t_0 = \int_0^1 \frac{da}{H_0(\Omega_0/a + 1 - \Omega_0)^{1/2}}. \tag{A.23}$$

For $\Omega_0 = 0$, this simplifies to

$$t_0 = H_0^{-1} \tag{A.24}$$

and, for $\Omega_0 = 1$,

$$t_0 = \frac{2}{3} H_0^{-1}. \tag{A.25}$$

Equation (A.23) can be solved for $0 < \Omega_0 < 1$ by putting

$$a = \frac{\Omega_0}{1 - \Omega_0} \sinh^2 \theta, \tag{A.26}$$

which gives

$$t_0 = \frac{2\Omega_0}{H_0 (1 - \Omega_0)^{3/2}} \int_0^{\theta_0} \sinh^2 \theta d\theta. \tag{A.27}$$

Integrating

$$t_0 = \frac{\Omega_0}{H_0 (1 - \Omega_0)^{3/2}} (\sinh \theta_0 \cosh \theta_0 - \theta_0), \tag{A.28}$$

where θ_0 is given by $\sinh^{-1}[(1 - \Omega_0)/\Omega_0)^{1/2}]$.

Similarly for $\Omega_0 > 1$,

$$a = \frac{\Omega_0}{\Omega_0 - 1} \sin^2 \theta, \tag{A.29}$$

which gives

$$t_0 = \frac{2\Omega_0}{H_0 (\Omega_0 - 1)^{3/2}} \int_0^{\theta_0} \sin^2 \theta d\theta. \tag{A.30}$$

Integrating

$$t_0 = \frac{\Omega_0}{H_0 (\Omega_0 - 1)^{3/2}} (\sin \theta_0 \cos \theta_0 - \theta_0), \tag{A.31}$$

where θ_0 is given by $\sin^{-1}[(\Omega_0 - 1)/\Omega_0)^{1/2}]$.

Both these functions (equations A.28 and A.31) are given by the excellent approximation,

$$t_0 = H_0^{-1}\left(1 + \frac{\Omega_0^{0.6}}{2}\right)^{-1}. \tag{A.32}$$

Note that as equation (A.7) is only valid for the matter-dominated regime, the integral in equation (A.21) should be from $t \approx t_{\rm eq}$, the epoch of matter–radiation equality, with another integral from t_0 to $t_{\rm eq}$ which is valid for the radiation-dominated regime. However, as $t_{\rm eq} \sim 10^6$ years and $t_0 \sim 10^{10}$ years, this does not introduce a serious error in the calculation.

A.4 The Cosmological Constant

The cosmological constant was introduced by Einstein to accommodate his theoretical preference for a static universe. Though it was later shown that the universe was expanding, and hence a static solution was not required, the cosmological constant is nonetheless an integral part of the general solution for the field equations. Like the general cosmological equation (A.7), the cosmological constant can be introduced via the Newtonian approximation as well as the full general relativistic theory. The introduction of the cosmological constant, Λ, introduces an extra term into Poisson's equation, namely

$$\nabla^2\phi + c^2\Lambda = 4\pi G\rho, \tag{A.33}$$

where c is the speed of light. Note that this term (Λ is positive) acts in the opposite sense to that of matter, thus the introduction of the cosmological constant introduces an "repulsive" force between matter. In the language of general relativity, space is curved in the absence of matter. This modifies equation (A.7) to

$$\ddot{a} = -\frac{4\pi}{3}\rho G a + \frac{1}{3}c^2\Lambda a \tag{A.34}$$

and, proceeding as before,

$$H^2 = -\frac{8\pi}{3}\rho G + \frac{1}{3}c^2\Lambda - \kappa/a^2. \tag{A.35}$$

Again, the cosmological constant can be seen to be acting in the opposite sense to that of matter. The presence of the cosmological constant has important implications as to whether the universe is closed or not. If $\Lambda > 0$ and $\kappa \leq 0$, then the universe will be open as H^2 can never reach zero. Only if $\kappa > 0$ can the universe be closed. The introduction of a cosmological constant also increases the age of the universe (§ 1.2.4). Note that the cosmological constant must be extremely small as otherwise its effect in equation (A.33) would be noticed locally. As it is, Newtonian gravity is an excellent approximation on local scales (where "local" is the solar system, the largest scale that Newtonian gravity has been tested).

The effect of the cosmological constant upon the physical parameters is best seen in the case of the deceleration parameter, q. This is defined as

$$q = -\frac{dH}{dt} = \frac{a\ddot{a}}{\dot{a}^2}. \tag{A.36}$$

Substituting for $\ddot{a}$ from equation (A.34) gives

$$\begin{aligned} q &= \left(\frac{4\pi}{3}G\rho\right)\frac{a^2}{\dot{a}^2} + \left(\frac{c^2\Lambda}{3}\right)\frac{a^2}{\dot{a}^2} \\ q &= \frac{4\pi}{3}G\rho/H^2 + \frac{c^2\Lambda}{3H^2}, \end{aligned} \tag{A.37}$$

but $\rho_c = 3H^2/8\pi G$, giving

$$q = \frac{1}{2}\Omega - \frac{c^2\Lambda}{3H^2}. \tag{A.38}$$

Again, this serves to reinforce the notion of the cosmological constant as a repulsive force that slows down the deceleration of the general expansion. Note that it is possible (*in principle*) to use the deceleration parameter as a test for Λ as q_0 can in principle be

determined from dynamics and Ω_0 from measurements of the density. In practice, difficulties in measuring both q_0 and Ω_0 (see § 1.2.3) make a determination of Λ impossible.

Appendix B

Linear Perturbation Theory

This appendix derives the equations governing the growth of density perturbations under linear perturbation theory. The crucial assumption is that the perturbations are small compared to the mean values, thus allowing all second and higher order terms to be ignored. The equations are solved for both the matter and radiation dominated regimes.

B.1 Matter-Dominated Regime

Treating the universe as an ideal fluid, the following fluid dynamics equations are required.

$$\begin{aligned} \frac{D\mathbf{v}}{Dt} &= -\frac{\nabla P}{\rho} - \nabla\phi && \text{(Euler's Equation)} \\ \frac{D\rho}{Dt} &= -\rho(\nabla\cdot\mathbf{v}) && \text{(Mass Conservation)} \\ \nabla^2\phi &= 4\pi G\rho && \text{(Poisson's Equation)} \end{aligned} \tag{B.1}$$

where ρ is the density, P the pressure, ϕ the gravitational potential, $\mathbf{v}$ the proper velocity and D/Dt the comoving derivative [$\equiv \partial/\partial t + (\mathbf{v}\cdot\nabla)$].

The equations can be linearised by assuming small perturbations to the mean quantities, i.e.

$$\begin{aligned} \rho &= \bar{\rho} + \delta\rho, \\ P &= \bar{P} + \delta P, \\ \phi &= \bar{\phi} + \delta\phi, \\ \mathbf{v} &= \bar{\mathbf{v}} + \delta\mathbf{v}. \end{aligned} \tag{B.2}$$

Noting that for the condition of homogeneity to be satisfied,

$$\nabla\bar{\rho} = \mathbf{0} \qquad \nabla\bar{P} = \mathbf{0}, \tag{B.3}$$

one can substitute the above expressions (equation B.2) into Euler's equation (B.1), giving

$$\frac{D(\mathbf{v}+\delta\mathbf{v})}{Dt} = \frac{1-\delta\rho/\bar{\rho}}{\bar{\rho}}\left[(\nabla\bar{P})+(\nabla\delta P)\right] - \nabla\bar{\phi} - \nabla\delta\phi. \tag{B.4}$$

Expanding the D/Dt notation gives

$$\frac{D(\mathbf{v}+\delta\mathbf{v})}{Dt} = \dot{\delta\mathbf{v}} + (\bar{\mathbf{v}}\cdot\nabla)\delta\mathbf{v} + (\delta\mathbf{v}\cdot\nabla)\bar{\mathbf{v}} + (\delta\mathbf{v}\cdot\nabla)\delta\mathbf{v} + (\bar{\mathbf{v}}\cdot\nabla)\bar{\mathbf{v}} + \dot{\bar{\mathbf{v}}}, \tag{B.5}$$

where the dot signifies the time derivative. Assuming that the perturbations are small (e.g. $\delta\rho \ll \bar{\rho}$), all second order terms can be ignored, giving the linear theory approximation,

$$\dot{\delta\mathbf{v}}+(\bar{\mathbf{v}}\cdot\nabla)\delta\mathbf{v}+(\delta\mathbf{v}\cdot\nabla)\bar{\mathbf{v}}+(\bar{\mathbf{v}}\cdot\nabla)\bar{\mathbf{v}}+\dot{\bar{\mathbf{v}}} = -\left[\frac{\nabla\bar{P}}{\bar{\rho}}+\nabla\bar{\phi}\right]+\frac{\delta\rho}{\bar{\rho}^2}(\nabla\bar{P})-\frac{\nabla\delta P}{\bar{\rho}}-\nabla\delta\phi. \tag{B.6}$$

But, $\nabla\bar{P} = 0$ and, from Euler's equation (B.1),

$$(\bar{\mathbf{v}}\cdot\nabla)\bar{\mathbf{v}} + \dot{\bar{\mathbf{v}}} = -\frac{\nabla\bar{P}}{\bar{\rho}} - \nabla\bar{\phi}, \tag{B.7}$$

giving

$$\dot{\delta\mathbf{v}} + (\bar{\mathbf{v}}\cdot\nabla)\delta\mathbf{v} + (\delta\mathbf{v}\cdot\nabla)\bar{\mathbf{v}} = -\frac{\nabla\delta P}{\bar{\rho}} - \nabla\delta\phi. \tag{B.8}$$

Similarly for the equation of conservation of mass (equation B.1) :

$$\frac{\partial(\bar{\rho}+\delta\rho)}{\partial t} + [(\bar{\mathbf{v}}+\delta\mathbf{v})\cdot\nabla](\bar{\rho}+\delta\rho) = -(\bar{\rho}+\delta\rho)[\nabla\cdot(\bar{\mathbf{v}}+\delta\mathbf{v})], \tag{B.9}$$

giving

$$\dot{\delta\rho} + (\bar{\mathbf{v}} \cdot \nabla)\delta\rho = -\bar{\rho}(\nabla \delta\mathbf{v}) - \delta\rho(\nabla \cdot \bar{\mathbf{v}}). \tag{B.10}$$

Following a similar process for Poisson's equation gives

$$\nabla^2 \delta\phi = 4\pi G \delta\rho. \tag{B.11}$$

Writing $\delta = \delta\rho/\bar{\rho}$ allows the equations to be simplified as does re-introducing the D/Dt notation, where D/Dt is now have given by

$$\frac{D}{Dt} \equiv \frac{\partial}{\partial t} + (\bar{\mathbf{v}} \cdot \nabla). \tag{B.12}$$

Substituting into equations (B.8), (B.10) and (B.11) gives

$$\frac{D(\delta\mathbf{v})}{Dt} + (\delta\mathbf{v} \cdot \nabla)\bar{\mathbf{v}} = -\frac{\nabla \delta P}{\bar{\rho}} - \nabla\delta\phi, \tag{B.13}$$

$$\frac{D\delta}{Dt} = -\nabla \delta\mathbf{v}. \tag{B.14}$$

$$\nabla^2 \delta\phi = 4\pi G \bar{\rho}\delta. \tag{B.15}$$

So far the equations have been expressed in proper coordinates, $\mathbf{x}$. Introducing comoving coordinates, $\mathbf{r}$, such that $\mathbf{x} = a\mathbf{r}$, gives $\mathbf{v} = \dot{\mathbf{x}} = \dot{a}\mathbf{r} + a\dot{\mathbf{r}}$. The contribution $\dot{a}\mathbf{r}$ is the contribution to the velocity of the Hubble expansion ($\equiv \bar{\mathbf{v}}$) thus $a\dot{\mathbf{r}}$ is the peculiar velocity, $a\mathbf{u} \equiv \delta\mathbf{v}$, where $\mathbf{u} \equiv \dot{\mathbf{r}}$ is the comoving peculiar velocity.

Introducing a coordinate transform (into comoving coordinates)

$$\nabla \rightarrow \frac{1}{a}\nabla, \qquad \frac{D}{Dt} \rightarrow \frac{\partial}{\partial t}, \tag{B.16}$$

it follows that

$$\dot{\delta\mathbf{v}} = \partial(a\mathbf{u})/\partial t = \dot{a}\mathbf{u} + a\dot{\mathbf{u}} \tag{B.17}$$

and

$$(\delta\mathbf{v}\cdot\nabla)\bar{\mathbf{v}} = \left[(a\mathbf{u})\frac{1}{a}\nabla\right]\dot{a}\mathbf{r} = \dot{a}\mathbf{u}. \tag{B.18}$$

Hence Euler's equation (B.13) becomes

$$\frac{\partial(a\mathbf{u})}{\partial t} + \dot{a}\mathbf{u} = -\frac{1}{a}\frac{\nabla\delta P}{\bar{\rho}} - \frac{\nabla\delta\phi}{a}. \tag{B.19}$$

Differentiating and dividing by a gives

$$\dot{\mathbf{u}} + \frac{2\dot{a}}{a}\mathbf{u} = -\frac{1}{a^2}\nabla\delta P\bar{\rho} - \frac{\nabla\delta\phi}{a^2} \tag{B.20}$$

Similarly, the mass continuity equation (B.14) becomes

$$\dot{\delta} = -\nabla\cdot\mathbf{u} \tag{B.21}$$

and Poisson's equation (B.15) becomes

$$\nabla^2\delta\phi = 4\pi G\bar{\rho}a^2\delta. \tag{B.22}$$

It is now possible to solve for δ by eliminating $\mathbf{u}$. Operating on equation (B.20) with ∇ gives

$$\nabla\cdot\dot{\mathbf{u}} + \frac{2\dot{a}}{a}\nabla\cdot\mathbf{u} = -\frac{\nabla^2\delta P}{a^2\bar{\rho}} - \frac{\nabla^2\delta\phi}{a^2}, \tag{B.23}$$

and differentiating equation (B.21) with respect to time gives

$$\ddot{\delta} = -\nabla \cdot \dot{\mathbf{u}}. \tag{B.24}$$

Substituting $(\nabla \cdot \mathbf{u})$ from equation (B.21), $\nabla^2 \delta\phi$ from equation (B.22) and $\nabla \cdot \dot{\mathbf{u}}$ from equation (B.24) in equation (B.23) gives

$$-\ddot{\delta} - \frac{2\dot{a}}{a}\dot{\delta} = -4\pi G\bar{\rho}\delta - \frac{\nabla^2 \delta P}{a^2 \bar{\rho}}. \tag{B.25}$$

This is an approximate solution for the linear case where $\delta \ll 1$. The final result is dependent on both the pressure and density of the dust. However, these are related by the sound speed, c_s, which is defined as

$$c_s^2 = \frac{\partial \bar{P}}{\partial \bar{\rho}} \tag{B.26}$$

and so

$$\frac{\nabla^2 \delta P}{a^2 \bar{\rho}} = c_s^2 \frac{\nabla^2 \delta \rho}{a^2 \bar{\rho}}. \tag{B.27}$$

Isolating a single wave of wavenumber k, one finds

$$\begin{aligned} \delta\rho &\propto \exp(-i\mathbf{k} \cdot \mathbf{x}), \\ \nabla^2 \delta\rho &\propto -k^2 \delta\rho. \end{aligned} \tag{B.28}$$

Thus

$$\ddot{\delta} + \frac{2\dot{a}}{a}\dot{\delta} = \delta\left(4\pi G\bar{\rho} - \frac{c_s^2 k^2}{a^2}\right). \tag{B.29}$$

If the bracket on the right-hand side of equation (B.29) is positive, the solution for δ will be a growing one. This corresponds to a crucial wavelength known as the Jeans' wavelength, the value of λ' $(= 2\pi/k)$ when the bracket is zero. This gives

$$4\pi G\bar{\rho} = \frac{c_s^2 k_J^2}{a^2} \tag{B.30}$$

or

$$\lambda_J' = \frac{c_s}{a}\sqrt{\frac{\pi}{G\bar{\rho}}}. \tag{B.31}$$

Thus for $\lambda' > \lambda_J'$ (i.e. $k < k_J$), there is a growing mode for the solution of δ. This defines the smallest possible wavelength for perturbations. Note that this is given above in comoving coordinates. In real coordinates $\lambda = a\lambda'$, giving

$$\lambda_J = c_s\sqrt{\frac{\pi}{G\bar{\rho}}}. \tag{B.32}$$

B.2 Radiation-Dominated Regime

For the radiation-dominated case, the relevant equations are the special relativistic analogues of those in equation (B.1)

$$\begin{aligned}
&\frac{D\mathbf{v}}{Dt} = -\nabla\phi && \text{(Euler's Equation)} \\
&\frac{D}{Dt}\left(\rho + \frac{P}{c^2}\right) = \frac{\dot{P}}{c^2} - \left(\rho - \frac{P}{c^2}\right)(\nabla\cdot\mathbf{v}) && \text{(Mass Conservation)} \\
&\nabla^2\phi = 4\pi G\left(\rho + \frac{3P}{c^2}\right) && \text{(Poisson's Equation)}
\end{aligned} \tag{B.33}$$

Note that Euler's equation has no (matter) pressure term as this is assumed to be small. This holds for $\lambda > \lambda_J$ (see § B.1). The above equations hold for $|\mathbf{v}| \ll c$ and as the universe is radiation dominated, one can write

$$P = \frac{1}{3}\rho c^2. \tag{B.34}$$

Linearising as before,

$$\begin{aligned} &\dot{\delta\mathbf{v}} + (\delta\mathbf{v}\cdot\nabla)\bar{\mathbf{v}} = -\nabla\delta\phi && \text{(Euler's Equation)} \\ &\frac{3}{4}\dot{\delta\rho} + (\bar{\mathbf{v}}\cdot\nabla)\delta\rho = -\delta\rho(\nabla\bar{\mathbf{v}}) - \bar{\rho}(\nabla\delta\mathbf{v}) && \text{(Mass Conservation)} \\ &\nabla^2\delta\phi = 8\pi G\delta\rho && \text{(Poisson's Equation)} \end{aligned} \tag{B.35}$$

Following a similar method of transforming variables into comoving coordinates and eliminating $\mathbf{u}$ gives

$$\ddot{\delta} + \frac{2\dot{a}}{a}\dot{\delta} = \frac{32\pi}{3}G\bar{\rho}\,\delta. \tag{B.36}$$

Note that this solution is only valid if pressure can be neglected, i.e. if $\lambda \gg \lambda_J$. Comparing this to the solution in the matter dominated regime with $\lambda \gg \lambda_J$, gives (from equation B.29)

$$\ddot{\delta} + \frac{2\dot{a}}{a}\dot{\delta} = 4\pi G\bar{\rho}\,\delta, \tag{B.37}$$

and one can see that the "driving" term is a factor 8/3 higher for a radiation dominated universe.

B.3 Solutions for δ

To solve equations (B.37) and (B.36), a solution must be found for the scale factor, a. The equation governing the time evolution of the scale factor is equation (A.7), which gives

$$\dot{a}^2 = \frac{8\pi}{3}\rho G a^2 - \kappa. \tag{B.38}$$

For early times, when the perturbations are small and linear theory holds, $\Omega \to 1$ (see equation A.20 and § 1.2.3). This means that $\kappa \to 0$ and can be ignored. This results in equation (A.7) being greatly simplified. Putting $\rho = \rho_0/a^3$ and solving for a gives

$$\dot{a} = \frac{8\pi}{3}\rho_0 G a^{-1}, \tag{B.39}$$

or,

$$a \propto t^{2/3}. \tag{B.40}$$

Substituting in equation (A.7) gives

$$4\pi G\rho = \frac{2}{3t^2}. \tag{B.41}$$

This is for a matter-dominated universe. For the radiation dominated case, the radiation density falls away as a^{-4}, the extra power of a arising from the redshifting of the radiation with expansion. Thus equation (A.7) becomes

$$\dot{a} = \frac{8\pi}{3}\rho_0 G a^{-2}, \tag{B.42}$$

or, solving for a,

$$a \propto t^{1/2}. \tag{B.43}$$

Substituting in equation (A.7) gives

$$\frac{32\pi G\rho}{3} = \frac{1}{t^2}. \tag{B.44}$$

Note that both these time-density relationships follow

$$t \propto \frac{1}{\sqrt{G\rho}}. \tag{B.45}$$

Using these four results it is possible to solve equations (B.37) and (B.36) for δ.

• Matter-Dominated Case

Equation (B.37) gives

$$\ddot{\delta} + \frac{4\dot{\delta}}{3t} = \frac{2}{3}\delta. \tag{B.46}$$

Putting $\delta \propto t^n$ gives

$$n(n-1) + \frac{4}{3}n = \frac{2}{3}, \tag{B.47}$$

$$\Rightarrow \quad n = \frac{2}{3} \quad \text{or} \quad n = -1. \tag{B.48}$$

• Radiation-Dominated Case

Equation (B.36) gives

$$\ddot{\delta} + \frac{\dot{\delta}}{t} = \frac{\delta}{t^2}. \tag{B.49}$$

Putting $\delta \propto t^n$ gives

$$n(n-1) + n = 1, \tag{B.50}$$

$$\Rightarrow \quad n = 1 \quad \text{or} \quad n = -1. \tag{B.51}$$

Thus the growing modes are

$$\begin{aligned} &\delta \propto t^{2/3} \ ; \quad \delta \propto a \ ; \quad a \propto t^{2/3}\,. \quad \text{(Matter Dominated)} \\ &\delta \propto t \ ; \quad \delta \propto a^2 \ ; \quad a \propto t^{1/2}\,. \quad \text{(Radiation Dominated)} \end{aligned} \tag{B.52}$$

Note that both these relationships hold for cases where the pressure is negligible. In the matter dominated regime, if $\lambda \lesssim \lambda_J$, then pressure becomes important and the perturbations undergo wave-like oscillations instead of growth.

Appendix C

Inflation

C.1 The Big Bang

As discussed in § 1.1.4, the Hot Big Bang model has become the standard theory of cosmology and has met with a great deal of success. Extrapolating backwards, the current expansion of the universe implies a phase when the universe was arbitrarily hot and dense. This is assuming that the known laws of physics can be extrapolated backward to this point. Under this assumption, the universe starts with a singularity at time $t = 0$ and has infinite temperature and pressure. It expands and begins to cool, but cannot be described by any classical theory until it is larger in size than the Planck length, 10^{-35} m.

Though the Big Bang theory has been remarkably successful (see § 1.1.4), all its successes arise from the state of the universe after about the first minute. The problems that arise all occur within the first 10^{-30} of a second, a time when the model does not make (and is unable to make) any predictions. These problems are:

• Horizon Problem

The microwave background radiation (§ 1.1.4) is very homogeneous. However, when the radiation decoupled from the matter in the early universe, different regions had no causal connection (Fig. C.1) and hence they could not have had time to come into thermal equilibrium. This means that the universe must have been homogeneous when it started its expansion and this must be included in the initial conditions of the Big Bang.

• Flatness Problem

As discussed in § 1.2.3, the density of the universe is close to the critical density (i.e. $0.2 \lesssim \Omega_0 \lesssim 2$). As $\Omega(z)$ diverges from $\Omega = 1$ with increasing look-back time, this means that if $\Omega_0 \neq 1$ then at very early times Ω would be very close to, but not exactly equal

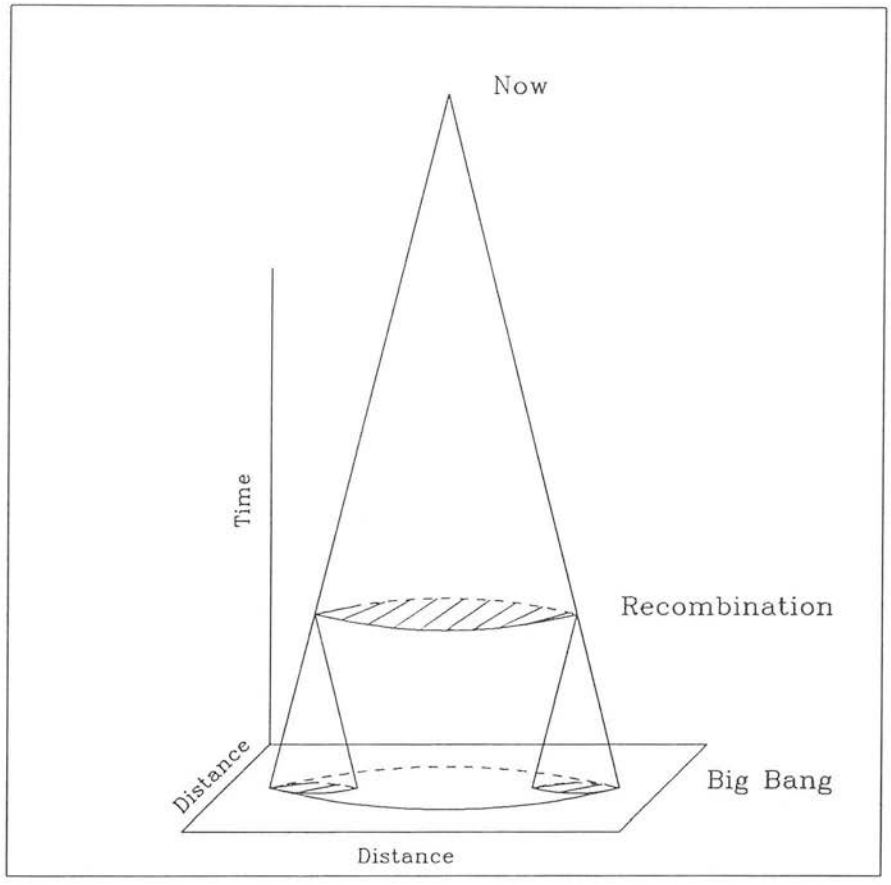

Figure C.1 The Horizon Problem: the space-time diagram shows our present position ("Now") along with our past light-cone, which represents the region of causal connection. At the time of recombination, two points at opposite side of our light horizon were at the same temperature, despite their own light horizons not overlapping. This means that no signal could have propagated between the two regions and thus they could not have come into thermal equilibrium. If the two regions were at the same temperature at the epoch of recombination, this implies that they were at the same temperature at the Big Bang. All the distances are comoving. Diagram adopted from Guth & Steinhardt (1984).

to, unity. Though such a value of Ω is not impossible, it is highly unlikely and needs to be introduced as an initial condition.

• Smoothness Problem

As discussed in § 1.3, the early universe was homogeneous to a very high degree (as witnessed by the homogeneity of the microwave background) and is now inhomogeneous on scales of up to at least $50\,h^{-1}$ Mpc. In the Big Bang theory, the initial fluctuations that give rise to these inhomogeneities are postulated to have formed at early times when the horizon was small. However, the largest scale fluctuations currently observable are on scales that would be greater than the horizon at those early times. This implies either a violation of causality or that such fluctuations must have already been present as part of the initial conditions.

• Magnetic Monopoles

Grand unification theories predict that during the very early universe all four fundamental forces were unified and as the universe cooled this symmetry between them was broken. A quite general consequence of this symmetry breaking is the production of topological defects (§ 1.3.4). One such defect is the magnetic monopole which is predicted to be very massive (about 10^{16} times the mass of a proton). They are also copiously produced and extremely stable. Theories predict that they should now be sufficiently numerous so as to raise the density of the universe well in excess of that needed for closure. This would mean that space would be so highly curved that the universe would have recollapsed by now!

There are many other examples of this sort (e.g. see Linde 1987) and any realistic model of the very early universe must account for these discrepancies while at the same time keeping the features of the standard theory that has led it to its successes. One such contender is the inflationary universe.

C.2 Inflation Theory

Originally proposed by Guth (1981), the initial inflation theories were a modification of the standard theory. They assumed that the very early universe contained regions of hot expanding matter at a temperature greater than $T_{\rm GUT}$, the temperature at which the various forces become unified in grand unification theories ($T_{\rm GUT} \sim 10^{27}$ K). The main difference between inflation and the standard theory is that instead of treating matter as an ideal gas at these high temperatures, it is treated in terms of quantum fields

coupled to general relativity. The theory assumes that the universe undergoes a period of exponential expansion in its very early moments. This expansion is coupled with a supercooling and so evolution is no longer adiabatic. Once this period of expansion is over the universe must reheat back to the temperature predicted by the standard model otherwise the successes of the standard model would be lost. In all of the inflation theories this expansion period is very short and after $\sim 10^{-35}$ seconds the expansion is over and the theory assumes that the universe evolves as in the Big Bang model.

In grand unification theories, the four fundamental forces are unified above T_{GUT}. The theories predict the existence of scalar fields (often called Higgs fields and denoted by ϕ). When these fields have values $\phi = 0$, symmetry is unbroken. However, when just one of these fields takes on a non-zero value the symmetry of the four forces will break in some way. It is predicted that for temperatures greater than T_{GUT} all the scalar fields are forced into $\phi = 0$ states. This state corresponds to the true minimum of the energy density of the field, $V(\phi)$. However, for $T = 0$ K, a new minimum has evolved at some $\phi = \epsilon$. In this state $V(\phi) = 0$ and hence it corresponds to the true vacuum. The minimum at $\phi = 0$ is now referred to as the false vacuum.

As the temperature drops to around T_{GUT}, the scalar fields condense into the false vacuum state. Here they begin to evolve exponentially. This evolution ends when the field decays into the true vacuum state and symmetry breaks. The energy which was stored in the false vacuum is released and reheats the universe.

By definition, the true vacuum has zero pressure. For regions of true vacuum to evolve and expand in a surrounding universe of false vacuum the pressure in the region of true vacuum must be greater than that of the false vacuum. As these regions have zero pressure, this means that the false vacuum must have *negative* pressure. It is this pressure that drives the expansion. Gravitational attraction is proportional to pressure, P, and also energy density, ρ, such that

$$\text{Attraction} \propto (3P/c^2 + \rho). \tag{C.1}$$

It can be shown that for the false vacuum the pressure is equal to minus the energy density. Thus the total attraction will be negative for negative pressure, i.e. repulsive gravitation and hence expansion (see Guth and Steinhardt 1984). For a detailed

mathematical argument as to why expansion occurs see Brandenberger (1985) and the references therein.

Once the system is in the true vacuum state, the scalar fields have non-zero values. These fields can alter the masses of the quanta mediating the different forces and so causes the symmetry between them to break. Once the field is in the minimum position it oscillates rapidly and this corresponds to the formation of very large mass Higgs particles. These particles then decay into more normal forms of matter and hence the universe heats up again.

It is the period of exponential expansion that characterises inflation and that also leads to a solution of the various problems discussed in § C.1, provided that the period of inflation is long enough.

• Horizon Problem

Due to inflation, a small, homogeneous region in the original universe, all parts of which lay within one light horizon at the time of expansion, could now have expanded to well beyond the present light horizon. Such a region would have had time to come into thermal equilibrium before expansion, which then explains why there is such large-scale homogeneity in the microwave background radiation.

• Flatness Problem

Despite its initial value, Ω is driven towards unity by the expansion. This then accounts for the flatness of the universe. An intuitive approach is to consider the universe as the surface of a balloon. Before the onset of rapid inflation a small area will be quite curved. After a period of exponential expansion the same area will seem quite flat. In general relativistic terms, inflation forces the curvature of space towards zero.

• Magnetic Monopoles

The magnetic monopole density is diluted as inflation takes place. The total number is conserved, but after inflation so few are left within the present light horizon that these are well below the observed maximum (none have so far been observed). Of course, no more monopoles must be produced after the end of the inflationary period as these would stay within our light horizon.

Note that the dilution that occurs to the magnetic monopoles would also occur to baryonic matter. Thus more baryons must be produced after the inflation to account for the present number of baryons. In order for this to happen grand unification theories require the temperature to be very near that of the symmetry breaking ($\sim T_{\mathrm{GUT}}$). Thus the universe must be reheated after expansion.

Inflation theory can also provide a natural mechanism for the generation of primordial fluctuations. In the standard Big Bang model, initial perturbations in the density and radiation fields are assumed to be part of the initial conditions. However, they can arise in inflation theory, giving a scale-invariant Harrison–Zel'dovich spectrum (§ 1.3.1).

Quantum fluctuations will be present in both the matter and radiation fields during inflation. Initially the wavelengths of these fluctuations will be small in size, but as the universe inflates, these wavelengths will inflate with it. Once the wavelength exceeds the light horizon the fluctuation it represents will cease to propagate as it is beyond the range of causal contact. Thus the amplitude of the fluctuation will be frozen, but its wavelength will continue to expand. Once inflation is over the wavelength will cease to grow and the fluctuation will be frozen until it recrosses the light horizon, which occurs as a result of the normal expansion of the universe. It then re-enters space as a perturbation, but now with the wavelength it had when inflation stopped. Thus small quantum fluctuations have been expanded by inflation to give perturbations on an astronomical scale. Furthermore, these fluctuations retain the same amplitude on entering the horizon as they did on leaving it. As the rate of expansion of the universe is constant, so the growth in amplitude of the fluctuations is constant, resulting in equal amplitude fluctuations at horizon crossing, which gives rise to a Harrison–Zel'dovich spectrum of initial perturbations.

C.3 Old and New Inflation Theories

Inflation theory thus predicts a period of exponential expansion for regions of false vacuum. The main feature of the theory is the manner in which the false vacuum decays into the true vacuum, as this governs the length and character of the inflation period and hence whether inflation can indeed solve the various cosmological problems in as suggested in § C.2.

Inflation was originally proposed by Guth (1981). He assumed that in the early universe the $\phi = 0$ state was the absolute minimum (see Fig. C.2). Once the temperature drops below T_{GUT}, $\phi = 0$ ceases to be the true minimum and inflation begins. The false vacuum is separated from the stable true vacuum by a potential barrier. It may decay to the true vacuum by tunnelling through this barrier and forming a bubble of true vacuum in a universe of false vacuum. Once this bubble has formed it quickly evolves to the true vacuum. Here the scalar field oscillates rapidly about the minimum and decays, releasing the energy that was stored in the false vacuum and reheating the universe. This reheating takes place on a very short time scale compared to that of the inflation and is non-adiabatic. The bubble then expands normally and the evolution of the universe continues as in the standard theory.

Though this gives rise to a region that underwent a period of inflation, Guth realised that the theory was fatally flawed as it produces a very unrealistic cosmology. When the energy is released during the reheating phase, about half of it goes into reheating the universe and the other half into the walls of the bubble. As these walls formed after the inflation, they would expand normally and lie within the present light horizon. These walls would have been detected as they would create energy density perturbations on a scale far above the current observational limits. The problem is that the bubbles do not percolate, that is, each bubble is a separate entity. The universe outside of the bubbles is dominated by the false vacuum and so decay has not taken place and inflation continues, sweeping apart the bubbles of true vacuum, which expand in the normal manner. This could be corrected by having a very high rate of bubble formation so that the bubbles can coalesce before they are swept apart. The rate depends on the lifetime of the false vacuum state and is sensitive to the details of the underlying grand unification theory. However, it is assumed to be low otherwise insufficient expansion would take place before bubble formation and the various problems discussed in § C.1 and § C.2 would persist. Thus, if bubbles form at a sufficient rate to allow percolation, there will have been insufficient expansion in the false vacuum state to the solve the flatness, horizon and monopole problems.

Despite this failure, the use of an inflationary period to solve various cosmological problems seemed very attractive and the idea was not abandoned. In 1982 Linde first proposed what was to become the new inflation theory. This was also proposed independently by Albrecht & Steinhardt (1982) a few months later. The difference in the new

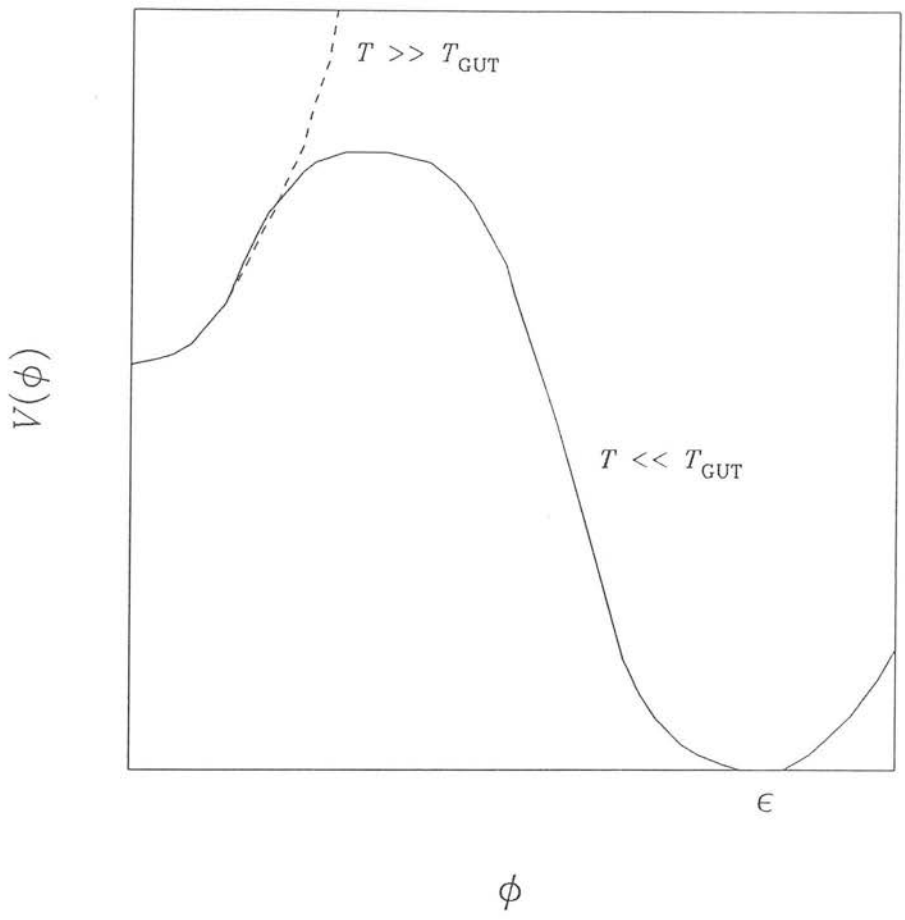

Figure C.2 The one-dimensional scalar field in the old inflationary model of Guth (1981). The broken line shows the potential before symmetry breaking, where the minimum at $\phi = 0$ is a true minimum, and the solid line is the potential after symmetry breaking, where the true minimum lies at $\phi = \epsilon$. Note that the field becomes trapped in the false vacuum at $\phi = 0$ and needs to tunnel through the potential barrier before it can evolve into the true vacuum state.

theory is the shape of the potential. This is based on a Coleman–Weinberg (Coleman & Weinberg 1973) potential with a local maximum at $\phi = 0$. The theory progresses as the old version, with the universe in a true vacuum phase at $\phi = 0$, which then condenses into a false vacuum phase as the temperature drops below T_{GUT}. Supercooling takes place and the false vacuum begins to expand exponentially. However, instead of tunnelling through a potential barrier in order to decay, the field can be displaced

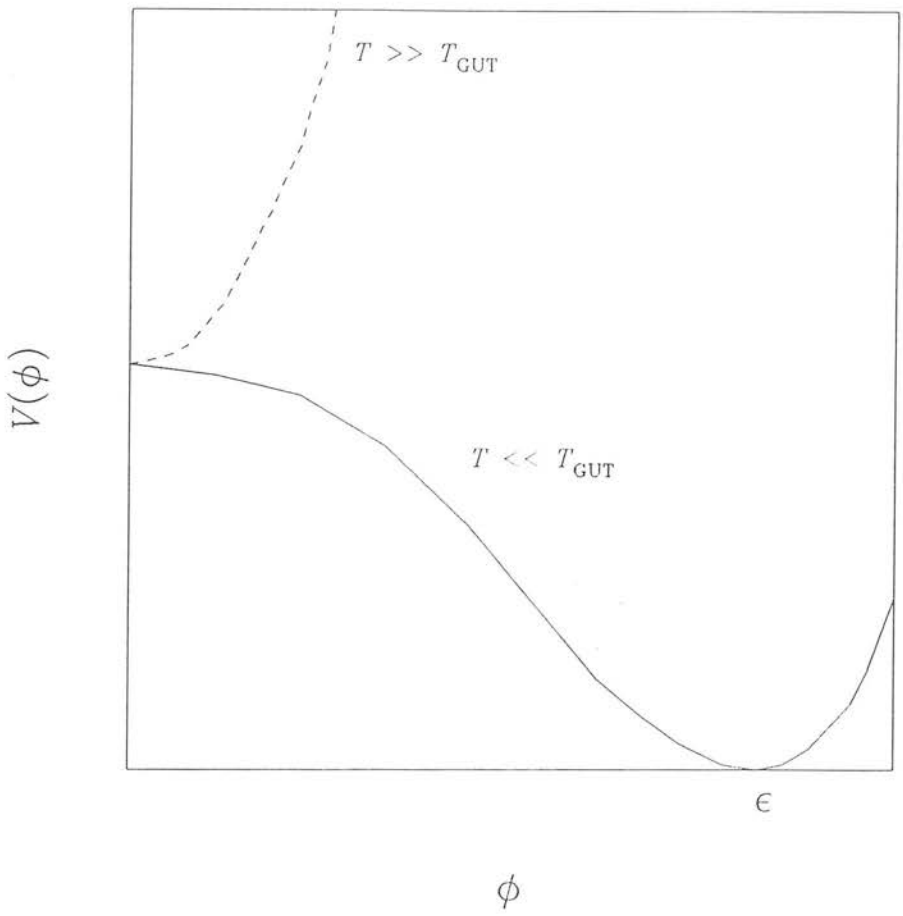

Figure C.3 The one-dimensional scalar field in the new inflationary model. The broken line shows the potential before symmetry breaking, where the minimum at $\phi = 0$ is a true minimum, and the solid line is the potential after symmetry breaking, where the true minimum lies at $\phi = \epsilon$. Note that there is no longer a minimum at $\phi = 0$, thus the field is free to evolve into the true vacuum state without the need for tunnelling.

from equilibrium by quantum fluctuations or small residual thermal fluctuations (see Fig. C.3). Once it has been displaced it will naturally evolve towards the minimum at $\phi = \epsilon$. This evolution will take place slowly due to the small gradient near the maximum. Thus the newly evolving state will have an energy density very close to that of the false vacuum and will continue its inflation in a quasi-exponential fashion. This is often called the "slow rolling" phase. Once the field has reached the "steep" part

of the potential it will quickly "roll" down to the minimum at $\phi = \epsilon$ and the inflation will stop. Once there it will oscillate as before and rapidly decay, thus reheating the universe. This solves the flatness, horizon and monopole problems as before and avoids the flaw of the old model as symmetry breaking occurs before the end of inflation, thus domain walls are swept out of the present horizon during the inflation period.

C.4 Summary

The main point of inflation theory is that there existed in the very early ($t \lesssim 10^{-35}$ seconds) universe a false vacuum which led to a period of exponential expansion, thus solving the horizon, flatness and monopole problems. This also provides a mechanism for the production of primordial perturbations from quantum fluctuations in the inflationary stage. The specific theories presented here ("old" and "new" inflation) are not the only mechanisms possible, they merely served to illustrate the general scheme. Other mechanisms include chaotic inflation (e.g. Linde 1987), which allows the initial, pre-inflation fields to be chaotic rather than in thermodynamic equilibrium, and double inflation, where there are two (or more) periods of inflation, each linked to its own scalar potential. This will introduce a more complicated initial perturbation spectrum which decouples large- and scale-small perturbations.

However, there are problems with inflation theory. The potential needs to be fine tuned so that (in "new" inflation at least) it is flat near the origin and remains flat long enough so that slow rolling gives rise to sufficient inflation. It also needs to be steep enough near the true vacuum in order that the universe may reheat to the correct level. Though inflation is quite generic, there are doubts as to whether the initial conditions in the very early universe will give rise to sufficient inflation, or even to inflation at all. Some also doubt the need for inflation (e.g. Turok 1991) and there are problems with the amplitude of the fluctuations generated during the inflationary period, which requires a fine tuning of the particular grand unification theory. Other theories, based on topological defects, also give rise to similar initial perturbations without the need for inflation (though such features can arise naturally during inflation), but with extra large-scale power (e.g. textures; see § 1.4.4), which means that inflation is by no means unique as a solution to the problems of the standard hot Big Bang theory.

Appendix D

Weighting Scheme for the Kinematical Method

This appendix derives a weighting scheme used by the kinematical method in order to give the walls in a two- or three-dimensional Voronoi foam a constant number density of particles.

D.1 Two Dimensions

The line density, ρ_{l}, of particles in a wall is given by :

$$\rho_{\mathrm{l}} = n/\delta l', \tag{D.1}$$

where $\delta l'$ is the length of wall projected by a small angle $\delta\theta$ from a Voronoi nucleus, N, and n is the number of particles within the area subtended by $\delta\theta$ and bounded by $\delta l'$ (see Fig. D.1).

However, $\delta l' = \delta l/\cos\theta = r\delta l/r_{\mathrm{p}}$ and $\delta l = r\delta\theta$ as $\delta\theta \to 0$. Thus

$$\rho_{\mathrm{l}} = \frac{nr_{\mathrm{p}}}{r^2\delta\theta}. \tag{D.2}$$

For a random distribution of particles n is proportional to the area, A, subtended by $\delta\theta$ and bounded by $\delta l'$:

$$n = \frac{n_0 A}{L^2}, \tag{D.3}$$

where n_0 is the total number of particles in the simulation and L is the length of the side of the simulation. Now, $A = \frac{1}{2}r\delta l = \frac{1}{2}r^2\delta\theta$ for small $\delta\theta$, giving

$$n = \frac{n_0 r^2\delta\theta}{2L^2}, \tag{D.4}$$

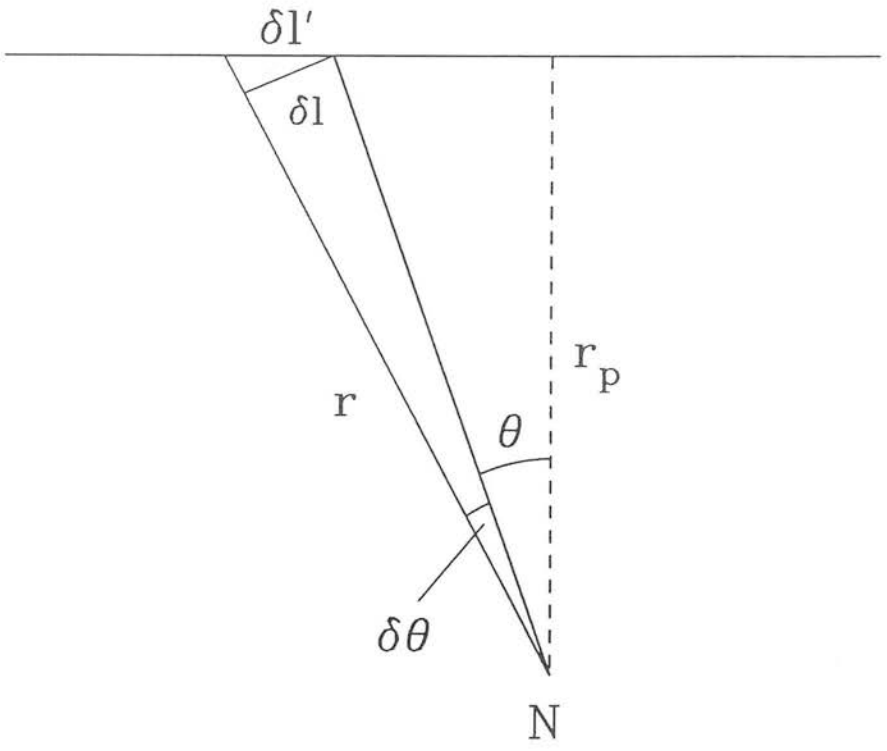

Figure D.1 Diagram showing the projection of particles within a small angle $\delta\theta$ onto a line element of wall, $\delta l'$.

and hence

$$\rho_{\mathrm{l}} = \frac{n_0}{2L^2}\, r_{\mathrm{p}}. \tag{D.5}$$

For particles located at the Voronoi nucleus, N, and uniformly distributed in angle over 2π radians (the "grenade model"), n is proportional to the angle $\delta\theta$:

$$n = \frac{n_{\rm p}\delta\theta}{2\pi}, \tag{D.6}$$

where $n_{\rm p}$ is the number of particles per nucleus. Hence

$$\rho_{\rm l} = \frac{n_{\rm p}}{2\pi}\frac{r_{\rm p}}{r^2}. \tag{D.7}$$

To ensure a constant line density each particle in the simulation must be weighted by a factor, W, inversely proportional to the actual line density, $\rho_{\rm l}$. Thus, for a random initial distribution of particles,

$$W \propto \frac{1}{r_{\rm p}}, \tag{D.8}$$

and for the "grenade" model,

$$W \propto \frac{r^2}{r_{\rm p}}. \tag{D.9}$$

D.2 Three Dimensions

The above derivation may also be extended into three dimensions. The line elements δl and $\delta l'$ become area elements δA and $\delta A'$ and the angle $\delta\theta$ becomes the solid angle, $\delta\Omega$. Thus the surface density, $\sigma_{\rm s}$, is given by :

$$\sigma_{\rm s} = n/\delta A' = \frac{nr_{\rm p}}{r^3\delta\Omega}, \tag{D.10}$$

since $\delta A' = \delta A/\cos\theta = r\,\delta A/r_{\rm p}$ and $\delta A = r^2\delta\Omega$ as $\delta\Omega \to 0$.

For a random distribution of particles, n is proportional to the volume, V, subtended by $\delta\Omega$ and bounded by $\delta A'$, where $V = \frac{1}{3}r\,\delta A = \frac{1}{3}r^3\delta\Omega$ for small $\delta\Omega$.

$$n = \frac{n_0 V}{L^3} = \frac{n_0 r^3\delta\Omega}{3L^3}, \tag{D.11}$$

giving

$$\sigma_s = \frac{n_0}{3L^3} r_p, \tag{D.12}$$

and hence the weighting, W, is the same as that for the two–dimensional case (equation D.8).

For particles located at the Voronoi nucleus, N, and uniformly distributed in solid angle over 4π steradians (the "grenade" model is three dimensions), n is proportional to the solid angle $\delta\Omega$:

$$n = \frac{n_p \delta\Omega}{4\pi}, \tag{D.13}$$

and hence,

$$\sigma_s = \frac{n_p}{4\pi} \frac{r_p}{r^3}, \tag{D.14}$$

giving a weight, W, for the three–dimensional grenade model of :

$$W \propto \frac{r^3}{r_p} \tag{D.15}$$

These results are summarised in Table D.1.

Model	Two Dimensions	Three Dimensions
Random Particles	$W \propto 1/r_p$	$W \propto 1/r_p$
"Grenade" Model	$W \propto r^2/r_p$	$W \propto r^3/r_p$

Table D.1 Weighting schemes for the kinematical method.

Appendix E

The Autocorrelation Function

This appendix lays out the basic Fourier transform relationships between the spatial correlation function (autocorrelation function) and the power spectrum. Consider a density perturbation, $\delta\mathbf{x} = \delta\rho(\mathbf{x})/\bar{\rho}$. This can be expressed as the sum over all phase-space of the perturbations at the point $\mathbf{x}$, i.e.

$$\delta(\mathbf{x}) = \sum_{k=0}^{\infty} \delta(\mathbf{k}) \exp(-i\mathbf{k}\cdot\mathbf{x}). \tag{E.1}$$

In the case of a continuous medium this goes over to an integral,

$$\delta(\mathbf{x}) = \frac{V}{(2\pi)^3} \int \delta(\mathbf{k}) \exp(-i\mathbf{k}\cdot\mathbf{x}) d^3\mathbf{k}, \tag{E.2}$$

where $V/(2\pi)^3$ is the density of states in phase-space over the finite volume, V.

Defining the Fourier transform of a function $f(\mathbf{x})$ to be

$$F(\mathbf{k}) = \int f(\mathbf{x}) \exp(i\mathbf{x}\cdot\mathbf{k}) d^3\mathbf{x} = \mathcal{F}[f(\mathbf{x})] \tag{E.3}$$

and its inverse to be

$$f(\mathbf{x}) = \frac{1}{(2\pi)^3} \int F(\mathbf{k}) \exp(-i\mathbf{x}\cdot\mathbf{k}) d^3\mathbf{k} = \mathcal{F}^{-1}[F(\mathbf{k})], \tag{E.4}$$

where $\mathcal{F}$ and $\mathcal{F}^{-1}$ refer to the Fourier transform and its inverse respectively, one can relate the real and phase-space density perturbations via Fourier transforms :

$$\begin{aligned} \delta(\mathbf{x}) &= V\mathcal{F}^{-1}[\delta(\mathbf{k})], \\ \delta(\mathbf{k}) &= \frac{1}{V}\mathcal{F}[\delta(\mathbf{x})]. \end{aligned} \tag{E.5}$$

Now, the spatial two-point correlation function is defined as

$$\xi(r) = \langle \delta(\mathbf{x})\delta(\mathbf{x}+\mathbf{r}) \rangle \tag{E.6}$$

where the angle brackets denote the expectation value, averaged over $\mathbf{x}$. It is written as a function of $r \equiv |\mathbf{r}|$ assuming isotropic fluctuations. This is equivalent to the definition used in § 4.2.2 (equation 4.8). For an ensemble average this goes over to an integral :

$$\xi(r) = \frac{1}{V} \int_{-\infty}^{\infty} \delta(\mathbf{x})\, \delta(\mathbf{x}+\mathbf{r})\, d^3\mathbf{x}. \tag{E.7}$$

The multiplication theorem of Fourier transforms states

$$\int_{-\infty}^{\infty} f_1(\mathbf{x})\, f_2(\mathbf{x})\, d^3\mathbf{x} = \frac{1}{(2\pi)^3} \int_{-\infty}^{\infty} F_1^*(\mathbf{k})\, F_2(\mathbf{k})\, d^3\mathbf{k}, \tag{E.8}$$

where $F_1^*(\mathbf{k})$ is the complex conjugate of $F_1(\mathbf{k})$. Identifying f_1 with $\delta(\mathbf{x})$ and f_2 with $\delta(\mathbf{x}+\mathbf{r})$ and using the shifting properties of Fourier transforms, namely :

$$\mathcal{F}[f(\mathbf{x}+\mathbf{r})] = F(\mathbf{k}) \exp(i\mathbf{k}\cdot\mathbf{r}) \tag{E.9}$$

one finds

$$\int_{-\infty}^{\infty} \delta(\mathbf{x})\, \delta(\mathbf{x}+\mathbf{r})\, d^3\mathbf{x} = \frac{V^2}{(2\pi)^3} \int_{-\infty}^{\infty} \delta^*(\mathbf{k})\, \delta(\mathbf{k})\, \exp(i\mathbf{k}\cdot\mathbf{r}) d^3\mathbf{k}. \tag{E.10}$$

However, as $\delta^*(\mathbf{k})\delta(\mathbf{k})$ is merely the power spectrum, $|\delta_k|^2$, and, using the definition in equation (E.3), the correlation function is simply the Fourier transform of the power spectrum:

$$\xi(r) = \frac{V}{(2\pi)^3} \int_{-\infty}^{\infty} |\delta_k|^2 \exp(i\mathbf{k}\cdot\mathbf{r}) d^3\mathbf{k} = \frac{V}{(2\pi)^3} \mathcal{F}[|\delta_k|^2] \tag{E.11}$$

and, from the inverse transform (equation E.4),

$$|\delta_k|^2 = \frac{1}{V}\int_{-\infty}^{\infty} \xi(r)\exp(-i\mathbf{k}\cdot\mathbf{r})d^3\mathbf{r} = \frac{(2\pi)^3}{V}\mathcal{F}^{-1}[\xi(r)]. \tag{E.12}$$

The power spectrum is used in this thesis in the form $\Delta^2(k)$, which is defined as the contribution to the variance per $\ln k$, i.e.

$$\Delta^2(k)\frac{dk}{k} = \frac{V}{(2\pi)^3}|\delta_k|^2 4\pi k^2 dk, \tag{E.13}$$

which, rearranging, gives

$$\Delta^2(k) = \frac{V}{2\pi^2}|\delta_k|^2 k^3. \tag{E.14}$$

One may also recast the relationship between the correlation function and power spectrum (equation E.11) using this definition of the power spectrum.

$$\xi(r) = \frac{V}{(2\pi)^3}\int_{-\infty}^{\infty} \frac{2\pi^2}{V}\frac{\Delta^2(k)}{k^3}\exp(i\mathbf{k}\cdot\mathbf{r})d^3\mathbf{k}. \tag{E.15}$$

Integrating over all space (assuming isotropy) leads to

$$\xi(r) = \frac{1}{4\pi}\int_0^{\infty} \frac{\Delta^2(k)}{k^3}\frac{\sin(kr)}{kr}4\pi k^2 dk, \tag{E.16}$$

which simplifies to

$$\xi(r) = \frac{1}{r}\int_0^{\infty} \Delta^2(k)\sin(kr)\frac{dk}{k^2}. \tag{E.17}$$

Appendix F

Limber's Equation

This appendix derives the equation giving the angular correlation function from the power spectrum via Limber's equation. Limber's equation links the angular and spatial correlation functions and is given by (e.g. Peebles 1980; Peacock 1991)

$$w(\theta) = \frac{\int_0^\infty y^4 S(y)^2 dy \int_{-\infty}^{\infty} \xi(\sqrt{x^2 + y^2\theta^2}) dx}{\left[\int_0^\infty y^2 S(y) dy\right]^2}, \tag{F.1}$$

where $S(y)$ is the selection function (see § 5.5.3, equation 5.12) and y is the comoving radial distance. The spatial separation, r, is given by $\sqrt{x^2 + y^2\theta^2}$. The second integral then becomes

$$I = 2\int_0^\infty \xi(\sqrt{x^2 + y^2\theta^2}) dx = 2\int_{y\theta}^\infty \frac{r\xi(r)}{(r^2 - y^2\theta^2)^{1/2}} dr. \tag{F.2}$$

Using the relationship between the correlation function and the power spectrum given in Appendix E (equation E.17),

$$\xi(r) = \frac{1}{r}\int_0^\infty \Delta^2(k) \sin(kr) \frac{dk}{k^2}, \tag{F.3}$$

this becomes,

$$I = \int_0^\infty \Delta^2(k) \left[2\int_{y\theta}^\infty \frac{\sin(kr)}{(r^2 - y^2\theta^2)^{1/2}} dr\right] \frac{dk}{k^2}. \tag{F.4}$$

Recasting the inner integral using the substitution $r = ty\theta$ gives an integral of standard form

$$\int_{y\theta}^\infty \frac{\sin(kr)}{(r^2 - y^2\theta^2)^{1/2}} dr = \int_1^\infty \frac{\sin(k\, y\, \theta\, t)}{(t^2 - 1)^{1/2}} dt, \tag{F.5}$$

which (from equation 9.1.24 of Olver 1965) is $\frac{\pi}{2}J_0(ky\theta)$, where J_0 is the Bessel function. Substituting into equation (F.1) gives

$$w(\theta) = \frac{\int_0^\infty y^4 S(y)^2 dy \int_0^\infty \pi \Delta^2(k) J_0(ky\theta) \frac{dk}{k^2}}{\left[\int_0^\infty y^2 S(y) dy\right]^2} \equiv \frac{I}{N^2}. \tag{F.6}$$

Using the selection function (equation 5.12)

$$S(y) = \exp\left(-\left[\frac{y}{y_*}\right]^2\right)\left(\frac{y_*}{y}\right)^{\frac{1}{2}}, \tag{F.7}$$

one can then proceed to solve equation (F.6). The numerator becomes

$$I = \int_0^\infty \pi \Delta^2(k) y_* \left[\int_0^\infty y^3 \exp\left(-\frac{2y^2}{y_*^2}\right) J_0(ky\theta) dy\right] \frac{dk}{k^2}, \tag{F.8}$$

and putting $\alpha = 2/y_*^2$, the inner integral becomes

$$\int_0^\infty y^3 \exp(-\alpha y^2) J_0(ky\theta) dy = -\frac{\partial}{\partial \alpha} \int_0^\infty y \exp(-\alpha y^2) J_0(ky\theta) dy. \tag{F.9}$$

This is now a standard integral (Luke 1965; equation 11.4.29), which is given by

$$\int_0^\infty y \exp(-\alpha y^2) J_0(ky\theta) dy = \frac{\exp(-k^2\theta^2/4\alpha)}{2\alpha}. \tag{F.10}$$

So, substituting and differentiating

$$I = \int_0^\infty \frac{\pi y_*^5}{8} \Delta^2(k) \exp\left(-[k\theta y_*]^2/8\right)\left(1 - [k\theta y_*]^2/8\right) \frac{dk}{k^2}. \tag{F.11}$$

Expanding the normalisation term gives

$$N = y_*^{1/2} \int_0^\infty y^{3/2} \exp\left[-\left(\frac{y}{y_*}\right)^2\right] dy, \tag{F.12}$$

and, writing $t = y^2/y_*^2$ gives

$$N = \frac{y_*^3}{2} \int_0^\infty t^{1/4} \exp(-t) dt, \tag{F.13}$$

which is the gamma function, $\Gamma(5/4)$.

Thus equation (F.6) becomes

$$w(\theta) = \frac{\pi}{2\Gamma^2(5/4)} \int_0^\infty \Delta^2(k) \exp\left(-[k\theta y_*]^2/8\right) \left(1 - [k\theta y_*]^2/8\right) \frac{dk}{k^2 y_*}, \tag{F.14}$$

which is the equation used in § 5.5 to calculate the angular autocorrelation function from the power spectrum.

Appendix G

Publications

(1) Williams, B.G., Heavens, A.F., Peacock, J.A. & Shandarin, 1991, *Monthly Notices of the Royal Astronomical Society*, **250**, 458. "Exact hierarchical clustering in one dimension"

(2) Williams, B.G., Peacock, J.A. & Heavens, A.F., 1991, *Monthly Notices of the Royal Astronomical Society*, **252**, 43. "Large-scale periodicity: problems for cellular models"

Mon. Not. R. astr. Soc. (1991) 252, Short Communication, 43P–46P

Large-scale periodicity: problems with cellular models

B. G. Williams,[1] J. A. Peacock[2] and A. F. Heavens[1]
[1]Department of Astronomy, University of Edinburgh, Royal Observatory, Blackford Hill, Edinburgh EH9 3HJ
[2]Royal Observatory, Blackford Hill, Edinburgh EH9 3HJ

Accepted 1991 July 19. Received 1991 July 19; in original form 1991 June 17

SUMMARY

We consider recent attempts to employ cellular models of galaxy clustering in order to explain the apparent large-scale periodicity seen in pencil beam surveys. We concentrate on the Voronoi foam model, which has been proposed to provide a natural explanation for both large-scale periodicity and the clustering of Abell clusters. We show that this model predicts a scale length for the galaxy–galaxy correlation function which is too large: $r_0 > 10h^{-1}$ Mpc (h is the Hubble constant in units of 100 km s^{-1} Mpc^{-1}). Similar problems arise for other models based on cellular structures: the observed value of the galaxy–galaxy correlation function sets a limit on how large the cells can be.

1 INTRODUCTION

Much interest has been aroused by the recent pencil-beam survey of Broadhurst *et al.* (1990) which shows regular clustering in the redshift distribution of galaxies separated by intervals of $128h^{-1}$ Mpc. A natural way of accounting for such apparent periodicity is to appeal to a cellular distribution of galaxies. One specific model that has been put forward is the Voronoi foam (e.g. Coles 1990; van de Weygaert 1991; Ikeuchi & Turner 1991). This is a simple statistical description of the distribution of galaxies in which they are confined to sheets, filaments and clusters surrounding voids. The structure is fully determined by the distribution of randomly placed nuclei, each cell containing a single nucleus. The walls that bound the cells are located at the planes midway between adjacent nuclei and intersect to form filaments which in turn intersect to form nodes.

Such a structure might approximate that of an explosion model of galaxy formation (e.g. Ostriker & Cowie 1981) but is also generic in the late stages of a model where structure forms through gravitational instability. Cellular structures are seen in N-body simulations (e.g. Matsuda & Shima 1984) and approximate models such as the adhesion model (e.g. Gurbatov, Saichev & Shandarin 1989). By identifying the nodes with Abell clusters, van de Weygaert & Icke (1989) have shown that higher estimates of the cluster–cluster correlation function can be reproduced by this model. Furthermore van de Weygaert (1991) has used the model to simulate the Broadhurst *et al.* (1990) survey, obtaining periodicities in the range 100–150 h^{-1} Mpc.

Thus the Voronoi foam model has been shown to account for both the cluster–cluster correlation function and the large-scale periodicity of the Broadhurst *et al.* (1990) survey. However, as we shall demonstrate below, the model is inconsistent with the observed galaxy–galaxy correlation function.

2 SIMULATIONS

We wish to investigate whether the Voronoi foam model is able to reproduce the galaxy–galaxy correlation function in addition to the periodicity and the cluster–cluster correlation function. We thus need to construct and populate the geometric skeleton of the Voronoi foam. We use computer simulations that rely on a kinematical technique described by van de Weygaert & Icke (1989). The essence of this method is that particles (nominally representing galaxies) are randomly distributed in space and given a velocity that is directed radially away from the nearest Voronoi nucleus. Each particle is moved in a series of time steps until it reaches a wall. The particle's velocity is then modified by cancelling its velocity perpendicular to the wall, thus constraining the particle to move along the wall until it reaches a filament. Its velocity is again modified, constraining it to move along the filament, until it reaches a node, where it stops.

By advancing the simulation a given number of time steps and recording the positions of each particle, it is possible to create snapshots of the structure at different stages. This allows us to explore different ways of populating the same geometrical structure. Particles progress from voids via walls and then filaments to nodes. Thus at early stages of the simulation most of the particles lie in voids and walls with a few in filaments and nodes; at later times this situation is reversed. An alternative is to record the position of each particle as it first reaches a wall, filament or node. This gives a 'static' picture of the skeleton.

Note that this is not the method used by van de Weygaert (1991) in his simulation of the Broadhurst *et al.* (1990) survey, though the 'static' method gives a very similar distribution of particles on the walls. His method is partly geometrical, using the known geometrical properties of the Voronoi

foam to determine where a cone (representing the field of view of the pencil-beam survey) would cut a wall. The area of wall cut by the cone is populated by a number of galaxies which are given random perpendicular distance from the wall and a luminosity drawn from a Schechter function. The galaxies are distributed randomly on the wall, the number density fixed by the size and shape of the wall. Although this method of populating the walls with galaxies differs from ours we believe this to be of little consequence as we shall show below.

3 RESULTS

All our simulations were run using 512 nuclei distributed randomly within a cubic volume with periodic boundary conditions. Our length scale is fixed by normalizing the number of nodes to the observed number density of richness ≥ 1 Abell clusters (6×10^{-6} h^3 Mpc^{-3}; van de Weygaert & Icke 1989; van de Weygaert 1991) giving a charcteristic inter-nucleus separation of 104 h^{-1} Mpc. This gives a box with side of length 832 h^{-1} Mpc. The node–node correlation function is described by the standard power-law, $\xi(r)=(r/r_0)^{-\gamma}$, with slope $\gamma=2$ and clustering length, $r_0=27$ h^{-1} Mpc. This agrees with the clustering length found for this model by van de Weygaert & Icke (1989) and is consistent with the correlation function for Abell clusters obtained by Bahcall & Soneira (1983). Problems arising for the Voronoi model if the actual correlation length of Abell clusters is significantly lower than this (e.g. Sutherland 1988) are discussed below.

The Voronoi foam provides three distinct sites where galaxies might be located: walls, filaments and nodes. It is instructive to look at the clustering properties of each site separately. This is done by recording the position of each particle when it first reaches a wall, filament or node. The three corelation functions corresponding to particles at walls, filaments and nodes are shown by the solid lines in Fig. 1. As one can see, both the amplitude and slope of the correlation function increase as the particles move from walls through filaments to nodes.

In the Voronoi model the geometric skeleton has zero thickness. Obviously this is not the case in the real Universe, so we have investigated the effects of finite thicknesses by giving each particle a random displacement characterized by a Gaussian of half-width $5h^{-1}$ Mpc. The effect of this is shown by the dashed lines in Fig. 1. Though this changes the correlation function it does so only on scales small compared to the clustering length. In order to reduce r_0 to $5h^{-1}$ Mpc we need to smooth on scales $\sim 15h^{-1}$ Mpc. This is clearly too large as the walls found in the Broadhurst *et al.* (1990) survey have an $8h^{-1}$ Mpc half-width and even this may be an anomalously large value (see Kaiser & Peacock 1991).

Fig. 1 suggests that the minimum correlation length arises from particles that are confined exclusively to the walls. However, even in this case $r_0\gtrsim 10h^{-1}$ Mpc, which is in conflict with the generally accepted observed value of 4–$7h^{-1}$ Mpc (Bean *et al.* 1983; Davis & Peebles 1983; Shanks *et al.* 1983 1989; de Lapparent, Geller & Huchra 1988). The first indication is thus that the Voronoi model as normalized above will generate excessive small-scale galaxy correlations. To see if this conclusion can be weakened we need to know how the correlation function is affected when the surface density of particles on the walls is varied.

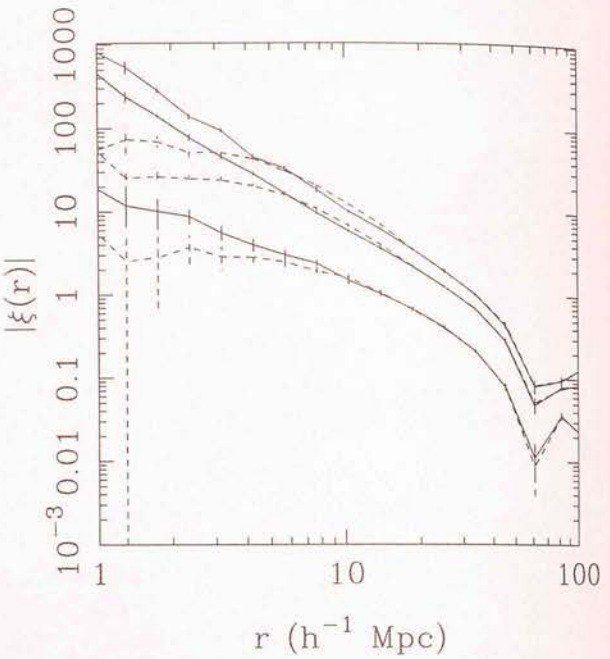

Figure 1. Two-point correlation function for particles when they first reach walls (bottom line), filaments (middle line) and nodes (top line) in a Voronoi foam. This gives a pseudo-random coverage of the walls, similar to that of van de Weygaert (1991). The dashed line shows the effect of adding a random displacement to each particle, drawn from a Gaussian of half-width $5h^{-1}$ Mpc, to simulate the finite thickness of the Voronoi skeleton. Between 5–$30h^{-1}$ Mpc all the correlation functions may be fitted by a power law $\xi(r)=(r/r_0)^{-\gamma}$ where, reading from left to right, $r_0=13h^{-1}$ Mpc, $\gamma\sim1.6$ (walls), $r_0=27h^{-1}$ Mpc, $\gamma\sim1.75$ (filaments) and $r_0=32h^{-1}$ Mpc, $\gamma\sim1.8$ (nodes). The reason that the node–node correlation function differs from that of van de Weygaert & Icke (1989) is that they weighted the nodes equally whereas we weighted the nodes according to the number of particles present at each node. The correlation functions are the mean of 10 independent simulations and the error bars represent the standard deviation on the mean.

To investigate this we have calculated the correlation function at different times during a simulation. Though this gives various distributions of particles, the correlation functions are very similar provided only the particles on the walls are included. Two sample correlation functions are shown in Fig. 2, one for an early time (dashed line) and one for a later time (dot-dash line). Both have $r_0\gtrsim 10h^{-1}$ Mpc.

So far the initial distribution of paticles has been random, giving a uniform initial density. An alternative is to place an equal number of particles (still distributed randomly) within each cell. This will result in a radical change in the surface density of particles on the walls. The effect of this is to raise the correlation length ($r_0\sim 20h^{-1}$ Mpc) and is shown by the dotted line in Fig. 2. A further change is to weight each particle according to its position on the wall. The weighting scheme used effectively gives each wall the same surface density of particles. The result of this is to lower the correlation length, but only to $r\sim 11h^{-1}$ Mpc. This is shown by the dot-dot-dash line in Fig. 2.

We have extensively tested this property of the correlation function and have found that it is very robust. For a wide range of distributions, $r_0\gtrsim 10h^{-1}$ Mpc. This is in agreement with Pierre, Shaver & Iovino (1988) who have also measured

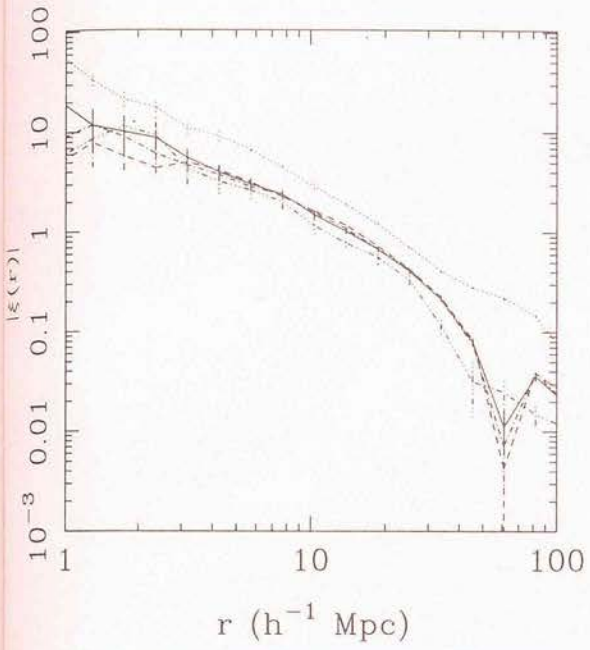

Figure 2. The two-point correlation function for all particles in alls. The different curves represent different methods for populat-g the walls. The solid line is the lower curve in Fig. 1, i.e. stopping articles when they first reach walls. The dashed and dot-dashed nes are the correlation functions of all particles on the walls at an rly (dashed, 60 per cent of particles still in voids) and late (dot-shed, 10 per cent of particles still in voids) stage of a dynamical mulation. The dotted line represents stopping the particles on the alls as in Fig. 1, but giving each cell an equal number of particles. he dot-dot-dash line is the same as the dotted line, but with the articles weighted so as to give the walls a constant surface density. he correlation functions are the mean of 10 independent simula-ons and the error bars represent the standard deviation on the ean.

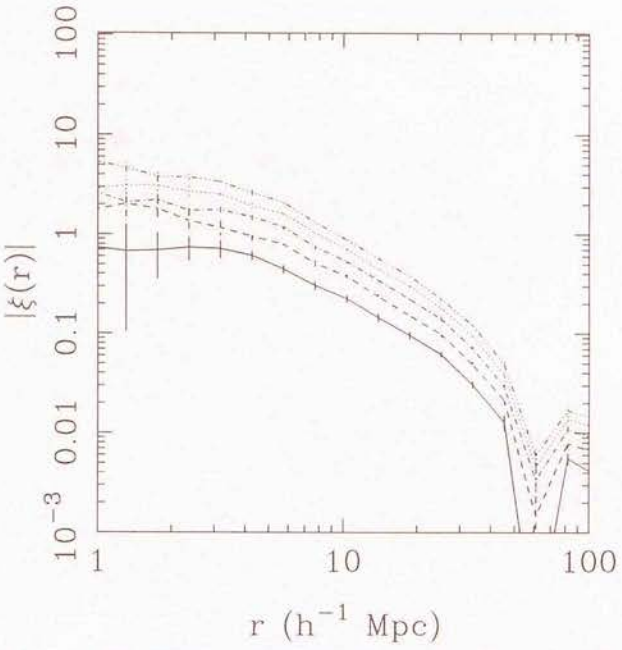

Figure 3. The two-point correlation function for all particles. The different curves represent different stages of the simulation. The percentages of particles in voids are 66 per cent (solid line), 58 per cent (dashed line), 51 per cent (dot-dash line), 46 per cent (dotted line) and 41 per cent (dot-dot-dash line). The correlation functions are the mean of 10 independent simulations and the error bars represent the standard deviation on the mean.

e 'galaxy–galaxy' correlation function of the Voronoi foam hile investigating quasar absorption line systems. They ed a characteristic inter-nucleus separation of $25h^{-1}$ Mpc, d obtained a correlation function with $\gamma \sim 1.6$ and $=3h^{-1}$ Mpc. Had they normalized their model in the same y as van de Weygaert (1991) this would have led to their rrelation function having $r_0 \sim 12h^{-1}$ Mpc, which is con-tent with our result.

It is only possible to reduce r_0 significantly by using highly ntrived configurations. For example, by placing six par-les at each nucleus and starting them one along each Car-sian axis we can reduce the correlation length to $5h^{-1}$ Mpc, t we also reduce the slope to ~ 1.3. The only way we have ceeded in reducing r_0 to that of the observed laxy–galaxy correlation function without such fine tuning the initial particle distribution is to include *all* the par-les. At late times this increases the correlation function as e particles in the nodes are more strongly clustered. How-er, for early times the inclusion of the void particles de-eases r_0. This is because they are still close to their initial ndom) positions. Fig. 3 shows the correlation function of particles at early times. Though this achieves the required w value of r_0, filling the voids with galaxies is unsupported observations. Visual inspection of redshift surveys such as e CfA survey (de Lapparent, Geller & Huchra 1986) and the southern redshift catalogue (Fairall *et al.* 1990) clearly show that though the voids are not entirely devoid of luminous galaxies, the percentage of galaxies found in voids is considerably less than the 40 per cent plus of particles in voids required by the correlation functions in Fig. 3.

This is supported by Fig. 4, which shows a $10h^{-1}$ Mpc deep slice through one of the simulations used to calculate the correlation functions in Fig. 3. As one can see, though the voids are well delineated by the particles in walls (filled circles), the other particles (open circles) fill the voids without exhibiting the any cellular structure. This is clearly at odds with observations. One further observation from Fig. 4 is that the characteristic linear dimensions of the voids are in the region of $80–100h^{-1}$ Mpc, far greater than the median void size of $29h^{-1}$ Mpc of the CfA survey (Pierre, Shaver & Iovino 1988). This further suggests that the Voronoi foam model over predicts the size of small-scale galaxy clustering.

4 DISCUSSION

The above estimates of the 'galaxy–galaxy' correlation function (i.e. the correlation function of particles in walls) show that although the Voronoi foam provides a good approximation to the Abell cluster–cluster correlation function and naturally reproduces the large-scale periodicity observed by Broadhurst *et al.* (1990), it is incapable of *naturally* reproducing the small-scale clustering of galaxies: the intrinsic clustering of the geometrical skeleton is too large.

The only freedom we have is in the normalization of the length scale. Our results suggest that the Voronoi model is capable of providing a reasonable description of galaxy

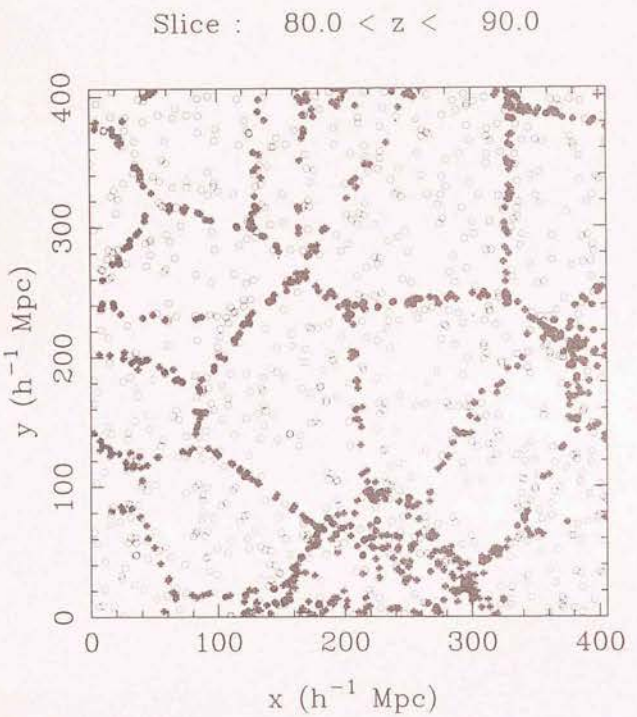

Figure 4. A $10h^{-1}$ Mpc slice through the bottom left hand corner of a Voronoi foam. Filled circles represent particles in walls and open circles those that have not yet reached walls. The slice is taken from one of the simulations used to calculate the correlation function in Fig. 3 shown by the dot-dash line.

clustering if we raise the density of the nodes by a factor 8 (i.e. to 5×10^{-5} h^3 Mpc^{-3}), corresponding to halving the length scale. This would predict $r_0 \sim 14h^{-1}$ Mpc for nodes, in agreement with some more recent work on Abell clusters (Sutherland 1988; Sutherland & Efstathiou 1991). However, our node density would then no longer be in agreement with the observed number density of richness ≥ 1 Abell clusters, though we could obtain agreement of number densities by including less-rich clusters. The problem is that by decreasing the length scale in this way we decrease the scale of the periodicity so that it is no longer in agreement with the Broadhurst *et al.* (1990) result.

We believe that other cellular models would also have similar problems. For example, a cubic lattice of cell size λ was shown by Heavens (1985) to have $r_0 = \lambda/8$: 16 h^{-1} Mpc if $\lambda = 128$ h^{-1} Mpc. The more reasonable value of $\lambda = 40$ h^{-1} Mpc will clearly not provide a natural explanation of the Broadhurst *et al.* (1990) periodicity.

In conclusion, cellular models face severe problems if they are to account for both small scale galaxy–galaxy clustering and the observed large-scale periodicity of the Broadhurst *et al.* (1990) survey. By requiring the cell size to be large enough to account for the latter, we find that the intrinsic clustering of the cellular structure is too large to be consistent with the observed galaxy–galaxy correlation function. If the large-scale galaxy distribution approximates a cellular structure then it is hard to see how the $128h^{-1}$ Mpc periodicity found by Broadhurst *et al.* (1990) can be a common feature of pencil-beam surveys.

ACKNOWLEDGMENTS

BGW is supported by an SERC studentship. We wish to thank the referee, W. J. Sutherland, for useful comments on the manuscript and for suggesting the inclusion of Fig. 4.

REFERENCES

Bahcall, N. A. & Soneira, R. M., 1983. *Astrophys. J.*, **270**, 20.
Bean, A. J., Efstathiou, G., Ellis, R. S., Peterson, B. A. & Shanks, T. 1983. *Mon. Not. R. astr. Soc.*, **205**, 605.
Broadhurst, T. J., Ellis, R. S., Koo, D. C. & Szalay, A. S., 1990. *Nature*, **343**, 726.
Coles, P., 1990. *Nature*, **346**, 446.
Davis, M. & Peebles, P. J. E., 1983. *Astrophys. J.*, **267**, 465.
de Lapparent, V., Geller, M. J. & Huchra, J. P., 1986. *Astrophys. J. Lett.*, **338**, L5.
de Lapparent, V., Geller, M. J. & Huchra, J. P., 1988. *Astrophys. J.*, **332**, 44.
Fairall, A. P., Palumbo, G. G. C., Vettolani, G., Kauffmann, G., Jones, A. & Baiesi-Pillastrini, G., 1990. *Mon. Not. R. astr. Soc.*, **247**, 21 P.
Gurbatov, S. N., Saichev, A. I. & Shandarin, S. F., 1989. *Mon. Not. R. astr. Soc.*, **236**, 385.
Heavens, A., 1985. *Mon. Not. R. astr. Soc.*, **213**, 143.
Ikeuchi, S. & Turner, E. L., 1991. *Mon. Not. R. astr. Soc.*, **250**, 519.
Kaiser, N. & Peacock, J. A., 1991. *Astrophys. J.*, in press.
Matsuda, T. & Shima, E., 1984. *Prog. theor. Phys.*, **71**, 855.
Ostriker, J. P. & Cowie, L. L., 1981. *Astrophys. J. Lett.*, **243**, L127.
Pierre, M., Shaver, P. A. & Iovino, A., 1988. *Astr. Astrophys.*, **197**, L3.
Shanks, T., Bean, A. J., Efstathiou, G., Ellis, R. S., Fong, R. & Peterson, B. A., 1983. *Astrophys. J.*, **274**, 529.
Shanks, T., Hale-Sutton, D., Fong, R., Metcalfe, N., 1989. *Mon. Not. R. astr. Soc.*, **237**, 589.
Sutherland, W. J., 1988. *Mon. Not. R. astr. Soc.*, **234**, 159.
Sutherland, W. J. & Efstathiou, G., 1991. *Mon. Not. R. astr. Soc.*, **248**, 159.
van de Weygaert, R., 1991. *Mon. Not. R. astr. Soc.*, **249**, 159.
van de Weygaert, R. & Icke, V., 1989. *Astr. Astrophys.*, **213**, 1.

Exact hierarchical clustering in one dimension

B. G. Williams, A. F. Heavens, J. A. Peacock and S. F. Shandarin

Mon. Not. R. astr. Soc. (1991) **250**, 458–476

Exact hierarchical clustering in one dimension

B. G. Williams,[1] A. F. Heavens,[1] J. A. Peacock[2] and S. F. Shandarin[3]★

[1] *Department of Astronomy, University of Edinburgh, Royal Observatory, Blackford Hill, Edinburgh EH9 3HJ*
[2] *Royal Observatory, Blackford Hill, Edinburgh EH9 3HJ*
[3] *Department of Physics and Astronomy, University of Kansas, Lawrence, KS 66045, USA*

Accepted 1991 January 8. Received 1991 January 2; in original form 1990 September 17

SUMMARY

We present the results of a series of one-dimensional simulations of gravitational clustering based on the adhesion model, which is exact in the one-dimensional case. The catalogues of bound objects resulting from these simulations are used as a test of analytical approaches to cosmological structure formation. We consider mass functions of the Press–Schechter type, together with modifications to this formalism based on density-peak theories, and also the two-point correlation function estimated from peak theory. With suitable choices of filter function for the linear density field, these techniques can give an excellent fit to the data. However, there are some restrictions: for a one-dimensional spectral index, $n > 3$, the characteristic mass scale grows faster than expected in the standard clustering hierarchy, and the multiplicity function has a shape quite different from the Press–Schechter form. For $n \gtrsim 0$, the correlation-function method also gives less satisfactory results as dynamical contributions to the correlations tend to dominate statistical ones in this case. Finally, we test to what extent the locations of individual collapsed objects can be predicted via linear theory. This turns out to be possible only for objects near the characteristic non-linear mass: results such as the low-mass slope of the multiplicity function can only be correct in a statistical sense.

1 INTRODUCTION

Although the Universe we see around us is highly non-linear on scales of up to at least the size of galaxy clusters, the microwave background provides very strong evidence that the Universe was once isotropic and homogeneous. In the context of the theories of inflationary cosmology the structure that we now see has grown via graviational amplification of small perturbations which originated from quantum fluctuations at very early times. One of the problems facing models of the evolution of the universe is to explain how these perturbations have grown into the present-day stucture.

However, it is not straightforward to calculate the final outcome of this process directly from a given set of initial conditions because of the highly non-linear nature of the problem. Considerable progress has been made via the use of n-body simulations, but these are hampered by limited resolution and dynamic range and by problems concerning the location of luminous objects with respect to structures formed. Thus there still remains a considerable motivation for finding analytical methods that directly link the statistical properties (such as mass and correlation functions) of the final structure to the initial conditions.

This paper is concerned with the comparison of such direct methods with numerical simulations. We restrict ourselves to one spatial dimension because in this case it is easier to attain the large dynamic range in mass necessary for a thorough test of the direct methods and because in one dimension our numerical model is *exact*.

The numerical simulations are based on the adhesion model (Gurbatov, Saichev & Shandarin 1989), which is a fully non-linear description of gravitational perturbations. The model is based on Burgers' equation (Burgers 1940, 1974) and can be viewed as an extension of the well known Zel'dovich approximation (Zel'dovich 1970) to include the notion of 'sticky' particles which forbids the crossing of particle trajectories, the point where the Zel'dovich approximation breaks down.

In this paper we compare our results with theoretical predictions of both the mass and two-point correlation functions for collapsed objects. We consider the mass function proposed by Press & Schechter (1974) and also the modifications suggested by Peacock & Heavens (1990) based on the consideration of Gaussian peaks in the linear density field. Similarly we consider the two-point correlation function for Gaussian peaks in a linear density field derived

★ Permanent address: Institute for Physical Problems, Academy of Sciences, Moscow 117334, USSR.

in Lumsden, Heavens & Peacock (1989); see also Coles (1989). We believe that testing these theories in one dimension is a valid approach as there are no specific features in these theories that make them unique in three dimensions. Therefore we conclude that our results can provide a useful guide for future studies in two and three dimensions.

The paper is arranged as follows. Section 2 discusses the adhesion model and the simulations. Section 3 examines the various direct methods that we have compared with the results of our simulations, which are presented in Section 4. We discuss the implications of our work and summarize our findings in Section 5.

2 THE SIMULATIONS

2.1 Basics of the adhesion model

Our simulations are based on the adhesion model which leads to Burgers' equation. The use of Burgers' equation in connection with the problem of large-scale structure has been discussed in several papers (Gurbatov & Saichev 1984; Gurbatov, Saichev & Shandarin 1984, 1985; Shandarin 1987; Weinberg & Gunn 1990; Nusser & Dekel 1990). The adhesion model as we implement it was first presented in the paper by Gurbatov *et al.* (1989) and for a full derivation we refer the reader to that paper. Here we reproduce the most important parts of the model.

The model is based on the equations describing the evolution of density inhomogeneities in an expanding dust-like medium in comoving coordinates. These are (Peebles 1980)

$$\frac{dV_i}{dt} + \frac{\dot{a}}{a} V_i = -\frac{1}{a} \frac{\partial \phi}{\partial x_i} \tag{1}$$

$$\frac{\partial^2 \phi}{\partial x_i^2} = 4\pi G a^2 [\rho(x_i, t) - \rho_b(t)] \tag{2}$$

$$\frac{\partial \rho}{\partial t} + 3\frac{\dot{a}}{a}\rho + \frac{1}{a}\frac{\partial}{\partial x_i}(\rho V_i) = 0, \tag{3}$$

where the peculiar velocity, V_i is given by

$$V_i = a\frac{dx_i}{dt} \tag{4}$$

in terms of comoving coordinates $x_i = r_i/a$. r_i is the Eulerian coordinate, ϕ is the perturbation of the gravitational potential, $a(t)$ is the scale factor (the dot signifies the time derivative), ρ the density and ρ_b the mean density.

The Zel'dovich approximation is given by

$$x_i = q_i + b(t) \cdot s_i(\boldsymbol{q}), \tag{5}$$

where x_i and q_i are comoving Eulerian and Lagrangian coordinates respectively, $b(t)$ is a function describing the time evolution of the growing mode of gravitational instability in the linear approximation and $s_i(\boldsymbol{q})$ is the potential vector field $s_i(\boldsymbol{q}) = \partial\Phi_0(\boldsymbol{q})/\partial q_i$ which describes the spatial structure of the gravitational perturbations in the linear stage. Φ_0 is proportional to the initial gravitational potential and it is related to ϕ by $\phi = 3\ddot{a}ab \cdot \Phi_0(\boldsymbol{q})$.

By assuming that the Zel'dovich approximation is valid outside any structure one can use it to calculate explicitly the acceleration for every point in the fluid. By defining a new set of variables

$$v_i(x_i, t) = \frac{1}{ab} V_i(x_i, t) \tag{6}$$

$$\eta(x_i, t) = a^3 \rho(x_i, t) \tag{7}$$

and using the Zel'dovich approximation one obtains the following set of equations describing the time evolution of the peculiar velocity and density.

$$\begin{aligned} &\frac{\partial v_i}{\partial b} + v_k \frac{\partial v_i}{\partial x_k} = 0 \\ &\frac{\partial \eta}{\partial b} + \frac{\partial(\eta v_i)}{\partial x_i} = 0. \end{aligned} \tag{8}$$

Thus the Zel'dovich approximation is equivalent to the fluid mechanics of a perfect inviscid fluid and therefore tells us nothing about the evolution of density once orbit crossing has occurred.

The adhesion model is an attempt to extrapolate the Zel'dovich approximation into the non-linear regime. To do this 'sticky' particles are used. Though the model is expressed in terms of a continuous medium, it is useful to think of it in terms of individual particles that move with the fluid. Every particle moves in accordance with the first equation in (8) until it runs into another particle whereupon the two particles 'stick' and move together with a common velocity that conserves momentum. In the case of a continuous medium this can be described mathematically by inserting a viscous term in the first equation in (8) giving

$$\frac{\partial v_i}{\partial b} + v_k \frac{\partial v_i}{\partial x_k} = \nu \frac{\partial^2 v_i}{\partial x_k^2}. \tag{9}$$

The form of the viscous term chosen leads us to an equation analogous to the Burgers' equation (Burgers 1940, 1974) which has a well known analytic solution.

For the study of large-scale structure we shall only consider potential motions, as in linear theory the growing mode is curl-free. Introducing a velocity potential related to the velocity field as

$$v_i(\boldsymbol{x}, b) = -\frac{\partial \Phi(\boldsymbol{x}, b)}{\partial x_i} \tag{10}$$

we may solve equation (9). Note that we observe the opposite sign convention to that taken by Gurbatov *et al.* (1989), who gave the exact solution in terms of the usual diffusive Green function.

$$v_i(\boldsymbol{x}, b) = \frac{\int (x_i - q_i)/b \exp\{-[1/2\nu] G(\boldsymbol{x}, \boldsymbol{q}, b)\} d^3q}{\int \exp\{-[1/2\nu] G(\boldsymbol{x}, \boldsymbol{q}, b)\} d^3q}, \tag{11}$$

where

$$G(\boldsymbol{x}, \boldsymbol{q}, b) = \frac{(\boldsymbol{x} - \boldsymbol{q})^2}{2b} - \Phi_0(\boldsymbol{q}), \tag{12}$$

which differs from the expression given by Gurbatov *et al.* (1989) only in the sign of Φ_0.

In the limit $\nu \to 0$ the main contribution to the integrals in equation (11) comes from the region where $G(\boldsymbol{x}, \boldsymbol{q}, b)$ has a minimum with respect to $\boldsymbol{q}$. In this case it can be shown that equation (11) simplifies to

$$v_i(\boldsymbol{x}, b) = \frac{x_i - q_i(\boldsymbol{x}, b)}{b} \tag{13}$$

where $q_i(\boldsymbol{x}, b)$ is the coordinate of the absolute minimum of $G(\boldsymbol{x}, \boldsymbol{q}, b)$ at given $\boldsymbol{x}$ and b, provided that this is a non-degenerate case.

2.2 The adhesion model in one dimension

We have analysed the adhesion model in one dimension using a geometrical technique which can also be extended to higher dimensions. Equation (13) is a solution of equation (9) if the function $G(x, q, b)$ (equation 12) has a minimum with respect to q at the point $q_i(x, b)$, which implies

$$x = q_i - b \left. \frac{\partial \Phi_0}{\partial q} \right|_{q_i}. \tag{14}$$

If we now wish to find the Eulerian position of a particle whose Lagrangian position is q_t we can do so by constructing a parabola, P

$$P = h + \frac{(x-q)^2}{2b} \tag{15}$$

(where h is a constant) and require it to be tangential to the potential $\Phi_0(q)$ at q_t. We shall show that x is then the Eulerian position of the particle at a time characterized by the function $b(t)$. The condition that the parabola is tangential to the potential requires

$$\left. \frac{\partial P}{\partial q} \right|_{q_t} = \frac{(q_t - x)}{b} = \left. \frac{\partial \Phi_0}{\partial q} \right|_{q_t} \tag{16}$$

and hence

$$x = q_t - b \left. \frac{\partial \Phi_0}{\partial q} \right|_{q_t}. \tag{17}$$

By comparing equations (14) and (17) it can be seen that $q_t = q_i$ is also a solution of equation (9) with the Eulerian position, x, given by equation (17), i.e. the solution of equation (9) is the minimum of the parabola.

It is clear from equations (13) and (16), that the velocity is given by the gradient of the potential:

$$v(x, b) = - \left. \frac{\partial \Phi_0}{\partial q} \right|_{q_t}. \tag{18}$$

Thus for a given time, characterized by $b(t)$, the parabola P is a solution to equation (9) in the limit $\nu \to 0$ and gives both the position (bottom of the parabola) and velocity (negative gradient of the potential) of a particle with Lagrangian co-ordinate q_t. We may therefore take every point in Lagrangian space and calculate its Eulerian position and velocity at a time characterized by $b(t)$ by simply constructing a parabola tangential to the parabola at that point.

So far this is nothing more than the Zel'dovich approximation. For early times $b(t)$ will be small and there is a one-to-one correspondence between points in Lagrangian and Eulerian space. As $b(t)$ increases and the parabola broadens there will come a time when a parabola will be tangential at more than one point in Lagrangian space and so the solution in equation (17) is no longer unique.

This is shown in Fig. 1. Matter from Lagrangian points q_1 and q_2 will simultaneously arrive at the point x, bringing with them all the matter in between to form a single 'pancake' at x. Because of the simplification of allowing $\nu \to 0$ the adhesion model tells us nothing of the internal structure of objects formed. In one dimension, all objects formed are point objects, completely specified by their location, mass and momentum.

The strength of the adhesion model is that the above process can be carried out for any value of $b(t)$ without the need to refer to previous steps, thus avoiding cumulative errors and also being faster than conventional n-body techniques. For our present investigation the most important advantage of the adhesion model is that it is *exact* in one dimension.

2.3 Computer simulations of the adhesion model

The simulations consist of an array holding the gravitational potential and its derivative which are sampled at a discrete number of points, equally spaced in Lagrangian coordinates. The potential and its derivative are generated by means of a fast Fourier transform of a specified power spectrum with random phases. Our boundary conditions are such that the potential is periodic. Each of the points is designated either 'free' if the point has not yet been included in any pancake or 'bound' if it has. The array is shifted so that the global maximum (always a free point) lies at the boundary of the array with the first point of the array immediately to the right of the maximum and the last point of the array immediately to its left.

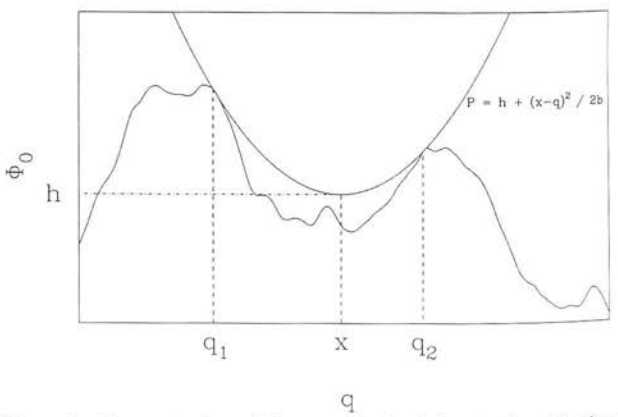

Figure 1. Demonstration of the graphical solution to the adhesion model. The parabola P touches the gravitational potential Φ_0 at two points, q_1 and q_2. As the parabola does not intersect the potential at any point, particles at q_1 and q_2 would both simultaneously end up at the bottom of the parabola, x. In one dimension it is obvious that all matter between these two points must also end up at x.

We use the technique described in Section 2.2 to locate the pancakes by looking for instances where a parabola is tangential to the potential at two separate points. For each point in the array, starting with the first, we check all others to the right to see if the parabola intersects the potential once, more than once or not at all. If the parabola does not intersect the potential at any other point then that point is free and we proceed to the next.

Because of the discrete nature of the potential we make the approximation that if the parabola intersects the potential at one and only one other point in the array then the parabola is tangential at that point. This then determines the right-hand edge of the pancake in Lagrangian space.

If the parabola intersects the potential more than once, then the point is bound and the left-hand edge of the pancake in Lagrangian space lies between the bound point and the previous (free) point. The position of the edge is found more accurately by conducting a binary search using values of the potential and its derivative interpolated from the free and bound points. The search continues until the approximate condition that the parabola is tangential at some other point (described above) is met which determines the position of the left-hand edge to high accuracy.

A further binary search is then conducted, fitting a parabola tangentially to interpolated points in the region of the right-hand edge until the parabola is found to intersect the potential once and only once in the region of the left-hand edge. The program then resumes at the next point immediately after the right-hand edge of the pancake as all intervening points are obviously bound.

The mass of the pancake is the linear distance between the two edges in Lagrangian space (i.e. we set the line density to unity). The pancake's momentum is the difference between the values of the potential at the two edges. The location of the pancake in Eulerian space is taken to be the average of the positions of the bottoms of the two parabolae that accurately determine the left- and right-hand edges of the pancake in Lagrangian space. These differ only by a fraction of a grid point.

We use two simple ways of internally checking the program. One is to calculate the total mass of the objects and the free points. With unit line density this should be equal to the size of the simulation. The other check is to sum the momenta of the objects and the free points which should come to zero.

3 DIRECT METHODS

3.1 The Press–Schechter mass function

In pressure-free linear theory the density perturbations, $\delta(\boldsymbol{x})=[\rho(\boldsymbol{x})-\rho_b]/\rho_b$, grow in proportion to the scale factor, a, as long as $\Omega=1$ [in which case the scale factor, a, is equivalent to the time dependent function $b(t)$ used in Section 2] and the density field rapidly becomes non-linear. For a large range of initial conditions the linear density field will be dominated by fluctuations on small scales, which will be the first to become non-linear, leading to a local collapse. The objects formed will then cluster together and merge to form larger objects as time goes on. The critical idea in continuing to apply linear theory to this non-linear situation is that the location and properties of the non-linear objects might nevertheless be found by *smoothing* the linear-theory density field on a given scale. This approach is aided by the fact that one is often interested in the case where the various Fourier components, δ_k, of the density field are assumed to have random phases, and hence the field is Gaussian. All the statistics of the situation are therefore specified simply by the power spectrum, $|\delta_k|^2$.

An early attempt at using such ideas to determine the mass function of collapsed objects analytically was made by Press & Schechter (1974). Their method was to evolve the density field according to the linear approximation and then, for a given time, implicitly smooth the field on different mass scales, M. Any point with $\delta(x)$ greater than some critical value $\delta_c(\sim 1)$ was assumed to have collapsed into an object of mass at least M.

Following this prescription it is relatively simple to derive their original mass function [$f(M)\,dM$ is the number density of objects in a mass range M to $M+dM$]:

$$f(M)=\frac{\rho_b\delta_c}{\sqrt{2\pi}\sigma_0 M^2}\exp\left(-\frac{\delta_c^2}{2\sigma_0^2}\right)\frac{d(\ln\sigma_0)}{d(\ln M)}, \tag{19}$$

where σ_0^2 is the variance of the smoothed density field, given in three dimensions by

$$\sigma_0^2(R_f)=A\int_0^\infty W(k,R_f)^2|\delta_k|^2 4\pi k^2\,dk, \tag{20}$$

A being a normalization constant and $W(k, R_f)$ a filter function, and the filter radius, R_f, representing smoothing on a given length scale, which corresponds to a given mass, M (see Section 3.3).

The variance, σ_0^2, is normalized so that it is equal to the square of the critical density, δ_c, for a given filter radius, R_*, corresponding to a cut-off mass, M_*, which represents the boundary between the linear and non-linear regimes. When filtered on a scale $M<M_*$ the density field is non-linear, but for filtering scales corresponding to masses above M_* the density field is still linear.

The Press–Schechter formalism accounts for only half of the mass as it does not include the underdense regions where $\delta<0$. To correct for this Press & Schechter (1974) inserted a factor of two in their mass function, thus doubling the *number* of objects at all masses without changing the actual mass of any of the objects. If the filter function contains a sharp truncation in k space, then this factor of two is naturally obtained (see Bond *et al.* 1990). However, for any differentiable filter function this is not the case and the mass function differs from the Press–Schechter form (Peacock & Heavens 1990).

3.2 Press–Schechter and peaks theory

Another conceptual problem posed by the Press–Schechter formalism is that objects form from spatially unconnected regions. Consider the density field smoothed on some radius R_f. A point with $\delta=\delta_c$ will be part of an object of mass $M(R_f)$, but adjacent points will have $\delta\neq\delta_c$. However, when smoothed on some other scale $R_f\pm\delta R_f$ these points will also have $\delta=\delta_c$ and thus be incorporated into objects of mass $M(R_f\pm\delta R_f)$, i.e. spatially adjacent points will become incorporated in different objects, a very unphysical process.

A better approach to the formation of structure, which avoids some of these conceptual problems, is to assume that

objects form at the sites of maxima in the linear density field (Peacock & Heavens 1985; Bardeen *et al.* 1986). The incorporation of such a constraint into the Press–Schechter formalism has been considered by Peacock & Heavens (1990). Their approach is to consider the fraction of mass associated with a peak above a given threshold, ν (defined as the dimensionless ratio δ/σ_0), when smoothed on a scale R_f. The physical basis for this approach is to assume that any material within a distance $\sim R_f$ of a peak which has collapsed is part of an object with mass at least $\sim \rho_b R_f^3$ (in three dimensions). The criterion for collapse is that any point in the peak has $\delta \geq \delta_c$. Note that the relationship between the mass of the object formed and the filter radius is very important in determining the final form of the mass function and its overall normalization. In general, for a pure power law the peak model predicts more lower mass objects than Press–Schechter, though this effect does depend on the mass assigned to a peak and is more pronounced in three dimensions (see below).

3.3 Filter functions

The above methods have two critical uncertainties: what form of filter function should be used, and what is the relationship between the filtering length, R_f, and the mass?

We shall discuss several different choices of filter. Note that in all cases we refer to the *real* space form of the filter function when referring to it by name, but all filter functions are applied in k space. The real and k space filter functions are a Fourier transform pair, where the normalization of the transform is contained within the normalization constant, A (see equation 20).

Press & Schechter used a top-hat filter function. This equally weights all points in real space out to a distance R_f from the centre of the filter function, leading to 'ringing' in k space as its Fourier transform is a sinc function. Is this an undesirable feature? Intuition says that the sidelobes indicate an unreasonable choice of filter, but we should recall that there are no absolute guidelines here. We are attempting to mimic the effect of non-linearities via a linear filter; if such an attempt is successful at all, the 'correct' filter can only be judged by its empirical performance. Nevertheless, the top hat does seem an unwise choice owing to its width in k space: for many power spectra of practical interest [cold dark matter (CDM), for example] the higher moments of the power spectrum which are of interest for determining the statistical character of the density field do not converge with this filter. This says that the top hat accepts power from too wide a range of wavenumbers; the whole idea of Press–Schechter-style filtering is to isolate fluctuations arising from a given scale. It is common for this reason to resort to the Gaussian filter, since this damps short wavelengths more severely. However, other choices are possible which differ in the rapidity of this damping; we shall also consider 'exponential' and 'power-law' filters, in order to gain some insight into the sensitivity of the results to filter choice. The definitions of these alternatives are given in Table 1.

Table 1. Filter functions.

Filter Name	$W(x,R_f) \propto$	$W(k,R_f) \propto$	Area under $W(x,R_f)$
Top Hat	R_f^{-1}, $\lvert x\rvert < R_f$	$\sin(kR_f)/(kR_f)$	$2R_f$
Exponential	$\exp\left(-\frac{\lvert x\rvert}{R_f}\right)$	$(1+k^2R_f^2)^{-1}$	$2R_f$
Power Law 1	$[1+(x/R_f)^2]^{-1}$	$\exp(-\lvert k\rvert R_f)$	πR_f
Power Law 2	$[1+(x/R_f)^2]^{-2}$	$(1+\lvert k\rvert R_f)\exp(-\lvert k\rvert R_f)$	$\pi R_f/2$
Gaussian	$\exp(-\frac{x^2}{2R_f^2})$	$\exp(-\frac{1}{2}k^2R_f^2)$	$\sqrt{2\pi}R_f$

The relationship between mass and filter radius is similarly open to choice and depends to a large extent on the filter function. One would expect the mass of an object filtered on a scale R_f to be related to the area under the filter function, which means in d dimensions that $M(R_f) \propto \rho_b R_f^d$.

The problem arises when trying to decide upon the constant of proportionality. For the top-hat filter in three dimensions, one has the motivation of the spherical collapse model to set $M = V\rho_b$, where V is the top-hat volume. In general, things are not so simple, and so we make the scaling

$$M = \beta V \rho_b, \tag{21}$$

where β is to be treated as a fitting parameter.

The importance of β depends on the power spectrum and the mass-function theory being adopted. For power-law spectra, $|\delta_k|^2 \propto k^n$, we have, in d dimensions,

$$\frac{\delta_c}{\sigma_0} = \left(\frac{M}{M_*}\right)^{(n+d)/2d}, \tag{22}$$

which is independent of β. However, M_* is defined to be $\beta\rho_b V_*$, where V_* is the volume of the filter function that corresponds to $\sigma_0 = \delta_c$. For pure Press–Schechter theory, $M^2 f(M)$ depends only on δ_c/σ_0 and hence is independent of β, except through its effect on the numerical value of M_*. A variation in β simply translates $M^2 f(M)$ by some amount in $\ln M$, but preserves its shape and normalization; the Press–Schechter fudge factor of 2 is not supplied by putting $\beta = 2$. However, as discussed in Section 4, the peak-based mass functions are sensitive in detail to β.

3.4 Correlation functions

The problem of calculating a two-point correlation function for peaks in a one-dimensional Gaussian field has been addressed by Lumsden *et al.* (1989) who have produced an exact form for ξ_{pk-pk}, the correlation function for all peaks above a threshold ν (see also Coles 1989). The result, which was unfortunately misprinted in the original paper, is

$$1 + \xi_{pk-pk}(r) = \frac{\sigma_0^2\sigma_2^2}{(2\pi)^3 M_{33}^{-1}(\det M)^{1/2} n_{pk}^2(>\nu)} \int_\nu^\infty\int_\nu^\infty\int_0^\infty q_2 \times \exp(-Q_0/2)\left[1 - \frac{\sqrt{2\pi}}{2}\exp(+a^2/2)\,a \times \operatorname{erfc}(a/\sqrt{2})\right] dq_2\, d\nu_2\, d\nu_1, \tag{23}$$

where

$$a = -\sigma_0\left(M_{13}^{-1}\nu_1 + M_{16}^{-1}\nu_2 - \frac{\sigma_2}{\sigma_0}M_{36}^{-1}q_2\right)\Big/\sqrt{M_{33}^{-1}}$$

$$Q_0 = M_{11}^{-1}\sigma_0^2(\nu_1^2+\nu_2^2)+2M_{14}^{-1}\sigma_0^2\nu_1\nu_2+M_{33}^{-1}\sigma_2^2q_2^2 - 2\sigma_0\sigma_2(M_{13}^{-1}\nu_1 q_1+M_{16}^{-1}\nu_2 q_2), \quad (24)$$

with

$$y^T\equiv(\delta_1,\delta_1',\delta_1'',\delta_2,\delta_2',\delta_2'') \qquad M_{ij}\equiv\langle y_i y_j\rangle. \quad (25)$$

Note that M_{ij}^{-1} indicates the ij component of the inverse of M. Explicit forms of M_{ij} can be found in Lumsden *et al.* (1989).

The expression for the number density of peaks above a height ν is given by equation (8a) in Lumsden *et al.* (1989) which can be integrated analytically (Cartwright & Longuet-Higgins 1956) to give

$$n_{pk}(>\nu)=\frac{1}{4\pi R}\left\{\operatorname{erfc}\left(\frac{\nu}{\sqrt{2(1-\gamma^2)}}\right) + \gamma e^{-(\nu^2/2)}\left[1+\operatorname{erf}\left(\frac{\gamma\nu}{\sqrt{2(1-\gamma^2)}}\right)\right]\right\}, \quad (26)$$

where γ and R are defined in terms of the $2j$th moments of the power spectrum by

$$\gamma=\frac{\sigma_1^2}{\sigma_2\sigma_0} \qquad R=\frac{\sigma_1}{\sigma_2} \quad (27)$$

and

$$\sigma_j^2\propto\int_0^\infty|\delta_k|^2k^{2j}\,dk. \quad (28)$$

Equation (23) is used in Section 4.4 to generate the correlation function of objects above a given mass as follows: the density field is smoothed on the mass scale of interest and the threshold, ν, is set such that the number of peaks found above the threshold matches the number of pancakes of that mass or above present in the simulation.

It should be noted that the peaks theory correlation function will always give $\xi_{pk-pk}=-1$ for small separations, i.e. for $r\lesssim R_f$. This is because when smoothed all substructure on scales less than about R_f will be removed and hence there will be no pairs on scales of R_f or less. However, the peaks correlation function deals only with the static clustering present within the power spectrum and takes no account of the movement of peaks. With a view to assessing on which scales such movement will affect the correlation function, we use the Zel'dovich approximation (equation 5) to relate the peculiar velocity, V, to the comoving displacement, $\Delta x(=x-q)$, using equation (4).

The mean square peculiar velocity may be obtained from equation 27.22 of Peebles (1980). We note that the rms velocity of the peaks in a Gaussian field is somewhat smaller than the rms peculiar velocity. The relationship between the two is given by equation (4.23) in Bardeen *et al.* (1986) and thus we may derive the rms comoving displacement of peaks is $\sigma_{\Delta x}=(b/a\dot{b})\sigma_{v,pk}=(b/a\dot{b})\sigma_v(1-\gamma_v^2)^{1/2}=\sigma_{-1}(1-\gamma_v^2)^{1/2}$, where $\gamma_v=\sigma_0^2/(\sigma_{-1}\sigma_1)$.

For a power-law spectrum (with $n>-1$) with a Gaussian filter function,

$$\sigma_{\Delta x}=\frac{2\sigma_0R_f}{(n+1)^{1/2}(n+3)^{1/2}} \quad (29)$$

Thus in one dimension for n not close to -1, peaks on the mass scale M_* where $\sigma_0\sim1$ will move $\sim R_f$. Note that this calculation ignores any correlation between the velocity of peaks which would be needed in order to determine ξ_{pk-pk}. However, it does demonstrate that the displacements associated with the peculiar velocities of the density perturbations are of the right order to lead to correlations on scales $<R_f$. Thus although the peaks theory predicts $\xi_{pk-pk}=-1$ for $r<R_f$ we would not expect this to be the case.

4 RESULTS

In this section we present the results of our computer simulations and contrast them with the predictions of the above methods. We used two sizes of simulations, those with a potential sampled on a 2^{14} point grid and larger simulations with a 2^{17} point grid. We assumed that there was a total mass equal to the size of the simulation which is initially smoothly distributed giving a line density of $\rho_b=1$.

For simplicity we restricted ourselves to power-law spectra with a short-wavelength Gaussian cut-off. This should not be confused with the smoothing processes discussed in Section 3. The power spectrum is given by

$$|\delta_k|^2=k^n\exp(-k^2R_i^2) \quad (30)$$

with R_i set to two grid points to ensure that the results are not affected by the sampling of short wavelength modes of a size close to that of the resolution of the simulation. The gravitational perturbations are related to the matter density perturbations via Poisson's equation to give

$$\Phi_k=-k^{-2}\delta_k. \quad (31)$$

The gravitational potentials, $\Phi(q)$, used in our simulations are calculated by fast Fourier transforming the gravitational perturbations, Φ_k. The variance is expressed as a direct sum, rather than the integral given in equation (20).

$$\sigma_0^2(R_f)=A\sum_{k_{min}}^{k_{max}}|\delta_k|^2\,W(k,R_f)^2, \quad (32)$$

where σ_0^2 is normalized in the same manner as before and $W(k,R_f)$ is given in Table 1 for the various filters.

The initial density field was normalized so that $\sigma_0=\delta_c$, corresponding to a smoothing length, $R_f=0$ and a scale factor, $a=1$. Under linear theory $\sigma_0(R_f)$, for some fixed R_f, grows in proportion to the scale factor, a. Using this and the fact that $\sigma_0(R_*)=\delta_c$ allows us to express the scale factor in terms of the corresponding cut-off mass, M_*, and its associated filter radius, R_*,

$$a=\delta_c\left[\frac{\sigma_0^2(0)}{\sigma_0^2(R_*)}\right]^{1/2} \quad (33)$$

For each power spectrum eight independent realizations of the gravitational potential were generated. We use several

independent realizations of a potential rather than a single, larger potential because the computational time for a single potential rises faster than the size of the potential. Also we were limited to a maximum size of $\frac{1}{8}$ million points per simulation.

Parabolae were fitted to each potential at eight different epochs, the results being combined at each epoch. This allows us to investigate the time evolution of the structure. The different epochs are characterized by the scale factor, a, and as the process of parabola fitting is independent of previous epochs we are free in our choice of the values of the scale factor for each epoch.

We calculate the scale factor at each epoch using equation (33) with values of R_* calculated from equation (21), the volume of the relevant filter function being given in Table 1. To provide a wide range of physical scales the values of M_* are logarithmically spaced with a maximum value of 1638.4, one tenth of the size of the 2^{14} point potentials. The scale factors depend on the spectral index and size of the potential used, but we scale to M_* at each epoch. This allows us to compare different potentials, assuming a Press–Schechter style scaling of the cut-off mass with epoch.

4.1 Mass functions

In this subsection we compare the mass functions obtained from our simulations to the theoretical mass function derived by Press & Schechter and from peaks theory. Figs 2–5 show plots of the mass function in 'multiplicity function' form, $M^2 f(M)$, versus the mass, M, scaled by the assumed time dependence of the cut-off mass, M_*. Fig. 2 shows the Press–Schechter mass functions (solid lines) calculated directly from equation (19), with σ_0^2 being calculated using equation (32) and the values of R_f obtained from equation (21). The parameter β is obtained by fitting the theoretical curve by eye. Here we set $\beta = 1.4$ for all power spectra, which corresponds to setting $\beta = 1$ and using values of δ_c of 0.92 for $n = -\frac{1}{2}$, 0.71 for $n = 1$ and 0.51 for $n = 3$ (see equation 22). It should be stressed that using a value of $\beta = 1$ and varying δ_c as given above would give identical results for the unmodified Press–Schechter theory.

One can see the excellent fit of Press–Schechter curves to the data over a wide range of masses. There are differences, however, at either end of the mass range. The data points from the simulations tail off faster at low mass than the Press–Schechter curves. This is due to the normalization of the Press–Schechter mass function which automatically accounts for all the mass. However, not all the matter in the simulation is incorporated in pancakes – there are still free points, and these are not included in the data. Thus the Press–Schechter curves will always overestimate the total amount of mass present in the pancakes. Also there is the effect of the finite sampling of the simulation. Obviously with the basic length (and hence mass) unit of one grid point this will be the minimum mass of pancake formed, and coupled with the initial removal of small scale power by smoothing on a scale R_f, there is a turn down in the number of pancakes at low masses. Note that, as one would expect, the difference between the curves is greater for early epochs which have

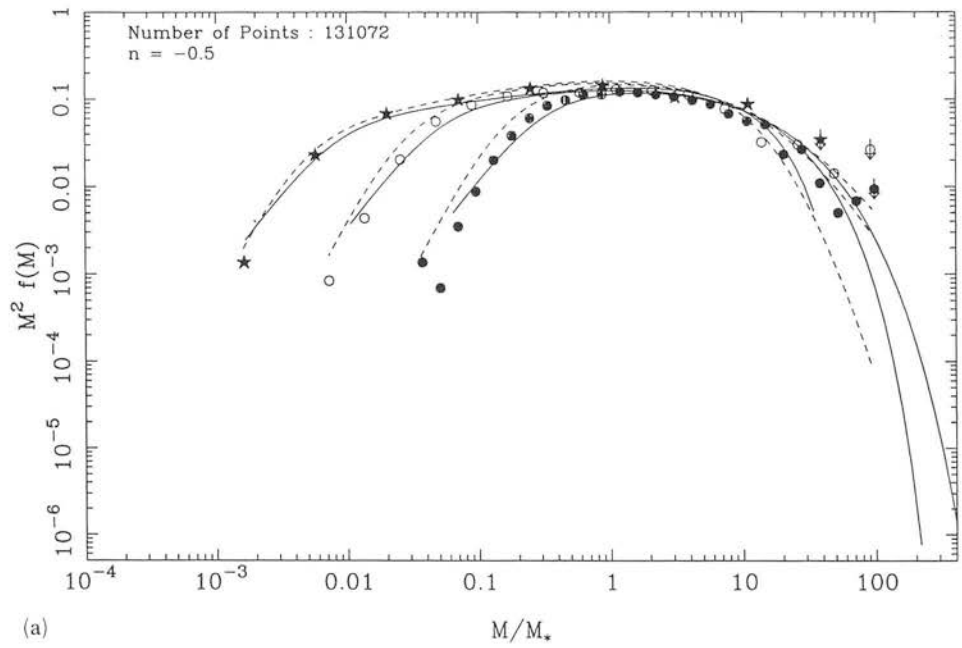

Figure 2. Plot of the mass function in the form $M^2 f(M)$ versus M/M_* as given by Press–Schechter (continuous line), peaks theory [dashed line in Fig. 2(a) and (b)] and simulations (data points). The three sets of data are for epochs 3 (●), 5 (○) and 7 (★). The last data point (marked by a superposition of a ↓) is an upper limit assuming one pancake in the bin after the last data bin. The three diagrams are for spectral indices (a) $n = -\frac{1}{2}$, (b) $n = 1$ and (c) $n = 3$ and are plotted on the same scales to facilitate comparison. For the Press–Schechter curves the parameter $\beta = 1.4$ for all spectral indices which corresponds to setting $\beta = 1$ and using a value of δ_c of (a) 0.92, (b) 0.71 and (c) 0.51. For the peaks theory curves the parameter β is set to unity and δ_c varied. For Fig. 2(a), $\delta_c = 0.92$ and for Fig. 2(b), $\delta_c = 0.71$.

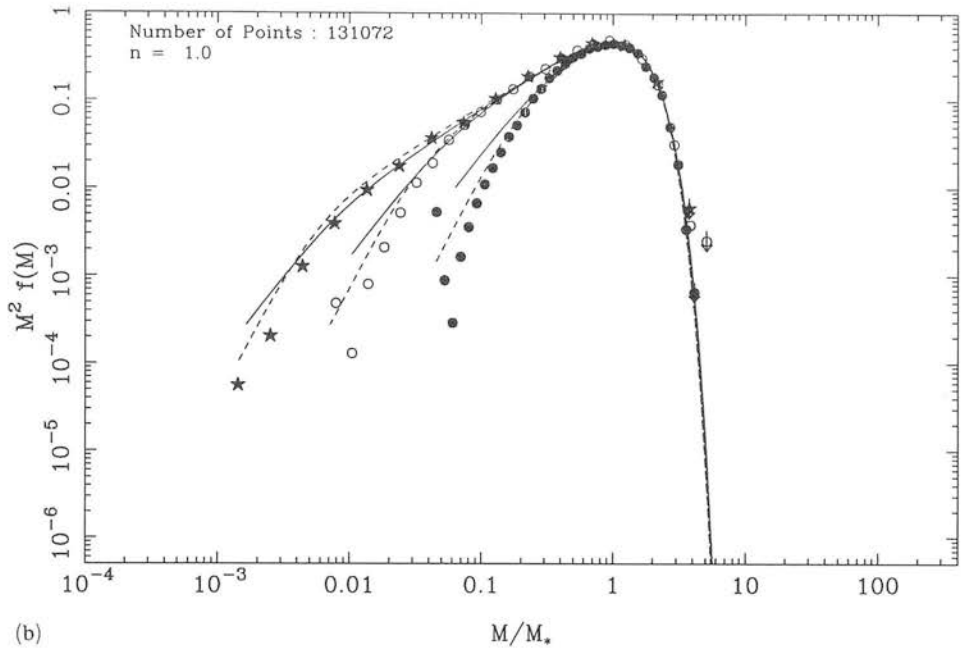

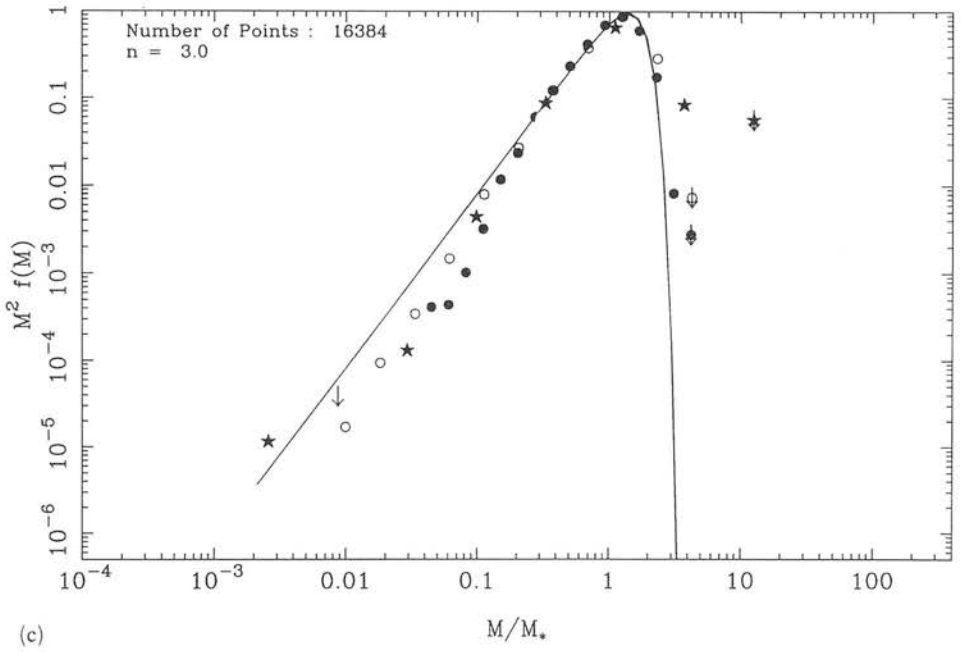

Figure 2 – *continued*

low values of M_* as here far more pancakes of mass $M \sim M_i$ form. For late epochs, when $M_* \gg M_i$, there is very little difference. Also for late epochs most of the mass is incorporated into pancakes and therefore the Press–Schechter overestimate is only very slight.

The differences at the high-mass end of the mass function are due to the heavy smoothing of a discretely sampled power spectrum. For large masses the smoothing radius, R_f, is sufficiently large that the filter function tends to zero even for very small wavenumbers, k, thus severely curtailing the sampling of the power spectrum. This can be seen in Fig. 2(a) by the rapid fall away of the Press–Schechter curves (continuous lines) at high mass, indicating that the $n = -\frac{1}{2}$ power spectrum is insufficiently sampled to produce the self-similar behaviour of a pure power law. Note that, as one would expect, this effect is more pronounced for later epochs as the cut-off mass, M_* and hence the filter radius, R_f, at the high mass end increase with time. In contrast Fig. 2(b) and (c) show that the Press–Schechter curves are self-similar at the high-mass end. This indicates that the $n = 1$ and $n = 3$ power spectra are fully sampled. This is due to the lack of large-scale power present in these power spectra, hence there are no pancakes of large enough mass to curtail the sampling by any noticeable amount.

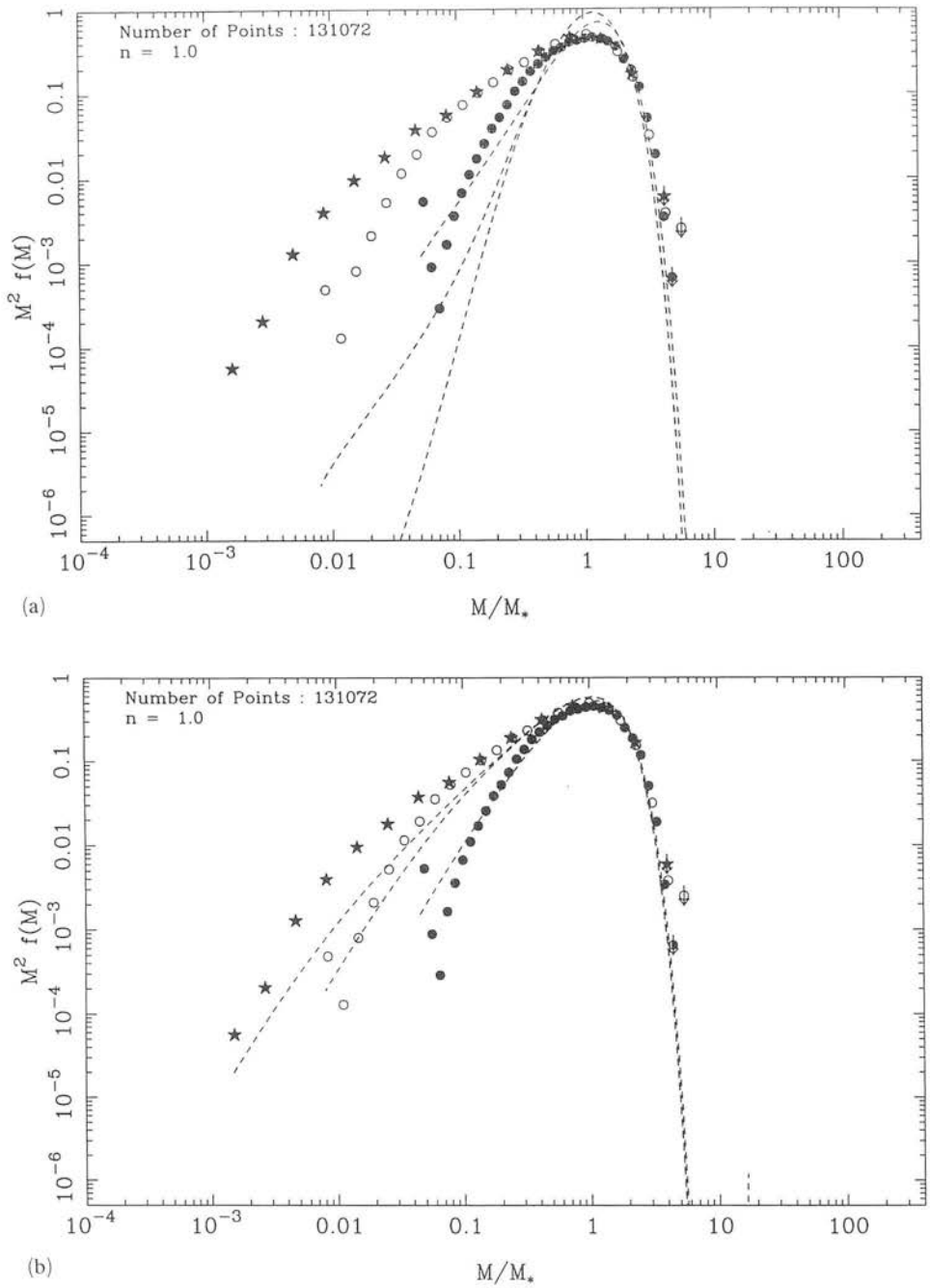

Figure 3. A plot of $M^2 f(M)$ versus M/M_* showing the effect of using different filter functions in the peaks theory mass functions (dashed lines). The three sets of data are as in Fig. 2. Both plots are for a spectral index of $n = 1$ with $\beta = 1.0$ and $\delta_c = 0.71$. Fig. 3(a) shows a power-law filter of k-space form $\exp(-kR_f)$ and Fig. 3(b) shows a modified power-law filter of k-space form $(1 + kR_f)\exp(-kR_f)$ (see Table 1).

Fig. 2(a) and (b) also show peaks theory mass functions (dashed lines) generated using a Gaussian filter. For the $n = -\frac{1}{2}$ power spectrum (Fig. 2a) we have set the parameter $\beta = 1$ and for δ_c we take the value of 0.92 (see above). One can see that while both curves agree quite well at the high-mass end the peaks curves give considerably better fits at the low-mass end, more accurately reproducing the tailing off of the data. The discrepancy between the low-mass end of the peaks curves and the data can be explained using similar arguments to those given above for the Press–Schechter curves. Note that the peaks curves also suffer from the sampling problem mentioned above, but to a lesser extent. For the $n = 1$ power spectrum (Fig. 2b) we take $\beta = 1$ and $\delta_c = 0.71$. Again the peaks curve provides a better fit to the data, especially at the low-mass end.

Fig. 3 shows the effect of using different filters in the peaks theory mass function. In Fig. 3(a) the peaks theory curves have been calculated using a power-law filter (see Table 1,

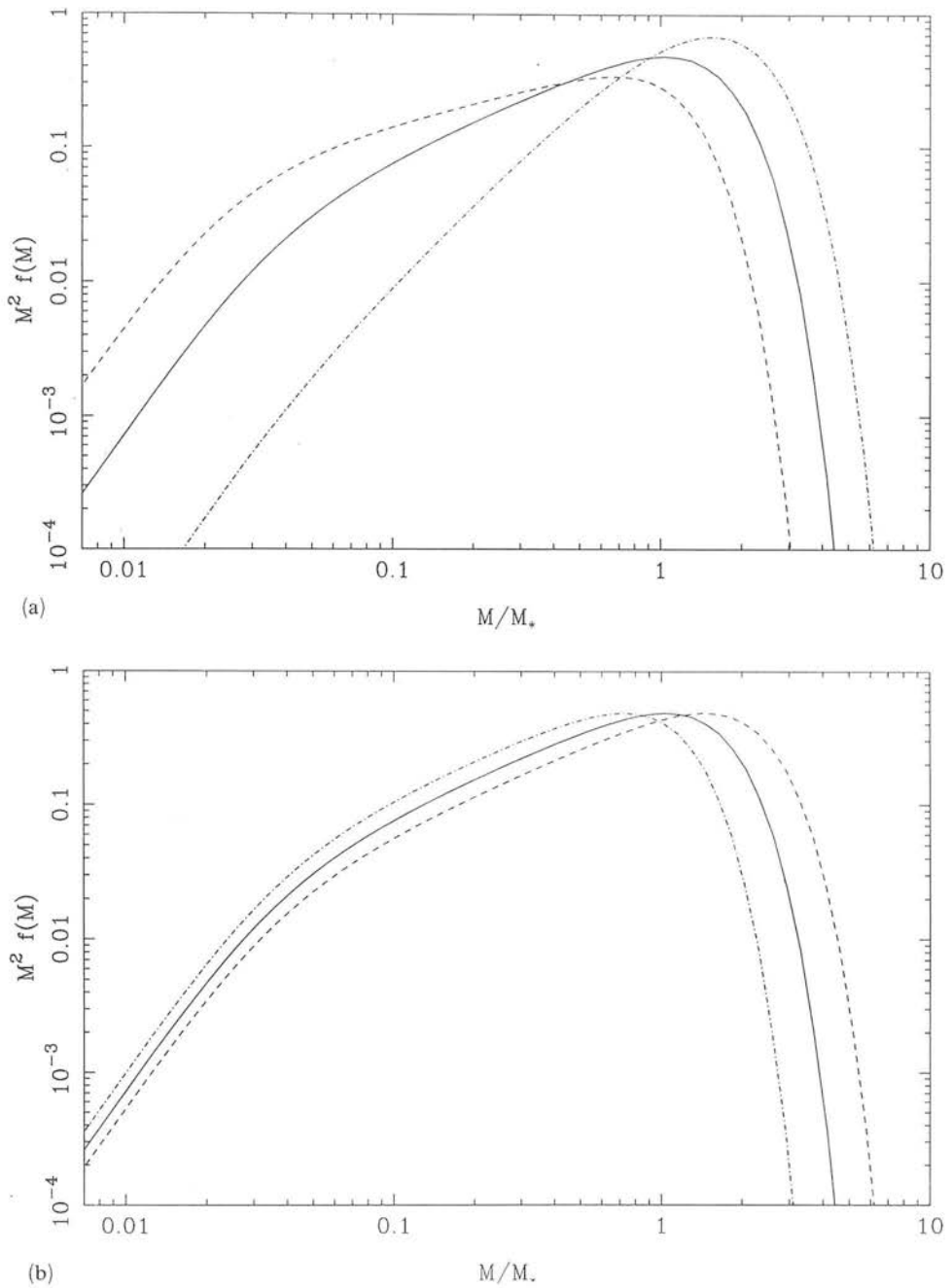

Figure 4. A plot of $M^2 f(M)$ versus M/M_* showing the effect of varying β and δ_c in the peaks theory mass function. The peaks curves have been calculated for a spectral index of $n=1$ using a Gaussian filter and normalized to the M_* value of the peaks curve denoted by the solid line. Fig. 4(a) shows the effect of varying the parameter β with δ_c kept at a constant value of 0.71. The three curves are $\beta=0.7$ (broken line), $\beta=1.0$ (solid line) and $\beta=1.4$ (dot-dash line). Fig. 4(b) shows effect of varying δ_c with $\beta=1.0$. The three curves are $\delta_c=0.5$ (broken line), $\delta_c=0.71$ (solid line) and $\delta_c=1.0$ (dot-dash line). Unlike the simple Press–Schechter case the variation of the two parameters is not equivalent.

'Power Law 1') for an $n=1$ spectrum with $\beta=1$ and $\delta_c=0.71$. One can see that the power-law filter gives a considerably worse fit than either the Press–Schechter or the peaks curve with a Gaussian filter (see Fig. 2b). The power-law filter vastly underestimates the number of pancakes at low mass and similarly overestimates the number of pancakes around the cut-off mass. Also it cuts off a fraction too soon. Fig. 3(b) shows a modified power-law filter (see Table 1, 'Power Law 2') which is a considerably better fit, but still underestimates the number of pancakes with low masses and overestimates those at the high-mass end. The exponential and top-hat filters given in Table 1 were not used here because the higher moments required by the peaks theory mass function do not always converge.

Fig. 4 shows the effect for the peaks theory of modifying both β and δ_c on an $n=1$ power spectrum using a Gaussian filter. Similar results were obtained for different spectral indices and different filter functions. As can be seen from

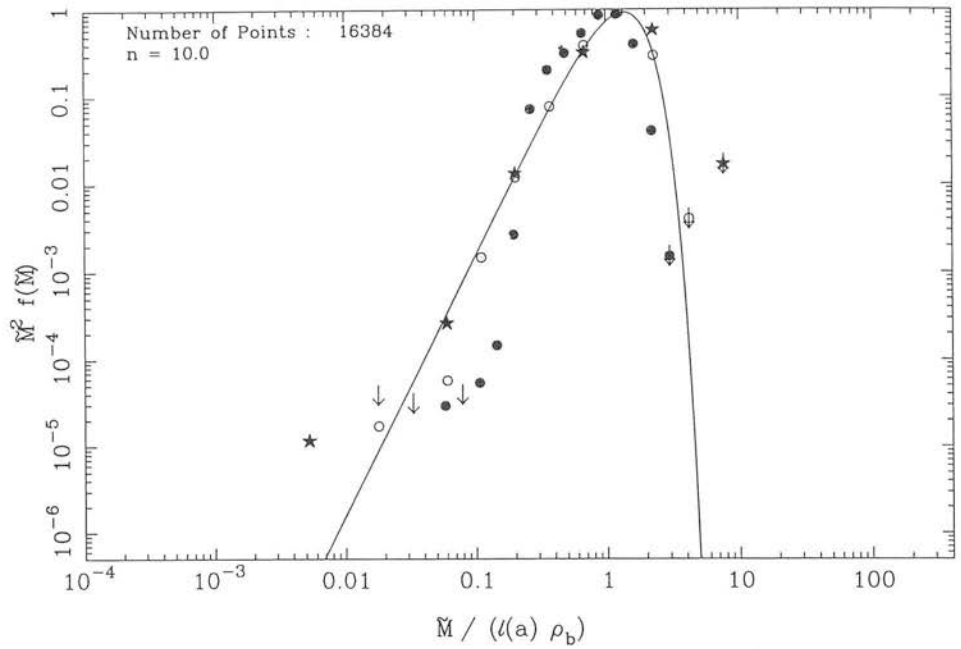

Figure 5. Plot of the mass function in the form $M^2 f(M)$ versus M/M_* as given by Kida (continuous curve) and simulations (data points) for a spectral index of 10. The three data sets are epochs 4 (●), 6 (○) and 8 (★). The first set (●) does not fit the theoretical curve as the latter is only valid for large values of the scale factor, a.

Fig. 4(a), modifying β has a major effect on the shape as well as the position of the mass function. The slope of the low-mass end of the mass function is steepened as β is increased, though the slope of the very low mass tailing off introduced by the artificial cut-off remains unaltered. As a result the theory predicts fewer low-mass pancakes which leads to an increased number of pancakes around the cut-off mass, which itself increases with increasing β. It is readily apparent from Fig. 4(a) that altering β, even by relatively small amounts, will significantly alter the mass function.

Unlike the original Press–Schechter case, changes in β and δ_c are not equivalent when using the peaks theory modifications. Altering δ_c (see Fig. 4b) produces very little change in the actual form of the mass function, mainly causing the cut-off mass to decrease as δ_c increases.

We conclude from this that the best procedure for normalizing the $M(R_f)$ relation in the context of the peaks theory mass function is to set $\beta = 1$ and that a best fit to the data is then obtained by varying δ_c, given approximately by $\delta_c \simeq 1.4^{-(n+1)/2}$ (see above). It seems that the approach of setting δ_c to a universal constant for all power spectra and then varying β will not give a reasonable fit to the data. Furthermore it is apparent that altering β and δ_c away from those values given for Fig. 3 will not significantly improve the fit to the data of the mass functions produced using the two power-law filters, thus leading us to the conclusion that out of the filters considered, the Gaussian filter is to be preferred.

4.2 Steep spectra

The assumptions that go into Press–Schechter type models are only valid for a limited range of spectral indices. It had been previously thought by various authors (e.g. Press & Schechter 1974; Peebles 1980) that the growth of non-linear perturbations would go as

$$M_* \sim M_0 a^{2d/(n+d)}, \tag{34}$$

where d is the number of dimensions. In one dimension this is indeed the case and our results presented in Section 4.1 confirm this.

It was widely believed that in three dimensions equation (34) would hold for spectral indices between $-3 < n \leq 4$. For spectra steeper than the 'minimal' $n = 4$ spectrum, it was proposed that the growth would take a limiting value given by

$$M_* \sim M_0 a^{6/7} \tag{35}$$

which is independent of the spectral index for $n \geq 4$. This arises due to the non-linear generation of the long wavelength part of the spectrum where mode-coupling terms dominate over an intrinsic large-scale power. Thus even if there are no long-wavelength perturbations at the linear stage (as is the case for steep spectra) the characteristic mass will grow at these scales with the limiting rate given above.

It was suggested by Gurbatov *et al.* (1989) that equation (34) only holds as long as the variance of the gravitational potential, $\sigma^2_{\Phi_0}$, diverges as $k \to 0$. For a pure power-law power spectrum with no smoothing but with a small wavelength cut-off (k_{max}) and the relationship between matter and gravitational perturbations given by equation (31), the variance in d dimensions is given by

$$\sigma^2_{\Phi_0} = \int_0^{k_{max}} k^{n+d-5}\, dk. \tag{36}$$

Thus one can see that $\sigma^2_{\phi_0}$ diverges for $n \leq 1$ in three dimensions and for $n \leq 3$ in one dimension, which is contrary to previous assumptions. In this case the limiting rate would be given by

$$M_* \sim M_0 a^{3/2} \tag{37}$$

in three dimensions and in one dimension by

$$M_* \sim M_0 a^{1/2}. \tag{38}$$

This conclusion is backed up by the work of Kida (1979) who effectively (although working in the context or turbulence theory) solved the Burgers model exactly in one dimension to obtain $f(M)$ in the limit of very steep spectra. Not only does M_* scale as above, but the form of $f(M)$ is greatly different from the Press–Schechter prediction (see below). We also note that similar work on the Burgers model has been carried out by Gurbatov & Saichev (1981), looking at one-dimensional turbulence with Gaussian fields, and Doroshkevich & Kotok (1990), looking at the problem in the context of galaxy formation. Both sets of authors derived a mass function in accordance with that given by Kida.

We have carried out simulations for a range of spectral indices above $n = 3$ which show that this is the point where the Press–Schechter mass function breaks down and also confirm that the cut-off mass grows approximately as predicted above. This supports previous work on one-dimensional power spectra by Kotok & Shandarin (1989).

Fig. 5 shows a plot of $M^2 f(M)$ for $n = 10.0$ and a theoretical curve taken from Kida (1979), where $f(M)$ is given by

$$f(M) = \frac{\pi \rho_b}{2} \frac{M}{[l(a)\rho_b]^3} \exp\left[-\frac{\pi}{4} \left(\frac{M}{l(a)\rho_b} \right)^2 \right], \tag{39}$$

where $l(a)$ is a characteristic scale given by

$$l(a) = \left(\frac{\pi a}{2B^{1/2}} \right)^{1/2} \left[\ln \left\{ \frac{A}{4} (\pi a)^{1/2} B^{-5/4} \right\} \right]^{-1/4} \tag{4.35}$$

and A and B are constants.

In Kida's work A and B are free parameters which arise in an ansatz that the probability that the highest peak is in the range $[\Phi_0, \Phi_0 + d\Phi_0]$ is

$$P(\Phi_0) = \frac{1}{n_{pk}} A \Phi_0^{\alpha} \exp(-B\Phi_0^{\beta}), \tag{40}$$

where n_{pk} is the total number density of peaks.

We can improve on Kida's analysis by using the properties of Gaussian fields to determine the values of α, β, A and B:

$$\alpha = 1, \quad \beta = 2, \quad A = \frac{1}{2\pi} \frac{\sigma_1}{\sigma_0^3} \quad \text{and} \quad B = \frac{1}{2\sigma_0^2}, \tag{41}$$

where σ_j^2 the $2j$th moment of the gravitational power spectrum, i.e.

$$\sigma_j^2 \propto \int_0^\infty |\Phi_k|^2 k^{2j}\, dk. \tag{42}$$

Note that this is not the exact form given by Kida, rather it is equivalent to the function $\tilde{f}(\tilde{\mu})$ given in his equation (4.38) and we have used the approximation to $l(a)$ given by his equation (4.35). Though at first sight the expression (4.38) may seem dimensionally odd, it is in fact valid as the potential, Φ_0, has dimensions of length squared.

Kida's analysis is only valid if the peaks are uncorrelated in position. This is the case for steep power spectra at large values of the scale factor ($a \gg 1$). The lack of any power above some critical length scale means that the peaks are uncorrelated on this scale and above. If the scale factor is sufficiently large, then in terms of the adhesion model the parabola will only touch the highest peaks; thus the separation of the touching peaks will be large. For a sufficiently steep spectrum and a large enough scale factor the peak separation will be greater than the critical length and the positions of the peaks are uncorrelated. Looking at Fig. 5 we can see that the fit of the theoretical curve to data points improves as we move from early (small a) to late epochs (large a), confirming the above conclusion. We have also fitted the mass function given in equation (39) to simulations with spectral indices ranging from $n = 4$ to $n = 15$ and all give good fits, though the fit improves with increasing n, as we would expect.

It is interesting to compare this to the Press–Schechter mass function under the assumption that for $n \geq 3$ in one dimension, one may use a constant value of $n = 3$ in the mass function. Both mass functions give the correct low-mass slope [$f(M) \sim M$ for $M \ll M_*$, where $M_* \sim l(a) \sim a^{1/2}$] but the cut-offs are different, Kida's formula going as $\exp[-(M/M_*)^2]$ whereas the Press–Schechter mass function would predict a cut-off going as $\exp[-\frac{1}{2}(M/M_*)^4]$, i.e. Press–Schechter cuts off too quickly, not producing enough high-mass objects. This is because the Press–Schechter formalism does not take into account the non-linear processes that generate the long-wavelength fluctuations.

4.3 Direct tests of the linear theory assumption

In this subsection we use our simulations to check the validity of one of the assumptions of linear theory, namely that pancakes of mass M form from regions with $\delta \simeq \delta_c$ when smoothed on a scale $R_f(M)$. We take the masses of all the pancakes formed in our simulations and bin them in 16 logarithmically spaced mass bins. We then smooth the density field with a filter radius $R_f(M)$ as given in equation (21) where M is the centre of the bin, and find the density contrasts at the Lagrangian coordinate half-way between the two points of touching of the parabola. We have also taken the alternative approach of finding the density contrast at the highest peak between the two points of touching. This is a direct test of the peaks modification of the Press–Schechter formalization decribed in Section 3.2 and makes no significant difference to the results presented below.

The results are given in Figs 6 and 7 for power spectra with $n = -\frac{1}{2}$ and $n = 1$. Two plots are shown for each power spectrum, the first showing the data for all epochs and the fourth showing data from pancakes of mass $M \geq M_*$. As it can be seen from the plots, the spread in values of δ is quite small for both spectral indices. Values for the position of the maximum of the distribution, the mean of the distribution, and of its width in terms of the full width at half maximum and standard deviation are shown in Table 2.

Looking at Figs 6 and 7 one can see the remarkable similarity between the shapes of the histograms and the overall

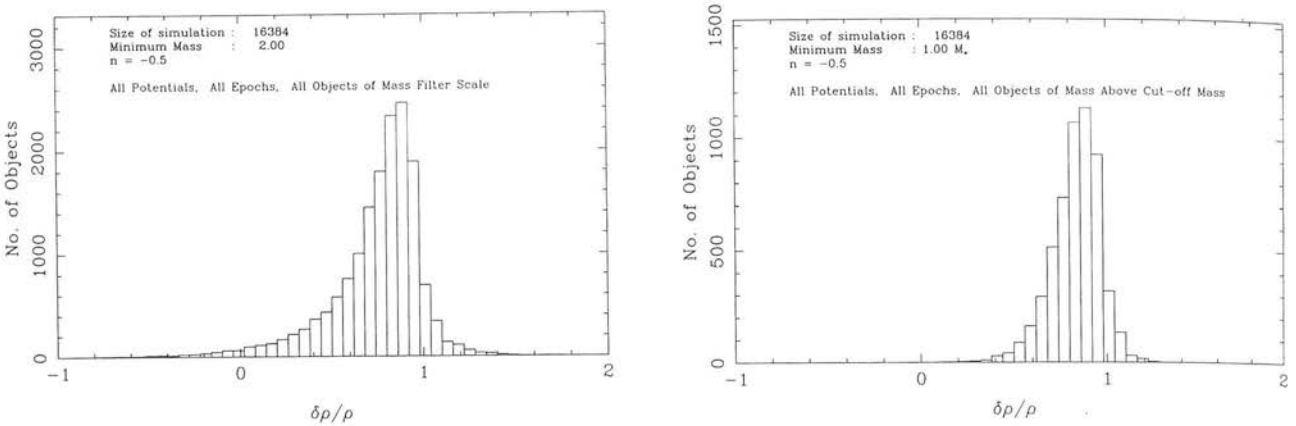

Figure 6. Histogram showing the distribution of $\delta\rho$ at the centre of the pancake in Lagrangian space when smoothed on a scale $\sqrt{2\pi}M\beta$ with $\beta = 1$. The data are for eight independent realizations of a 2^{14} point simulation with spectral index, $n = -\frac{1}{2}$. The plots are for (a) all points above a minimum mass of 2 grid points for all epochs and (b) all points above the cut-off mass M_* for all epochs.

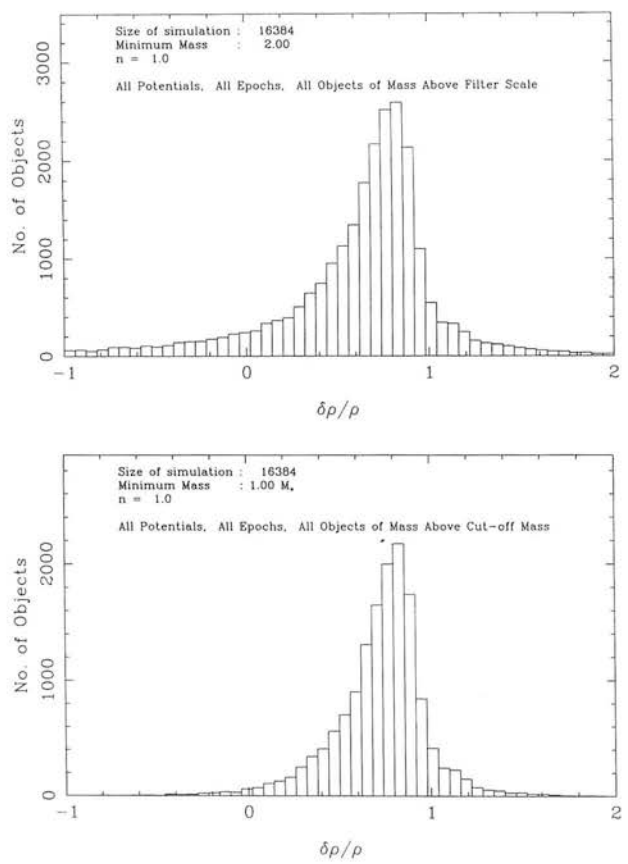

Figure 7. As Fig. 6, but for $n = 1$.

trends in the characteristics of the peak of the distributions given that they are for two dissimilar power spectra. This is confirmed by looking at Table 2. However, though the two different power spectra have very similar peak positions and full width half maxima, there is considerable difference between the mean and standard deviations of the two distributions. This is almost entirely due to the tails of the distribution present for the $n = 1$ power spectrum (Fig. 7). These are absent in the $n = -\frac{1}{2}$ power spectrum, and arise from pancakes forming in regions where the smoothed density field has $|\delta| \gg 1$. The absence of such extreme variations in the $n = -\frac{1}{2}$ power spectrum arises because there is relatively little small-scale power, and hence large local fluctuations are avoided. The location of pancakes in such regions in the $n = 1$ power spectrum can be taken as showing that the linear theory prediction of pancakes forming in regions with $\delta \sim \delta_c$ is not 100 per cent accurate, though inspection of Fig. 7 by eye shows that the majority of pancakes are contained within a narrow band $0 < \delta < 1$.

Table 2. Data for $\delta\rho/\rho$ distributions.

Figure	n	Epoch	Min. Mass	Peak	FWHM	$\bar{x}$	σ_0
6a	$-\frac{1}{2}$	ALL	2.0	0.88±0.02	0.29±0.02	0.75	0.26
6b	$-\frac{1}{2}$	ALL	M_*	0.94±0.02	0.24±0.02	0.83	0.13
7a	1	ALL	2.0	0.85±0.02	0.30±0.02	0.32	3.20
7b	1	ALL	M_*	0.85±0.02	0.30±0.02	0.73	0.26
	$-\frac{1}{2}$	1	2.0	0.91±0.02	0.19±0.02	0.86	0.09
	$-\frac{1}{2}$	8	2.0	0.65±0.05	0.65±0.05	0.51	0.44
	1	1	2.0	0.83±0.02	0.21±0.02	0.80	0.10
	1	3	2.0	0.70±0.05	0.70±0.05	0.52	0.48

Note that if the peaks theory is a correct interpretation of the physical processes involved in pancake formation then we would expect the histograms to be delta functions located at $\delta = \delta_c$. In linear theory δ_c is expected to be unity in one dimension. However, we obtained a best fit for the peaks theory mass functions (see Section 4.1) using values of $\delta_c = 0.92$ and 0.71. Though the data presented in Figs 6 and 7 do not support a unique value of δ_c for a given power spectrum they certainly point towards the majority of

pancakes being formed in regions where $\delta < 1$. In all cases the distribution is noticeably skewed towards the left, i.e. low values of δ.

We have also looked at data for individual epochs. The statistics of some of these epochs are shown in Table 2. From this we may deduce a general trend with epoch. At early times the data show a marked decrease in half width, both from that of later times and to the whole data set. We also note that at later times the distribution becomes much less peaked (as signified by the rapid increase in half width) and the peak moves away from unity. In the $n = 1$ case this is markedly so, and for late epochs, there is only a broad peak in the range $-2 < \delta < 2$.

This behaviour is to be expected as for early times the masses of the pancakes will be close to M_*, whereas at late times the majority of the pancakes have mass considerably less than M_*. This can be seen by looking at Fig. 2, where for late epochs there is a considerable tail to the distribution into the region where $M \ll M_*$. We expect the assumption that pancakes form when $\delta = \delta_c$ to be more likely to hold for pancakes of mass $M \simeq M_*$. This can be borne out when we consider Figs 6(b) and 7(b) showing data from all pancakes of mass $M \geq M_*$. For the $n = -\frac{1}{2}$ case there is a shift in the peak towards unity and a decrease in the full width, though this is not the case for the $n = 1$ power spectrum. However, both power spectra show a marked decrease in standard deviation and on visual examination of Figs 6(b) and 7(b) it can be seen that both distributions have lost their broad wings. In view of this we find it surprising that both the Press–Schechter and especially the peaks theory mass functions predict the correct low-mass slope and give such a good fit to the simulations, especially at late epochs where the values of δ vary most markedly.

4.4 Correlation functions

In this subsection we compare the two-point correlation function derived from our simulations with that calculated from the peaks theory. We define the two-point correlation function for pancakes as

$$\xi_p(r) = \frac{n_{\text{pairs}}}{n_{\text{exp}}} - 1, \tag{43}$$

where n_{pairs} is the number of pairs at a given separation, r, and n_{exp} is the expected number of pairs at that separation in a random (unclustered) catalogue.

Figs 8 and 9 show the correlation function for 2^{17} point simulation with spectral indices of $n = -\frac{1}{2}$ and 1, respectively. The four different sets of data are for different epochs, showing the time evolution of the correlation function. The conclusions that one may draw from these figures are heavily dependent on the spectral indices, unlike those in previous sections.

Considering the data for the $n = -\frac{1}{2}$ power spectrum (Fig. 8a) we can see that there is very little change in the correlation function with time if one considers the correlation function calculated using all the pancakes. However, looking at Fig. 8(b), which shows the correlation function for all pancakes with a mass above $M_*/2$, we can clearly see an increase in amplitude with time which we might naively expect from the evolution of the autocorrelation function under linear theory.

The difference between the two plots is obviously due to the small-mass pancakes which dominate the counts at all epochs. These low-mass pancakes show very little evolution with time, perhaps because the relative positions of nearby pancakes change little in the absence of small-scale power. Since the low-mass objects dominate the counts, the correlation function of all pancakes shows little evolution. The correlation function of the high-mass pancakes (Fig. 8b) has the same slope as the correlation function of all pancakes (Fig. 8a) but there is an increase in amplitude by up to an order of magnitude.

In the case of the $n = 1$ power spectrum, Fig. 9 reveals the trends towards higher correlation amplitudes with time except at small separation. It should be noted that, while this effect is similar to that for the $n = -\frac{1}{2}$ case, the sign of the correlation function is different in the two cases. For the $n = -\frac{1}{2}$ case the correlation function is positive on all except very large scales, but in the $n = 1$ case the correlation function is negative, except at very large scales; thus an increase in correlation amplitude means a more negative value of $\xi_p(r)$, i.e. fewer pancakes than expected at a given separation. This is probably due to the large amount of small-scale power leading to high relative motions and mergers of pancakes which gives rise to a complicated evolution of the correlation function.

Figs 10 and 11 show plots from the same simulations for an expansion factor corresponding to $M_* = 40.48$. In Fig. 10 the four sets of data represent correlation functions calculated using only pancakes above $M_*/8$, $M_*/4$, $M_*/2$ and M_* respectively. The four continuous curves are correlation functions calculated using peaks theory (equation 23) and correspond to the simulations, the density field being smoothed on a mass scale equivalent to the minimum mass of pancake used. In Fig. 11 the $M_*/8$ curve is not shown.

Considering Fig. 10 one can see that there is quite good agreement between the peaks theory correlation functions and those from the simulations and the same general trends are obeyed. However, Fig. 11 shows that the peaks theory correlation functions bear no resemblance to the simulations for the $n = 1$ case. This is due to the complicated evolution of the correlation function which dominates any statistical clustering present in the initial conditions. As the peaks theory is a static model, which does not take this evolution into account, one would not expect the model to fit the simulations in this case. Also, there is very little power on large scales in the $n = 1$ power spectrum. This means that the correlation amplitude drops rapidly for large separations. However, because peaks theory gives $\xi_{pk-pk} = -1$ for $r \lesssim R_f$, and the ampitude of ξ_{pk-pk} goes to zero for $r \gtrsim R_f$, there is only a very small range over which there is sufficient signal to compare the two correlation functions.

Note that in both cases, although the peaks theory predicts $\xi_{pk-pk} \to -1$ for $r \lesssim R_f$, this is not the case in the experimental data. As suggested in Section 3.4, $\xi_{pk-pk} \neq -1$ for $r \lesssim R_f$ due to movement of peaks over distances of order R_f. This assertion may be further supported by performing cross correlations between the pancake positions and the positions of peaks in the density field when smoothed on a scale $R_f(M)$, where M is the mass of the pancake. Fig. 12 thus shows the cross-correlation function (filled circles) and two-

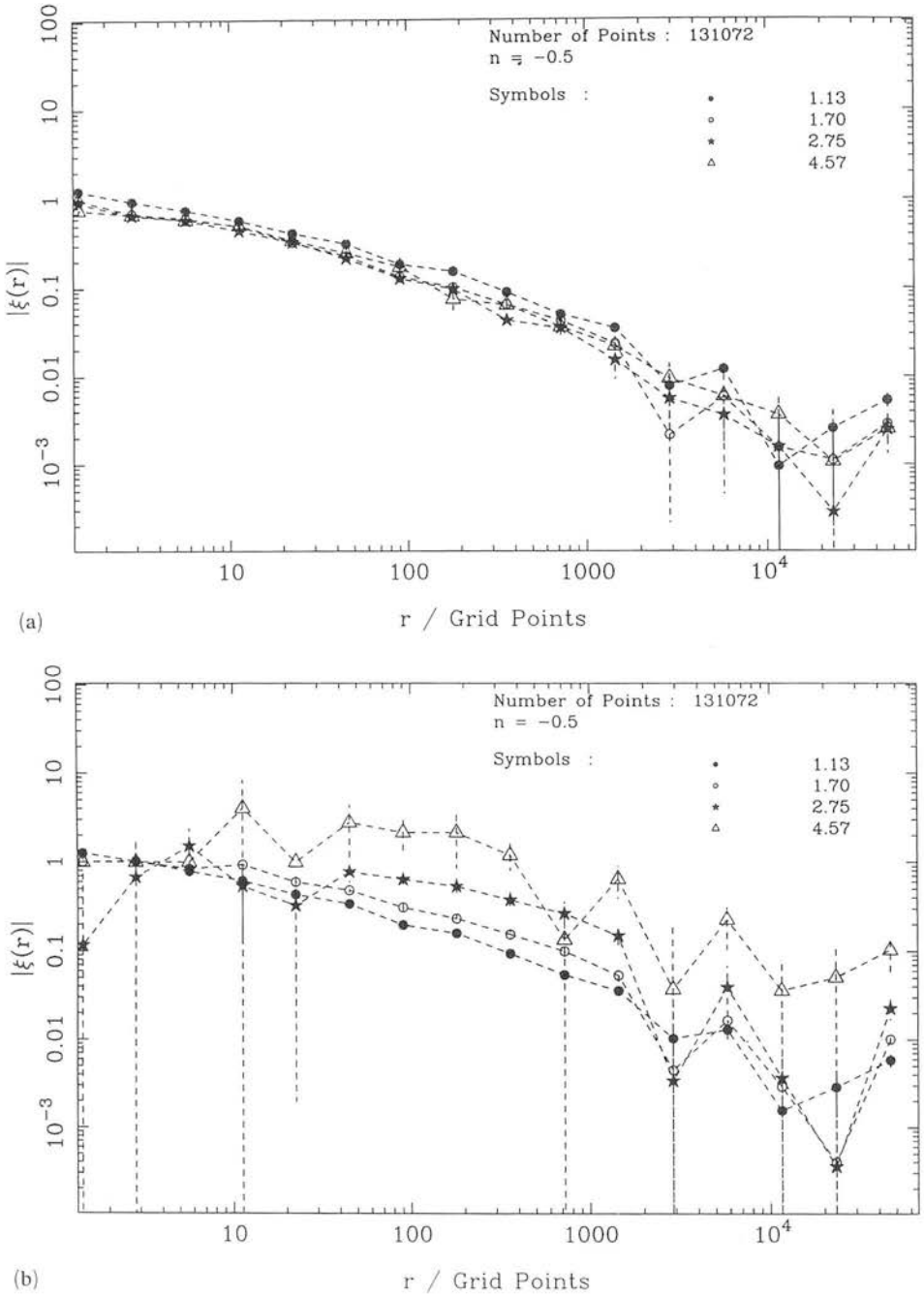

Figure 8. The correlation function ξ_p for an $n = -\frac{1}{2}$ spectrum. The data points are the average over eight potentials for a 2^{17} point run, the errors being a measure of the deviation from the mean. Each curve represents a different time characterized by the scale factor, shown on the plots. The two plots show the correlation function calculated using (a) all the pancakes, (b) all pancakes above $M_*/2$.

point correlation function (open circles) for a spectral index of $n = -\frac{1}{2}$ at a late epoch. For small r there are no pairs at all, but as r increases so the cross-correlation function increases until for $r \sim 700$ one recovers the two-point correlation function. In this case $M_* \simeq 700$ giving $R_* \simeq 1750$. This suggests that though there is not an exact one-to-one correspondence between peaks and pancakes (we would expect a single, large peak at $r = 0$ if this were the case), it is the case that pancakes are located within $\sim R_f$ of peaks, accounting for the reduced amplitude of the cross-correlation function in that region. This is consistent with the hypothesis that pancakes form at peaks in the linear density field and then move away from the site of formation by distances of up to $\sim R_f$. Indeed the cross-correlation function suggests that R_f should be considered an upper limit to the movement of a pancake.

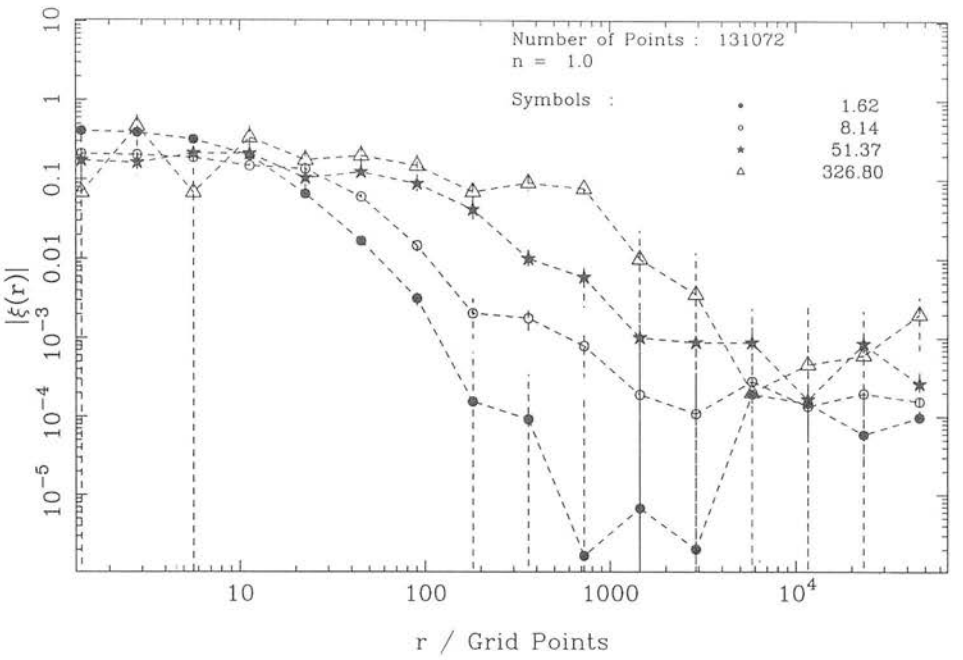

Figure 9. As Fig. 8(a) but for a spectral index of $n = 1$.

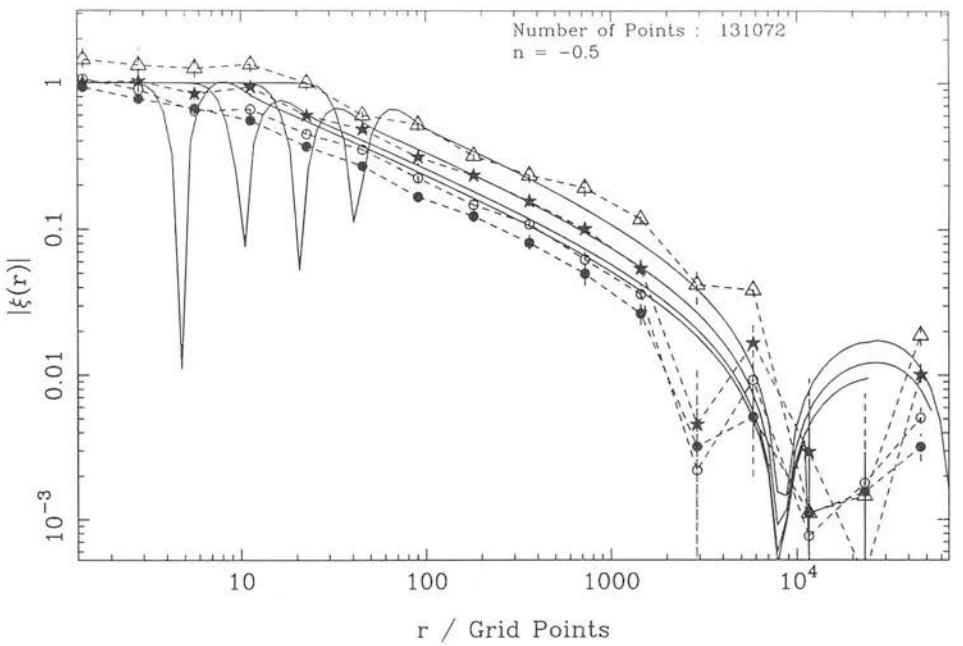

Figure 10. The correlation function ξ_p (broken line) and the peaks theory correlation function (ξ_{pk-pk}) using a Gaussian filter (solid line) for an $n = -\frac{1}{2}$ spectrum. The data points are the average over eight potentials for a 2^{17} point run, the errors being a measure of the deviation from the mean. All curves are for the same scale factor and show the correlation function calculated using all pancakes above $M_*/8$ (●), $M_*/4$ (○), $M_*/2$ (★) and M_* (△).

Note that this movement of peaks is not sufficient to explain the discrepancy between the data and the peaks theory correlation functions in Fig. 11. Whereas the movement of the peaks described in Section 3.4 arises from peculiar velocities in the *linear* density field, the dynamical evolution that causes the clustering for the $n = 1$ power spectrum is non-linear in origin and thus beyond the scope of the peaks theory.

We have also investigated the effect of using different filter functions on the peaks correlation theory. Fig. 13 shows the correlation function calculated using a power-law filter equivalent to that used to produce the mass functions in Fig.

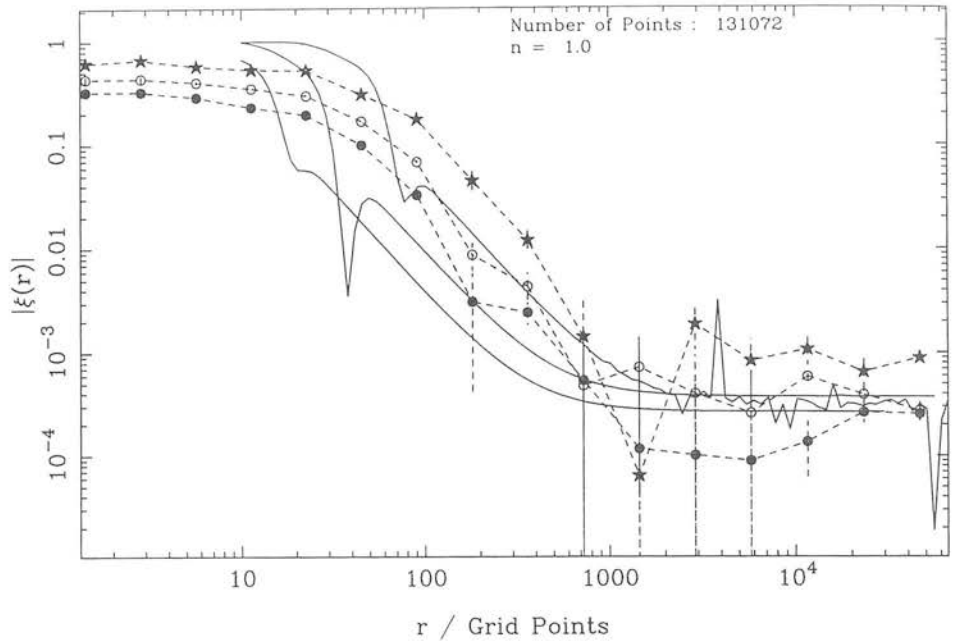

Figure 11. As Fig. 10 but for a spectral index of $n = 1$. The excessive ringing present in the peaks theory curves is caused by the under sampling of the integral in equation (23).

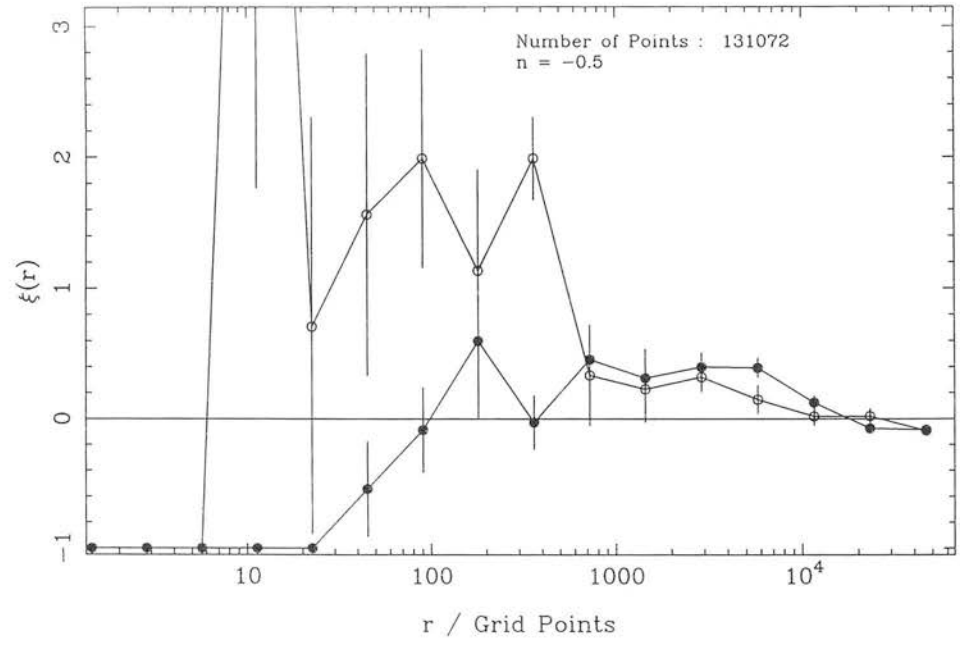

Figure 12. The cross-correlation function (●) and the two-point correlation function (○) for an $n = -\frac{1}{2}$ power spectrum at a late epoch with $M_* = 714.3$.

4(b) (see Section 4.1). This clearly predicts far too much clustering on all scales of interest. As with the mass function, the Gaussian filter appears to be the best choice out of the alternative filters we have investigated.

5 CONCLUSIONS

We have shown the adhesion model to be a useful tool in the analysis of gravitational clustering and have used it to test various direct methods, such as the Press–Schechter mass function and the peaks theory mass function of Peacock & Heavens. The tests we have made are essentially of two types: statistical tests and direct tests of some of the underlying assumptions of linear theory.

Into the first category come the comparisons between the mass and correlation functions which both show remarkably good agreement. Into the second category comes the investigation of whether pancakes form in regions where $\delta \simeq \delta_c$ and

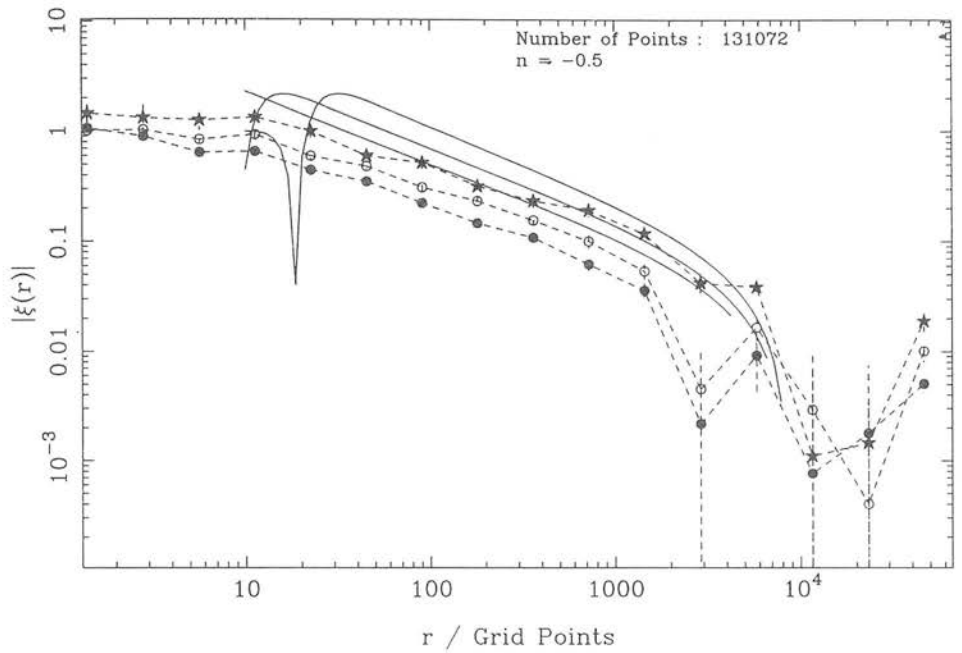

Figure 13. As Fig. 10 but with the peaks theory correlation function calculated using a power-law filter.

whether pancake positions are closely correlated with the positions of peaks in the smoothed density field.

Both mass functions give accurate fits to the data provided that the spectral index lies in the range $-1 < n \leq 3$. Outside this range the mass function breaks down completely. The peaks theory mass functions provide a better fit to the data, especially at late times. A best fit is obtained using a Gaussian filter with $\beta = 1$ and δ_c varied according to the power spectrum, but given approximately by $\delta_c \simeq 1.4^{-(n+1)/2}$. For a given power spectrum the values of β and δ_c give a good fit to the data for all epochs.

The peaks theory also fares better for low masses where there is a non-power-law feature in the power spectrum owing to artificial cut-off imposed by the initial small-scale smoothing. This feature is much more accurately reproduced in the mass function by the peaks theory than Press–Schechter, suggesting that it is a better technique in general.

We have also shown that *in one dimension* the onset of non-linear effects on the linear part of the perturbation spectrum occurs for lower values of the spectral index than previously thought and have confirmed the validity of the mass function derived for steep spectra by Kida (1979).

We support our use of $\delta_c < 1$ by considering the density contrast of the smoothed density field at the location of the pancakes. Our histograms clearly show that the vast majority of pancakes form in regions where $\delta < 1$, although there is too much spread in the data to supprt any single value for δ_c for a given power spectrum.

Looking at the two-point correlation function of the pancake positions we have found considerable differences in behaviour between different power spectra. We note that peaks theory, which predicts the correlation function from the statistical properties of the initial linear density, fits well for a spectral index of $n = -\frac{1}{2}$ but not for a spectral index of $n = 1$. In the latter case there is little positive correlation statistically and most of the correlation presumably arises out of dynamic evolution of the system. One may speculate that where there is a significant amount of statistical clustering, peaks theory provides an excellent approximation. However, where statistical clustering is absent, or anticlustering present, the peaks theory is unable to produce an accurate fit to the data.

We have investigated the use of different filter functions, both for generating mass functions and correlation functions and have found that the Gaussian filter is preferred over the exponential and power-law filters.

Despite the underlying assertion of peaks theory, namely that objects form from peaks in the linear density field with $\delta = \delta_c$, being incorrect in detail, the resulting mass function is an excellent statistical approximation to the mass function obtained from our adhesion model simulations. Also, where the power spectrum contains a significant amount of statistical clustering, the peaks theory correlation function is an excellent approximation to the results of our simulations.

ACKNOWLEDGMENTS

We thank Lev Kofman for many helpful discussions on this subject and especially for introducing us to the work of Kida. SFS acknowledges NASA grant NAGW-1793 and NSF grant AST-8911327 for support of this work. BGW is supported by an SERC studentship.

REFERENCES

Bardeen, J. M., Bond, J. R., Kaiser, N. & Szalay, A. S., 1986. *Astrophys. J.*, **304**, 15.

Burgers, J. M., 1940. *Proc. R. Neth. Acad. Sci.*, **43,** 2.
Burgers, J. M., 1974. *The Nonlinear Diffusion Equation,* Reidel, Dordrecht, Holland.
Cartwright, D. E. & Longuet-Higgins, M. S., 1956. *Proc. R. Soc. A.*, **237,** 212.
Coles, P., 1989. *Mon. Not. R. astr. Soc.*, **239,** 319.
Doroshkevich, A. G. & Kotok, T. V., 1990. *Mon. Not. R. astr. Soc.*, **246,** 10.
Gurbatov, S. N. & Saichev, A. I., 1981. *Soviet Phys. JETP,* **53,** 347.
Gurbatov, S. N. & Saichev, A. I., 1984. *Iv. Radiofizika,* **27** (in Russian).
Gurbatov, S. N., Saichev, A. I. & Shandarin, S. F., 1984. *Inst. Appl. Math., Preprint No. 152,* Moscow (in Russian).
Gurbatov, S. N., Saichev, A. I. & Shandarin, S. F., 1985. *Soviet Phys. Dokl.*, **30,** 921.
Gurbatov, S. N., Saichev, A. I. & Shandarin, S. F., 1989. *Mon. Not. R. astr. Soc.*, **236,** 385.
Kida, S., 1979. *J. Fluid Mech.*, **93,** 337.
Kotok, E. V. & Shandarin, S. F., 1989. *Soviet Astr.*, **32,** 351.
Lumsden, S. L., Heavens, A. F. & Peacock, J. A., 1989. *Mon. Not. R. astr. Soc.*, **238,** 293.
Nusser, A. & Dekel, A., 1990. *Astrophys. J.*, **362,** 14.
Peacock, J. A. & Heavens, A. F., 1985. *Mon. Not. R. astr. Soc.*, **217,** 805.
Peacock, J. A. & Heavens, A. F., 1990. *Mon. Not. R. astr. Soc.*, **243,** 133.
Peebles, P. J. E., 1980. *The Large Scale Structure of the Universe,* pp. 136–137, Princeton University Press.
Press, W. H. & Schechter, P., 1974. *Astrophys. J.*, **187,** 425.
Shandarin, S. F., 1987. *Large Scale Structures of the Universe, IAU Symp. No. 130,* p. 273, eds Audouze, J., Pelletan, M.-C. & Szalay, A., Kluwer, Dordrecht.
Weinberg, D. H. & Gunn, J. E., 1990. *Astrophys. J.*, **352,** L25.
Zel'dovich, Ya. B., 1970. *Astr. Astrophys.*, **5,** 84.